UPCYCLING MINERAL WASTES: THEIR CHARACTERISATION AND ACTIVATION FOR USE IN SUSTAINABLE CEMENTITIOUS BINDERS

By

Surya Maruthupandian

School of Physics, Engineering and Computer Science

submitted to the University of Hertfordshire in partial fulfilment of the requirements of the degree of Doctor of Philosophy

November 2023

(Page intentionally left blank)

Author’s Declaration

I declare that the work in this dissertation was carried out in accordance with the requirements of the University’s Regulations and Code of Practice for Research Degree Programmes and that it has not been submitted for any other academic award. Except where indicated by the specific reference in the text, the work is the candidate’s work. Any views expressed in the dissertation are those of the author.

Signed: Surya Maruthupandian Date: 11 November 2023

ABSTRACT

The widespread use and production of Portland cement, amounting to 4.1 billion tonnes annually, poses challenges in acquiring quality raw materials. The emissions of carbon dioxide, particulate matter, nitrous oxides, and sulphur oxides associated with cement production also contribute to climate crisis and pose major health risks related to respiratory and pulmonary diseases. Despite exploring various options such as alternative cements, fuels, and technologies to reduce the impacts of cement production, the current solutions meet only 10 -15% of the projected demands. The declining production of well-established supplementary cementitious materials, such as fly ash and blast furnace slag, adds to the complexity of the situation as alternative sources of these materials are required.

On the other hand, the demands associated with the global development had led to intensified mining and significant mineral waste production, the quantity of which is about 217 km^3 at present with a predicted annual addition of 12.3 km^3 to this volume. This poses major environmental, economic, social, and legal concerns. Construction and demolition waste (CDW) is another significant source of waste globally and the recycling plants mainly focus on the recycling of coarse aggregates and certain finer fractions. The finer fractions in the size range of silt particles and below are unused and are disposed of in landfill, leading to an increasing proportion of finer fractions generated from CDW recycling in landfill.

The Construction and Building materials research under Horizon 2020 program of Europe 2020 strategy promotes the materials for energy efficiency including materials with low embodied energy and materials capable of reusing a high waste content. Mineral waste, with a composition similar to supplementary cementitious materials, emerges as a potential solution. However, documented challenges, such as crystallinity, variations physical, chemical, and mineralogical characteristics, acid mine drainage, and heavy metal leaching, hinder its immediate use as a cement precursor.

This study focuses on developing a suitable treatment for mineral waste for its use as a binder precursor. A three-phase experimental methodology was designed to meet the objectives also in consideration with the scope and limitations.

In the initial stage, the raw and activated mining tailings and CDW derived silt were characterized. Mineral wastes investigated in this study, namely mine tailings and CDW derived silt exhibited a high silica composition, containing approximately 54-58% SiO_2. The initial screening by XRD analysis guided the selection of calcination and milling regimes. A calcination temperature of 650°C, 750°C and 850 °C for mine tailing and 750°C and 850 °C for CDW derived silt were adopted. Milling balls and a milling container made of tungsten carbide were used for grinding using milling times of 30 minutes, 60 minutes, and 90 minutes.

The median particle sizes (D$_{50)}$ of mine tailings decreased by 55.54% and CDW-derived silt, decreased by 72% after 90 minutes of milling. The results obtained from X-ray diffraction and Rietveld analysis revealed the oxidation of graphite and decomposition of clinochlore, and chlorite in mine tailings, as well as the decomposition of calcite and gypsum in CDW derived silt. Alterations in the quantities of all the mineral phases have been observed in both mine tailing and CDW derived silt with the activation methods adopted. It was found that the mine tailing samples calcined at 850 °C (MTCT850) and CDW silt samples calcined at 750 °C

(STCT750) exhibited higher heat of hydration compared to other samples within a simulated cementitious matrix in adapted R3 tests. These samples also indicated Si and Al solubility higher than the raw mineral waste during dissolution in an 8M NaOH solution.

Based on these observations MTCT850 and STCT750 were determined to be the samples subjected to optimum treatment. Following this, paste mixes were prepared by replacing 10%, 20%, and 40% of cement with activated mineral waste and with water to binder ratio 0.3, 0.4 and 0.5. The findings revealed that the setting time increased and the heat of hydration decreased with increase in percentage of cement replacement.

The examination of mineralogical properties and microstructure of the cementitious pastes over a period of 7 to 90 days at different ages revealed an ongoing process of hydration. The XRD analysis of the pastes showed presence of biotite, quartz, feldspar, oligoclase from the mineral waste. This observation was also confirmed by SEM images which showed the presence of unhydrated MTCT850 and STCT750 particles in the cement paste samples. However, FTIR studies revealed ongoing variations in the chemical makeup and molecular bonding in the hydration products confirming the densification of the matrix and ongoing hydration as observed in the microstructure.

The strength development and durability properties of mortar mixes with various percentages of cement replacement (10%, 20%, and 40%) and a water to binder ratio of 0.4 were evaluated in phase III. The strength tests revealed at the end of 90 days the OPC samples had a strength of 70.68 MPa, and the MT mixes exhibited strength in the range of 51.8 MPa and 63.8 MPa, and the same for ST mixes were 63 MPa to 69.8 MPa. Based on the observed strength development, it can be determined that the mixes with 20% MTCT850 (MT20) and mixes with 20% STCT750 (ST20) can be considered the optimum mixes. The MT20 and ST20 mixes also displayed better performance compared to OPC in terms of carbonation and demonstrated satisfactory performance in terms of sorptivity.

The current study also estimated that the use of mineral wastes can reduce carbon dioxide emissions by 6% to 27% and energy by approximately 3% to 15%, equivalent to a range of 122 to 579 MJ/ tonne of binder.

The aforementioned results collectively and individually suggest that the treatment processes employed, (i.e.) calcination and ball milling, has resulted in effective alterations to the particle size, morphology, and mineralogy of the material. The findings of this research emphasize the potential of mineral waste as a sustainable component in modern and high-performance cementitious binders, contributing to a greener and more environmentally responsible construction industry.

Dedicated to My Brother

Once upon a time
Many moons ago,
I slipped and fell in a pool, and you saved me from drowning.
Ever since,
you have always saved me from drowning and not essentially in water.

‘I am’ because ‘You are’.

ACKNOWLEDGEMENTS

They say it takes a village to raise a child, but when it comes to completing a Ph.D., it takes not only a village but also a village's ration of coffee. I am deeply grateful for the invaluable help and unwavering support I received from numerous kind-hearted individuals throughout this project. While it is impossible to express my gratitude to each and every one of them individually, with a cup of coffee I attempt to make a sincere effort to acknowledge their contributions here.

Firstly, I’d like to thank my Supervisor Dr. Antonios Kanellopoulos. When I first started my Ph.D., I was very nervous before meeting him and when I met him the first thing, I noticed was he was wearing a Batman lanyard. Somehow, suddenly and effortlessly I felt at ease. He took me on a lab tour and at the end of the tour I texted my brother, “I believe I am in good hands”. Throughout the course of my work many things changed, the work plan, objectives, the team and even the world became COVID and post COVID world. But that one thing never changed, I was in good hands. In this time, I have always felt guided, valued, mentored, and supported. Be it a faulty equipment, a badly written draft, visa issues, or any problems I took to Antonios, he always said “leave it with me and carry on with your work”. And I left knowing what Ayn Rand meant when she wrote, “a complex problem could rest safely on three syllables pronounced by a man who knew what he was saying”. It would be an understatement if I simply say this wouldn’t have been possible without his support. I thank him immensely for his guidance and support.

I extend my sincere gratitude to Prof. Andreas Chrysanthou for his guidance and expertise throughout my research journey. His unwavering support has been invaluable, and I am appreciative of the insightful discussions we've had, covering topics ranging from mineralogy and microscopy to carbon footprint and energy considerations. Prof. Chrysanthou's comments and suggestions have played a pivotal role in enhancing the quality of my research and in my growth as a researcher.

They say a journey of thousand miles begin with a single step. When I started this academic journey, Anna held my hand and walked with me during the early stages, introducing me to the intricate workings of the lab and engaging in valuable discussions. I am profoundly thankful for Dr. Anna Chalisaou’s presence on this path.

I express my heartfelt and deepest gratitude to Prof Pandelis Kourtessis and members of Doctoral Training Alliance, a special mention to Jennie, Heather, and Ellie for making this PhD program possible. I would like also to express my gratitude to Dr Theodore Hanein and Dr Aniruddha Baral of the University of Sheffield, for their help with the XRF data.

I'd like to acknowledge and thank our technical manager, Alex Kingstrom. When I started my experimental work, Alex was the Lab manager. They say that it can be challenging to establish a sense of belonging in a new environment, especially when one is working in isolation. However, Alex made me feel like an integral part of the team with effortless ease. I owe Alex a profound debt of gratitude for his commitment to expediting the approval of my risk assessments and ensuring a seamless supply of the materials I needed, both during the lockdown and beyond. Thank you, Alex.

My attempts to express my gratitude to Lewis leaves me at a loss for words. I’d like to thank Lewis Batt, the lab manager, for all his help in the lab, for his exceptional skills in fixing various equipment, for his taste in music, his friendship and most importantly for keeping all the tools I need within easy reach on the lower shelves. He has been thoughtful, kind and incredibly supportive during all the time I have known him. If I had thanked him as many times as I had wanted to, most of our conversations would have sounded like Golden Globe Awards acceptance speech. So, here I express my heartfelt thank you to Lewis for everything.

I thank Dr. Shannon and Dr. Sufyan for all their help in the Duncan Calder lab and for sharing my love for microscopy; Dr. Yuvraj and Dr. Sundar, for their indisputable love for concrete and for the invaluable discussions on its tests and results.

I'd like to express my gratitude to every member of the Technical Support Group of SPECS and LMS who directly or indirectly contributed to this work, a special mention to Giorgos, Vince, Azunka, Lewis Ner, Jack, Eugene, Arthur, Bear, Malcolm, Steve, James, and Christine.

I am sincerely grateful to CBRI as well as my postgraduate thesis supervisors, Prof. Lakshmi, and Prof. V.V.L. Kanta Rao, for leading my path to this research.

In addition to the invaluable assistance and support I received during my time in the laboratory, my personal relationships played a pivotal role in enhancing my work. To echo the heartfelt words of Mary Haskell to Kahlil Gibran, "Your work is You, not less than you, not parts of you. These days when you 'cannot work' are accomplishing it, are of it, like the days when you 'can work'." I am profoundly grateful to these individuals who stood by me during those moments when I "cannot work”. Words feel flimsy when I try to express just how much their love and kindness means to me, I express my deepest gratitude:

To Muhammad and Mahmoud. For being there, being the person they are, and being the calm, I look forward to on my chaotic days.

To Ritesh, Lianne, Vignesh, Angelika, Alexx, Waruna, Adrian, Hamza, Sourabh, Shantanu, and Kirthika; for the amazing conversations and the endless calories we consumed together. To Aaqib for all this, along with his fondness for fixing things which came to my help in the Materials lab.

To Bharathi, for being the only known constant when I stepped into a stream of infinite unknowns and for being an incredible friend. To Vasumathi & family, for being a home away from home. To the lovely ladies of Rore café and Hatfield library for their warmth and welcome, and of course the coffee and books.

To my personal cheerleader and lifeline, Srini. Whoever thinks female friendships are not supportive, has not met my girl. To Lala and Lincy, for challenging the age-old notion "out of sight, out of mind".

To Monica and Balaji, for being my friends; faring many years and across many seas. For taking this journey before I did. Balaji for always reminding me that everything will be 'alright,' and Monica, for reminding me that things have never been 'alright,' yet I managed well nonetheless."

To authors Ayn Rand and Harper Lee, in presence of whose words, I never felt alone. To all my pets. I spent most of my life trying to become half as good as the person they thought I were. They inspired me to be curious, concerned and observant about a world that doesn't use words and has a lot to say. And I believe that's what lead me to research.

Last but not least, To my beautiful and loving family. Because of them I think bright and clearly. Because of them I embrace failure fearlessly. Because of them I love and laugh abundantly. Because of them I Live.

To Life for all the second chances.

TABLE OF CONTENTS

LIST OF FIGURES

LIST OF TABLES

CHAPTER 1
INTRODUCTION

1.1 General / Background

Portland cement used in preparation of concrete is one of the most used and manufactured materials in the planet [1] with about 4.1 billion tonnes being produced annually [2]. The production of cement is associated with significant carbon emissions at a rate of about approximately 866 kg/ t [3], of which 60 – 70% are from the decarbonisation of limestone to calcium oxide during the clinkerisation process and 30 - 40% are from the combustion of fuels and plant operation [1,3]. This makes the cement industry responsible for about 7 – 8% anthropogenic CO_2 emissions [4]. This quantity is expected to increase in the coming years. The latest population projections by the United Nations reports that the global population is expected to grow to around 8.5 billion in 2030, 9.7 billion in 2050 and 10.4 billion in 2100 [5] with about 58 – 60% of this population being expected to live in cities [6]. This will impose a strain on open land, existing infrastructure, and services available. It will also require substantial infrastructure investments [6].

The sustainable development goals (SDGs), Industry, Innovation and Infrastructure aims to build resilient infrastructure, promote inclusive and sustainable industrialization and foster innovation (SDG 9) and Sustainable Cities and Communities aims to make cities and human settlements inclusive, safe, resilient, and sustainable (SDG 11) before 2030 [7]. Meeting the aforementioned requirements and objectives before 2030 not only places a significant burden on the availability of quality construction materials, but also necessitates an enhanced and environmentally conscientious approach to their production and acquisition in order to mitigate emissions and other waste production. In the year 2020, the global demand for limestone reached a total of 5.4 Gt, while the demand for aggregates amounted to 17.5 Gt [8]. It is anticipated that these figures will continue to rise in order to adequately address the growing demands. Therefore, it is imperative to reduce the consumption of and preserve the pristine natural resources. On the other hand, cement production is also associated with emissions of particulate matter of size less than 2.5 µm and 10 µm, nitrous oxides and sulphur oxides. This poses major health risks associated with respiratory and pulmonary diseases [8],making cement production play a major role in not only global economy and environment but also health.

Though various options such as alternative cements [1,4,9], alternative fuels [10–12] and alternative technologies [10,13] are being explored to meet these increasing demands and reduce the impacts of cement in a sustainable manner, this would not be enough to meet more than 10 -15% of the projected demands[8]. The production of well-established supplementary cementitious such as fly ash and granulated blast furnace slag are in decline [14] granulated blast furnace slag is by product from production of steel using blast furnace. Steel industry is responsible for emission of about 3.7 Gt of carbon di oxide and 86% of which is from blast Furnace. The IEA’s Net Zero calls for at least 53% of steel production by electric arc furnace by 2050, which is more energy efficient and has lower emissions [15,16] . With this shift the production of granulated blast furnace slag will also decrease. Though, it might not be a pivotal shift immediately across the globe, these changes might affect the availability of these materials locally.

Similarly, as a part of climate action [17] and all industries are spearhead towards use of renewable energy. As a result of which all the coal fuelled power plants will gradually shift towards a greener fuel making the availability of fly ash scarce. The production of fly ash is already decreasing in the countries like UK and is expected to face a shortage after 2023 [14].

This development in construction sector along with all sectors of our economies require mineral products and the production of these products in turn require raw materials. These raw materials required are obtained by extracting useful materials from the earth's surface by a process called mining. Mining is an energy intensive process and is associated with the production of enormous quantities of waste. Mineral waste can be defined as the *"residues, tailings or other non-valuable material produced after the extraction and processing of material to form mineral products"* [18]. The term mineral waste encompasses the quarry and crushed rocked wastes, mineral wastes, red mud, coal refuse, wash slime and any other unusable waste left after mineral processing. The current estimate of stored/ dumped quantity of mine tailing alone is 217 billion tonnes which is about 217 km^3 and predicted annual growth is 12.3 km^3 [19,20].

The global initiatives on climate action, as well as the European Union's "Clean planet for all" campaign, advocate for the adoption of clean energy technologies. These technologies include photovoltaic conversion, wind and thermal energy harvesting, energy storage, electric mobility, and digital technologies such as robotics, and 3D printing [17,21]. The production of all these items is extremely dependent on minerals, both critical and non-critical, necessitating significant quantities of such materials. For example, the demand for platinum a major component of fuel cells in e-mobility is forecast to increase to 24 t in 2030 and 59 t in 2050 [21]. Such an increase in demand will also pose a need to explore lower quality ores for extraction. The use of low-quality ore also means production of more quantities of waste in the process.

The term "mining waste" arises in a lot of forms including coarse wastes such as stripped soil, weathered rock, and fine-grained wastes such as tailings red mud, coal refuse, wash slime and any other unusable waste left after mineral processing etc [22,23]. These fine wastes are typically of particle size less than 1 mm [22]. Solid form mineral wastes are disposed in landfills. The fine wastes are in general disposed in form of slurry to avoid air pollution due to fine particles during transport and disposal [22]. The slurry is disposed into a cell, confinement, pond, or dam [23], called mine tailing dam. Mineral wastes may be alkaline, contain metals and acidic substances [24]. Thus, making mineral waste management a crucial issue as the physico-chemical characteristics of the wastes have severe impact on the soil and ground water including acid drainage [25].

Besides the physico chemical characteristics of the wastes, the sheer quantity itself poses major environmental issues, especially on occurrence of mine tailing dam failure. According to a mine tailing folklore, "no tailing dam has ever been completely without at least one failure during deposition of particles" [26]. The rate of major failure of a tailing dam is approximately 1 in 700 whereas it is 1 in 10, 000 for water retaining dam [25] Even if all the necessary precautions are taken during the tailings dam construction natural calamities such as earthquake and flood always impose an increased risk of failure. It is interesting to note that the major failures are most likely, about 85% of the time to happen in an active tailing dam than in an abandoned dam [23,25,27] and this failure almost always happen when there is a booming demand for particular material [27]. This can be explained by the lack of time for consolidation of the old material before disposal of the new material on top of it leading to failure. Such failures are catastrophic and is always associated with life loss and environmental loss where the entire downstream region is covered in a slurry of toxic, irritant, or chemically aggressive material, making the land or water unsuitable for intended use. This makes the recycling and reuse of mineral waste a major environmental, economic, social and legal concern.

Construction and demolition waste (CDW) is another significant source of waste generation worldwide, accounting for a substantial percentage of the total waste generated in many countries. In the year 2016, the European Union (EU) alone generated about 374 million tonnes [28]. At the same time the equivalent amount for the UK was 66.2 million tonnes [29]. Considering this EU developed waste framework directive which targeted re-use, recycling and other material recovery of about 70% of the non-hazardous construction and demolition waste. The global CDW management industry grew from an economy of $179.51 billion in 2022 to $188.81 billion in 2023 [30]. A recent report [31] shows that in 2021 of the total 253 Mt of aggregates consumed in the UK, 63 Mt were recycled aggregates. However, these recycling plants mainly focus on the recycling of coarse aggregates and certain finer fractions [32,33]. The finer fractions in the size range of silt particles are unused and are disposed of in a landfill. Therefore, there is an increasing proportion of finer fractions generated from CDW recycling contributing to the increasing volumes of waste in landfill.

Sustainable development is of paramount significance for Horizon 2020 through climate action and resource efficiency and represents at least 60% of the overall budget. As the construction sector keeps utilising large volumes of pristine natural, non-renewable, materials for the manufacture of cement and concrete, the Construction and Building materials research under Horizon 2020 program of Europe 2020 strategy promotes materials for energy efficiency including materials with low embodied energy and materials capable of reusing a high waste content [34].

One such waste that can be used in construction is the mineral waste or mining and quarrying wastes. Every year more than 700 million tons of mineral wastes are being disposed in landfills globally [34] and in UK mineral wastes constitute about 35% of the total waste disposed [35]. The mine tailing derived from mining processes and CDW silt derived from CDW recycling processes constitute a significant quantity of the total mineral waste and are herein after referred to as mineral waste collectively.

1.2 Research Significance

The mineral residues generated from the processes of ore and mineral extraction exhibit a chemical composition that shows resemblance to that of Portland cement. Several investigations have also documented the cementitious characteristics of mineral wastes [36–39]. Nevertheless, there are also documented limitations associated with their use. The mineral wastes exhibit a high degree of crystallinity and can be characterised as non-reactive or inert [40,41]. Mineral wastes refer to the accumulated byproducts resulting from the processing of diverse source mineral ores using different processes and technologies, resulting in variations in their physical, chemical, and mineralogical characteristics [18]. The existing methods of waste disposal, such as the mine tailing dams and landfills, pose serious environmental concerns due to their substantial quantities and physico-chemical properties contributing to acid mine drainage and the leaching of heavy metals. The effective and efficient neutralisation and treatment of mineral waste to immobilise heavy metals prior to reuse is a significant concern due to the presence of hazardous metals and metalloids, including nickel (Ni), zinc (Zn), cobalt (Co), arsenic (As), antimony (Sb), as well as sulphide minerals.

According to recent estimates, the total quantity of stored or disposed mine tailings is around 217 billion tonnes. It is projected that there will be an annual increase in this quantity at rate of 12.3 km^3 [19,20]. It is anticipated that the amounts of mineral wastes would see a rise in the forthcoming years due to global initiatives such as Clean Planet for All and the Sustainable Development Goals. These activities heavily rely on resources and technologies using significant amounts of mineral products. Likewise, with the Waste Framework directive by EU and similar zero waste initiatives [42], it is noteworthy that the worldwide market for the management of CDW experienced an increase from $179.51 billion in 2022 to $188.81 billion in 2023[30]. Hence, the fine fractions derived from the recycling CDW are concurrently experiencing a proportional increase. The increasing quantities of mineral waste and decreasing availability of commonly used supplementary cementitious materials, such as fly ash and ground granulated blast furnace slag, has led to the exploration of mineral waste as a viable alternative for incorporation into cementitious binders.

However, use of mineral wastes in cement production is hindered by the variability in their chemical characteristics and their lack of reactivity. However, it should be noted that the chemical properties of these mineral wastes are generally appropriate for their incorporation into cement. Therefore, the conversion of non-reactive phases into reactive phases and subsequent stabilisation of hazardous leachate poses a significant challenge when considering the use of mineral waste as a precursor for binder materials.

Therefore, this study focuses on developing a suitable treatment for mineral waste for its use as a binder precursor. Previous research (A comprehensive literature analysis is provided in Chapter 2) suggests that mineral wastes have significant potential for utilisation in cementitious binders. Nevertheless, previous studies have also highlighted the absence of systematic activation mechanism or mix design procedure. The past studies also highlight a need for more information on characterisation and performance of the mineral waste to encourage their use with more confidence in cementitious binder.

1.3 Research Scope

After a careful evaluation of the current state of the art, the present study envisages,

To utilize mineral wastes in the development of alternative cementitious binders which will lead to cement-based systems less dependent on pristine natural resources and with lower embodied energy.

This shall be attained by satisfying the following objectives.

Objective 1
Characterization of the mineral wastes and assessment of its suitability for use in cementitious binder.

Objective 2
Determination and optimization of the treatment processes (activation methods) to convert non-reactive, crystalline, and inert phases of the mineral waste to amorphous and reactive phases.

Objective 3
Preparation of binders with the activated mineral wastes and evaluation of their properties.

1.4 Outline of Thesis

The present thesis comprises seven chapters, with the introductory chapter being the first. Chapter 1 provides an overview of the research conducted in this study and explains the motivation behind the chosen research topic. Additionally, the study's scope and objectives are presented.

Chapter 2 provides an overview of mineral wastes. In addition, a detailed literature review was performed to gain insights on the sources of mineral waste, as well as its physical, chemical, and mineralogical characteristics. The review also includes the need for activation and various approaches used for activation of mineral wastes. This study also outlines the different ways of incorporating mineral wastes into cementitious binders and examines their performance within cementitious matrices.

Chapter 3 provides a comprehensive account of the materials and experimental methods employed in the subsequent research work.

Chapter 4 of this research study centres on the assessment of the suitability of materials with regard to the study's objective. It discusses the findings from physical, chemical, and mineralogical characterization of the mineral wastes, both prior to and subsequent to activation. Furthermore, it provides further details regarding the outcomes of the pozzolanic activity test.

Chapter 5 of this study delves into the evaluation of the performance exhibited by the cementitious matrices that were prepared. This chapter includes various characteristics, including the setting time and heat of hydration, of fresh paste samples. The discussion also encompasses the microstructure, mineralogy, strength development, and durability aspects of the hardened samples.

Chapter 6 of the study focuses on the comparative analysis between the prepared binder and traditional Ordinary Portland Cement (OPC) in terms of their environmental impact, specifically carbon di oxide emissions and energy consumption.

The concluding Chapter 7 concludes the thesis by summarizing the key findings from each chapter. It reiterates the importance of the study's contributions, addresses the research objectives, and discusses the implications of the results. The scope for future studies is also provided in this section.

CHAPTER 2
REVIEW OF LITERATURE

2.1 Introduction

This chapter provides a comprehensive analysis of the relevant research on the utilisation of mineral waste in cementitious binders. The present research investigates the utilisation of mine tailings and construction and demolition waste (CDW) derived silt. The literature review primarily concentrates on previous studies that have assessed the potential uses of these materials. This chapter provides an account of the challenges in the construction industry, along with a specific focus on the origins, sources, and problems related to mineral waste. The characteristics, activation processes, and performance of these materials in cementitious matrices are also examined. The chapter concludes by addressing the challenges related to the upcycling of mineral wastes, proposing potential strategies to mitigate these challenges, and highlighting the existing gaps in the current state of the art. These existing gaps stand as a rationale behind the work presented in the thesis.

2.2 General

The use of natural resources has been the basis of growth in civil infrastructure for at least 100 years. At the same time, the exploitation of natural resources and the pollution associated with their extraction and processing have been already stretching the limits of our natural habitat, putting significant pressure on the environment and human well-being. According to the United Nations, the world's urban population has quadrupled since the 1950s, reaching 4.7 billion today, and with an estimated 6.6 billion people living in cities by 2050 [6]. To sustain this rapid urbanisation rate, billions of tonnes of construction materials are required annually.

All evidence and projections suggest that civil infrastructure growth will keep expanding to meet the needs of modern urban societies, including essential development for poverty reduction and provision of fundamental infrastructure to the billions currently living in deprived areas, for the decades to come. A recent report from the Organisation for Economic Co-operation and Development (OECD) projects a rapid growth in the production and use of construction materials in the next 40 years [43]. This translates into a massive demand for pristine natural raw materials. Such demand will have a detrimental effect on the environment, depleting natural resources and causing large scale destruction of landscapes [44].

The manufacture of construction materials is a process that utilises enormous amounts of raw materials and energy, due to the sheer scale of the industrial processes required. Concrete is the dominant construction material and the key element in most infrastructure assets. However, concrete manufacture on a gigatonne scale per annum imposes extremely high energy and resource demands: with >4 billion tonnes of cement being produced annually, accounting for ~8% of global anthropogenic CO_2 emissions and yielding an annual production of ~2 tonnes of concrete for every person on the planet [3]. In Europe, the construction sector alone is responsible for 36% of CO_2 emissions and for the 40% of all energy consumption [45]. Cement manufacture is a major contributor with the whole clinkerisation process consuming ~3.5 GJ/ton [46].

This chapter is based on the following paper: Maruthupandian, Surya, A. Chaliasou, and Antonios Kanellopoulos. "Recycling mine tailings as precursors for cementitious binders–Methods, challenges and future outlook." Construction and Building Materials 312 (2021): 125333.

At the same time, with increase in demand for mineral commodities such as coal, copper, iron, aluminium, gold, tungsten, zinc etc., the quarrying for aggregates and mining of ores has increased while low grade ores have started being explored [22]. The lower the quality of the ore, the higher is the quantity of waste produced such as solids, crushed rocks, overburden soil and tailings.

These wastes are mainly composed of oxides of silicon, aluminium, calcium, magnesium, and iron. This composition is similar to that of widely used building materials such as cement, fine and coarse aggregates, and supplementary cementitious materials. This, in addition to their vast quantities, gives scope for exploring the use of mineral wastes in the construction industry.

2.3 Challenges in Construction Industry

Despite their heavy carbon footprint, shifting away from conventional cements is difficult. Concrete and the related cement-based materials are the construction industry's favourites for a variety of reasons including: (i) ease and low cost of construction compared to alternatives (e.g., steel); (ii) robustness under a variety of exposure scenarios; (iii) ability to construct a large variety of complex geometries; (iv) excellent mechanical performance, and (v) the almost global abundance of raw materials to produce them. Limestone and argillaceous materials (silica, alumina, iron) are extracted from the earth's crust, and through an intensive thermomechanical process converted to clinker, which is ground to be sold as cement. Then potable water and good quality natural aggregates are added to produce concrete. To satisfy this vast demand for concrete production globally, approximately 27 billion tonnes of natural aggregates and nearly 3 billion tonnes of fresh water are required [47]. The environmental impact with respect to depletion of natural resources is enormous. The International Energy Agency in its recently published roadmap for a sustainable transition in the cement and concrete industries has strongly highlighted two important elements: (i) the need to switch to alternative raw materials by 2025 and (ii) to switch to alternative cementitious binders by 2035 [48]. This strategy is also promoted by the European Cement Association in its latest report on decarbonisation of cement [49].

Reducing the environmental impact of cement-based materials is the focus of research the last 15-20 years. At the forefront of these attempts is the use of supplementary cementitious materials (SCMs). These are typically rich in silica and are soluble siliceous, alumino-siliceous, or calcium-alumino-siliceous fine powders that can be used as partial clinker replacement in cements or as partial replacement of Portland cement (PC) in concrete mixtures. SCMs are by-products of industrial operations (e.g., coal fired power plants; steel industry; ferrosilicon industry) and their chemical structure and mineral nature makes them compatible with the cementitious matrix. The three-best known SCMs are fly ash, ground granulated blast furnace slag, and silica fume. These materials do not directly reduce the environmental impact of clinker, but they rather reduce the need for it. In fact, recent studies show strong indications that the use of such minerals to reduce the clinker demand is the most viable option for the industry [50]. However, several problems that are summarised below are associated with the existing SCMs:

(i) Even though SCMs currently account for about 20% of cementitious materials within the UK cement and concrete industries [51], the global reduction in emissions as a result of SCMs use is not more than about 10% [48]. This signals that more amounts are needed and more efficient material use is necessary.

(ii) The existing SCMs rely heavily on specific industrial waste mainstreams which are currently either under major revision or threat. Coal combustion processes which lead to the production of fly ash are expected to considerably reduce to meet the global demand for lower CO_2 emissions, and biomass combustion or co-combustion products are not as suitable for use in most concretes. In the UK it is planned to retire all coal-fired power plants by 2025 and in the Netherlands by 2030 [52]. It is apparent that the global production of fly ash is expected to decline significantly.

(iii) The existing SCMs are not as abundant as natural raw resources. In addition, they are not readily available in large quantities around the world. This results in either excessive use of cement (in absence of SCMs) or the generation of more CO_2 emissions associated with transportation of such compounds in locations where they are not available.

On the other hand, to meet the increased infrastructure requirements of modern urban societies, existing buildings are being upgraded, repaired, retrofitted or demolished producing enormous amounts of wastes. Construction and demolition waste (CDW) refers to the waste generated during the construction, retrofit, and demolition of buildings and infrastructure. It is a significant source of waste generation worldwide, accounting for a substantial percentage of the total waste generated in many countries. Rapid urbanisation and upgrade of national infrastructures are responsible for the vast amounts of CDW. In the year 2016, the European Union (EU) alone generated about 374 million tonnes and according to the European Commission, CDW accounts for approximately one third of total waste generated within EU [28]. At the same time the equivalent amount for the UK was 66.2 million tonnes [29]. It is therefore critical for the sector to look into upcycling possibilities for CDW rather than only recovery. Research in the field so far has predominantly focused on recovery rather than creating value. The main focus has been directed to granular components of CDW and CDW derived fines were either not considered or considered much less.

Sustainable development is of paramount significance for Horizon 2020 through climate action and resource efficiency and represents at least 60% of the overall budget. As the construction sector keeps utilising large volumes of pristine natural, non-renewable, materials for the manufacture of cement and concrete, the Construction and Building materials research under Horizon 2020 program of Europe 2020 strategy promotes materials for energy efficiency including materials with low embodied energy and materials capable of reusing a high waste content [34].

One such waste that can be used in construction is the mineral waste or mining and quarrying wastes. Every year more than 700 million tons of mineral wastes are being disposed in landfills globally [34] and in UK mineral wastes constitute about 35% of the total waste disposed [35].

2.4 Mineral Wastes

Mineral wastes can be defined as the “residues, tailings or other non-valuable material produced after the extraction and processing of material to form mineral products” [18]. The term mineral wastes encompass the quarry and crushed rock wastes, mineral wastes, red mud, coal refuse, wash slime and any other unusable waste left after mineral processing.

These mineral products are used as raw materials which form the basis of our technological development in all sectors of our economies. From building and construction operations to the manufacture of bespoke electronic components, raw materials and minerals are important. World mining data shows significant increase in the extraction of mining products the last 35 years (Fig. 2.1).

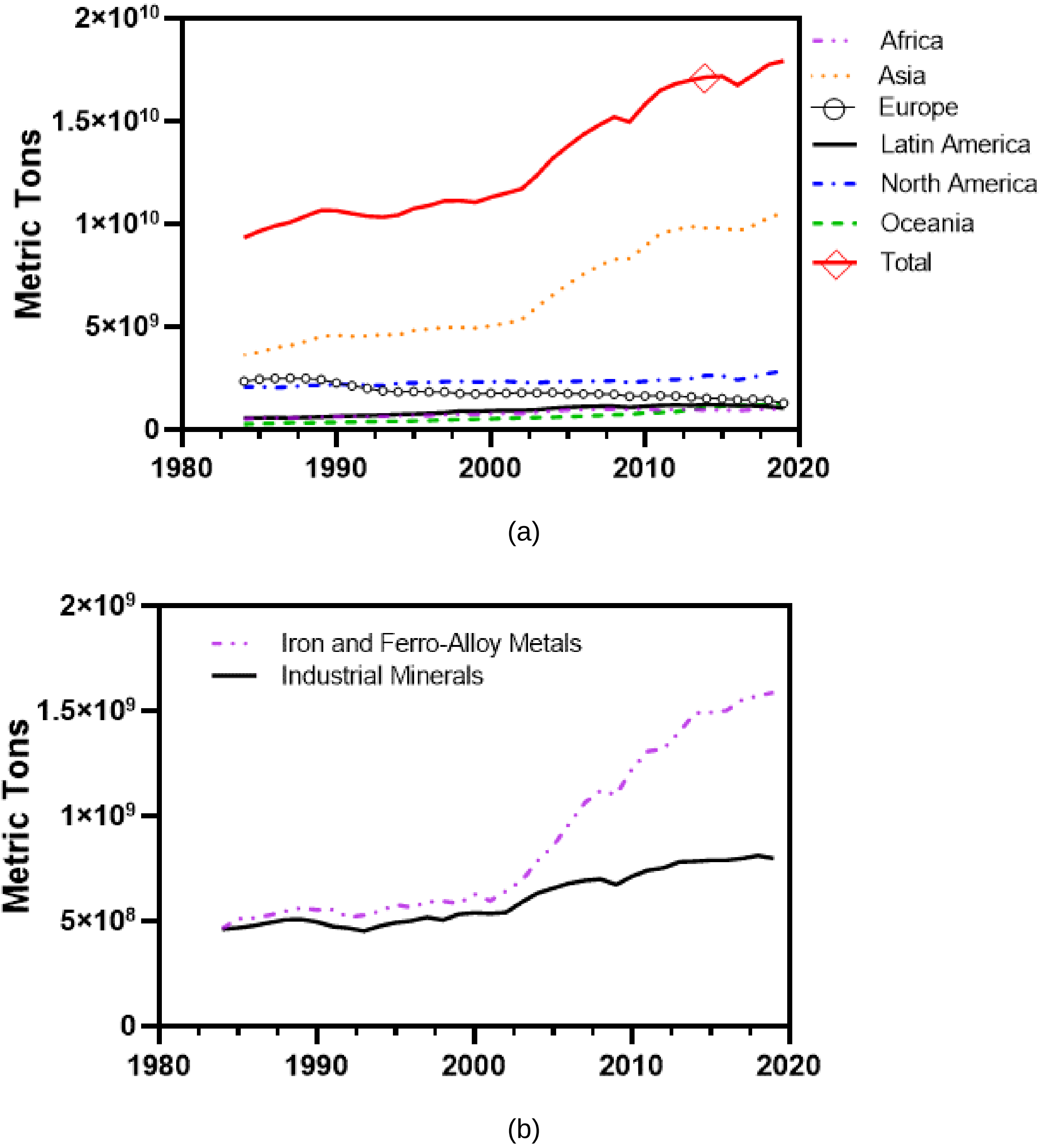

Fig. 2.1: Production of mining products between 1985 and 2020: (a) all mining products per geographical region and (b) global production of two major mining commodities (Data obtained from World Mining Data [53]).

Since 2000, there is a steady increase of mining production except for Europe. For Asia and Australia, this increase has been considerable (Fig. 2.2).

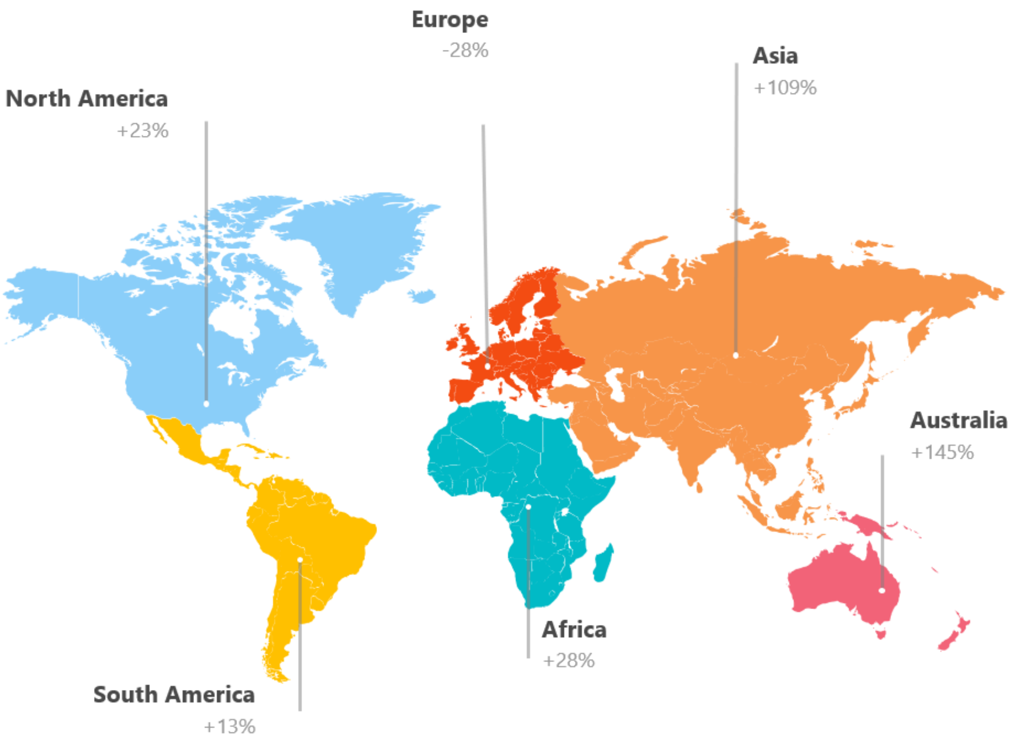

Fig. 2.2: Production growth of mining products per geographic region between 2000 and 2020 (Data obtained from World Mining Data [53]).

At the same time, the sustainability goals (SDGs), which in many countries are now part of the legislation, have created the perfect growth conditions for low-carbon technologies. From wind turbines to solar panels and electric cars, these developments require vast volumes of minerals for production and manufacturing. Therefore, the road to a low-carbon sustainable future will be a very mineral intensive road. Industrial level mining directly and positively impacts: the development of good jobs and economic growth (SDG8); provides raw materials that support the development of renewable energy technologies (SDG7) which in turn facilitates innovation and infrastructure (SDG9).

At the same time, it can negatively impact terrestrial ecosystems (SDG15) as well as sustainable clean water consumption and availability (SDG6). The effects of mining are also found to impact attaining the goals related to life below water (SDG14), actions related to climate change (SDG13), ensuring healthy lives for all communities (SDG 3) and responsible consumption and production patterns (SDG12) [54]. These negative impacts mainly stem from the quantity and nature of wastes associated with the mining activities. Taking these into consideration, the Responsible Mining Foundation proposed a framework for responsible mining [55]. This report declares mineral waste management as a major environmental responsibility. The efficient tailing management shall improve good health (SDG3), sustainable cities and communities (SDG11), responsible consumption (SDG12), climate action (SDG13), life below water (SDG14). When the quantity of tailings disposed in land and into water bodies and confined dams are reduced contamination of land and water is avoided and hence improves life on land (SDG15) and clean water and sanitation (SDG6).

Mineral wastes can be generally disposed by either direct or indirect methods. The former involves disposal of mineral wastes in rivers/sea, while the latter encompasses disposal of mineral wastes in the form of slurry (25-30% solid) into a cell, confinement, pond or dam [23]. Solid form mineral wastes may also be disposed in landfills. Mineral wastes may be alkaline, contain metals and acidic substances [24]. Thus, making mineral waste management a crucial issue as the physico-chemical characteristics of the wastes have severe impact on the soil and ground water including acid drainage [25]. The disposal of such waste is a major environmental challenge and liability especially in the light of some recent catastrophic disasters involving the collapse of mineral waste dams leading to considerable loss of life [56]. In addition to such catastrophic events, stockpiling such vast amounts of wastes can significantly alter and affect the natural habitat and the biodiversity of the surrounding local communities [57]. The failure of mine waste dams has also led to about 237 catastrophic accidents worldwide since 1917 [23]. Such failures have resulted in life loss, job loss and irreversible damages to the surrounding agricultural land and water bodies. If a mineral waste has high amounts of sulphide minerals and low amounts of minerals such as carbonates which will neutralize them, their oxidation in natural conditions may also lead to acid mine drainage [58]. If the mine drainage is neutralized, neutral effluents generated may consist of toxic metals and metalloids, such as Ni, Zn, Co, As, and Sb. This makes the recycling and reuse of mineral waste a major environmental concern.

2.5 Sources

Mining is the term used to describe the process of excavation of earth’s crust to extract minerals and ores. Valuable components or metals are extracted from the minerals and ores by different mineral separation processes. At the end of the mineral separation process, a valuable component, which is a concentrate of base metal or mineral, is extracted. As part of this process, the mineral separation process residues (tailings) are generated [26]. Tailings do not bear any significant monetary value and occur in form of sludge with a varying water content ranging from 18 to 32% [36,59–61]. The quantity of tailings generated varies, depending on several factors: (i) the type of material extracted; (ii) the process followed and (iii) the quality of ore. Ince et al [62] reported that for low quality ores in copper extraction about 128 tons of tailings are generated for the production of 1 ton of copper. In the contrary, high-quality ores can generate 1.5 tons of tailings for every ton of copper produced [63]. Nonetheless, even the optimum 1 to 1.5 ratio will lead to the production of immense volumes of waste material that currently remains unused affecting the environment and local communities. On the other hand, the presence of oxides of silicon, aluminium, calcium, magnesium, and iron make the composition of these materials more similar to that of cement and other supplementary cementitious materials such as fly ash, silica fume etc.

Likewise, rapid urbanisation and upgrade of national infrastructures are responsible for the increasing amounts of CDW. In the recent past CDW recovery rates have increased also. According to Eurostat data, the average recovery rate of CDW reaches upto 90%, however it varies from country to country from as low as 10% up to more than 90%. Albeit recovery levels are high, recycling and upcycling of CDW in the manufacture of dominant construction materials, such as concrete, is very low. This discrepancy roots itself on the fact that recovery takes place in low-end, low-quality applications such as backfilling, or low-strength non-structural concrete. Past studies [5]–[7] explored the possibility of reuse of CDW in construction as coarse aggregate and fine aggregates in the manufacture of concrete. [64–66]. While this approach faces a significant number of technological challenges, at the same time the processing of such wastes to produce aggregates is always associated with production of silt, powder and other forms of waste which cannot be used in construction directly [32,33]. Processing of fine fractions from CDW is an area of research and development with growing interest, primarily due to the mineralogy of such waste fines that make them good potential candidates to be utilised within binder systems (cement-based or alkali-activated).

The utilization of mineral waste in cementitious binders necessitates a deeper understanding of its physical, mineralogical, and chemical composition in order to enhance confidence in its application. Understanding the impact of the mineralogical composition on the behaviour of the binders is of significant importance as well. Past studies have investigated the properties of mineral waste and its application in cementitious matrices and cement-like matrices. This encompasses research efforts that have employed mineral waste as supplementary cementitious materials (SCMs), as a raw material for clinker production, as a direct substitute for cement (with or without activation), and as alkali-activated binders.

2.6 Physical, Chemical, Mineralogical properties

2.6.1 Physical properties

Mineral wastes are crystalline, relatively loose and porous in microstructure [67]. The specific gravity of such compounds ranges between 2.70 – 4.29, depending on the source and its composition [68–70]. Mineral wastes are reported to have a high-water absorption, up to 7.15% [71]. This can raise concerns if the mineral wastes are intended for use in concrete as aggregates. However, such porous materials can have alternative uses. Recent studies have shown that a percentage of highly porous aggregates can facilitate internal curing processes [72,73]. In addition, it has been demonstrated that porous aggregates can be used as carriers for healants in promoting self-healing processes in cementitious matrices [74,75].

The pH of mineral wastes is generally in near neutral or slightly alkaline region ranging between 8.0 – 9.3 for carbonate rich wastes [76] and 6.7 – 10.0 for silicon rich wastes [77–80]. Though the pH of mineral wastes is generally alkaline, the chemical and mineral composition determines the possibility of acid mine drainage especially in case of mine tailings. If a mineral waste has high amounts of sulphide minerals and low amounts of minerals such as carbonates, which will neutralize them, their oxidation in natural conditions may also lead to acid mine drainage [58]. If the mine drainage is neutralized, neutral effluents generated may consist of toxic metals and metalloids, such as Ni, Zn, Co, As, and Sb [81]. This makes the effective and efficient recycling and reuse of such wastes a major environmental concern.

The particle size of mineral wastes varies amongst cement sized, silt sized and sand sized particles. Argane et al., [82] reported a silt sized tailing of D_{50} 210 -270 µm whereas cement sized mineral waste of 17 µm [26] and cement sized silt of D_{50}14.15 – 27 µm [83] were also reported. The particle size distribution of mineral waste observed in various studies are as given in Fig. 2.3.

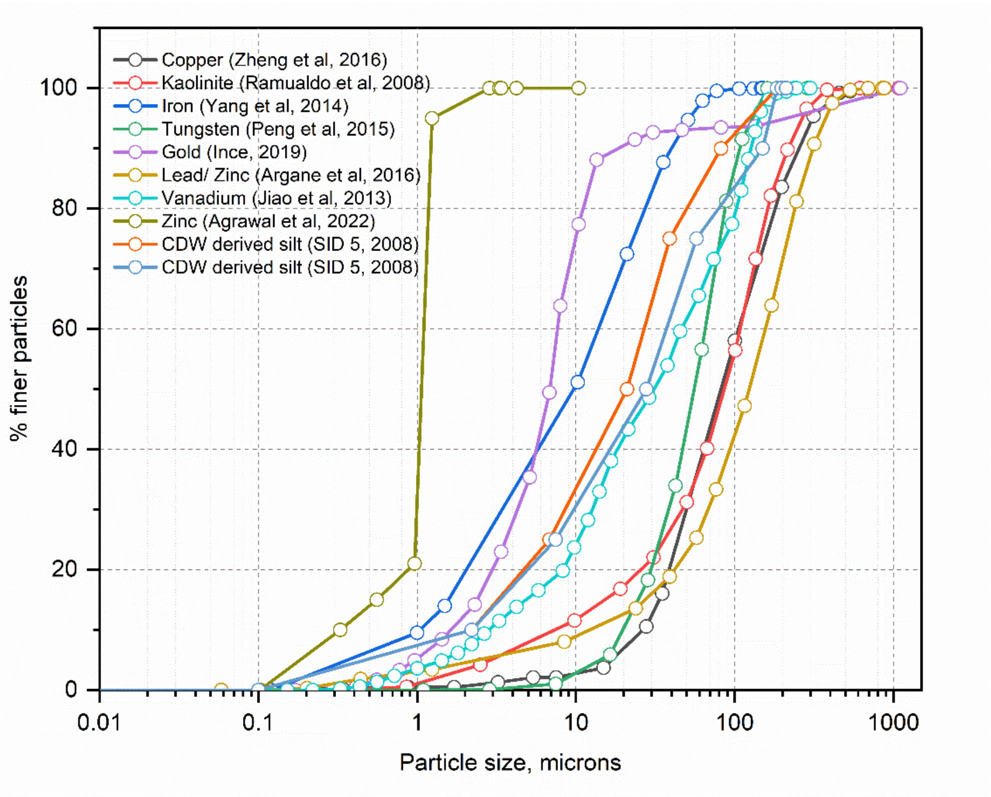

Fig. 2.3: Particle size distribution of various mineral wastes.

The variation in the size enabled various attempts on recycling the mineral wastes as fine aggregates [84,85] and as a binder component [83,86–89]. However, the feasibility of using mineral wastes as aggregate or cement mainly depends on its chemical composition, rate of dissolution and its ability to produce hydration products like that of cement.

2.6.2 Chemical and mineralogical properties

The composition of mineral wastes varies highly due to the variation in source mineral, process of extraction, mineral extracted and quality of the ore. Table 2.1 shows the chemical composition of various mineral wastes discussed across several studies. It can be seen from the table that bauxite, coal, graphite, gold, iron, kaolinite, CDW derived silt and lead-zinc mineral waste are predominantly composed of silicate. Phosphate, tungsten, and zinc mineral waste have a considerable amount of CaO, whilst bauxite, coal and kaolin mineral waste have a considerable amount of Al_2O_3. The Si/Al ratio and basicity modulus (calculated as shown in Table 2.1) serve as indicators of a material's potential for alkali activation [90]. The modulus of hydraulicity (calculated as shown in Table 2.1) assesses the ability of the material to form reaction products and harden upon reaction with water. The higher the value, the greater the material's ability to react, harden and strengthen when in contact with water. [91,92]. The ratio of silica to alumina (SiO_2/Al_2O_3) of mineral wastes ranges from 0.86 – 9.12, modulus of hydraulicity [92] ranges between 0.02 – 3.98 and the modulus of basicity are between 0.03 – 5.28. Shi et al [90] recommended a Si/Al value of 1.5 – 2.5 and basicity modulus range between 0.7 to 1.2 for a material to be suitable for alkali activation. However, these conventional indicators of hydraulicity or geopolymerisation may not be suitable to determine the reactivity of the mineral wastes, as the mineral wastes are crystalline in nature [84] and aluminates and silicates present are not always available in a form suitable for dissolution that will yield them suitable for participation in chemical reactions. Therefore, the mineralogical composition of the material plays a significant role in determining its reactivity and selection of appropriate and effective treatments can only be done when the fraction of reactive components in a tailing are identified [93].

Table 2.1: Chemical composition of a variety of mineral wastes reported in the literature.

Mine type	**Bauxite** [94]	**Boron** [95]	**Coal** [96]	**Copper** [97]	**Gold** [88]	**Iron** [98]	**Kaolin** [99]	**Graphite** [100]	**Phosphate** [101]	**Quartz** [102]	**Tungsten** [103]	**Vanadium** [104]	**Zinc** [105]	**Copper & Zinc** [106]	**Lead & Zinc** [40]		**CDW derived silt** [89]
Chemical Composition															**Silicate**	**Carbonates**	
CaO (%)	3.15	14.36	1.06 - 8.41	8.14	14.89	6.20	0.2	15.547	34.2	0.51	28.02	6.51	33.66	0.84	1.99	19.83	3-19
SiO_2 (%)	32.24	19.57	52.34 - 61.92	44.54	44.62	24.40	59.5	62.50	22.8	79.53	36.52	61.92	6.20	25.16	68.44	7.16	54-98
Al_2O_3 (%)	37.39	6.17	19.50 - 36.34	16.18	8.64	10.95	32.9	10.21	2.5	9.52	8.70	7.35	2.06	6.41	9.38	3.09	7.9-12.4
Fe_2O_3/ TFe (%)	8.67	2.85	6.42 - 8.35	-	26.1	31.15	2.7	5.07	0.9	3.22	11.71	4.12	0.19	19.24	2.22	2.11	4.6-5.8
SO_3/ S (%)	-	0.34	0.11 - 0.65	5.14	2.31	-	0.1	-		-	0.16	7.14	1.46	26.18	1.12	7.51	0.1-0.8
MgO (%)	0.85	4.26	1.0 - 1.57	-	0.51	0.99	-	2.33	4.1	0.64	1.12	1.24	9.94	1.69	0.48	11.27	0.3-0.7
K_2O (%)	-	2.31	2.65 - 4.02	-	0.55	0.86	0.1	2.26	0.4	3.24	0.05	1.25	0.24	0.41	5.46	0.48	2.0-3.2
TiO_2 (%)	2.31	-	0.85 - 1.21	-	0.41	0.42	2.0	-	-	0.52	0.12	0.46	0.09	0.09	-	-	0.6-0.8
Na_2O (%)	0.85	0.18	0.17 - 0.53	-	1.63	0.28	-	-	0.8	0.72	-	2.66	0.30	0.23	0.7	0.1	0.8-1.2
MnO (%)	-	-	0.06 - 0.14	-	0.09	-	-	-	-	0.16	2.56	-		0.07			0.1
Cl (%)	-	-		-	0.02		-	-	-	-	-	-		0.04			
ZnO/ Zn (%)	-	-	27 - 46 ppm	0.65	0.11	-	-	-	-	78.82 mg/kg	0.02	-	1.77	0.31	230 ppm	260 ppm	
PbO/ Pb (%)	-	-	-	-	-	-	-	-	-	195.90 mg/kg	-	-	0.15	0.14	4710 ppm	5940 ppm	
Cu (%)	-	-	-	-	-	-	-	-	-	75.24 mg/kg	-	-		0.19			
Cr_2O_3/ Cr (%)	-	-	-	-	-	-	-	-	-	-	0.03	-		0.02			
WO_3 (%)	-	-	-	-	-	-	-	-	-	-	0.03	-		-			
V_2O5/ V (%)	-	-	-	-	-	-	-	0.308	-	-	0.02	0.42		50.30 ppm			

SrO/ Sr (%)	-	0.51	-	-	-	-	-	-	-	-	-	-		21.40 ppm	1.12	7.51	
BaO/ Ba (%)	-	-	-	-	-	-	-	-	-	-	-	-	0.31	0.008			
P_2O_5 (%)	-	-	-	-	-	-	0.4	-	-	-	-	-	0.27	0.04			
ZrO_2/ Zr (%)	-	-	-	-	-	-	0.1	-	-	-	-	-		0.003			
LOI (%)	13.74	21.06	1.81 - 5.61	18.92	-	6.95	2.0	0.65	19	2.46	2.30	6.93	43.35	18.68			0.3-1.0
SiO_2/Al_2O_3	*0.86*	*3.17*	*1.70-2.68*	*2.75*	*5.16*	*2.23*	*1.81*	*6.12*	*9.12*	*8.35*	*4.20*	*8.42*	*3.01*	*3.93*	*7.30*	*2.32*	*4.35-11.11*
Basicity Modulus $(\frac{CaO+MgO}{SiO_2+Al_2O_3})$	*0.06*	*0.72*	*0.03-0.10*	*0.13*	*0.29*	*0.20*	-	*0.25*	*1.51*	*0.01*	*0.64*	*0.11*	*5.28*	*0.08*	*0.03*	*3.03*	*0.03-0.31*
Hydraulicity Modulus $(\frac{CaO}{Fe_2O_3+SiO_2+Al_2O_3})$	*0.04*	*0.50*	*0.01-0.08*	*0.13*	*0.19*	*0.09*	*0.002*	*0.20*	*1.31*	*0.01*	*0.09*	*3.98*	*0.02*	*0.02*	*1.60*	*0.04*	*0.03-0.28*

*The chemical compositions reported in the table are indicative for a particular type of tailing observed in a study and does not represent a mean or median.

** All values given in the table are in percentage unless otherwise specified.

Table 2.2 provides an outlook of various minerals present in different mineral wastes. Quartz, Kaolinite, Calcite, and Muscovite are some of the minerals most widely found in the mineral waste. Similarly, many phyllosicate, alumino silicate, calcium alumino silicate and carbonate minerals were also present. It can be seen that SiO_2 is found in non-reactive quartz form [107,108] or reactive cristobalite form [109,110]. Similarly, TiO_2 occurs as low reactive Rutile [111,112] and in the form of anatase which is more reactive [113]. Minerals may also occur as a member of a series such as feldspar, biotite, phyllosilicates, iron oxides, alumina silicates, with different crystallinity and reactivity [114,115]. Hence, conversion of non-reactive phases to reactive phases and making them more amorphous is important for exploring the potential of mineral wastes as binders.

Table 2.2: Mineral composition of a variety of mineral wastes (Note: The percentage composition of minerals is reported only in a few studies).

	Mineral waste	Mineral	% Composition		Mineral waste	Mineral	% Composition
1	Bauxite [94]	Kaolinite				Hematite	1.07
		Diaspore				Other	4.03
		Anatase		8	Low sulphide Lead - Zinc Carbonate dominant (80%) [58]	Dolomite	
		Corundum				Calcite	
		Quartz				Ankerite	
		Mullite				Barite	
2	Boron [107]	Hydroboracite				Kaolinite	
		Montmorillonite				Smithstone	
		Colemanite		9	Kaolin [73]	Kaolinite	
		Illite				Mica	
		Quartz				Quartz	
		Calcite		10	Phosphate [109,116,117]	Quartz	0.9 – 12.44
3	Coal [118,119]	Quartz	29 – 37			Apatite	9.6
		Mica	25			Fluorapatite	34.09 - 44
		Calcite	15 – 17			Calcite	11.15
		Kaolinite	14 – 15			Dolomite	9.45 – 89.5
		Dolomite	5			Illite	9.46
		Feldspar	2			Palyrgorskite	21
		Amorphous	17			Hematite	1.4
4	Copper [97,120,121]	Albite		11	Tungsten [87,122]	Garnet	88.14
		Gypsum				Amphibole	5.46
		Sanidine				Chlorite	4.27
		Quartz				Quartz	2.13
		Augite				Muscovite	
		Dolomite		12	Vanadium [123]	Quartz	
		Phlogopite				Feldspar	
		Amphibole				Diopside	
		Clinochrysotile		13	Low sulphide Lead - Zinc Silicate dominant (90% silicate) [84]	Quartz	
		Calcite				Orthoclase	
		Talc				Chlorite	
		Clinochlore				Albite	
		Siderite				Barite	
		Hematite				Fluorite	
		Pyrite		14	Desulphurized pyrrhotite tailings [112,124]	Magnetite	2.56
		Mullite				Orthoclase	1.37
		Muscovite				Pentlandite	0.29
5	Gold [71,86,125,126]	Albite				Pyrrhotite	0.64
		Gypsum				Quartz	1.60
		Quartz				Rutile	0.30
		Dolomite				Actinolite	29.75
		Muscovite				Albite	2.76
		Microcline				Arsenopyrite	0.01
		Pyrite				Calcite	2.17
		Sodium Alumn. silicate				Chalco Pyrite	0.25
		calcite					
		Sanidine				Clinochlore	26.48
		Mica				Lizardite	31.81
		Montmorillonite		15		Pyrite FeS_2	

6	Graphite [111]	Quartz	43.15		High sulphide tailings Copper and Zinc [106,127]	Anhydrite $CaSO_4$	
		K-Feldspar	12.42			Caldecahydrite $CaAl_2O_4$ $10.H_2O$	
		Albite	5.08			Quartz SiO_2	
		Anorthite	3.31			Smithstone	
		Biotite	8.34			Diopside	
		Muscovite	4.82			Calcite	
		Epidote	2.05			Albite	
		Chlorite	3.13			Sodium copper sulfide	
		Rutile	0.72				
7	CDW derived silt [89]	Illite		16	Iron tailing [63,128]	Hematite	
		Quartz				Quartz	
		Montmorillonite/ kaolinite				Kaolinite	
		Calcite				Goethite	
		Albite				Biotite	
		Dolomite				Clinochlore	
		Pyrite				Talc	

2.7 Activation Procedures

The structural stability of any material is associated with its chemical reactivity. Materials with more defects in their microstructure, more distortion in their lattices, or materials existing in an amorphous state are considered to have less stability and tend to have a high reaction activity [129]. Since mineral wastes, are highly crystalline their processing is essential to render them more reactive for use in cementitious systems as part of the binder phase. This processing is commonly known as “activation”. Activation processes can be either mechanical, chemical, thermal or a combination of them (see Fig. 2.4). For use in cementitious matrices, the mineral waste can be alumino-silicate, calcium-alumino-silicate or predominantly silicate. The energy required in the processing of mineral waste should be of sufficient magnitude to rearrange the crystalline lattice or impart damage to it. For example, in case of an alumino-silicate mineral if the binding energies of the Al-O-Si, Si-O-Si or other structural forms present in the raw material are strong, energy higher than binding energy may be required to disrupt the bonds in crystalline lattice and make ions available for further reaction [130]. The thermal activation is achieved by calcination of the material in a high temperature furnace. The mechanical activation/ mechanochemical activation can be performed by means of ball mill, ring mill, planetary ball mill, vibratory ball mill, stirred ball mill or jet mill [131–133]. The chemical activation is achieved by use of an activator to induce chemical reactions for release of Si, Al and other ions and enabling further reactions. When alkalis are used for this purpose, the process is known as alkali activation [134]. The following sections discuss the various activation processes found in the literature. Table A1 in the Appendix provides detailed information about the application of activation processes for individual minerals as reported in published research.

(a) Mechanical Activation

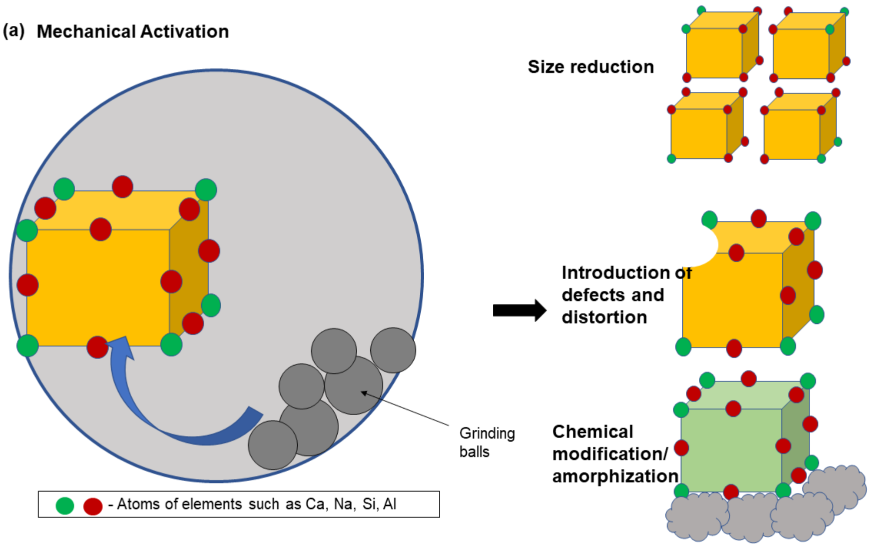

(b) Chemical Activation

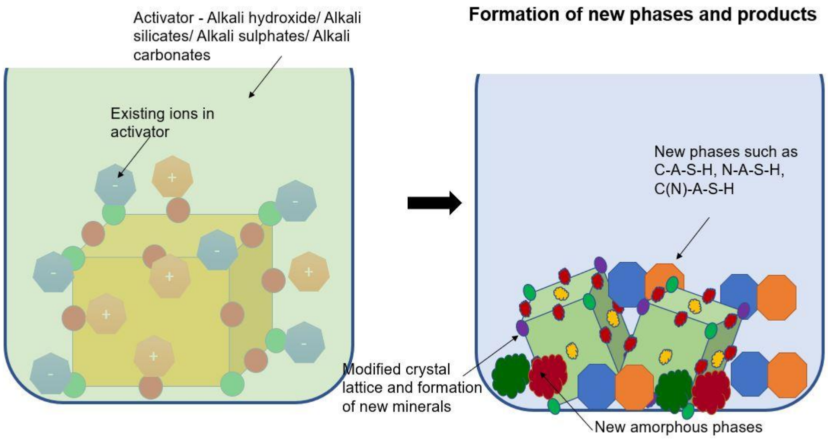

(c) Thermal Activation

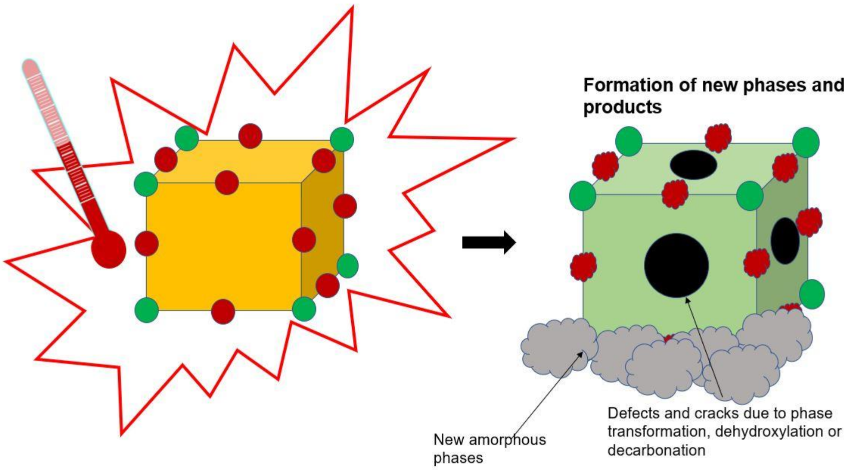

Fig. 2.4: Schematic representation of the mineral activation processes: (a) Mechanical; (b) Chemical and (c) Thermal activation.

a) Mechanical and Mechano-chemical Activation

Mechanical activation utilises mechanical actions to induce changes on the microstructure of minerals. Mechanical processing essentially decreases the particle size and increases the surface area of the materials. This in turn improves the reactivity [86]. The most commonly used mechanical activation is grinding which involves a combination of pressure and shearing actions on the material. Research indicates that grinding improves reactivity of mineral waste by dynamic creation of new surfaces, by creating defects in crystal lattice and phase transformations. [129,135–137]. It was also reported that during grinding due to friction and impact of the grinding media on the material a localised increase in temperature may be observed in a small area leading to mechanically activated chemical reactions [137]. The electron energy at such localised contact points is about 10 eV which is higher than energy of thermal treatment at 1000°C (4 eV) [138]. These reactions are mechanically induced chemical reactions in solids and the process is therefore known as mechano-chemical activation [133] . The variation in specific surface area of different mineral waste with respect to grinding time is given in Fig. 2.5. A phenomenon called selective grinding occurs when minerals of high and low hardness are present in the same material and the minerals with higher hardness act as a grinding media for minerals of lower hardness and accelerate the grinding process [87,137]. Minerals of high hardness such as garnet and quartz have a particle size larger than other minerals after grinding of the mine waste. A bimodal particle size distribution curve after grinding represents the presence of minerals with different relative grindability present in the same material [103]. This variation in size reduction of different minerals when subjected to the same grinding energy is referred to as grinding performance or grindability. Enhancing the grinding performance is crucial for achieving optimal economic and environmental efficiency. [139].

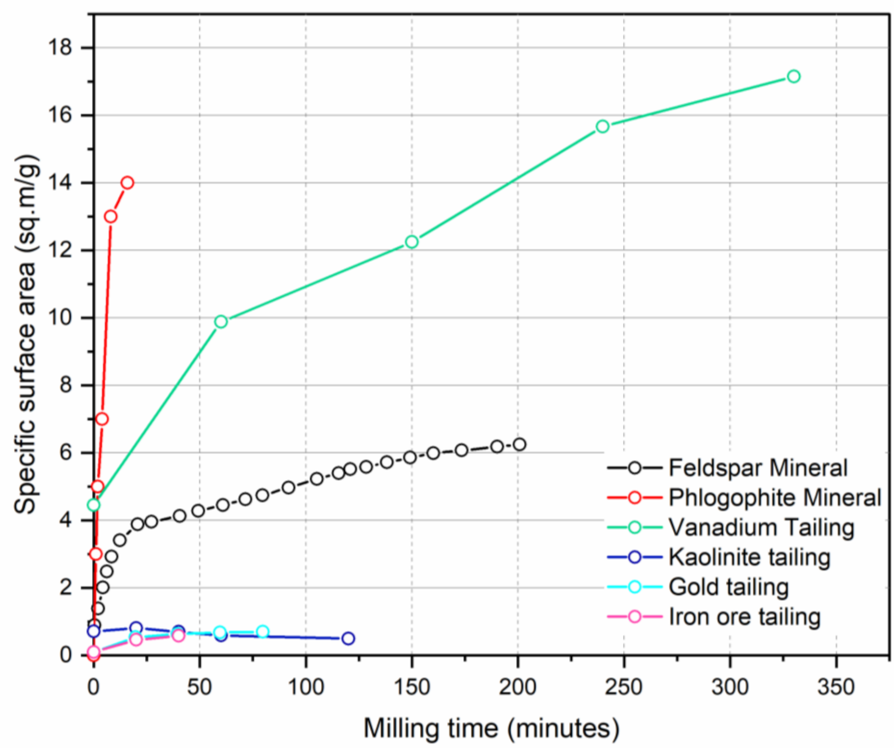

Fig. 2.5: The specific surface area of mineral waste with respect to grinding time [86,104,140–143].

In certain cases, grinding also breaks the Al-O-Si, Si-O-Si bonds further improving the reactivity of minerals. A recent study has shown that the content of reactive Si and Al increased from 300 to 1500 mg/ L and from 100 to 315 mg/ L respectively after 5.5 hours of grinding [135]. Similarly, Yu et al. [144] reported an increase in reactive Si and Al content by 26.03% and 96.33% respectively, after 4 hours of grinding. Grinding beyond 3 h leads to increased surface energy which in turn results in agglomeration of particles. Therefore, an increase in the particle size is observed after 3 h of grinding in case of copper tailings and 4 hours grinding in case of iron tailings [144,145]. This phenomenon was explained by Tole et al [137] as given in Fig 2.6.

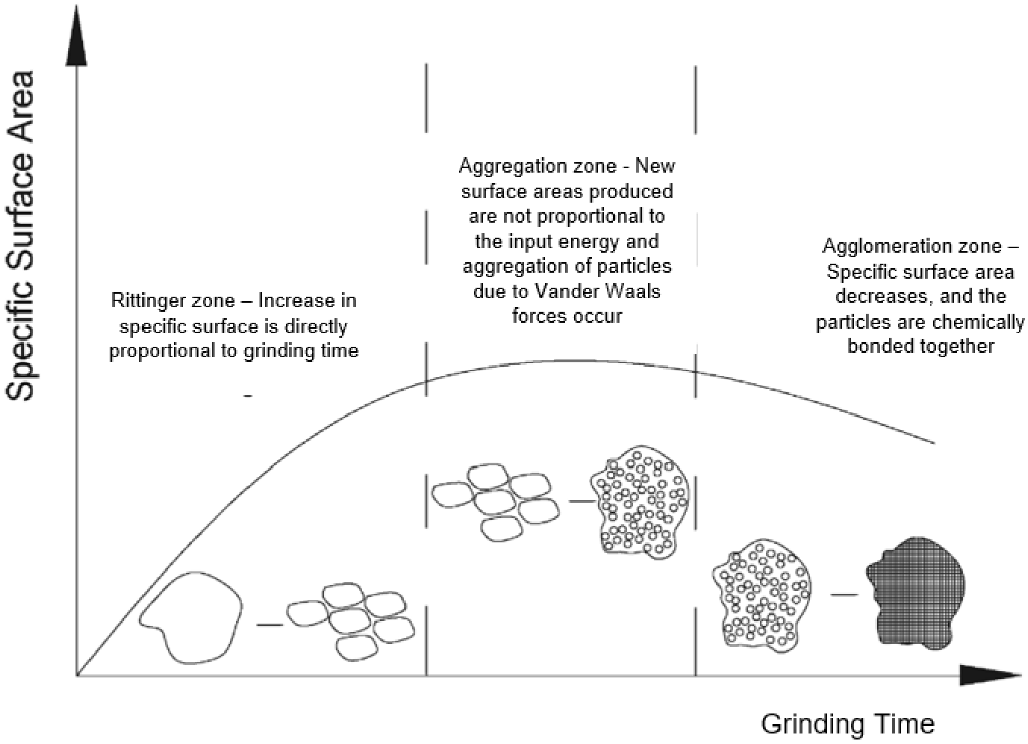

Fig. 2.6: Reaction evolution of particles during mechano-chemical activation. Image reproduced from [137].

The XRD analysis showed that intensity of quartz, endenite, albite, hematite and feldspar peaks were significantly decreased after 4-5 hours of grinding [144,145]. After melting, quenching and grinding the reactivity of phlogopite increased from 1% to 40% [93]. Yao et al [136] reported that the relative crystallinity of muscovite reduced to 37% whereas the crystallinity of quartz reduced only to 80% after 80 minutes of grinding. Clinochlore exhibited a complete collapse of mineral structure after 16 minutes of milling [146]. The increase in amorphous content of different mineral wastes and minerals with grinding is given in Fig. 2.7 while in the literature researchers have also used TEM (see Fig. 2.8) to confirm the formation of amorphous phases pre- and post- mechanical treatment.

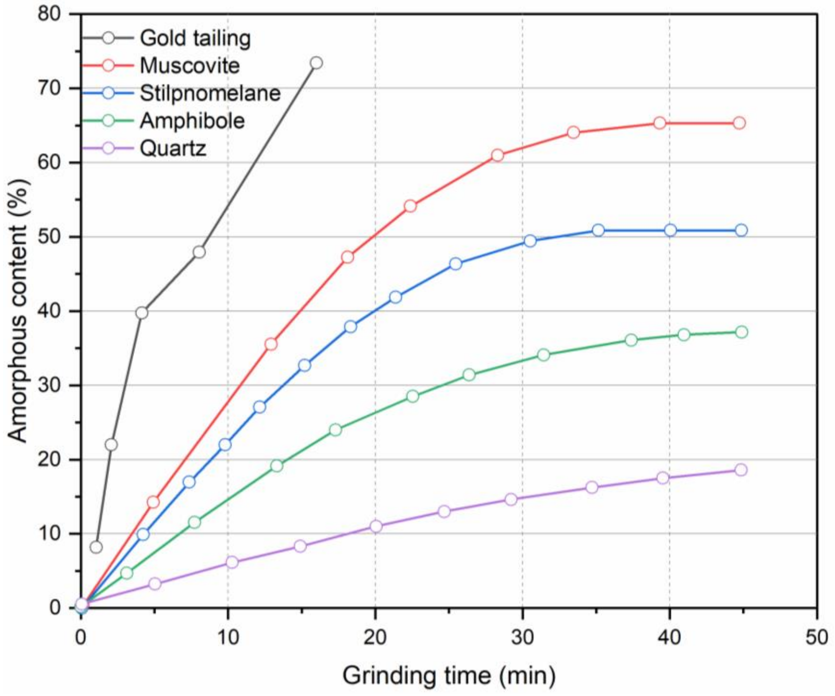

Fig. 2.7: Amorphous content of different mineral waste and minerals with respect to grinding time.

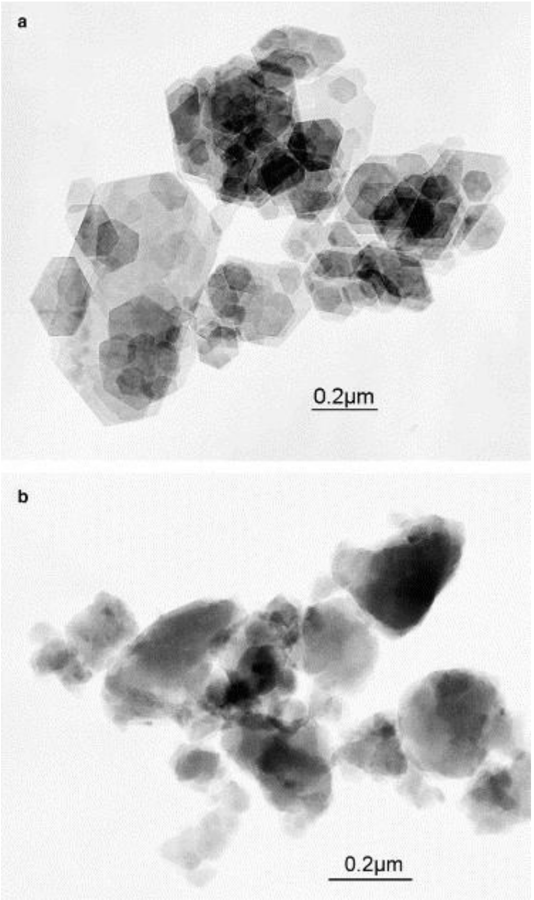

Fig. 2.8: TEM images of kaolinite-talc mixture: (a) before and (b) after grinding. The well-developed pseudo hexagonal crystals were converted to shapeless amorphous materials after 60 minutes of grinding. Image reproduced from [141].

b) Thermal activation and thermo-chemical activation

As the formation of crystalline phases in the minerals is a function of temperature, calcination is known to impart changes in the crystal structure of the minerals. The changes in the crystal structure include release of hydroxyl group by formation of water molecule, (i.e.) dehydroxylation and decarbonisation where bicarbonate, carbonate and carbon are removed by release of carbon dioxide.

The minerals which undergo these modifications during the calcination are:

(i) ***dehydroxylation*** of hydroxides in minerals such as kaolinite at about 580 °C and mica at about 700 °C [147]

and (ii) ***decarbonation*** in carbonate minerals such as calcite, dolomite, siderite smithsonite etc [84,148]

The dehydroxylation of phyllosilicate minerals improves the reactivity as the loss of hydroxides generates more disorder and exposure of Al ions favouring their dissolution. [149]. Therefore, this method of activation has been found suitable for mineral waste containing a large amount of phyllosilicate or carbonate minerals. However, minerals such as albite though they exhibit dehydroxylation at a higher temperature do not exhibit any change in crystal structure [150]. The calcination also involves alpha – beta transformation of quartz. Such transformations are generally accompanied by increase in volume and hence lead to formation of cracks thus further improving the reactivity by exposing new surfaces available for reaction [151]. Past studies show that minerals such as albite [150], apatite [38], arsenopyrite [152], calcite [96], chlorite [153], clinochlore [154,155], corundum [156], diaspore [94], dolomite [153], feldspar [157], hematite [158,159], hydroboracite [107], montmorillonite [149], talc [160], undergo modifications when calcined at temperatures between 540 °C and 1450 °C. Therefore, thermal treatment shall be effective for mineral waste with these minerals as major phases.

The choice of treatment temperature also depends on the minerals present in the mineral waste in their raw form. Torgal and Jalali reported that calcination of mineral wastes at 750 °C had no effect on the compressive strength of the cementitious matrix containing them. However, further increase of the calcination temperature to 950 °C resulted in an increase in the compressive strength values due to formation of amorphous products [161]. Beyond 950 °C, thermal treatment resulted in the formation of crystalline phases crystalline phases, such as mullite, which reduced the reactivity and hence did not yield an improvement in the measured mechanical properties.

Calcination in presence of alkali or alkaline roasting or thermo-chemical activation

Calcination of tungsten mine waste in presence of sodium carbonate yielded a maximum strength at a calcination temperature of 500 °C instead of 950 °C [161]. Minerals such as albite when calcined in the presence of NaOH or Na_2CO_3 they completely shift to an amorphous state due to loss of crystalline ordering of Al and Si [150]. Similarly, calcination of mine tailing in presence of alkalis at 600 °C indicated decrease in crystalline silica and albite and formation of biotite. Also, it is important to take into account the disintegration temperature of activator during alkaline roasting, or else the disintegrated compounds may lead to leaching or formation of efflorescence during hydration [162]. Kaze et al [163] in their study reported that the presence of high amounts of iron (almost 50%) led to a structural disorder in clay minerals where Al ions are replaced by Fe ions. These inherent defects result in reduction in crystallinity and requires lower thermal activation energy.

c) Chemical activation – Alkali activation

Alkali activation of mineral waste refers to the use of alkalis to stimulate the potential activity by dissolution. It is not to be confused though with the term "alkali activation" that refers to alternative to cement binders, in some cases known as "geopolymers". In both cases, the alkalis used for this purpose are known as activators. In mineral waste treatment, the most widely used activators are MOH, M_2SiO_3, M_2SO_4 and M_2CO_3 where M refers to either sodium or potassium [90]. The dissolution of silica and alumina from the source material is generally dependant on: (i) the strength Si-O-Al bonds; (ii) the formation of soluble species from the source; (iii) the pH of the solvent medium (i.e., activators) and (iv) the temperature of the system in which reaction takes place [164,165]. Studies showed that the time and rate of release of Al and Si ions play a crucial role in strength gain. Though the rate of dissolution of Si can be increased with increased alkali concentrations, the concentration of Si, Al, Ca in the binder, the glass content and the fineness of the precursor, played the most important role in strength gain [164,165]. Most studies therefore used alkali activation in combination with other activation methods such as grinding and calcination to attain the optimum conditions [59,107,146].

When it comes to geopolymerisation, it was found that grinding improved the rate of reaction due to increase in the specific surface area [104]. Xu and Deventer [166] suggested that alkali activation can be performed both on calcined and non-calcined materials, and calcined materials had better reactivity due to their more amorphous nature. Their study also reported that geopolymerisation of multiple minerals combined is possible, showing alkali activation can be suitably applied for mineral waste. Torgal et al [167] observed that the compressive strength increased with increase in molarity of the activator while past studies indicate that the better strength was achieved when the SiO_2/Al_2O_3 ratio of the system (precursor + activator) ranged between 3.0 – 3.8 [168]. Liew et al [169] found that the optimum SiO_2/Al_2O_3, SiO_2/Na_2O, Al_2O3/Na_2O and H_2O/Na_2O molar ratios were 3.10, 2.69, 0.87 and 14.23 respectively, for calcined phyllosilicate minerals whereas Xu and Deventer [170] observed a higher compressive strength for alkali feldspar minerals when the Si/Al ratio was maintained between 2.21 – 2.38.

In general, when the precursor's Si/Al ratio value does not fall within the above-mentioned range, an additional source of silica as sodium silicate activator and/or alumina are added. The most commonly added materials are silicafume, metakaolin, ground granulated blast furnace slag, fly ash, milled glass waste, [89,105,171–174]. Kiventera et al [175] adopted Si/Al value less than 3, between 1.5 - 2.5 and Na/Al ratio in the range of 1.0 – 1.29, to proportion a mixture of fly ash, ground granulated blast furnace slag and gold mineral waste. The mix was found to have better strength and microstructure when metakaolin was added and the Si/Al was 2.5 and Na/Al was 1.0. Peng et al., [103] activated mineral waste rich in garnet and quartz, using $Ca(OH)_2$, gypsum and sodium silicate as different activators and found that the reactivity of mineral waste improved by 67.65%, 27.73% and 36.29 % respectively. CDW derived silt was activated using NaOH with and without fly ash and metakaolin. It was reported that the mixes with 20% metakaolin and 80% silt had compressive strength 24.7 – 63 % higher than the mixes with 100% silt and 19.2 – 24.7% higher than mixes with 20% fly ash and 80% silt [89]. Others have used NaOH in presence of fly ash and metakaolin to activate calcined tailings comprising calcite, quartz, dolomite and mullite [174]. When fly ash was used quartz, dolomite, calcite, mullite, hydro-sodalite, chabazite were present in the activated paste whereas the use of metakaolin led to the formation of quartz, dolomite, calcite, hydro-sodalite and sodium aluminium silicate [174]. The presence of dolomite, calcite and quartz phases before and after activation indicated that they were unaffected by alkali activation [174]. However, the interlocking of unreacted large particles contributed to strength development after hardening [103]. Jiao et al. [123] activated ground tailing using Na_2SiO_3 and found Si/Al = 3.3, Na/Al = 1.0 and H_2O/Na = 1.6 were optimum for activation. The studies with both sodium and potassium activators indicated that a geopolymer paste with highly reactive precursor when used with a low viscous activator such as KOH or K_2SiO_3 exhibits cracks due to accelerated evaporation of water which otherwise would have been available for geopolymerisation [176]. Koohestani et al [177] reported a formation of silica gel when the pH of the system was 8.7. Evidence in the literature suggests that high calcium content in the mineral wastes can turn the tailing itself to an activator [79]. Furthermore, mineral wastes can be used as an inert filler in geopolymers in presence of a co-binder [178]. In case of alkali activation of minerals rich in Fe [163,179], it was observed that Al^{3+} ions were replaced by Fe^{3+}. This resulted in formation of Si-O-Fe linkages and hence Fe^{3+} binders are formed. Peys et al [179], from their study reported that the synthesis of this phase is observed when the Na/Fe^{3+} is almost equal to 1 and Si/Fe^{3+} is almost equal to 3. The study also reported that the Fe^{2+} ions after dissolution is oxidised to Fe^{3+} during or after the synthesis of geopolymer.

The major advantage of alkali activation of mineral waste is that, unlike the other two methods of activation, alkali activated mineral wastes can be used as a standalone cement. Alkali activation also: (i) helps in encapsulation of heavy metals and metalloids and thus prevents its leaching; (ii) it has low energy consumption demand and (iii) has better acid resistance [172,180]. Mineral waste alkali activation can be considered akin to engineering the same waste to cater different needs by modifying the activators, e.g. tungsten mine waste when activated with NaOH and $Ca(OH)_2$ exhibited optimum mechanical properties with shrinkage less than OPC whereas when activated with Na_2CO_3 had high early age strength but performed poorly under water [181]. However, the disadvantage in using mineral wastes is the effect of presence of Cu^{2+}, Fe^{2+}, Fe^{3+} in the formation of geopolymer chains, which is still not well established. Also, the alkali activation may form hydration products which are unstable thus the binder exhibits high early strength and decrease in strength at later ages [162].

2.8 Mineralogy and Microstructure

Understanding the mineralogy and microstructure of binders containing mineral waste is very important towards properly understanding their behaviour. The studies found in the literature are still limited but some useful initial conclusions have been drawn already. Generally, the microstructure and mineralogy of the binders containing mineral waste were affected by various factors including the percentages of mineral waste, type of usage (as admixture, SCM or cement replacement), water content, activator, and presence of mineral admixtures.

2.8.1 Alkali activated binders

In geopolymers with alkali activated calcined Kaolin mine waste, poorly crystalline pseudo zeolitic alumino silicate gel, anatase and kaolinite were observed when SiO_2/ Al_2O_3 ratio was high (sodium silicate activator). However, in systems activated only with NaOH, the crystalline products of hydrosodalite and Trona were identified [99]. Though a highly alkaline environment favours the dissolution of aluminosilicate compounds by breaking Si–O–Si and Al–O–Al bonds and release of Si and Al ions into solution from the mineral waste excessive amount of NaOH was found to affect the strength negatively [89]. Sedira et al. [182] activated tungsten mine waste with brick waste using NaOH and Na_2SiO_3. Poorly formed K-A-S-H, C-A-S-H, N-A-S-H gels were observed indicating alkaline activation of the products was not complete. Samples with more brick waste had lesser pore diameter and pore volume than the mixes with mine waste alone. Similar observation was made with the use of GGBFS, where the unreacted particles of the mineral waste and slag found to be surrounded by newly formed reaction products [183]. An area of concern is that mixes with mineral waste can potentially lead to matrices with increased porosity [184]. Silva et al [185] reported that when alkali activated, chamosite is converted to crystalline phase zeolite type (sodalite). With use of sodium silicate activators, minerals such as gypsum, quartz, sodium aluminium silicate, magnesium sulphate, magnesite, pyrite were formed in the alkali activated paste whereas sodium aluminium silicate, quartz, magnesium sulphate, pyrite, akermanite, magnesite were present in the raw tailing. Sedira et al [186] reported that mixes with sodium silicate and sodium hydroxide exhibited more cracks due to higher shrinkage when compared to mixes with sodium hydroxide only. Also, the mixes with higher solid to liquid ratio had a more cohesive microstructure. Wang et al [187] in their study with garnet tailings showed that on third day as given in Fig 2.9 (a), the matrix appeared as if many particles of 2-5 µm are glued together. This can be attributed to the high crystallinity of the raw material. However, at later ages (7 days and 28 days) it the original large sized particles present formed a three-dimensional crosslinked structure. Fig. 2.9 (a), (d-f) show that the initial dissolution of the particle has been accelerated by the presence of metakaolin (20%) in the system. It is evident from the absence of large sized particle in Fig. (d) of geopolymer paste made of garnet tailing with metakaolin captured at 3 days.

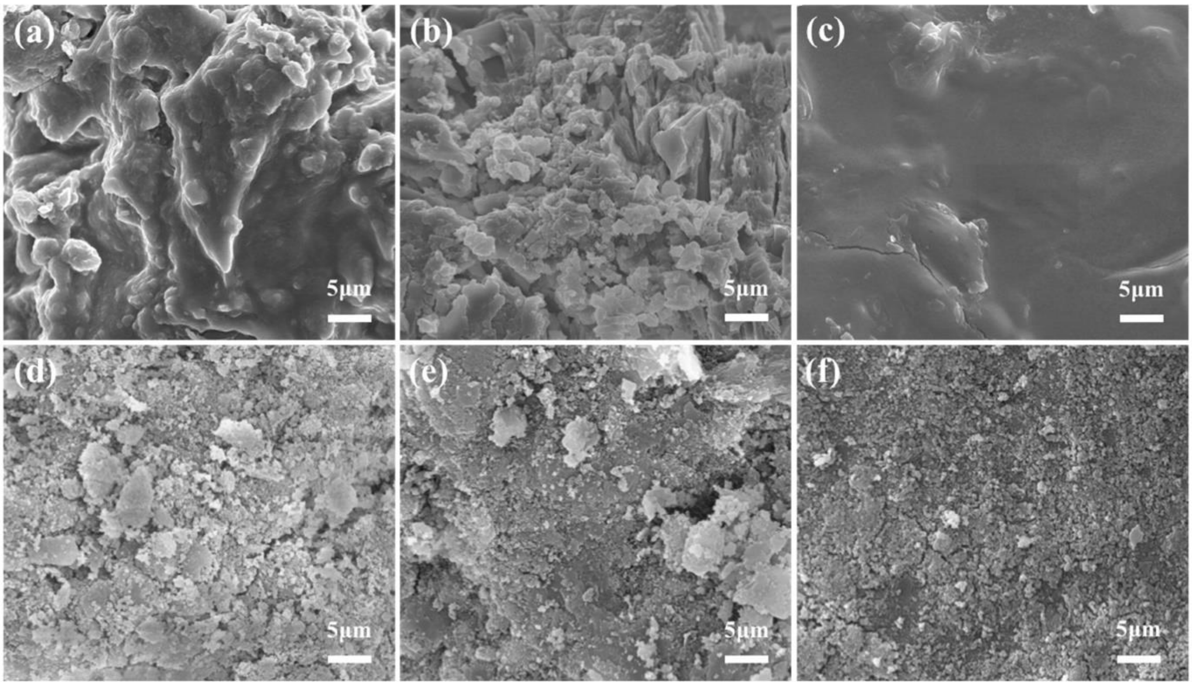

Fig. 2.9: Microstructure of garnet mineral waste based geopolymer at 3, 7 and 28 days (Image reproduced from Wang et al [125]).

2.8.2 Portland cement replacement and supplementary cementitious material

In the literature, one can find several combinations of how mineral wastes are incorporated in cementitious matrices. Mixes with mineral waste, lime powder (10%) and OPC indicated the formation of quartz, calcite, dolomite, pyrite, siderite, muscovite, clinochlore, hematite and ettringite [188]. Phases such as portlandite, quartzite, alite, quartz, ettringite, calcium ferric aluminate hydrate, albite and epidote were found in mixes with 20% mineral waste and OPC. This indicates that all phases in mineral waste cannot be consumed by hydration [189]. Martinez et al. reported that total porosity increased by 28% and mean pore size decreased by 42% with 50% replacement of OPC by activated coal mine waste [190]. Ince [88] reported both reduction in pore size and pore volume with increase in percentage of mineral waste. The study reported that the porosity decreased from 37.5 % to 32 % for 30% cement replacement. Cheng et al [129] reported that mixes with mineral waste had a flocculent structure in their calcium silicate hydrates (C-S-H) accompanied by lesser quantity of portlandite crystals and attributed this to the lower Ca/Si value. However, the overall microstructure was more compact and uniform. A similar observation was made by Liu et al [191] in samples of 90 days age, whereas at 3 days it was seen that the Ca/Si value was high due to faster dissolution of Ca from the cementitious system than Si from the mineral waste. This gradually reduces with age and hydration and resulting in secondary reactions leading to formation of flocculant C-S-H as seen in Fig. 2.10.

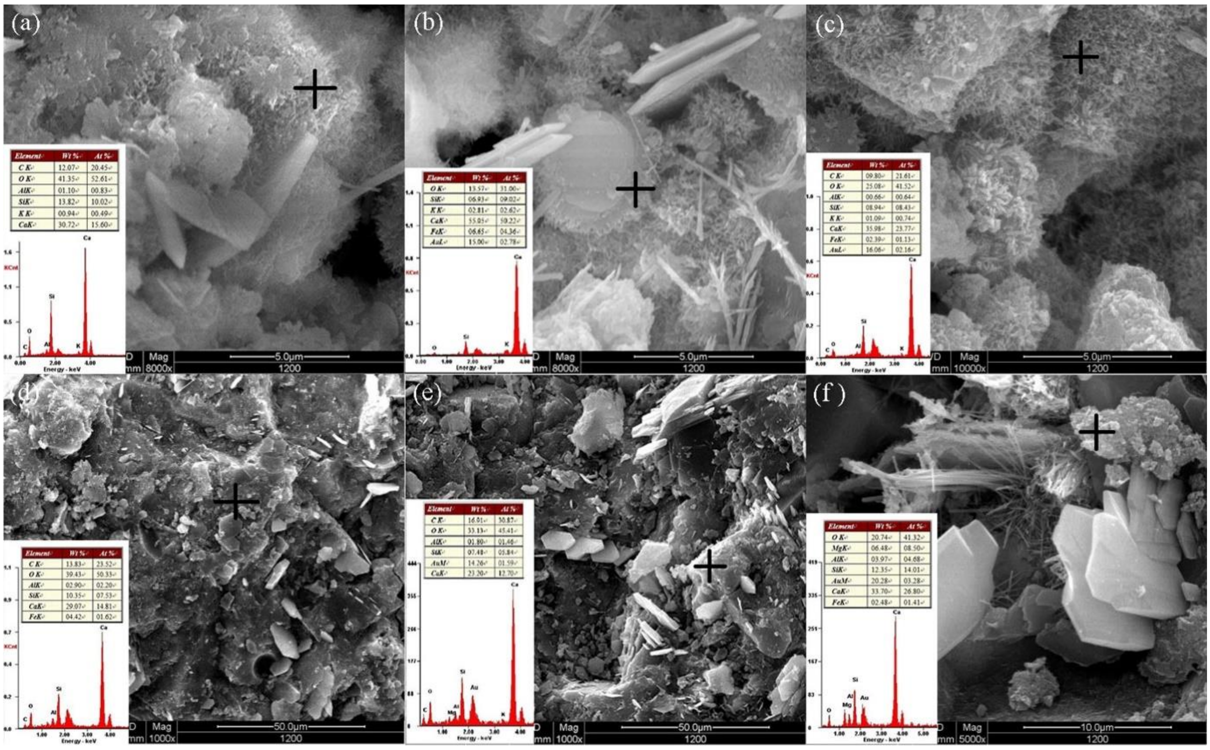

Fig. 2.10: Microstructure of cement paste with 0, 15, 45 % mineral waste at ages 3 (a-c) and 90 (e -f) respectively (Image reproduced from Liu et al [191]).

2.9 Hydration and Fresh Properties

Early age properties are rather critical for any binder. Fresh properties define placement and handling whereas hydration kinetics affect setting times and hence have a knock-on effect on the evolution of properties. It is well known fact in concrete technology that the addition of powdered additions has an impact on early age properties. While the published data on traditional SCMs is quite rich and conclusive, for mineral wastes it is still early days. The available research is very limited and far from conclusive.

2.9.1 Alkali activated binders

Rao and Liu [192] reported workability as a function of alkali concentration and reported mixes made with activator at pH 14 had better workability than activator at pH 12, whereas Kiventera et al., [193] reported that the workability decreased with increase in concentration of alkalis in case of the highly sulphidic mineral waste. Perumal et al., [194] reported that the setting behaviour of alkali activated mineral waste was mainly dependant on the minerals present in it for the same activators used. Koohestani et al [177] reported that increase in sodium silicate delayed the setting of pastes. While it can be comprehended that the workability of the mineral waste is a function of minerals present and the concentration of activator, it can be seen clearly from Fig. 10 that the crystallinity of the mineral waste had an impact on hydration and the matrix formation of the pastes after alkali activation. The mechanism of polymer formation involves the following steps: i) dissolution; ii) poly-condensation; iii) gelation and iv) hardening [90,114,127,130]. This mechanism is summarised for mineral waste in Fig. 2.11.

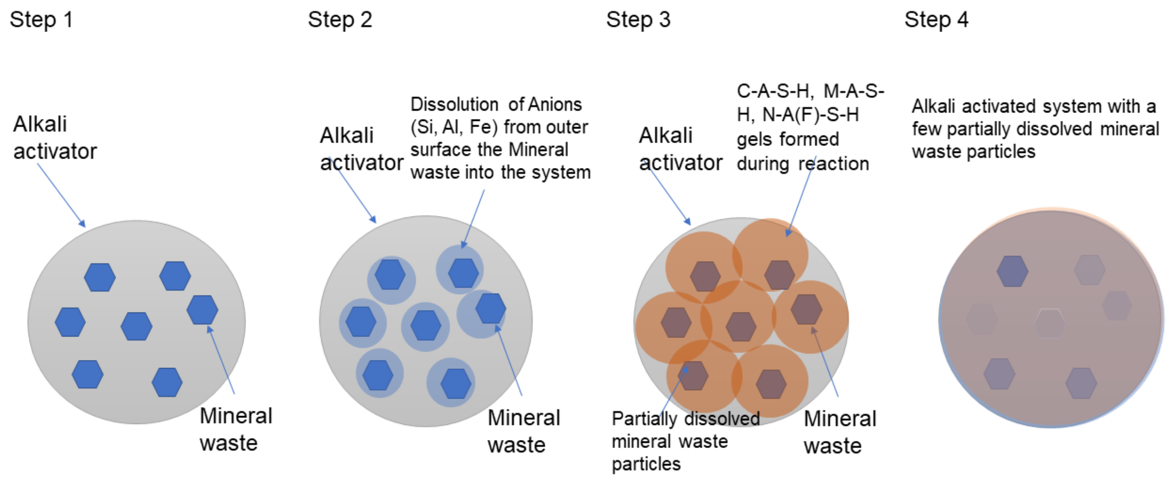

Fig. 2.11: Mechanism of alkali activation of mineral waste: Step 1: dissolution; Step 2: poly-condensation; Step-3: gelation and Step 4: hardening.

2.9.2 Portland cement replacement and supplementary cementitious material

The general trend observed in the published studies is that increasing mineral wastes addition in cementitious binders increases the water demand [68,88,173,195]. The addition of coal mineral waste as a raw material for clinkering increased the setting time due to its high lead (Pb) content [196]. The replacement of cement tailing by 30% phosphate mine waste led to an increase in setting time, bleeding and delayed the induction phase of hydration. The study confirms the use of phosphate tailing as direct cement replacement not only has a dilution effect but also a retarding effect due to dissolution of phosphate. Increasing the proportion of phosphate tailings led to a significant drop in the yield stress, plastic viscosity, and an increase in the thixotropy of the mix [197]. Other studies do not show significant effect on setting times with 10% addition having no effect on initial setting time whereas 20% addition increasing the setting time only marginally [96]. Ince et al [195] reported that the increase in quantity of mineral waste replacement from 0% to 20% led to decrease in setting time in both lime mortar from 1250 minutes to 1180 minutes and cement-based mortar from 280 minutes to 220 minutes. The yield stress and plastic viscosity of the mortar decreased with increase in percentage of mineral waste replacement and were found to be 30.4% and 35.8% lesser than control concrete for a replacement percentage of 30% [198]. Of course, the rheological effects depend on the fineness and reactivity of mineral wastes and therefore more detailed and extended research is needed. There is also some early evidence that heat of hydration and induction period are also affected. Liu et al showed that the addition of mineral wastes resulted in dilution of calcium ions in the cementitious system and hence delayed the saturation point and further strength gain [199]. Therefore, it can be considered that in the initial days of hydration, mineral wastes act only as fillers. To summarise, the presence of mineral waste provides additional Si required for the pozzolanic reaction and facilitate the production of secondary C-S-H. However, this Si is available at a much later age due to slow reactivity of the mineral waste and sometimes leads to formation of C-S-H with a low Ca/Si ratio resulting in a low C-S-H density. Therefore, to achieve binder of better mechanical performance it is imperative to adjust the percentage replacement or improve the reactivity of mineral waste to facilitate the additional Si is available at the right time and quantity for reaction. Also, the presence Cu^{2+}, PO_4^{3-} and impurities such as oil from production process affect the strength gain.

2.9.3 Filler

Using mineral waste as fillers, Siddique et al reported that with increase in mineral waste the flow of mortar decreased even for the same water to binder ratio [200]. Similarly, Onuaguluchi and Eren [68] found that flow decreased with increase in percentage of mineral waste and Zheng et al [116] reported that the addition of mineral waste of a particle size higher than cement led to lesser total surface area and hence reducing the water demand. The study also reported a delayed setting time due to release of phosphorous ions which acts as retarder into the hydrating system. Studies reported that as a filler the mineral wastes increased the water demand due to its higher surface area which in turn could delay the hydration and setting. Also, as mineral wastes might act as a reactive filler, it is important to consider its influence both in packing density as well as chemical reaction.

2.10 Mechanical Properties

Studies on mortars containing mineral wastes have shown compressive strength up to 75 MPa as given in Table 2.3 and the relative compressive and flexural strengths are given in Fig 2.12 and 2.13. From all existing data it is evident that there is no generic trend of increase or decrease in strength with the increase in percentage of mineral wastes. The absence of specific patterns can be attributed on various factors including particle size, type of cementitious binder, curing temperature, type and extent of activation and the limited number of studies currently existing. However, a point of convergence between studies is that 20-30% replacement appears to be an optimum value so far.

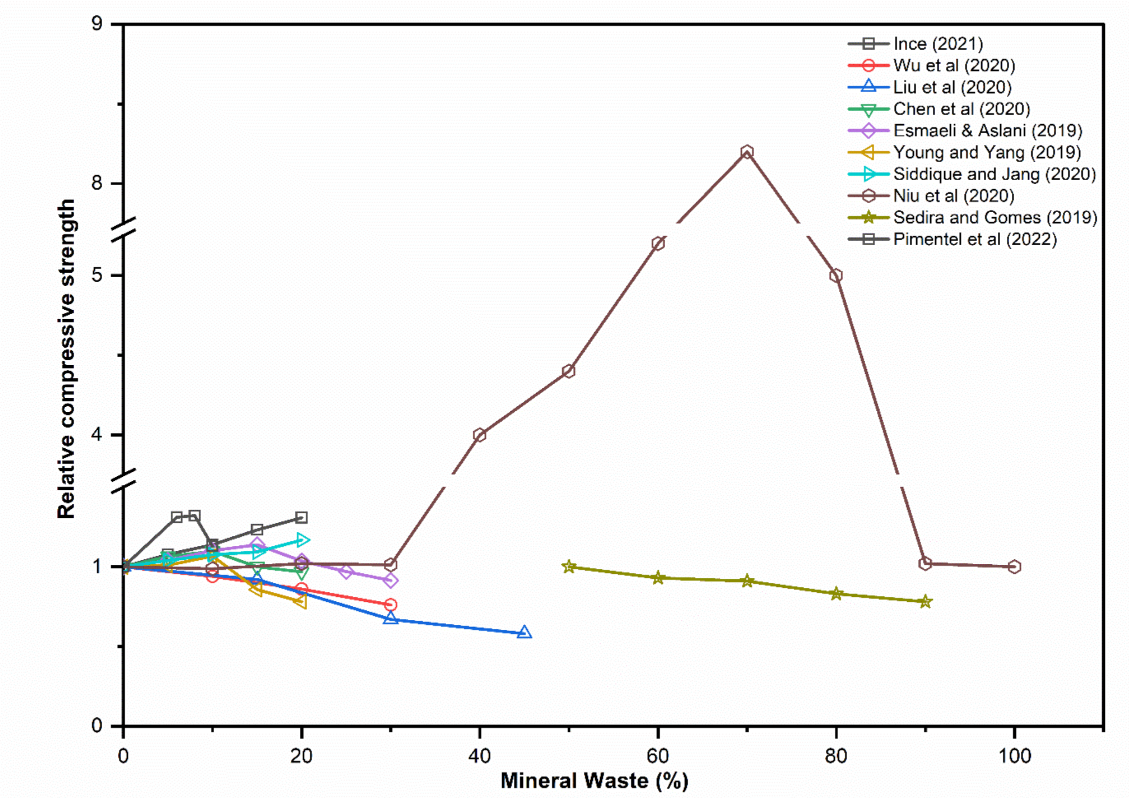

Fig. 2.12: Variation in compressive strength of samples with different percentages of mineral wastes.

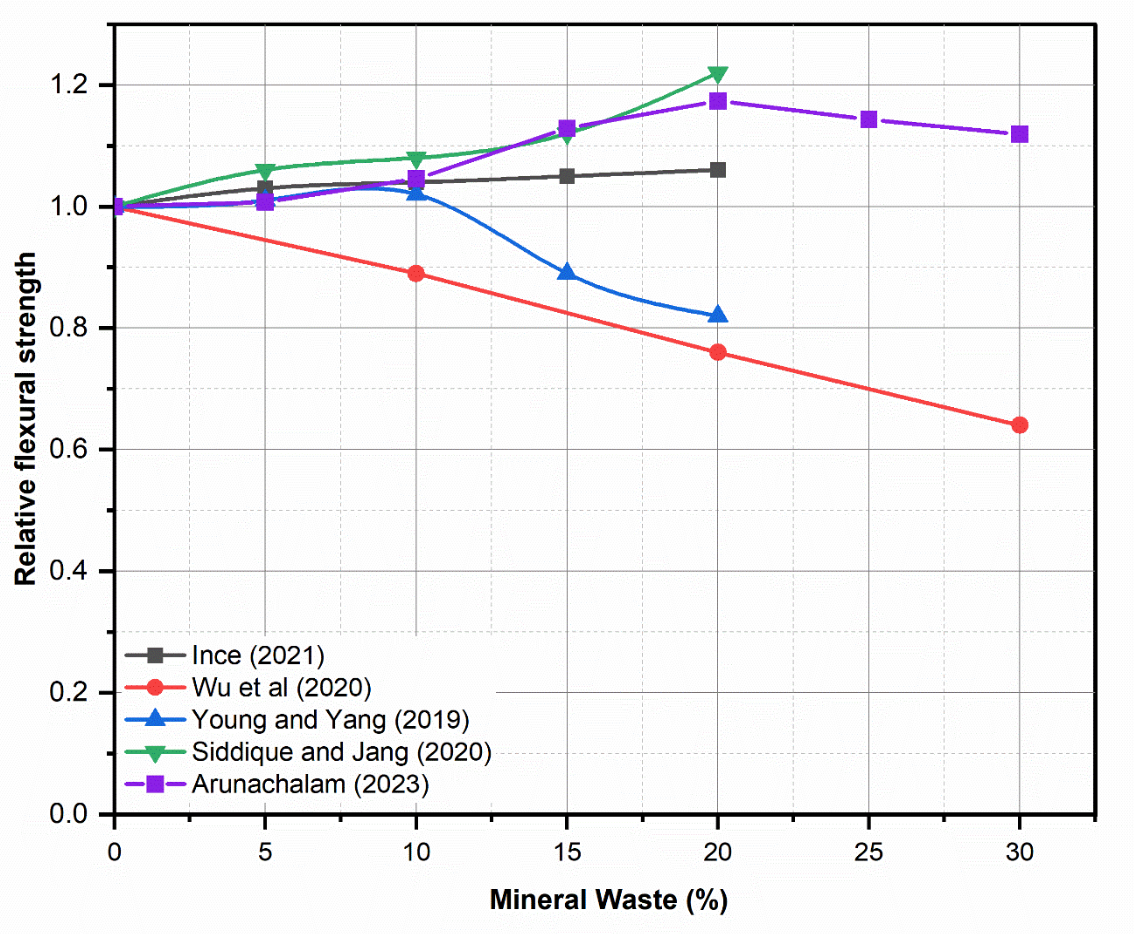

Fig. 2.13: Variation in flexural strength of samples with different percentages of mineral wastes.

Table 2.3: Compressive strength variation observed in various studies

As cement replacement and supplementary cementitious material									
Sl. No	**Type of mineral waste**	**Mix**	**Admixture**	**w/b ratio**	**Activation Process**	**Percentage replacement**	**Max. Compressive strength (MPa)**	**Variation in compressive strength compared to control concrete (%)**	**Study**
1	Gold	Mortar	-	0.62	-	30% as cement replacement	37	13.9	[88]
2	Copper	Mortar	-	0.485	Mechanical activation	10% as cement replacement	46.5	35.5	[68]
3	Coal	Mortar	-	0.50	Thermo mechanical activation	10% as cement replacement	64	- 8.3	[96]
4	Tungsten	Mortar	GGBFS	0.52		10% as cement replacement	35	-14.6	[76]
5	Coal	Mortar		0.30	Thermal activation	6 % as cement replacement	59	-1.7	[201]
6	Coal	Mortar		0.50	Clinkering	7% as clinker raw material	60	1.7	[202]
7	Coal	Mortar	-	0.50	Mechano-Thermal activation	20 % as cement replacement	55.7	-11.9	[190]

Alkali activated cements							
Sl. No	**Type of mineral waste**	**Mix**	**Admixture**	**Activation Process**	**Percentage replacement**	**Maximum Compressive strength achieved (MPa)**	**Study**
1	Vanadium	Mortar	Sodium hydroxide and Metakaolin	Thermo chemical activation (Alkaline roasting)	70 % mineral waste and 30% metakaolin	55.7	[203]
2	Kaolin	Paste	Sodium hydroxide, Sodium silicate,	Thermo mechanical treatment followed by Alkali activation	100% mineral waste	75	[99]
3	Boron	Mortar	Sodium silicate, sodium hydroxide	Thermo mechanical treatment followed by alkali activation	100 %	30.7	[95]
4	Tungsten	Mortar	calcium hydroxide, sodium hydroxide, sodium silicate	Thermal treatment followed by alkali activation	100%	75	[204]
5	Tungsten	Mortar	Sodium silicate, sodium hydroxide Potassium Hydroxide and ground granulated blast furnace slag	Alkali activation	90% mine waste and 10% GGBFS	33	[186]

6	CDW derived silt	Mortar	Sodium hydroxide	Alkali activation	80% silt + 20% metakaolin	32.3	[89]
Alkali activated material as a replacement of OPC							
1	Tungsten	Mortar	Sodium silicate, gypsum, lime	Mechano-chemical activation	30% cement replacement	56.95	[103]

2.10.1 Alkali activated binders

The mineral Albite, calcined in presence of alkali, when used as a one-part cement achieved a strength of up to 44 MPa at 28 days [205]. Tungsten mine waste calcined in presence of Na_2CO_3, yields high early age strength up to 45 MPa on alkali activation with NaOH, and the strength decreases at later ages due to the formation of unstable compounds due to ineffective activator combination [162]. The molarity of NaOH solution found to have an effect on the development of compressive strength of binders with activated tungsten mine waste [162]. More specifically, about 18 MPa, 30 MPa and 70 MPa were achieved using 8 M, 14 M, and 24 M NaOH solution for activation of the waste, in presence of $Ca(OH)_2$. Geopolymers synthesized from non-calcined raw materials display a higher increase in the compressive strength in the later stage of the geopolymerisation reaction [206]. Jiao et al [207] indicated the curing temperature played an important role in strength gain of geopolymers with mineral wastes where the compressive strength increased from 35.1 MPa to 55.7 MPa when the curing temperature was increased from 20 ^{o}C to 60 ^{o}C. At room temperature curing, the strength gain happens at a later age about at 14 days [177]. The feasibility of development of sodium silicate from mineral waste was studied. It was found that the sodium silicate produced from the mineral waste were able to successfully activate a metakaolin based system as geopolymers and achieve a strength up to 32.1 MPa as compared to a strength of 40 MPa by commercial sodium silicate [208].

2.10.2 Portland cement replacement and supplementary cementitious material

Malagon et al [202] used 7% of coal mining waste as raw material for producing cement clinker and observed a 9-14% decrease in strength due to hindering of hydration by the Cu ions present in the mine waste. A replacement of 30% cement with phosphate tailings causes a decrease in flexural strength by 25% and compressive strength by 34.7%, 38.9%, 40.7% at 3 days, 28 days and 90 days, respectively [197]. Similar observation was made by Liu et al [199] where the compressive strength decreased from about 88 MPa to 35 MPa when the replacement percentage was 45%.

Martinez et al., [209] suggested when activated coal mine waste was used as cement replacement up to 20% attained strengths were at the 42.5 MPa class grade range whereas increasing the replacement to 50% performance dropped to 32.5 MPa class. Esmaeli and Aslani [210] proposed an optimum replacement percentage for copper mineral wastes at which the compressive strength was greater than the control mixes by 5% and elastic modulus and split tensile strength were greater by 10% and 12 %, whereas Vargas and Lopez [211] reported all percentage of replacements lead to decrease in strength and use of copper mineral waste as an addition to the matrix as a filler improved the strength. Similarly, Liu et al found that at all water cement ratios the strength reduced with increase in graphite tailing content by up to 29% - 42% for 15% cement replacement due to free graphite and hydrocarbon oil leading to improper bonding and hydration [212]. Ince [88] reported a maximum compressive strength of about 37 MPa was achieved when the percentage replacement of cement by mineral waste was 30%, proving to be the optimum and all mineral waste mixes had compressive strength values higher than mixes with 100% cement. In their recent study, Ince et al [195] reported that the compressive strength of mixes increased with increasing percentage of mineral wastes for both cement and lime mortars up to a replacement of 20% as shown in Fig 8. The mortars developed by Ince et al [195] were then used to join masonry units and it was found that the dewatering of the mortar (i.e. water movement towards the masonry) had an impact on the evolution of properties. When dewatering happened before curing the cement mortar mixes with 20% mineral waste had approximately 20% lesser strength than that of control. The study also reported a reduction in split tensile and flexural strengths of the dewatered cement mortar with use of mineral wastes whereas the same improved with increase in percentage of mineral wastes for dewatered lime mortar. The mechanisms that underpin better behaviour in lime mortars are not yet well studied. Jian et al [213] observed that addition of up to 2-6% of mineral waste as a clinker raw material affected negatively the strength development of the cementitious matrix, with the exception of 2% replacement at 60 days. More specifically, for 0%, 2%, 4% and 6% replacement the strength of the cementitious matrix at 28 days was 44.1 MPa, 18.6 MPa, 11.3 MPa and 5.7 MPa respectively; while at 60 days it was 66.8 MPa, 71.5 MPa, 48.9 MPa and 25.3 MPa respectively.

2.10.3 Filler

Existing data suggests that the use of mineral wastes as fillers in cementitious matrices is also not conclusive. Some suggest that the filler effect can lead in the improvement of mechanical properties probably due to better packing, while others report reduction in properties. Sidique and Jang showed that incorporation of 5%, 10%, 15% and 20% mineral wastes led to an increase of 3%,1%,10% and 16% in compressive strength and 2%, 5%, 24% and 17% in flexural strength respectively [214]. All the tailing added mixes had better resistance to abrasion and impact as compared to control concrete. However, Zheng et al [116] reported a decrease in performance of mortar mixes with increase in percentage of mineral wastes. The study reported a 25% decrease in flexural strength and a 35.9% decrease in compressive strength for a 30% addition of mineral waste as a filler. This decrease in performance compared to control mixes could be due to the dilution effect as the study aimed reduction in cement usage by replacing cement by a filler.

It can be outlined from the past studies that obtaining a binder of high compressive strength up to 75 MPa is possible with the use of different mineral wastes. However, the published results are not yet conclusive while at the same time there is a large spread of processing techniques and replacement percentages (for the mineral wastes used). Therefore, there is a need for a systematic approach and clear understanding of: the mineralogy (and its variability) of mineral wastes; suitable activation techniques; optimum duration of processing; choice of activator(s); optimum concentration of activator(s) and the percentage of replacement of cement in traditional cementitious binders.

2.11 Durability

The durability of the mineral waste binders was in most cases found to be a function of porosity and microstructure. The performance of mineral wastes with respect to corrosion behaviour, chloride penetration and resistivity were affected by the presence of conductive elements such as graphite and iron. Though, the past studies do not indicate a standard trend in improvement or reduction in durability performance with increase in percentage of mineral waste, it was always observed in certain cases that optimum ranges for mineral wastes’ utilisation exist and within these optimum ranges the binders performed well.

2.11.1 Alkali activated binders

Jiao et al [123] reported a high thermal stability of geopolymer mixes with mineral wastes. The compressive strength of the samples was unaffected up to an exposure temperature of 600°C, and it increased up to a temperature of 900°C due to densification. Ahmari and Zhang [215] found that there were no visible efflorescence, disintegration, or cracks even after four months of immersion in solutions of pH 4 and 7, however the unconfined compressive strength decreased by 59.3% and 53.3% from 11 MPa respectively, after immersion. A similar result was reported by Kiventera et al [193]. Their study showed that mineral wastes mixed with pure NaOH produced a binder which performed poorly after immersion in water. However, the same performance was improved by use of ground granulated blast furnace slag in combination with tailings as a precursor. Falah et al [216] reduced the water absorption of alkali activated concrete with mineral waste by using 30% submicron sized mineral wastes. Perumal et al [146] in their study reported that alkali activated mineral waste pastes exhibited a water absorption of 35%, 30%, 26%, 22.5% and 20% when the grinding time was varied from 1,2,4,8, 16 minutes respectively.

2.11.2 Portland cement replacement and supplementary cementitious material

In general, water absorption of the mixes with mine waste were found to be higher than that of mixes with OPC and increased with increase in percentage of mineral wastes [68,190]. When OPC was replaced by 50% coal mine waste, the water absorption increased by 32% [190]. However, Esmaeli and Aslani [210] reported that the water absorption decreased up to an optimum percentage of replacement and increased beyond that. In another study [77] mixes with optimum replacement ratio of 15% and 20% mineral wastes had marginally lower water absorption (~2%), when compared to control concrete (2.4%). The depth of water absorption was also reported to decrease up to 20% replacement and increase beyond 20% cement replacement. Though the depth of water penetration increased after 20% replacement, it was still found to be lesser than control concrete (29.3 mm) at 30% replacement (24.2 mm) [210]. Similarly, Cheng [129] reported an optimum replacement percentage of 30% beyond which the performance of samples after immersion in water starts declining. Similar increase in trend was also observed in case of water absorption under pressure where the depth of water penetration for 0%, 20% and 50 % cement replacement were 3.6 mm, 6.5 mm and 15.8 mm respectively [190]. The study also reported primary absorption coefficient through capillary sorption measurements where it was similar for samples with 50% replacement and control mixes whereas samples with 20% replacement performed better than control. Ince et al [195] reported that water penetration depth and porosity increased with increase in percentage of mineral wastes for cement mortar and decreased with increase in percentage of mineral wastes for lime mortar. It is evident, that the reported data is scattered and to a certain extent confusing. Two studies that focused on freeze thaw performance concluded that the reduction in pore-size (as a result of the addition of mineral wastes) led to a poor freeze thaw performance with the mixes containing graphite mineral wastes reported a mass loss of about 5% after 25 cycles of freeze and thaw [88,217].

Ince reported that carbonation depth decreased from 9.8 mm to 5.6 mm for 30% cement replacement [88] whereas Cheng et al [129] reported that the carbonation depth increases with increase in percentage of mineral wastes. However, the mixes with mineral wastes had better compactness and were reported to be less porous. On the chloride ion penetration front, mixes with mine waste exhibited a better chloride resistance, irrespective of the type of mine waste used. The samples with 50% coal mine waste had a chloride resistance 5 times greater than that of control samples and samples exposed to chloride indicated the formation of Fridel’s salt which was in line with the behaviour of samples with fly ash [209]. The chloride migration test indicated that the samples with mineral wastes performed better than the control sample in chloride migration test. The samples with mineral waste fell in the category of high chloride diffusivity and the control samples were in the category of very high chloride diffusivity [210]. A study on the corrosion development, found that the corrosion onset time increased linearly with increase in percentage of mine waste, indicating that the mineral wastes delayed the initiation of corrosion [218]. Graphite tailing improved the electrical conductivity of concrete which, on the other hand, can be problematic when it comes to corrosion. The surface resistivity decreased from 62 kΩ·cm for normal concrete to 32 kΩ·cm for concrete with 15% graphite tailing [100]. The surface change for samples with graphite tailing was almost twice as that of control. The surface temperature reduced rapidly with increase in percentage of graphite tailing [217].

2.11.3 Filler

Incorporation mineral wastes as fillers increased density and lowered water absorption and total void content. After 24 hours of exposure to water the mixes with 20% mineral wastes recorded a 11% decrease in rate of water absorption [214]. The mixes with 10% mineral wastes were highly resistant to sulphate attack. Though the mixes with 15% and 20% mineral waste exhibited higher strength loss and weight loss compared to mixes with 10% mineral wastes, all the mixes with mineral wastes performed better than control mixes. Similarly mixes with 10% mineral waste were more resistant to acid attack [214]. Mass loss and depth of chloride penetration decreased with increase in percentage of mineral waste, depth of penetration was 10.7 mm for control mixes whilst 3.5-3.7 mm for mixes with mineral waste, similarly 4.3% and 3.4-3.7% mass loss for both the mixes. The mass loss of the sample when exposed to HCL was 4.3% for control and 3.4% - 3.7 % for samples with mineral waste [68]. Addition of mineral waste also increased the drying shrinkage, however the drying shrinkage of mixes with 10% mineral waste was lower than the mixes with 5%, 15%, 20% and 25% mineral wastes [116].

Figure 2.14 shows published data on the variation of measured porosity for different percentages of mineral waste used in the binders.

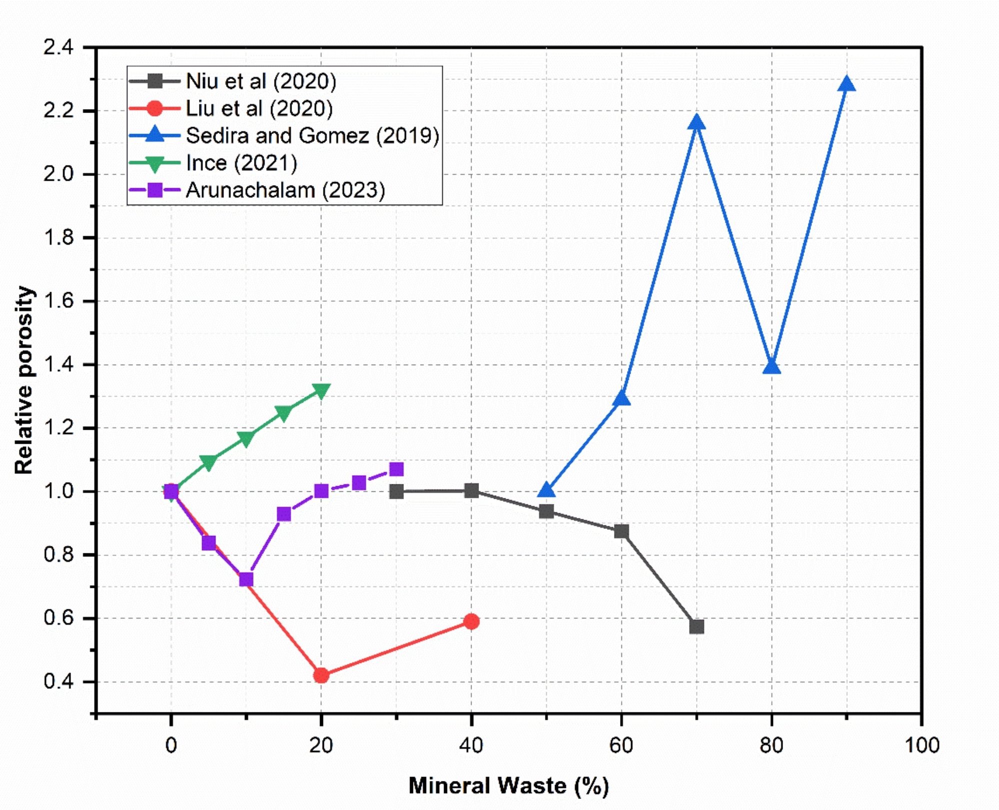

Fig. 2.14: Variation in porosity of samples with different percentages of mineral wastes.

2.12 Environmental Properties - Leaching of Heavy metals

Table 2.1 indicates that mineral wastes are in general obtained with the presence of heavy metals such as Pb, Zn, Cd, Cu, Ar, Cr, V, Zr. This always poses a danger of leaching of heavy metals into the environment over the period when mineral waste is used as a construction material. Immobilising heavy metals is very critical in this discussion. Heavy metals can become a part of a 3-dimensional chain and thus get immobilised, and this process is known as locking. The ionic size and valence of the heavy metals are the major factors influencing locking.

2.12.1 Alkali activated binders

Wan et al., [105] studied immobilisation of lead from lead nitrate addition by alkali activation of sphalerite floatation mineral waste (Zinc tailings) using sodium silicate and reported that about 97.9 – 99.5% of heavy metals were immobilised when metakaolin was used as an additive and 92.26% were immobilised when only mineral wastes were used. Similarly, for the same amount of alkali activated of tungsten mine waste the heavy metals leaching decreased with increase in percentage of GGBFS. In either case, the leaching value was less than the permissible value given by Korean guidelines, TCLP toxic limits [219] and European guidelines [220] for cadmium, zinc, copper and lead [76]. Gomes et al., [221] reported that alkali activated tungsten mine wastes when water cured stabilizes at a pH of 7 after about a week. This makes it fall within the range of 2-8.5 in which arsenic leaching is negligible. Peng et al., [103] reported that the Pb in tungsten mine waste are solidified in the garnet crystal and therefore cannot leach.

2.12.2 Portland cement replacement and supplementary cementitious material

Ince [88] found that when sulphidic gold mineral waste was used as a cement or sand replacement the leaching was always within the limits specified by US Code of Federal Regulations (CFR). And it was also observed that when the percentage of replacement was higher the leaching was lower due to pore structure refinement. The Cr, Pb and Cd leached was 0.153, 0.0004, 0.00007 mg/ L when the percentage replacement was 10% and it decreased to 0.129, 0.0003 and 0.00005 mg/L respectively, when the percentage replacement was 30%. When compared with other standards it can also be seen that these wastes qualified as non-hazardous as per the TCLP toxic limits [219] and as non-toxic as per the framework for eco-toxic materials as per European guidelines [220]. Gou et al., [222] also reported that the clinkering and hydration of cement with mineral waste prevents the leaching of heavy metals when mineral wastes are used as a cement replacement. In a similar line, Nouairi et al., [223] reported that 75% of Pb, 85% of Zn and 80% of Cu were immobilized by hydration of Zn-Pb mineral wastes in mortar. Pyo et al., [102] reported that though the As, Pb, Zn and Cd content of quartz tailing were higher than the other silica powder their values were within the permissible limits. The study also reported the reduction in leaching due to physical and chemical encapsulation of heavy metals when used in ultrahigh performance concrete as supplementary cementitious material.

2.13 Future outlook and Identified research gaps

This chapter has highlighted the chemical and mineralogical similarities between mineral wastes and pristine raw materials used in the manufacture on cement-based binders. However, the current state-of-the-art in the field of utilising mineral waste in such binders albeit showing some promising results is limited and largely inconclusive as discussed in the preceding sections. A list of limitations for such use is given in Table 2.4. All these challenges highlight the importance of extensive and systematic research on this area, something that can lead to large scale valorisation of mineral waste streams in large manufacturing processes such as cement and concrete.

Table 2.4: Challenges for use of mineral wastes in cementitious binders and potential solutions

Challenges	**Potential solutions**
Variability in property and quality of various mine streams	It is difficult to assign a single method of reuse/recycle for all wastes. However, proposing a classification system based on certain key parameters from characterisation and providing customised solution for each category shall be more practical from industry point of view. Clustering mineral waste streams and mapping their properties can allow the development upper/lower limits in their use, increasing the confidence of post-processors and/or end-users.
High crystallinity and non-reactive nature of mineral wastes.	The reactivity of the mineral wastes shall be improved by mechanical, thermal, or

	chemical activation. The field of mechanochemistry can provide vital assistance on this issue.
Presence of heavy metals and metalloids such as Hg, Pb, Cr, V, Cd, Mn, Zn etc in variable quantities is observed in mineral wastes. This may leach into the environment when used in binders in construction.	Heavy metals and metalloids get encapsulated and are prevented from leaching when used in cementitious binder [222,223]. Also, under the aegis of circular zero waste economy, options are being explored to mine heavy metals from the mineral wastes before their disposal. This may help in removal of heavy metals prior to their disposal and eliminate the risk of leaching.[224].
Presence of Cu^{2+}, PO_3^{2+} which interfere with the hydration and setting processes.	The presence of such ions shall be noted, and the percentage of replacement shall be decided as to keep these ions within permissible limits. Cement technology methods can be utilised to alleviate hydration and/or setting issues.
Lack of guidelines and standards. The existing guidelines and standards do not explicitly provide a methodology for suitability assessment of mineral waste as an SCM or precursor for alkali activation.	More research and development should be carried out in this area to strengthen the knowledge data base to provide a rational approach and guideline towards use of mineral wastes or any new waste in cementitious binder. Currently with advent of Horizon Europe program and the United Nations SDGs, various research and innovation projects are spearheaded in this direction.

Identified research gaps

The past studies indicate a high potential for use of mineral wastes in cementitious binders. However, existing research also points out the following gaps

The absence of an activation method or mix design procedure which is more systematic rather than trial and error is evident.

In addition, there is no thorough study on zeolitic chemistry and geopolymerisation for the efficient use of mineral wastes. Future research should focus on kinetics of the reaction, reaction products, mathematical models for the strength and performance predictions, assessment of effect of contaminants.

2.14 Conclusions

The past studies discuss here provides an insight into the utilization potential and problems associated with the use of mineral waste in cementitious binders. It also indicates the areas in which more research is required. Based on these findings the present study shall address the following through the course of progress

i) Lack of assessment methods for a crystalline binder precursor
ii) Lack of systematic method for activation of mineral waste

CHAPTER 3
MATERIALS AND METHODS

3.1 General

This chapter provides the properties of materials used in the study and the experimental procedure adopted. The relevance of the findings of a particular test to the overall objective of the study is also briefly discussed. The description also includes sample preparation, test parameters, standard guidelines or reference adopted for a particular test.

3.2 Materials

3.2.1 Mineral Waste

This study aimed to investigate the feasibility of utilising two different mineral wastes. The objective is to assess the suitability of the implemented methodology for various waste streams characterised by its unique mineralogical compositions.

(a) Mine tailing

The mine tailing used in this study, is a by-product of graphite mining from Talga Group, Germany. The tailing used is generated from the floatation process of the finer ore concentrate. It is predominantly silicate and was provided in dry state which comprised a few lumps up to a size of 20 cm. A 100 kg of mine tailing was sampled and homogenised before use. The mine tailing was grey in colour and can be denoted by N4 as per Munsell scale [225].

(b) Silt

The silt used in this study was collected from Eco Aggregates, construction waste recycling facility in Hertfordshire, United Kingdom. The facility processes washed aggregates derived from construction and demolition waste, and the wash water is treated in a thickener tank with a flocculant. Lime solution is combined with the settled silt from the thickener vessel. The lime solution reacts with any clay present in silt, which increases solid sedimentation and improves filter drainage. The mixture is placed in a filter press, and the pure water is then drained away. Filter cakes composed of sediment are left on the filter. Fig. 3.1 illustrates the procedure. The particle size of these filter cakes ranges from 0.002 to 0.05 mm and were of a brown colour 5YR 6/4. To avoid any potential misleading and the confusion with natural silt, the silt used in this study will hereinafter be referred to as CDW derived silt.

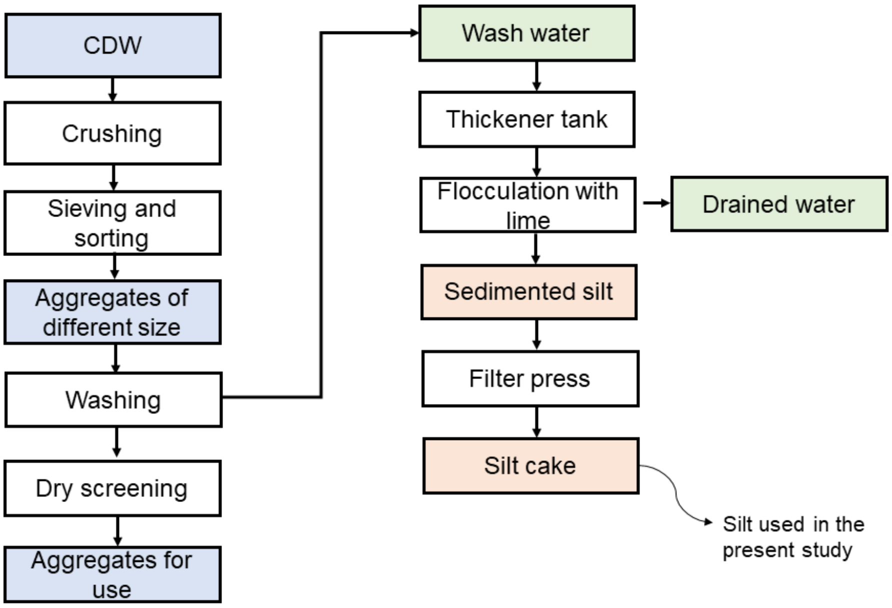

Fig. 3.1: Process of silt formation in the CDW recycling plant which was used for sampling in this study.

Fig. 3.2 shows a visual comparison of mine tailing and CDW derived silt with cement, fly ash and silica fume. The colour of fly ash, cement and silica fume can be denoted as N4, N5 and 4PB5/3 as per Munsell scale [225].

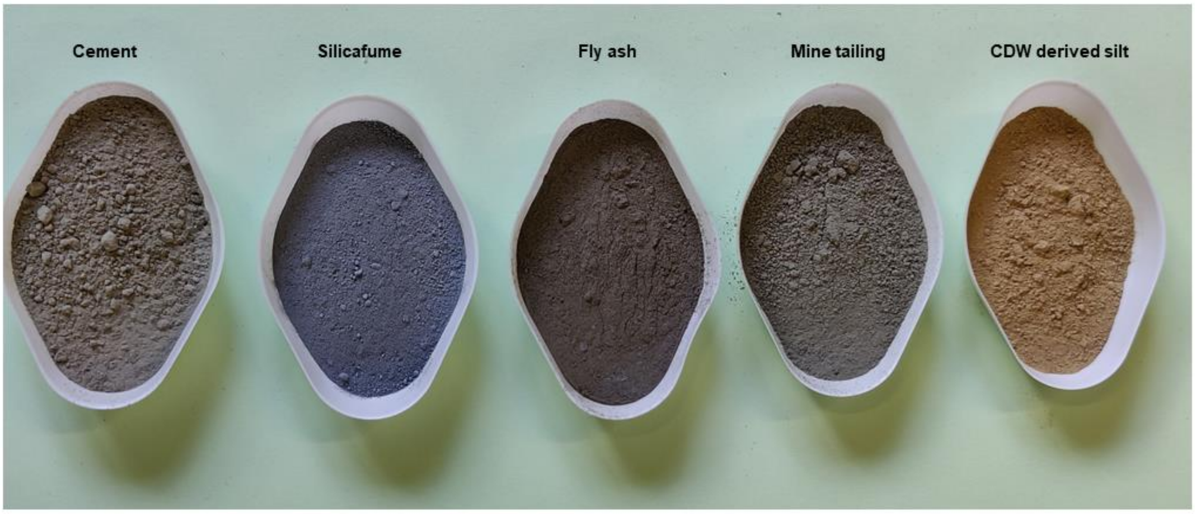

Fig. 3.2: Colorimetric comparison of cement, mine tailing, fly ash silica fume and CDW derived silt.

Both mine tailing and CDW silt are fully characterized in Chapter 4.

3.2.2 Chemicals and reagents

Laboratory grade chemicals and reagents were used in this study. Sodium hydroxide pellets of 98% extra pure grade from Acros Organics were used to prepare sodium hydroxide solution of required molarity using deionized water for dissolution studies. Potassium hydroxide, of 85% extra pure flakes, calcium hydroxide of 98% purity, and granular potassium sulphate of 99% purity from Acros organics were used in anhydrous form for the modified R3 tests along with calcium carbonate precipitate in powder form from Fisher scientific. Concentrated hydrochloric acid of specific gravity 1.18 and concentration 37% from Fisher scientific was used for pH adjustment of leachate for dissolution studies.

Concentrated HCl was diluted using deionized water used to prepare a 1 M HCl solution. Isopropyl alcohol of 99.7% purity was used for dispersion and cleaning to avoid contamination during analytical studies (SEM, TEM, ICP, XRD) and for hydration arrest of paste samples. Commercially available fly ash and silica fume were used for benchmarking purposes. The Si and Al ICP standard solution of concentration 1000 mg/mL in HNO_3 from Reagecon was used for calibration of ICP instrument in dissolution studies. Anatase from Thermo scientific and purity 98+% was used as a standard for XRD analysis. Phenolphthalein solution 1% in methylated spirit by Fisher scientific was used for carbonation tests.

3.2.3 Portland cement

Commercially available CEM-I 52.5 N high strength cement was used in the study. This cement confirms with the requirements of BS EN 197-1.

3.2.4 Fine aggregate

Graded silica sand confirming to EN 196-1 of size range 0.08 mm to 2.00 mm, as shown in Fig. 3.3 was used. For the duration of this research, the sand was stored in room temperature and dry conditions.

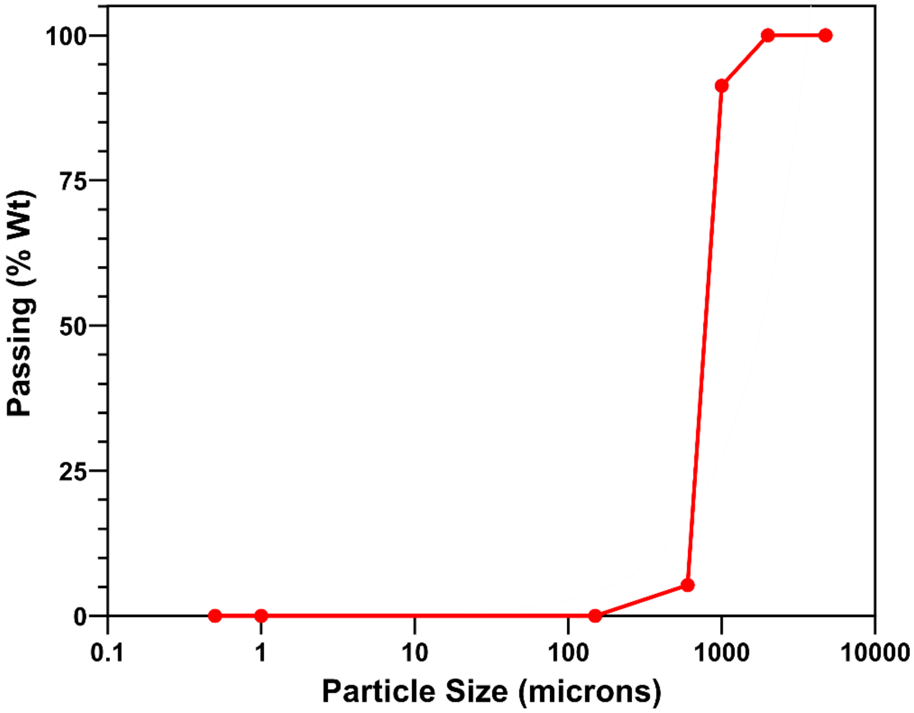

Fig. 3.3: Particle size distribution of sand used in the present study.

3.2.5 Water and super plasticizer

Deionised water was used for preparation of all the chemicals, paste and mortar mixes. Sika ViscoFlow - 2000 (GB), a polycarboxylate polymer based high range water reducing concrete admixture with enhanced workability retention was used to adjust the workability of paste and mortar mixes.

3.2.6 Silica fume and fly ash

Commercially available silica fume and low calcium fly ash were used for establishing a standard of comparison. A comparison of the heat of hydration was carried out across fly ash, silica fume, mine tailing and CDW-derived silt in R3 tests and cementitious paste mixes. The particles size distribution of cement, fly ash and silica fume used are given in Fig. 3.4.

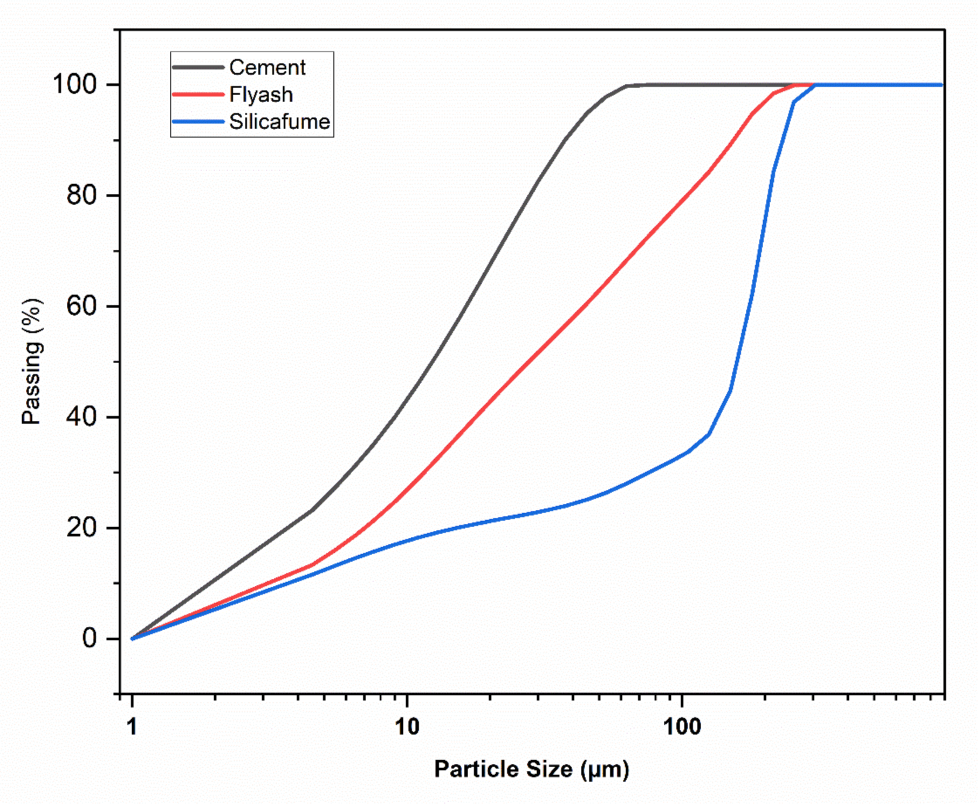

Fig. 3.4: Particle size distribution of cement, fly ash and silica fume used in the present study.

3.3 Experimental Methodology

The experimental methodology was designed in order to achieve the research objectives, as illustrated in Figure 3.5. The research was carried out in three phases. In the initial stage, analyses were conducted to characterise the raw mining tailings and CDW derived silt. Different activation methods were employed, taking into consideration the mineralogical characteristics. The research entailed analysis and comparison of the characteristics of untreated mine tailings and treated mine tailings, along with untreated CDW derived silt and treated CDW derived silt. In the second phase of the study, the samples that were activated optimally were chosen. Following this, paste mixes were prepared by replacing 10%, 20%, and 40% of cement with activated mineral waste and with water to binder ratio 0.3, 0.4 and 0.5. The rationale behind this selection was to explore variations both above and below the commonly accepted optimum replacement rate of 20% [226]. This approach was adopted to ensure a comprehensive assessment across a broader range of replacement percentages, and potential impacts on the material properties. The evaluation included an assessment of the microstructure development and mineralogical characteristics of the aforementioned paste mixes. The strength development and durability properties of mortar mixes with various percentages of cement replacement (10%, 20%, and 40%) and a water to binder ratio of 0.4. were evaluated in phase III.

3.3.1 Overview

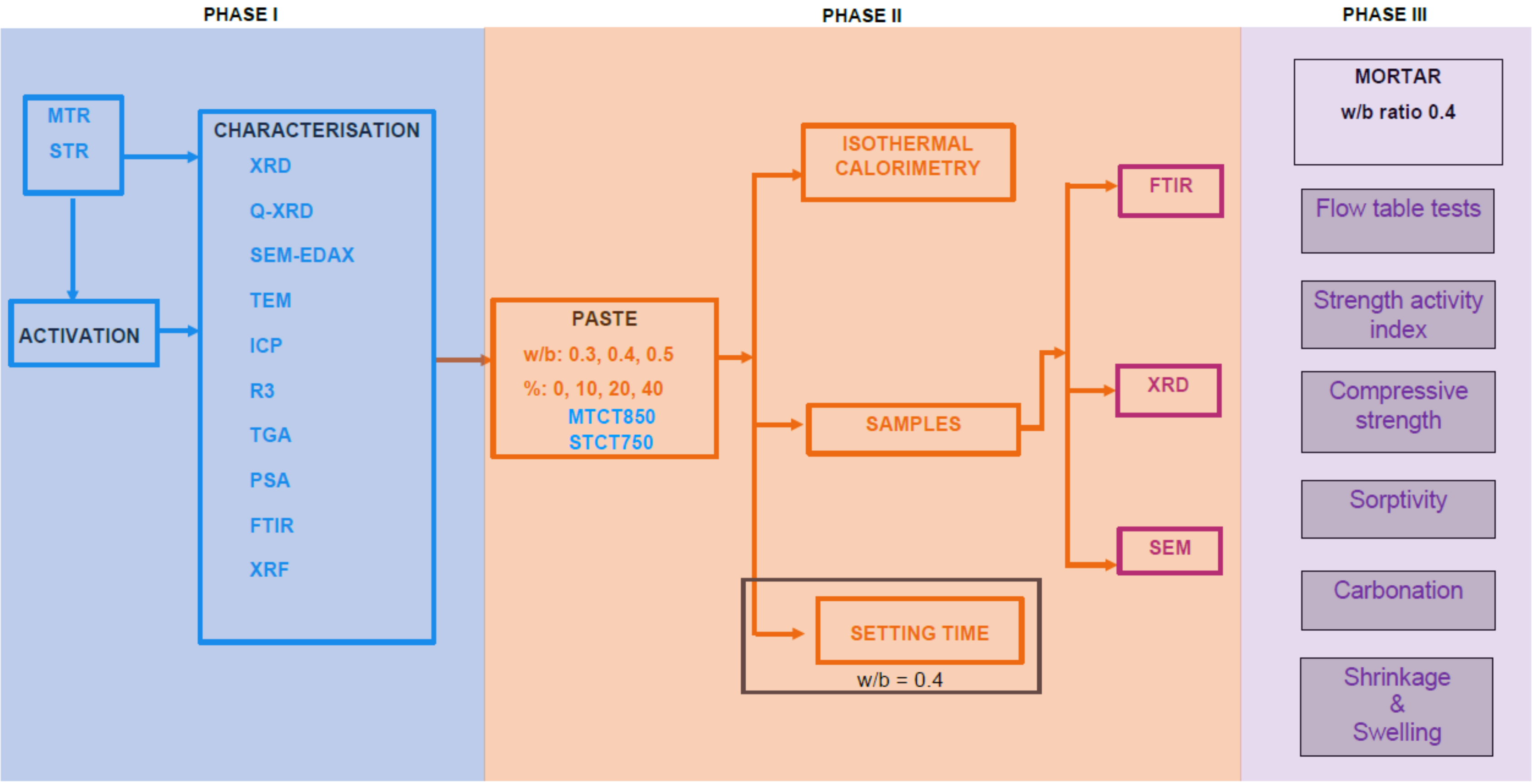

Fig. 3.5: Overview of the experimental methodology adopted in the study.

3.3.2 Activation of materials

The selection of the activation methods and the associated parameters was done following the identification of the mineral phases existing in the mine tailing and the CDW derived silt. Following the completion of activation procedures, the treated materials were then characterized and compared with the characteristics of untreated mine tailing and the untreated CDW derived silt to understand the change in properties following activation.

The as received tailings and the CDW derived silt were oven dried at 80°C for 24 hours and any lumps present were broken to pass the material through 600 μm. This was done to homogenise and achieve uniformity of sample. These samples were stored in airtight containers and placed in a vacuum chamber. Hereinafter, the oven dried and homogenised mine tailing and CDW derived silt will be referred to as MTR and STR respectively. MTR and STR were used for particle size analysis, microscopy, and chemical reactivity tests. For as analytical and microstructural studies (e.g., XRD, XRF and FTIR) which required finer samples, the prepared MTR/STR were ground using an agate mortar and pestle to pass through 150 μm sieve.

a) Thermal activation

The calcination temperatures were determined based on the minerology of the samples and recommendations from existing literature. As the initial XRD indicated presence of kaolinite, graphite and phlogopite, the calcination temperatures were chosen to be above 650°C. Literature reports that heating above 900 °C in presence of clay minerals such as kaolinite, illite leads to formation of new crystalline alumino silicate mineral phases such as mullite, which may reduce the reactivity of the activated mineral waste [227,228]. Therefore, calcination temperatures of 650°C, 750°C and 850 °C were adopted for mine tailing. In case of CDW derived silt the preliminary analysis indicates presence of calcite whose decomposition temperature is between 700°C and 800 °C [229]. A calcination temperature of 750°C and 850 °C were adopted for CDW derived silt.

Two regimes of calcination were adopted in this study: (i) sudden heating and cooling and (ii) uniform heating and cooling. In first method the samples were introduced inside a furnace in a cup shaped fused alumina crucible of 250 ml capacity, preheated to a set temperature of 650°C, 750°C or 850 °C and calcined for 2 hours. Once the calcination was complete the materials were transferred to a companion chamber at room temperature for cooling. These samples are designated MTCC650, MTCC750, MTCC850 and STCC750, STCC850. It was noted that the sample's calcination in this method of calcination was not uniform, producing a non-homogeneous powder. The final product, which had undergone calcination, was more red in colour towards the crucible's surface than it was at its bottom, which had a more grey coloured appearance. This demonstrates that the amount of calcination and oxidation varies depending on the depth of the material. Therefore, this CC series of samples were characterised thoroughly but considering the non-homogeneity was not considered for further studies in cementitious matrices.

In the second method, a tray shaped fused alumina crucible (of internal dimensions 217x95x60 mm and a wall thickness of 16 mm) was used. In this regime, a ramp-up rate of 300°C / hour was used to comply with the thermal expansion of crucible and prevent fracture due to thermal shock. To ensure uniform heating of the sample, this was evenly spread in the crucible to a height of 1.5 cm The samples remained at set temperature for 2 hours to ensure complete calcination. The standing time of two hours was chosen based on the methodology adopted in similar studies which confirmed that the phase transformation of iron bearing minerals can be ensured after calcination for 2 hours [228]. Following this, samples allowed to cool gradually in the furnace to avoid thermal shock due to sudden exposure to the atmosphere and removed when it reached room temperature. These samples were named MTCT650, MTCT750, MTCT850 and STCT750, STCT850. The adopted calcination regimes are shown in Fig. 3.6 and the crucibles are shown in Fig. 3.7 (a).

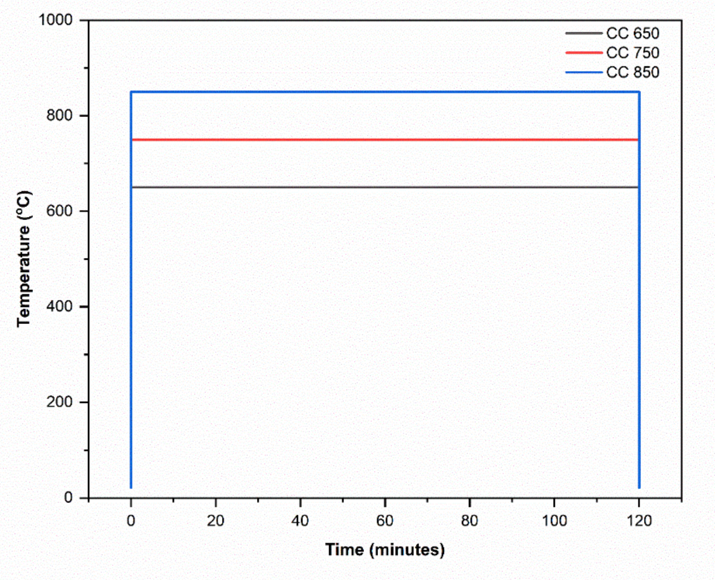

(a)

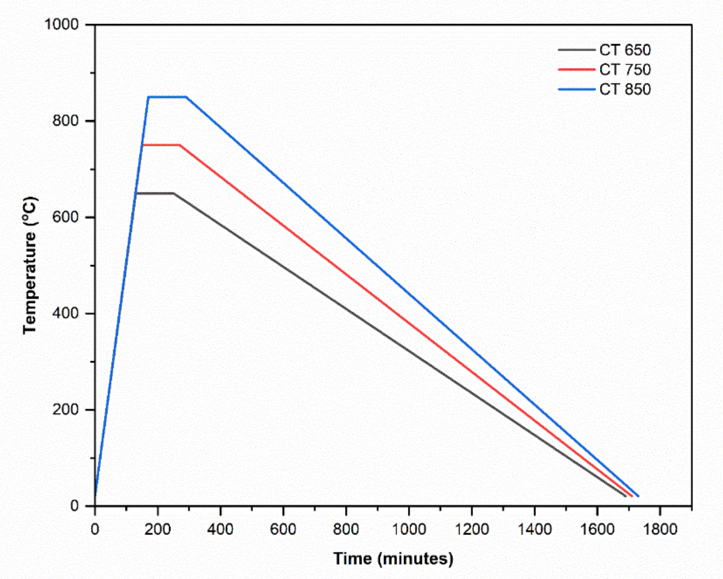

(b)

Fig. 3.6: Heat treatments adopted in the study. (a) heating and cooling adopted for CC samples (b) uniform heating and gradual cooling adopted for CT samples.

b) Mechanical-chemical activation

Mechano-chemical treatment refers to structural and/or chemical changes that increase reactivity of minerals [133]. In this study, this was facilitated by ball-milling with the intention to increase structural disorder in the minerals which in turn will improve their chemical reactivity. The milling was carried out in a Fritsch Pulversiette 6 planetary ball mill as shown in Fig. 3.7 (b). The initial screening of MTR/STR with XRD (See Chapter 4, Section 4.4) indicated presence of minerals of hardness 2-7 in the Mohs hardness scale. Indicatively, diamond's hardness is a 10 at Mohs scale while calcite is at 3 [230]. Therefore, balls and jar made of tungsten carbide, of hardness 9 at the Mohs scale were used for grinding, to prevent wear/tear of the balls and jar, and subsequent contamination of the material. The milling time of 30 minutes (MTBM30 & STBM30), 60 minutes (MTBM60& STBM60) and 90 minutes (MTBM90& STBM90) were adopted following relevant observations reported in the literature [86]. It has been reported 20 minutes of milling led to reduction of integral intensity of crystalline peaks and after 80 minutes of milling there was reduction in crystallinity of quartz, albite (plagioclase) and muscovite [86]. The kinetic energy imparted during milling is directly proportional to the diameter of the balls raised to the power four [231]. As the maximum particle size of the material used for grinding is expected to be less than 600 microns after sieving, the maximum suitable size of 10 mm balls was used, to optimize the diameter and the imparted collision energy (kinetic energy) [231]. Twenty 10 mm balls each weighing 10g were used to grind 80 g of powder in a 250 mL jar, making the ball weight to powder ratio by mass to be 2.5. The highest safe operation speed of ball mill used in this study was 500 rpm and the same was adopted in the present study.

Crucibles used for calcination

(b)
Planetary ball mill

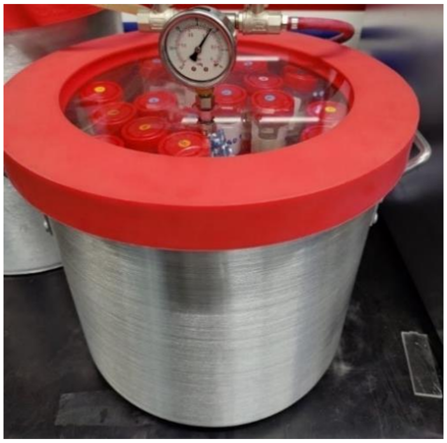
(c)
Vacuum chamber


(d)
Preparation of paste samples


(e)
Curing of paste samples


(f)
Preparation of mortar samples


(g)
Flow table test

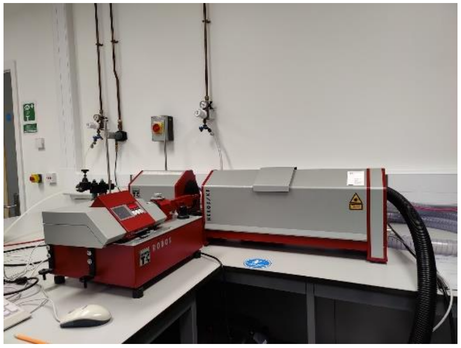
(h)
Laser particle size analyser

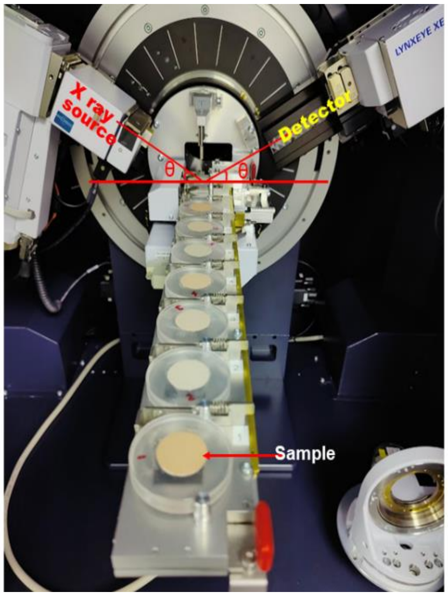

(i)
X-ray Diffractometer

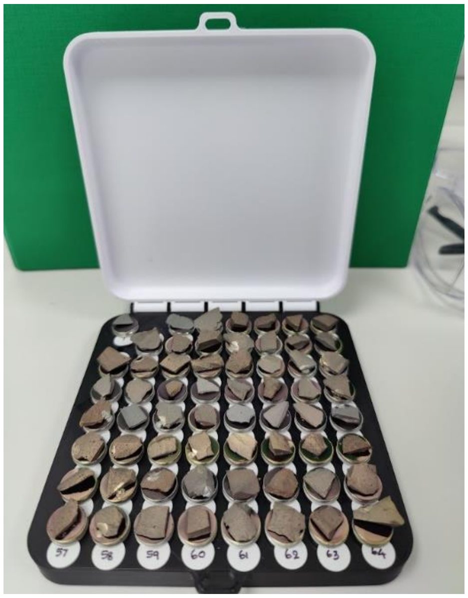

(j)
Gold coated paste samples for SEM

(k)
Scanning electron microscope

(l)
Fourier transformed infrared spectrometer

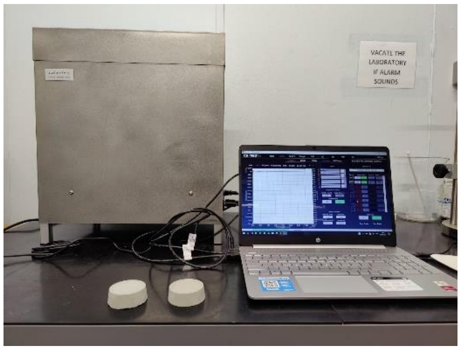

(m)
Isthermal calorimeter

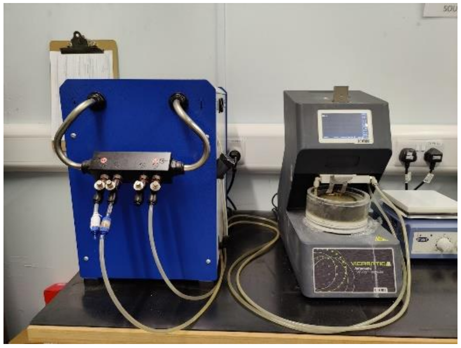

(n)
Automatic Vicat apparatus

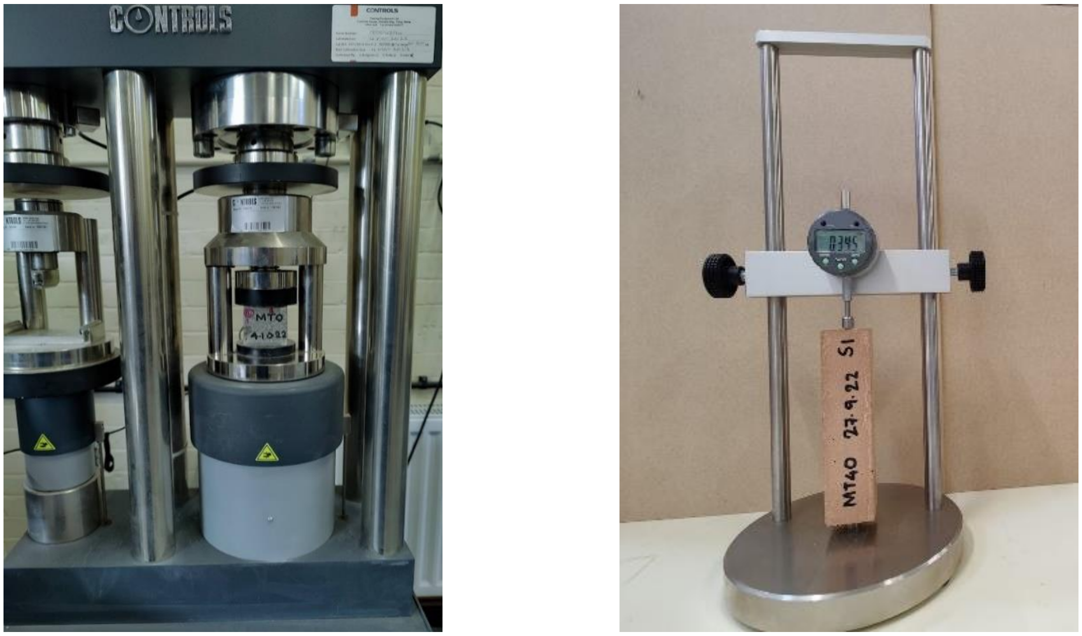

(o)
Compression testing machine

(p)
Length comparator

(q)
Carbonation chamber

(r)
Climate chamber

Fig. 3.7: Sample preparation and test set up for different tests.

c) Sample nomenclature

The nomenclature used in this study is as follows: The mine tailing samples have the prefix MT and silt samples have the prefix ST. Raw samples without any treatment are indicated by R. The samples heated and cooled rapidly in cup shaped crucibles are called CC and gradually heated and cooled in tray are called CT. The ball milled samples are called BM. The number indicates calcination temperature or milling time depending on the followed procedure. The nomenclature used for different samples in the present study are given in Table 3.1.

Table 3.1: Associated nomenclature and description of samples used in this study

Sample	**Description**
MTR	Raw Mile Tailing
STR	Raw CDW derived Silt
MTCC650	Mine tailing calcined at 650ºC in a cup shaped crucible
MTCC750	Mine tailing calcined at 750ºC in a cup shaped crucible
MTCC850	Mine tailing calcined at 850ºC in a cup shaped crucible
STCC750	Silt calcined at 750ºC in a cup shaped crucible
STCC850	Silt calcined at 850ºC in a cup shaped crucible
MTCT650	Mine tailing uniformly calcined at 650ºC in a tray shaped crucible
MTCT750	Mine tailing uniformly calcined at 750ºC in a tray shaped crucible
MTCT850	Mine tailing uniformly calcined at 850ºC in a tray shaped crucible
STCT750	Silt uniformly calcined at 750ºC in a tray shaped crucible
STCT850	Silt uniformly calcined at 850ºC in a tray shaped crucible
MTBM30	Mine tailing ball milled for 30 minutes
MTBM60	Mine tailing ball milled for 60 minutes
MTBM90	Mine tailing ball milled for 90 minutes
STBM30	Silt ball milled for 30 minutes
STBM60	Silt ball milled for 60 minutes
STBM90	Silt ball milled for 90 minutes

3.3.3 Sample preparation

a) Samples for microstructural analysis and mineralogy

Powder

The powder samples were prepared as discussed in section 3.3.2 and stored in airtight containers in a vacuum chamber as shown in Fig. 3.7 (c).

Cementitious matrices

Based on the findings of the characterisation of untreated and treated mine tailings and CDW derived silt, MTCT850 and STCT750 were found to be more suitable for replacement of cement in binders (The findings are discussed in detail in Chapter 4). Hence, the further studies on paste and mortar were performed with these samples and compared with OPC.

A total of 21 paste mixes as given in table 3.2 were prepared with 0, 10, 20 and 40% of MTCT850 and STCT750 as cement replacement. The water cement ratios of 0.3, 0.4 and 0.5 were adopted.

Required amount of dry powder was mixed and homogenised in an airtight container. Estimated amount of water and required amount of superplasticizer were added to the mixed powder. The dosage of superplasticizer was varied to ensure that a constant workability was maintained across all the mixes. The water was gently stirred into the container and mixed using a vortex mixer for 2 minutes. This mix was then used for testing setting time, heat of hydration or cast into samples. The samples were cast in plastic containers in form of cylindrical discs of 50mm diameter and 25 mm height as shown in Fig. 3.7 (d). The samples were demoulded and cured in a water bath set at 23°C as seen in Fig. 3.7 (e). These samples were tested at the ages of 7, 14, 28, 56 and 90 days.

Samples were taken out of the water bath at the test age and air dried for 2 hours. These air-dried samples were broken into smaller pieces of size less than 2 cm using a hammer. These smaller pieces were immersed in isopropyl alcohol for 48 hours to remove all the water. These samples were oven dried at 60°C for 24 hours to evaporate the iso propyl alcohol. The oven dried samples were stored in an airtight container in a vacuum chamber. SEM analyses were performed on these fractured pieces. These pieces were taken out of vacuum just before test and ground to a fine powder of size less than 150 µm using an agate mortar and pestle. This powder was used for XRD and FTIR.

Table 3.2: Nomenclature and description for binder paste mixes

Nomenclature	**w/c ratio**	**OPC (%)**	**Replacement**	
			Material	**%**
OPC W30	0.30	100	-	0
OPC W40	0.40	100	-	0
OPC W50	0.50	100	-	0
MT10 W30	0.30	90	MTCT850	10
MT20 W30	0.30	80	MTCT850	20
MT40 W30	0.30	60	MTCT850	40
MT10 W40	0.40	90	MTCT850	10
MT20 W40	0.40	80	MTCT850	20
MT40 W40	0.40	60	MTCT850	40
MT10 W50	0.50	90	MTCT850	10
MT20 W50	0.50	80	MTCT850	20
MT40 W50	0.50	60	MTCT850	40
ST10 W30	0.30	90	STCT750	10
ST20 W30	0.30	80	STCT750	20
ST40 W30	0.30	60	STCT750	40
ST10 W40	0.40	90	STCT750	10
ST20 W40	0.40	80	STCT750	20
ST40 W40	0.40	60	STCT750	40
ST10 W50	0.50	90	STCT750	10
ST20 W50	0.50	80	STCT750	20
ST40 W50	0.50	60	STCT750	40

b) Samples for strength and durability tests

Mortar mixes of comparable consistency (detailed in section 3.3.12) as listed in table 3.3 with water cement ratio 0.4 and cement to sand ratio 1:1.5 were prepared. A mixing time of 2 minutes of dry mixing, 2 minutes of low-speed wet mixing and 1 minute of high-speed wet mixing was adopted. These mixes were cast into cubes and prisms as shown in Fig. 3.7 (f) for various tests as given in table 3.4. The moulds were filled in three layers and tamped 25 times using a steel tamping rod after each layer. After the final layer was filled the mould were vibrated for 60 seconds to achieve compaction. The excess mortar was struck off and the samples' surfaces were finished using a steel trowel. At all stages care was taken to make sure there was no bleeding or segregation of the mix.

Table 3.3: Nomenclature and description for mortar mixes

Nomenclature	OPC (g)	Replacement		Water (g)	SP dosage (g)
		Material	(g)		
OPC W40	4000	-	0	1600	-
MT10 W40	3600	MTCT850	400	1600	12
MT20 W40	3200	MTCT850	800	1600	24
MT40 W40	2400	MTCT850	1600	1600	38
ST10 W40	3600	STCT750	10	1600	12
ST20 W40	3200	STCT750	20	1600	24
ST40 W40	2400	STCT750	40	1600	36

Table 3.4: Details of samples per mix for study of bulk properties

Test	Sample size (mm)	Number of samples	Remarks
Compressive strength test and Strength activity index	Cube 50×50×50	15	Samples were tested at different ages 7, 14, 28, 56, and 90 days. The strength values from the same samples were used to calculate strength activity index
Sorptivity	Cube 50×50×50	3	The test was performed after curing the sample for 28 days.
Shrinkage	Cube 160×40×40	6	A set of 3 samples were used for shrinkage and 3 for expansion.
Carbonation	Cube 160×40×40	6	A set of 3 samples were placed in carbonation chamber and 3 in companion chamber with same temperature and humidity conditions.

3.3.4 Particle size analysis

Laser diffraction is the process of measurement of particle size distributions by measuring the angular variation in intensity of light scattered as a laser beam passes through a dispersed particulate sample. The particle size distribution of the raw and ball milled samples was determined using a laser particle size and particle distribution instrument (HELOS/KF) with RODOS dry dispersion as shown in Fig. 3.7 (g). In this study, the R5 lens was used, covering the size range between 0.5 – 875 µm.

3.3.5 Powder X ray diffraction

In the technique of X-ray powder diffraction, the surface of the sample is exposed to a monochromatic X-ray beam at an angle θ, as depicted in Figure 3.7 (i). The X-rays experience constructive interference after diffraction by the crystalline phases within the sample, and are then detected by a goniometer at an angle θ. The Bragg's law illustrates this principle. [232] (Eq. 3.1). Scanning over a range of angles of X ray incidence produces a pattern characteristic for the analysed crystalline phase. This can be used to derive insights about the crystalline phases present in the material such as spacing between the lattice planes which can then be used to identify the crystalline phases.

$$n\lambda = 2d \times \sin\theta \qquad \text{Eq. 3.1}$$

where,

n is the order of interference band
λ is the wavelength of X rays
d is the spacing between crystal planes
θ is the angle of incidence.

X-ray diffractometry in this study was performed using a Bruker D8 Advance X-ray diffractometer (XRD) with Cu-Kα radiation of wavelength 1.540549 Å and radiation energy of 8.04 keV to study the mineralogy. The fine powder (prepared as described in 3.3.2 and 3.3.3) was spread on the sample holder and a glass plate was used to strike of the excess material and achieve a flat and smooth surface. The smooth surface ensured that there are no preferred orientation and eliminates any variations in intensity arising because of it.

The XRD analysis for performed for a 2θ value ranging between 5° and 80°, at a speed of 0.01 ° / step and 1 sec/ step for characterization of raw and activated mineral waste samples. And the 2θ value ranging between 5° and 60°., at a speed of 0.05 ° / step and 2 sec/ step was adopted for analysis of hydration arrested paste samples. In order to provide a comprehensive examination of the material, the characterization of samples was conducted using a broader range of 2θ values and smaller step intervals. This approach was employed due to the uncertain nature of the phases present in the material.

HighScore Plus X-ray diffraction software was used for the analysis of the XRD results [233]. For quantification of phases Rietveld analysis was performed using Anatase as an internal standard.

3.3.6 Electron microscopy and energy dispersive X-ray analysis

When an incident electron beam interacts with the surface of a material, it undergoes a sequence of elastic and inelastic collisions before leaving from the surface. The electrons emerging from the surface are collected by a charged detector, thereby generating an image that depicts the topographical features of the material. [232]. A scanning electron microscope facilitates such observation. In this study microstructural morphology observations of the samples were conducted using a scanning electron microscope (SEM) (JSM-5700F, JEOL) operated at 20kV and 16 mm to 22 mm working distance. The working distance varied with the sample and the magnification at which it was observed. Aluminium pin stubs of 12.5mm diameter, 3.2 x 8mm pin with carbon adhesive discs were used for preparation of samples for SEM analysis. Powder samples were used for mineral waste samples before and after activation and fractured pieces of size less than 10 mm were used for cementitious paste samples as shown in Fig. 3.7 (j). The samples were sputter coated with gold. The coating time was adjusted to be between 45 s to 60 s and was finalised after a trial observation through the microscope in Fig. 3.7 (k).

EDAX X-ray microanalysis was also performed to identify the elements present. An acceleration voltage of 15kV and a spot size of 47μm was adopted to get a clear image based on trials. An average of two obtained spot values are reported in this study.

Transmission electron microscopy (TEM) was performed at 200 kV using a JEOL JEM-1400F for observations of physical and morphological changes in the individual particles with the applied treatment. Isopropyl alcohol was added to 1 g of powder sample (listed in Table 3.1) in a test tube till it formed a colourless suspension. This suspension was subjected to ultrasonication for 1 minute at a frequency of 20 kHz. A drop of this dispersed sample was mounted on a holey carbon film on 300 mesh copper grids (from Agar scientific) using a micro pipette. The grid was allowed to dry at a drying chamber at 27^{o}C for 3 hours allowing the isopropyl alcohol to evaporate completely. Following this, the grids were placed in the TEM chamber for analysis.

3.3.7 X-ray fluorescence analysis

Panalytical Zetium WDXRF (Wavelength Dispersive X-ray Fluorescence) and Panalytical SuperQ software, was used to determine the oxide composition of the silt. The data was calibrated using the WROXI (wide-ranging oxides) standard to calculate the oxide concentration in weight percentage. The test was performed on a 40 mm diameter fused bead prepared in a platinum crucible and casting dish by mixing 10 g lithium tetraborate and 1 g clinker at 1065°C using a Claisse LeNeo Fluxer.

3.3.8 Fourier-transform infrared analysis

The application of Fourier transform infrared spectrometric analysis (FTIR) is commonly employed in mineral research for the examination of molecular structure and nature of chemical bonds in the mineral phases present. The molecular bonds exhibit absorption of distinct resonant frequencies that correspond to the vibration and rotation energies, thereby revealing the attributes of a molecular structure [234,235]. The findings of these studies in connection with the XRD results can help corroborate the efficiency of the treatment process or the phase development during hydration. FTIR studies were performed to identify the structural changes in the chemical bonds present in the mineral waste before and after activation. The changes in powdered hydration arrested cementitious paste samples at different ages were also studied.

ATR-FTIR Spectroscopy instrument by Shimadzu IRSPIRIT Infra-red spectrometer igiven in Fig. 3.7 (l) was used for the FTIR studies. Attenuated total reflectance (ATR) is a sampling technique that allows for the direct analysis of solid or liquid samples without the need for additional preparation. The process employs total internal reflection to produce an evanescent wave that infiltrates the sample, generating valuable molecular information. The ATR crystal was wiped cleaned using an isopropyl alcohol solvent. The swivel press was lowered to establish optical contact with the crystal and FTIR reading was recorded. This is considered as the background data for testing the sample. This data provides the results of interaction of IR with atmosphere and was eliminated from the sample data to ensure any atmospheric influence is eliminated from the test results. Subsequently, the powder sample (prepared as described in section 3.3.3) was placed onto the ATR crystal and firmly pressed down using the swivel press to provide the optimal contact between the sample and crystal. Measures were implemented to ensure a consistent pressure was maintained between the press and the crystal for all the samples. For each sample 16 scans were taken between 4000 cm^{-1} and 600 cm^{-1} using the LabSolutions IR Spectrum software.

3.3.9 Dissolution of Si and Al

Solubility of Si and Al in NaOH are good indicators of availability of Si and Al within an alkali activated system for condensation and gel formation [164,236]. Identifying, the solubility of Si and Al, conclusions can be drawn as to whether the activated mineral waste can be utilized a key compound to produce alkali-activated binders. Moreover, Si and Al are of particular significance, as they are the key elements participating in pozzolanic reactions to form C-S-H, C-A-H and C-A-S-H phases.

The solubility tests were carried out with 8M NaOH. For each 1g oven dried material passing through 150 µm sieve, 50 g alkaline solution was added and mixed using a magnetic stirrer for 6 hours. The solution was filtered through a 0.45 µm pore size filter. The leachate was diluted using deionized water at 1:50 ratio. This diluted leachate was acidified to a pH of 2 using 1M HCl to prevent settling of the ions. An Inductive Coupled Plasma Optical Emission Spectrometer (ICP-OES) fitted with a sea spray nebulizer and SPS3 autosampler was used for determining Si and Al leached into the alkaline solution from the mineral waste.

3.3.10 Isothermal calorimetry

Chemical reactivity by adapted R3 test

The assessment of the chemical reactivity (pozzolanicity) of the treated tailings within a simulated cementitious matrix was performed following the provisions of R3 test (ASTM C1897(2020)) but at modified temperature (60^oC instead of 40^oC). Due to the low reactivity observed in both the MTR and STR samples, i the heat of hydration for these samples in R3 test were rather low when the test was performed at 40 ^oC, this resulted in heat flow values indistinguishable from system noise. It has been reported [237] that the latent hydraulic reaction and pozzolanic reactions in presence of calcium hydroxide can be activated by increase in temperature. Therefore, the test temperature was increased from 40^oC to 60^oC consequently, enhancing the reactivity for non-reactive and less reactive materials [237]. Nevertheless, it is crucial to take into account that performing the test at an elevated temperature renders the results not comparable to the typically performed R3 test values and also results in a reduction in the recorded heat of hydration [237].

The experimental procedure involved producing a mix containing 10g mineral waste, 30g calcium hydroxide, 5g calcium carbonate and 54 g potassium solution. The potassium solution contains 4.00 g/L potassium hydroxide and 20.0 g/L of potassium sulphate dissolved in deionised water. The heat of hydration of this mix was monitored, using an I-Cal HPC - High Performance Calorimeter, for a period of 7 days under the constant temperature of 60^oC. The first 75 minutes of the tests were not taken into consideration due to temperature differences as recommended [238–240]. Cumulative heat, at the end of three and seven days, per gram of material was reported. The higher heat of hydration indicates a higher degree of reactivity.

To minimize the difference in temperature all the materials and the containers used were conditioned at 60^oC for 24 hours prior to the start of the procedure. If the first 75 minutes of the heat of hydration are truncated during the R3 test at 60C, there is a larger likelihood of losing crucial information on initial hydration process. The maturity of concrete is a function of time and temperature. The concrete maturity at a temperature of 60°C after a duration of 75 minutes is equivalent to the concrete maturity after a duration of 112 minutes at a temperature of 40°C. This suggests that doing the R3 test at 60°C results in a loss of data equivalent to the first 112 minutes at 40°C. Therefore, in addition to the mineral waste samples, for benchmarking purposes the R3 test was performed at 60°C for silica fume and fly ash which are known for their reactivity in cementitious systems.

Heat of hydration of cementitious pastes

The heat of hydration of the cementitious binder mixes listed in table 3.2 was recorded for 72 hours using I-Cal HPC - High Performance Calorimeter shown in Fig. 3.7 (m) at 23^oC. 50 g of paste prepared as described in section 3.3.3 was placed in airtight containers which were in turned placed in the calorimeter for measurement of heat of hydration. The heat of hydration was recorded was 72 hours. The first 8 minutes of the test was neglected to remove the effects of temperature difference between the sample and the calorimeter. The cumulative heat of hydration at the end of test period is reported as Joule/g of cementitious binder. The average heat of hydration of 2 samples were considered for a particular mix.

3.3.11 Setting time

The setting time tests were performed in accordance with BS EN 196 -3: 2016 [241] , using an automatic Vicat apparatus, Vicamatic 3 from controls. The setting time tests were performed for the 7 different mixes of paste samples with water to cementitious binder ratio 0.4 given in Table 3.2. As the strength test samples were prepared with water to cementitious binder 0.4, the setting time results can be correlated to the findings. The paste prepared as described in section 3.3.3 (a) was filled in Vicat mould and this mould was placed in the base of the cylindrical Perspex pot and mounted on the stage of Vicat apparatus. This pot was filled with deionised water and the circulator set at 23^{o}C. This ensured that the test performed under controlled conditions throughout the overall duration of the process. The test temperature was chosen to be the same as that of the heat of hydration tests performed in Isothermal calorimetry to ensure findings of tests were comparable. The plunger was programmed to drop 44 times as per the standard at different time intervals throughout the test. The initial setting time was reported as the time at which the depth of penetration was 5 mm from the bottom of the plate.

3.3.12 Workability by flow table test

Initial trial mixes were prepared for the mixes mentioned in section 3.3.3, without the use of a superplasticizer. The mixes were poured into a truncated conical brass mould with dimensions of 60 mm in height, 100 mm in bottom diameter, and 70 mm in top diameter. The mould was positioned above a flow table and subsequently filled in a two-layers. To ensure adequate compaction, each layer was stroked ten times. The excess mortar was carefully struck off, and the mould was removed vertically. The flow table was subjected to 15 jolts, and the diameter of the mortar spread of mortar as shown in Fig. 3.7 (g) was measured at right angles. The OPC mixes has a spread diameter of 135mm. It was also observed that the spread decreased with increase in percentage of mineral waste. Super plasticiser was added in increments until all the mixes had a comparable workalibity, where the diameter of the spread was 130 mm – 140 mm. These dosages of superplasticiser were recorded and used for preparation of mortar samples for other tests.

3.3.13 Strength development

The compressive strength of the mixes was determined by testing 50×50×50 mm cubes at the age of 7, 14, 28, 56 and 90 days. The samples were tested using Automax multitest controlling a 300kN compression frame in Fig. 3.7 (o). The samples were loaded till failure at a rate of 2.4 kN/s and the failure load was noted. The compressive strength (fc) was calculated Eq. 3.2. Three samples were tested for a given age and the average was reported as strength values.

$$fc = \frac{P_{max}}{A} \qquad \text{Eq. (3.2)}$$

where

P_{max} is the failure load
A is the area of sample

3.3.14 Shrinkage

The shrinkage tests were performed in accordance with BS EN 12617-4 [242]. A set of 6 samples were prepared per mix. 40×40×160 mm prism samples were cast with recessed cylindrical stainless-steel studs of diameter 10 mm and length 10mm were embedded in the samples at the time of casting to facilitate the shrinkage measurement. Of the 6 samples, 3 were stored in a water bath at 21±2ºC for swelling measurement and 3 were stored at a temperature 21±2ºC of and a relative humidity of 60±10% in a TAC - Advance Climatic Cabinets by Controls for shrinkage measurements. The samples were removed from the storage condition, the studs were wiped clean, and the length and mass of the sample were recorded. Measurement of length of the sample was performed using a length comparator of accuracy 0.001 mm as shown in Fig. 3.7 (p). The length change readings were monitored for a period of 150 days. The shrinkage and expansion were calculated using the formula given in Eq. 3.3 and reported as shrinkage or swelling strain for the particular age.

$$\Delta L = \frac{L_{t-} L_i}{L} \qquad \text{Eq. (3.3)}$$

where,

ΔL is the change in length of sample represented in %
L_t is the Length of sample after curing time t
L_i is the length of sample on the first comparator reading
L is the length of the reference rod, 160 mm

3.3.15 Carbonation

Carbonation tests were performed in accordance with BS EN 13295: 2004 [243]. A set of 6 prism samples of size 40×40×160 mm was cast per mix. These samples were demoulded after 24 hours and cured in water bath for 27 days. After 28 days from casting the samples were shifted to a climatic chamber at a temperature of 21±2ºC and a relative humidity 60±10%. TAC - Advance Climatic Cabinets by Controls was used for this purpose. After 14 days of conditioning, 3 samples were moved to a carbonation chamber set at a temperature of 21±2ºC, a relative humidity 60±10% and an atmosphere of 1% CO_2. Memmert CO_2 incubator ICO was used to maintain the sample in above said conditions. Remaining 3 samples remained the climatic chamber and served as a control measurement for the carbonation studies.

These samples were removed at an age of 7,28 and 56 days and 1.5 cm pieces were taken from the sample. The fractured surface of these pieces was sprayed with phenolphthalein (the details of which are described in section 3.2.3) and the depth of colouration was measured after 1 hour. The change in colour of phenolphthalein from colourless to pink indicates absence of carbonation. Measurements were taken on all four sides of the piece from the outer edges and 5 measurements were taken per side. The average of above readings was reported as carbonation value.

3.3.16 Sorptivity

Sorptivity of a material represents ability of the material to absorb and transmit water through it via capillary suction[244]. Cube specimens, with dimensions 50x50x50 mm, were cast and subjected to curing until reaching the requisite testing age of 28 days. A triplicate of samples were used per mix. Following this curing period, the specimens were carefully removed from a water bath, surface dried and subsequently transferred to an oven maintained at a controlled temperature of 40°C for a duration of 72 hours, as stipulated in reference [245].

The oven dried specimens were taken out of the oven and enveloped on all four side faces with adhesive tape, a precautionary measure to prevent any inadvertent water absorption. The exposed lower surface of each specimen was then placed on a support such that the bottom surface of the samples is in contact with water, and the change in specimen weight was methodically recorded over a time span of 4 hours and 16 minutes. The water level was maintained throughout the duration of test.

3.4 Conclusions

This chapter serves as a comprehensive overview of the essential elements that underpin the present study. It emphasizes the significance of materials, outlines our experimental procedures including sample preparation and relevance of the findings with respect to the aim of the study. In summary this chapter serves as the foundation for the subsequent chapters, where we will discuss in detail the specific experiments and their results. The information presented here provides context and sets the stage for the detailed analysis to follow.

CHAPTER 4
CHARACTERIZATION OF MATERIAL AND CHEMICAL REACTIVITY

4.1 Introduction

This chapter provides an overview of the chemical, morphological, and mineralogical characterization studies conducted on the mine tailing and CDW silt samples, both before and after activation. The chapter presents findings that led to the selection of mixes for the evaluation of cementitious matrices.

However, it is to be noted that, though the thermally activated CC samples are characterized, due to non-homogeneity of the powder prepared by this method they were not considered for further studies in cementitious matrices. The issue of non-homogeneity with CC samples was discussed in the preceding chapter.

4.2 Particle Size Distribution

The process of mechano-chemical activation, and more specifically through high energy milling, introduces notable alterations in the physical and structural properties of materials. Among these changes, the particle size emerges as a crucial physical characteristic. Hence, the examination of particle size distribution prior to and subsequent to milling provides valuable insights into the alterations induced by the milling process. Fig. 4.1 presents the results of particle size distribution analysis conducted on the mine tailing and CDW derived silt samples. The charts presented in Fig. 4.2 illustrate the decrease in D_{50} and D_{90} values for mine tailing and CDW derived silt samples as a result of the milling process where the value corresponding to D_{50} indicates that 50% of the particles are smaller than this size and D_{90} indicates 90% of the particles are smaller than this size.

The MTR samples had about 99% of particles finer than 67 µm. This was further reduced to 15.66 µm after 90 minutes of milling. The particle size distribution as shown in Fig. 4.1 indicates a uniform size distribution of the samples and the gradual reduction in particle size after milling for 30 minutes (MTBM30), 60 minutes (MTBM60) and 90 minutes (MTBM90). The median particle sizes (D_{50}) were reduced by 37.82%, 46.67% and 55.54% from the initial particle size after 30, 60 and minutes of milling respectively, whereas for D_{90} the reductions were 4.36%, 15.06% and 76.62% respectively. This indicated that the longer duration of milling is more effective for reducing the particle size of coarser particles and did not have a significant effect on the finer particles for the chosen size of grinding balls, 10 mm. Although it is possible to reduce the particle size further by reducing the ball size [231] , it was not explored within the scope of this study.

The CDW derived silt used in the study classified also as a fine material with 99% of its particles being finer than 123.58 µm, making it slightly coarser than the mine tailing used in the study. It can be observed from Fig. 4.1) that the STR was uniformly graded, and particle size reduced with milling. However, the effect of milling on reduction of particle size was less prominent after 30 minutes of milling. As seen from Fig. 4.2, the D_{50} and D_{90} values reduced by 52% and 82%

respectively after 30 minutes (STBM30), whereas it was 66.7% and 86% after 60 minutes (STBM60), and 72 % and 85.5% after 90 minutes of milling (STBM90).

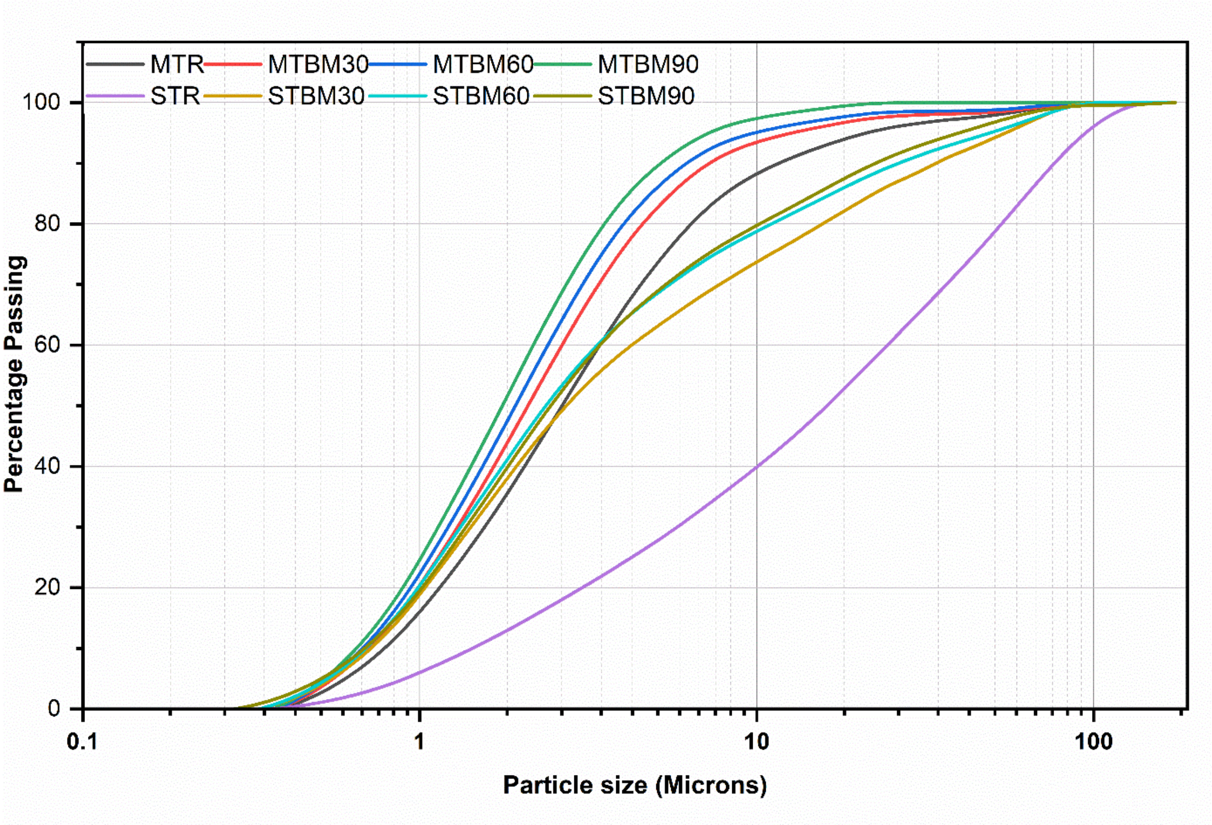

Fig. 4.1: Particle size distribution of mine tailing and CDW derived silt samples before and after milling.

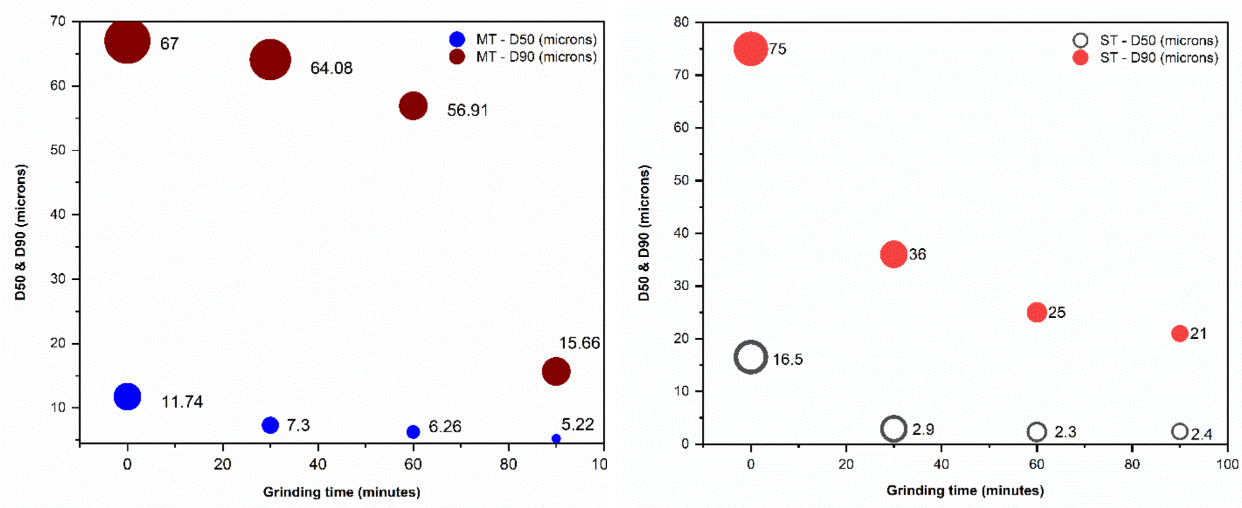

Fig. 4.2: Decrease in D90 and D50 particle size of mine tailing and CDW derived silt with increase in milling time.

4.3 Chemical Composition

The oxide compositions of MTR and STR used in the study were determined using XRF analysis and are given in Table 4.1. For comparison, similar compositions of cement, mine tailing and CDW derived silt from published research, and other commercially available supplementary cementitious materials (SCM) such fly ash, silica fume, and GGBFS are also provided. It can be seen from Table 4.1 that SiO_2, Al_2O_3 and Fe_2O_3 and CaO are the major oxides present in MTR and STR which is similar to that of cement and other SCM. The SiO_2, Al_2O_3 and Fe_2O_3 constitute about 82.74% of MTR and, SiO_2, Al_2O_3 and CaO constitute about 88.03% of STR. The observed composition of MTR and STR appears to be in line with the composition of mine tailing and CDW-derived silt reported in the literature but does not correspond to the composition of the other reference materials reported in Table 4.1. While the SiO_2 and Fe_2O_3 values of both MTR and STR are comparable to those of fly ash, their Al_2O_3 content is lower than that of fly ash. The CaO content of MTR is comparable to that of fly ash, while the CaO content of STR is approximately five times greater than that of fly ash. Due to the incorporation of lime in the process of CDW-based silt formation, as discussed in Chapter 3, section 3.2, it is anticipated that the STR will possess a higher CaO content.

The modulus of hydraulicity (M_h) as determined by Eq. (4.1) assesses the ability of a material to undergo hardening through the formation of reaction products upon contact with water [91,92].The strength activity index is reported to increase with increase in modulus of hydraulicity [91] . The M_h value of of MTR is 0.029 and STR is 0.29.

$$M_h = \frac{CaO}{Fe_2O_3+SiO_2+Al_2O_3} \qquad \text{Eq. (4.1)}$$

Similarly, the modulus of basicity/ basicity coefficient (M_b) [90] determined by Eq. 4.2 is 0.11 for MTR is and is 0.33 for STR.

$$M_b = \frac{CaO+MgO}{SiO_2+Al_2O_3} \qquad \text{Eq. (4.2)}$$

The recommended range for modulus of basicity is between 0.7 – 1.2 [90] for the material to be suitable for alkali activation. Nevertheless, the computed values of basicity modulus and hydraulicity modulus for MTR and STR do not accurately represent the reactivity of these materials. This is because these ratios do not consider the proportion of ions that are readily available for reaction, as well as the presence of non-reactive ions in crystalline form within the material. Therefore, it is important to take into consideration the mineralogical composition and crystallinity to determine the reactivity of the material. The loss on ignition value of 10.61% for MTR and 18.43% for STR indicate the presence of volatile materials, phases such as carbonates and hydroxides and combined water both chemically bonded as in case of gypsum or physically adsorbed.

Table 4.1 (a): Comparison of oxide composition of MTR used in the present study with that of graphite mine tailing, fly ash, silica fume, GGBFS and cement from literature

Oxides	**MTR**	**Graphite mine tailing in other studies** [111,246,247]	**Fly ash** [9]	**Silica Fume** [9]	**GGBS**[9]	**Cement** [232]
SiO_2	58.46	59.24-64.5	48.20-51.90	94-98	33-37	19.3
Al_2O_3	14.56	10.21 – 15.05	26.00-30.10	0.1-0.4	8-35	3.7
Fe_2O_3	9.72	5.07- 5.80	5.50-11.30	0.02-0.15	0.5-2.0	4.1
Na_2O	4.36		1.0-3.70	0.1-0.4		0.28
MgO	5.91	1.82 – 3.91		0.3-0.9	6-14	2.1
K_2O	2.31	2.26		0.2-0.7		0.88
CaO	2.43	0.84-15.55	2.10-4.20	0.08-0.3	34-43	63.2
SO_3	0.27		0-0.1		0.8-2.0	4.0
TiO_2	1.08					0.29
BaO	0.43					
Mn_3O_4	0.02				0.3-1.1	
V_2O_5	0.05					
ZnO	0.06					
ZrO_2	0.03					
NiO	0.03					
P_2O_5	0.19					0.17
LOI	10.61					

Table 4.1 (b): Comparison of oxide composition of STR used in the present study with that of CDW derived silt, calcareous fly ash, silica fume, GGBFS and cement from literature

Oxides	**STR**	**CDW derived silt in other studies** [89,248]	**Calcareous Fly ash** [249–251]	**Silica Fume** [9]	**GGBS**[9]	**Cement** [232]
SiO_2	56.87	54-98	33.6-54.7	94-98	33-37	19.3
Al_2O_3	10.16	7.9-12.4	6.2-27.8	0.1-0.4	8-35	3.7
Fe_2O_3	5.53	4.6-5.8	3.6-8.8	0.02-0.15	0.5-2.0	4.1
Na_2O	0.45	0.8-1.3	0-1.9	0.1-0.4		0.28
MgO	1.25	0.3-0.7	1.3-6.4	0.3-0.9	6-14	2.1
K_2O	1.67	2.0-3.3	0.1-1.5	0.2-0.7		0.88
CaO	21	3.0-18.4	16.4-27.5	0.08-0.3	34-43	63.2
SO_3	1.39	0.1-0.9	1.4-5.4		0.8-2.0	4.0
TiO_2	0.71	0.6-0.8	0.7-1.5			0.29
BaO	0.48					
Mn_3O_4	0.06	0.1	0.03-0.06		0.3-1.1	
V_2O_5	0.02					
ZnO	0.02					
ZrO_2	0.04					
NiO	0.02					
P_2O_5	0.29		0.1-1.3	0.10-0.33		0.17
LOI	18.43		1.85-2.73			

4.4 Mineralogy

The XRD patterns of mine tailings given in Figs. 4.3 (a) to (c) revealed that chlorite (96-900-4189), clinochlore (96-901-0130), kaolinite (96-155-0599), muscovite (96-901-5624), phlogopite (96-900-2830), biotite (96-900-0468), quartz (96-50-0036), hornblende (96-900-1245), graphite (96-901-2231), anhydrite (96-500-0041) and plagioclase minerals such as oligoclase (96-901-1423), anorthite (96-900-0362) and albite (96-900-9664), are the mineral phases present in MTR and no new phases were observed in the activated mine tailing. The symbols used for identification of minerals in spectral pattern are given in table 4.2 (a). In order to enhance the comprehensibility of the X-ray diffraction (XRD) patterns, certain subgroup minerals, such as clinochlore, are annotated with the corresponding parent group to which they belong, such as chlorite. Similarly, oligoclase and anorthite are marked as plagioclase. The quantities of various phases present determined by Rietveld analysis are given in table 4.2 (b). It can be observed that the MTR was 42.60% amorphous and the treated mine tailings were in the range of 38.33% to 47.52% amorphous.

Table 4.2 (a): The list of minerals identified in the mine tailing and the corresponding symbols used for annotation in diffractogram

Symbol	**Mineral name and remarks**	**COD reference number** [233]	**Chemical formula** [233]
Chl	Chlorite	96-900-4189	$Si_{3.00}Al_{1.20}Mg_{5.00}Fe_{0.10}Cr_{0.70}O_{18.00}H_{7.90}$
Kln	Kaolinite	96-155-0599	$Al_{4.00}Si_{4.00}O_{18.00}H_{8.00}$
Ms	Muscovite	96-901-5624	$K_{4.00}Al_{12.00}Si_{12.00}O_{48.00}$
Phl	Phlogopite	96-900-2830	$Al_{2.16}Si_{5.84}Mg_{6.00}K_{2.00}O_{24.00}H_{4.00}$
Bt	Biotite	96-900-0468	$Mg_{4.00}Al_{4.00}K_{2.00}Si_{6.00}O_{24.00}$
Qz	Quartz	96-50-0036	$Si_{3.00}O_{6.00}$
Hbl	Hornblende	96-900-1245	$Si_{13.84}Al_{2.16}Mg_{6.88}Fe_{3.44}Ca_{3.40}Na_{0.92}O_{48.00}$
Gr	Graphite	96-901-2231	$C_{4.00}$
Anh	Anhydrite	96-500-0041	$Ca_{4.00}S_{4.00}O_{16.00}$
Pl	Plagioclase	96-901-1423	$Na_{1.64}Ca_{0.36}Al_{2.36}Si_{5.64}O_{16.00}$

Figs. 4.3 (a) and (b) show XRD patterns of calcined samples CC series and CT series. Fig. 4.3 (c) presents the diffraction pattern of ball milled samples. The individual peaks with significant changes such as biotite/ phlogopite and quartz / graphite are given in Fig. 4.3 (d) and (e). The results are interpreted and discussed by observing these patterns collectively along with the findings reported in Table 4.2 (b).

Table 4.2 (b) shows that upon calcination the chlorite and clinochlore composition becomes zero and the graphite content decreases. It is to be noted that about 4.75% - 12.38% of the crystalline phase constituted by graphite disappears due to calcination or the heat generated during mechanical activation. This phase is expected to have converted to carbon dioxide and would not contribute to either amorphous or crystalline phase quantities. This reduction in the total quantity of the material might contribute to the seemingly increased quantities of phases such as biotite, quartz and phlogopite at calcination temperatures 650ºC and 750 ºC. The intensification of phlogopite and quartz peaks upon calcination in samples MTCC650, MTCC750, MTCT650 and MTCT750 in comparison to MTR as seen in Fig. 4.3 (d) and (e) indicate that these phases are unaltered by the heat treatment at this temperature. Similar observations have been reported in other studies[228]. The decomposition of phlogopite begins at 800ºC and this leads to a decrease in the quantity of phlogopite at 850ºC as in case of samples MTCT850 and MTCC850. However, the phlogopite peaks do not disappear as the decomposition is not complete at this temperature.

The phlogopite/ biotite peaks of ball milled samples in Fig. 4.3 (d) show that the peak intensity decreases with increase in milling time. The change in peak shape, peak shifting and peak narrowing were also observed reflecting the changes in crystal structure of the corresponding phases during milling. Similar to this the quartz and graphite appearing as a twin peak at the 2θ range 26.2 to 27 (Fig. 4.3 (e)), show modifications with milling and calcination. The quartz peaks show intensification upon calcination and the graphite phase starts decomposing. Whereas upon milling though the graphite phase does not disappear completely the layered arrangement of the graphite crystal structures are altered resulting in change of the peak shape.

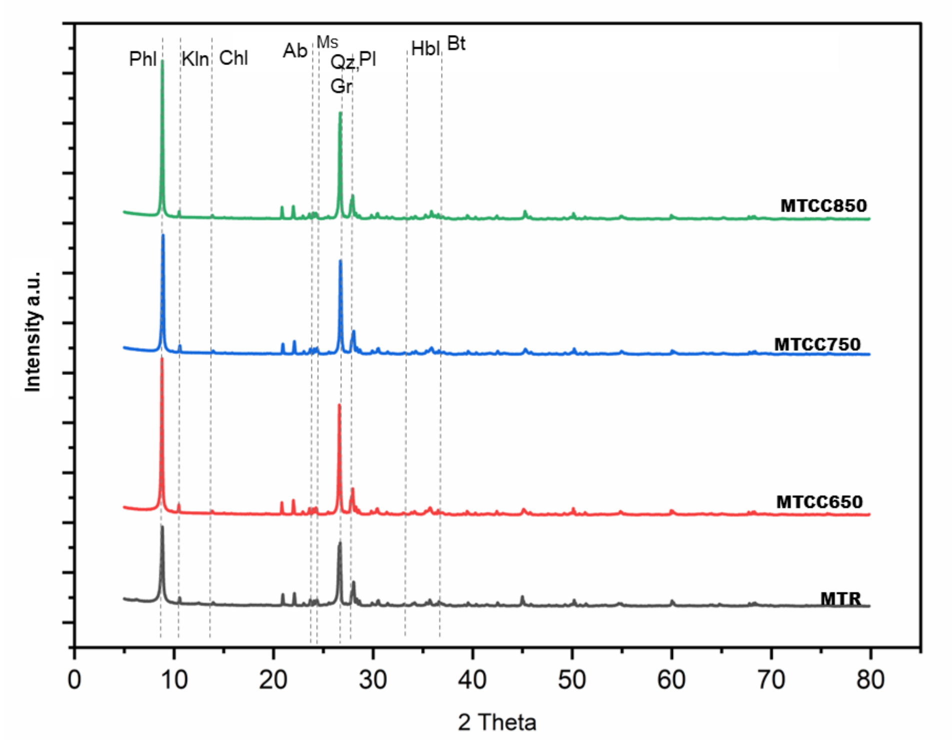

(a)

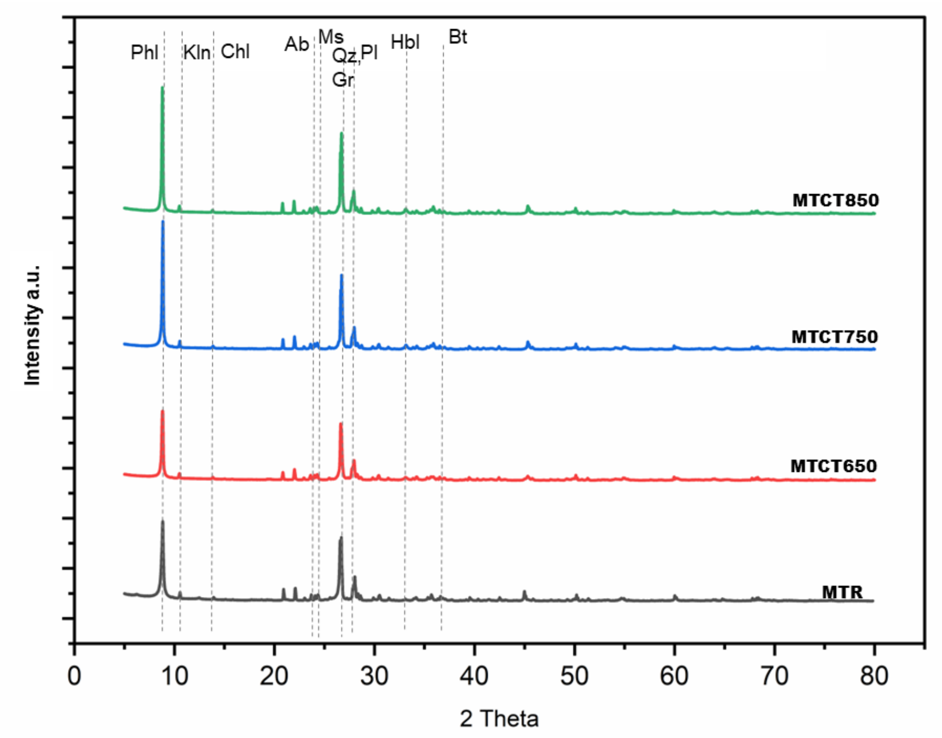

(b)

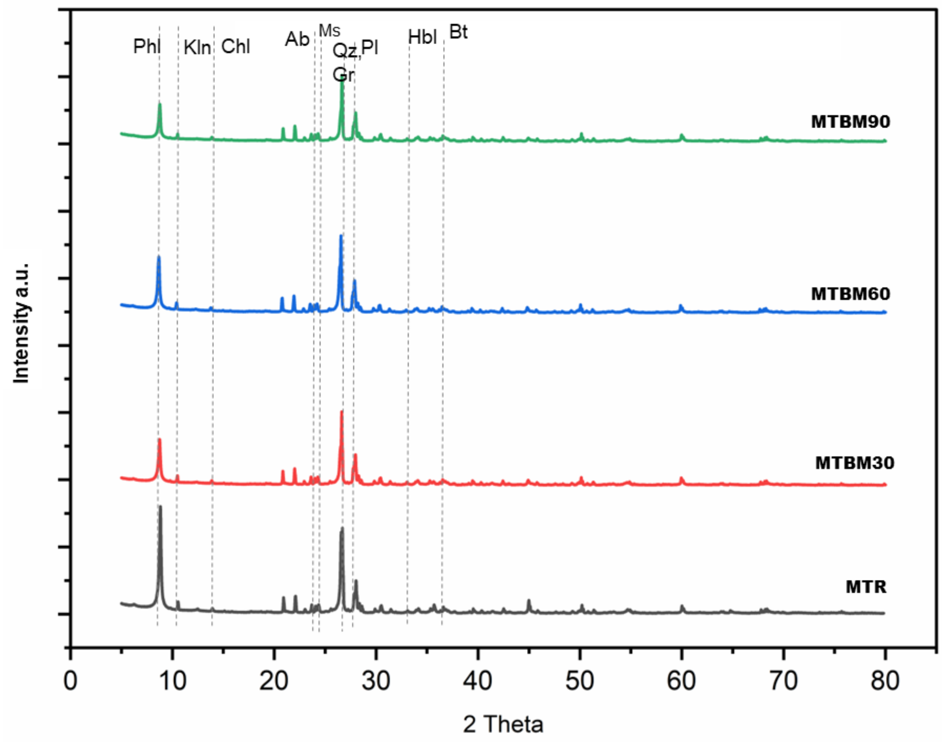
Phl
Kln
Chl
Ab
Ms
Qz,
Gr
Pl
Hbl
Bt
MTBM90
MTBM60
MTBM30
MTR
Intensity a.u.
0
10
20
30
40
50
60
70
80
2 Theta

(c)

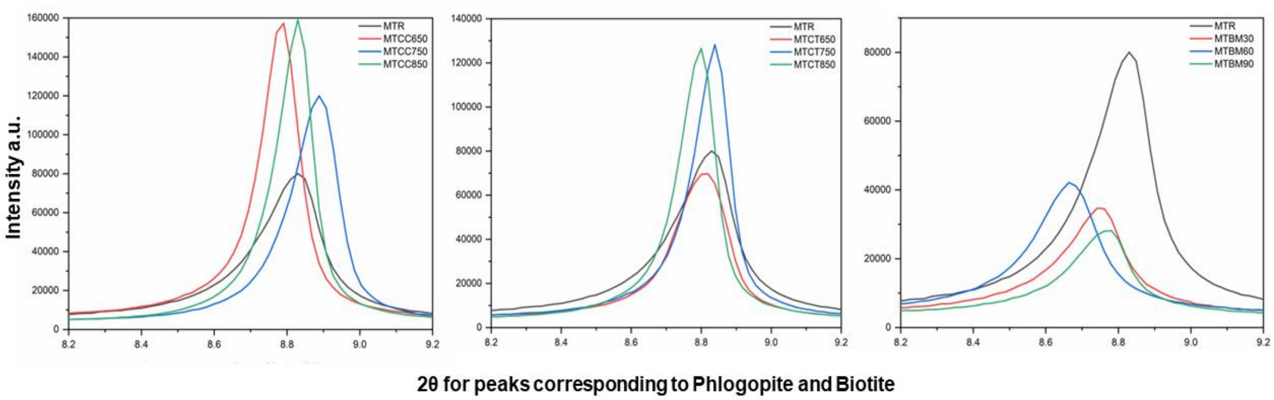
MTR
MTCC650
MTCC750
MTCC850
MTCT650
MTCT750
MTCT850
MTBM30
MTBM60
MTBM90
Intensity a.u.
160000
140000
120000
100000
80000
60000
40000
20000
0
8.2
8.4
8.6
8.8
9.0
9.2
2θ for peaks corresponding to Phlogopite and Biotite

(d)

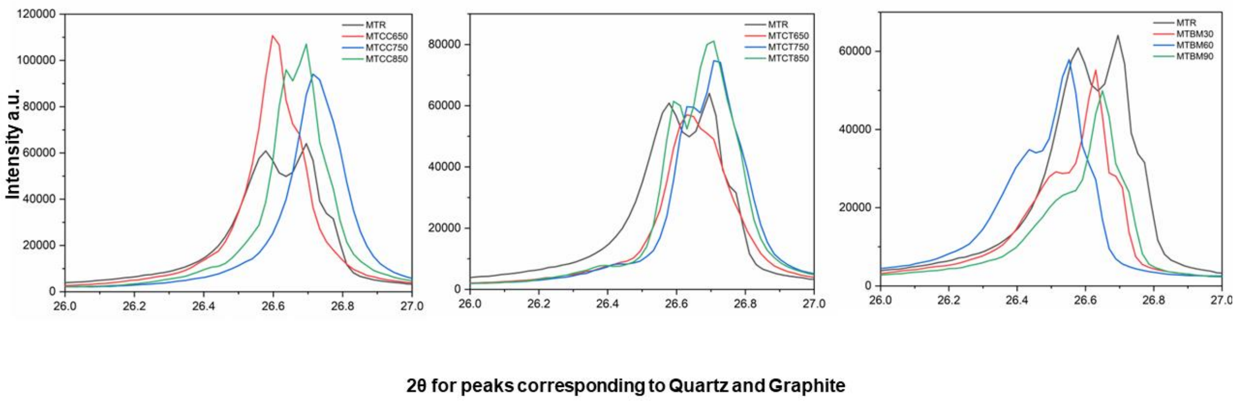

(e)

Fig. 4.3: (a) XRD phases of mine tailing samples before and after calcination, CC series, (b) XRD phases of mine tailing samples before and after calcination, CT series, (c) XRD phases of mine tailing samples before and after milling, BM series (d) Peaks corresponding to phlogopite and biotite (e) Peaks corresponding to graphite and quartz.

Table 4.2 (b): Mineral phases in mine tailing and their respective percentages

Mineral phases	MTR	MTCT650	MTCT750	MTCT850	MTBM30	MTBM60	MTBM90
Kaolinite	0.64	0.25	0.34	0.11	0.61	0.54	0.59
Quartz	8.55	11.05	10.51	12.42	10.12	8.81	9.88
Anorthite	5.09	7.90	7.56	7.11	2.27	3.68	5.03
Biotite	0.75	4.63	5.28	9.58	0.74	0.97	1.95
Hornblende	1.85	2.78	1.14	1.37	2.39	2.11	1.95
Phlogopite	10.52	8.77	15.00	1.47	13.80	10.76	12.19
Chlorite	0.12	0.00	0.00	0.00	0.00	0.00	0.00
Albite	2.31	2.35	2.27	1.26	3.25	3.08	3.20
Clinochlore	0.12	0.00	0.00	0.00	0.43	0.32	0.30
Graphite	13.29	6.98	0.91	0.68	8.53	8.54	6.45
Muscovite	0.81	1.11	0.74	1.05	0.98	0.86	0.89
Anhydrite	0.29	0.19	0.11	0.32	0.25	0.22	0.18
Oligoclase	13.06	15.68	12.90	17.11	17.79	14.22	16.45
Amorphous	42.60	38.33	43.24	47.53	38.83	45.89	40.95

Note: As the samples from CC series were not homogenous, the Rietveld analysis results were misrepresentative and therefore not included as a part of this discussion.

The XRD patterns of CDW derived silt given in Fig. 4.4 (a) to (c) indicated the presence of following phases: hematite (96-101-1268), K-feldspar (96-155-7002), gypsum (96-500-0040), Orthoclase (96-900-0163), ferrosilite (96-900-0356), hornblende (96-900-1227), feldspar (96-900-3089), anhydrite (96-900-4097), microcline (96-900-4192), albite (96-900-9664), illite (96-900-9666), quartz (96-900-9667), chlorite (96-901-0166), muscovite (96-901-2887), phlogopite (96-901-

3832), calcite (96-901-6707). The symbols used for identification of minerals in diffraction patterns are given in table 4.3 (a) and the quantities of various phases present determined by Rietveld analysis are given in table 4.3 (b). Figures 4.4 (a) and (b) depict XRD patterns of the calcined CDW derived silt samples from the CC series and CT series, respectively. Figure 4.4 (c) displays the diffraction pattern of samples subjected to ball milling. Figure 4.4 (d) and (e) show the peaks associated with notable modifications particularly calcite and gypsum. These XRD patterns observed collectively, along with the data shown in Table 4.2 (b), are utilised to analyse and discuss the results.

Table 4.3 (a): The list of minerals identified in the CDW derived silt, and the corresponding symbols used for annotation in diffractogram

Symbol	**Mineral name and remarks**	**COD reference number** [233]	**Chemical formula** [233]
Phl	Phlogopite	96-900-2830	$Al_{2.16}Si_{5.84}Mg_{6.00}K_{2.00}O_{24.00}H_{4.00}$
Hbl	Hornblende	96-900-1245	$Si_{13.84}Al_{2.16}Mg_{6.88}Fe_{3.44}Ca_{3.40}Na_{0.92}O_{48.00}$
Cl	Chlorite	96-900-4189	$Si_{3.00}Al_{1.20}Mg_{5.00}Fe_{0.10}Cr_{0.70}O_{18.00}H_{7.90}$
Gp	Gypsum	96-500-0040	$Ca_{4.00}S_{4.00}O_{24.00}$.
Ilt	Illite	96-900-9666	$K_{0.65}Al_{2.0}[Al_{0.65}Si_{3.35}O_{10}](OH)_2$
Or	Orthoclase	96-900-0163	$K_{4.00}Si_{12.00}Al_{4.00}O_{32.00}$
Ab	Albite	96-900-9664	$Na_{1.96}Ca_{0.04}Si_{5.96}Al_{2.04}O_{16.00}$
Anh	Anhydrite	96-500-0041	$Ca_{4.00}S_{4.00}O_{16.00}$
Ms	Muscovite	96-901-5624	$K_{4.00}Al_{12.00}Si_{12.00}O_{48.00}$
Qz	Quartz	96-50-0036	$Si_{3.00}O_{6.00}$
Fs	K-feldspar	96-155-7002	$K_{1.86}Na_{0.14}Al_{2.00}Si_{6.00}O_{16.00}$
Cal	Calcite	96-901-5391	$Ca_{6.00}C_{6.00}O_{18.00}$
K-Fsp	K-feldspar	96-155-7002	$K_{1.86}Na_{0.14}Al_{2.00}Si_{6.00}O_{16.00}$
Fsp	Feldspar	96-900-3089	$Ca_{0.80}Sr_{3.20}Si_{8.00}Al_{8.00}O_{32.00}$
Hem	Hematite	96-101-1268	$Fe_{12.00}O_{18.00}$

The diffraction patterns shown in Fig. 4.4 (a) and (b)and the individual peaks shown in Fig. 4.4 (e) show that in CC and CT series samples the peaks corresponding to calcite disappear upon calcination Fig and it is also confirmed by the Rietveld quantification given in table 4.3, where the calcite percentage decreases from 15.5% in STR to 2.2% in STCT750 and 0.86% in STCT850.Similarly, the calcination of gypsum leads to removal of chemically bound water molecule and formation of anhydrite as shown in Eq. 4.3. It is also evident from Fig. 4.4 (d) where the gypsum peak disappears in both CC and CT samples. Table 4.3 (b) shows that the quantity of gypsum decreases, and anhydrite increases with calcination indicating the decomposition of gypsum to anhydrite.

$$CaSO_4.2H_2O \rightarrow CaSO_4 + 2H_2O \qquad \text{Eq. (4.3)}$$

Also, decomposition of chlorite and dehydroxylation of Illite occurs upon calcination in both CC and CT series, and this can be seen in the diffraction patterns given in Fig. 4.4 (a) and (b). A reduction in Illite percentage from 15.3% to 2.59% at 750 ºC and 15.3% to 0.97% at 850ºC was observed in table 4.3 (b). It is also observed that associated with dehydroxylation of illite the haematite percentage increases to 1.26% from 0.27% indicating that the dehydroxylation of Illite leads to formation of amorphous silica and alumina and the traces of iron present in the Illite oxidises to form hematite as reported in the past studies[149,226]. The table 4.3 (b) also showed that the quantity of amorphous phases increased with calcination.

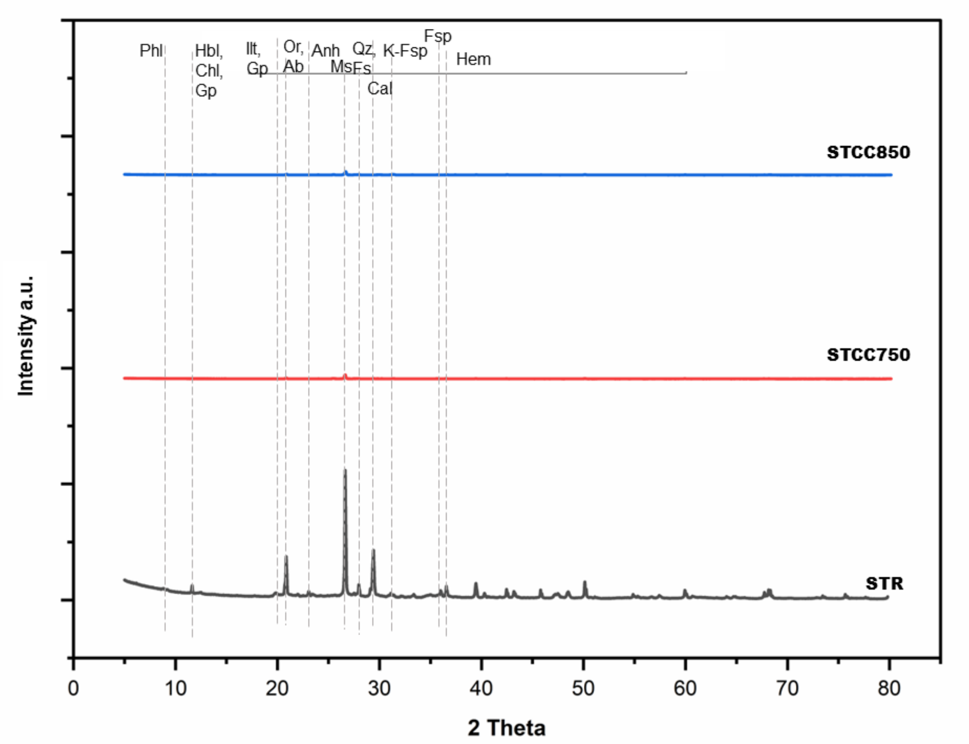

(a)

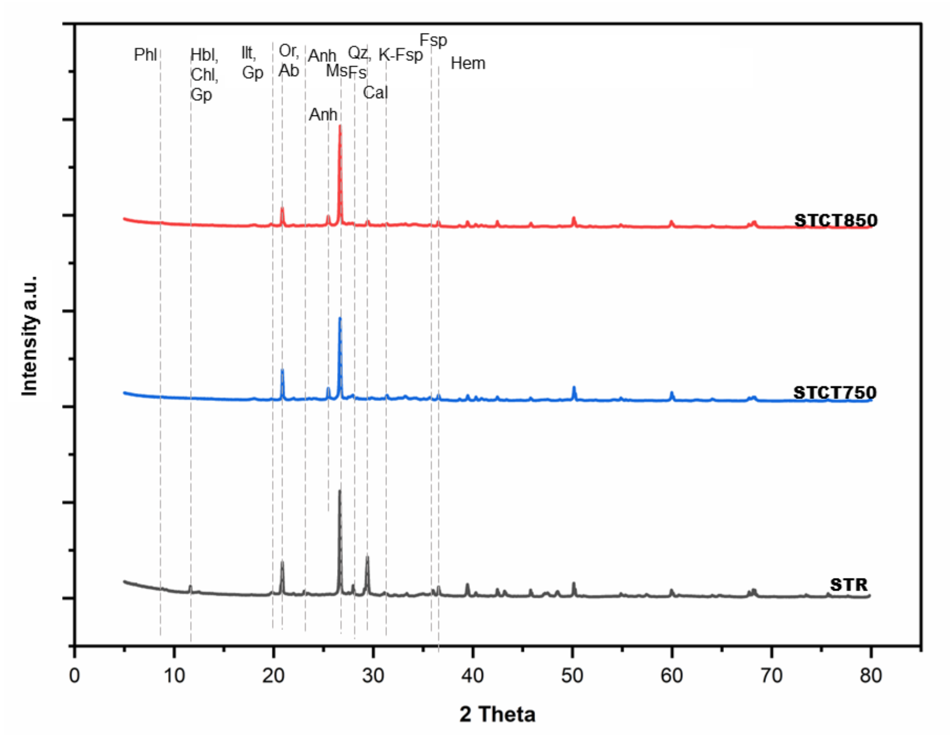
Phl
Hbl, Chl, Gp
Ilt, Gp
Or, Ab
Anh
Anh
Ms
Qz, Fs
Cal
K-Fsp
Fsp
Hem
STCT850
STCT750
STR
Intensity a.u.
0
10
20
30
40
50
60
70
80
2 Theta

(b)

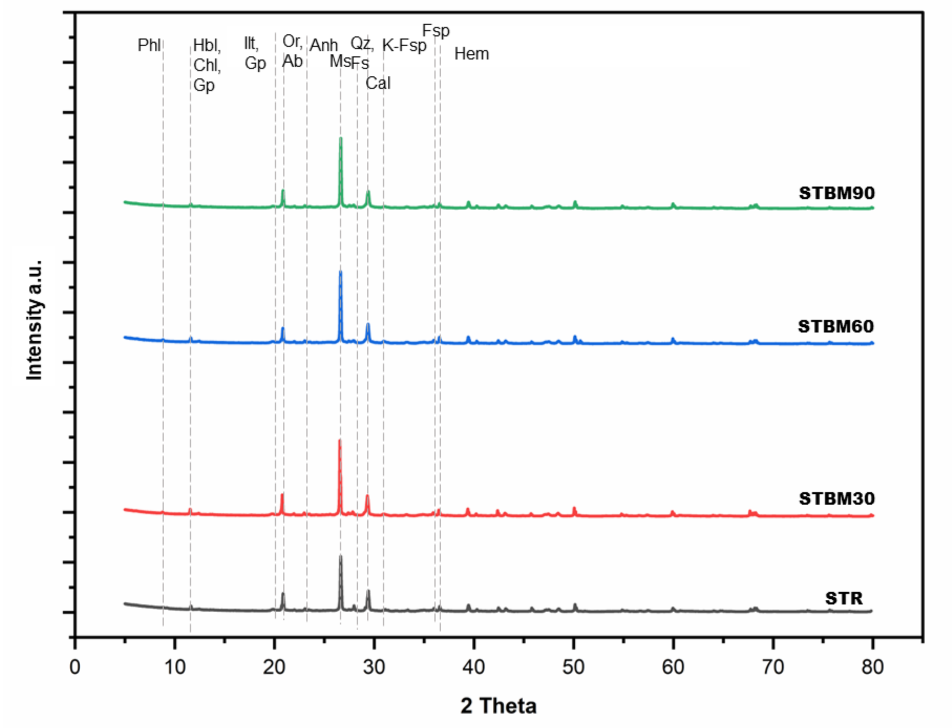
Phl
Hbl, Chl, Gp
Ilt, Gp
Or, Ab
Anh
Ms
Qz, Fs
Cal
K-Fsp
Fsp
Hem
STBM90
STBM60
STBM30
STR
Intensity a.u.
0
10
20
30
40
50
60
70
80
2 Theta

(c)

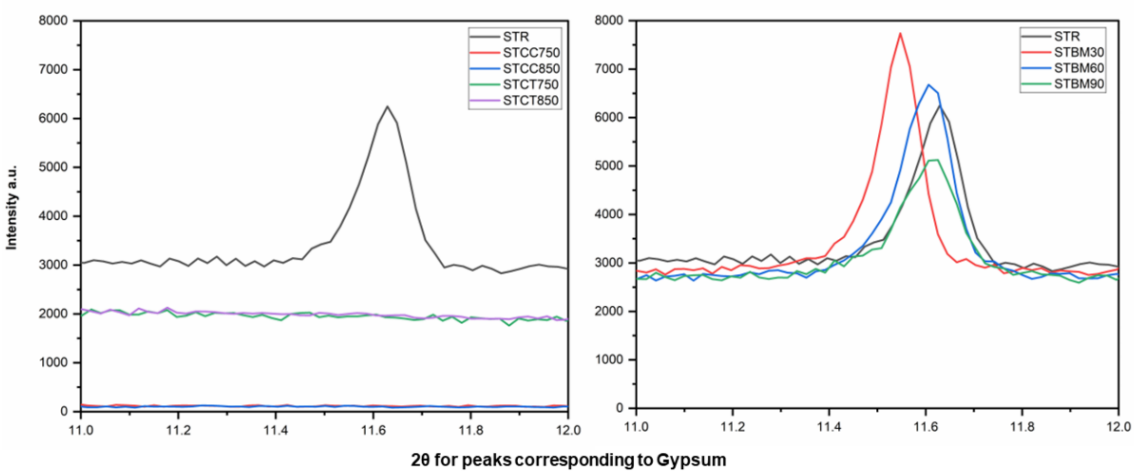

(d)

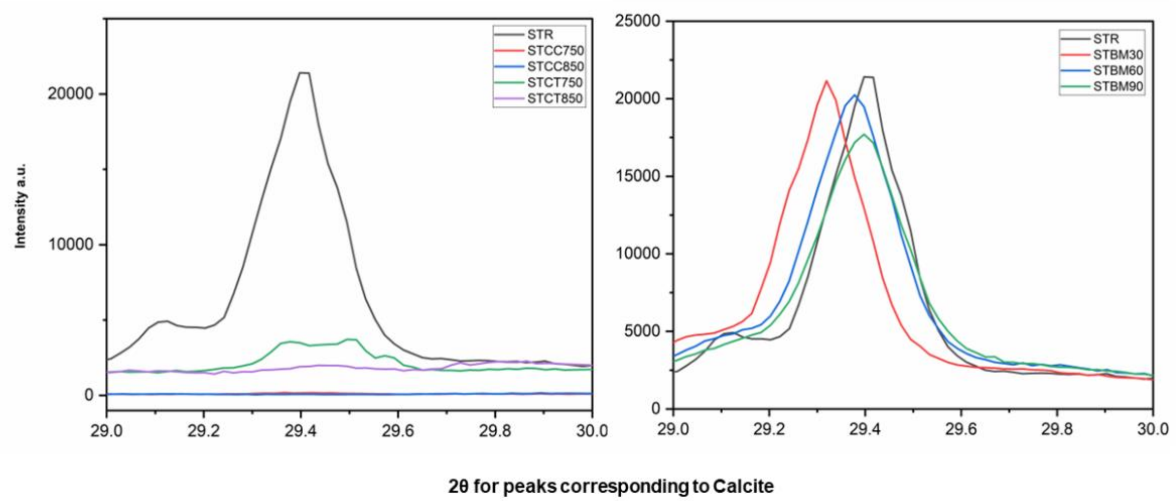

(e)

Fig. 4.4: (a) XRD phases of CDW derived samples before and after calcination, CC series, (b) XRD phases of CDW derived samples before and after calcination, CT series, (c) XRD phases of CDW derived samples before and after milling, BM series (d) Peaks corresponding to gypsum (e) Peaks corresponding to calcite.

Table 4.3 (b): Mineral phases in CDW derived silt and their respective percentages

Mineral Phases	STR	STCT750	STCT850	STBM30	STBM60	STBM90
Hematite	0.27	0.84	1.26	0.35	0.42	0.41
K-feldspar	0.48	2.21	0.63	0.21	0.00	0.00
Gypsum	3.88	0.32	0.69	4.61	4.30	2.12
Orthoclase	1.16	1.82	1.49	1.70	1.48	1.44
Ferrosilite	1.02	1.82	1.89	0.78	0.28	0.62
Hornblende	0.20	1.17	1.14	0.14	0.00	0.00
Feldspar	0.34	0.91	1.14	0.71	0.35	0.48
Anhydrite	0.14	5.00	4.57	0.14	0.28	0.21
Microcline	1.09	1.17	1.94	1.77	1.62	1.44
Albite	4.83	6.17	9.20	5.74	6.90	5.89
Illite	15.37	2.60	0.97	13.62	12.68	14.25
Quartz	22.72	35.13	29.14	23.55	24.01	24.86
Chlorite	0.54	0.00	0.00	0.85	0.85	0.55
Muscovite	0.20	2.078	0.63	0.21	0.35	0.34
Phlogopite	0.41	1.62	1.66	0.35	0.42	0.27
Calcite	15.51	2.21	0.86	16.17	16.41	15.62
Amorphous	31.84	34.94	42.80	29.08	29.65	31.51

Note: As the samples from CC series were not homogenous, the Rietveld analysis results were misrepresentative and therefore not included as a part of discussion.

4.5 FTIR studies

FTIR spectra of the tailing and CDW derived silt, before and after activation, are given in Fig. 4.5 (a) to (c) and 4.6 (a) to (c), respectively. The peak assignments, based on existing literature, for mine tailing and CDW-silt samples are given in Table 4.4 and Table 4.5, respectively.

The FTIR spectra of activated mine tailing samples and MTR samples are depicted in Fig. 4.5 (a) to (c). The Figs. 4.5 (a) to (c) reveal a reduction in relative peak intensity by approximately 4 to 20% in the activated mine tailing compared to the MTR.

Table 4.4: FTIR absorbance bands and assignments for mine tailing

Wavelength (cm^{-1})	**Assignment**	**Reference**
667 - 795	Si-O-Si symmetrical streching	[183][252][183]
950 - 1200	Asymmetric streching of Al-O and Si-O	[253][169][122]
1600 – 1700 1620, 1680	Bending vibration H-O-H Gypsum	[122,254]
3500, 2100-2200 599.28, 1091, 1643, 3060 and 3091	Triple covalent C bonds C-OH, C-H, CO, C-C, OH bonds corresponding to oxidation reduction of graphite	[255]
2200 - 3600	Stretching and bending of $O\text{-}H^-$	[122,169,228]

Fig. 4.5 (a) shows CC samples and 4.5 (b) shows CT samples in comparison with MTR. In both the Figs. (i.e. calcined samples) the observed peaks at 779 cm^{-1} and 795 cm^{-1} can be attributed to the presence of Si-O-Si bonds in quartz, as indicated by peak assignments. The peaks exhibit minimal changes following activation in all samples, with the exception of MTCC750. The peak observed in MTCC750 exhibited alterations in its shape and displayed increased asymmetry indicating structural changes in the crystal. The most significant peak is observed at approximately 966 cm^{-1}, a characteristic frequency commonly associated with the asymmetric stretching of Si-O and Al-O bonds [253][169][122]. A reduction in intensity of the peak by up to 20% was observed for both CC and CT samples, especially for MTCC750, MTCT850, MTCC750 and MTCC850. These peaks were also observed to shift slightly towards the higher wave number. The observed phenomenon can be attributed to the alterations in the structural configuration of the Al-O and Si-O chemical bonds within the constituent phases found in tailings. The lower internal order of the bonds in the mine tailing due to calcination may lead to peak broadening of the entire envelope, which in this case might be attributed to formation of Q^o silicate tetrahedra species [256]. The observed peaks within the spectral range of 1900 to 2350 cm^{-1} are also indicative of distinct carbon bonds, including C-OH, C-H, CO, C-C, and OH. The alterations in the shape, intensity, and symmetry of these peaks of can also be ascribed to oxidation and chemical interactions occurring within the graphite phase during the calcination processes [255]. The peaks at wavenumbers 1558 cm^{-1} and 1653 cm^{-1} are indicative of the bending vibrations of the H-O-H bond. These peaks intensified upon calcination in both CC and CT samples indicating the changes in phases with H-O-H bonds upon calcination. The spectral region spanning from 3300 to 3750 cm^{-1} which can be associated with the stretching and bending vibrations of O-H bonds exhibits a development of new peaks and intensification of existing peaks. A closer look of which is provided in Fig. 4.5 (d). The observed alterations in O-H bonds may be attributed to the variations in the crystal structure and composition of chlorite, biotite, phlogopite, kaolinite and hornblende following the process of calcination [122,169,228]. All these compounds possess O-H bonds and demonstrate changes in

their crystal structure upon calcination, as indicated by the XRD patterns and quantitative analysis.

Figure 4.5 (c) displays the FTIR spectrum of the ball milled samples. The observed peaks at 779 cm-1 and 795 cm-1 are indicative of the presence of Si-O-Si bonds within the quartz crystal. The peaks exhibited minimal alterations both prior to and subsequent to the milling process. The peak observed at around 966 cm-1 is widely recognised as being indicative of the asymmetric stretching of Si-O and Al-O bonds that are typically found in the alumino silicate mineral phases present in tailings. A small shift towards the lower wavenumber accompanied by a marginal decrease in intensity of less than 5% was observed for milled samples. The observed behaviour can be explained by the changes in the structural arrangement of the Al-O and Si-O chemical bonds present in the constituent phases present in tailings. The observed shift in this study can be related to alterations in the Al-O and Si-O bonds of alumino silicate minerals, specifically phlogopite and biotite [122,169,228]. The peak intensity of these minerals notably decreased during the milling process, as indicated by the XRD results.

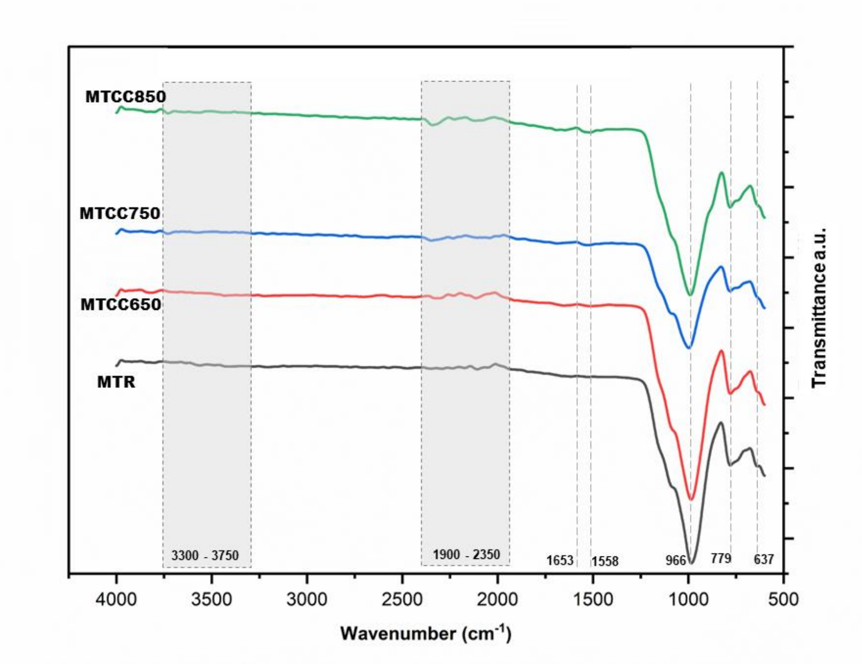

(a)

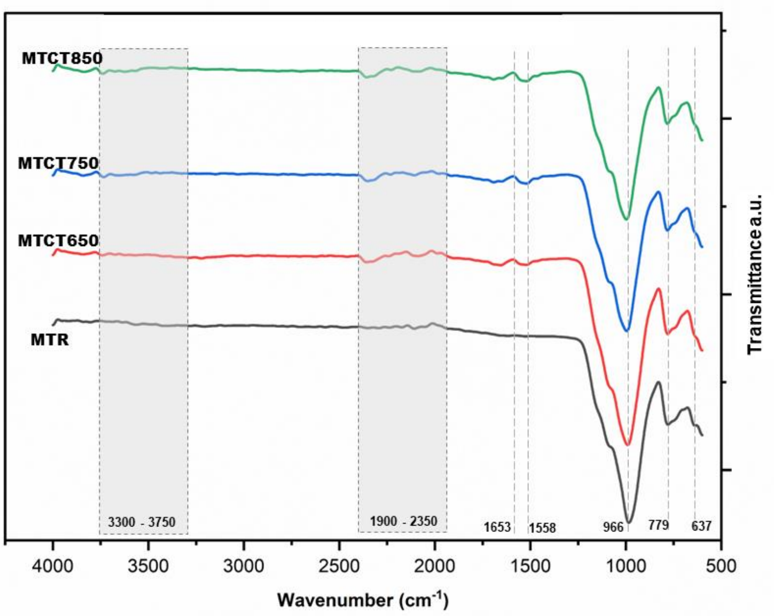
MTCT850
MTCT750
MTCT650
MTR
3300 - 3750
1900 - 2350
1653
1558
966
779
637
4000
3500
3000
2500
2000
1500
1000
500
Wavenumber (cm^{-1})
Transmittance a.u.

(b)

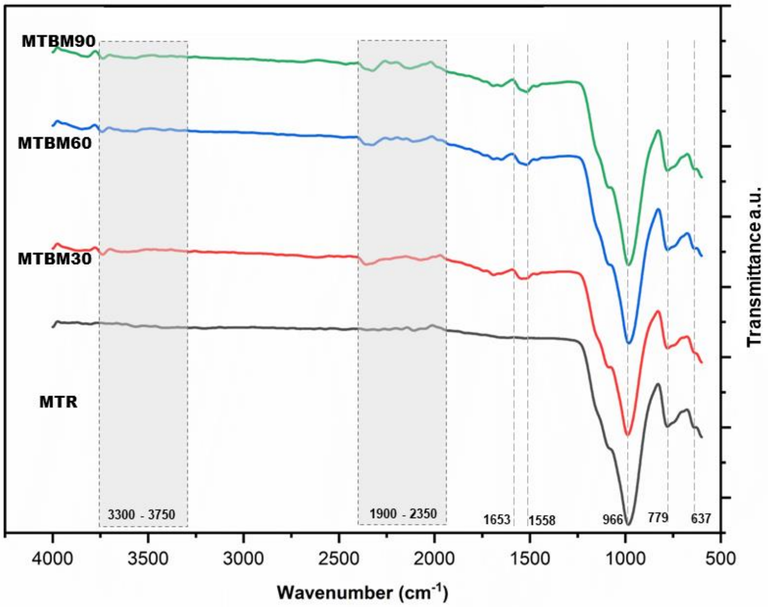
MTBM90
MTBM60
MTBM30
MTR
3300 - 3750
1900 - 2350
1653
1558
966
779
637
4000
3500
3000
2500
2000
1500
1000
500
Wavenumber (cm^{-1})
Transmittance a.u.

(c)

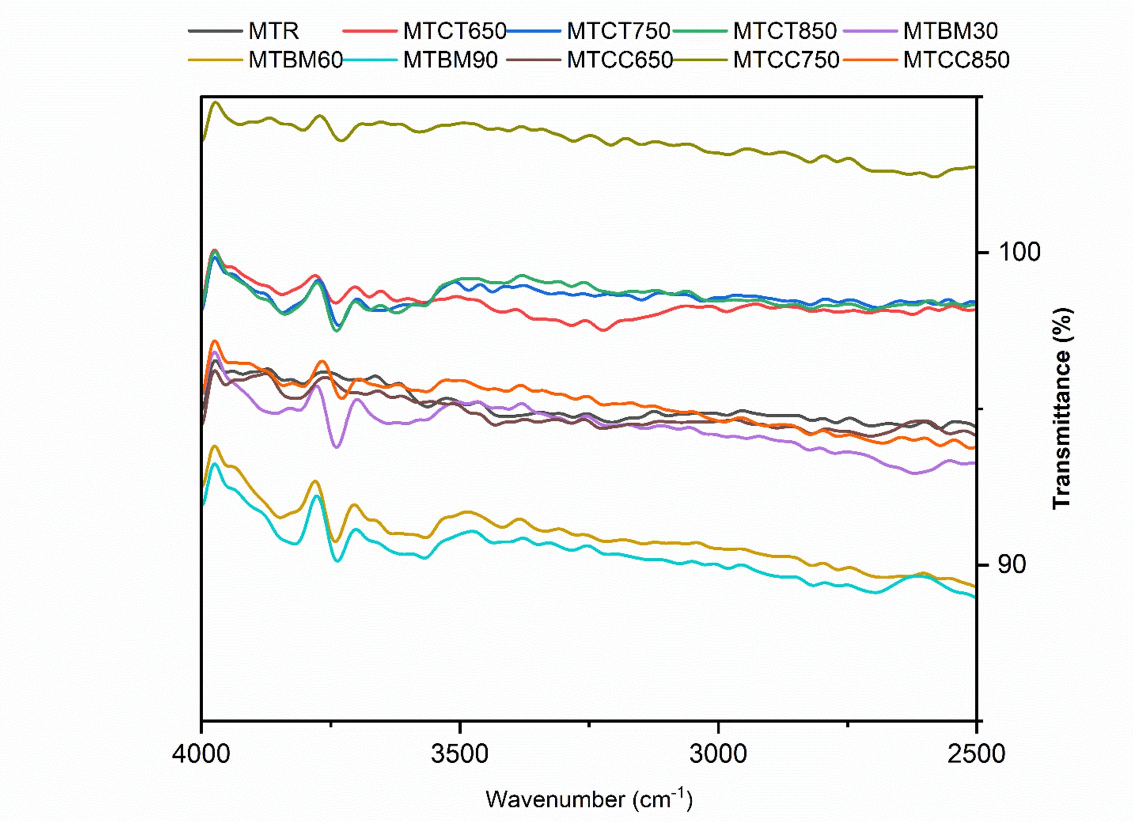

(d)

Fig. 4.5: (a) FTIR spectra of mine tailing before and after activation by calcination, CC series, (b) FTIR spectra of mine tailing before and after activation by calcination, CT series (c) FTIR spectra of mine tailing before and after activation by milling, BM series (d) FTIR spectral region corresponding to 2500 cm^{-1} to 4000 cm^{-1}.

Table 4.5 FTIR absorbance bands and assignments for CDW derived silt

Wavelength (cm^{-1})	**Assignment**	**Reference**
657 - 795	Si-O-Si symmetrical stretching	[183,252]
950 - 1200	Asymmetric stretching of Al-O and Si-O	[122,169,253]
1419 - 1490	C-O peaks corresponding to calcite	[257]
1600 – 1700 1620, 1680	Bending vibration H-O-H Corresponds to gypsum	[122,254]
2200 – 3600 3400, 3520	Stretching of $O\text{-}H^-$ Corresponds to gypsum	[122,169,254]

The FTIR spectra in of calcined CC, CT and ball milled BM samples are given in Fig. 4.6 (a) to (c), respectively.

Figs. 4.6 (a) and (b) show that the relative peak intensities of FTIR patterns decreased by up to 29% upon calcination. A potential explanation for this phenomenon could be attributed to the process of decomposition of phases during calcination. According to the data presented in Table

4.5, it is seen that the peaks observed at 657 cm^{-1} and 773 cm^{-1} are indicative of symmetrical stretching of Si-O-Si bonds. This can be designated to quartz, and these peaks remain without undergoing any substantial changes following activation. The peaks associated with the asymmetric stretching of Al-O and Si-O, located at 950 cm^{-1}, become combined with the prominent peak at 1025 cm^{-1}, and are only discernible in calcined samples subsequent to the decrease in intensity of the 1025 cm-1 peak. This observation is depicted in Fig. 4.6 (a) and (b) reveals an asymmetrical peak at 950 cm^{-1} in calcined samples, accompanied by the formation of a shoulder in the spectral region corresponding to a wavenumber of 1250 cm-1. The observed peak at 1025 cm^{-1} can be attributed to the in-plane stretching of Si-O bonds in illite [252] In calcined samples, this peak is observed to broaden, which can be attributed to the dehydroxylation process of Illite where the crystal structure shifts from ordered to disordered orientation. This observation is supported by the observed reduction in the quantity of illite as determined through XRD analysis. The peak observed at 1428 cm^{-1} can be attributed to the presence of C-O bonds in calcite[257]. This peak is not observed in calcined samples indicating the decomposition of, which is consistent with the results obtained from XRD analysis. The peaks at wavenumbers 1558 cm^{-1} and 1653 cm^{-1} are indicative of the bending vibrations of the H-O-H bond The peaks observed in the range of 2000-2450 cm^{-1} and 3300-3700 cm^{-1} correspond to the bending and stretching vibrations of the H-O-H molecule [252], However, the spectra exhibit a flattened appearance in this region for calcined samples, suggesting the occurrence of dehydration in gypsum and dehydroxylation in Illite and a range of OH species from other phases removed during calcination. The peaks at 1620 cm^{-1}, 1680 cm^{-1}, 3526 cm^{-1} and 3402 cm^{-1} corresponding to gypsum[254] disappear with calcination as observed in Fig. 4.6 (d). This observation is further supported by the results of XRD analysis where the Illite and gypsum peaks disappear upon calcination and Rietveld analysis exhibits change in quantities of these phases.

Figs. 4.6 (c), the FTIR spectra for ball milled samples demonstrated a decrease in relative peak intensities of approximately 38% after the milling process. The peaks at 657 cm^{-1} and 773 cm^{-1} indicate Si-O-Si bonds of quartz and remain without any significant alterations after milling. The peaks associated with the asymmetric stretching of Al-O and Si-O, located at 950 cm^{-1}, become combined with the prominent peak at 1025 cm^{-1} which corresponds to the in-plane Si-O bonds of Illite [252] The peak at 1428 cm^{-1} corresponding to C-O bonds in did not show any significant changes upon milling. The peaks at wavenumbers 1558 cm^{-1} and 1653 cm^{-1} are indicative of the bending vibrations of the H-O-H bond The peaks observed in the range of 2000-2450 cm-1 and 3300-3700 cm-1 correspond to the bending and stretching vibrations of the H-O-H molecule and peaks at 3526 cm^{-1} and 3402 cm^{-1} correspond to gypsum [252]. These peaks remain unchanged even after the milling process.

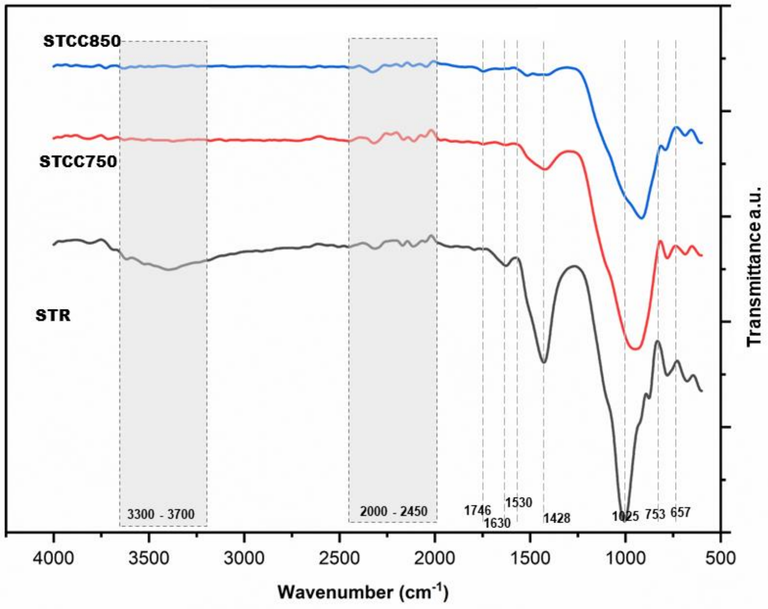
STCC850
STCC750
STR
3300 - 3700
2000 - 2450
1746
1630
1530
1428
1025
753
657
4000
3500
3000
2500
2000
1500
1000
500
Wavenumber (cm^{-1})
Transmittance a.u.

(a)

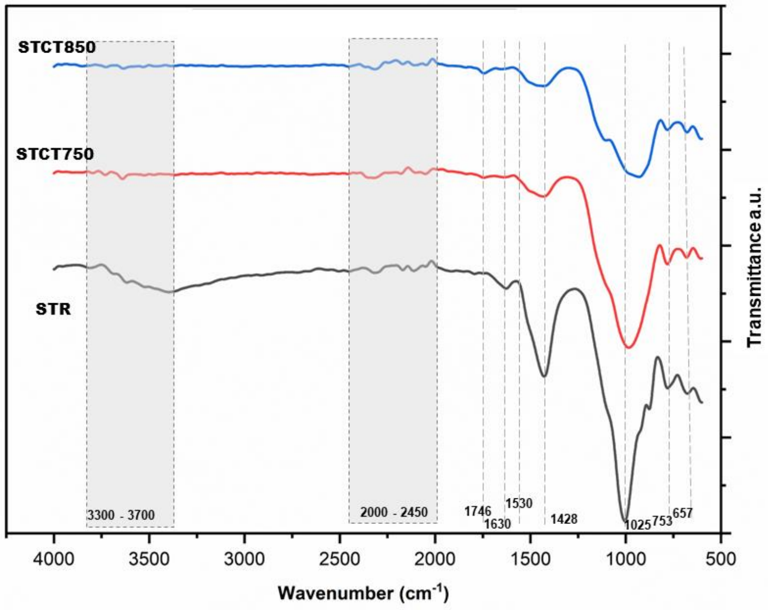
STCT850
STCT750
STR
3300 - 3700
2000 - 2450
1746
1630
1530
1428
1025
753
657
4000
3500
3000
2500
2000
1500
1000
500
Wavenumber (cm^{-1})
Transmittance a.u.

(b)

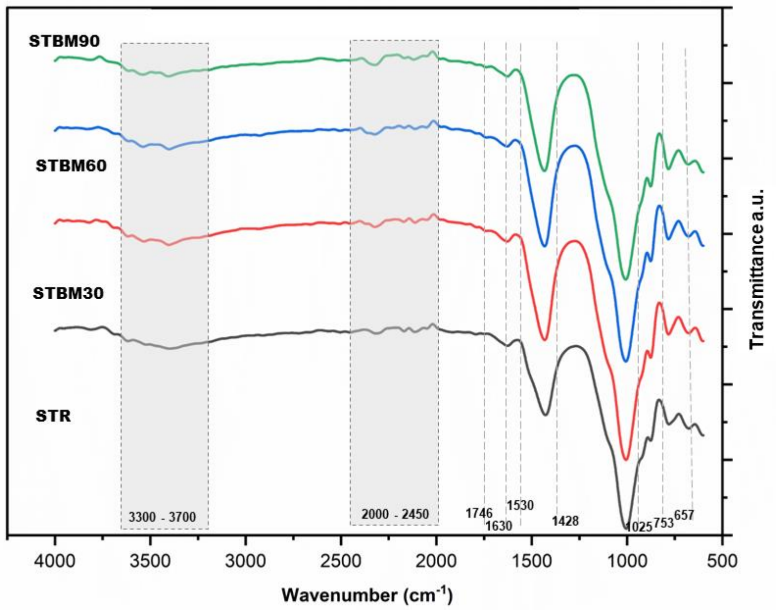

(c)

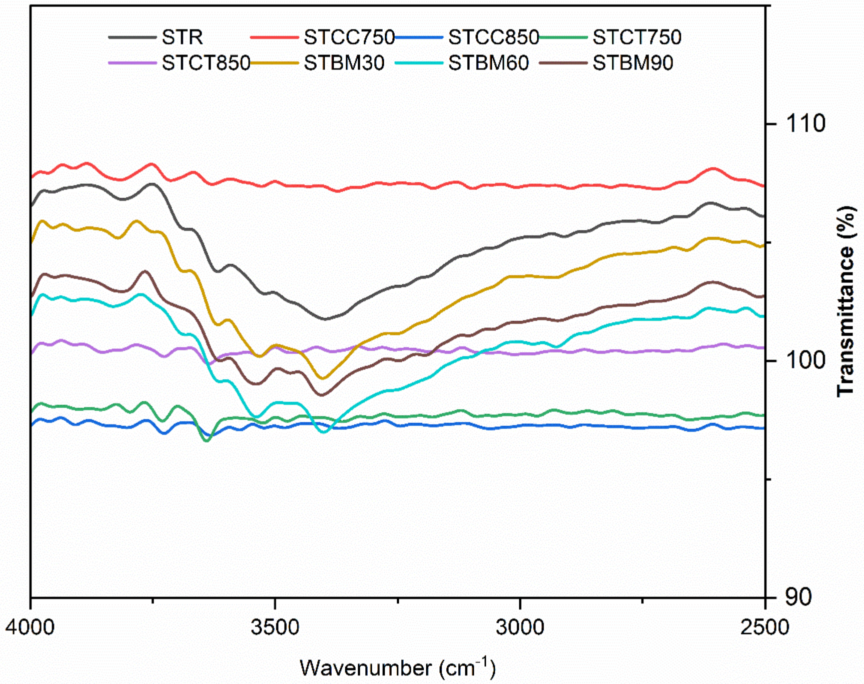

(d)

Fig. 4.6: (a) FTIR spectra of CDW derived silt before and after activation by calcination, CC series, (b) FTIR spectra of CDW derived silt before and after activation by calcination, CT series (c) FTIR spectra of CDW derived silt before and after activation by milling, BM series (d) FTIR spectral region corresponding to 2500 cm^{-1} to 4000 cm^{-1}.

4.6 Microstructure and EDAX Analysis

4.6.1 Mine tailing

The microstructure of samples observed by SEM is given in Fig.4.7 (a) to (c). The MTR samples Fig. 4.7 appear highly crystalline with dense particles of size ranging from about 1 µm to 70 µm, which broadly matches the findings from the particle size analysis. Crystallinity observations are in line with, earlier discussed, XRD indications of the existence of highly crystalline quartz and Ca/Si rich feldspars such as albite, anorthite and oligoclase. The particles appear angular with sharp edges and with an uneven particle size distribution. The MTR sample shows signs of agglomeration where the smaller particles adhere to the surface of the larger particles. These observations are similar to those made by Yu et al [67] and Ren et al [258]. Wu et al [189] suggested that this particle agglomeration of mine tailing can negatively influence the rheology of mine tailing-based cements.

On a higher magnification, (Fig. 4.7 (a) MTR inner image), sheet-like layers observed indicating the existence of phyllosilicate crystals [98]. Phyllosilicates are a class of silicates with a stratified structure of sheets at different orientations. This observation is in agreement with previously discussed XRD findings on the MTR, that indicated the existence of minerals belonging on the phyllosilicate family such as phlogopite, biotite, and muscovite.

The calcination process up to a certain extent will lead to the transformation of mineral particles from being angular and sharp to becoming more hazy/cloudy [Fig. 4.7 (a) and (b) (MTCC750 and MTCT650, inner image)]. This is an indication that the thermal treatment leads to structural changes with similar being reported in the literature et al [67]. Nonetheless, there is thermal treatment saturation point, beyond which mineral particles can exhibit partial vitrification and melting [MTCC850 and MTCT850 in Figs. 4.7 (a) and (b)]. Further heating, from this point onwards, could lead to the fusing and melting of certain phases which would result in the formation of the newer crystalline phases in the sample which might further reduce the reactivity of the sample [259].

The sample after milling had more small sized particles of size less than 5 µm (Fig. 4.7 (c) and the large sized particles (25 µm or larger) appeared to have cracks as shown in Fig. 4.7 (c) [MTBM30 inner image and MTBM60]. No agglomeration of samples was observed until 90 minutes of milling. The presence of fewer large sized particles and more smaller size particles can be attributed to the phenomenon of selective grinding. Selective grinding is a phenomenon where the milling energy applied has a more pronounced effect on minerals of lower hardness and the minerals of lower hardness had a better particle size reduction for the same milling energy [87]. This results in the minerals of higher hardness having a larger particle size [32]. This is also in agreement with the observations made from particle size analysis where the D_{90} of the particles was about 5.7 times that of D_{50} before milling, whereas that value was 8.8 times D_{50} after 30 minutes of milling. This indicates that the initial milling had an effect on particles of lesser hardness such as phlogopite, graphite and biotite and not on the ones with higher hardness such as quartz, leading to significant change in the difference between D_{50} and D_{90}. The effect on phlogopite and biotite was also confirmed through the identified structural changes discussed earlier in the XRD and FTIR sections.

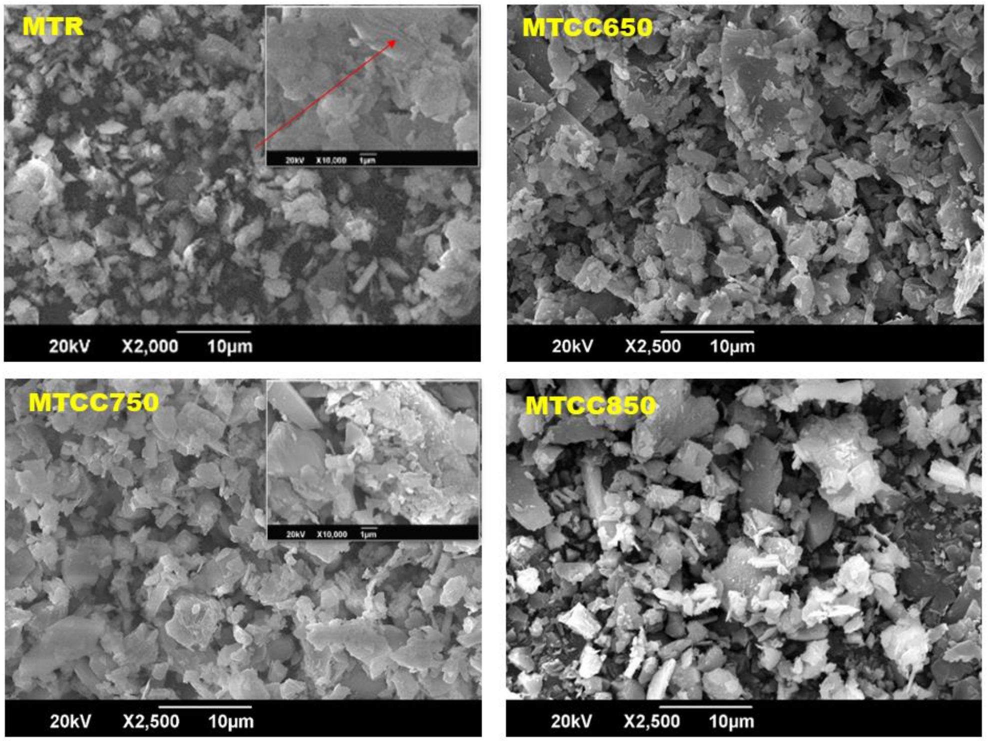

)

(a)

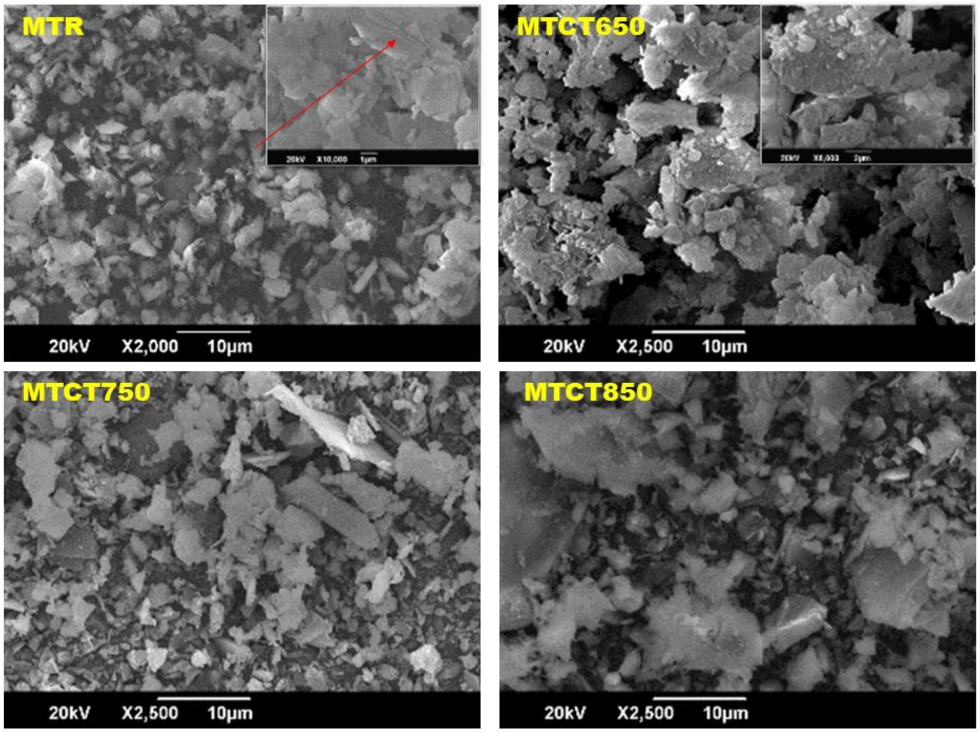

(b)

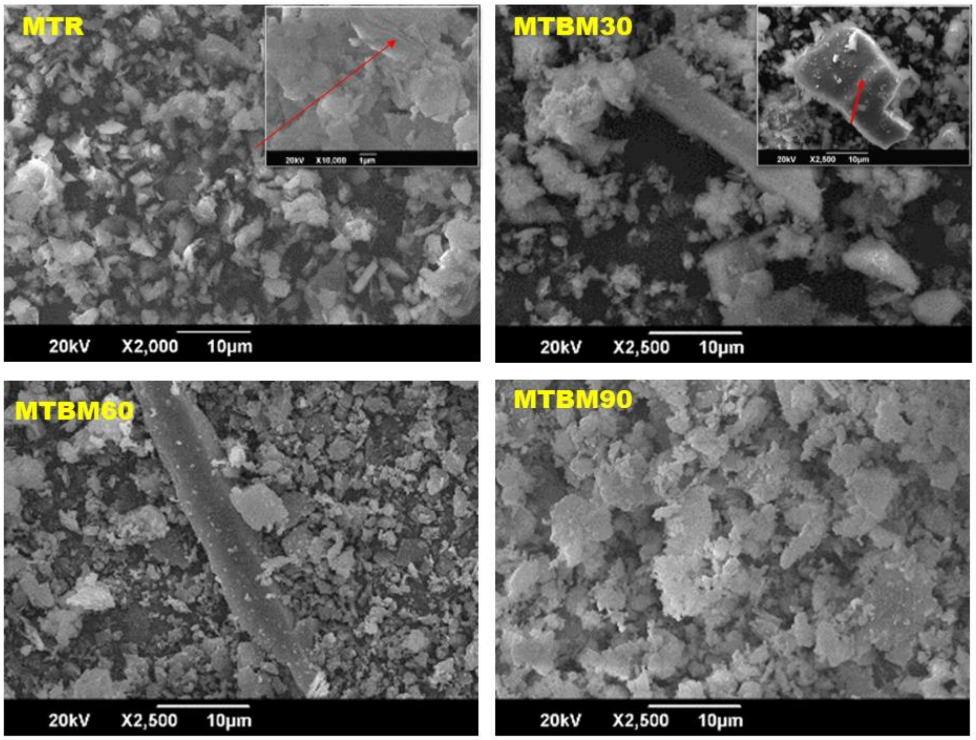

(c)

Fig. 4.7: SEM images of mine tailing samples used in this study. (a) MTR Inner image - Sheetlike appearance of phyllosilicates in MTR samples; Red arrow points at the layered appearance of phyllosilicates (a) MTCC750 Inner image - Appearance of flocculant particles in MTCC750. **(**b) MTCT650 Inner image - Appearance of flocculant particles MTCT650; (c) MTBM30 inner image - Red arrow points at the development of cracks in particles of MTBM30.

4.6.2 CDW derived silt

The SEM images of the CDW derived silt microstructure are presented in Fig. 4.8(a) and (b). The STR particles albeit being crystalline with particles of varying size, morphologically appeared different to the MTR samples. In STR the large sized particles were rounded, whereas smaller particles were flaky or needle-like. It can be inferred based on the findings of the XRD and the morphology of the observed material that the rounded particles are quartz, the needle/ rod like particles are of calcium carbonate in aragonite form and the flaky particles of irregular shapes are phyllosilicates. This observation is in line with the results of other studies where a similar mineralogy was reported [83,89,260,261].

The calcination of CDW derived silt affected the physical morphology of the particles. The changes can be appreciated as seen from in Figs. 4.8 (a). As the temperature of calcination increased from 750°C to 850°C the needle-like structures in both STCC850 and STCT850 disappeared due to decomposition of calcium carbonate during calcination, supporting the inference that the observed mineral is calcite and is also in line with the findings of XRD and FTIR studies. The STCT850 in Fig.4.8 (a) also indicates formation of cracks in the material because thermal stresses due to calcination. All the calcined samples STCC750, STCC850, STCT750 and STCT850 The appearance of cracks or flocculant appearance of particles after calcination are consistent with the findings of Zhao et al in their calcined materials [262]. The STCC850 and STCT850 also showed signs of vitrification. This indicates that the thermal treatment adopted in this study has led to structural changes in the crystal and hence affecting the morphology of the material observed.

In this study, in line with the discussion in section 4.6.1 the thermal saturation point appears to be the calcination temperature of 850 ^{o}C agglomeration of particles due to melting is shown for both tailing and CDW-silt samples (CT-series).

The ball milled CDW derived silt samples are given in Figs. 4.8 (b). The average particle size of the milled samples reduced to less than 10 µm when compared to STR samples except for a few large sized particles of size about 20 µm. This can be attributed to the selective grinding due to difference in grindability index of different minerals and the large particles could be of quartz which is of higher hardness [87]. The milled samples also appeared more flaky and has reduced the average particle size. This shows that the milling process imparted significant physical changes to the material. However, as observed from the findings of XRD milling did not have any significant effect on reduction in crystallinity.

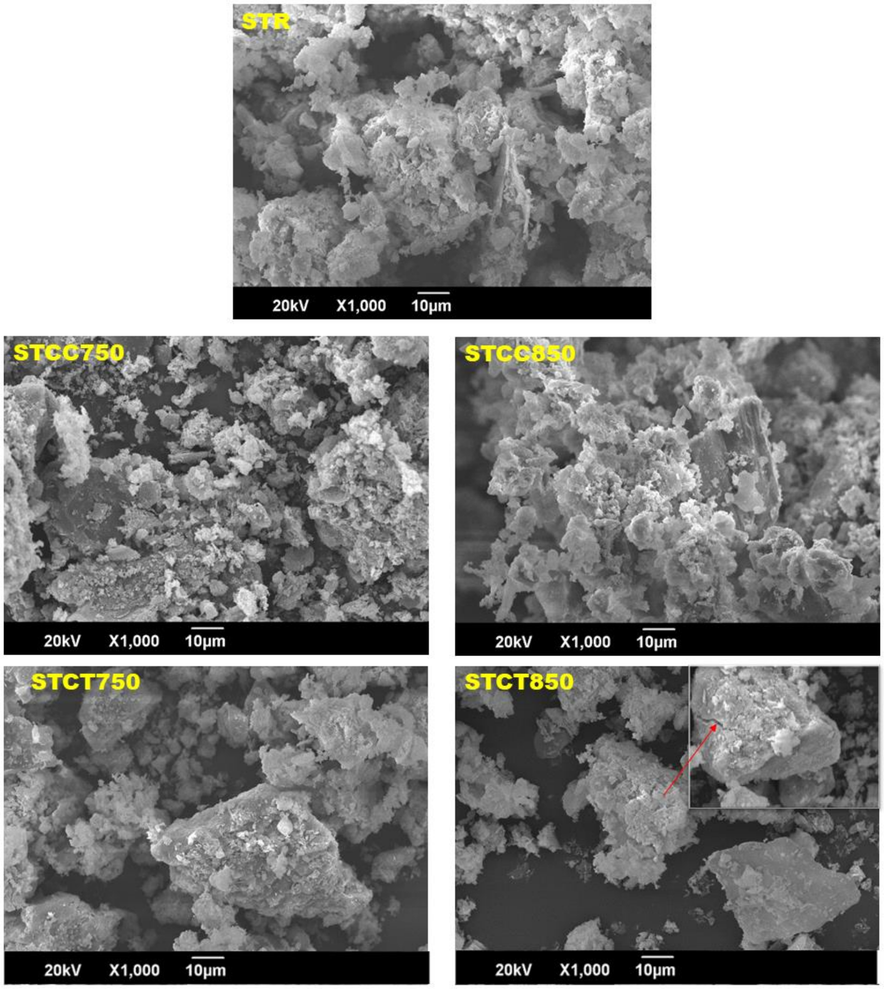

(a)

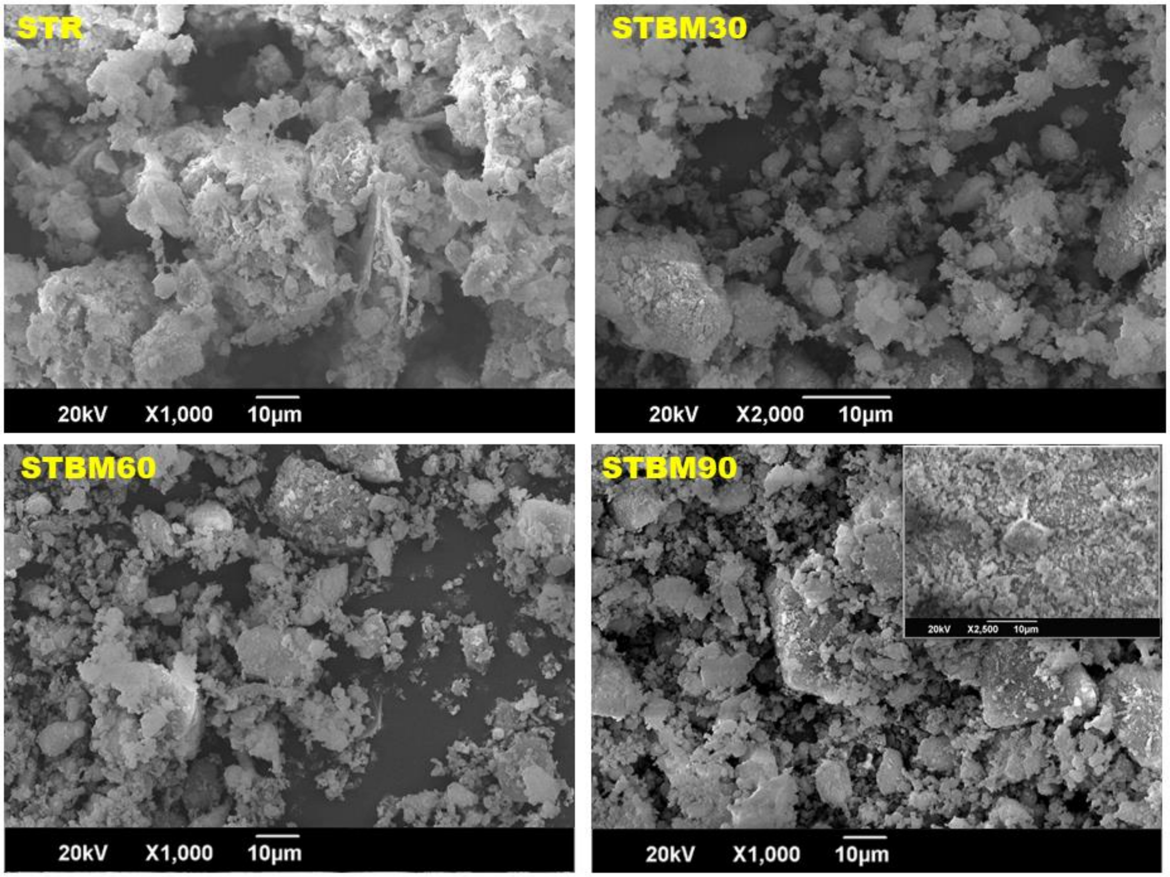

(b)

Fig. 4.8: SEM images of CDW derived silt samples used in this study. a) STCT850 - Inner image – appearance of crack during calcination b) STBM90 Inner image - A few large sized particles observed after milling contributing to selective grinding

Morphological features of individual crystals were also confirmed using TEM [Fig. 4.9 (a) to (c)]. The primary particle observation indicated that the mine tailing particles were polycrystalline, validating the findings from crystallography and scanning electron microscopy. Tailing particles in general had sharp angular edges.

Figure 4.9 (a) presents a comparison between MTR samples and CC series samples. The analysis reveals that MTCC650 and MTCC750 exhibit a higher degree of crystallinity and sharper edges, but with slight alterations in morphology, such as indications of aggregation and sintering. Visible evidence of aggregation and sintering were observed in certain regions of the particle within the MTCC850, while other areas exhibited a crystalline structure. The calcined samples of the CT series, as depicted in Figure 4.9 (b), displayed notable alterations in morphology. Furthermore, it was discovered that the agglomeration and sintering neck development occurred uniformly throughout the particle, rather than being localised to a specific portion of the particle as reported in the case of CC samples. The aggregation is due to the primary crystallites forming solid bridges during the calcination process [37]. It is evident that with increasing temperatures the morphology of the particle changes as a result of crystal structure changes. The changes observed in the CT samples were found to be consistent and homogeneous, similar to the findings observed through visual examination [37].

Similarly, the microscopic structure of particles of milled samples are given in Fig. 4.9 (c) indicate that the particles became more rounded in appearance after milling. The observed particles also showed a reduction in particle size with increase in milling period.

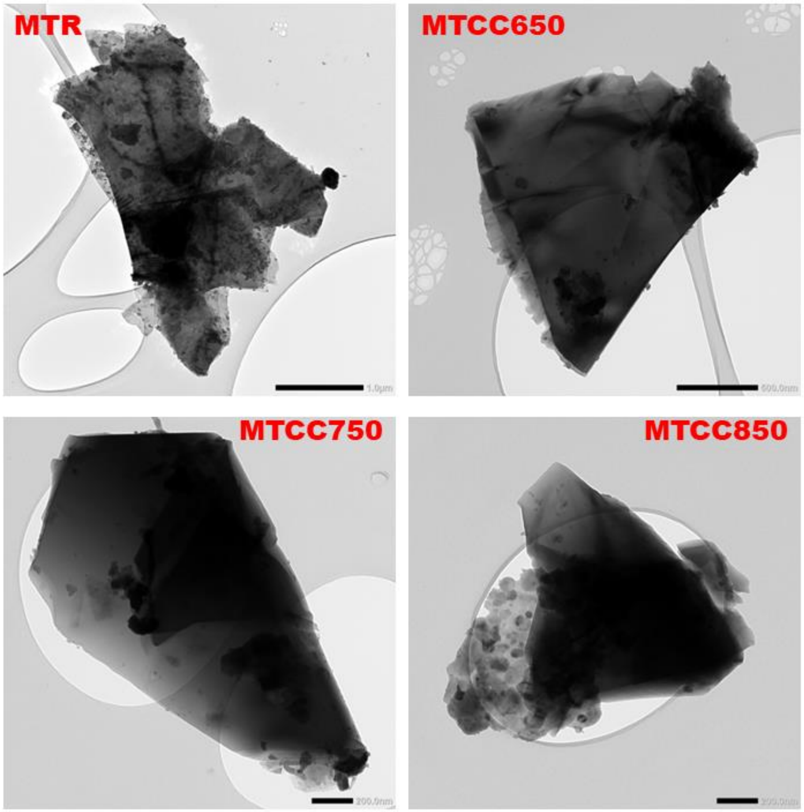

(a)

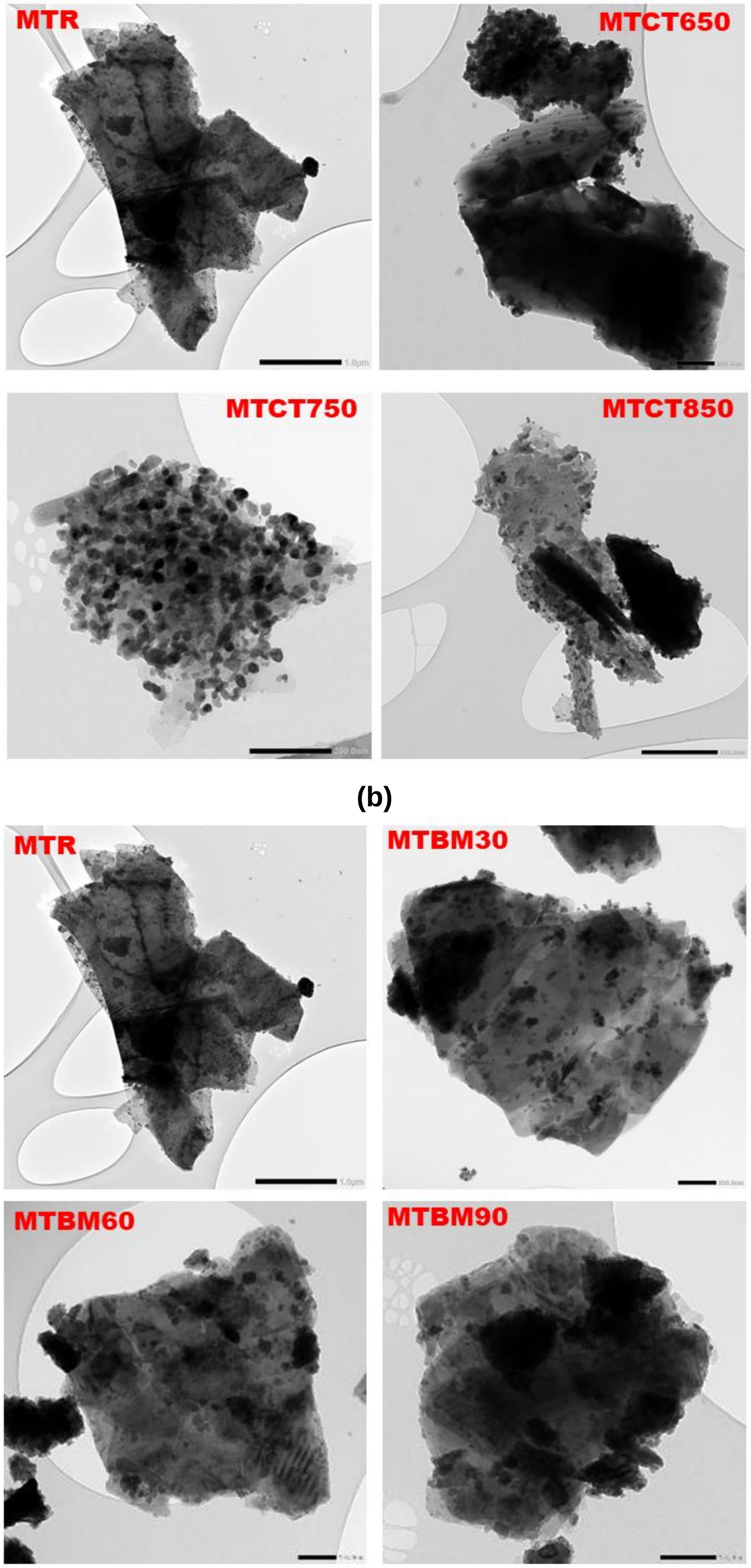

(b)

(c)

Fig. 4.9: TEM images of untreated and processed mine tailing samples.

The microstructure of calcined and ball milled CDW-silt particles observed using TEM are given in Fig 4.10 (a) and (b), respectively. The primary particle observation in Fig. 4.10 (a) indicated that the STR particles were polycrystalline and appeared to have softer edges and irregular shape compared to that of mine tailing. It can also be seen that the particles appear to have been composed of smaller particles with internal voids. Samples STCC750 and samples STCC850 indicate slight changes in morphology along the edges of the samples. Samples STCT750 and STCT850 indicate formation of necking as shown in Fig. 4.10 (a). This could be due to the primary crystallites forming solid bridges during calcination process [263]. The milled samples STBM30, STBM60 and STBM90 in Fig. 4. 10 (b) appeared with rounded edges and reduced particle size.

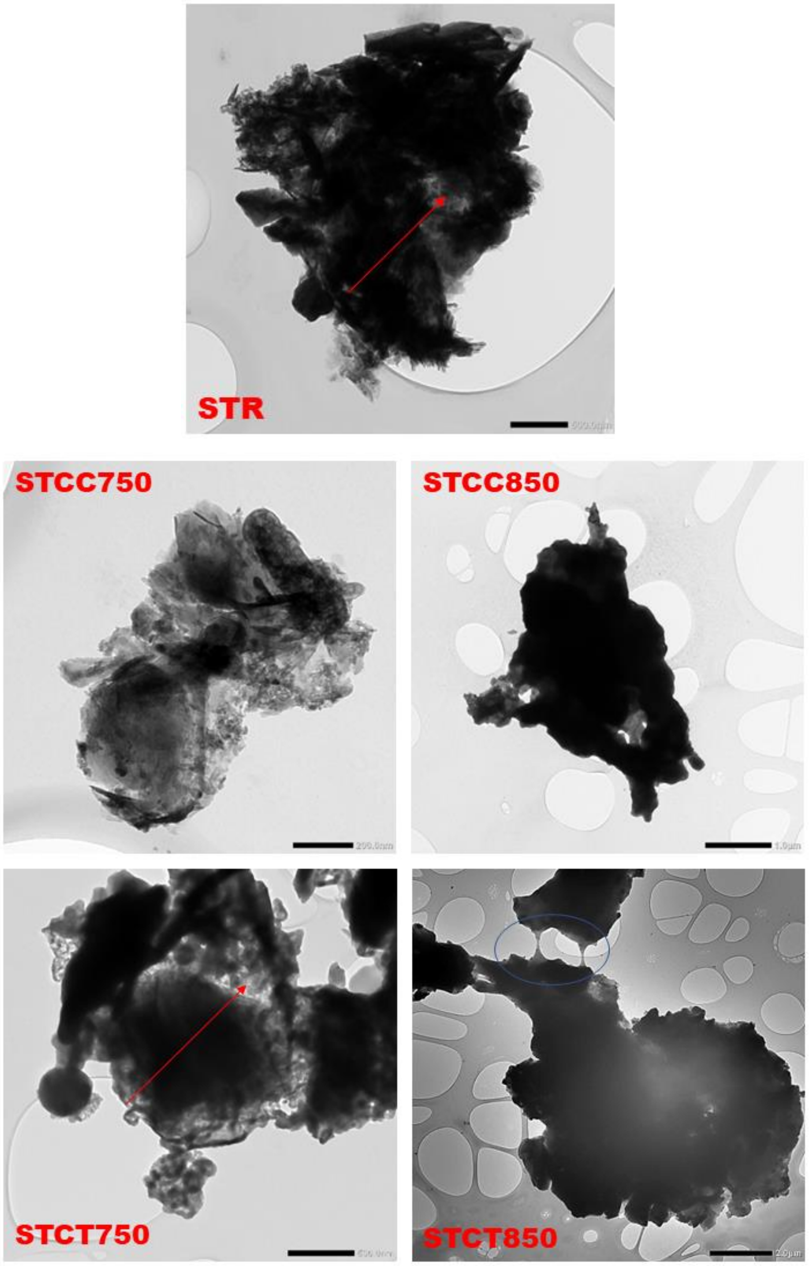

(a)

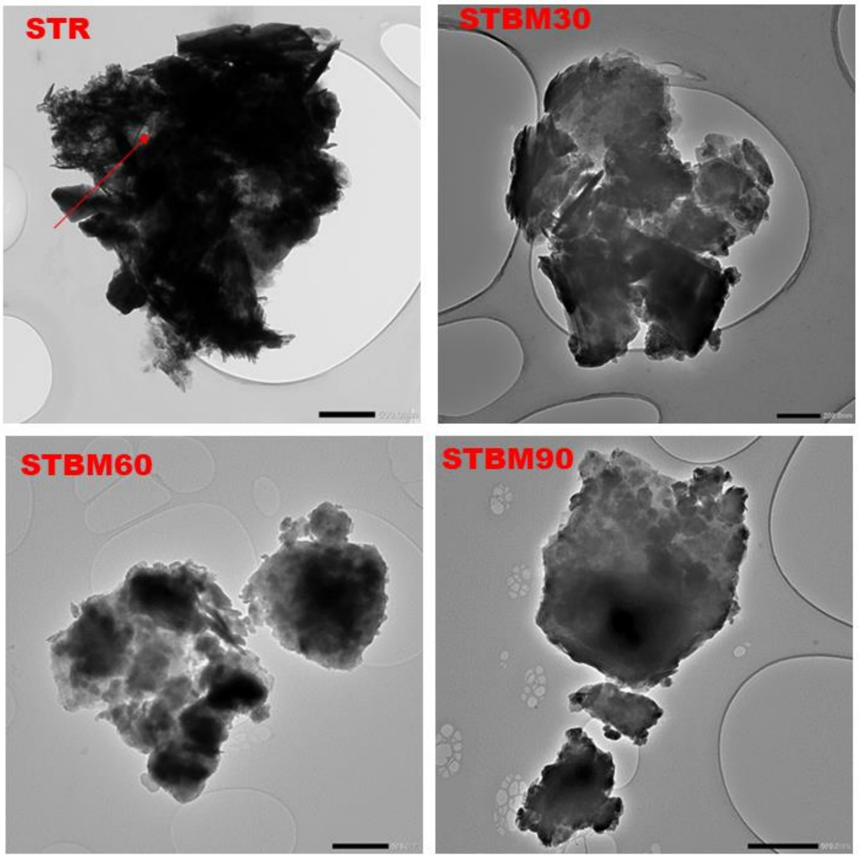

(b)

Fig. 4.10: TEM images of untreated and processed CDW derived silt samples. (a) and (d) red arrows point at internal voids., (e) The crystallite formation by sintering is indicated by the blue circle.

Tables 4.6 provides the EDAX assessment results for the mine tailing CDW derived silt before and after activation. The analysis revealed that silicon (Si), calcium (Ca), aluminium (Al), and iron (Fe) were the predominant elements detected. The elemental composition showed that the Si/Al ratio observed for MTR was 3.6, whilst the Si/Al ratio for MTCC fell within the range of 3.45-3.56. Similarly, the Si/Al ratio for MTCT was found to be within the range of 3.48-3.50, and for MTBM it ranged from 3.55 to 4.01.

Similar to mine tailing samples, the Si/Al ratio observed for STR was 2.86, while the Si/Al ratio for STCC fell within the range of 2.96-3.13. Similarly, the Si/Al ratio for STCT was found to be within the range of 2.14-2.97, and for STBM it ranged from 2.48-2.68. This observed variation may suggest alterations in composition that occur during the treatment procedures.

The process of graphite decomposition in mine tailings and calcite decomposition in CDW derived silt results in the production of carbon dioxide, consequently leading to alterations in the composition ratios of the respective samples. Nevertheless, the inclusion of carbon in the elemental composition is disregarded due to the utilisation of carbon tapes for sample mounting during the analysis. Hence, the elemental composition values obtained from the EDAX analysis are more indicative than absolute. However, the observed alterations in the elemental composition do suggest modifications in the associated minerals throughout the treatment process which is also supported by the findings of XRD and FTIR analyses.

The elemental composition of the milled tailing samples exhibits an increase in the percentage of Fe which was in range of 11.85% - 15.45% from 3.96% for MTR. This observation suggests that the milled tailings undergo structural alterations, leading to the liberation of ions into the sample because of mineral phases' breakdown. This modification is anticipated to have a significant impact on iron bearing minerals such as muscovite, phlogopite, biotite, and clinochlore, which possess a low hardness level ranging from 2-3 on the Mohs hardness scale.

In a similar manner, CDW derived silt exhibited decomposition of illite and calcite upon calcination, resulting in a range of values in the compositions, such as Ca between 7.74 and 24.11% for calcined samples in comparison to 11.34% Ca in STR. The Fe content in BM samples ranged between 7.46 % – 11.31% whereas the same for STR was 3.78%. These observed changes in elemental composition indicates changes to the mineralogical composition with the treatment adopted.

The EDAX analysis demonstrates an alteration in the elemental composition of mineral waste prior to and after activation. While the synthesis of new elements is not feasible during activation, the dehydroxylation and decarbonization that occur during thermal and mechanical treatments result in the removal of carbon, hydrogen, and oxygen from MTR and STR samples. This alters the overall quantity of elements in the samples prior to and following activation. The change in overall elemental composition is noticed by a variation in the percentage of different elements in the activated samples. This phenomenon is especially noticeable in cases of comparatively heavier elements such as iron and calcium

Table 4.6: Elemental composition of mine tailing samples and CDW derived silt samples.

Sample ID	Elemental composition		
MTR	**Element**	**Weight (%)**	**Atom (%)**
	O	51.32	65.495
	Na	3.81	3.385
	Mg	3.29	2.765
	Al	7.425	5.62
	Si	26.755	19.455
	S	0.795	0.505
	K	1.185	0.62
	Ca	0.935	0.475
	Fe	3.96	1.45
MTCC650	**Element**	**Weight (%)**	**Atom (%)**
	O	47.40	62.21
	Na	3.78	3.45
	Mg	3.39	2.93
	Al	8.01	6.23
	Si	27.91	20.87
	S	1.16	0.76
	K	1.30	0.70
	Ca	1.27	0.67
	Fe	0.49	0.22
MTCC750	**Element**	**Weight (%)**	**Atom (%)**
	O	50.4	64.66
	Na	4.035	3.60
	Mg	2.97	2.51
	Al	7.88	6.00
	Si	27.165	19.88
	S	0.935	0.60
	K	1.055	0.56
	Ca	0.965	0.50
	Fe	0.335	0.15
MTCC850	**Element**	**Weight (%)**	**Atom (%)**
	O	46.34	61.20
	Na	3.86	3.55
	Mg	3.36	2.92
	Al	8.11	6.35
	Si	28.85	21.70
	S	0.98	0.65
	K	1.41	0.76
	Ca	1.08	0.57
	Fe	0.63	0.28
MTCT650	**Element**	**Weight (%)**	**Atom (%)**
	O	47.29	61.96
	Na	3.88	3.54
	Mg	4.37	3.76
	Al	7.91	6.14
	Si	27.49	20.52
	S	0.86	0.56
	K	1.47	0.79

Sample ID	Elemental Composition		
STR	**Element**	**Weight (%)**	**Atom (%)**
	O	52.96	69.21
	Na	0.57	0.52
	Mg	1.19	1.02
	Al	6.90	5.35
	Si	19.76	14.71
	S	1.43	0.94
	K	1.25	0.67
	Ca	11.34	5.91
	Fe	3.78	1.42
STCC750	O	48.97	63.70
	Na	0.79	2.20
	Mg	1.61	2.12
	Al	7.37	6.23
	Si	20.93	18.55
	S	1.27	0.78
	K	1.49	0.71
	Ca	12.29	3.66
	Fe	4.48	0.91
STCC850	O	47.79	64.64
	Na	0.63	0.60
	Mg	1.17	1.05
	Al	7.07	5.67
	Si	22.16	17.07
	S	1.28	0.86
	K	1.32	0.73
	Ca	14.17	7.65
	Fe	3.99	1.55
STCT750	**Element**	**Weight (%)**	**Atom (%)**
	O	35.38	53.095
	Na	0.44	0.46
	Mg	0.97	0.965
	Al	7.595	6.755
	Si	22.54	19.27
	S	2.32	1.735
	K	2.265	1.395
	Ca	24.11	14.44
	Fe	4.375	1.885
STCT850	**Element**	**Weight (%)**	**Atom (%)**
	O	48.02	66.61
	Na	0.7	0.67
	Mg	1.64	1.5
	Al	7.54	6.2
	Si	16.19	12.79
	S	2.01	1.39
	K	0.75	0.42
	Ca	7.74	4.28
	Fe	15.42	6.13
STBM30	**Element**	**Weight (%)**	**Atom (%)**

	Ca	1.04	0.55
	Fe	4.88	1.83
MTCT750	**Element**	**Weight (%)**	**Atom (%)**
	O	48.02	62.95
	Na	3.62	3.30
	Mg	3.74	3.23
	Al	7.57	5.88
	Si	26.53	19.82
	S	1.38	0.90
	K	1.43	0.77
	Ca	1.48	0.77
	Fe	5.43	2.04
MTCT850	**Element**	**Weight (%)**	**Atom (%)**
	O	48.04	62.76
	Na	4.32	3.92
	Mg	3.46	2.97
	Al	7.78	6.03
	Si	27.21	20.25
	S	0.76	0.50
	K	1.54	0.82
	Ca	1.02	0.54
	Fe	5.29	1.98
MTBM30	**Element**	**Weight (%)**	**Atom (%)**
	O	31.94	48.12
	Na	2.52	2.64
	Mg	3.89	3.86
	Al	8.05	7.19
	Si	32.28	27.72
	S	1.63	1.22
	K	2.56	1.57
	Ca	1.69	1.02
	Fe	15.45	6.68
MTBM60	**Element**	**Weight (%)**	**Atom (%)**
	O	36.22	52.24
	Na	3.06	3.08
	Mg	3.62	3.44
	Al	8.30	7.10
	Si	31.16	25.60
	S	1.93	1.39
	K	2.05	1.21
	Ca	1.83	1.06
	Fe	11.85	4.91
MTBM90	**Element**	**Weight (%)**	**Atom (%)**
	O	34.30	50.71
	Na	2.44	2.52
	Mg	4.90	4.76
	Al	8.30	7.28
	Si	29.43	24.81
	S	1.22	0.90
	K	3.15	1.90
	Ca	1.50	0.89
	Fe	14.79	6.27
	O	37.78	56.24
	Na	0.52	0.54
	Mg	1.14	1.12
	Al	8.29	7.32
	Si	20.57	17.45
	S	2.51	1.87
	K	2.04	1.25
	Ca	15.86	9.43
	Fe	11.31	4.83
STBM60	**Element**	**Weight (%)**	**Atom (%)**
	O	45.29	63.55
	Na	0.75	0.73
	Mg	1.36	1.26
	Al	6.85	5.70
	Si	17.64	14.11
	S	3.14	2.20
	K	1.95	1.11
	Ca	13.22	7.41
	Fe	9.82	3.95
STBM90	**Element**	**Weight (%)**	**Atom (%)**
	O	44.36	62.18
	Na	0.79	0.77
	Mg	1.24	1.14
	Al	7.35	6.11
	Si	19.72	15.75
	S	2.50	1.75
	K	1.66	0.95
	Ca	14.93	8.36
	Fe	7.46	3.00

4.7 Chemical Reactivity by Dissolution of Si and Al

The solubility of Si and Al in alkaline environment is obtained from ICP. This gives an indication of the Si and Al available for formation of hydration products in an alkaline environment and hence the value is directly proportional to the reactivity of the material in an alkali activated cement or in a cementitious system [164]. The Si/Al ratio obtained from the test can provide an indication on type of activator that would be suitable if the material is used as a precursor for alkali activation (sodium hydroxide, sodium silicate etc) or if it should be used in combination with an Al rich source (in the form of alumina, red mud, kaolinite etc).

Fig. 4.11 shows the Si and Al solubility of the tailing samples. The concentration of Si and Al in the leachate was 0.34 mg/L and 0.03 mg/L respectively for MTR. The values ranged between 0.38 – 0.58 mg/L Si and 0.04 – 0.05 Al for CC samples, 0.51 – 0.80 mg/L Si and 0.05 – 0.06 Al for CT samples and 0.51 – 1.0 mg/L Si and 0.04 – 0.08 Al for BM samples. It is observed that the percentage of Si and Al in the leachate increased with the treatment, especially milling. The amount of Al was 154% higher and Si was 196% higher than MTR for MTBM90. In the case of calcination, Al quantity increased 60-66%, while Si was 116-134% higher for MTCT650 and MTCT750 than MTR. However, in case of MTCT850 there was an increase of 49% for Si and 61% for Al than MTR. This implies that milling of samples was more effective in improving the dissolution of Si and Al from mine tailings than calcination. The mine tailing samples had an Si/ Al value of 10.32 for MTR and ranged from 9.13 to 10.86 for CC samples, 9.57 – 14.27 for CT samples 12.00 – 13.92 for BM samples. The Si/Al values observed in this dissolution study exhibit a significant difference when compared to the Si/Al ratio acquired using EDAX, which fell between the range of 3.44 – 4.00 for mine tailing samples. This confirms that the Si and Al present in the samples may not always be available in the matrix for reaction. Furthermore, the findings indicate that the treatment techniques induce different responses from various minerals, resulting in variations in the leachate's Si and Al availability. These variations are also dependent upon the specific composition and percentage of different elements present in the mineral under discussion.

The test results (of the diluted leachate for CDW derived silt samples is given in Fig. 4.12. It can be seen that concentration of Si and Al in the leachate was 3.33 mg/L and 0.45 mg/L respectively for STR. The values ranged between 2.63 – 7.10 mg/L Si and 0.34 – 1.26 Al for CC samples, 3.45 – 9.09 mg/L Si and 0.48 – 1.05 Al for CT samples and 4.12 – 4.50 mg/L Si and 0.37 – 0.49 Al for BM samples. It shows that STCT750 had a higher solubility, 9 mg/L of Si and 1.05 mg/L Al than the other samples. This was about 134% higher for Al and 172% higher for Si than STR samples. This indicates the silt samples calcined at 750°C (STCT750) shall have more Si and Al available in the matrix for reaction in case of alkali activation. The milling process increased the Al solubility by 23% to 35% and Si solubility ranged between 82% to 107.5% of STR. The Si/ Al values for STR was 7.40 and that of STCC samples was between 5.64 – 7.68, STCT was between 7.22 and 8.62 and STBM was between 9.30 – 11.15. The Si/ Al values for CDW derived samples as determined from EDAX analysis was in range of 2.15 – 3.13. Similar to the findings of mine tailing samples, CDW derived silt also shows that the available Si and Al is different from the elemental composition of the material.

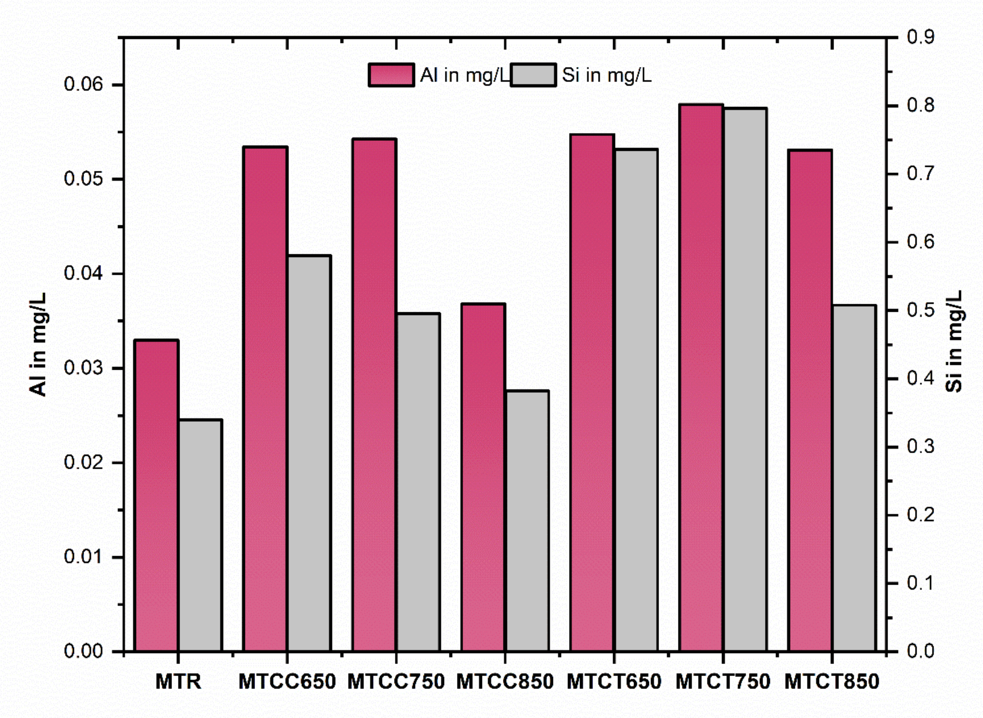

(a)

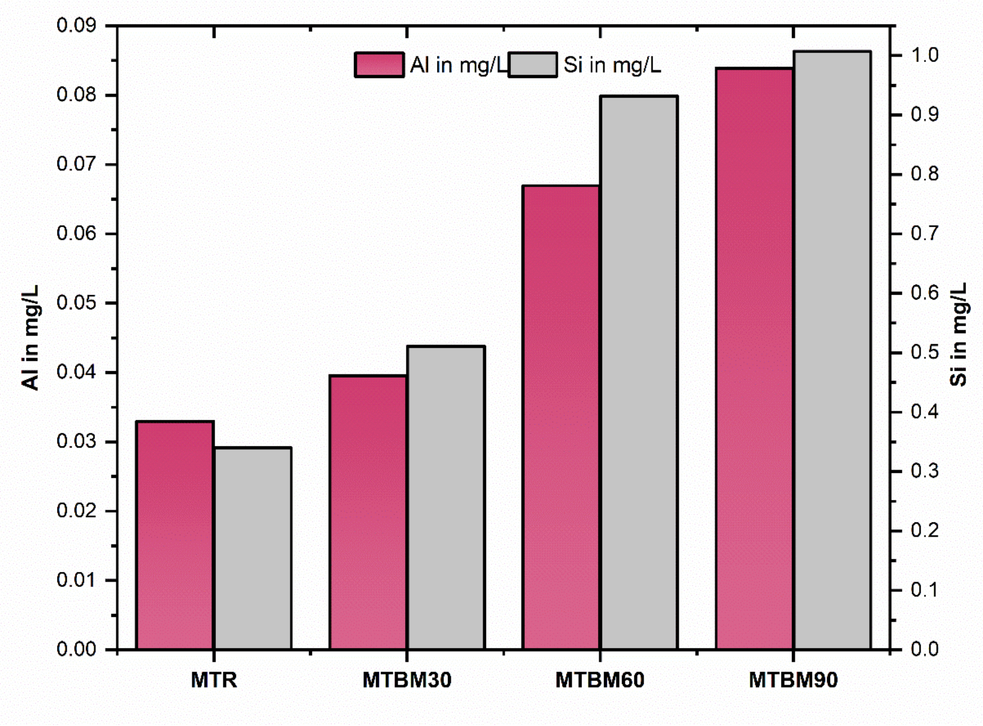

(b)

Fig. 4.11: Solubility of Si and Al from mine tailing (a) raw and thermally treated mine tailing and (b) raw and mechanically treated mine tailing. Both studies performed in 8M NaOH.

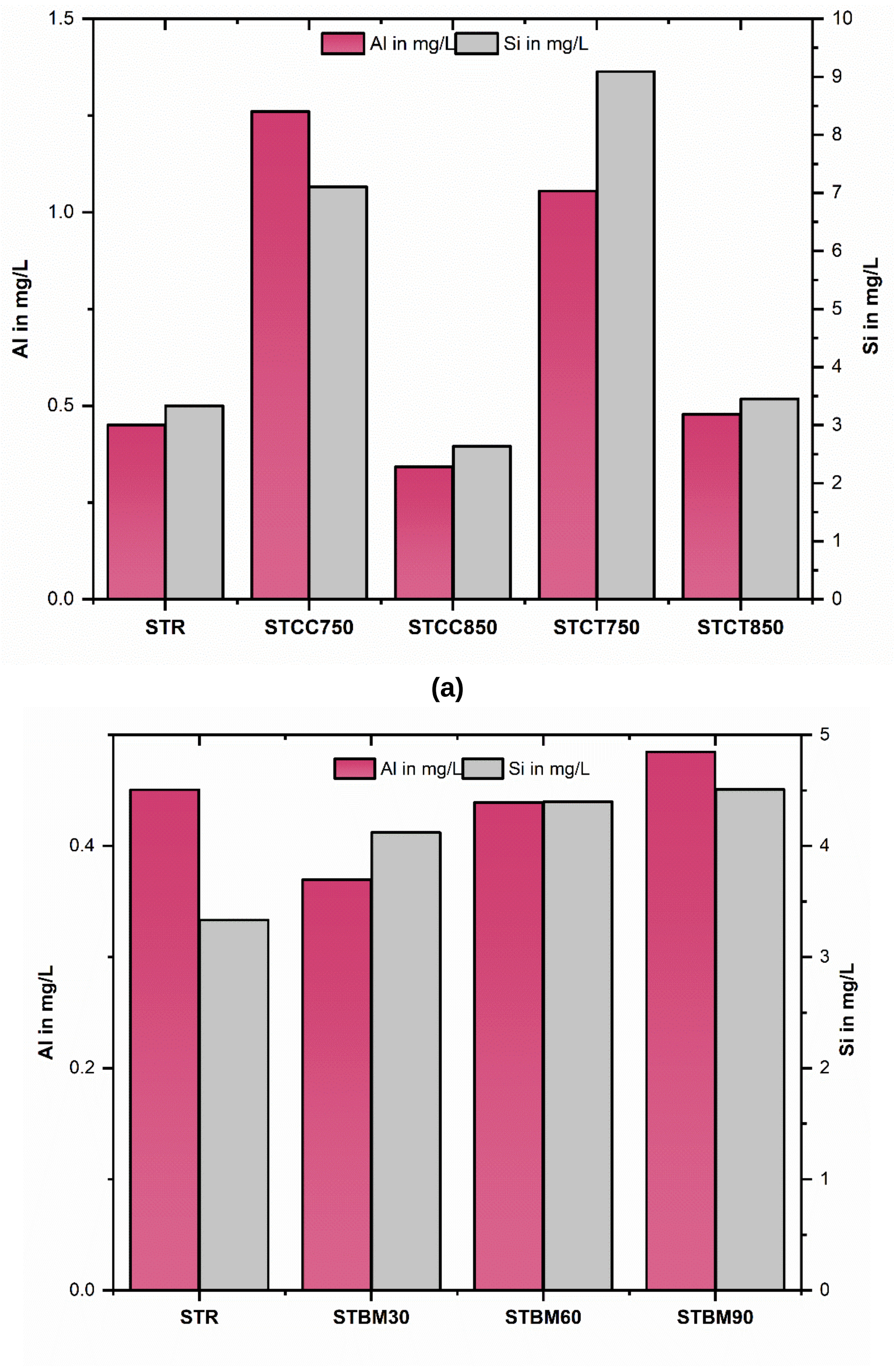

(a)

(b)

Fig. 4.12: Solubility of Si and Al from CDW derived silt (a) raw and thermally treated CDW derived silt and (b) raw and mechanically treated CDW derived silt. Both studies performed in 8M NaOH.

4.8 Chemical Reactivity by adapted R3 test

The heat of hydration of mine tailing with time is reported in Fig. 4.13 (a), (b) and (c). The data show that the initial high heat of hydration followed by slower or almost no heat of hydration shows a typical trend of a highly reactive supplementary cementitious material as reported in the literature. From Figs. 4.13 (a) – (c), it is evident that the behaviour of silica fume fits this description [237,264]. And a gradual increasing heat of hydration is typical for a slow reactive pozzolan such as fly ash.

From Fig. 4.13 (a) MTR, MTCC650, MTCC750 and MTCC850 were almost inert. While Fig. 4.13 (b) shows that MTR and MTCT650 samples were found to be almost inert, MTCT750, and MTCT850 show a trend similar to that of a slow reactive material [237,265], a trend which is also verified by the behaviour of fly ash. From Fig. 4.13 it can also be inferred that reactivity of fly ash and MTCT850 was better than that of silica fume at later ages (after 3 days) and MTCT750 was almost equal to that of silica fume at the end of seven days. These findings link very well with previous observations made in this study in relation to the confirmed structural changes on the mineral samples. It seems that while the calcination at 650 ^{0}C does not have any influence on the mine tailing, treatment at 750 ^{0}C and 850 ^{0}C has yielded a reactive compound that resembles fly ash in terms of pozzolanic behaviour. In the case of MTCT850, the performance of the tailing appears even better than that of fly ash, with heat of hydration about 1.35 times higher compared to fly ash.

Whereas from Fig. 4.13 (c) it can be seen that ball-milling seems to have a similar effect for the longest milling duration, with MTBM90 being very similar to MTCT750. Nonetheless, calcination appears more effective at this stage. The observed reduction in particle size with increase in milling time suggests a correlation. However, based on the dissolution test findings, it can be deduced that the Si/Al ratio of MTBM60 was 13.92, whereas the Si/Al ratios of MTBM30 and MTBM60 were 12.91 and 12.00, respectively. This observation suggests that there is a variation in the concentration of elements, including Si, Al, Ca, Fe, and Mg, leaching from the samples. This leaching mechanism contributes to the ions available for the formation of hydration products and hence influence the heat of hydration.

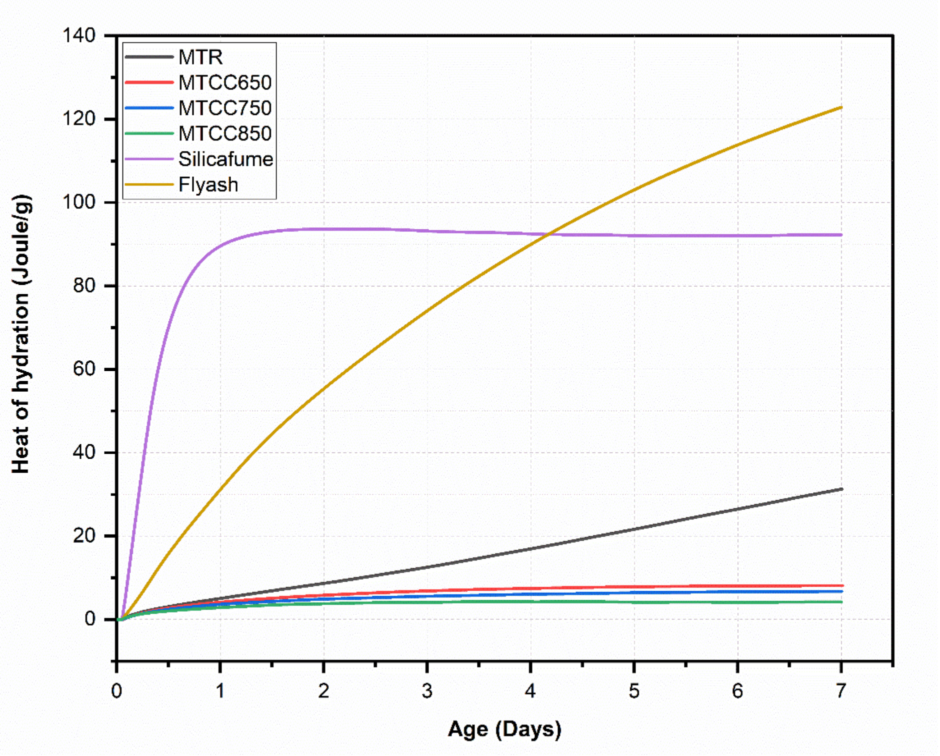

Heat of hydration (Joule/g)
Age (Days)
MTR
MTCC650
MTCC750
MTCC850
Silicafume
Flyash
0
20
40
60
80
100
120
140
0
1
2
3
4
5
6
7

(a)

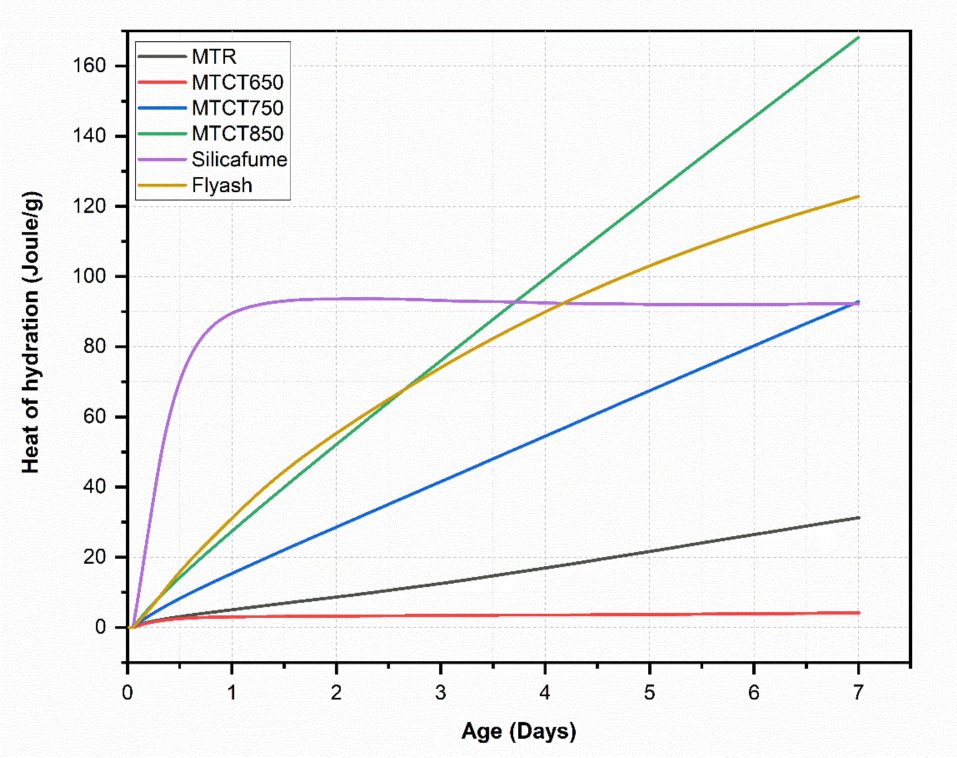

Heat of hydration (Joule/g)
Age (Days)
MTR
MTCT650
MTCT750
MTCT850
Silicafume
Flyash
0
20
40
60
80
100
120
140
160
0
1
2
3
4
5
6
7

(b)

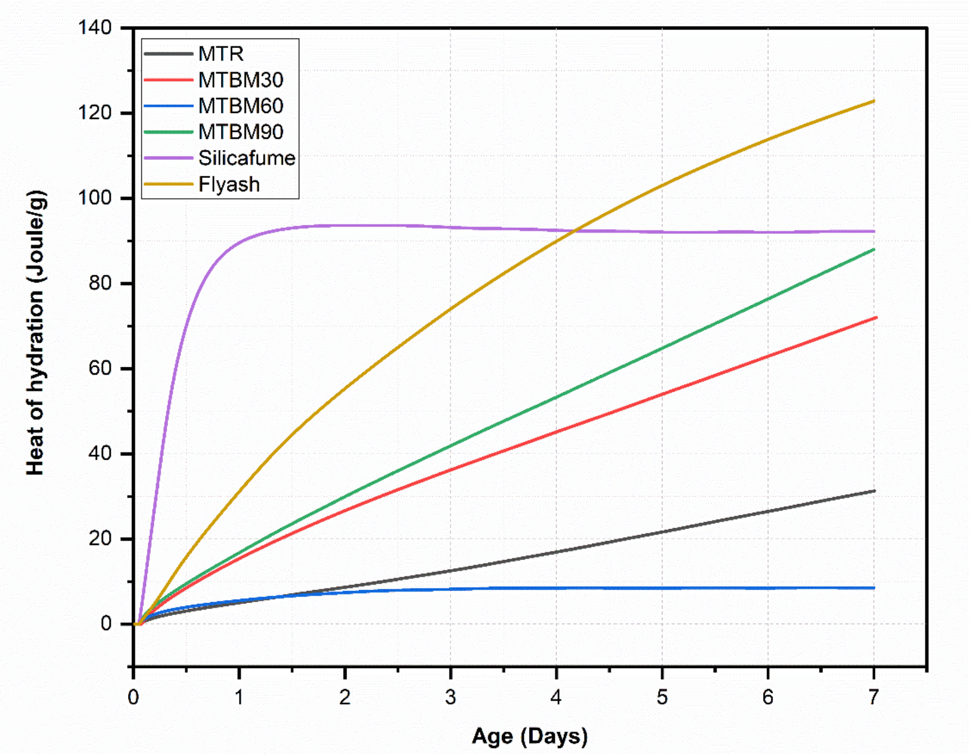

(c)

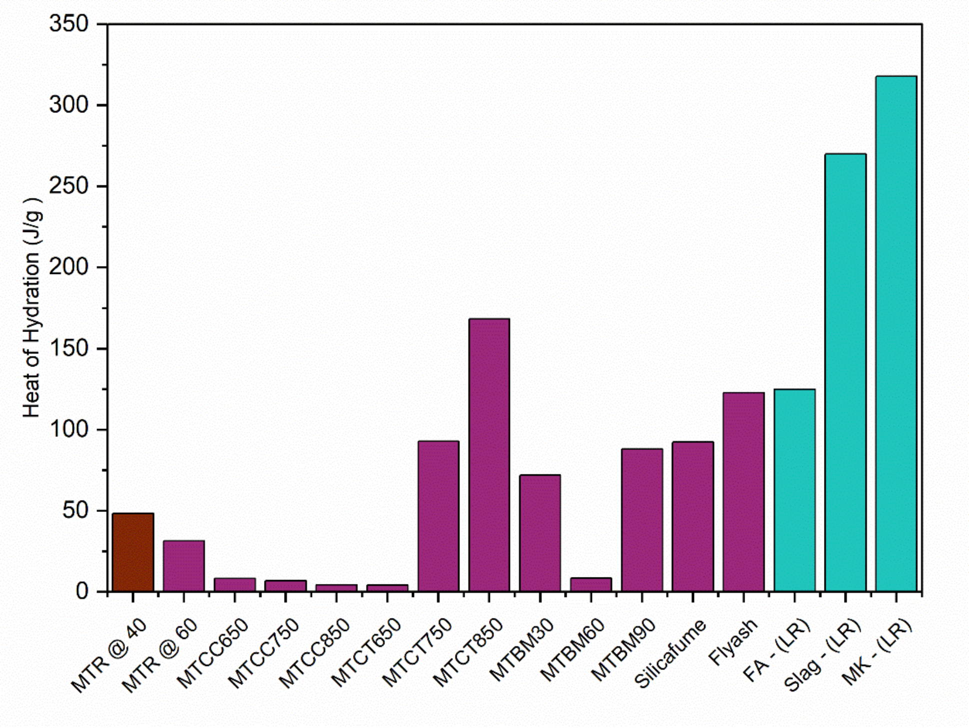

(d)

Fig. 4.13: Cumulative heat of hydration from adapted R3 test of mine tailings at 60 °C. (a) MTR and calcined mine tailings in CC series (b) MTR and calcined mine tailings in CC series (c) MTR and ball milled mine tailings, BM series (d) Cumulative heat of hydration at end of seven days compared with the past studies [237,265]..

The heat of hydration of the CDW derived silt samples is given in Fig. 4.14 (a) to (c). Results in Figs. 4.14 (a) to (c). show that STR, STBM60 and STBM90 are almost inert. Though STCC750, STCC850, STCT750 and STBM60 were having a heat of hydration lower than fly ash and silica fume, they performed comparatively better than the other samples. This indicates that in these two cases a degree of pozzolanicity is expected. The heat of hydration of fly ash was about 2.4 times that of STCT750 and 2.6 times that of STBM60. Similarly, heat of hydration of silica fume was about 1.8 times that of STCT750 and 2 times that of STBM60.

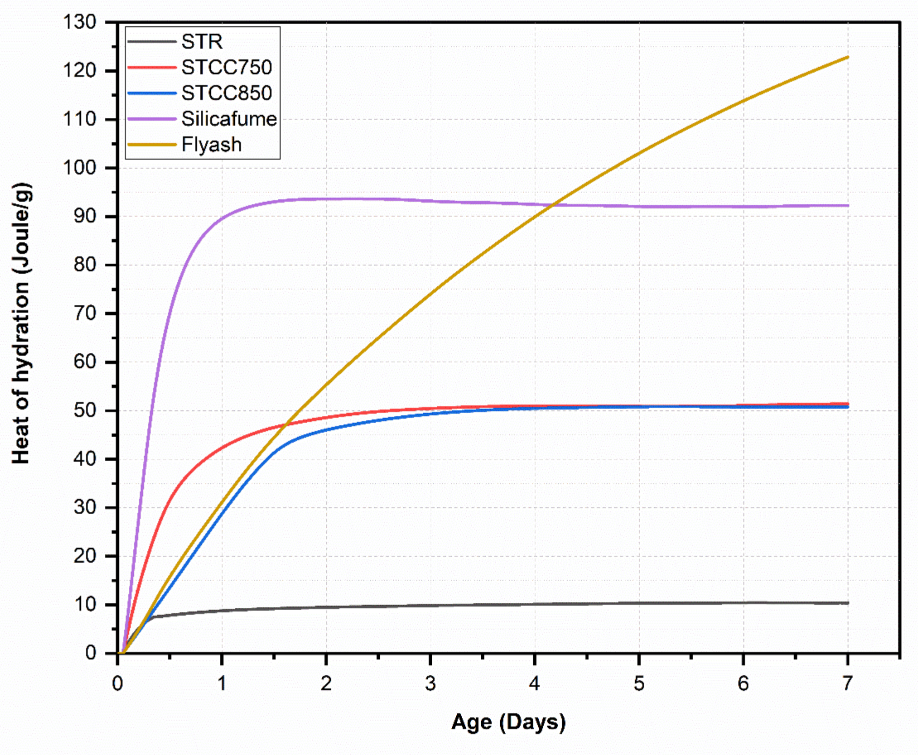

(a)

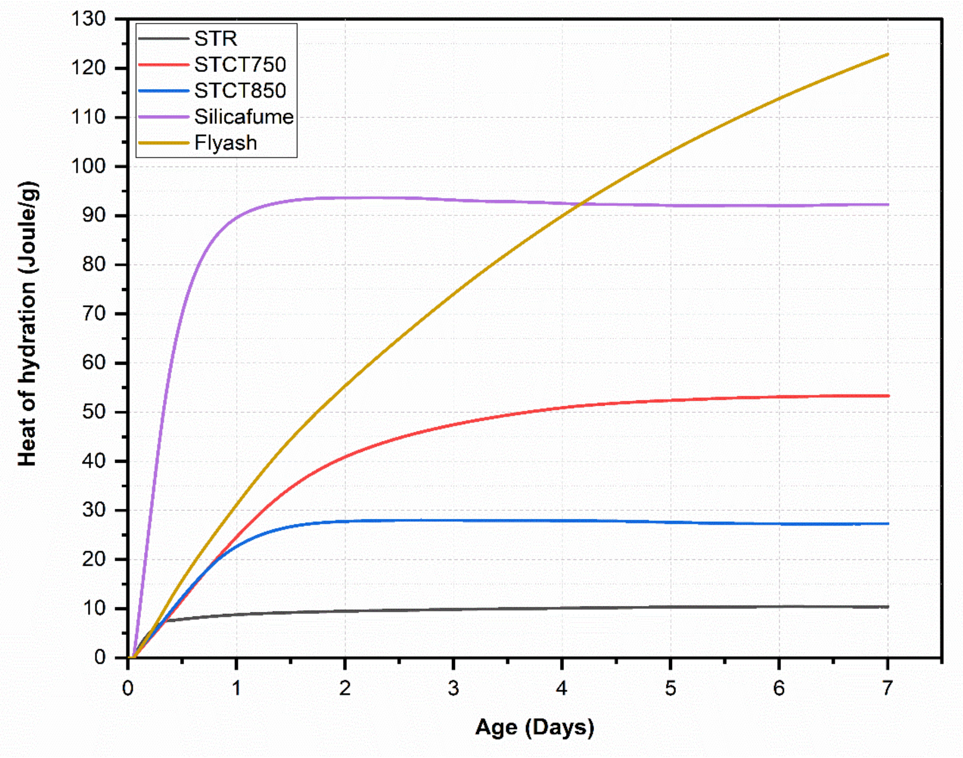
Heat of hydration (Joule/g)
Age (Days)
0
10
20
30
40
50
60
70
80
90
100
110
120
130
0
1
2
3
4
5
6
7
STR
STCT750
STCT850
Silicafume
Flyash

(b)

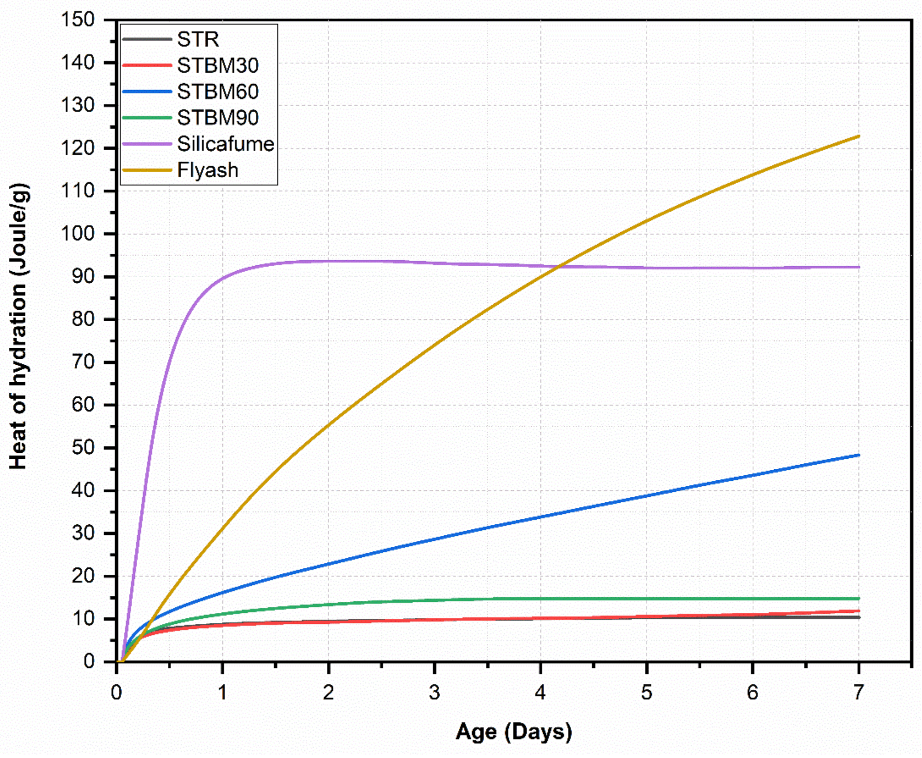
Heat of hydration (Joule/g)
Age (Days)
0
10
20
30
40
50
60
70
80
90
100
110
120
130
140
150
0
1
2
3
4
5
6
7
STR
STBM30
STBM60
STBM90
Silicafume
Flyash

(c)

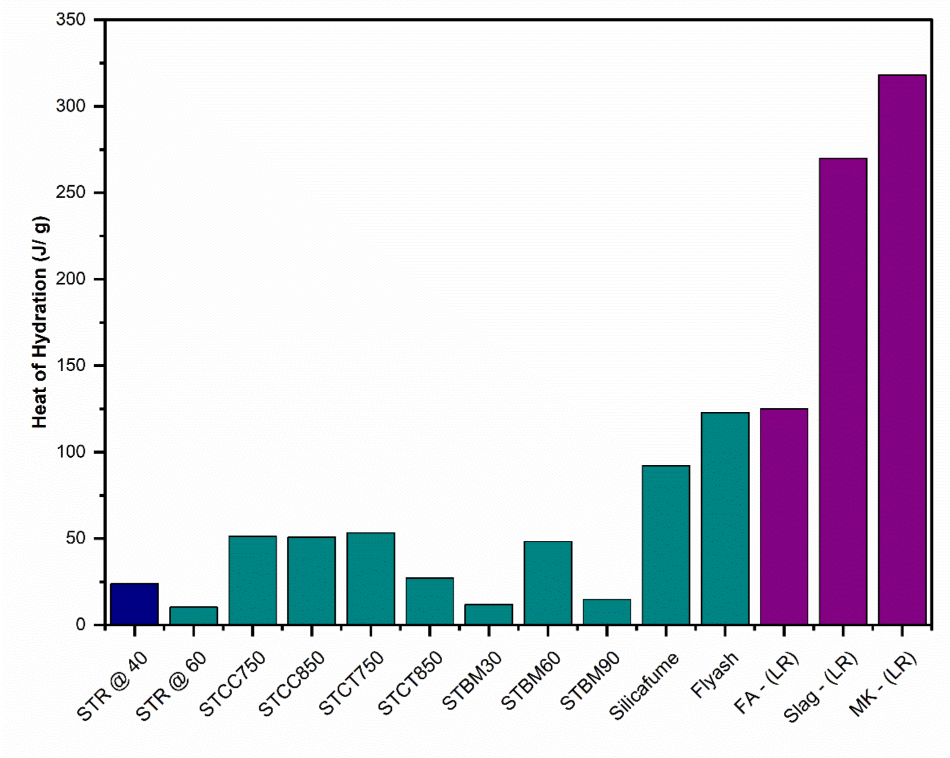

(d)

Fig. 4.14: Cumulative heat of hydration from adapted R3 test of CDW derived silt at 60 °C. (a) STR and calcined CDW derived silt in CC series (b) STR and calcined CDW derived silt in CC series (c) STR and ball milled mine tailings, BM series (d) Cumulative heat of hydration at end of seven days compared with the past studies [237,265].

It can be seen from Figs. 4.13 (d) and 4.14 (d), that MTCT850 and STCT750 exhibited highest the heat of hydration and it can also be noted that heat of hydration values of MTCT850 was higher than that of STCT750. Considering the trend of the heat of hydration curves it can also be seen that the STCT750 has plateaued within 7 days (a trend that resembles a fast-reacting pozzolan such as silica fume) whereas MTCT850 show the possibility of heat of hydration beyond seven days. When a fast-reacting pozzolan is placed in the calorimetry chamber at a higher temperature (60^{o}C) it takes time for the temperature and signal to stabilize, and the initial reading is eliminated (75 minutes in this case, equivalent to 112 minutes if the test was performed at 40 ^{o}C ; see Chapter 3 section 3.3.10). This leads to an under estimation of overall heat of hydration [266] and it is also evident from the heat of hydration of MTR and STR tested at 40 ^{o}C reported in this. Fig. 4.13 (d) and 4.14 (d). The heat of hydration of fly ash, metakaolin and slag as reported in other studies determined using modified R3 test 50 ^{o}C are also given for comparison . Also, STCT750 has higher CaO content as the source STR has about 21% CaO as compared to MTCT850. Based on the high SiO_2 and CaO contents of the STCT750 it can be inferred that the material has a potential to self-react when it comes in contact with water and exhibit latent hydraulic property [265].

4.9 Conclusions

The present chapter discussed the findings that have contributed to our understanding of the physical, chemical, and morphological characteristics of the mineral wastes investigated in this study, namely mine tailings and CDW derived silt. Both materials exhibited a high silica composition, containing approximately 54-58% SiO_2. It was found that the mine tailings exhibited a comparatively smaller particle size compared to the CDW derived silt, as indicated by their respective D_{90} values of 67 µm and 75 µm.

Mineralogical composition of the mineral samples was assessed with X-ray diffraction (XRD). The MTR samples exhibited the presence of various minerals including chlorite, clinochlore, kaolinite, muscovite, phlogopite, biotite, quartz, hornblende, graphite, anhydrite, and plagioclase minerals such as oligoclase, anorthite, and albite. On the other hand, the STR samples indicated the presence of hematite, k-feldspar, gypsum, orthoclase, ferrosilite, hornblende, feldspar, anhydrite, microcline, albite, illite, quartz, chlorite, muscovite, phlogopite, and calcite. he selection of activation methods was determined by the mineralogical composition of minerals present.

The Rietveld analysis, Fourier Transform Infrared Spectroscopy (FTIR), determination of elemental composition, and examination of microstructure collectively revealed alterations in the mineral phases and morphology resulting from the treatment processes employed. The reactivity of the activated samples was evaluated by examining their solubility in an alkaline environment using ICP-OES and measuring their heat of hydration using adapted R3 tests. It was determined that MTCT850 and STCT750 exhibited a higher heat of hydration. The STCT750 and MTCT850 samples exhibited a greater concentration of soluble silicon (Si) and aluminium (Al) in sodium hydroxide solution, in comparison to the MTR and STR samples.

Although the mine tailings and CDW derived silt from the CC series exhibited certain favourable outcomes in terms of alterations in their morphology and reactivity, it should be noted that the lack of uniformity in the samples prevented the establishment of a correlation between the results obtained from different tests. Furthermore, it was not feasible to achieve repeatability and reliability in the findings obtained from the CC samples. Therefore, they have not been included in the selection process for further studies.

The evaluation of cementitious matrices in the next chapter focuses on samples prepared with STCT750 and MTCT850, as indicated by the findings discussed in this chapter.

CHAPTER 5
PERFORMANCE OF CEMENTITIOUS MATRICES

5.1 General

This chapter presents a comprehensive analysis of the performance characteristics exhibited by cementitious matrices incorporating varying proportions of activated mine tailing and CDW derived silt. The selection of MTCT850 and STCT750 for investigation in cementitious matrices was made based on the findings from the characterization studies discussed in the preceding chapter. (Hereinafter, mixes containing MTCT850 are called MT mixes and STCT750 are called ST mixes.)

The investigation centred on examining the hydration properties, microstructural attributes, and mineralogical composition of the paste specimens. The strength development and durability were studied for the mortar mixes.

5.2 Fresh Properties

5.2.1 Setting time

The initial setting time was determined for cementitious paste samples containing MTCT850 and STCT750 (10%, 20% and 40%) as a cement replacement and water/ cementitious binder ratio (w/c ratio) of 0. 4. The obtained values for setting time are presented in Table 5.1. It is evident that the setting time increased with increase in percentage of cement replacement.

The setting time of OPC was found to be 260 minutes and the setting time of the MT mixes ranged from 305 minutes to 325 minutes. The reason for the time delay can be ascribed to the presence of mineral phases, such as quartz, oligoclase, anorthite, and biotite, which collectively make up approximately 47% of MTCT850 (see Section 4.4, Chapter 4). The aforementioned phases exhibit lower reactivity in comparison to the mineral phases such as alite and belite, found in ordinary Portland cement. These phases are relatively slow in forming hydration products compared to the phases in OPC. The addition of these phases increases the concentration of elements such as silica and alumina, which in turn reduces the amount of calcium available in the matrix for the formation of hydration products leading to an increase in setting time.

The observed setting time of ST mixes varied from 275 minutes to 340 minutes. The delay in setting time with addition of STCT750 is more pronounced than MTCT850. The mineralogical composition (see Section 4.4, Chapter 4) of STCT750 suggests the presence of quartz, orthoclase which is inert and does not participate in cement hydration reactions, as well as anhydrite. Anhydrite, a dehydrated variant of calcium sulphate. Anhydrite which is an anhydrous form of calcium sulphate readily transforms to gypsum upon exposure to water as given in eq. 5.1. The presence of gypsum actively retards the setting of cement and thus contributes to a delayed initial setting time.

$$CaSO_4 + H_2O \rightarrow\ CaSO_4.2H_2O \qquad \text{Eq. (5.1)}$$

The delay in setting time with addition of mineral waste was also reported in various other studies, where the delay was either due to slow reactivity of the material [62], or due to active influence of ions and molecules present in the material [116,267].

Table 5.1: Initial setting time of mixes used in this study

Mix Designation	Setting time (min)
OPC W40	260
MT10 W40	305
MT20 W40	305
MT40 W40	325
ST10 W40	275
ST20 W40	315
ST40 W40	340

5.3 Heat of hydration

Cementitious paste samples were prepared using different proportions of MTCT850 and STCT750, with w/c ratios of 0.3, 0.4, and 0.5, as elaborated in Chapter 3. The heat of hydration of these mixes was measured over a period of 72 hours at 23^{o}C and compared to that of similar mixes containing fly ash and silica fume.

Figs. 5.1 (a) – (g) show the heat of hydration of MT mixes. Figs. 5.1 (a) to (d) are the estimate of heat of hydration per gram of binder and figs. 5.1 (e) to (g) are the estimate per gram of cement. The cumulative heat of hydration at the end of 72 hours for OPC mixes was between 256.30 to 322.63 J/g and the MT mixes was between 186.20 J/g to 295.30 J/g. The decrease in heat of hydration with increase in the percentage of MTCT850 is evident from Figure 5.1 (a) to (c). The data presented in Figure 5.1 (a) indicates that when the w/c ratio is 0.3, the heat of hydration for mixes containing 10%, 20%, and 40% MTCT850 is approximately 97.9%, 88.4%, and 72.6% respectively, compared to mixes containing OPC. The highest heat of hydration was observed in OPC, with the subsequent highest heat of hydration observed in MT10. The MT20 mixes exhibited similar performance to the mixes containing 10% silica fume and 10% fly ash, with heat of hydration values that were 88.7% and 87.3% of those observed in ordinary Portland cement (OPC) mixtures, respectively. MT40 mixes exhibited a heat of hydration comparable to mixes containing 40% fly ash, but higher than mixes containing 40% silica fume.

According to the results presented in Figure 5.1 (b) and (c), it can be observed that the heat of hydration for a w/c ratio of 0.4 displayed values of 92.0%, 86.7%, and 67.6% for mixes containing 10%, 20%, and 40% MTCT850, respectively. Similarly, for a w/c ratio of 0.5, the corresponding heat of hydration values were 91.5%, 84.5%, and 63.5%. The heat of hydration of mixes containing 10% silica fume and MT20 exhibited similar values at w/c ratios of 0.4 and 0.5%. Specifically, the heat of hydration was approximately 86% of OPC at a w/c ratio of 0.4, and 85% of OPC at a w/c r ratio of 0.5% for both the mixes.

According to the findings presented in Figure 5.1 (d), it is evident that the heat of hydration was higher values for mixes with w/c ratios of 0.4 and 0.5, in comparison to mixes with a w/c ratio of 0.3. The heat of hydration for OPC mixes exhibited an increase of 19 % and 25 % for w/c ratios of 0.4 and 0.5, respectively when compared to mixes with 0.3 w/c ratio. In the case of mixes containing MTCT850, the heat of hydration was approximately 11-17% higher for a w/c ratio of 0.4 and 10-17% higher for a w/c ratio of 0.5 than mixes with 0.3 w/c ratio. The increased heat of hydration observed at 0.5 w/c ratio can be attributed to the availability of surplus water for hydration reaction and thus promoting the hydration of the cementitious material at early ages.

It can be observed from the results below that the heat of hydration exhibited by mixtures containing 10% and 20% MTCT850 is comparable to or greater than that observed in mixtures incorporating silica fume and fly ash. For this reason, MTCT850 was selected as the optimum MT treated regime for the rest of the cement-based matrix experimental work.

Figs. 5.1 (e) to (g) shows the heat of hydration of the mixes per gram of cement. Therefore, the findings from these plots can be used to distinguish the contributions of the mineral addition to the total heat of hydration of the MT mixes. It can be observed from 5.1 (e) to (g) that the heat of hydration per gram of cement of OPC mixes were in the range of 256 J/g whereas the MT mixes were in the range of 279 J/g to 345 J/g depending on the percentage of MTCT850 and the water cement ratio. It can be observed that the difference in heat of hydration increased with increase in percentage of MTCT850. This increase could be contributed by the participation of MTCT850 in hydration, creation of additional nucleation sites for hydrate phases due to presence of MTCT850 and increase the water to cement ratio due to replacement of cement by MTCT850, which increases the long-term hydration degree by providing more space for the hydrates to precipitate [232].

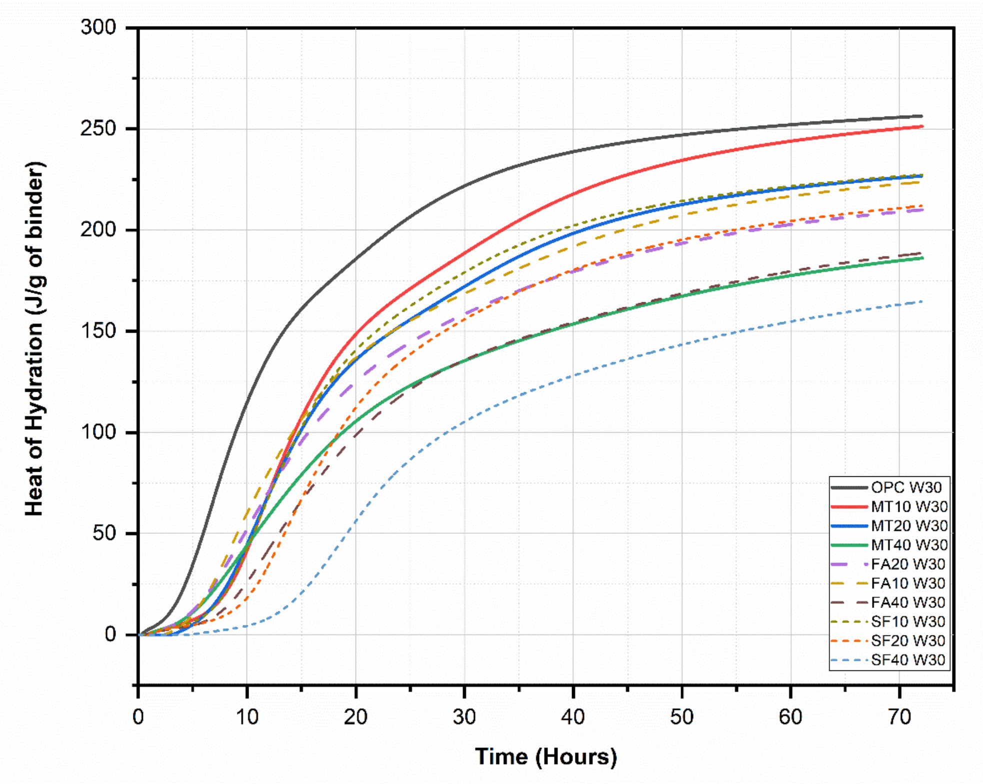
Heat of Hydration (J/g of binder)
Time (Hours)
300
250
200
150
100
50
0
0
10
20
30
40
50
60
70
OPC W30
MT10 W30
MT20 W30
MT40 W30
FA20 W30
FA10 W30
FA40 W30
SF10 W30
SF20 W30
SF40 W30

(a)

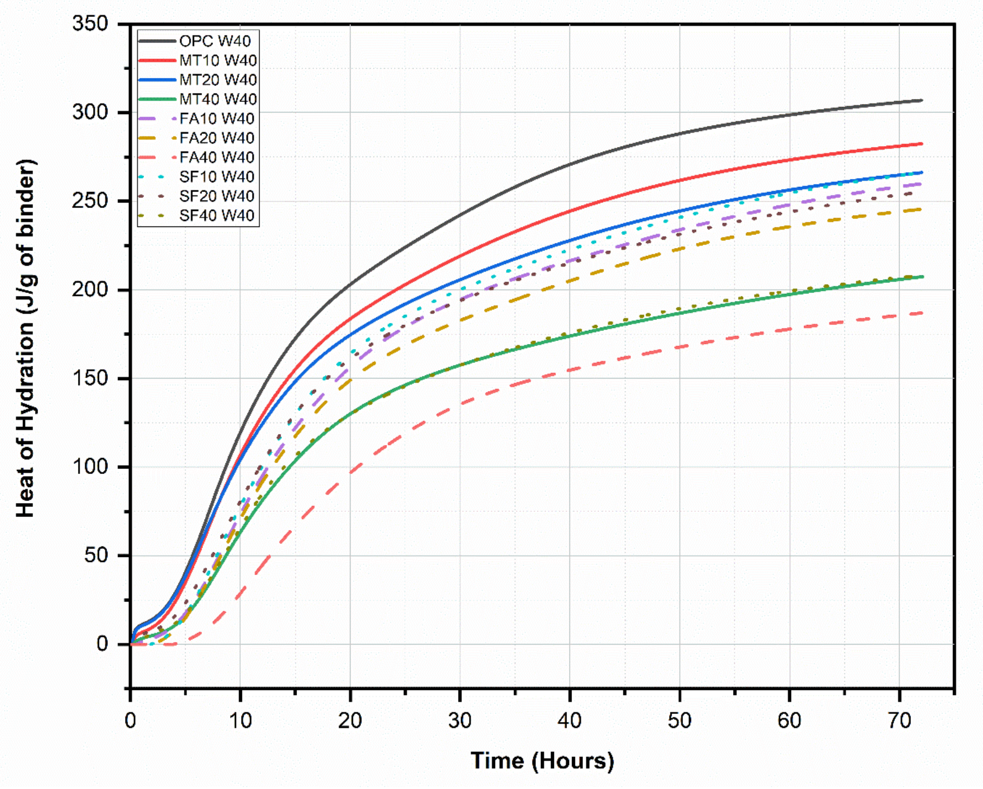
Heat of Hydration (J/g of binder)
Time (Hours)
350
300
250
200
150
100
50
0
0
10
20
30
40
50
60
70
OPC W40
MT10 W40
MT20 W40
MT40 W40
FA10 W40
FA20 W40
FA40 W40
SF10 W40
SF20 W40
SF40 W40

(b)

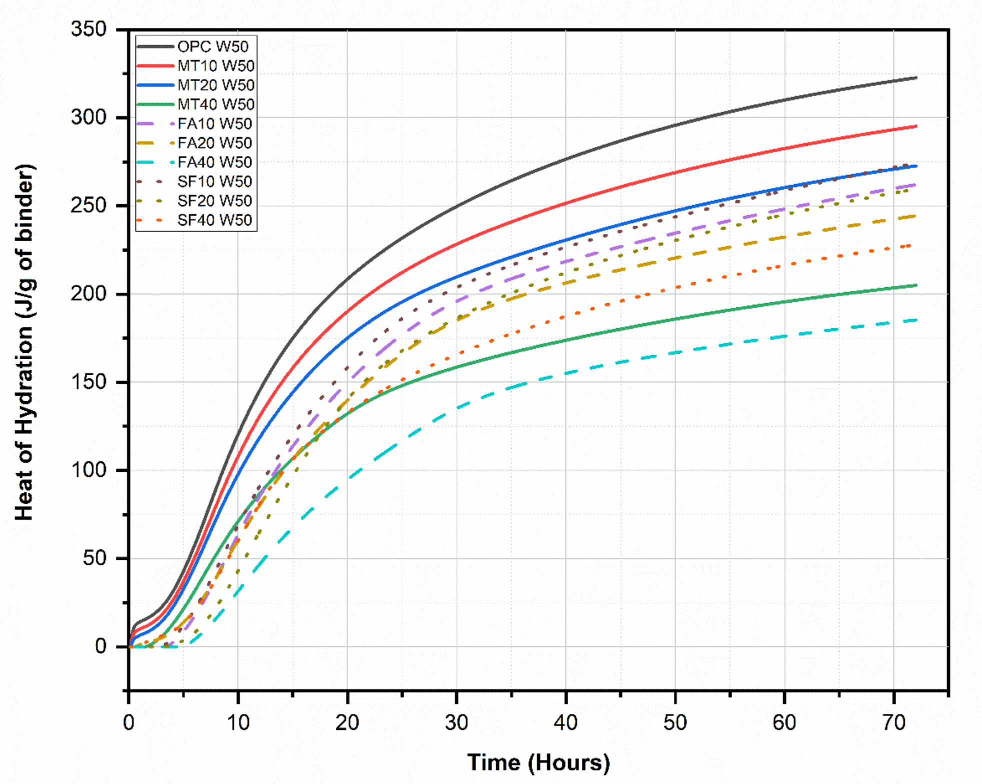

350
300
250
200
150
100
50
0
Heat of Hydration (J/g of binder)
0
10
20
30
40
50
60
70
Time (Hours)
OPC W50
MT10 W50
MT20 W50
MT40 W50
FA10 W50
FA20 W50
FA40 W50
SF10 W50
SF20 W50
SF40 W50

(c)

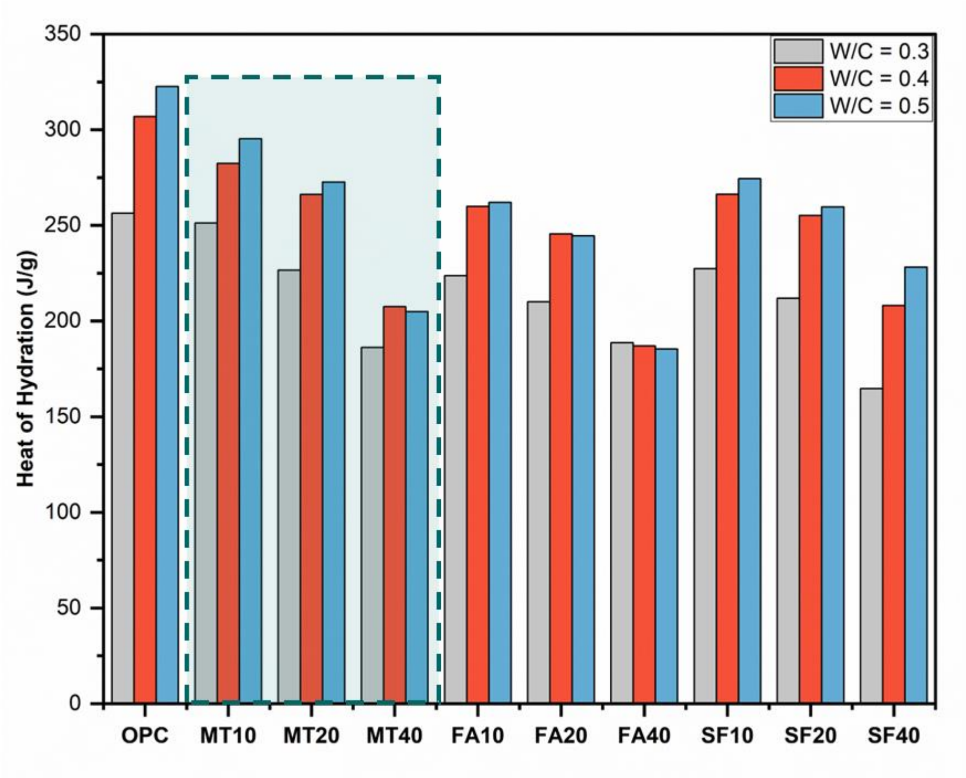

350
300
250
200
150
100
50
0
Heat of Hydration (J/g)
OPC
MT10
MT20
MT40
FA10
FA20
FA40
SF10
SF20
SF40
W/C = 0.3
W/C = 0.4
W/C = 0.5

(d)

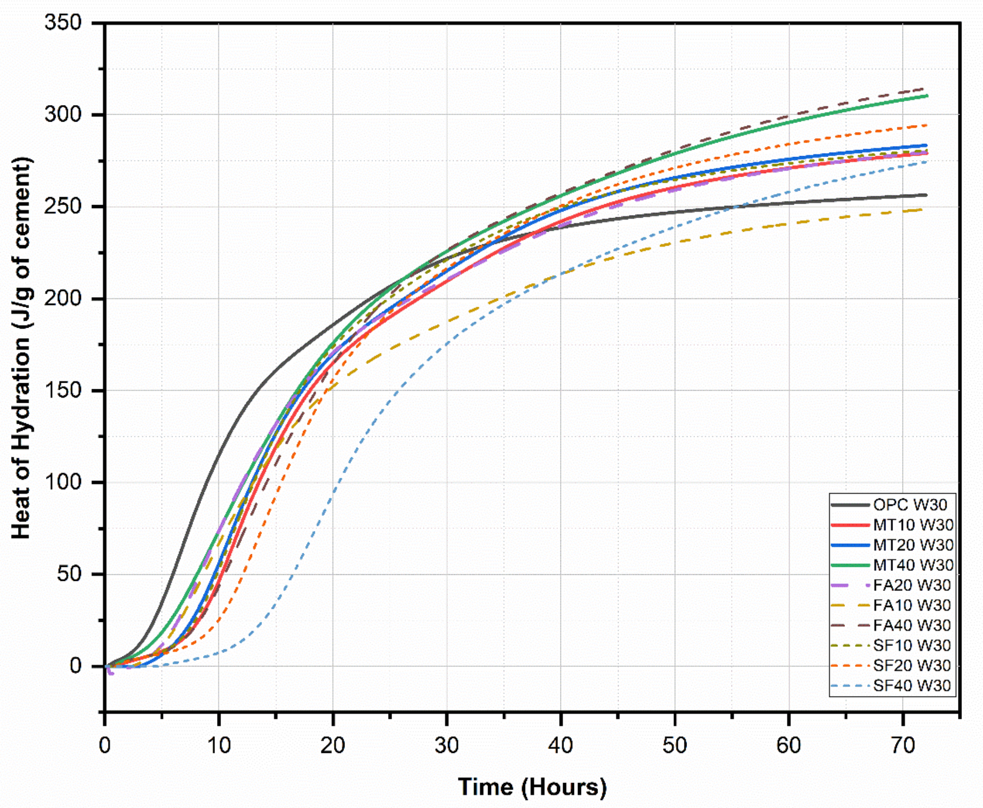
Heat of Hydration (J/g of cement)
Time (Hours)
350
300
250
200
150
100
50
0
0
10
20
30
40
50
60
70
OPC W30
MT10 W30
MT20 W30
MT40 W30
FA20 W30
FA10 W30
FA40 W30
SF10 W30
SF20 W30
SF40 W30

(e)

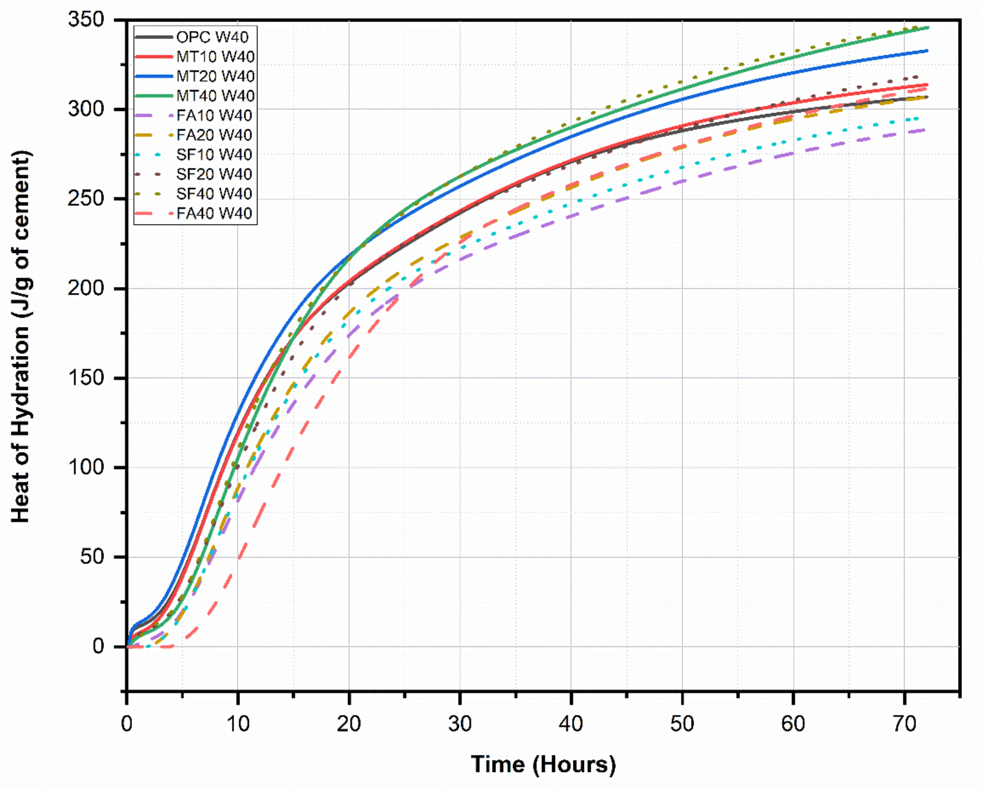
Heat of Hydration (J/g of cement)
Time (Hours)
350
300
250
200
150
100
50
0
0
10
20
30
40
50
60
70
OPC W40
MT10 W40
MT20 W40
MT40 W40
FA10 W40
FA20 W40
SF10 W40
SF20 W40
SF40 W40
FA40 W40

(f)

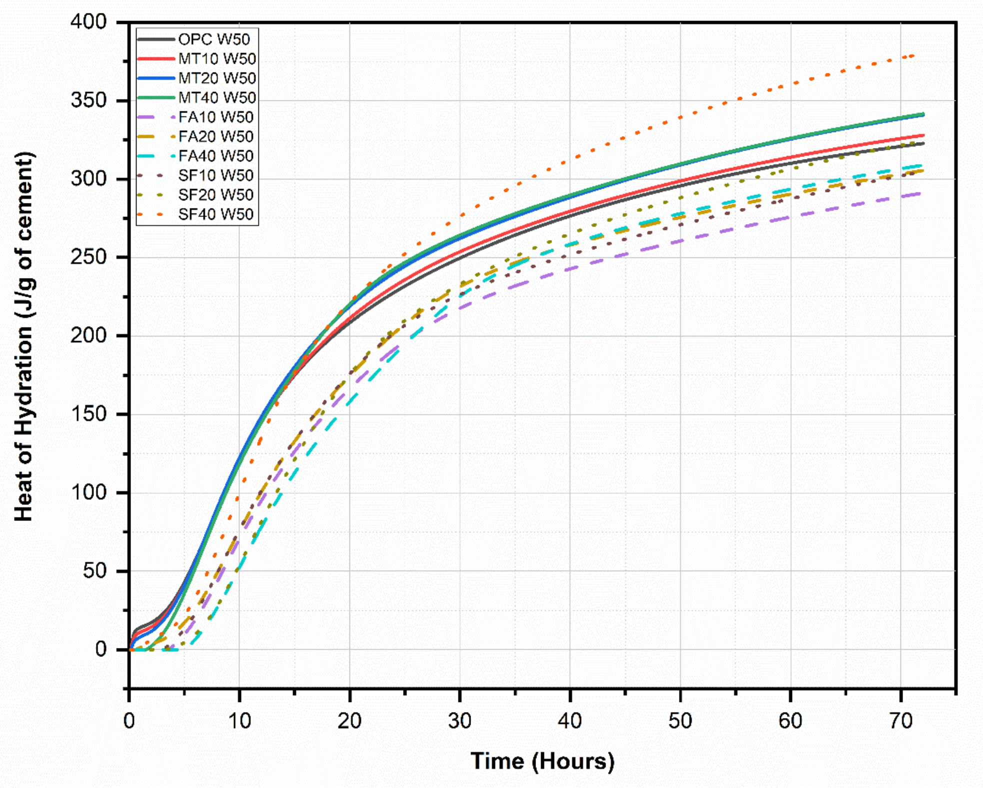

(g)

Fig. 5.1: Evolution of heat of hydration of cementitious paste mixes with 10%, 20% and 40% MTCT850 (a) mixes with w/c ratio 0.3 (b) mixes with w/c ratio 0.4 (c) mixes with w/c ratio 0.5 (d) Cumulative heat of hydration of the mixes at the end of 72 hours

Figures 5.2 (a) through (d) present data on the heat of hydration of OPC and ST mixes. The heat of hydration the ST mixes varied between 186.12 and 290.23 J/g as compared to between 256.30 to 322.63 J/g for OPC. According to the findings presented in Figure 4.2 (a), there was a decrease in the heat of hydration as the percentage of STCT750 increased. The heat of hydration for mixtures containing 10%, 20%, and 40% of STCT750 was approximately 90.05%, 84.9%, and 72.6% respectively, of that of OPC. The heat of hydration observed ST10 mixes was found to be greater than that observed in mixes containing silica fume and fly ash. The ST20 mixes displayed an approximately 2% higher heat of hydration compared to the mixes containing 20% fly ash and silica fume.

Examining the data presented in Figures 5.2 (b) and (c), it can be observed that the mixes containing 10%, 20%, and 40% STCT750 exhibited heat of hydration values equivalent to 90.8%, 86.5%, and 70.5% of the heat of hydration of Ordinary Portland Cement (OPC) at a w/c ratio of 0.4. The observed values for a w/c ratio of 0.5% were found to be 90%, 82.2%, and 66.5% of that of OPC, respectively. The ST40 mixes exhibited a heat of hydration ranging from 66% to 72% of Ordinary Portland Cement (OPC) across all w/c ratios.

Based on the data presented in Figure 5.2 (d), it is evident that, similar to MT mixes, the ST mixes exhibited a higher heat of hydration when the w/c ratio was 0.4 and 0.5, in comparison to the heat of hydration observed at a w/c ratio of 0.3. The heat of hydration of ST mixes exhibited an increase of 16% to 22% compared to OPC when the w/c ratio was 0.4. Similarly, when the w/c ratio was 0.5, the heat of hydration for these mixtures was found to be 15% to 25% higher than OPC. While the heat of hydration ST10 and ST20 was found to be lower than that of OPC and MT mixes, it was observed that their heat of hydration was higher than or comparable to mixes incorporating silica fume and fly ash.

The reduction in heat of hydration with addition of mineral wastes, as observed in the present study, is reported in various studies [116,213,268]. Nevertheless, it is crucial to acknowledge that these observations were solely conducted within the initial 72-hour timeframe subsequent to the mixing process. While these tests provide an insight into the hydration process and subsequent strength development, it is important to note that the strength measured at different ages may not consistently exhibit a uniform or comparable pattern as discussed here. Addition of mineral wastes which are rich in Si leads to dilution of Ca ions in the system. And these materials added (MTCT850 and STCT750) acts more as slow reactive supplementary cementitious materials in the initial period of hydration and later provide additional Si needed for the formation of secondary C-S-H [6,7] contributing to the strength gain [191,226].

The observed delayed onset of hydration in the ST10W30 in Fig. 5.2 (a) can be attributed to the low w/c ratio and delayed hydration specific to this particular mix and not a general trend of ST mixes.

Similar to the results of MTCT850, Figures 5.2 (e) to (g) display the amount of heat released during the hydration process for each gram of cement in the mixes with STCT750. Hence, the results obtained from these plots can be utilised to determine the effect of the mineral addition on the total heat of hydration of the ST mixes. From 5.2 (e) to (g), it is evident that the heat of hydration per gram of cement for OPC mixes ranged from 256 J/g. On the other hand, for ST mixes, the range varied from 256 J/g to 414 J/g, depending on the percentage of STCT750 and the water cement ratio. The difference in heat of hydration was found to increase as the amount of STCT750 increased. This increase could be attributed to the involvement of STCT750 in the hydration process, the creation of more nucleation sites for hydrate phases due to the presence of STCT750, and the increase in the water to cement ratio as the cement is replaced by STCT750 which contributes to enhancement of the long-term hydration degree by allowing more space for the hydrates to form [232].

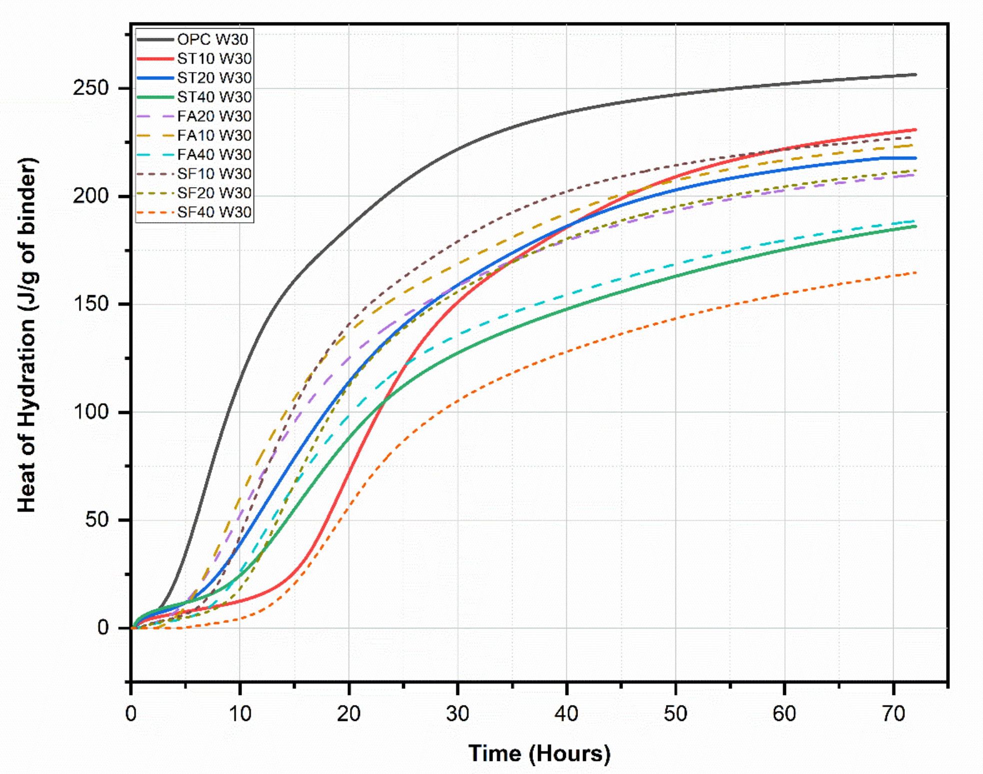
OPC W30
ST10 W30
ST20 W30
ST40 W30
FA20 W30
FA10 W30
FA40 W30
SF10 W30
SF20 W30
SF40 W30
Heat of Hydration (J/g of binder)
Time (Hours)
0
50
100
150
200
250
0
10
20
30
40
50
60
70

(a)

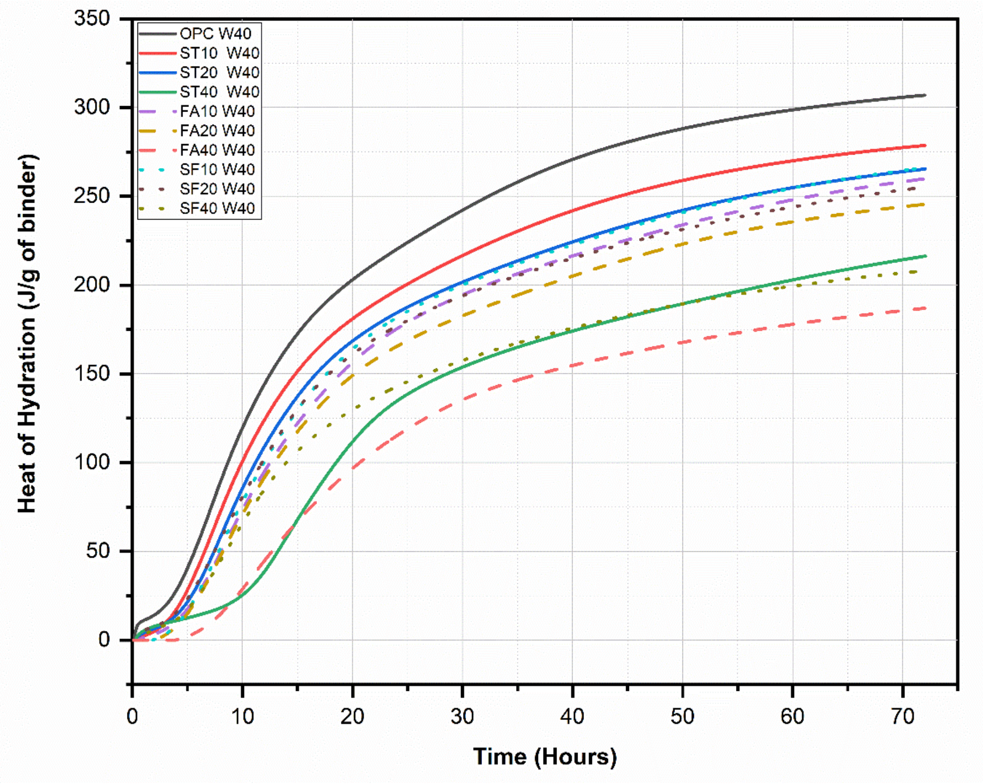
OPC W40
ST10 W40
ST20 W40
ST40 W40
FA10 W40
FA20 W40
FA40 W40
SF10 W40
SF20 W40
SF40 W40
Heat of Hydration (J/g of binder)
Time (Hours)
0
50
100
150
200
250
300
350
0
10
20
30
40
50
60
70

(b)

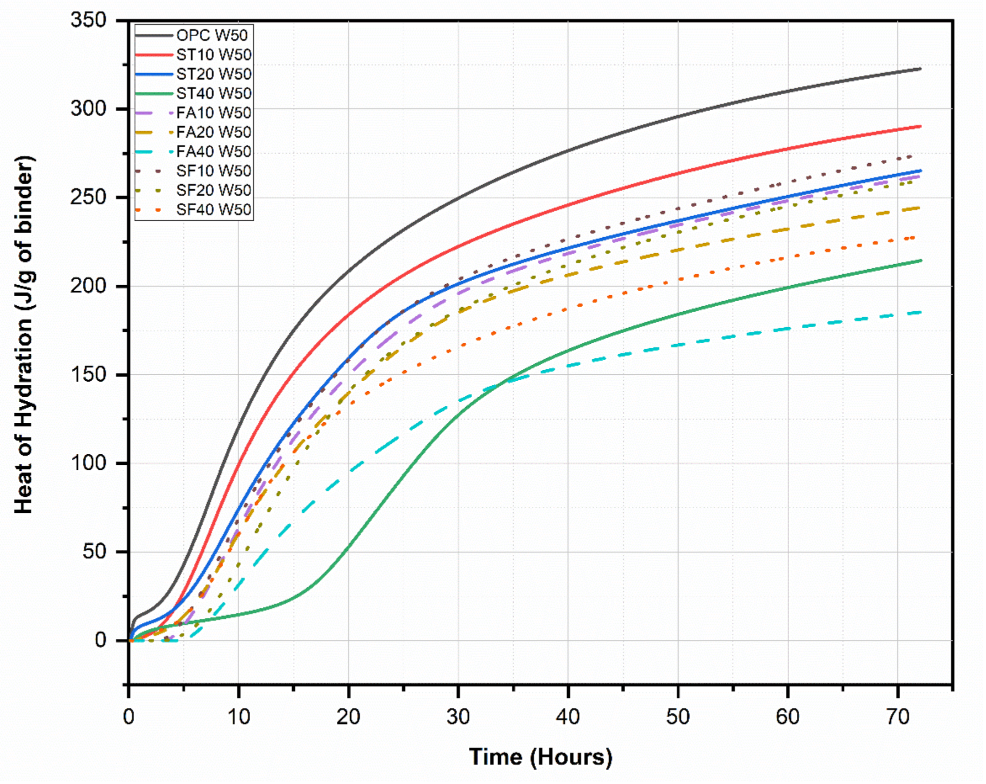

OPC W50
ST10 W50
ST20 W50
ST40 W50
FA10 W50
FA20 W50
FA40 W50
SF10 W50
SF20 W50
SF40 W50
Heat of Hydration (J/g of binder)
Time (Hours)
0
50
100
150
200
250
300
350
0
10
20
30
40
50
60
70

(c)

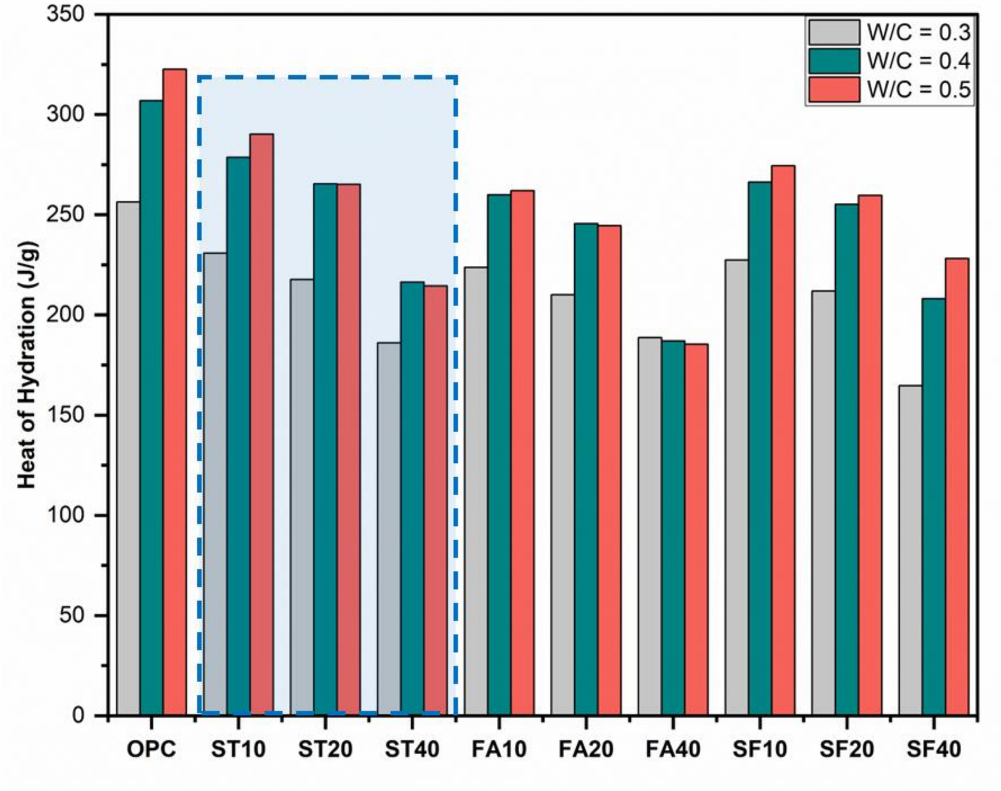

W/C = 0.3
W/C = 0.4
W/C = 0.5
Heat of Hydration (J/g)
0
50
100
150
200
250
300
350
OPC
ST10
ST20
ST40
FA10
FA20
FA40
SF10
SF20
SF40

(d)

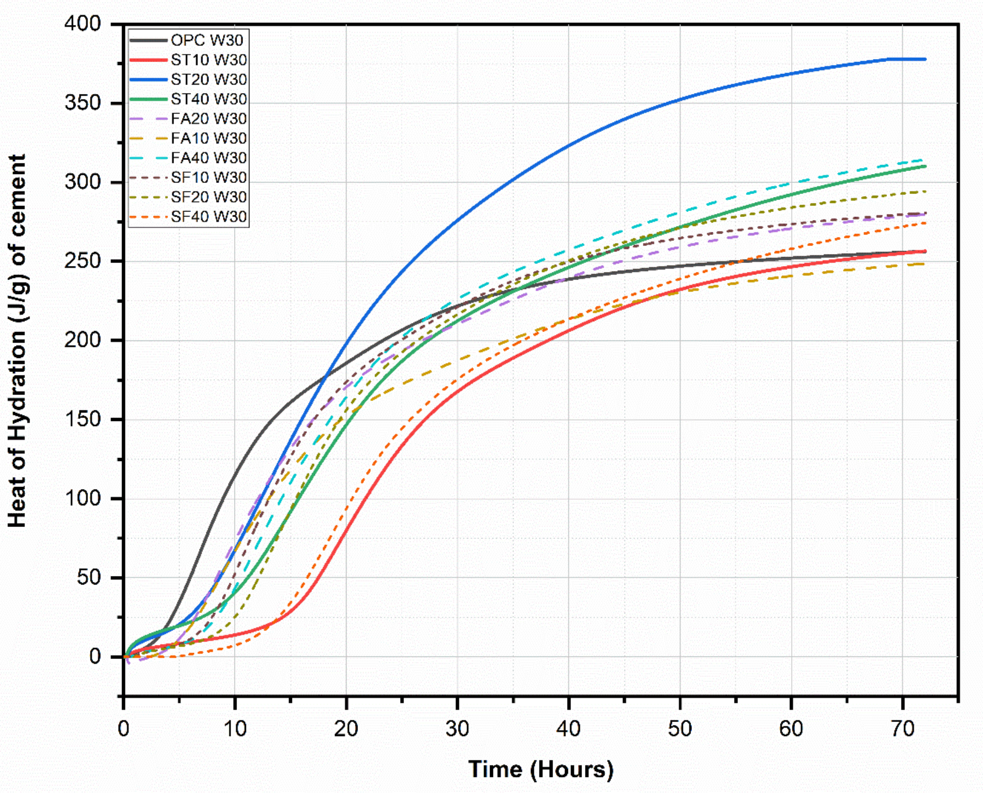
OPC W30
ST10 W30
ST20 W30
ST40 W30
FA20 W30
FA10 W30
FA40 W30
SF10 W30
SF20 W30
SF40 W30
Heat of Hydration (J/g) of cement
0
50
100
150
200
250
300
350
400
0
10
20
30
40
50
60
70
Time (Hours)

(e)

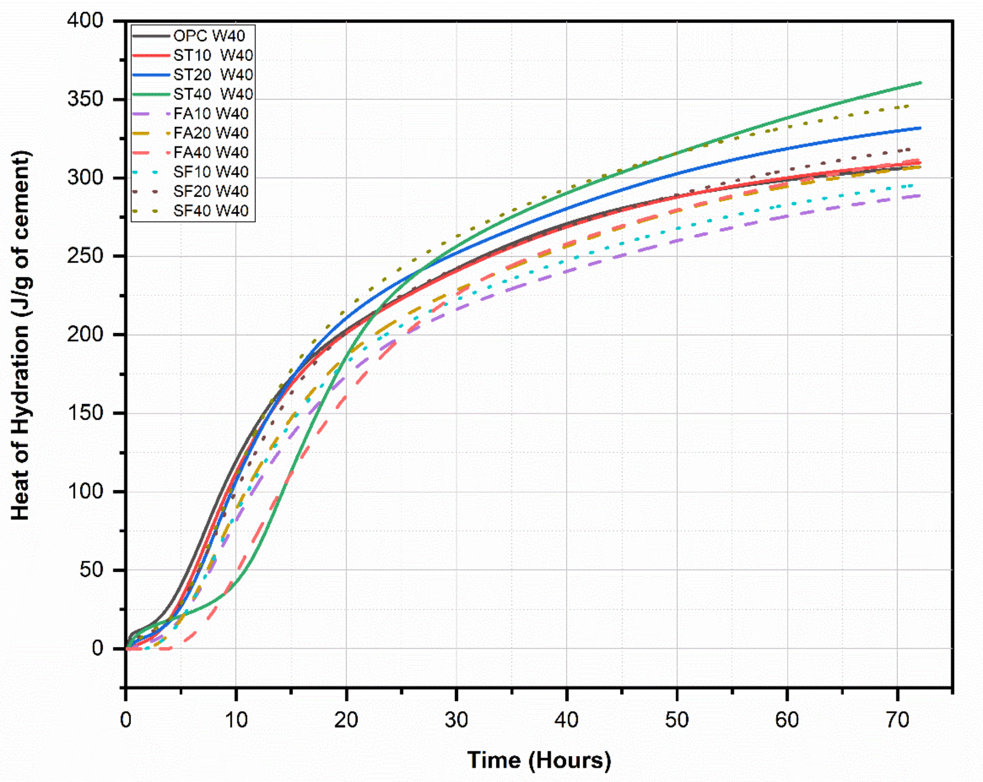
OPC W40
ST10 W40
ST20 W40
ST40 W40
FA10 W40
FA20 W40
FA40 W40
SF10 W40
SF20 W40
SF40 W40
Heat of Hydration (J/g of cement)
0
50
100
150
200
250
300
350
400
0
10
20
30
40
50
60
70
Time (Hours)

(f)

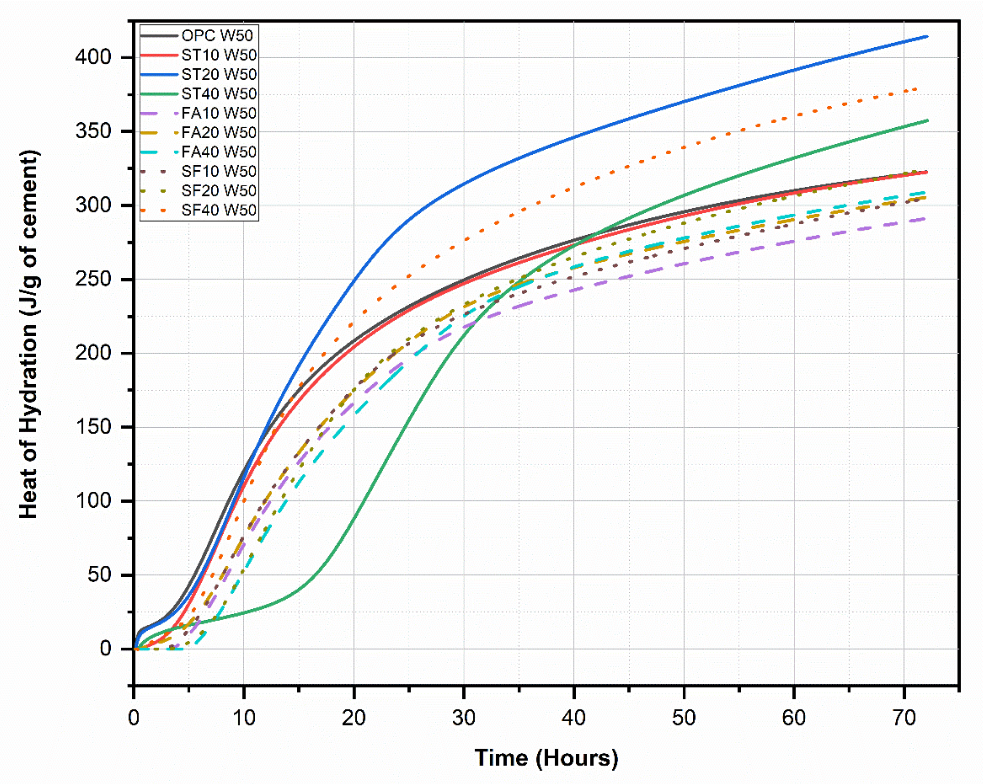

(g)

Fig. 5.2: Evolution of heat of hydration of cementitious paste mixes with 10%, 20% and 40% STCT750 (a) mixes with w/c ratio 0.3 (b) mixes with w/c ratio 0.4 (c) mixes with w/c ratio 0.5 (d) Cumulative heat of hydration of the mixes at the end of 72 hours.

5.4 Mineralogy

The Ordinary Portland cement comprises mineral phases, namely alite, belite, tricalcium aluminate, and tetra calcium alumino ferrite, which undergo a chemical reaction with water resulting in the formation of hydration products as shown in Eq. 5.2, 5.3 and 5.4 [9].

$$3.CaO.SiO_2 + xH_2O \rightarrow YCaO.SiO_2(x+Y-3)H_2O + (3-Y)Ca(OH)_2 \quad \text{Eq. (5.2)}$$

$$2.CaO.SiO_2 + zH_2O \rightarrow ACaO.SiO_2(z+A-2)H_2O + (2-A)Ca(OH)_2 \quad \text{Eq. (5.3)}$$

$$3.CaO.Al_2O_3 + yH_2O \rightarrow ZCaO.Al_2O_3(y+Z-3)H_2O + (3-Y)Ca(OH)_2 \quad \text{Eq. (5.4)}$$

Nevertheless, the mineral composition of cementitious matrix undergoes modifications when the treated mineral wastes (e.g., MTCT850 and STCT750) become part of the binder as shown in Eq. 5.5. Consequently, the hydration reaction differs, resulting in the formation of new hydration products. The examination of these phases after hydration provides valuable information into the mechanisms involved in the hydration process of the cementitious binder that is generated.

$$2Al_2SiO_3 + 2Ca(OH)_2 + yH_2O \rightarrow CaO.SiO_2(x)H_2O + CaO.2.Al_2O_3.SiO_2(y+2-x)H_2O \quad \text{Eq. (5.5)}$$

X-ray diffraction (XRD) analysis was used to identify the mineralogical phases present in the hydrated cementitious phases containing MTCT850 and STCT750. As the mineral phases in cement hydration products contain multiple overlapping peaks, the phase identification and peak assignments were achieved by comparing the observed peaks in the sample to all the major peaks in the reference pattern of the identified mineral. Any peak that exhibited intensities higher than 50% (as given in the reference pattern) was classified as a major peak. Furthermore, as a result of alterations in the crystal structure during activation and hydration, the software identified multiple minerals belonging to the same crystal group for the same observed 2θ values. In order to prevent any potential misinterpretation, all the minerals such as phlogopite, albite, K-feldspar and sanidine were identified as the group they belong to, i.e., biotite and feldspar rather than as the individual mineral. Though oligoclase belongs to plagioclase feldspar group, it was mentioned by its mineral name as the identification was irrefutable. For ease of the discussion the diffraction patterns are grouped based on the age of the samples and w/c ratio in the reported Figures. The minerals in the XRD patterns are annotated using IMA abbreviations [269] and the hydration products of cement are identified using the common terms [232] . The annotations used and the corresponding minerals are given in Table 5.2.

Table 5.2: The list of minerals identified in the OPC, MT and ST cementitious pastes and the corresponding symbols used for annotation in the diffractogram

Symbol	**Mineral name and remarks**	**COD reference number** [233]	**Chemical formula** [233]
Bt	Biotite	96-900-1348	$K(Mg, Fe)_3AlSi_3O_{10}(F, OH)_2$
Ett	Ettringite	96-901-1577	$Ca_6Al_2S_3O_{49}$
CAS	Calcium Aluminium Silicate in various zeolitic forms mainly gismondine, mordenite	96-153-7306	$O_{49.28}Ca_{3.67}Si_{8.80}Al_{7.20}$
Ocl	Oligoclase	96-901-1423	$Na_{1.64}Ca_{0.36}Al_{2.36}Si_{5.64}O_{16.00}$
CH	Portlandite	96-100-1769	$Ca(OH)_2$
Qz	Quartz	96-900-9667	SiO_2
Cal	Calcium carbonate in calcite or vaterite form	96-901-5391 96-900-0966	$CaCO_3$
C_2S	Belite	96-231-0925	$Ca_2\,(SiO_4)$
C_3S	Alite	96-154-0705	$O_{30.00}Ca_{18.00}Si_{6.00}$
HC	Hemicarbonate	96-210-5253	$Al_{6.00}Ca_{12.00}O_{55.50}C_{1.50}$
Fsp	Feldspar	96-900-1258 96-155-7002	$Al_{2.00}Si_{6.00}Na_{2.00}O_{16}$ $K_{1.86}Na_{0.14}Al_{2.00}Si_{6.00}O_{16.00}$

The figures presented in Figs. 5.3 through 5.7 illustrate the diffraction patterns of cementitious pastes that incorporate different proportions (10%, 20%, and 40%) of MTCT850 at different ages of curing (7 days, 14 days, 28 days, 56 days, and 90 days). The identified major phases are biotite, ettringite, calcium aluminium silicate ohases in zeolitic form mainly gismondine, mordenite, oligoclase, portlandite, quartz, calcite, belite, and alite.

It can be seen in Figs. 5.3 – 5.7, that both the OPC and MT pastes indicated presence of cement hydration products such as ettringite, portlandite, and some phases of unhydrated cement such as alite and belite. The samples also indicated presence of calcite which could be a product of carbonation during curing or exposure of the hydration arrested samples to atmosphere after removing from vacuum chamber and before gold coating. Despite implementing thorough measures to store the sample in a tightly sealed container in order to prevent carbonation, even a brief exposure to the atmosphere, as little as 2 hours, can result in the occurrence of carbonation [232]. Nevertheless, this phenomenon of carbonation is evident in both OPC and MT samples. The cementitious pastes with MTCT850 indicated the presence of biotite, quartz and oligoclase minerals which were also observed in the MTR and MTCT850 samples (Ref Section 4.4, Chapter 4). It is also observed that the intensity of peaks corresponding to biotite, quartz and oligoclase increased with increase in percentage of MTCT850. This was observed for all the w/c ratios adopted and for samples at all ages as shown through Figs. 5.3 – 5.7.

The observed trend in Figures 5.3 (a) – (c) and 5.4 (a) – (c) indicates a decrease in the intensity of alite and belite peaks with an increase in the percentage of MTCT850. In the context of w/c ratios of 0.4 and 0.5, and at ages beyond 28 days, it can be observed from Figures 5.5 (b) and (c), 5.6 (b) and (c), and 5.7 (b) and (c) that the peaks corresponding to alite and belite gradually diminish. The calcium aluminium silicate phases exhibits varying peak intensities across different ages and w/c ratios. This indicates some changes in calcium aluminium silicate phases with hydration. However, there is no discernible trend in these variations in intensity. This is because the changes in calcium aluminium silicate peaks are also influenced by the modifications in the ettringite structure over time, which in turn causes changes in intensities of ettringite peaks that are in close proximity to and overlap with the calcium aluminium silicate peaks.

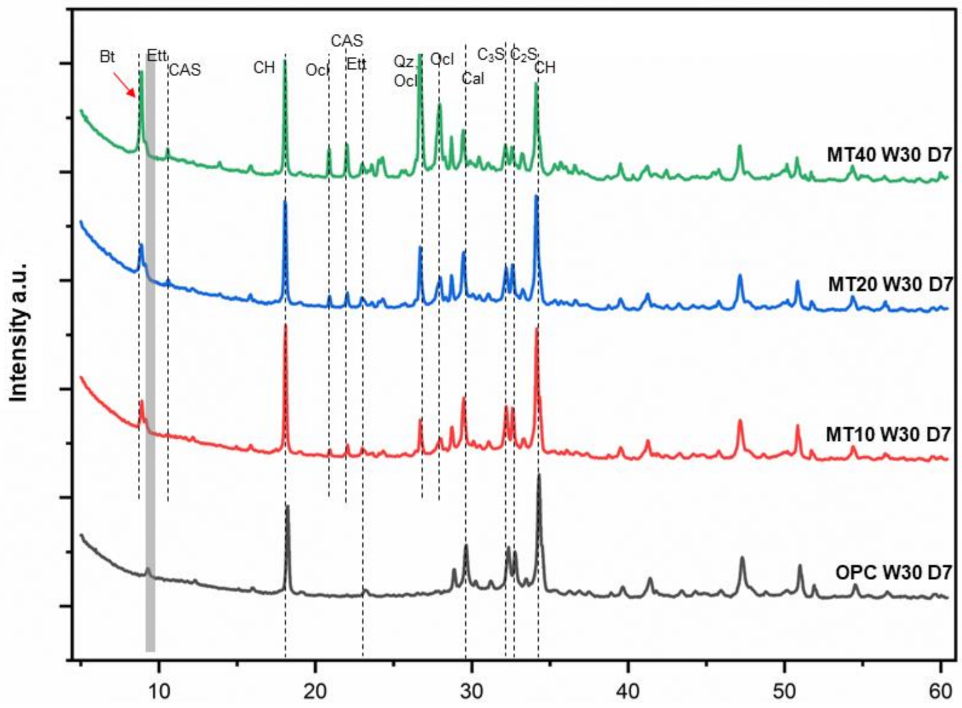

(a)

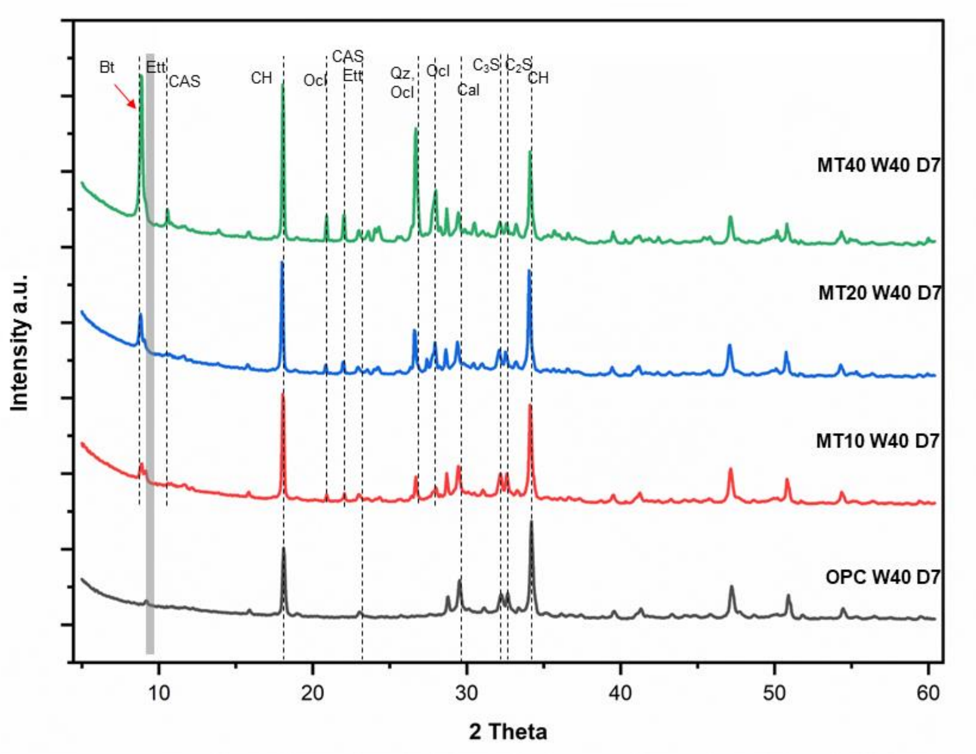

(b)

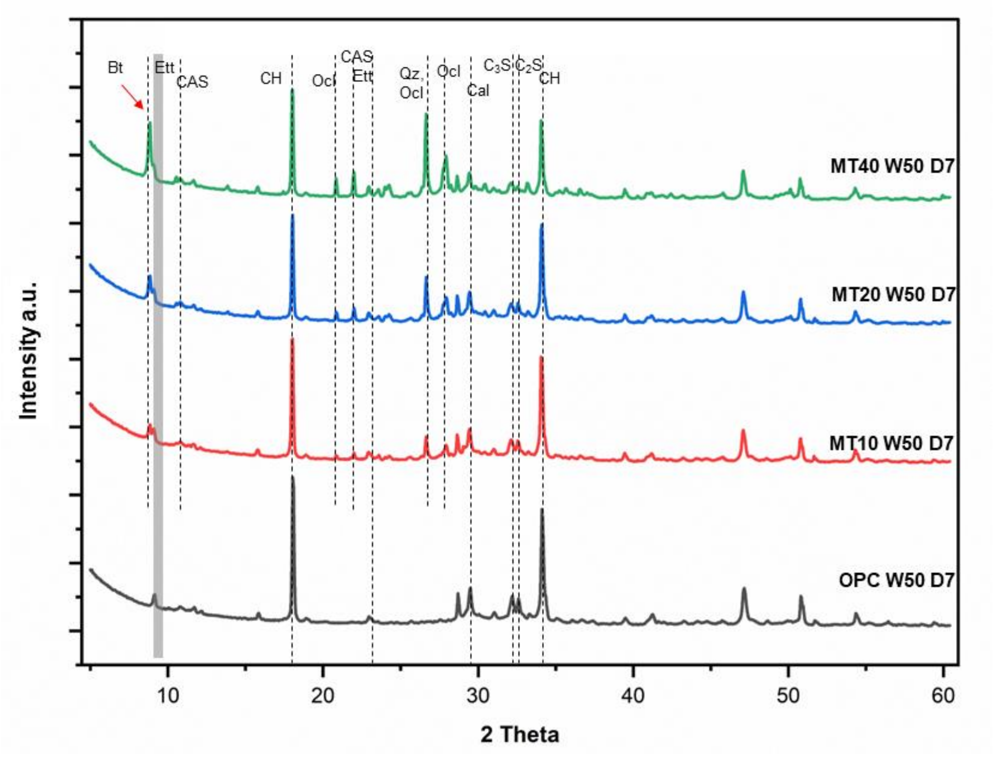

(c)

Fig. 5.3: XRD diffraction patterns of cementitious pastes containing 10%, 20% and 40% MTCT850 after 7 days of curing. (a) w/c ratio = 0.3, (b) w/c ratio = 0.4, (c) w/c ratio = 0.5.

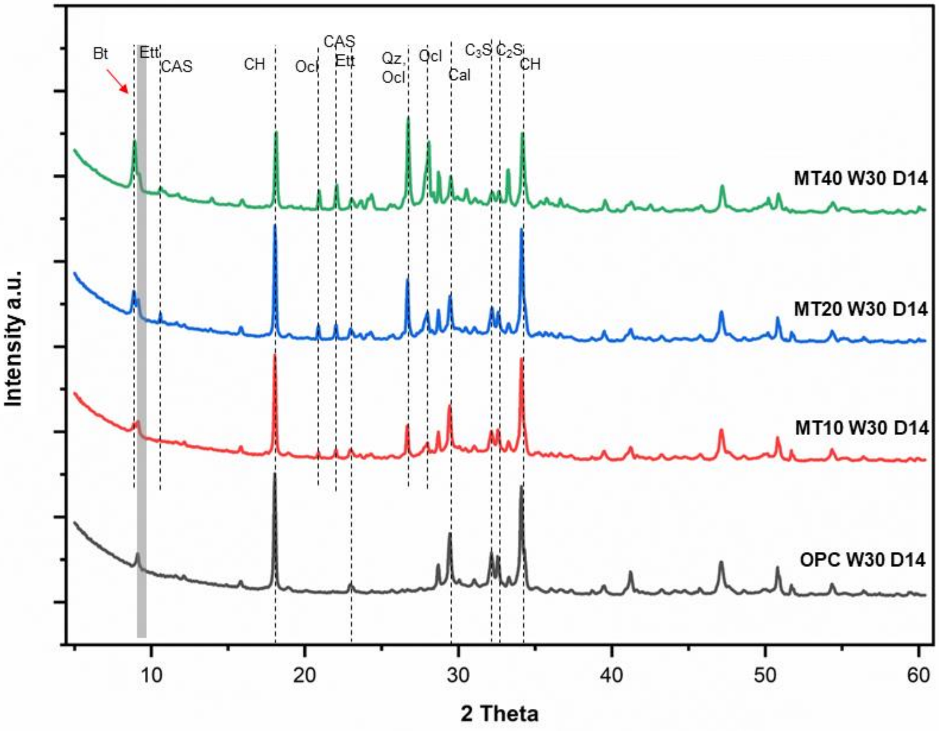
Bt
Ett
CAS
CH
Ocl
CAS
Ett
Qz,
Ocl
Ocl
Cal
C_3S
C_2S
CH
MT40 W30 D14
MT20 W30 D14
MT10 W30 D14
OPC W30 D14
Intensity a.u.
2 Theta
10
20
30
40
50
60

(a)

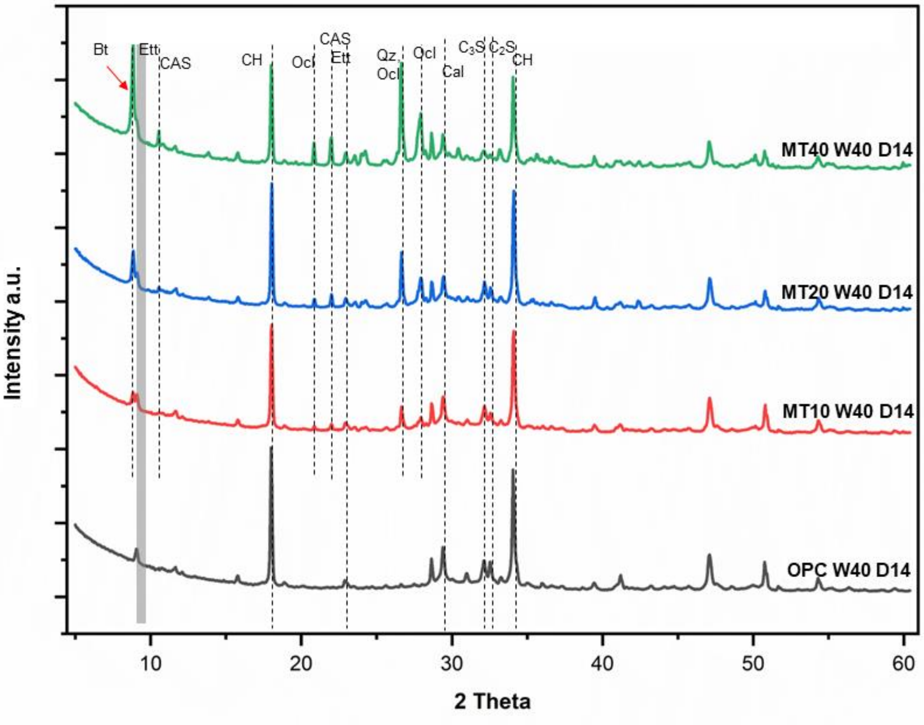
Bt
Ett
CAS
CH
Ocl
CAS
Ett
Qz,
Ocl
Ocl
Cal
C_3S
C_2S
CH
MT40 W40 D14
MT20 W40 D14
MT10 W40 D14
OPC W40 D14
Intensity a.u.
2 Theta
10
20
30
40
50
60

(b)

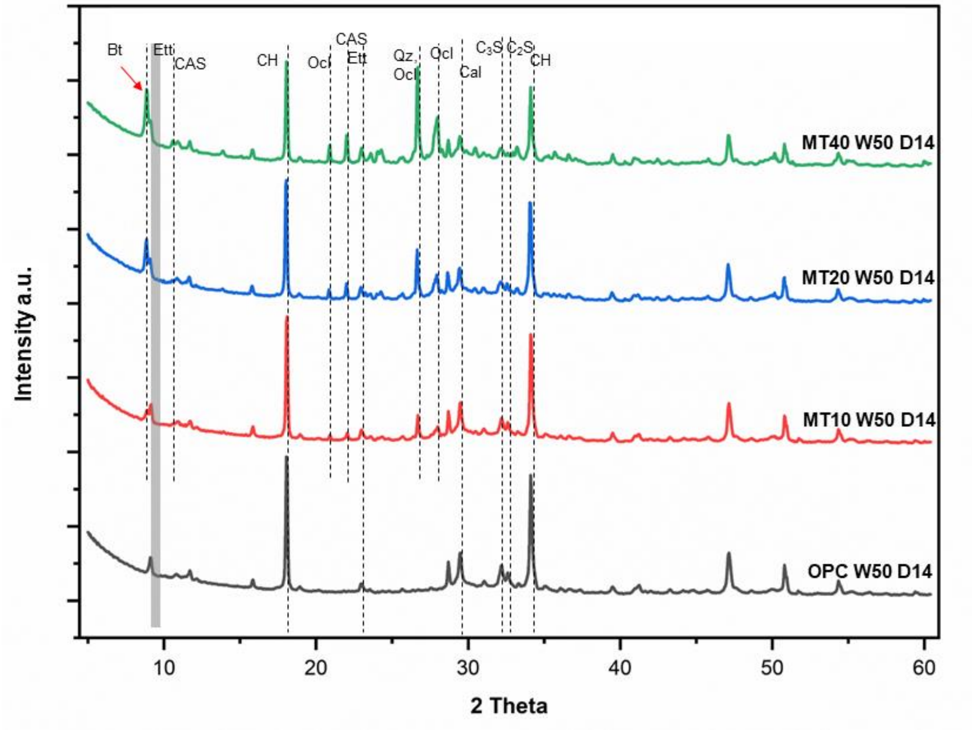

(c)

Fig. 5.4: XRD diffraction patterns of cementitious pastes containing 10%, 20% and 40% MTCT850 after 14 days of curing. (a) w/c ratio = 0.3, (b) w/c ratio = 0.4, (c) w/c ratio = 0.5.

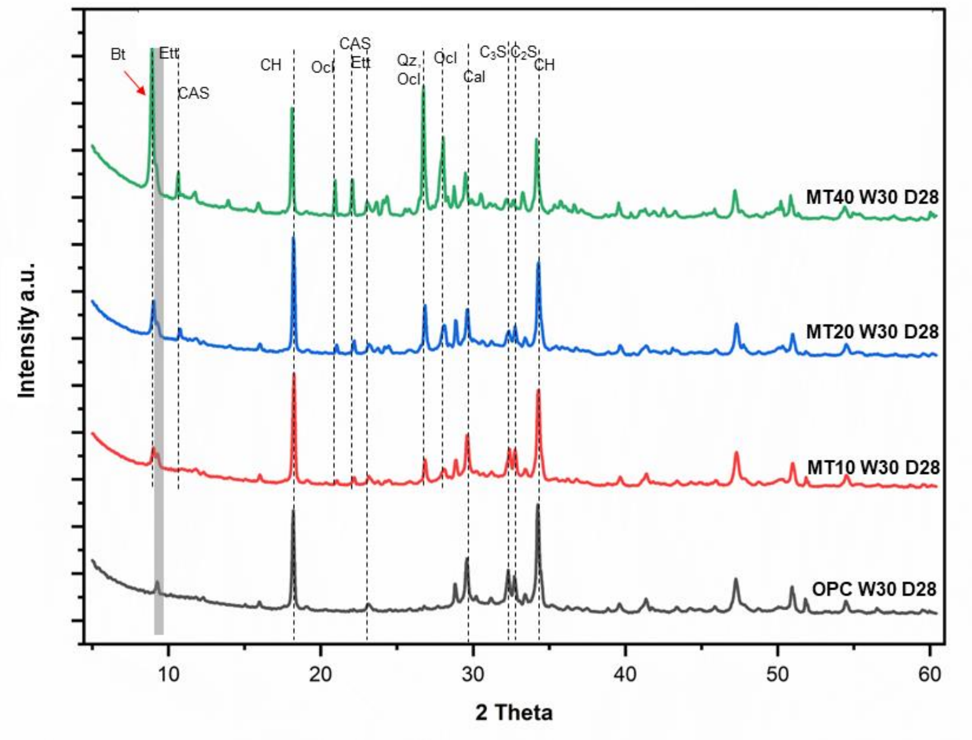

(a)

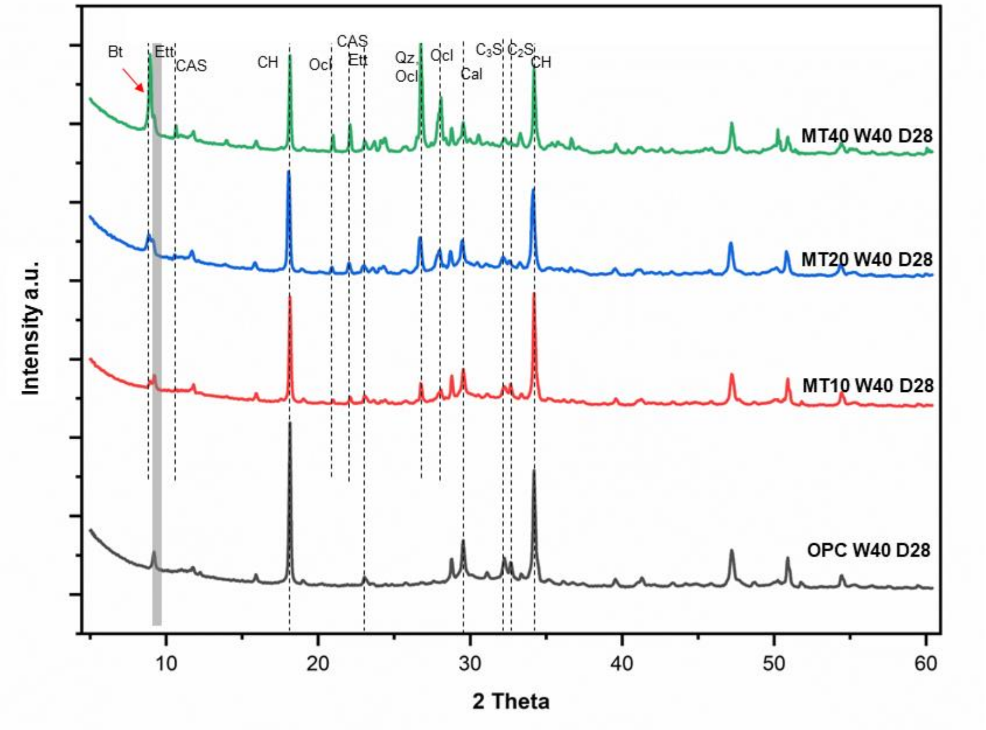

(b)

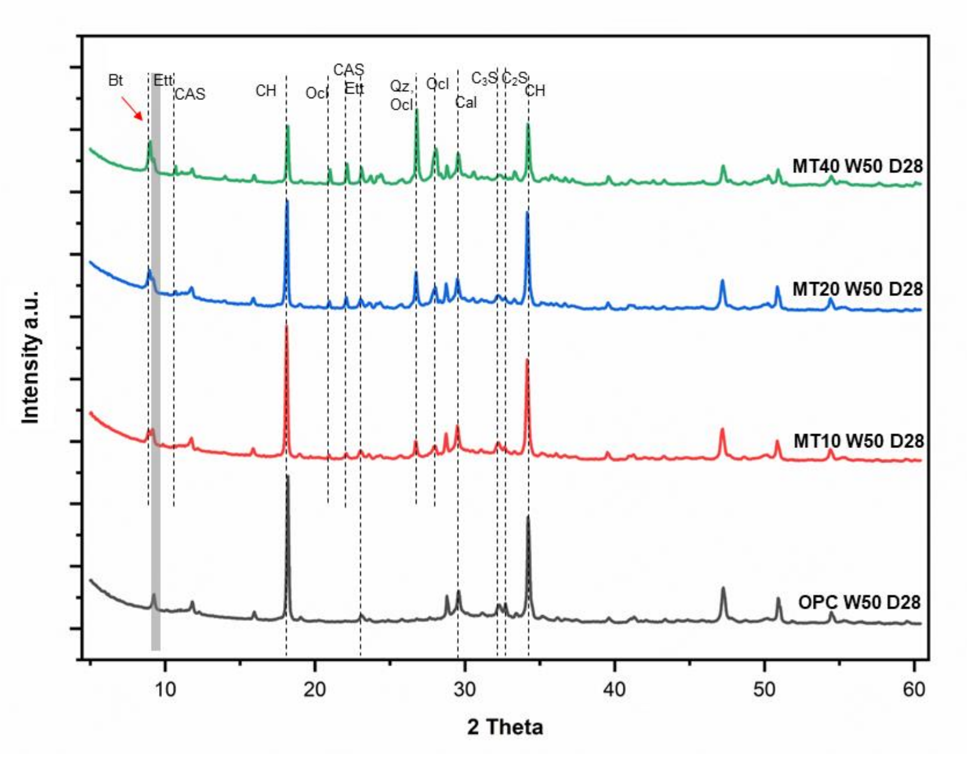

(c)

Fig. 5.5: XRD diffraction patterns of cementitious pastes containing 10%, 20% and 40% MTCT850 after 28 days of curing. (a) w/c ratio = 0.3, (b) w/c ratio = 0.4, (c) w/c ratio = 0.5.

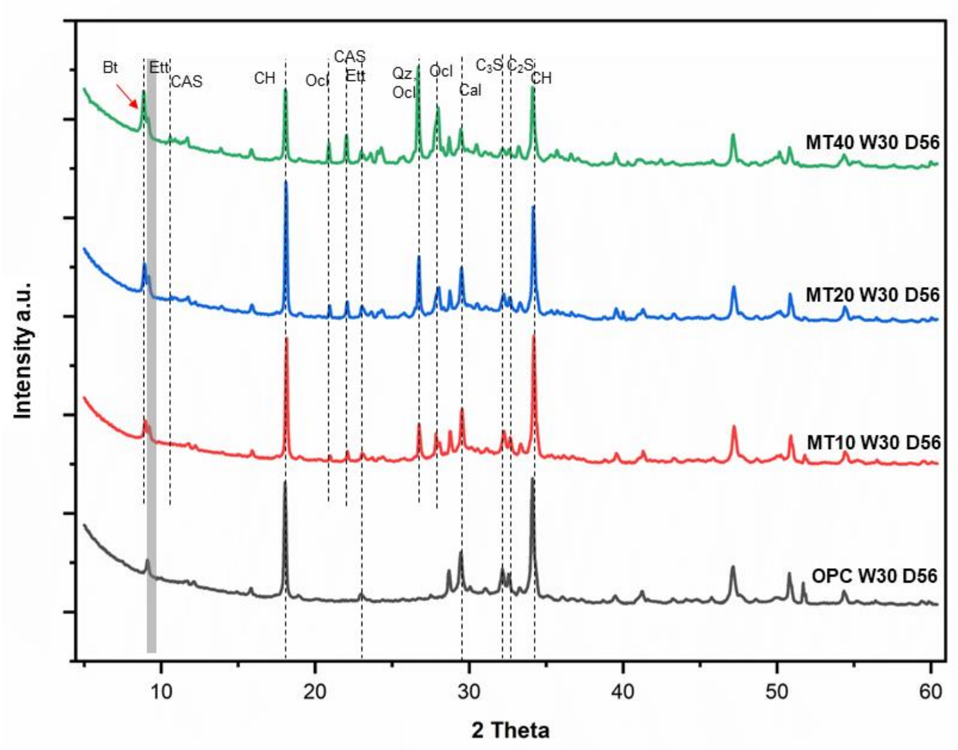
Bt
Ett
CAS
CH
Ocl
CAS
Ett
Qz
Ocl
Ocl
Cal
C₃S
C₂S
CH
MT40 W30 D56
MT20 W30 D56
MT10 W30 D56
OPC W30 D56
Intensity a.u.
2 Theta
10
20
30
40
50
60

(a)

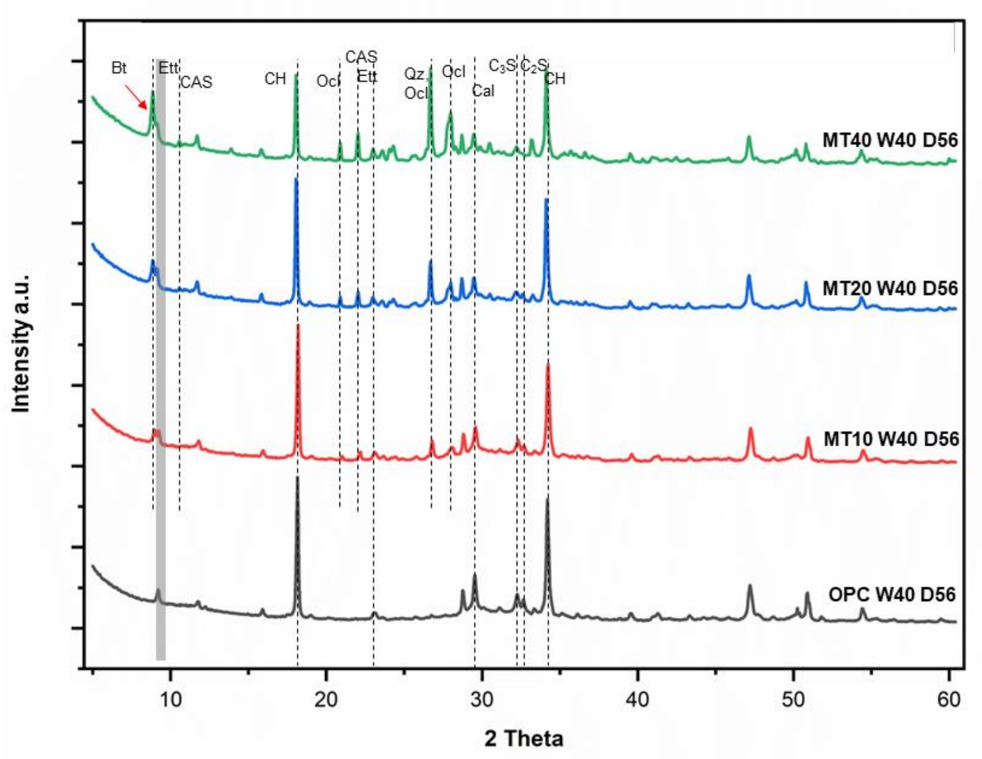
Bt
Ett
CAS
CH
Ocl
CAS
Ett
Qz
Ocl
Ocl
Cal
C₃S
C₂S
CH
MT40 W40 D56
MT20 W40 D56
MT10 W40 D56
OPC W40 D56
Intensity a.u.
2 Theta
10
20
30
40
50
60

(b)

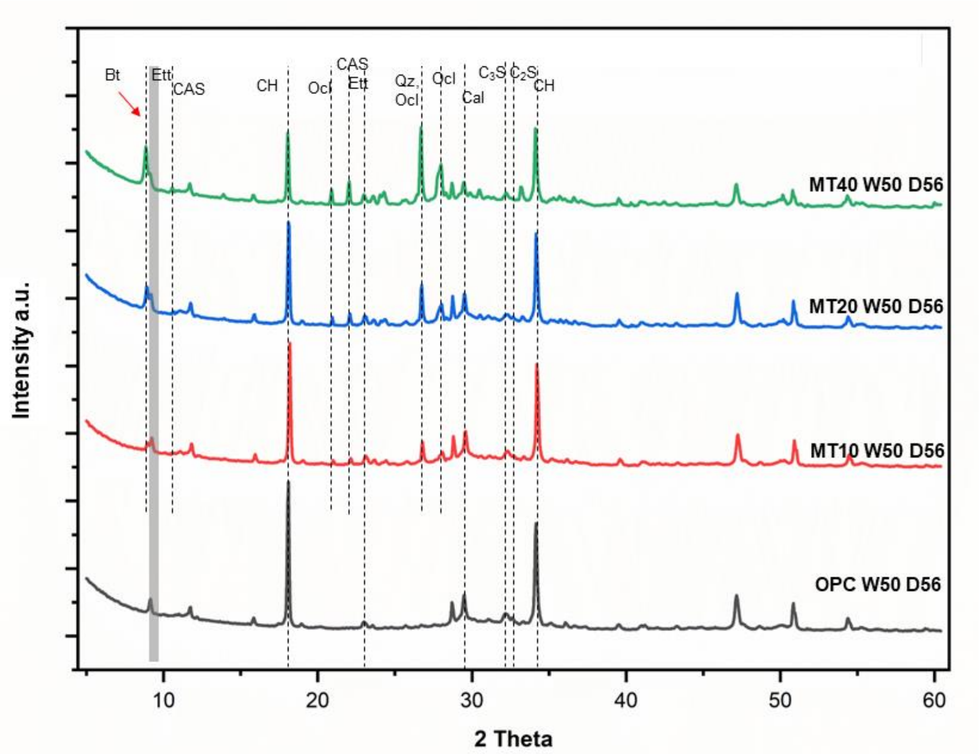

(c)

Fig. 5.6: XRD diffraction patterns of cementitious pastes containing 10%, 20% and 40% MTCT850 after 56 days of curing. (a) w/c ratio = 0.3, (b) w/c ratio = 0.4, (c) w/c ratio = 0.5.

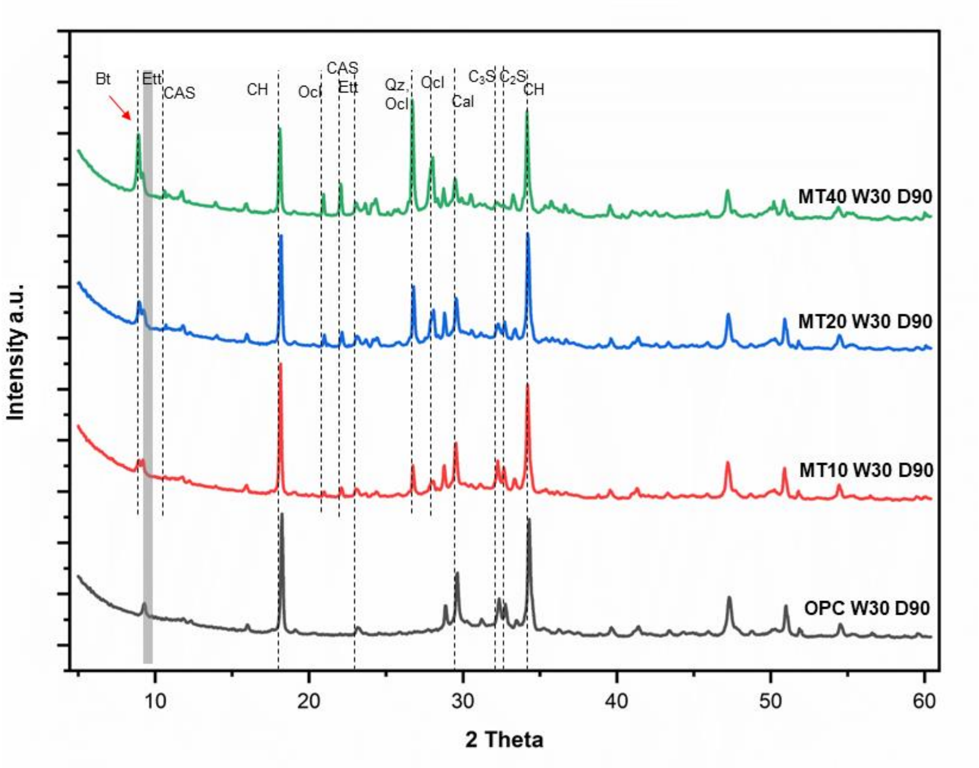

(a)

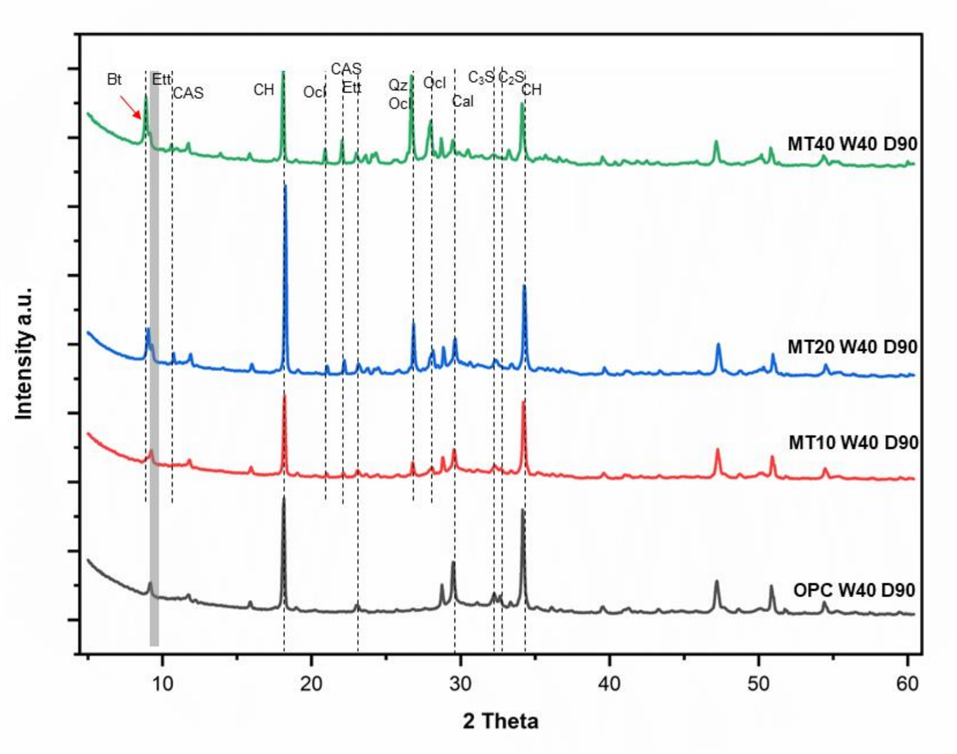

(b)

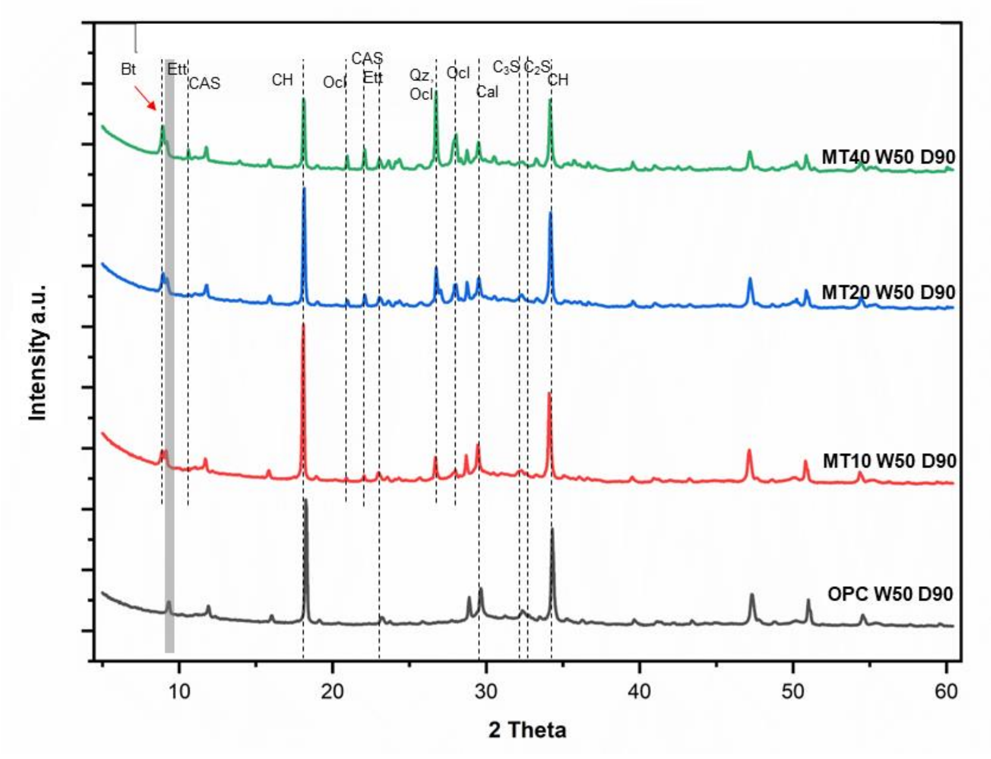

(c)

Fig. 5.7: XRD diffraction patterns of cementitious pastes containing 10%, 20% and 40% MTCT850 after 56 days of curing. (a) w/c ratio = 0.3, (b) w/c ratio = 0.4, (c) w/c ratio = 0.5

The diffraction patterns of cementitious pastes containing 10%, 20% and 40% of STCT750 at the ages 7 days, 14 days, 28 days, 56 days and 90 days are given in Figs. 5.8 through 5.12. From the diffraction patterns in the Fig. 5.8 – 5.12, the major phases identified were ettringite, hemi carbonate, calcium aluminium silicate phases in zeolitic form mainly gismondine, mordenite, feldspar, portlandite, quartz, calcite, belite and alite. The cement hydration products ettringite and portlandite, and the unhydrated cement phases alite and belite were found both in ST and OPC mixes. The phases of calcium aluminium silicate, quartz and hemi carbonate were found only in ST mixes. Formation of hemi carbonate is favoured in a system with anhydrite and calcite [270]. The rate of formation of this hemi carbonate depends on the solubility of calcite and availability of alumina [270] . In the mixes with STCT750 anhydrite and calcite are present as indicated by the XRD patterns in Fig. 5.8 through 5.12, Ca^{2+} developed from decomposition of calcite present in STR during calcination (Ref Table 4.3, Chapter 4) is also available for reaction. The albite, feldspar and K-feldspar present in the STCT750 remain unhydrated and are identified as feldspar peaks at all ages and at different w/c ratios as seen in Figs. 5.8 to 5.12. The intensity of these peaks increases with increase in percentage of STCT750. The presence of calcite was also observed in all the samples. The Fig. 5.8 indicates the presence of alite and belite peaks whose intensity decreases with increase in percentage of STCT750. Fig. 5.9-5.12 show that the alite and belite peaks gradually diminish with aging and hydration. This effect is more pronounced in mixes with higher w/c ratio.

The peak intensities of hemi carbonate and calcium aluminium silicate vary with ages and w/c ratios. As in the case of MT mixes the changes in these peak intensities are also influenced by the ettringite peaks.

Although the hydration products include the formation of calcium-silicate-hydrate (C-S-H) and calcium-aluminate-silicate-hydrate (C-A-S-H) gel (in case of ST and MT), it is important to note that these products exhibit a semi-crystalline nature. Consequently, when analysing X-ray diffraction (XRD) patterns, the presence of these hydration products is typically observed as a modification in the background rather than as a distinct peak. The observed changes in the peaks and background of the diffraction patterns corresponding to 2θ values at 21.5^o, 17.5^o, and 68^o are indicative of the formation of C-A-S-H gel [183,271]. Similarly, the changes in the intensities of peaks in the 2θ values at 15° – 19°, 25^o, 29.5^o, 31^o, 44^o, and 50^o are associated with the formation of C-S-H gel [183,232,271,272]. However, these observations can be confirmed only by performing a microstructure study of the corresponding cementitious pastes.

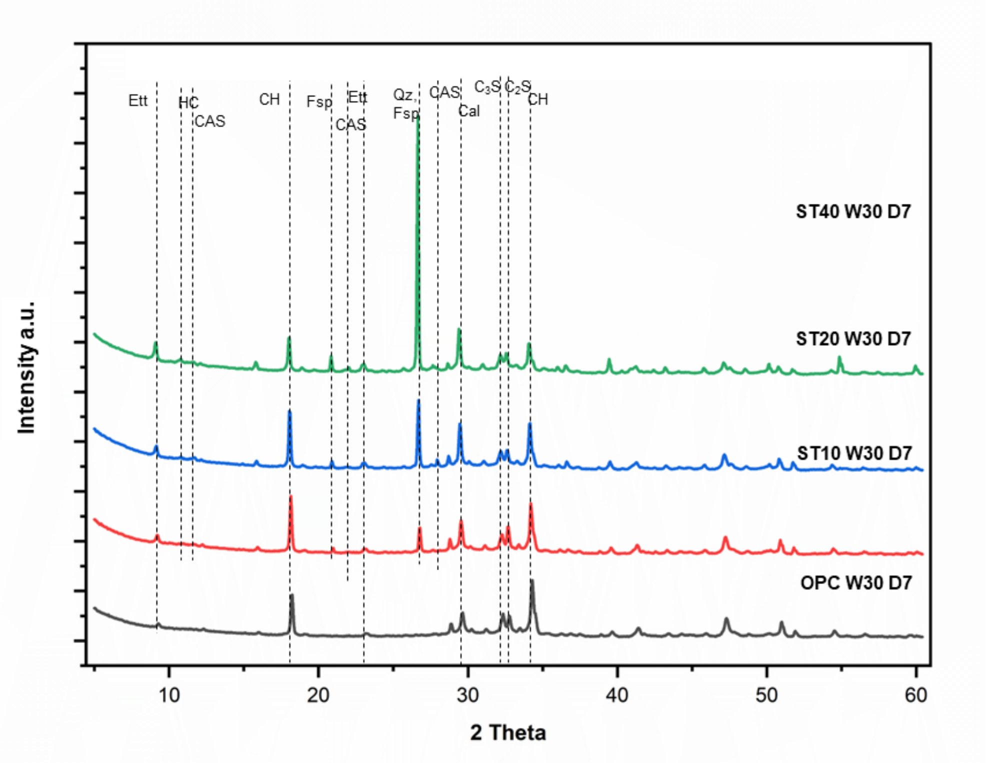
Ett
HC
CAS
CH
Fsp
Ett
CAS
Qz,
Fsp
CAS
Cal
C_3S
C_2S
CH
ST40 W30 D7
ST20 W30 D7
ST10 W30 D7
OPC W30 D7
Intensity a.u.
10
20
30
40
50
60
2 Theta

(a)

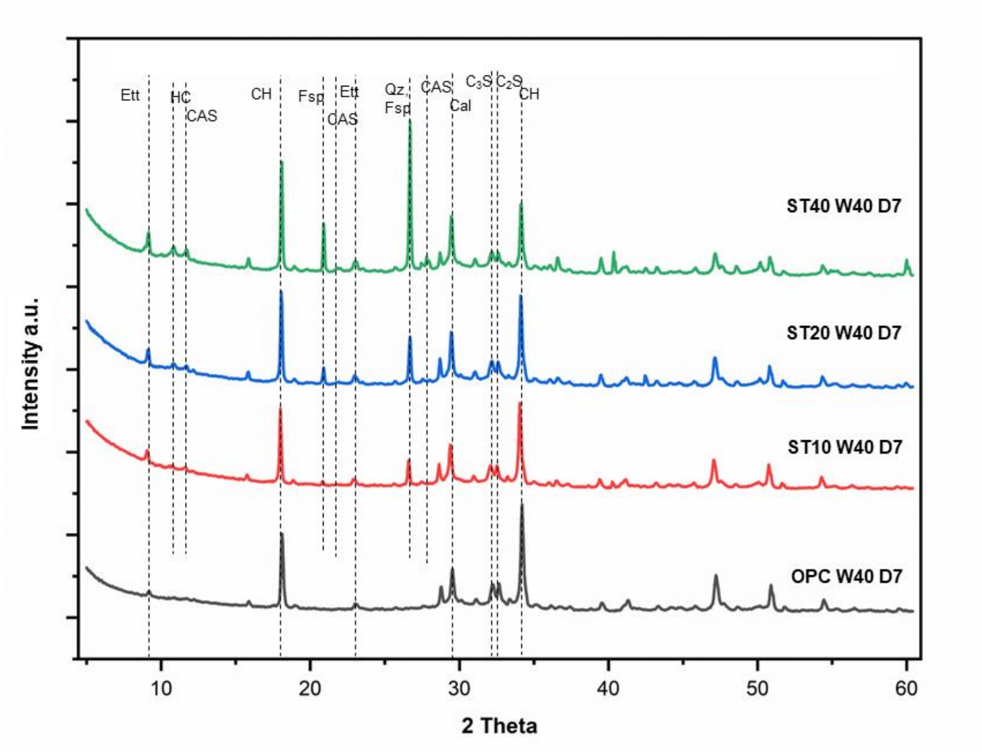
Ett
HC
CAS
CH
Fsp
Ett
CAS
Qz,
Fsp
CAS
Cal
C_3S
C_2S
CH
ST40 W40 D7
ST20 W40 D7
ST10 W40 D7
OPC W40 D7
Intensity a.u.
10
20
30
40
50
60
2 Theta

(b)

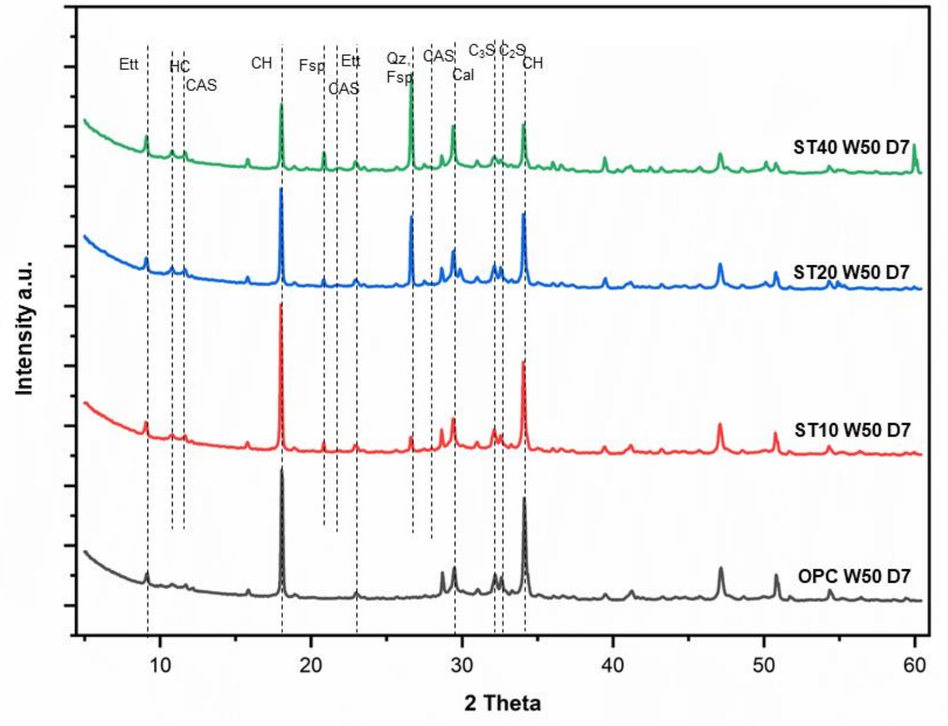

(c)

Fig. 5.8: XRD diffraction patterns of cementitious pastes containing 10%, 20% and 40% STCT750 after 7 days of curing. (a) w/c ratio = 0.3, (b) w/c ratio = 0.4, (c) w/c ratio = 0.5.

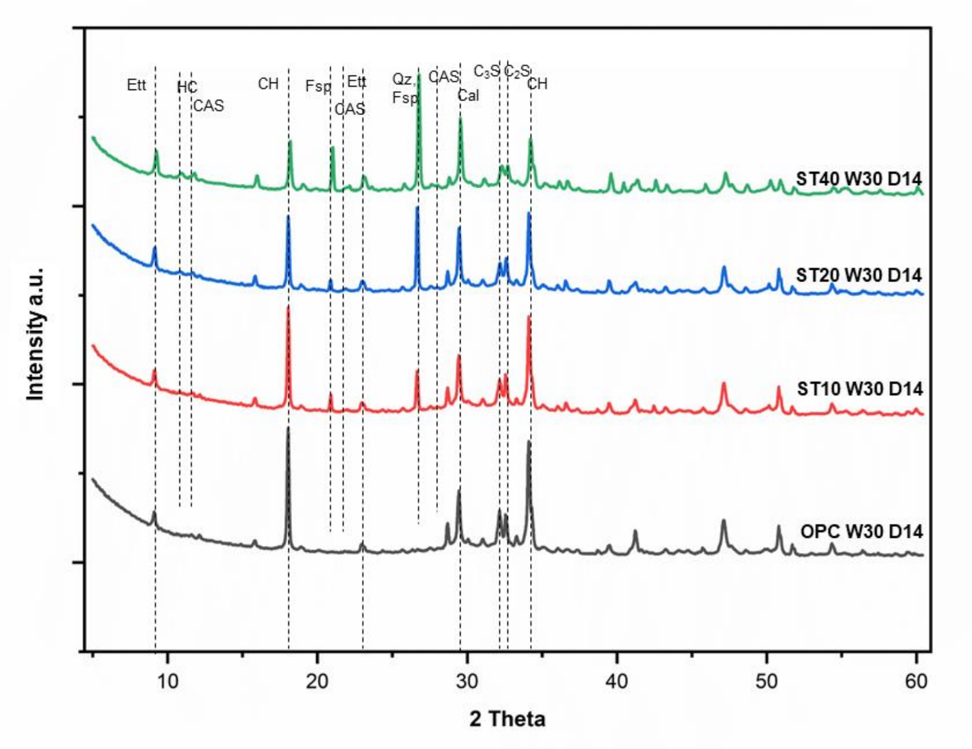

(a)

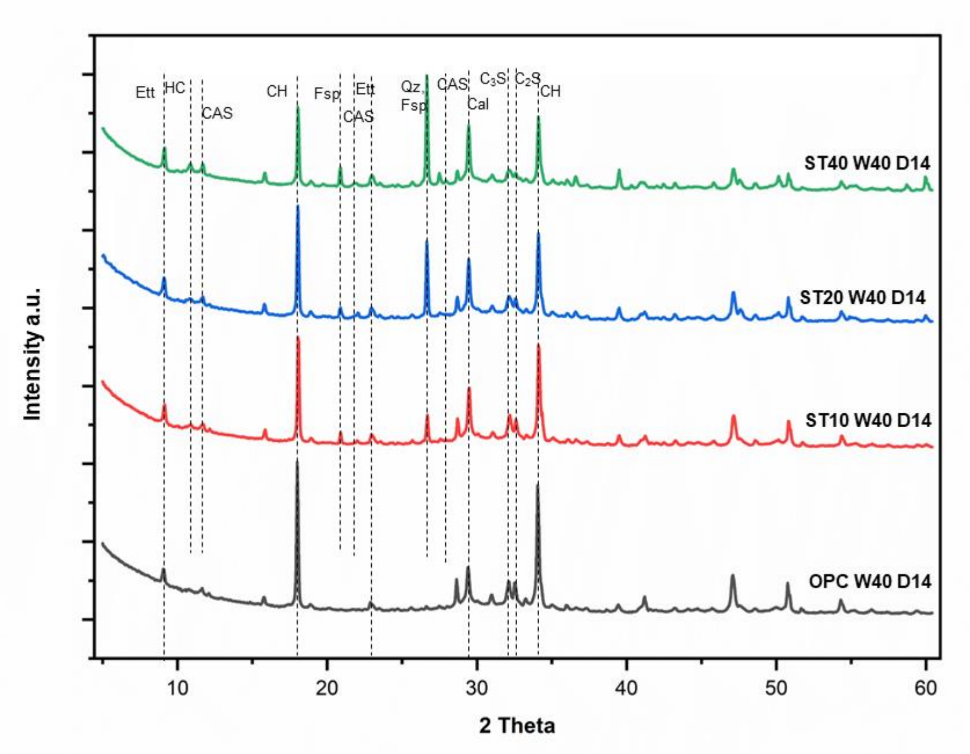

(b)

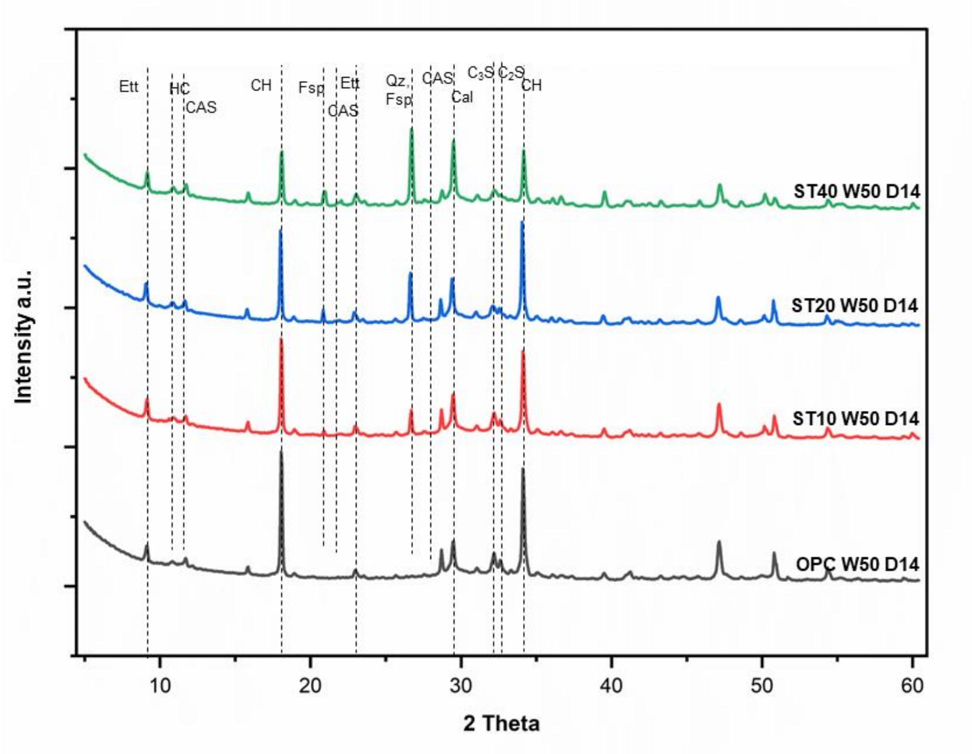

(c)

Fig. 5.9: XRD diffraction patterns of cementitious pastes containing 10%, 20% and 40% STCT750 after 14 days of curing. (a) w/c ratio = 0.3, (b) w/c ratio = 0.4, (c) w/c ratio = 0.5.

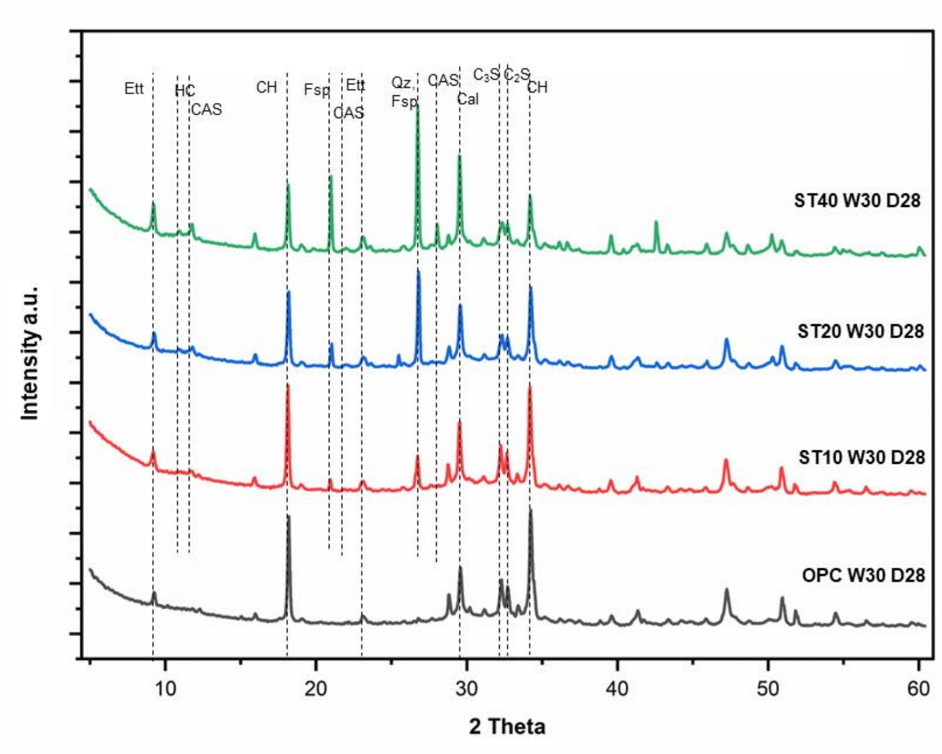
Ett
HC
CAS
CH
Fsp
Ett
CAS
Qz,
Fsp
CAS
Cal
C_3S
C_2S
CH
ST40 W30 D28
ST20 W30 D28
ST10 W30 D28
OPC W30 D28
Intensity a.u.
10
20
30
40
50
60
2 Theta

(a)

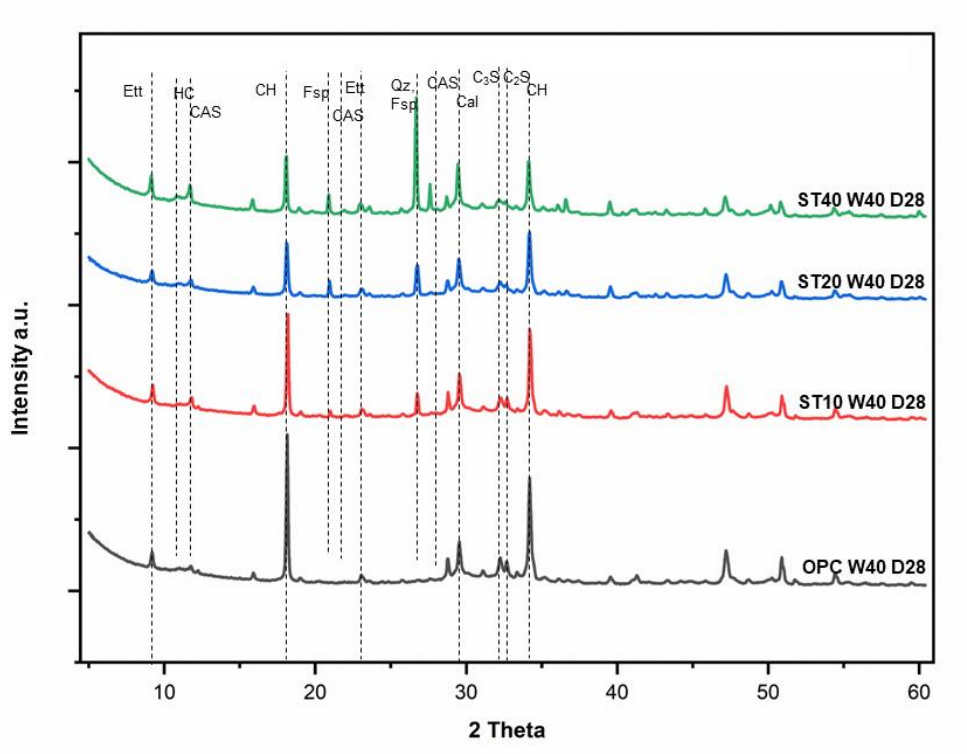
Ett
HC
CAS
CH
Fsp
Ett
CAS
Qz,
Fsp
CAS
Cal
C_3S
C_2S
CH
ST40 W40 D28
ST20 W40 D28
ST10 W40 D28
OPC W40 D28
Intensity a.u.
10
20
30
40
50
60
2 Theta

(b)

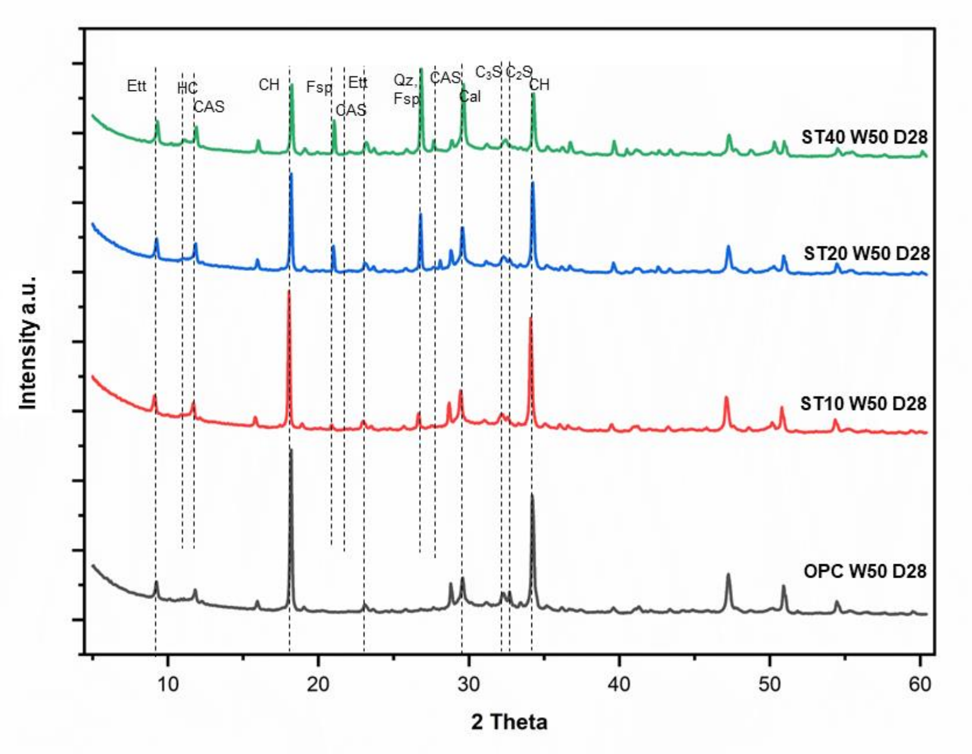

(c)

Fig. 5.10: XRD diffraction patterns of cementitious pastes containing 10%, 20% and 40% STCT750 after 28 days of curing. (a) w/c ratio = 0.3, (b) w/c ratio = 0.4, (c) w/c ratio = 0.5

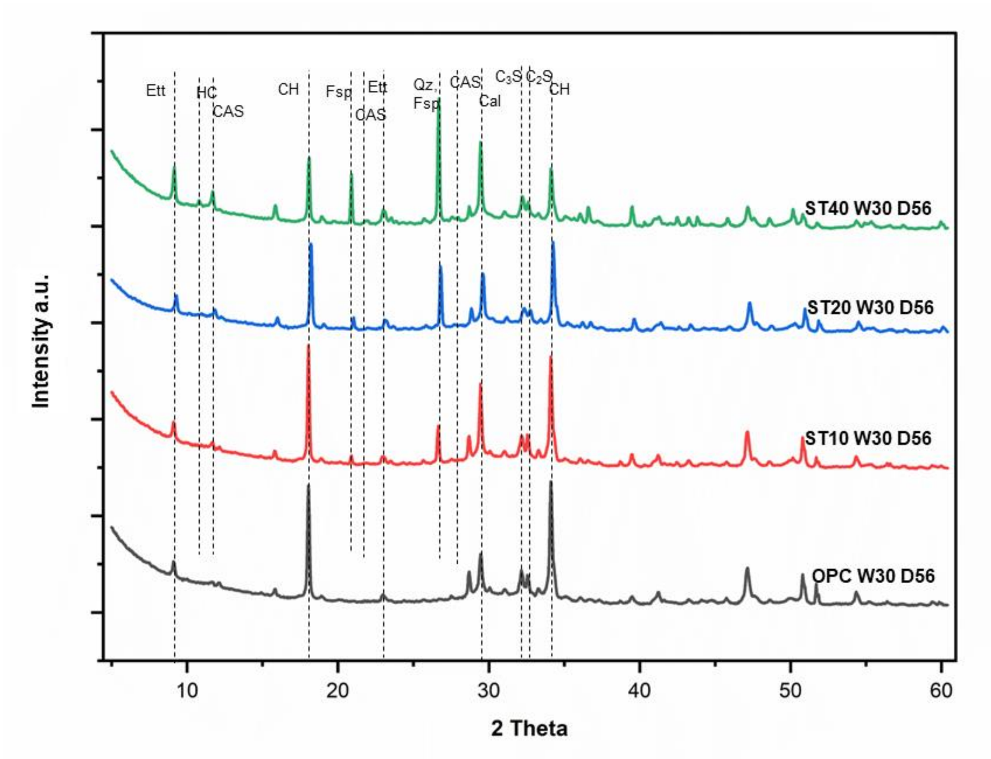

(a)

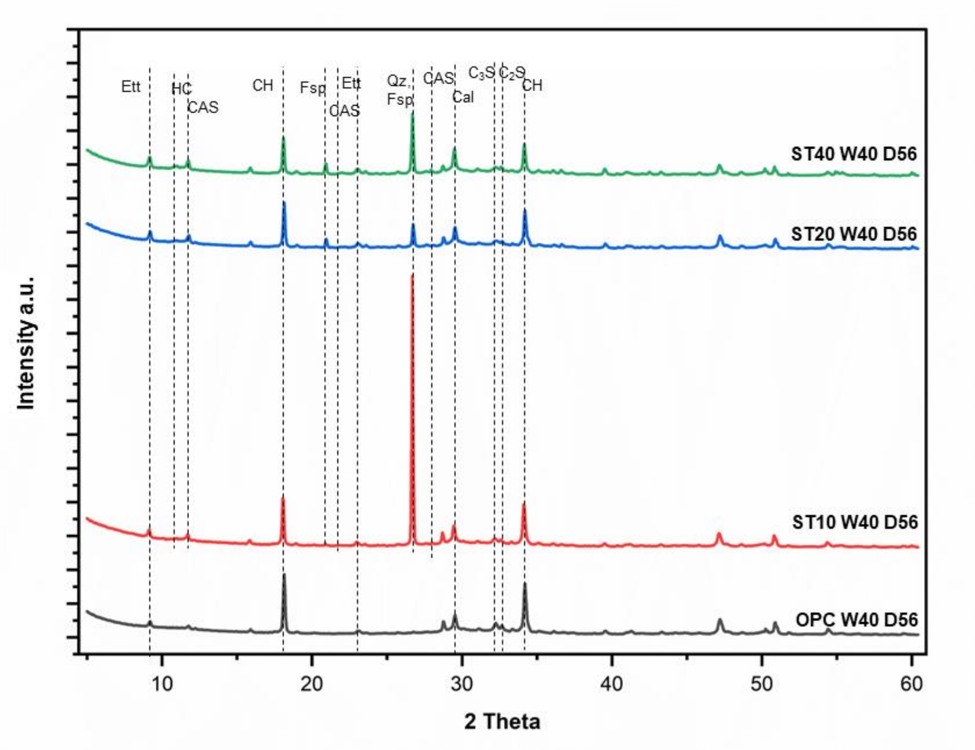

(b)

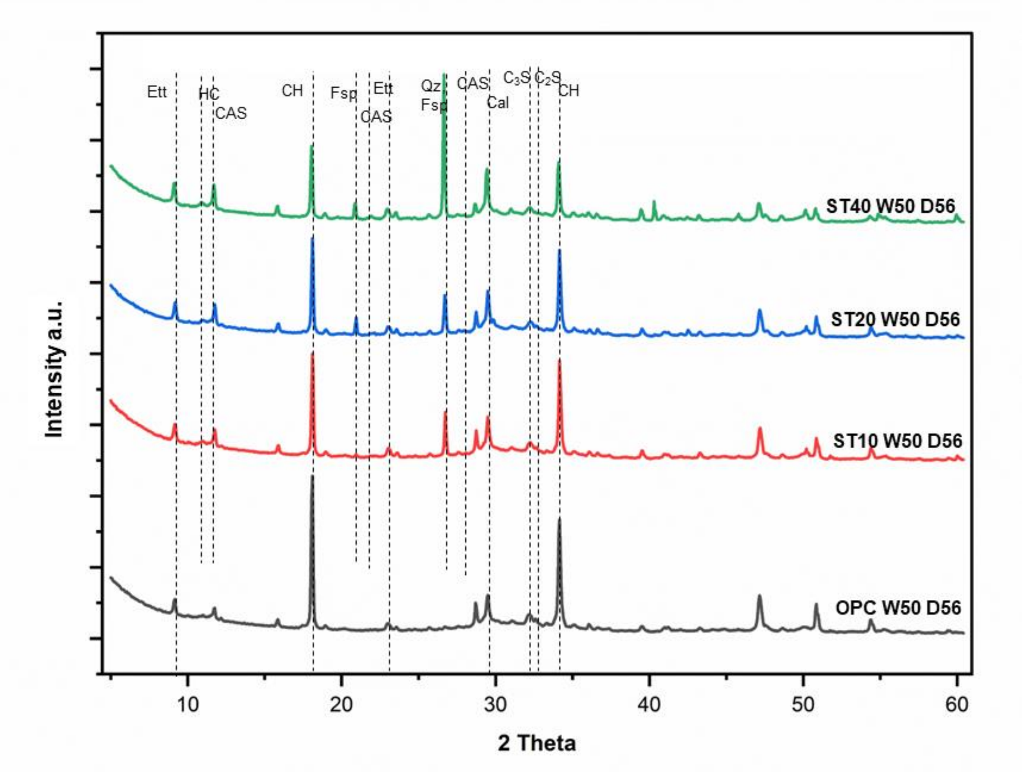

(c)

Fig. 5.11: XRD diffraction patterns of cementitious pastes containing 10%, 20% and 40% STCT750 after 56 days of curing. (a) w/c ratio = 0.3, (b) w/c ratio = 0.4, (c) w/c ratio = 0.5

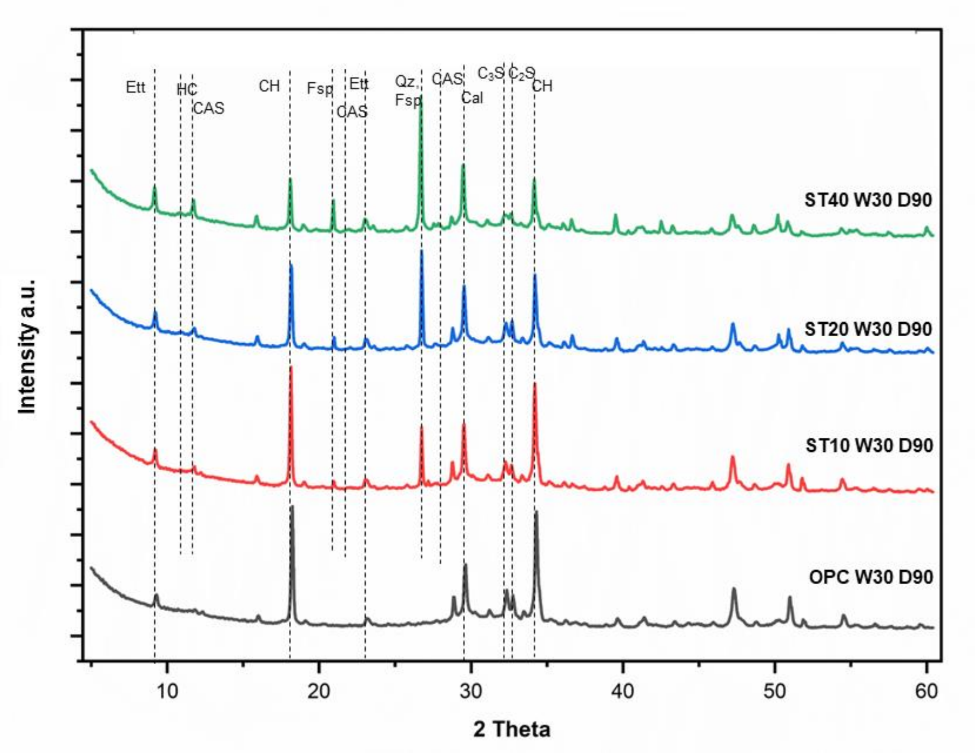
Ett
HC
CAS
CH
Fsp
Ett
CAS
Qz,
Fsp
CAS
Cal
C_3S
C_2S
CH
ST40 W30 D90
ST20 W30 D90
ST10 W30 D90
OPC W30 D90
Intensity a.u.
10
20
30
40
50
60
2 Theta

(a)

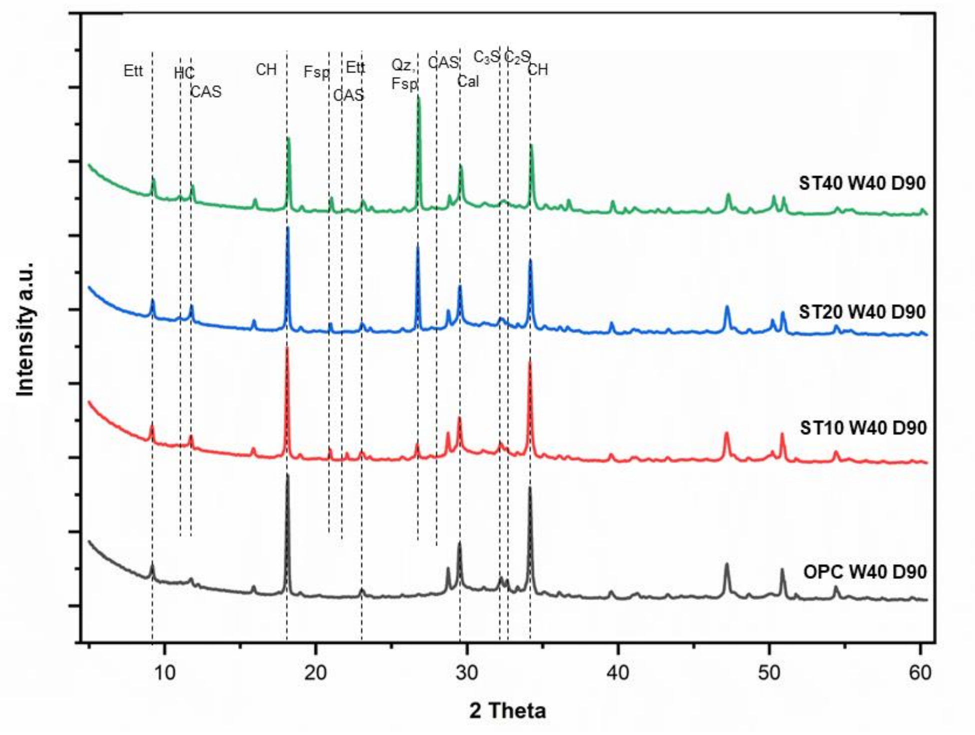
Ett
HC
CAS
CH
Fsp
Ett
CAS
Qz,
Fsp
CAS
Cal
C_3S
C_2S
CH
ST40 W40 D90
ST20 W40 D90
ST10 W40 D90
OPC W40 D90
Intensity a.u.
10
20
30
40
50
60
2 Theta

(b)

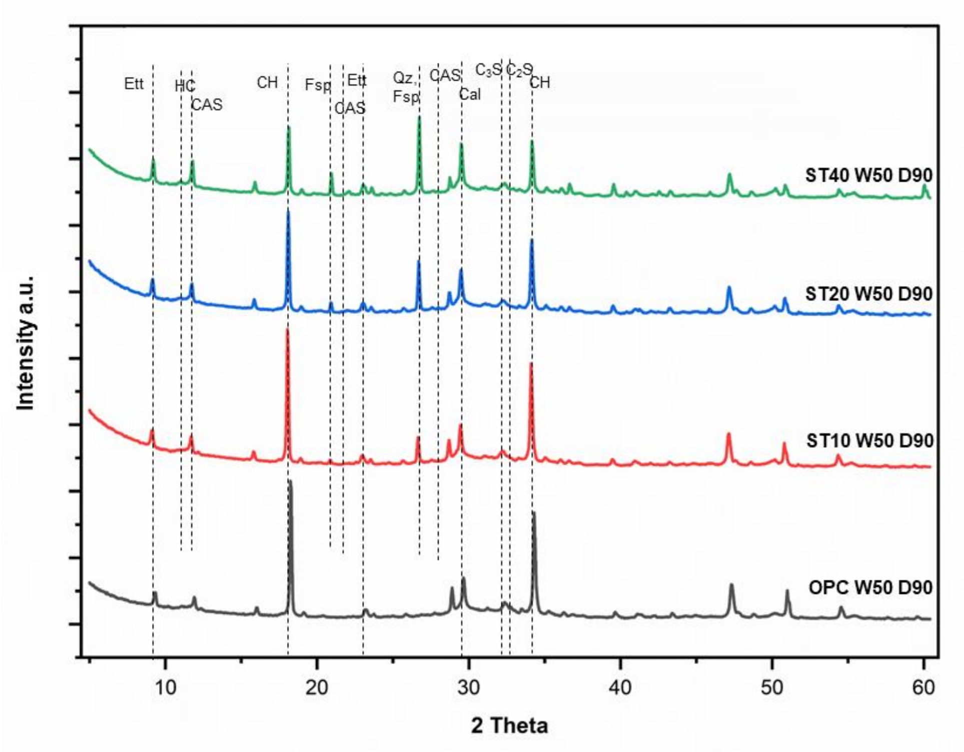

(c)

Fig. 5.12: XRD diffraction patterns of cementitious pastes containing 10%, 20% and 40% STCT750 after 90 days of curing. (a) w/c ratio = 0.3, (b) w/c ratio = 0.4, (c) w/c ratio = 0.5

5.5 Microstructural assessment with SEM

This section investigates the microstructure of hydrated cementitious pastes containing varying percentages (10%, 20%, and 40%) of MTCT850 and STCT750, with w/c ratios of 0.3, 0.4, and 0.5. The examination of the microstructure was conducted at different time intervals, specifically 7, 14, 28, 56, and 90 days of curing. The investigation was conducted on fractured surfaces in order to gain insights into the evolution of microstructure [232], rather than on polished surfaces. The small fragments used for the study were obtained from disc-shaped paste samples (described in Chapter 3, section 3.3.3) using a hammer and chisel and as a result some of the observed samples exhibited the presence of minuscule cracks. These cracks are therefore ignored from the discussions. Furthermore, it was observed that certain samples still exhibited the presence of unhydrated MTCT850 and STCT750 particles, which were found to charge and discharge electrons when examined using a scanning electron microscope. This mainly occurs because the unhydrated mineral waste surface is more porous than the hydrated cement paste. This leads to accumulation of electrons, which interferes with the interaction of electrons from the incidence beam and the sample surface during imaging. As a result, the image obtained is very bright, blurry and unclear. When this happened, the image capture time (previously set at 160 seconds per image) was decreased to 10 or 20 seconds, resulting in a slight reduction in resolution for the captured images. As the morphology of samples were observed and the microscopic images were captured, the microstructural elements present in the images were identified to be different phases based on the observations made in literature as indexed below in Table 5.3.

Table 5.3: Phases identified from microstructure analysis and their references

C-S-H formations	[232,273–275]
CH formations (Portlandite)	[232,276]
Ettringite	[232]
Vaterite ($CaCO_3$ formations)	[277,278]
Mordenite	[279]
Biotite	[279]
Feldspar	[279]
C-A-S-H	[280]

The microstructural characteristics of the samples containing MTCT850 at different ages (7, 14, 28, 56, and 90 days) are shown in Figures 5.13 to 5.17. The microstructural analysis of both the OPC and MT samples at all the ages revealed the presence of ettringite in a needle-like form, as well as the presence of C-S-H and portlandite crystals. At the age of seven days, the matrix showed ettringite needles with a length of approximately 5 µm, as depicted in Figure 5.13 (a) to (d).

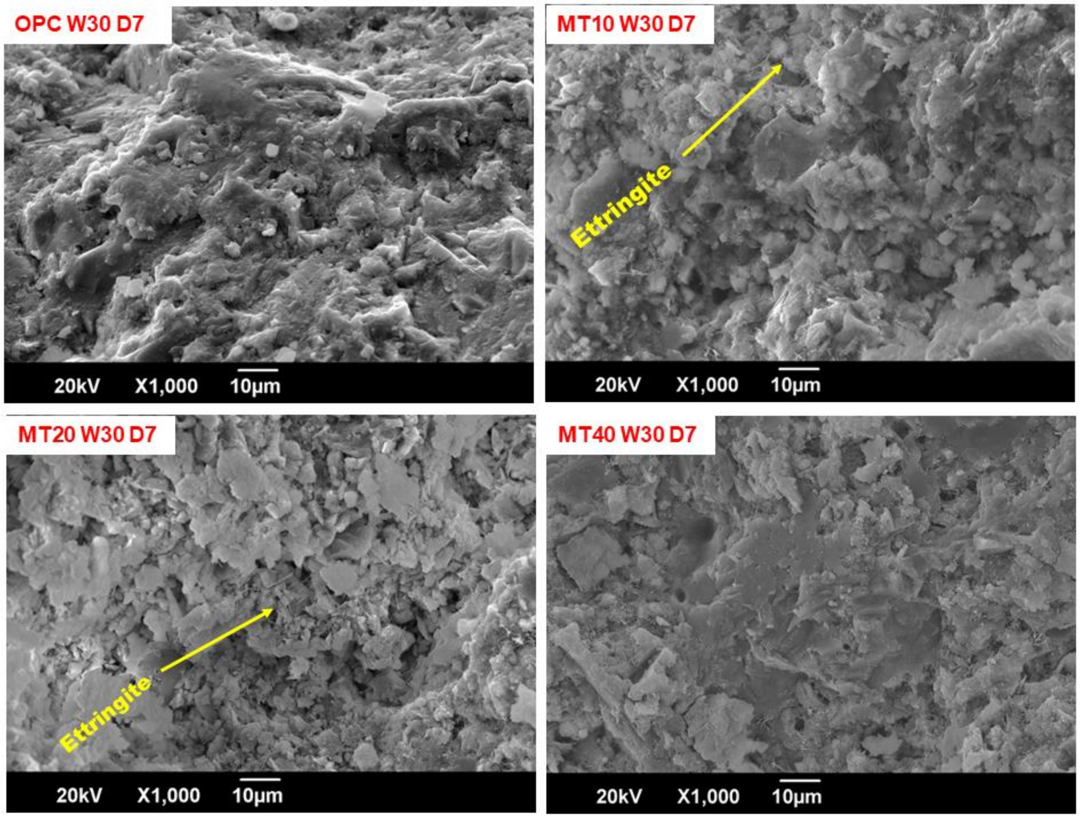

(a)

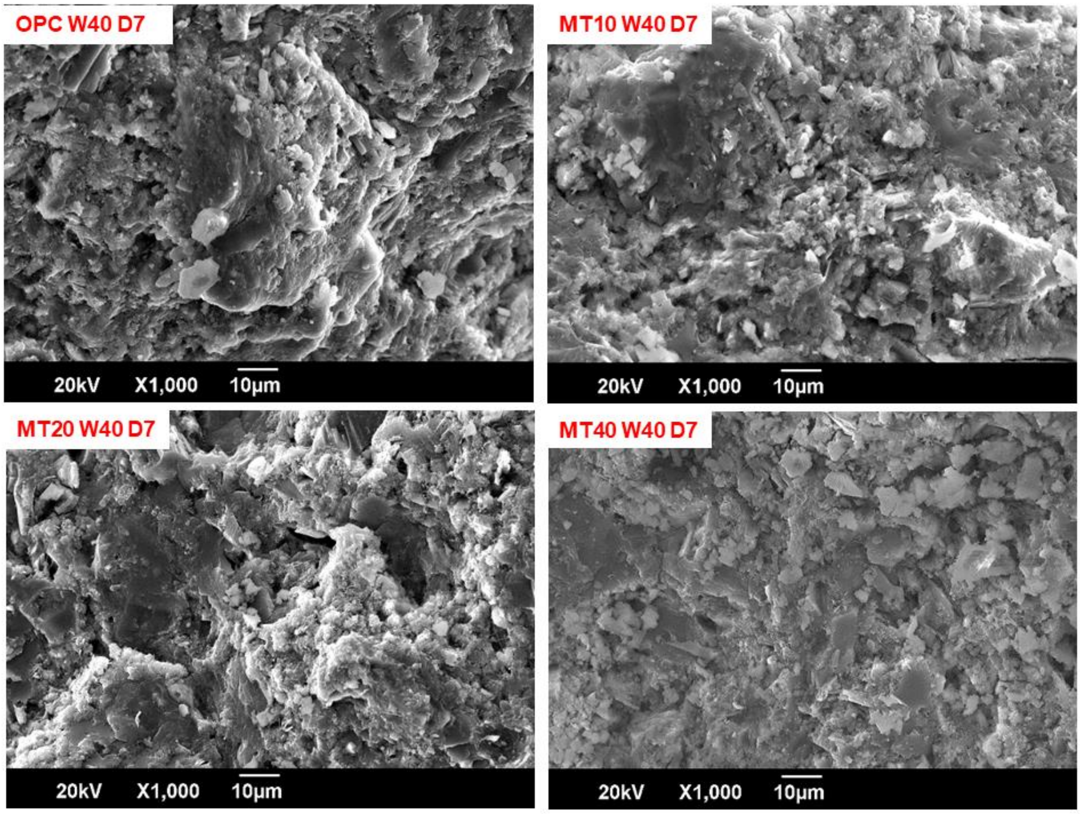
OPC W40 D7
MT10 W40 D7
MT20 W40 D7
MT40 W40 D7
20kV X1,000 10µm

(b)

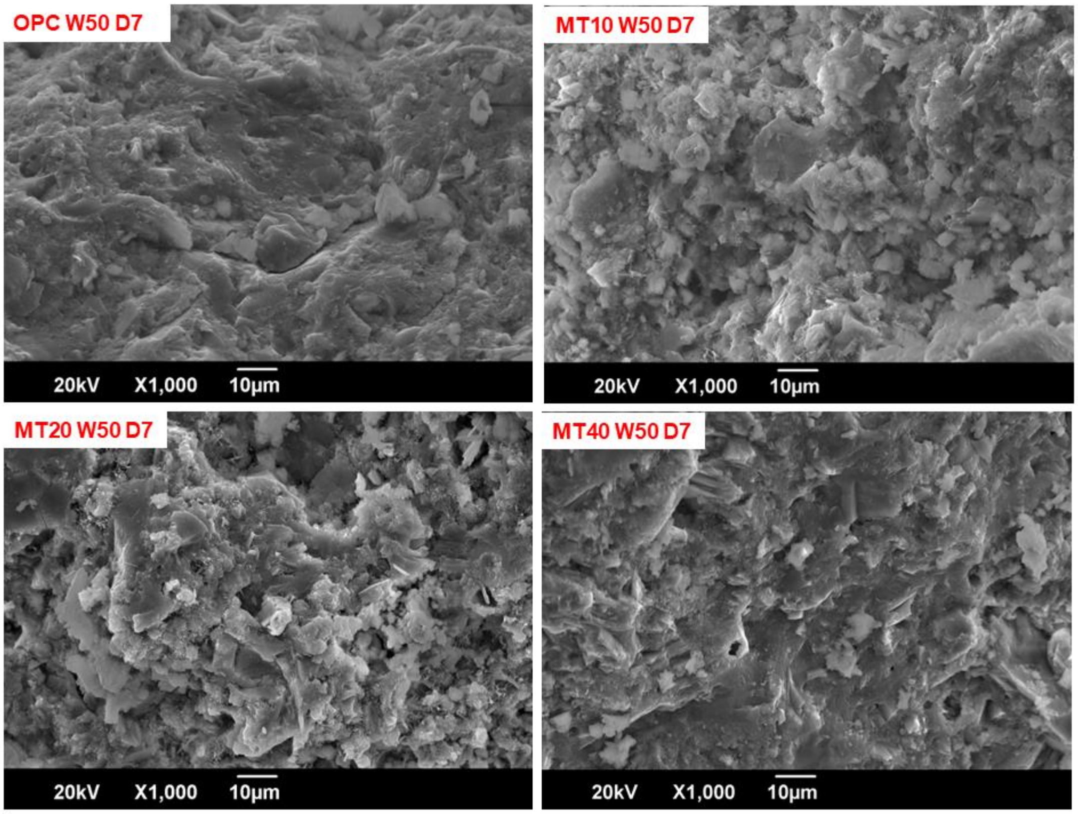
OPC W50 D7
MT10 W50 D7
MT20 W50 D7
MT40 W50 D7
20kV X1,000 10µm

(c)

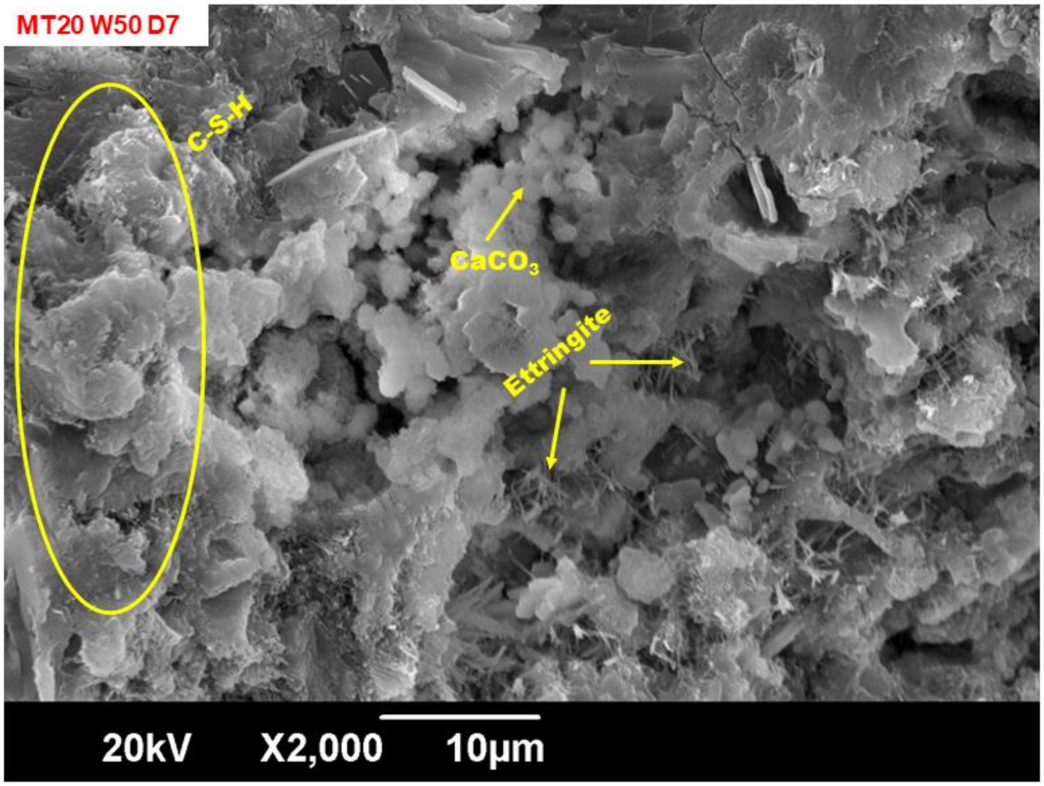

(d)

Fig. 5.13: SEM images of microstructure of cementitious pastes containing 0%, 10%, 20% and 40% MTCT850 after 7 days of curing (a) w/c ratio 0.3, (b) w/c ratio 0.4, (c) w/c ratio 0.5 (d) MT20W50 D7 showing phases of calcium carbonate, ettringite and C-S-H

The C-S-H observed during this stage exhibited a flaky or needle-like morphology. The calcite form of calcium carbonate was observed, as depicted in Figure 5.13 (d), and its presence was further confirmed through X-ray diffraction (XRD) analysis. As the hydration progressed the matrix exhibited a formation of portlandite with a more organised structure, as depicted in Figure 5.14 (a) to (e).

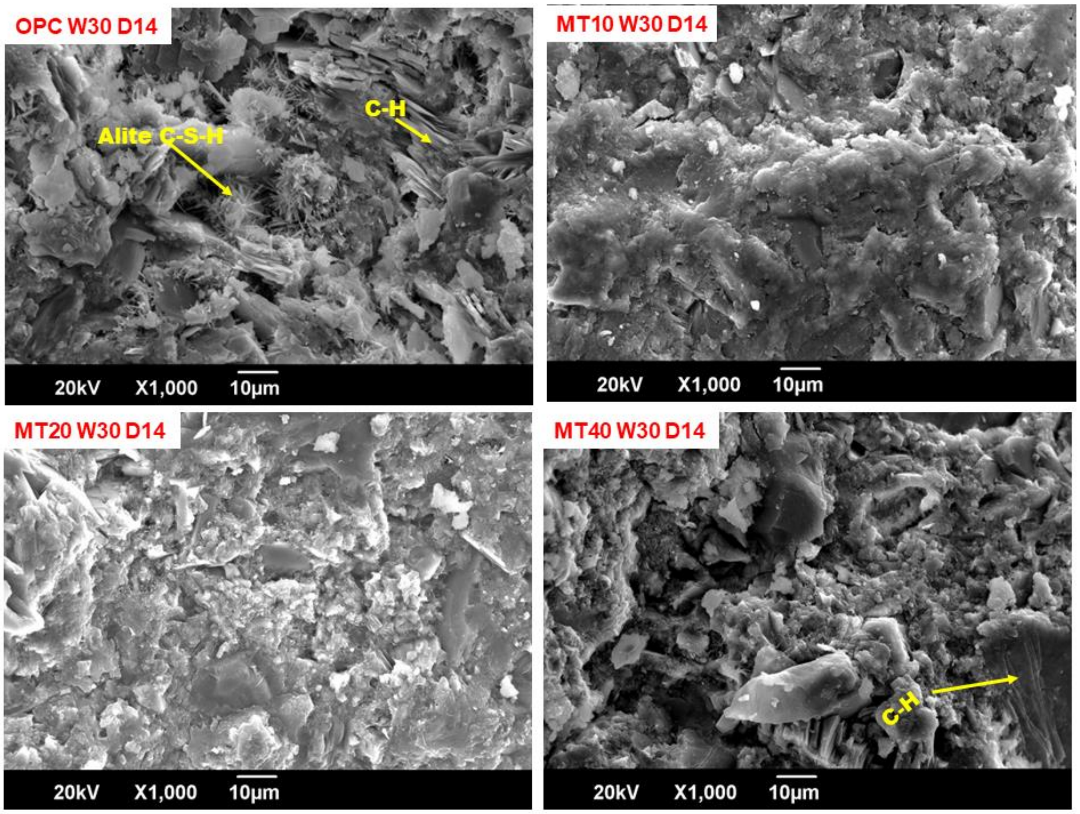
OPC W30 D14
Alite C-S-H
C-H
20kV X1,000 10µm
MT10 W30 D14
20kV X1,000 10µm
MT20 W30 D14
20kV X1,000 10µm
MT40 W30 D14
C-H
20kV X1,000 10µm

(a)

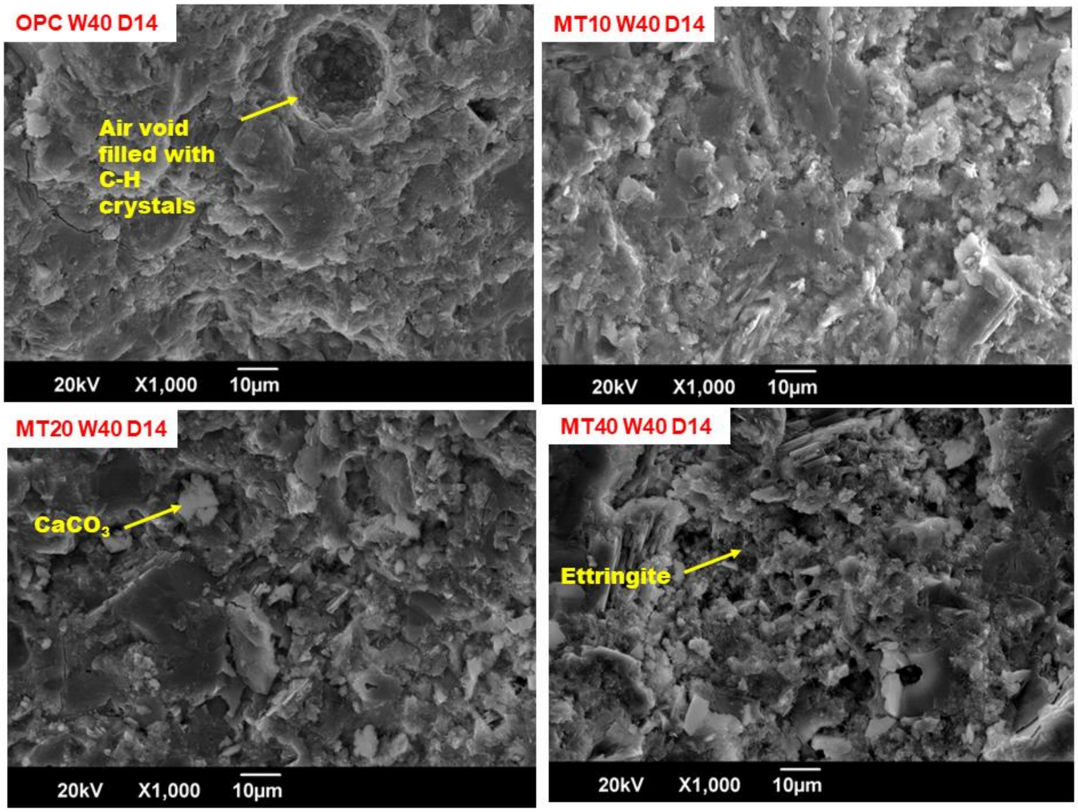
OPC W40 D14
Air void filled with C-H crystals
20kV X1,000 10µm
MT10 W40 D14
20kV X1,000 10µm
MT20 W40 D14
$CaCO_3$
20kV X1,000 10µm
MT40 W40 D14
Ettringite
20kV X1,000 10µm

(b)

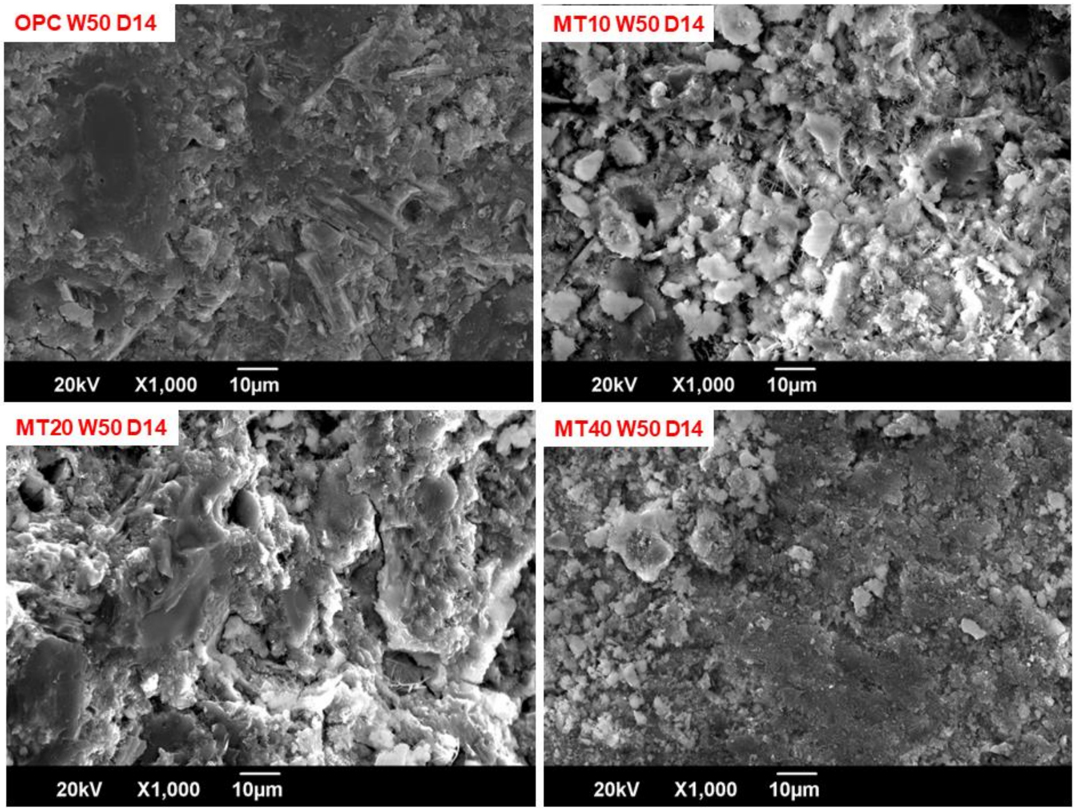
OPC W50 D14
20kV X1,000 10µm
MT10 W50 D14
20kV X1,000 10µm
MT20 W50 D14
20kV X1,000 10µm
MT40 W50 D14
20kV X1,000 10µm

(c)

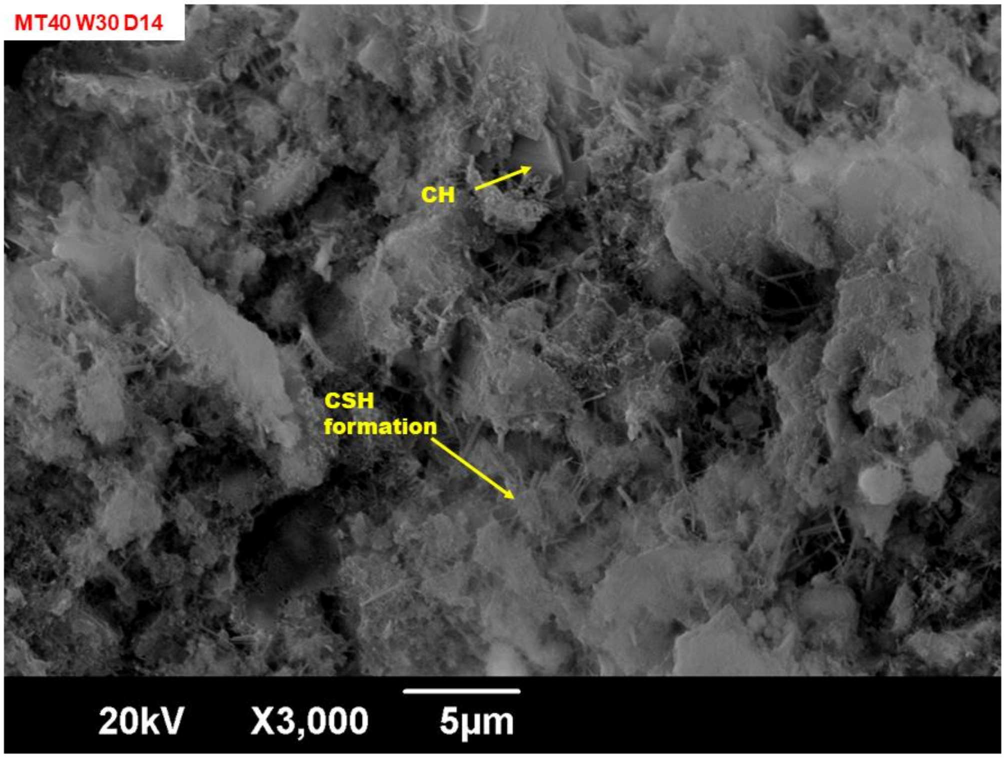
MT40 W30 D14
CH
CSH formation
20kV X3,000 5µm

(d)

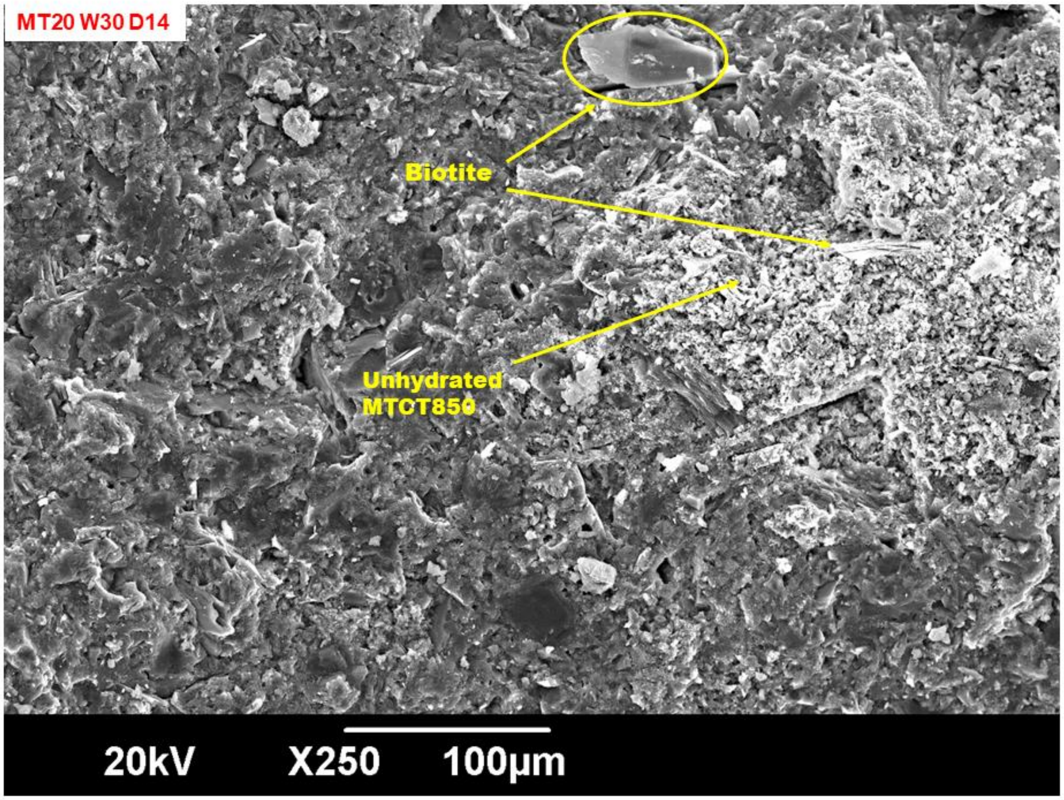

(e)

Fig. 5.14: SEM images of microstructure of cementitious pastes containing 0%, 10%, 20% and 40% MTCT850 after 14 days of curing (a) w/c ratio 0.3, (b) w/c ratio 0.4, (c) w/c ratio 0.5 (d) MT40W30 D14 showing formation of CH, ettringite and C-S-H (e) MT20W30D14 showing unhydrated particles of MTCT850.

The precipitation of needle like C-S-H on the alite crystals, and the presence of layered portlandite was observed in the case of ordinary Portland cement (OPC). The MT mixes displayed the presence of flaky C-S-H, as well as a matrix of crumpled foil like C-S-H. This matrix contained embedded portlandite crystals and ettringite rods, as seen in Figure 5.14 (d). The crumpled foil shaped C-S-H observed in MT mixes is similar to the C-S-H formed in cementitious binders containing supplementary cementitious material [232,273–275]. This formation is explained by the fact the fine particle structure of the supplementary cementitious material and the presence of high Si results in constrained space and hence C-S-H adapting a foil like structure rather than fibrillar structure [274] and formation of similar C-S-H structures were also observed in case of other siliceous mine tailings [129]. This observation suggests that the matrix becomes more compact as a result of hydration. The analysis of the MT samples revealed the existence of unhydrated MTCT850 particles that were found to be embedded within the matrix, as represented in Figure 5.14 (e). The unhydrated particles had a similar morphology to that of the powdered sample (discussed in detail in Chapter 4) This observation of unhydrated particles and mineral phases is consistent with the other studies which confirmed that the consumption of all the mineral waste is not possible by hydration [189]. Nevertheless, it is important to acknowledge that w/c ratio of the mix in this particular instance is quite low (w/c = 0.3). Therefore, achieving complete hydration of the particles, particularly within a 14-day period, is not possible. The presence of unhydrated MT particles was noted in the majority of samples, particularly in samples with w/c of 0.3 and when the MT content was at 20% and 40%. The identification of biotite particles in Figure 5.14 (e) was made easier by their layered arrangement and the vitreous appearance commonly observed in mica minerals [281]. While the other particles of MTCT850 were potentially observable, they lacked any particular features that would help them to be definitively identified.

Figure 5.15 (a) through (d) displays the OPC and MT samples after curing of 28 days. The matrix appears more compact because of ongoing hydration. The C-S-H exhibited a flaky and corrugated morphology. The voids present in the specimen were filled by C-S-H and ettringite, as depicted in Figure 5.15 (d). For both w/c ratios, OPC matrices exhibit strong presence of portlandite crystals. The presence of portlandite appears to reduce with the incorporation of MT into the system, which leads to the formation of hazy/cloudy-like hydration products.

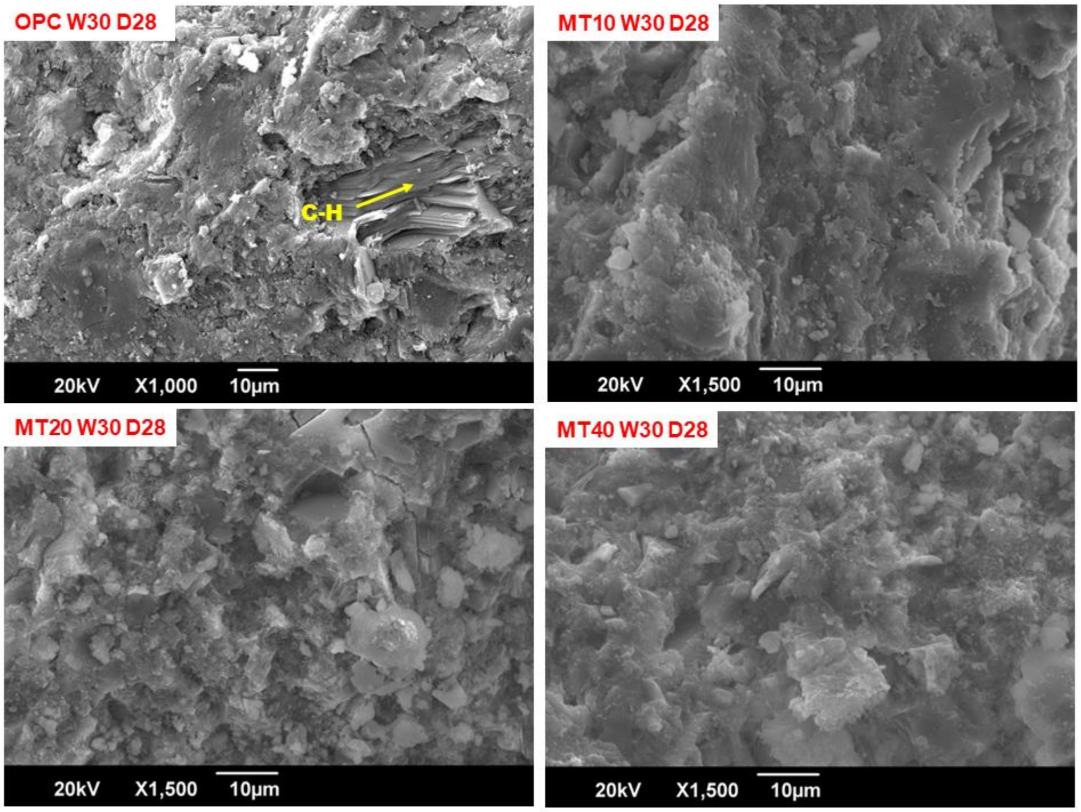

(a)

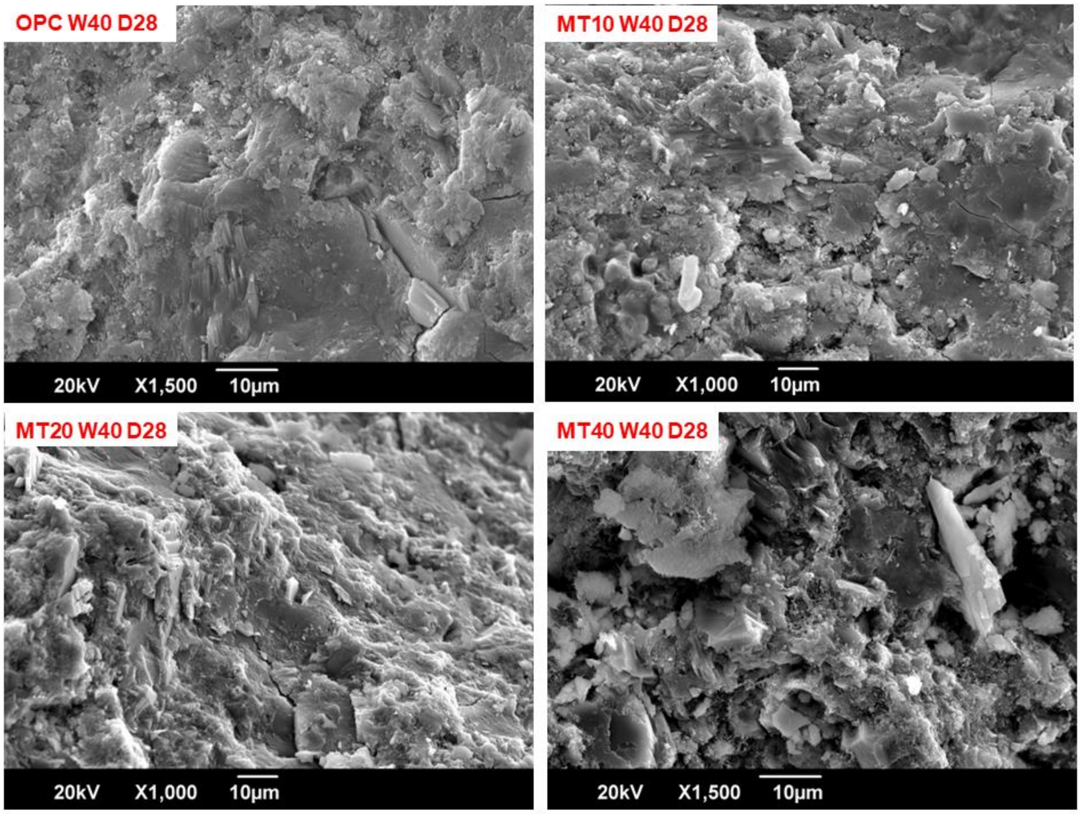
OPC W40 D28
20kV X1,500 10µm
MT10 W40 D28
20kV X1,000 10µm
MT20 W40 D28
20kV X1,000 10µm
MT40 W40 D28
20kV X1,500 10µm

(b)

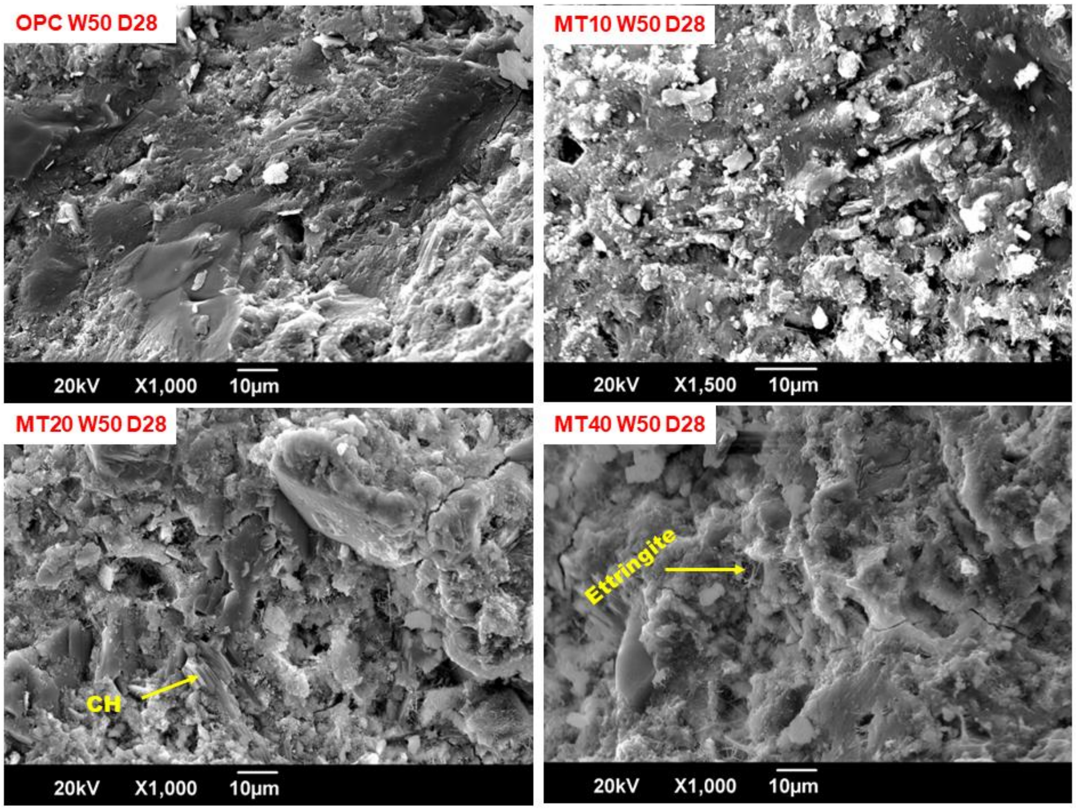
OPC W50 D28
20kV X1,000 10µm
MT10 W50 D28
20kV X1,500 10µm
MT20 W50 D28
CH
20kV X1,000 10µm
MT40 W50 D28
Ettringite
20kV X1,000 10µm

(c)

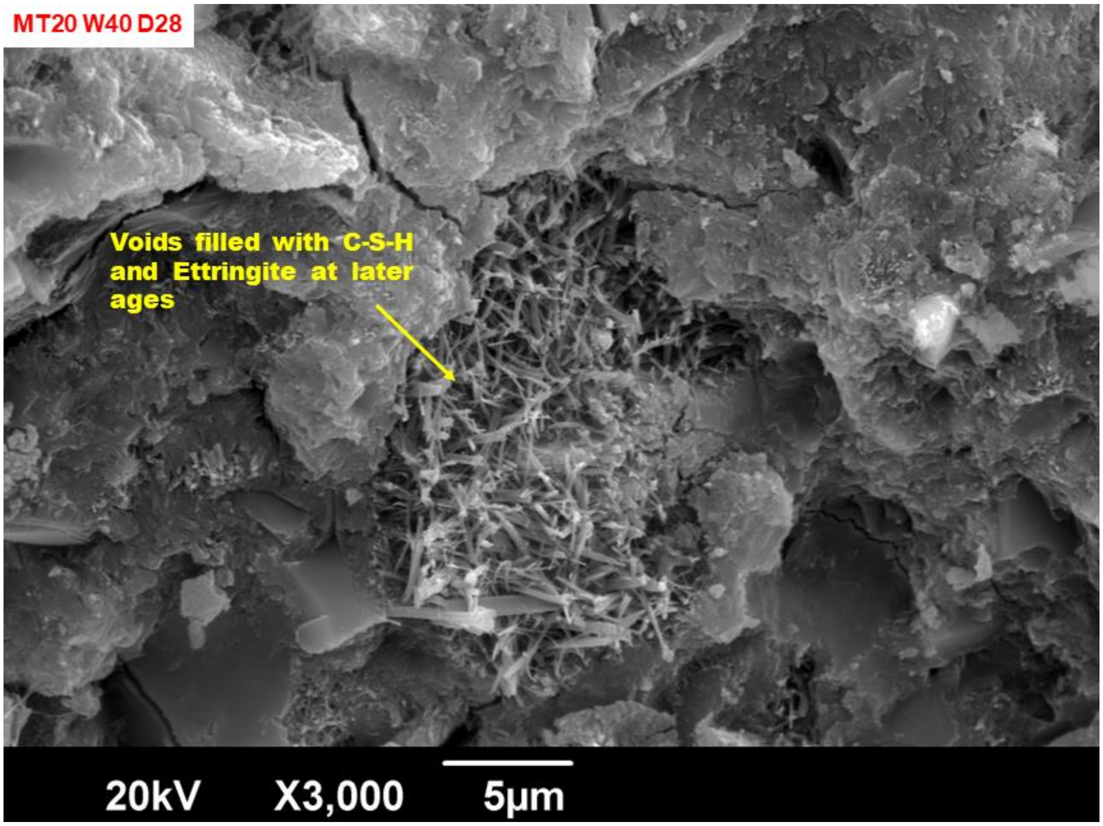

(d)

Fig. 5.15: SEM images of microstructure of cementitious pastes containing 0%, 10%, 20% and 40% MTCT850 after 28 days of curing (a) w/c ratio 0.3, (b) w/c ratio 0.4, (c) w/c ratio 0.5 (d) MT20W40 D28 showing a void filled by hydration products.

The samples at the age of 56 days are shown in Figure 5.16 (a) to (i). The portlandite appeared more orderly and compact in all the mixes. In the case of the MT samples, the C-S-H and ettringite minerals were observed to be enmeshed in a reticular network. It can also be seen from Figs. 5.16 (d) and (e) that the mixes with 40% MTCT850 appeared to have more C-S-H and portlandite was embedded in the matrix with flaky, crumpled foil like and corrugated C-S-H and needle shaped ettringite. In case of mixes with 10% MTCT850 the portlandite was well-formed and appeared distinctly. The phenomenon under consideration can be explained by examining the nucleation of portlandite samples, as depicted in Figure 5.16 (f). Nucleation occurs during later stages and results in the formation of C-S-H gel in the presence of mineral waste containing impurities like iron, manganese, and magnesium. Low reactivity of these materials leads to delayed release of these ions which then acts as nucleation sites [128,282].

The MT samples exhibit a higher concentration of these elements in comparison to the OPC, resulting in increased nucleation and subsequent formation of C-S-H at later stages. Figure 5.16 (g) depicts the presence of corrugated C-S-H structures and needle-like formations, measuring approximately 10 µm in length, which are identified as C-A-S-H formations. Although the matrices exhibited a more condensed structure and demonstrated enhanced connection among the hydration products, the analysis revealed that the samples continued to exhibit the presence of unhydrated MTCT850, as depicted in Figure 5.16 (h). Additionally, certain samples exhibited the presence of mordenite fibres as shown in Fig. 5.16 (i), which can be recognised as one of the zeolitic calcium aluminium silicate phases in XRD analysis.

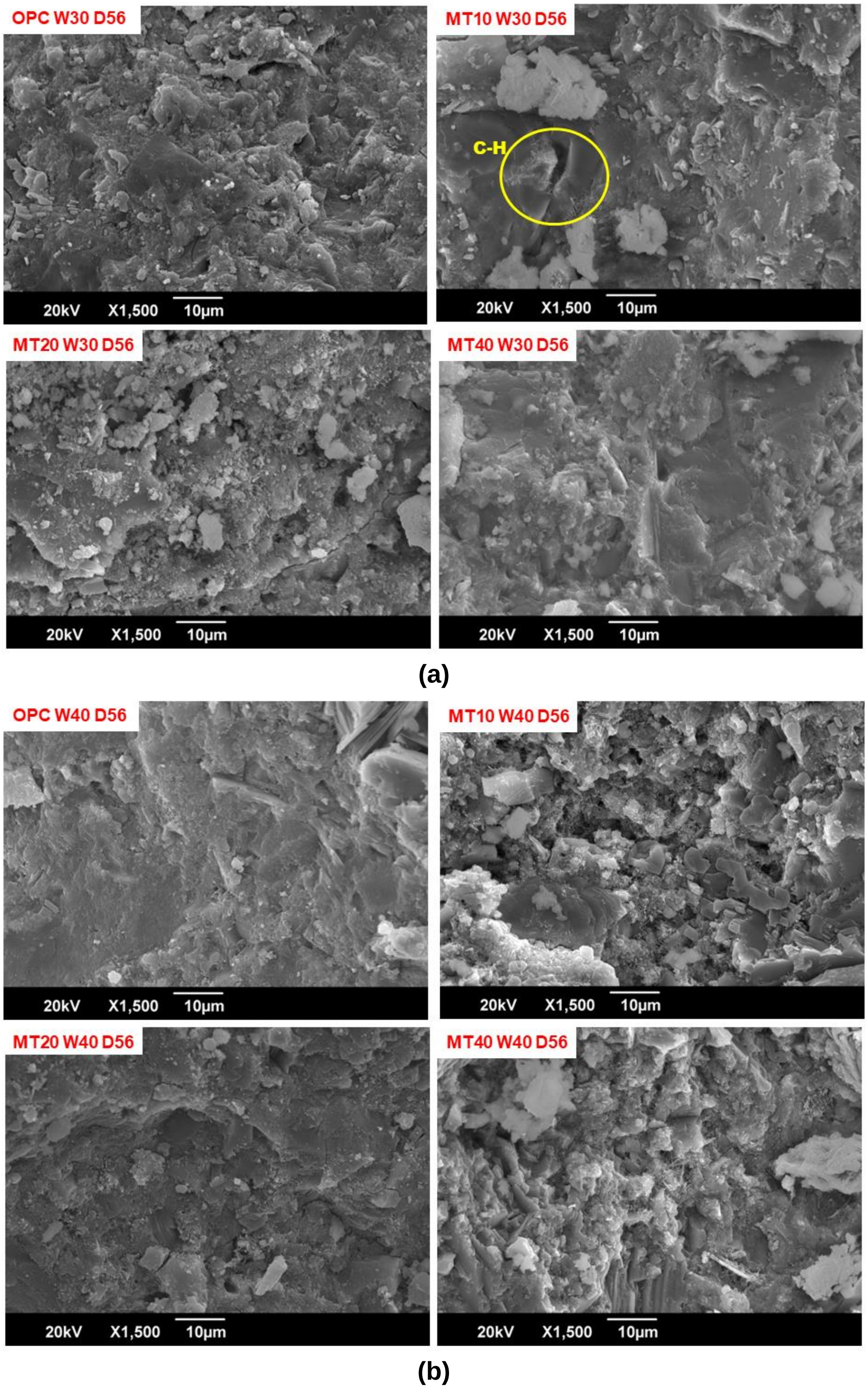

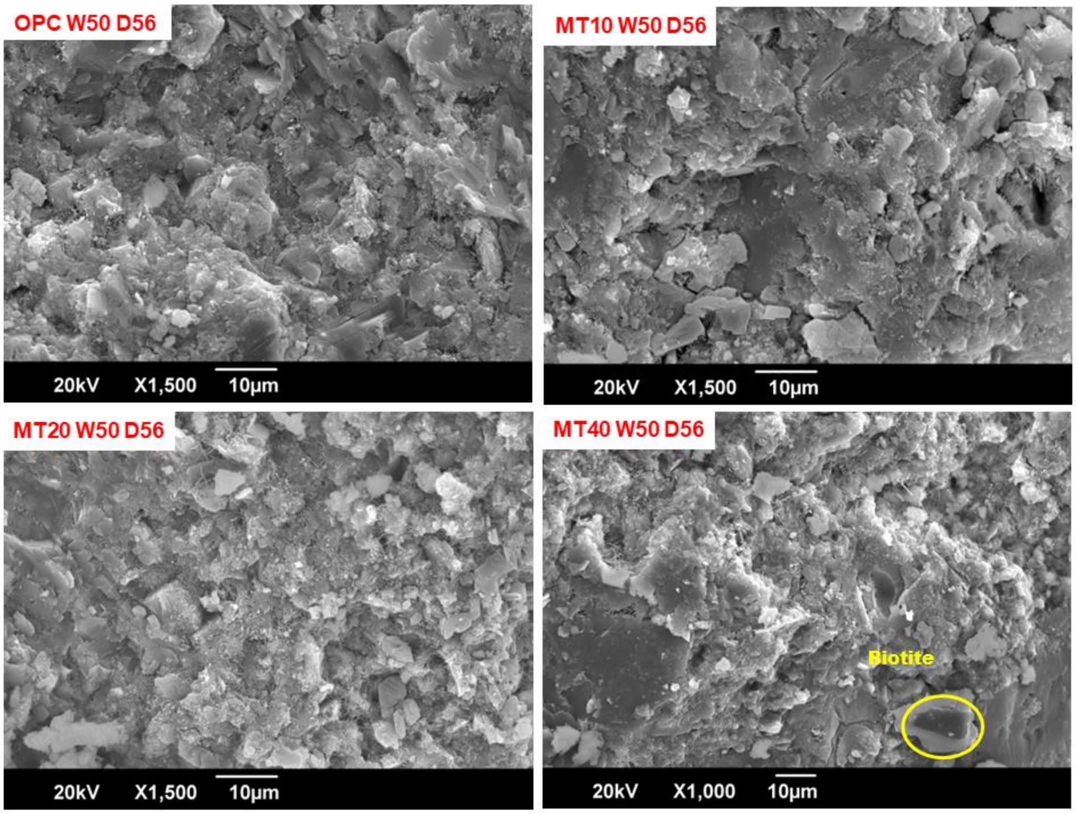
OPC W50 D56
20kV X1,500 10µm
MT10 W50 D56
20kV X1,500 10µm
MT20 W50 D56
20kV X1,500 10µm
MT40 W50 D56
Biotite
20kV X1,000 10µm

(c)

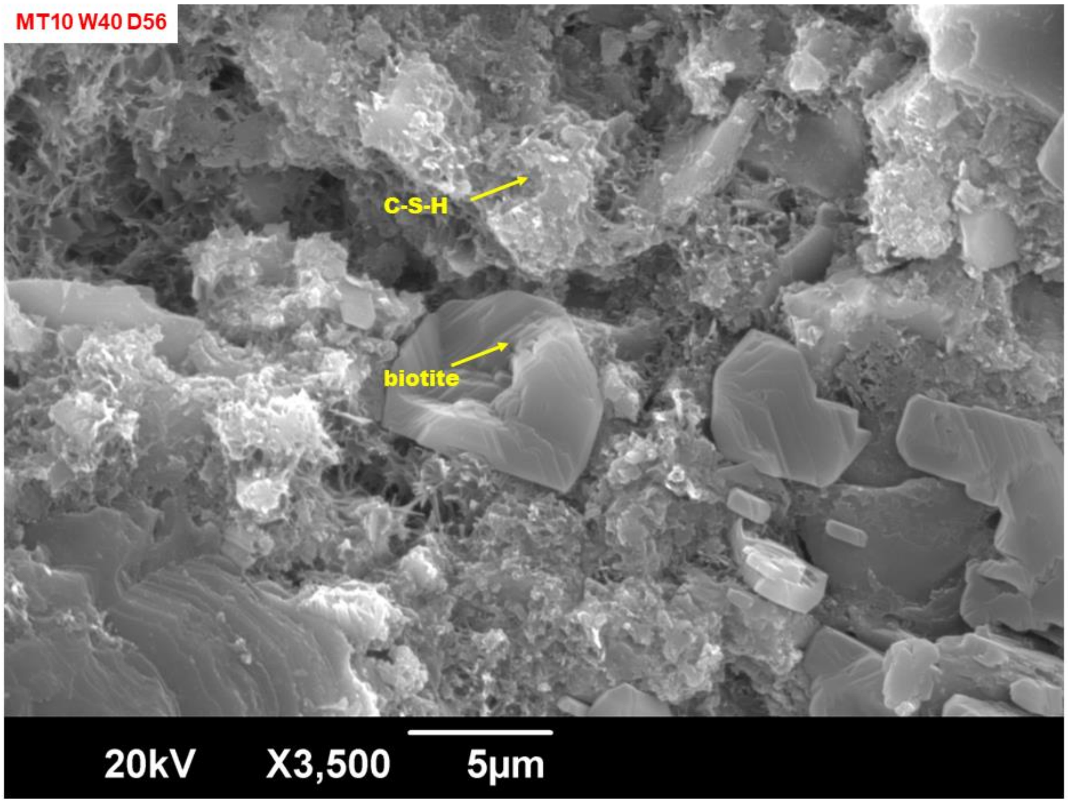
MT10 W40 D56
C-S-H
biotite
20kV X3,500 5µm

(d)

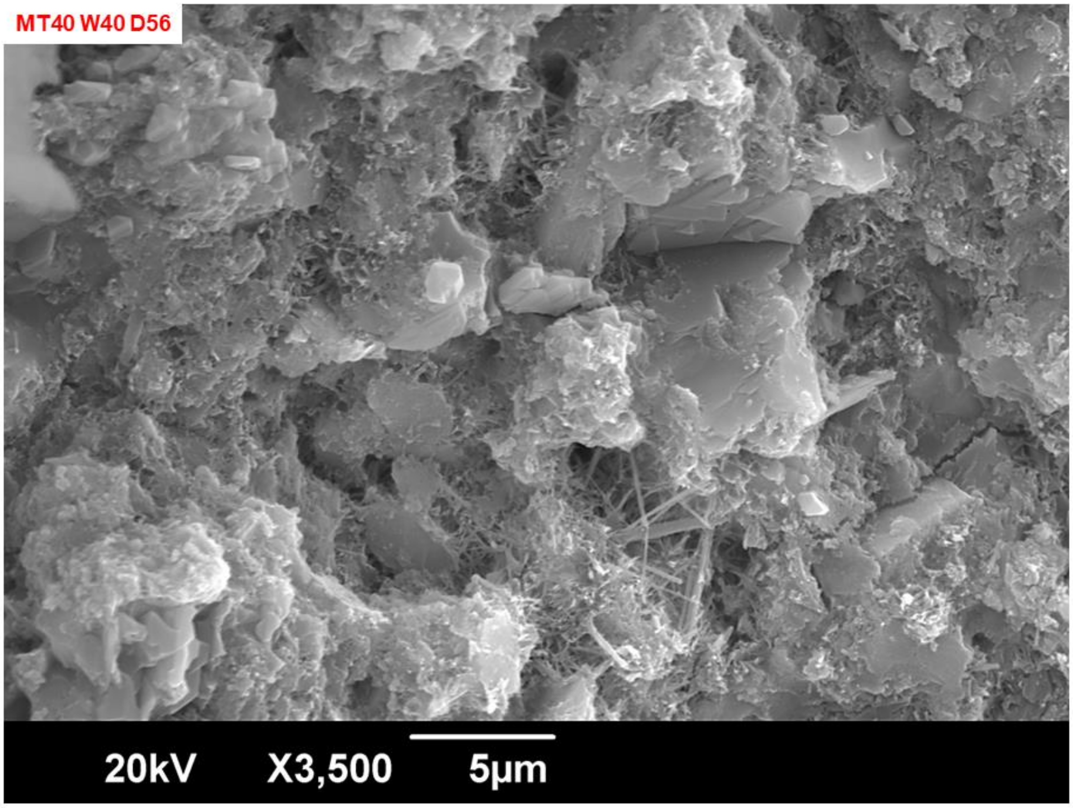
MT40 W40 D56
20kV
X3,500
5μm

(e)

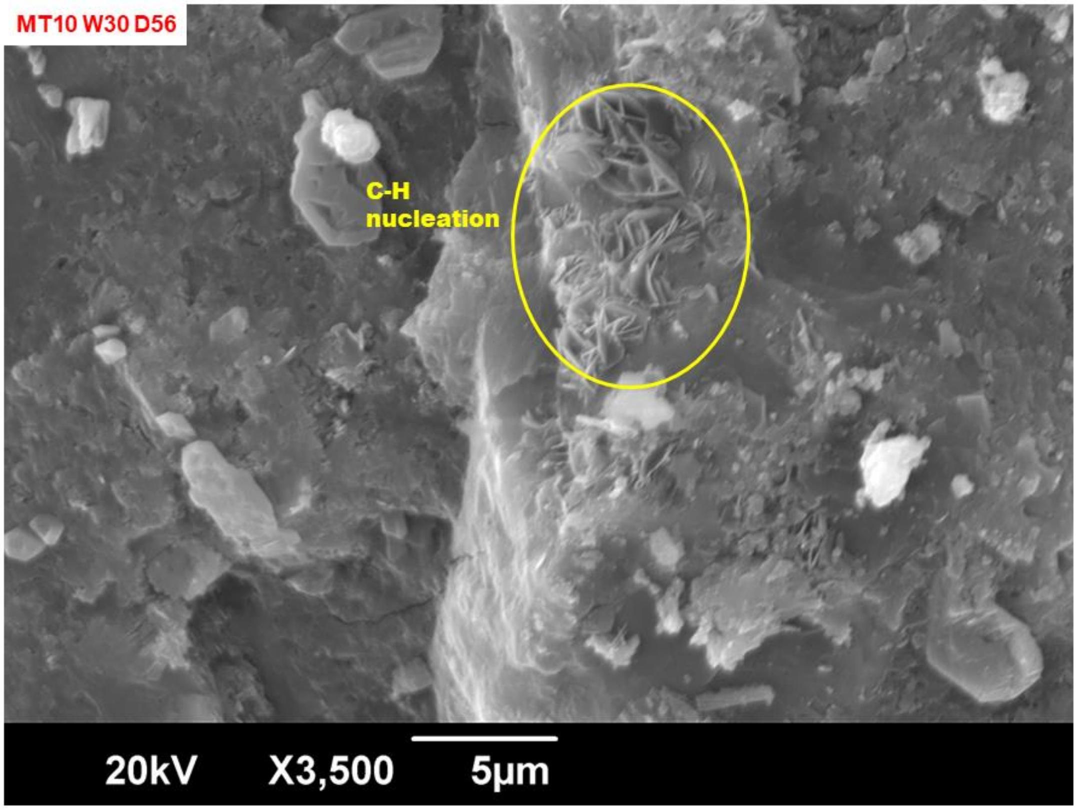
MT10 W30 D56
C-H
nucleation
20kV
X3,500
5μm

(f)

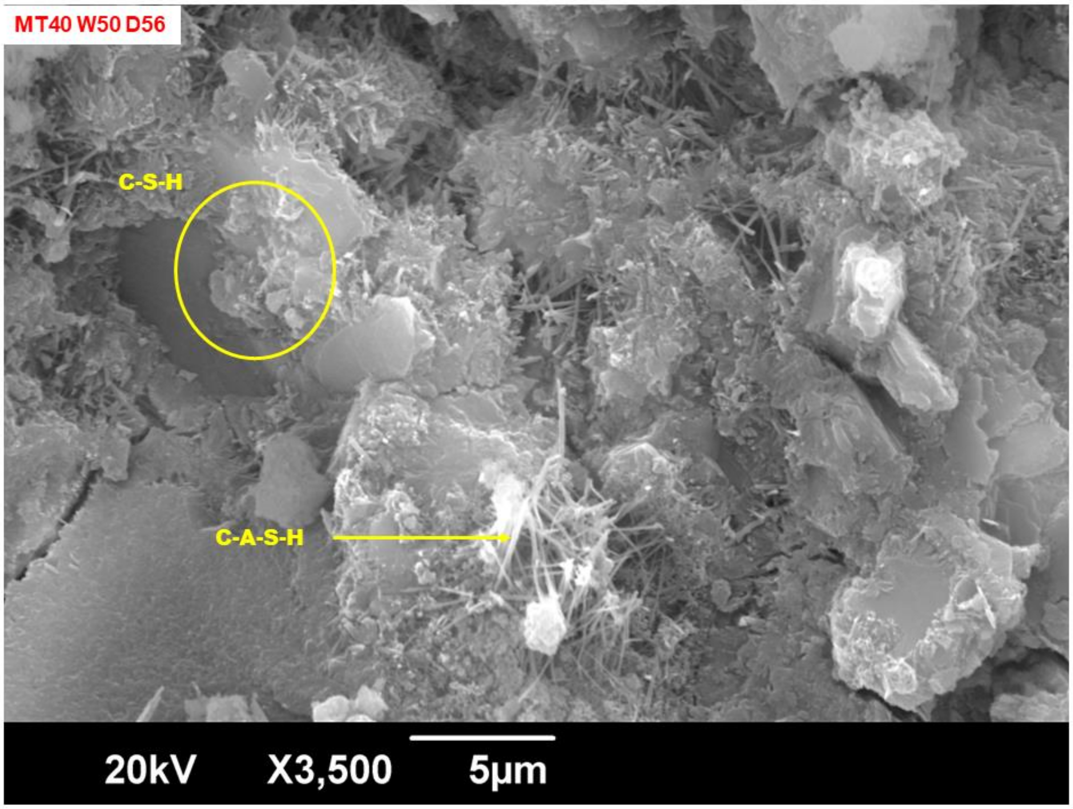
MT40 W50 D56
C-S-H
C-A-S-H
20kV
X3,500
5μm

(g)

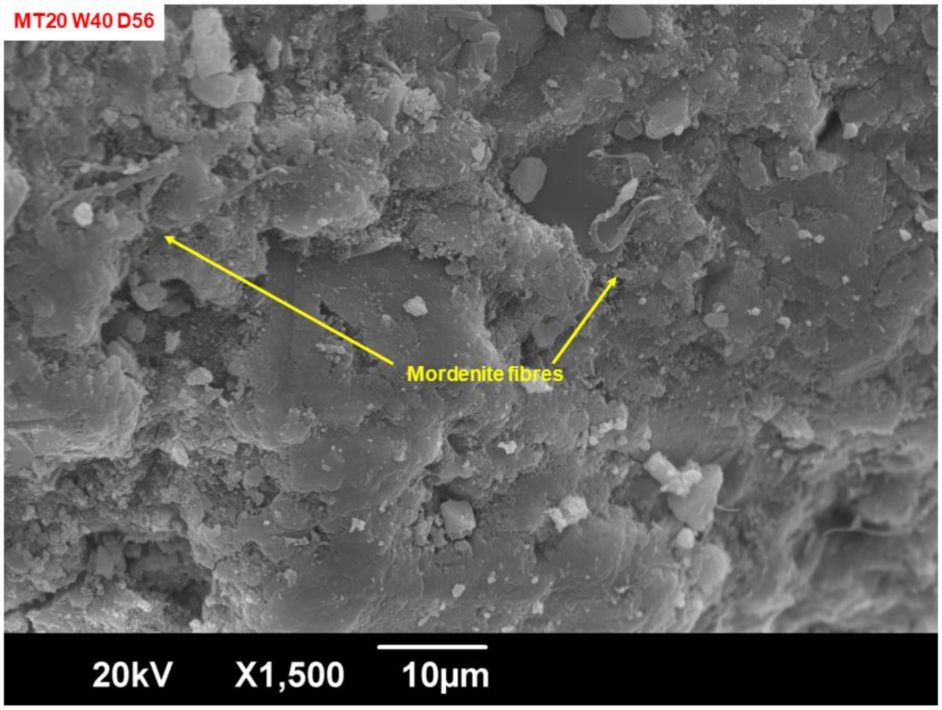
MT20 W40 D56
Mordenite fibres
20kV
X1,500
10μm

(h)

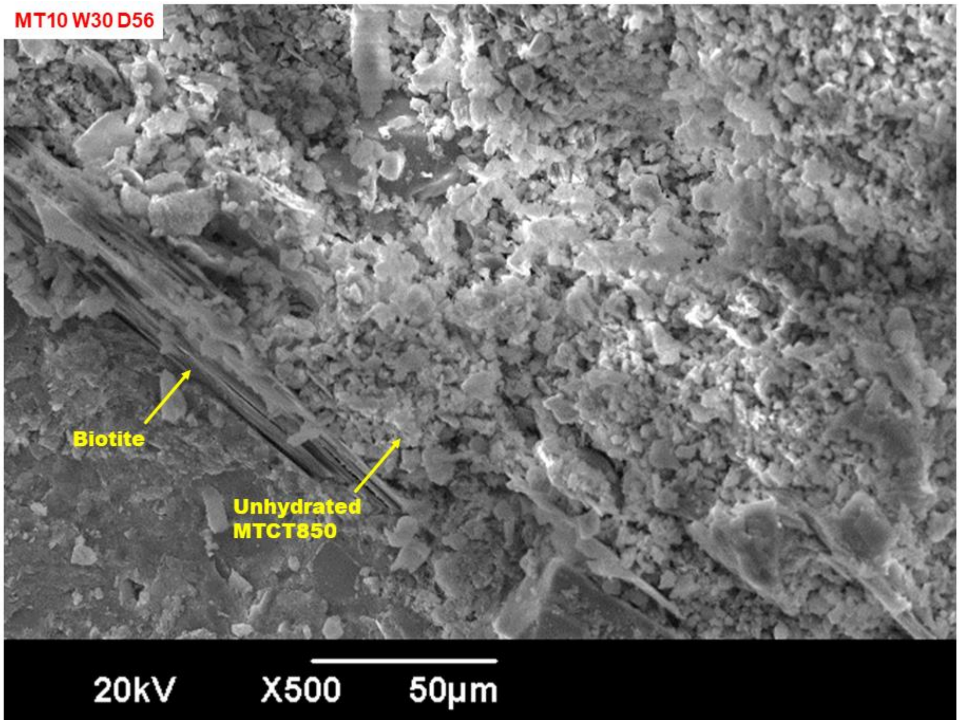

(i)

Fig. 5.16: SEM images of microstructure of cementitious pastes containing 0%, 10%, 20% and 40% MTCT850 after 56 days of curing (a) w/c ratio 0.3, (b) w/c ratio 0.4, (c) w/c ratio 0.5 (d) MT10W40D56 showing phases of portlandite, ettringite and C-S-H (e) MT40W40 D56 showing phases of portlandite, ettringite and C-S-H (f) MT10W30D56 showing nucleation in portlandite (g) MT40W50D56 showing presence of C-A-S-H (h) Presence of mordenite fibres in MT20W40D56 (i) MT10W30D56 showing presence of unhydrated particles

Figure 5.17 (a) to (d) illustrates the morphological characteristics of the OPC and MT pastes after a period of 90 days. The samples exhibited the presence of C-S-H, portlandite, and ettringite in all instances. Furthermore, the presence of fibrillar long C-A-S-H was also detected, as depicted in Figure 5.17 (c).

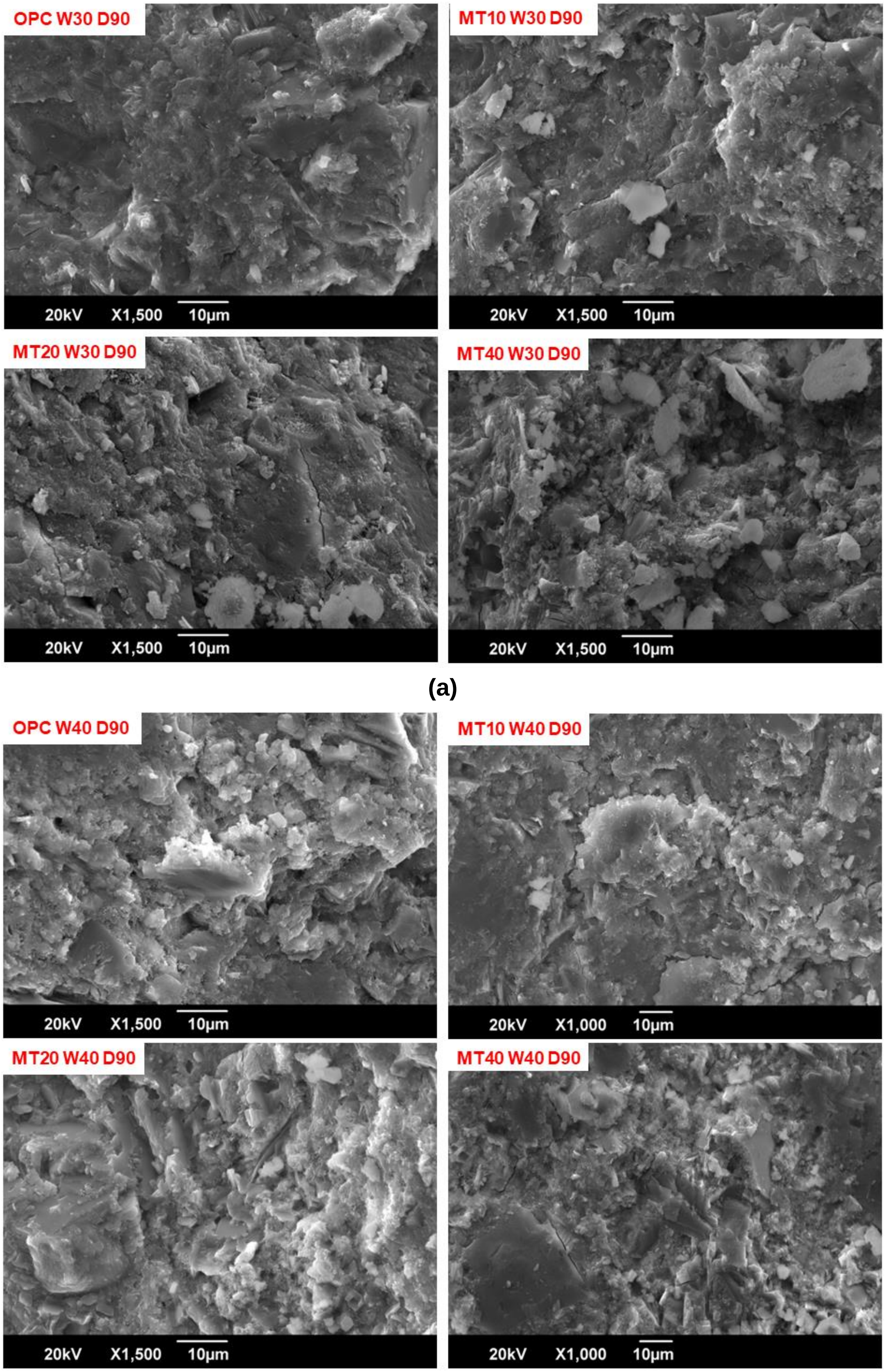
OPC W30 D90
20kV X1,500 10μm
MT10 W30 D90
20kV X1,500 10μm
MT20 W30 D90
20kV X1,500 10μm
MT40 W30 D90
20kV X1,500 10μm
OPC W40 D90
20kV X1,500 10μm
MT10 W40 D90
20kV X1,000 10μm
MT20 W40 D90
20kV X1,500 10μm
MT40 W40 D90
20kV X1,000 10μm

(a)

(b)

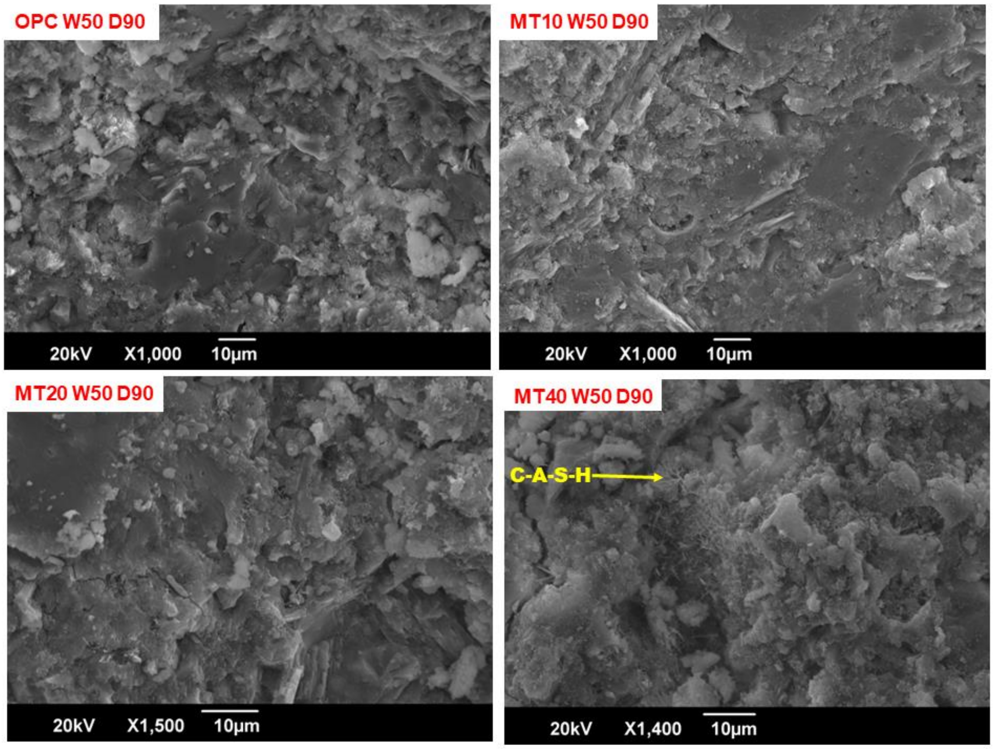

(c)

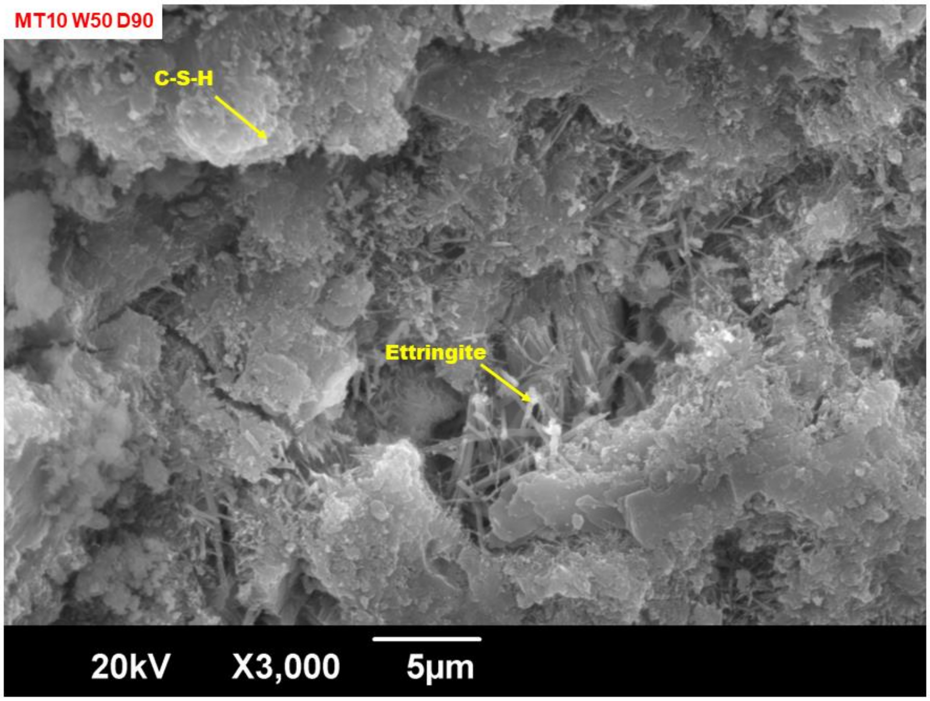

(d)

Fig. 5.17: SEM images of microstructure of cementitious pastes containing 0%, 10%, 20% and 40% MTCT850 after 90 days of curing (a) w/c ratio 0.3, (b) w/c ratio 0.4, (c) w/c ratio 0.5 (d) MT10W50D90 showing phases of ettringite and C-S-H.

The morphology of the samples containing STCT750 at different ages (7, 14, 28, 56, and 90 days) are shown in Figures 5.18 to 5.22. The microstructural analysis of both the OPC and MT samples at all the ages revealed the presence of ettringite in a needle-like form, as well as the presence of C-S-H and portlandite crystals.

Figs. 5.18 (a) through (d) shows OPC and ST samples after 7 days of curing. The samples exhibited presence of ettringite, C-S-H, portlandite. The ettringite observed in ST mixes this stage is short about 7 µm long and is more prevalent than in case of OPC. The higher presence of ettringite in ST sample could be due to the presence of anhydrite in STCT750 which in turn leads to availability of more sulphates for ettringite formation in ST samples. The C-S-H was flaky in structure and portlandite was more compact and layered. The ST samples also exhibited presence of unhydrated STCT750 and one such observation is made in Fig. 5.18 (a) where a degraded feldspar crystal is found embedded in the matrix.

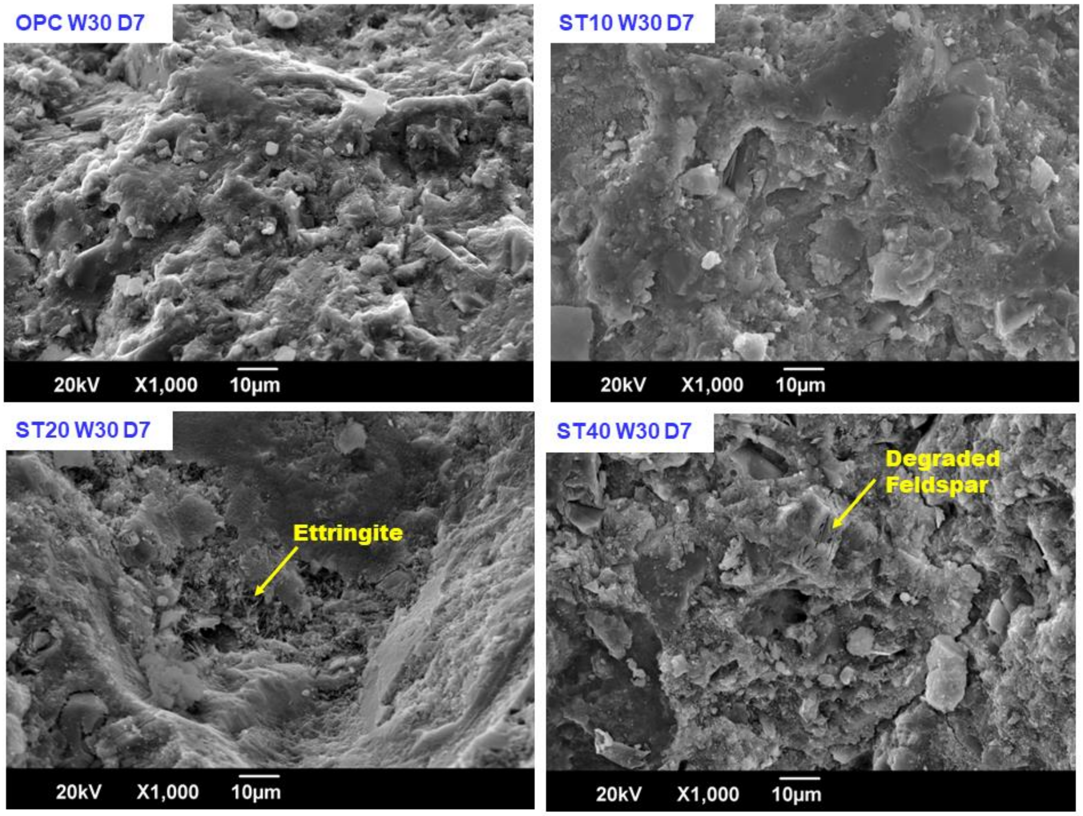

(a)

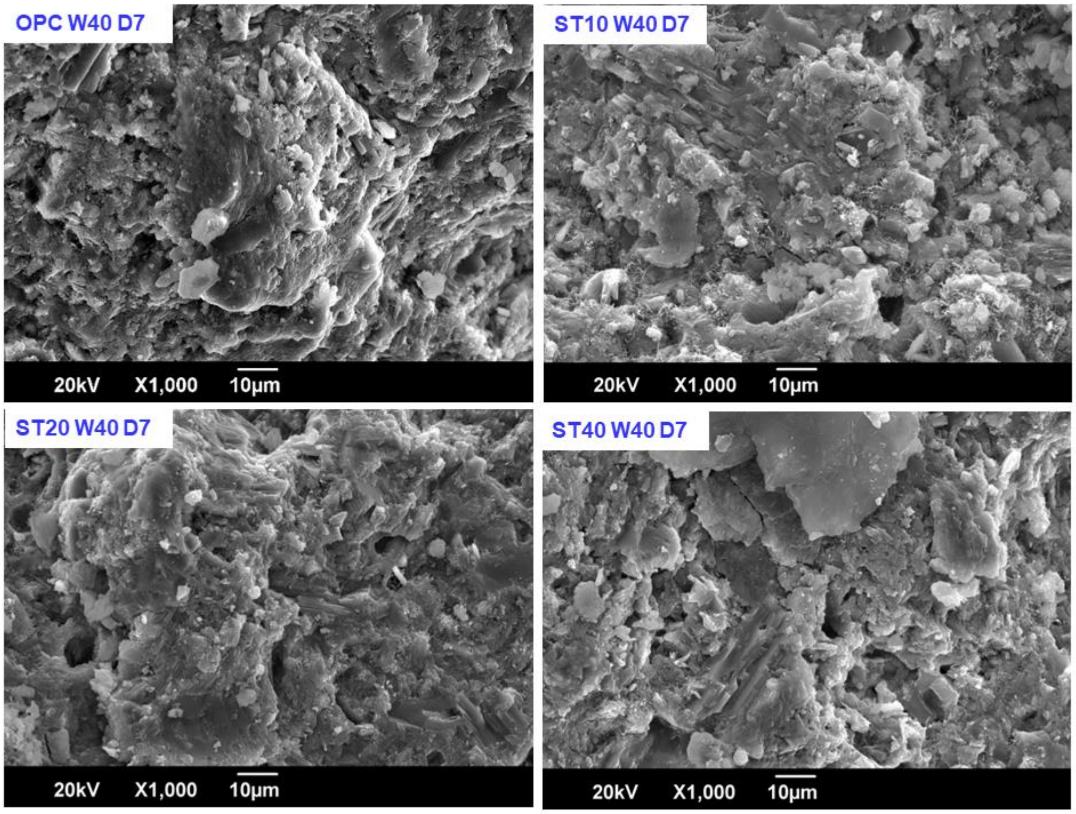
OPC W40 D7
20kV X1,000 10µm
ST10 W40 D7
20kV X1,000 10µm
ST20 W40 D7
20kV X1,000 10µm
ST40 W40 D7
20kV X1,000 10µm

(b)

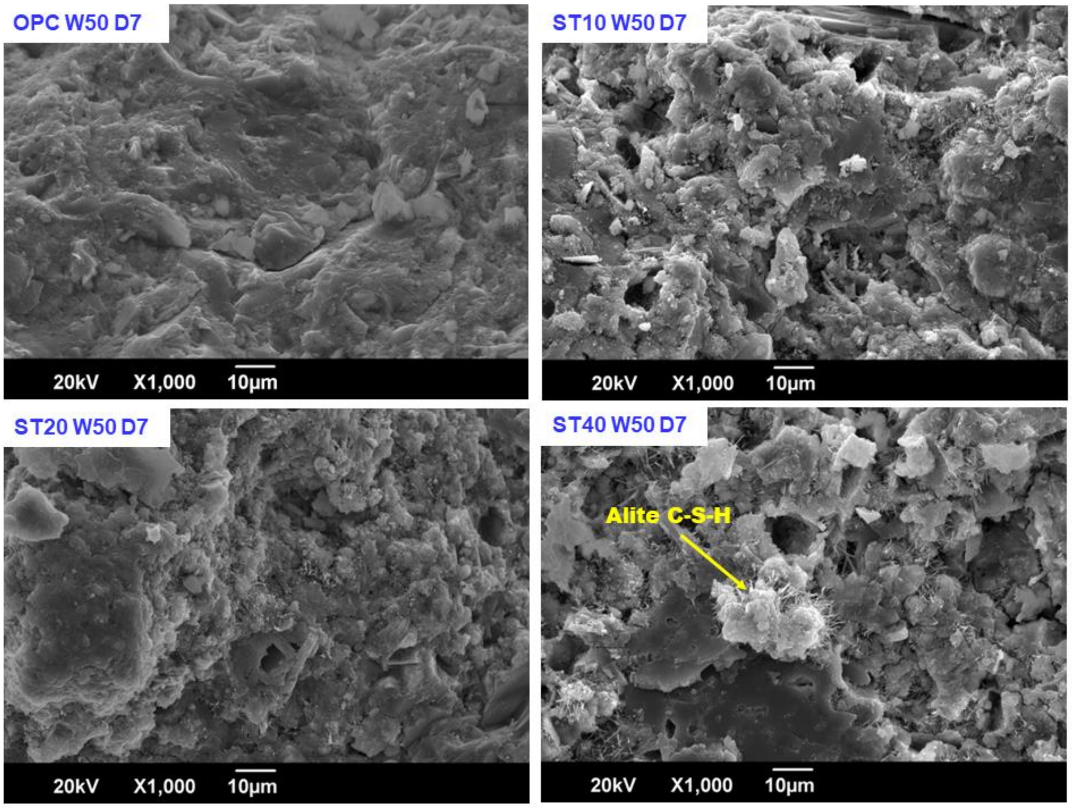
OPC W50 D7
20kV X1,000 10µm
ST10 W50 D7
20kV X1,000 10µm
ST20 W50 D7
20kV X1,000 10µm
ST40 W50 D7
Alite C-S-H
20kV X1,000 10µm

(c)

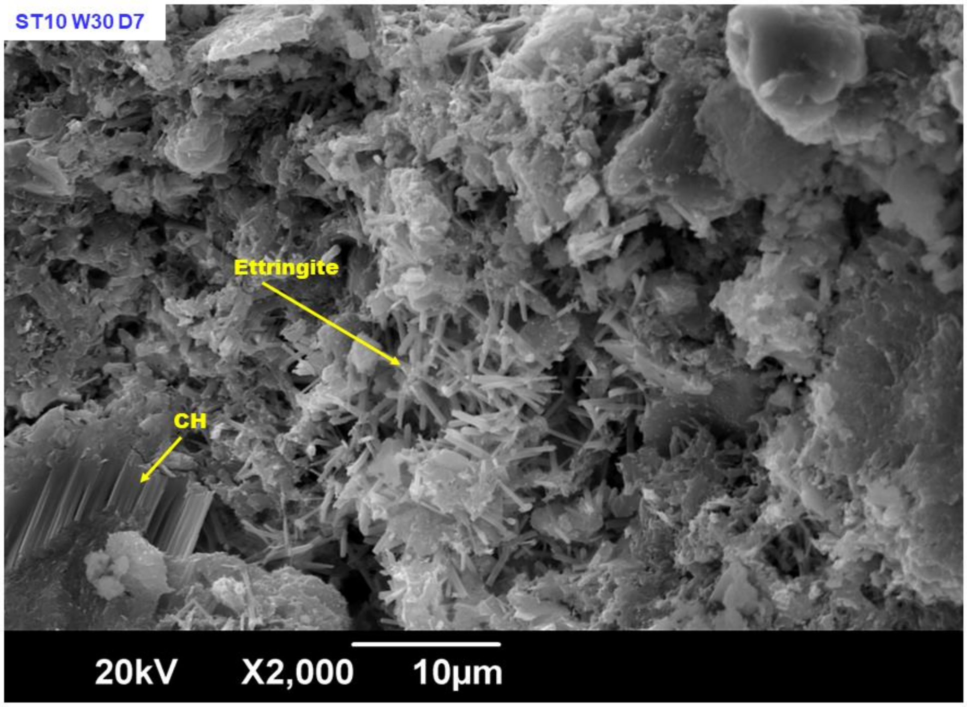

(d)

Fig. 5.18: SEM images of microstructure of cementitious pastes containing 0%, 10%, 20% and 40% STCT750 after 7 days of curing (a) w/c ratio 0.3, (b) w/c ratio 0.4, (c) w/c ratio 0.5 (d) ST10W30D7 showing phases of ettringite portlandite and C-S-H.

Fig. 5.19 (a) to (g) shows OPC and ST samples at 14 days of age needle like CSH and layered portlandite were observed in case of OPC, whereas the ST samples indicated more of flaky and crumpled foil like C-S-H and needle shaped ettringite throughout the matrix. Figs. 5.19 (d), (e) and (f) show reticular network of crumpled foil like C-S-H with ettringite and portlandite embedded in it. Fig. (g) shows presence of calcium carbonate in vaterite form on portlandite and surrounded by ettringite.

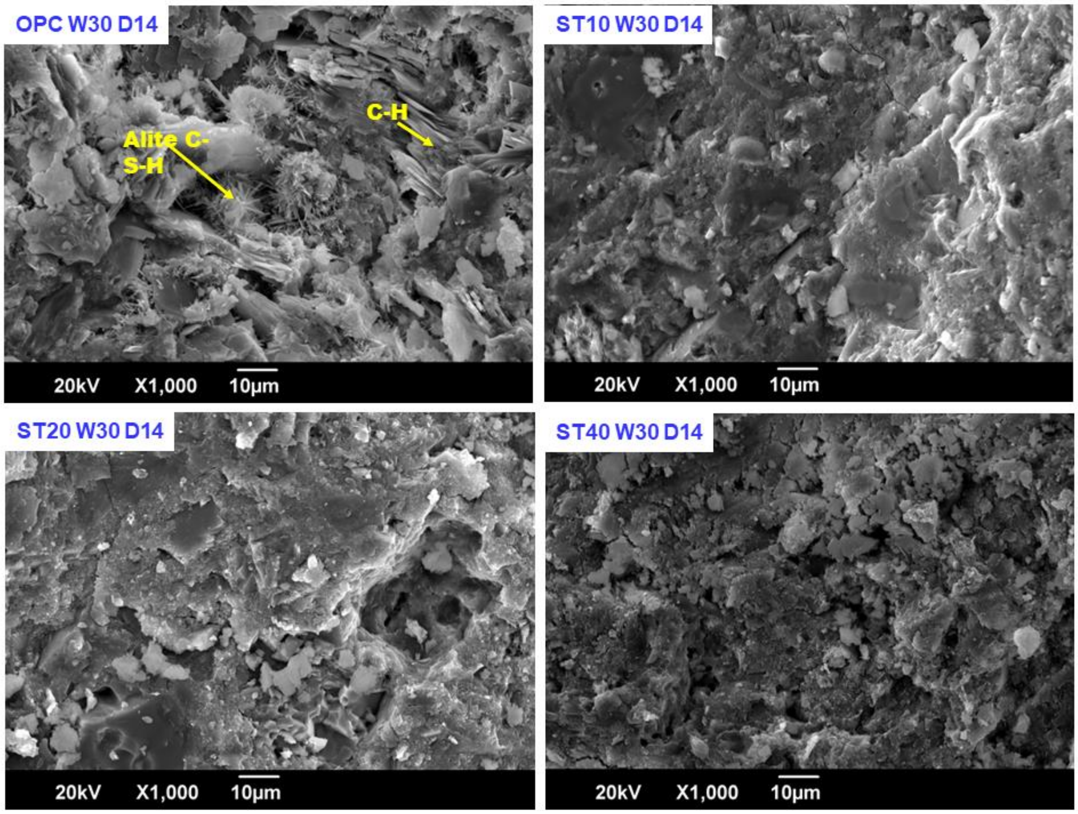
OPC W30 D14
Alite C-S-H
C-H
ST10 W30 D14
ST20 W30 D14
ST40 W30 D14
20kV X1,000 10µm

(a)

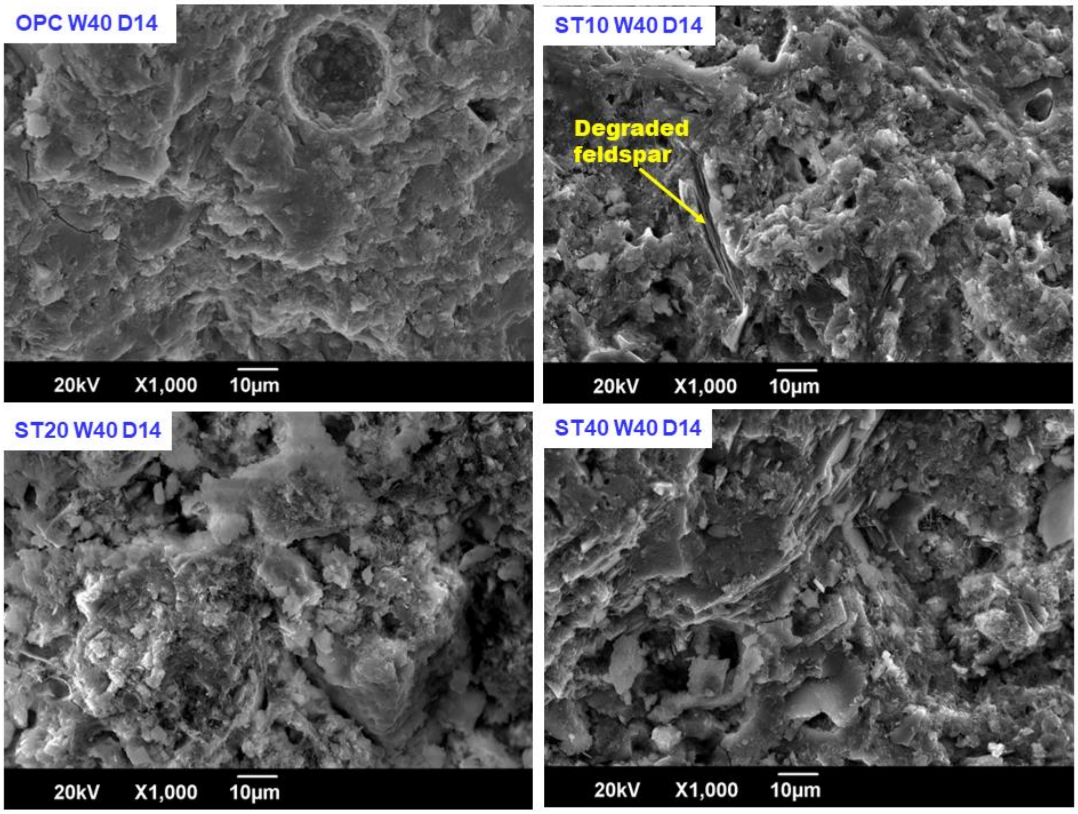
OPC W40 D14
ST10 W40 D14
Degraded feldspar
ST20 W40 D14
ST40 W40 D14
20kV X1,000 10µm

(b)

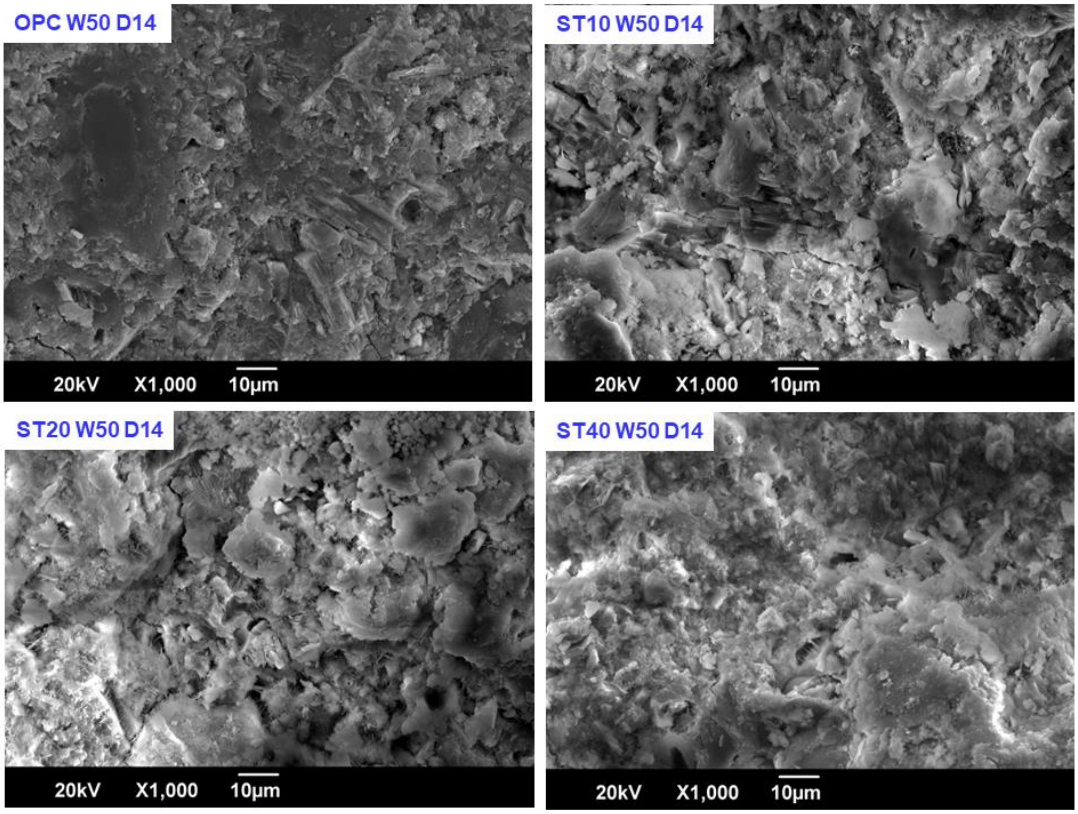
OPC W50 D14
20kV X1,000 10μm
ST10 W50 D14
20kV X1,000 10μm
ST20 W50 D14
20kV X1,000 10μm
ST40 W50 D14
20kV X1,000 10μm

(c)

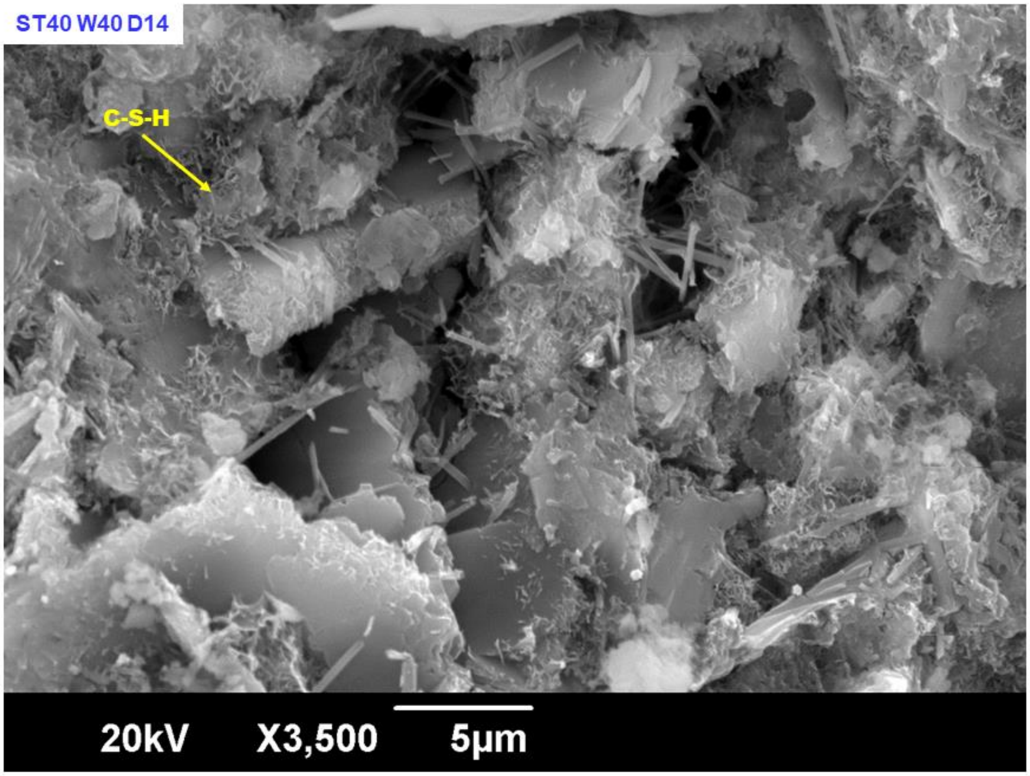
ST40 W40 D14
C-S-H
20kV X3,500 5μm

(d)

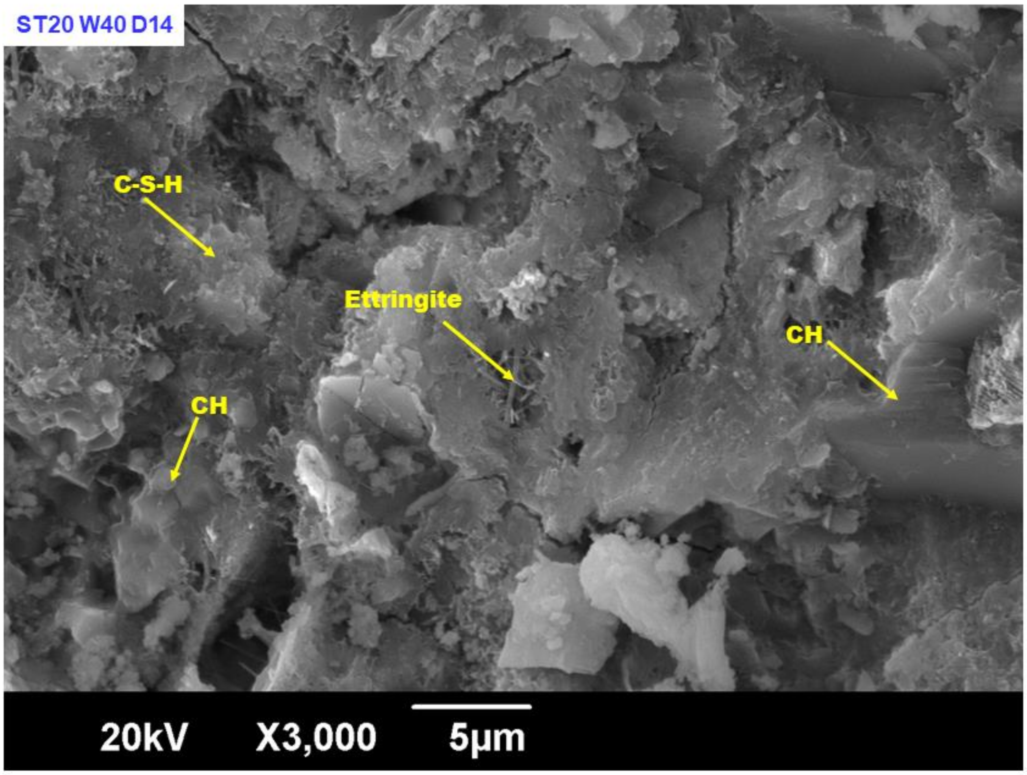
ST20 W40 D14
C-S-H
Ettringite
CH
CH
20kV X3,000 5µm

(e)

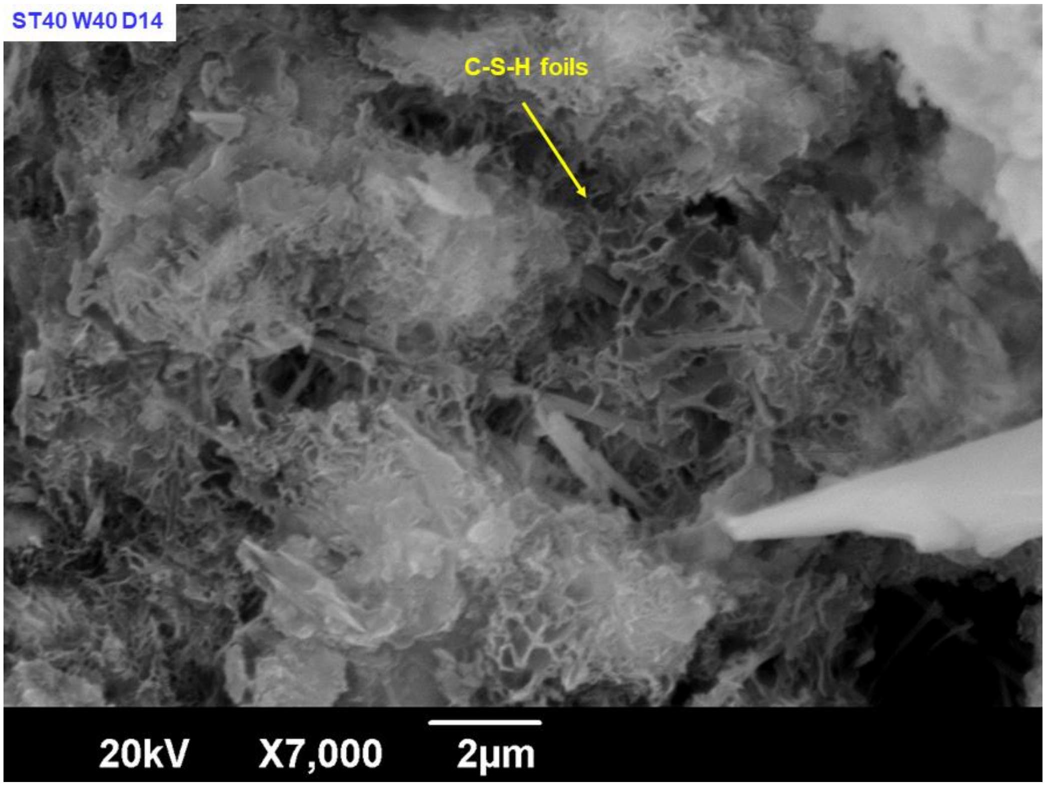
ST40 W40 D14
C-S-H foils
20kV X7,000 2µm

(f)

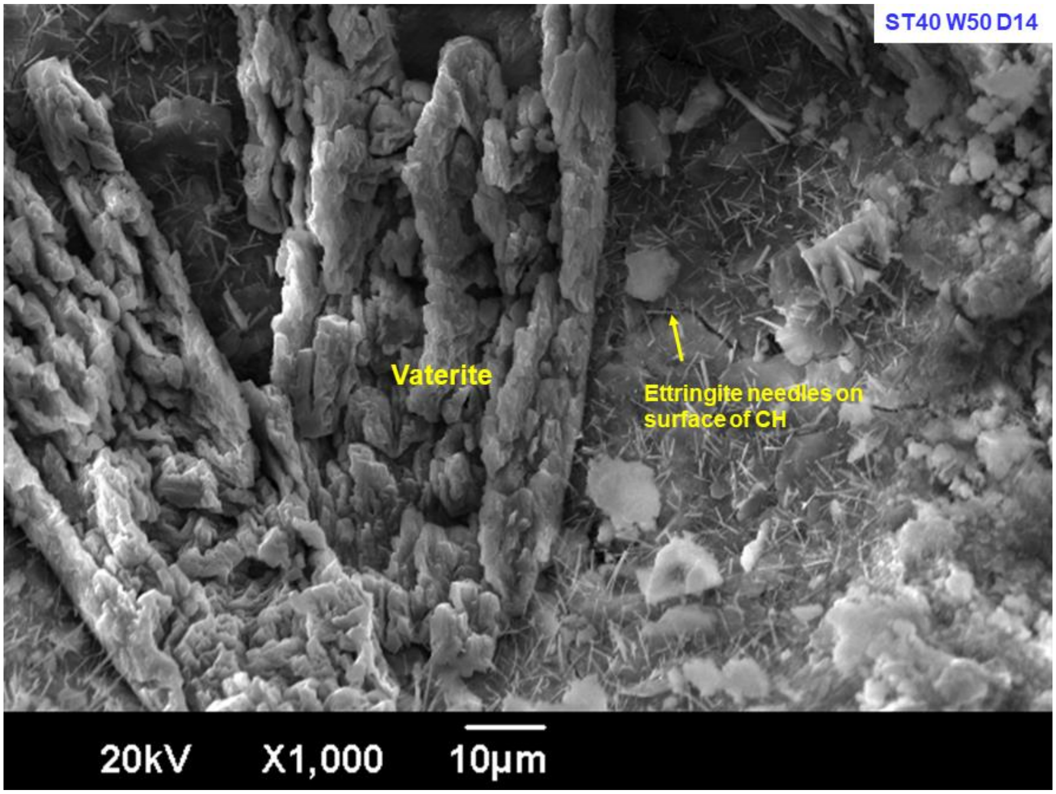

(g)

Fig. 5.19: SEM images of microstructure of cementitious pastes containing 0%, 10%, 20% and 40% STCT750 after 14 days of curing (a) w/c ratio 0.3, (b) w/c ratio 0.4, (c) w/c ratio 0.5 (d) ST40W40D14 showing phases of ettringite portlandite and C-S-H embedded together. (e) ST40D14 showing phases of phases of ettringite portlandite and C-S-H (f) ST40W40D14 with crumbled CSH foils and embedded ettringite needles (g) ST40W50D14 showing flaky vaterite formations

The microstructure of ST and OPC paste samples at the age of 28 days is given in Fig. 5.20. (a) to (e). The samples appeared more compact. The portlandite formed in samples with ST40 at w/c ratios appear to have been precipitated with ettringite, C-S-H and calcium carbonate as shown in Fig. 5.20 (b) and (c). The voids in ST samples were filled with C-S-H, ettringite and calcium carbonate in vaterite form as seen in Fig. Fig. 5.20 (e).

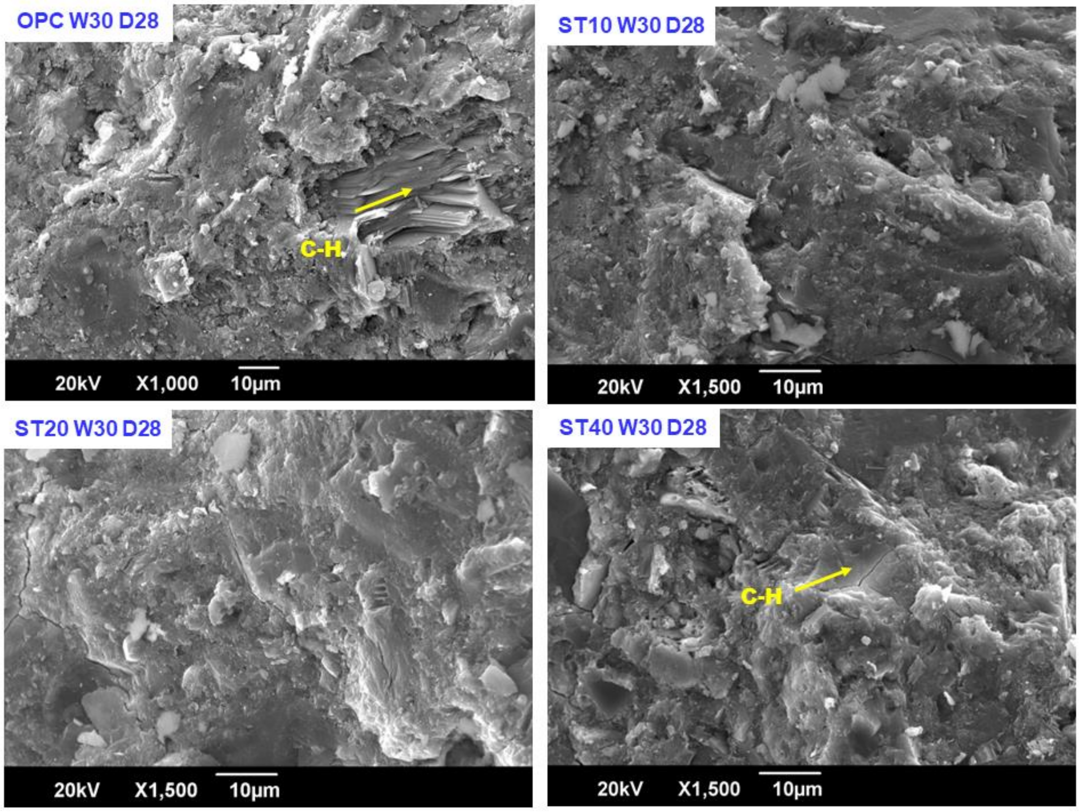
OPC W30 D28
C-H
20kV X1,000 10µm
ST10 W30 D28
20kV X1,500 10µm
ST20 W30 D28
20kV X1,500 10µm
ST40 W30 D28
C-H
20kV X1,500 10µm

(a)

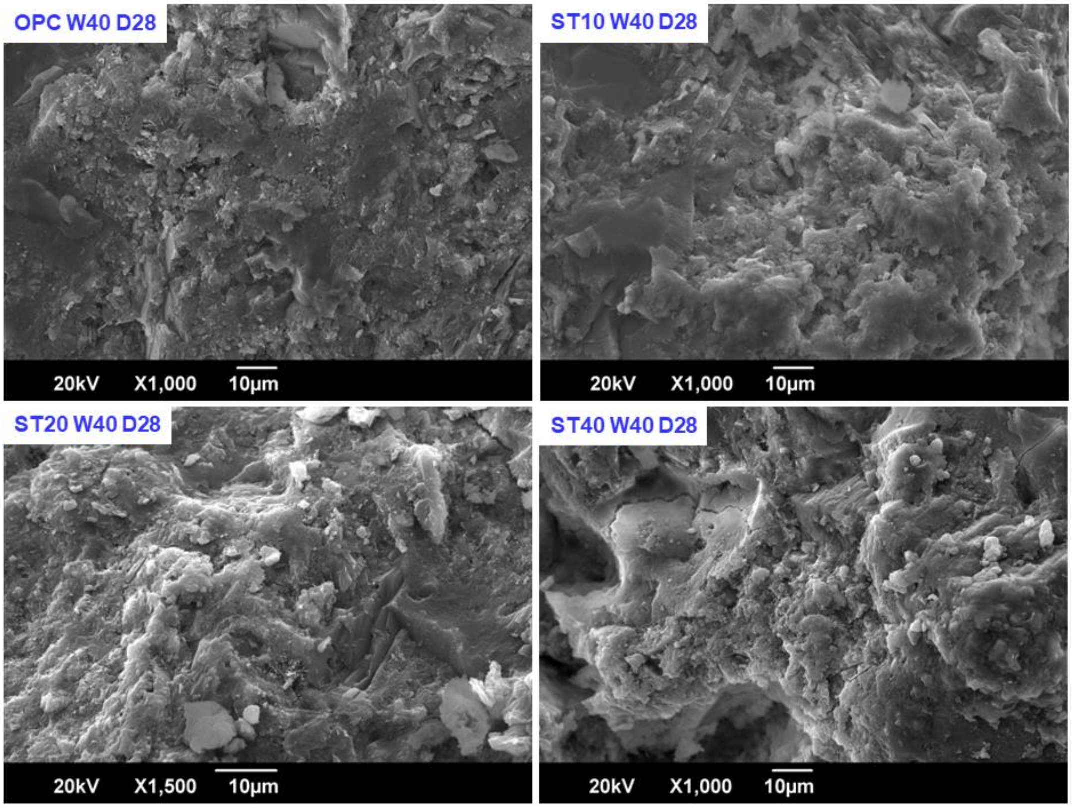
OPC W40 D28
20kV X1,000 10µm
ST10 W40 D28
20kV X1,000 10µm
ST20 W40 D28
20kV X1,500 10µm
ST40 W40 D28
20kV X1,000 10µm

(b)

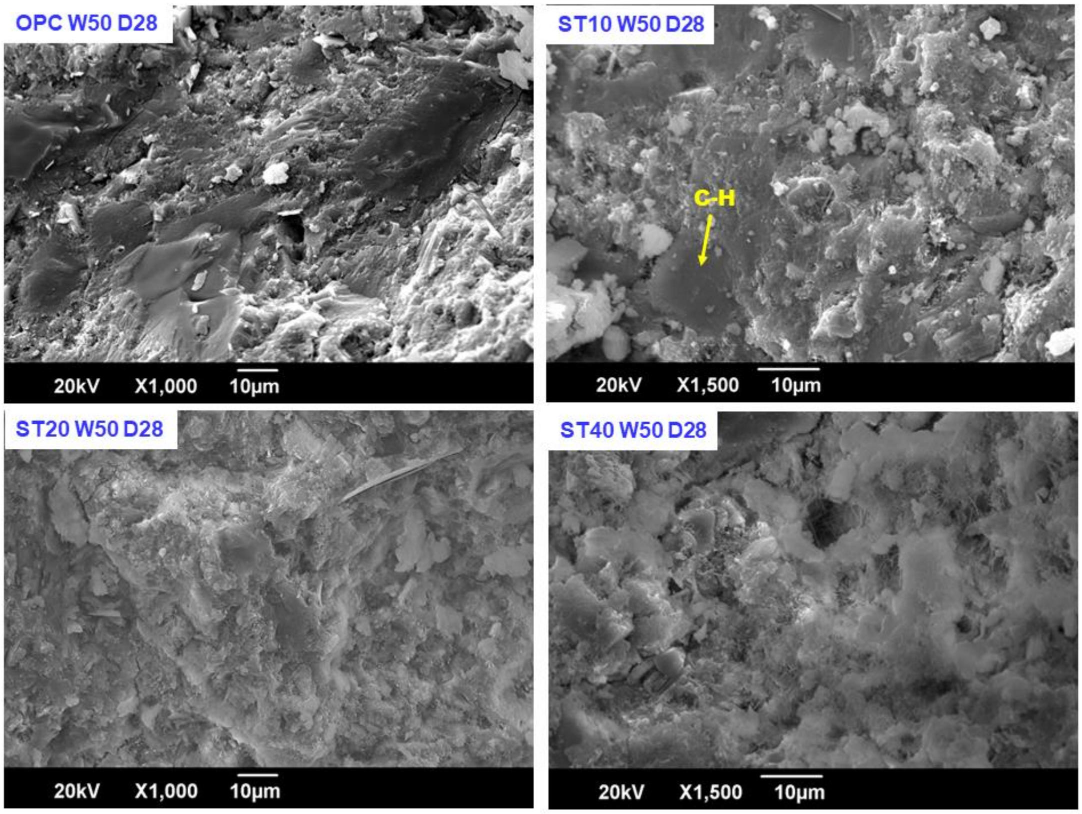
OPC W50 D28
20kV X1,000 10µm
ST10 W50 D28
C-H
20kV X1,500 10µm
ST20 W50 D28
20kV X1,000 10µm
ST40 W50 D28
20kV X1,500 10µm

(c)

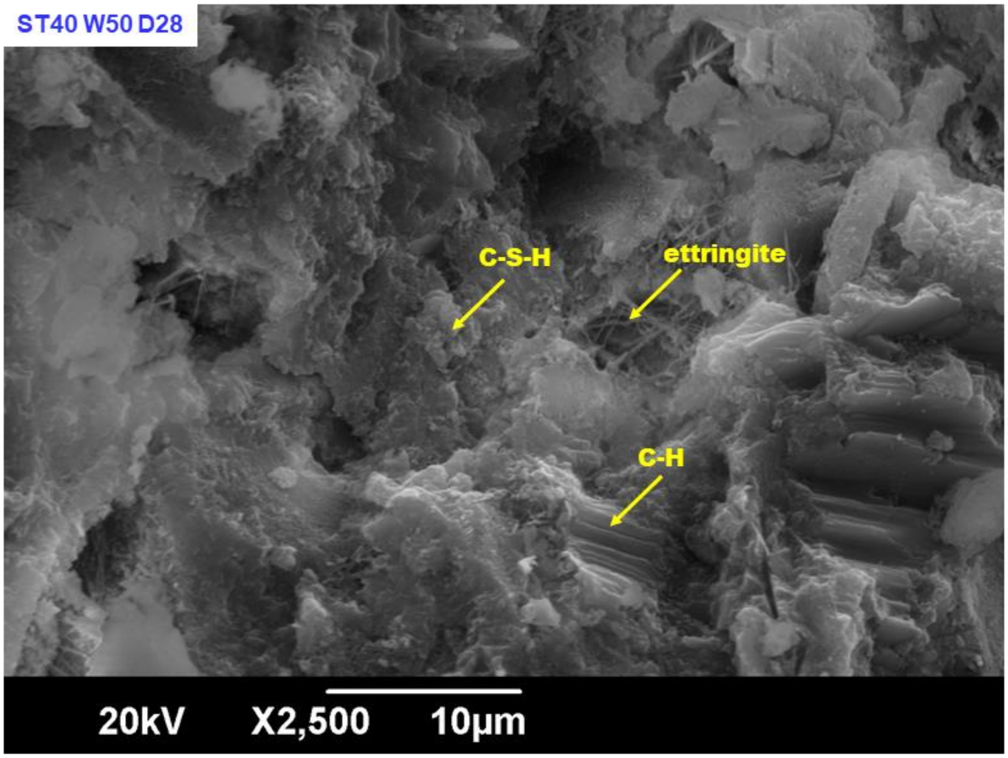
ST40 W50 D28
C-S-H
ettringite
C-H
20kV X2,500 10µm

(d)

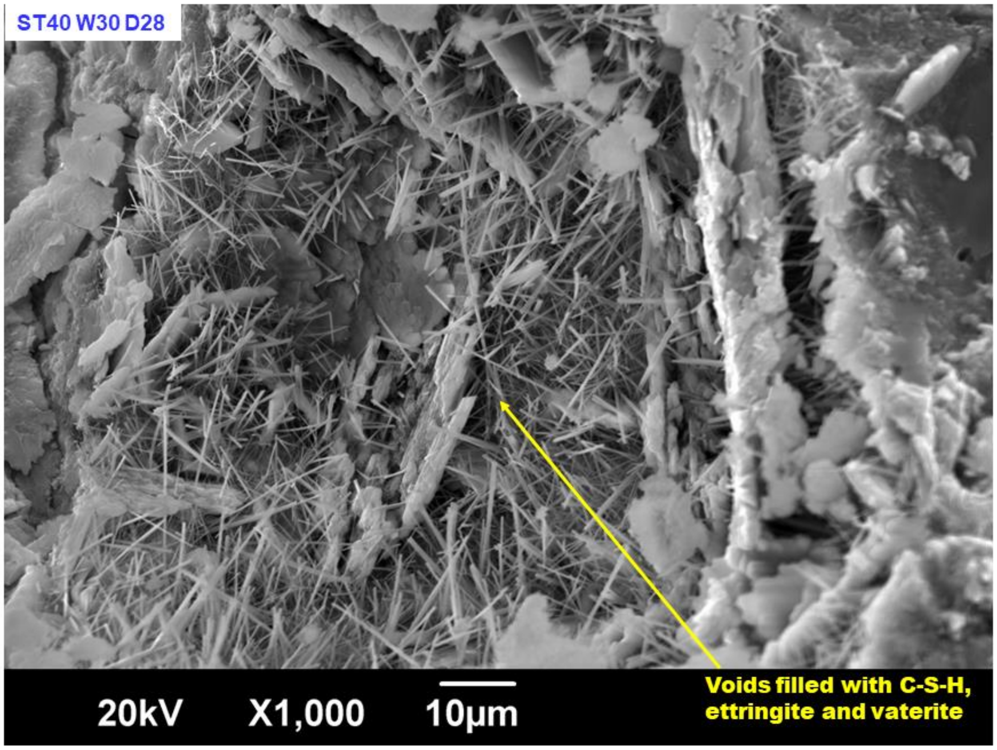

(e)

Fig. 5.20: SEM images of microstructure of cementitious pastes containing 0%, 10%, 20% and 40% STCT750 after 28 days of curing (a) w/c ratio 0.3, (b) w/c ratio 0.4, (c) w/c ratio 0.5, (d) C-S-H, ettringite and portlandite as observed in ST40W50D28 (e) A void filled with hydration products in ST40W30D28 sample.

The microstructure of ST and OPC samples studied at 56 days are reported in Figs. 5.21 (a) to (d). The ST samples appeared have denser and more compact portlandite and flaky shaped C-S-H. In Fig. 5.21 (d) nucleation of portlandite is observed in samples with 40% ST and this phenomenon is similar to that of MT.

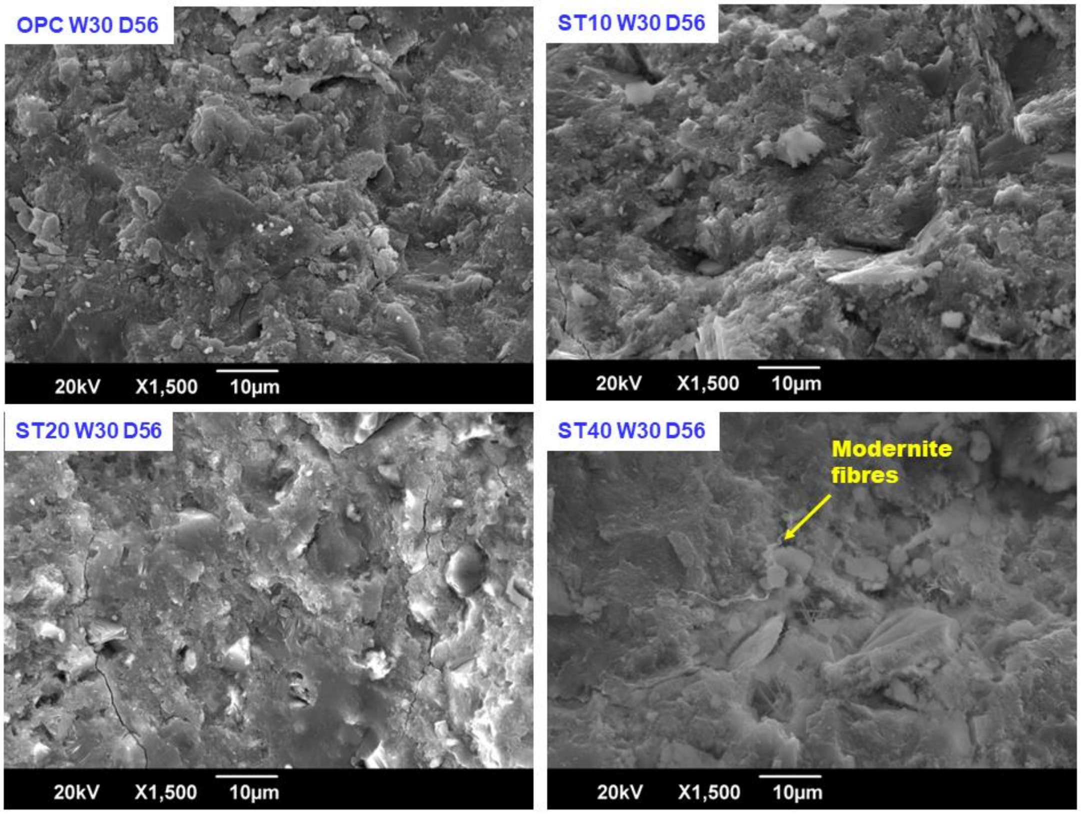
OPC W30 D56
20kV X1,500 10µm
ST10 W30 D56
20kV X1,500 10µm
ST20 W30 D56
20kV X1,500 10µm
ST40 W30 D56
Modernite fibres
20kV X1,500 10µm

(a)

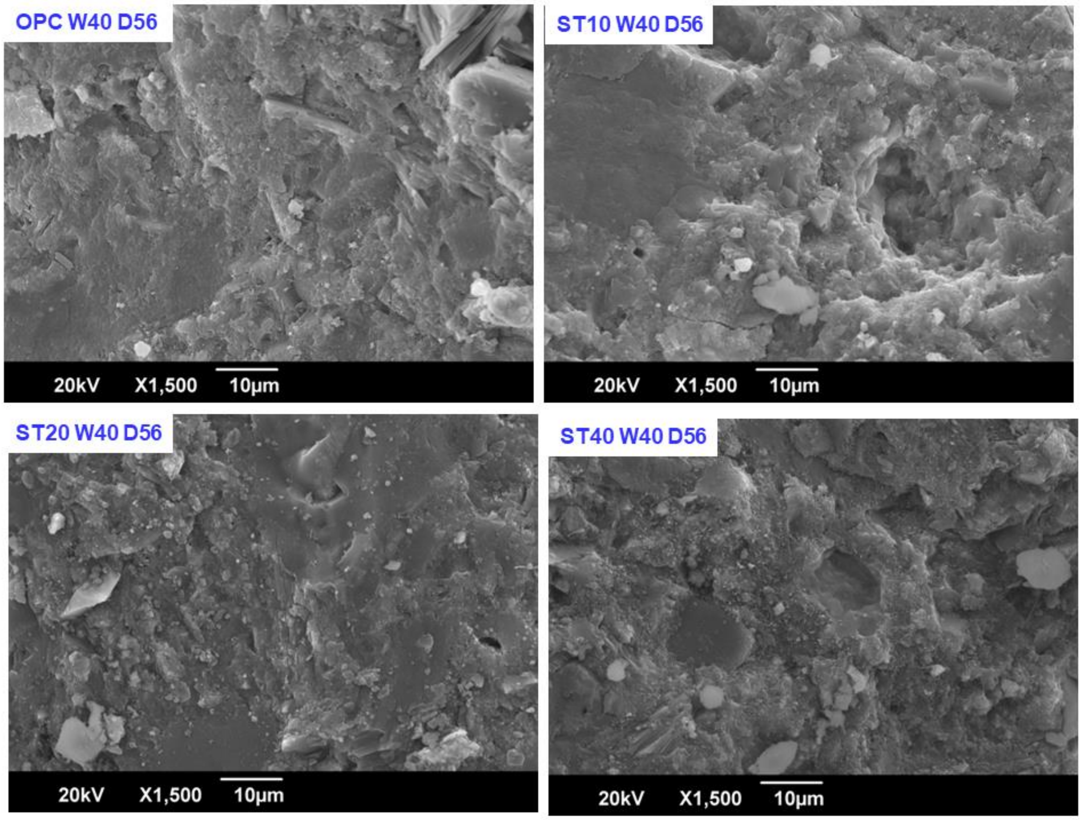
OPC W40 D56
20kV X1,500 10µm
ST10 W40 D56
20kV X1,500 10µm
ST20 W40 D56
20kV X1,500 10µm
ST40 W40 D56
20kV X1,500 10µm

(b)

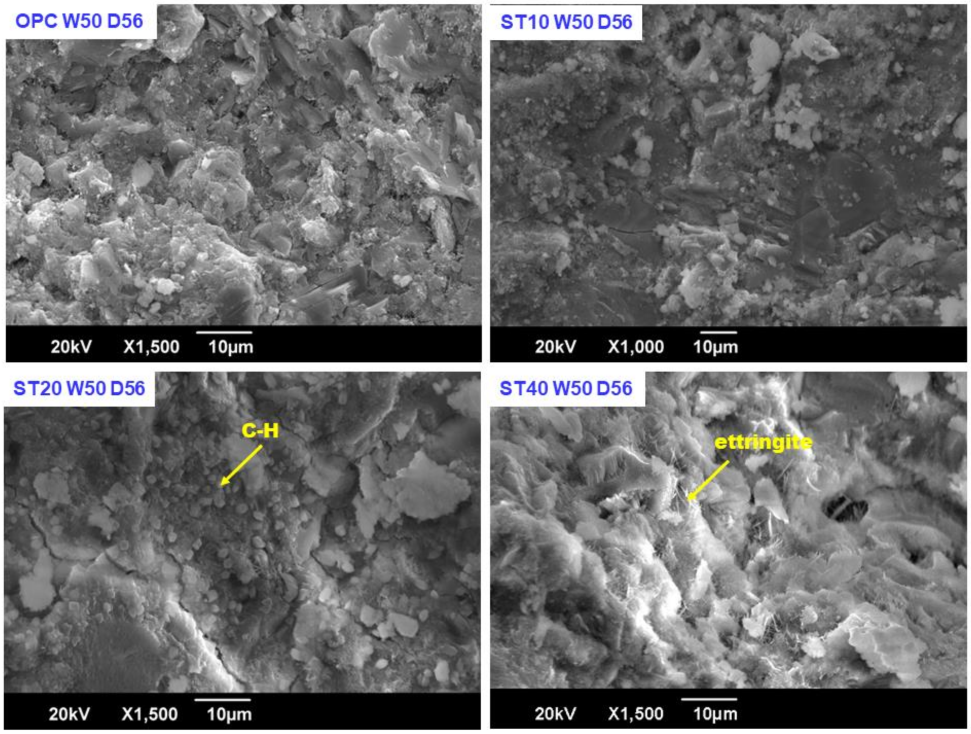

(c)

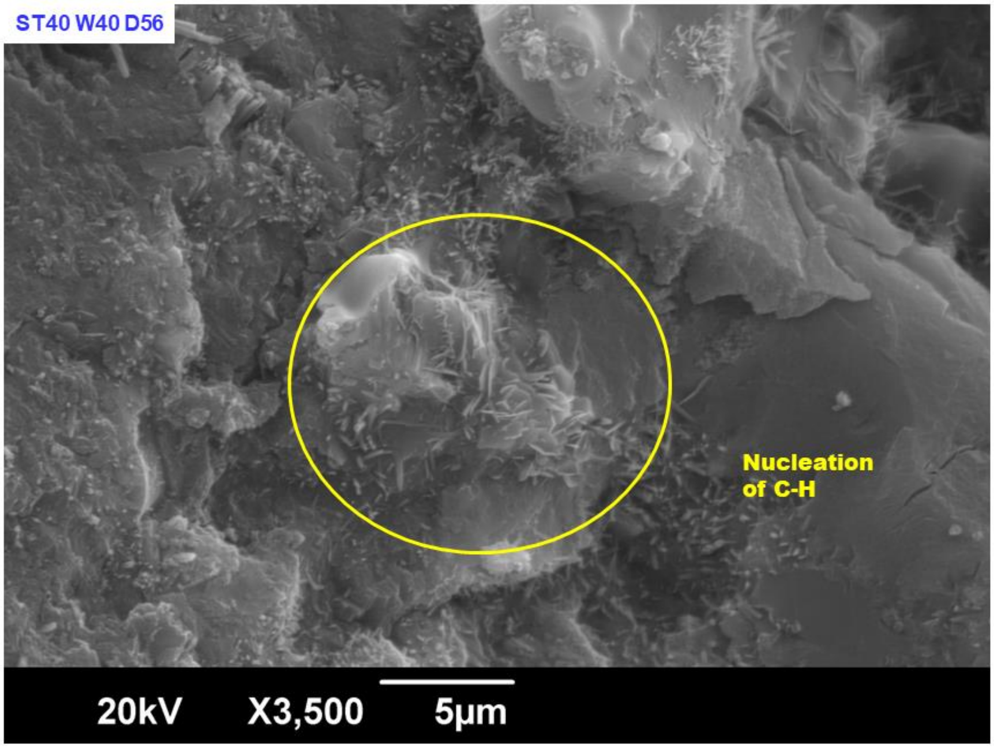

(d)

Fig. 5.21: SEM images of microstructure of cementitious pastes containing 0%, 10%, 20% and 40% STCT750 after 56 days of curing (a) w/c ratio 0.3, (b) w/c ratio 0.4, (c) w/c ratio 0.5 (d) Nucleation in portlandite of STW40D56 samples.

At 90 days the samples exhibited dense microstructure and compact portlandite formations as seen Fig. 22 (a) to (d). It is also observed that the matrix had more of flaky C-S-H than foil like C-S-H. The unhydrated STCT750 particles in Fig. 5.22 (d) appeared to be covered in hydration products and more intact than the one observed in Fig. 5.21 (e), indicating a later age reaction.

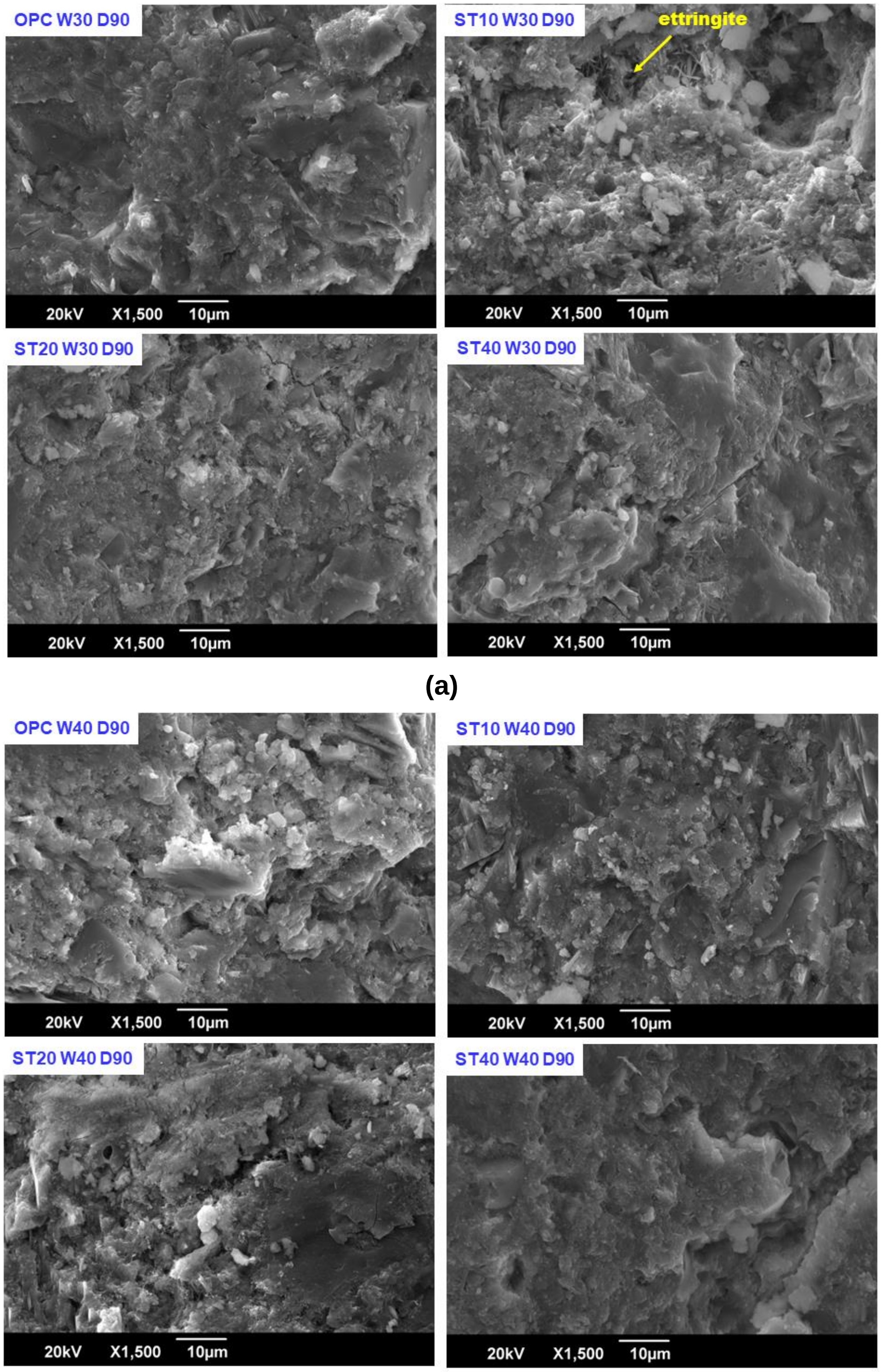

(a)

(b)

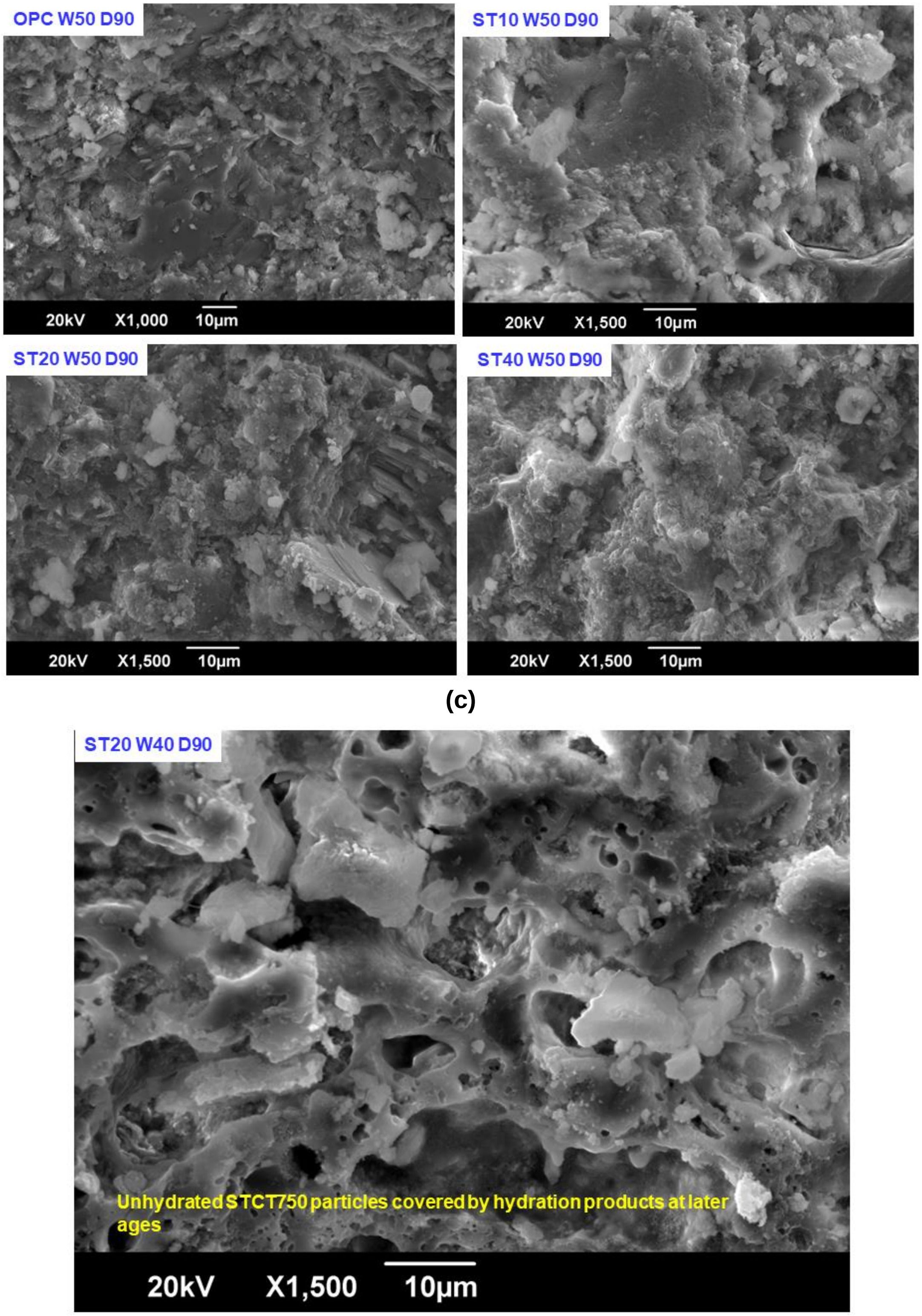

(c)

Unhydrated STCT750 particles covered by hydration products at later ages

(d)

Fig. 5.22: SEM images of microstructure of cementitious pastes containing 0%, 10%, 20% and 40% STCT750 after 90 days of curing (a) w/c ratio 0.3, (b) w/c ratio 0.4, (c) w/c ratio 0.5, (d) ST20W40D90 showing unhydrated STCT750 covered in hydration products.

5.6 FTIR analysis

The FTIR analysis of hydrated cementitious pastes containing varying percentages (10%, 20%, and 40%) of MTCT850 and STCT750, with w/c ratios of 0.3, 0.4, and 0.5 at the ages 7, 14, 28, 56 and 90 days are discussed in this section. The absorption or transmittance of the IR radiation passed through a sample gives a molecular fingerprint of the functional groups present in the sample. In this case, alterations of the molecular fingerprint indicate the changes happening to the existing mineral phases or formation of new mineral phases during hydration. The band assignments in the present study have been based on the findings of the analysis XRD and literature specific to cement paste with mineral admixture as supplementary cementitious material as given in Table. 5.4.

Table 5.4: The list of functional groups identified in the OPC, MT and ST cementitious pastes and the corresponding wavenumber

Wavenumber (cm^{-1})	**Assignment**	**Reference**
667 - 795	Si-O-Si bending and stretching	[283]
705 - 710	Al-O stretching	[283]
712 - 727	Asymmetric stretching vibrations of C- O	[284]
778, 796	Si-O stretching	[252]
800 - 1200	Asymmetric stretching of Si-O-Si, Al-O matrix	[252,283,284]
1420 - 1490	C-O bonds	[283–285]
1600 – 1700 1620, 1680	Bending vibrations of H-O-H bonds Gypsum	[283,284]
1900 - 2350	O-H bonds	[235]
3500 – 3700 3640	O-H stretching vibrations in water molecules Portlandite	[235,283–288]
421, 667, 1190	S-O functional groups	[289]

The IR spectra of the cementitious pastes with OPC, MTCT850 and STCT750 at different ages are given in Figs. 5.23 to 5.32. It can be seen that the peaks were observed around the wavenumbers 670 cm^{-1}, 810 cm^{-1}, 890 cm^{-1}, 966 cm^{-1}, 1025 cm^{-1}, 1430 cm^{-1}, 1650 cm^{-1}, 1900-2350 cm^{-1}, 3300-3700 cm^{-1}. These peaks were present in all the samples through all the ages with minor shifts (±50 cm^{-1}) in their location. These regions of interest are marked on the figures with these wavenumbers for ease of comparison and actual shifted wave numbers are detailed in the discussion section.

Fig. 5.23 (a) to (d) show the IR spectral patterns for the samples at the MT and OPC 7 days. Considering the Fig. 5.23 (a), all the samples have a minor peak at around 670 cm^{-1}, including

OPC. This peak corresponds to the S-O bond corresponding to the ettringite formation in the paste samples. There is an absorbance peak in the range of 810 cm^{-1} for MT40, 795 cm^{-1} for MT10 and MT20, for OPC this peak is at 780 cm^{-1}. This region corresponds to Si-O bonds typically in tetrahedral bonds and generally corresponds to quartz mineral. This explains the higher intensity of these peaks for MT samples than OPC sample (which was 30-37.5% of the MT peaks). In case of OPC this peak corresponds to the formation of C-S-H and the existing alite and belite phases undergoing hydration. The next major peak present at 966 cm^{-1} is also integrated with peaks at 890 cm^{-1} and 1025 cm^{-1}. In case of OPC this peak occurs at 955 cm^{-1} whereas the same is at 975 cm^{-1} for MT40, 950 cm^{-1} for MT20 and 943 cm^{-1} for MT10., also when compared to MT40, the intensities were 60 and 65% for MT10 and MT20, and it was 17% for OPC. Similarly, the peak at 861 cm^{-1} for OPC was at 859 cm^{-1}, 878 cm^{-1}, 873 cm^{-1} for MT10, MT20 and MT40, respectively. These peaks correspond to stretching and bending of Si-O-Si and Al-O bonds [252,283,284]. These, peaks at 810 cm^{-1}, 966 cm^{-1} and 1025 cm^{-1} for OPC and corresponding slightly shifted for MT mixes are the characteristic of C-S-H bands, where the peaks represent Q^1, Q^2 and Q^{3and4} formation of Si-O bonds. The slight shift in these peaks in MT mixes is attributed to the lengthening of silica chains in C-S-H. The presence of excess silica leads to dilution of Ca^{2+} ions and leads to higher degree of polymerization of C-S-H chains. This in FTIR appears as a shift in the peaks towards a higher wave number due to lower contribution of Q^1 species in C-S-H formation [287]. During hydration the bonds in alite, belite, ferrite and aluminate stretch, bend, and modify to form C-S-H, ettringite and other compounds.

All the observed changes in this region of spectra of OPC correspond to these changes. In case of MT along with these changes the phases of MTCT850 which remained unhydrated such as quartz, biotite and orthoclase also contain Si-O and Al-O bonds. The higher intensity of peaks of MT samples can also be attributed to the presence of these phases. The peak at 1430 cm^{-1} for MT samples and 1411 cm^{-1} for OPC samples correspond to C-O bonds, indicating presence of carbonate compounds, calcium carbonate in this case, which is also confirmed by XRD. The peaks at 1650 cm^{-1} are present only in the MT samples. These peaks correspond to bending vibration of H-O-H in water molecules, indicating the peaks correspond to the changes in the water adsorbed in the zeolitic C-A-S phases. The band corresponding to wavenumber 1900 – 2350 cm^{-1} correspond to O-H bonds a closer view of which is given in Fig. 2.3 (d).. The band corresponding to wavenumber correspond 3300-3700 cm^{-1} to O-H stretching vibrations in water molecules. The sharp peak at around 3640 cm^{-1} correspond to portlandite and the peaks at 1620 cm^{-1}, 1680 cm^{-1}, 3526 cm^{-1} and 3402 cm^{-1} correspond to gypsum [254] This region also indicates changes in the O-H species in other phases which shows the changes during C-S-H formation hydration. Similar observations were made in Fig. 5.23 (b) and (c).

The IR spectrum of OPC and MT samples observed at 14 days is given in Fig. 5.24 (a) to (d). The peak locations in the spectra were similar to that of 7 days. However, the peaks at 670 cm^{-1} corresponding to S-O bonds and absorbance peak at 810 cm^{-1} corresponding to Si-O tetrahedral bonds intensifies for MT samples indicating structural changes in the bonds. This implies the changes in ettringite phases and the phases containing SiO_4 groups such as quartz and belite. At 14 days the OPC mixes exhibited formation of peaks at 1650 cm^{-1} corresponding to water molecules and a shoulder formation between 1430 cm^{-1} and 1025 cm^{-1}. The formation of peaks at

1650 cm^{-1} indicates the formation of phases with adsorbed water such as C-S-H and the shoulder formation indicate the stretching of corresponding C-O and Si-O and Al-O phases.

The Figs. 5.25 (a) to (d) show the IR spectrum of MT and OPC samples at 28 days, The OPC samples exhibit intensification of peaks at 670 cm^{-1} and 810 cm^{-}1 due to changes in S-O groups in ettringite and SiO_4 in belite. The MT mixes with all w/c ratios as indicated in Figs. 5.25 (a), (b) and (c) exhibit a shoulder flattening in the region between 1025 cm^{-1} and 1430 cm^{-1} and asymmetric widening of peaks at 1430 cm^{-1}. 1430 cm^{-1} corresponds to calcium carbonate and these changes in the peak indicate modifications in the calcium carbonate phases present in the samples. These changes collectively indicate the changes in belite, ettringite, gypsum and the alumino silicates in MT during hydration and carbonation of the samples with time.

The Fig. 5.26 (a) to (d) show the IR pattern at 56 days and Fig. 5.27 (a) to (d) show the pattern at 90 days. These Figs. show the peaks at band positions similar to that of 7 days with minor shifts and peak widenings/ change in peak shapes with hydration of cementitious materials present in the sample. The alterations in the location and shape of the peaks signify the modifications in the chemical bonds present in the OPC and MT. During the process of hydration, the alite and belite phases are consumed, as evidenced by the XRD data. Additionally, the presence of secondary hydration products, such as crumpled C-S-H as evidenced by microscopy (SEM) images, is also noted. This observation collectively signifies the alterations in both the chemical composition and morphology of the hydration products that are generated as the samples undergo curing and hydration over time.

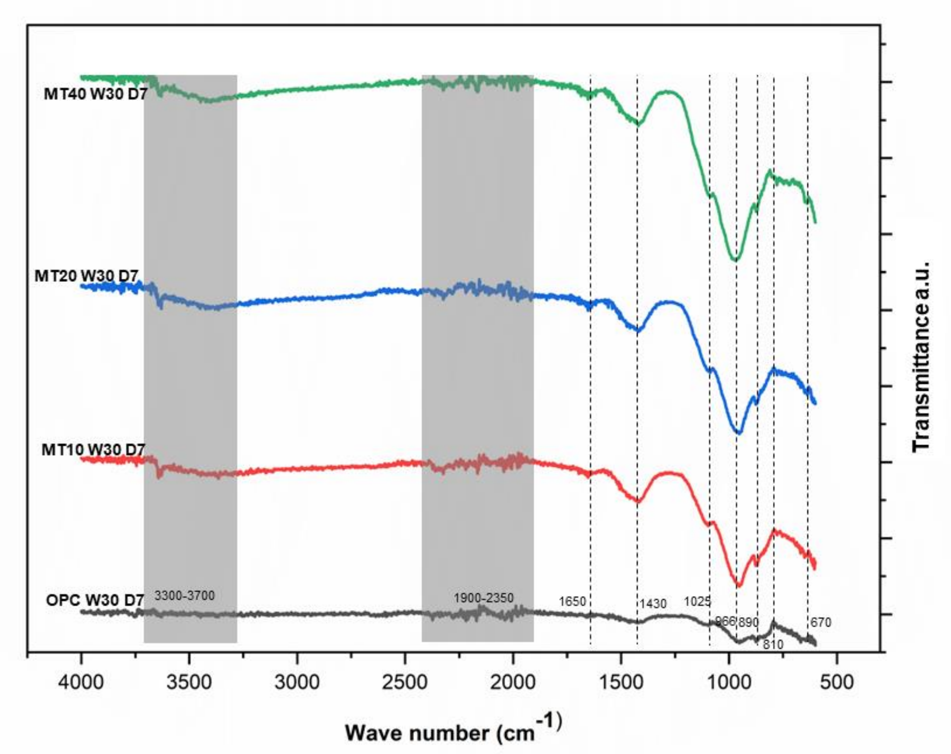

(a)

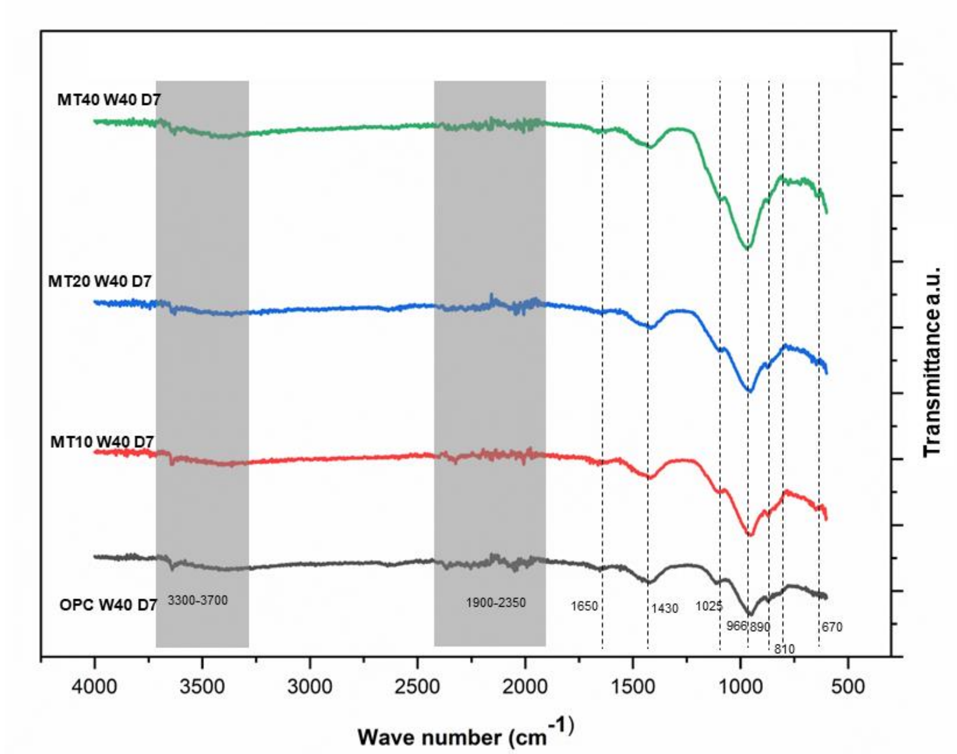
MT40 W40 D7
MT20 W40 D7
MT10 W40 D7
OPC W40 D7
3300-3700
1900-2350
1650
1430
1025
966
890
810
670
4000
3500
3000
2500
2000
1500
1000
500
Wave number (cm^{-1})
Transmittance a.u.

(b)

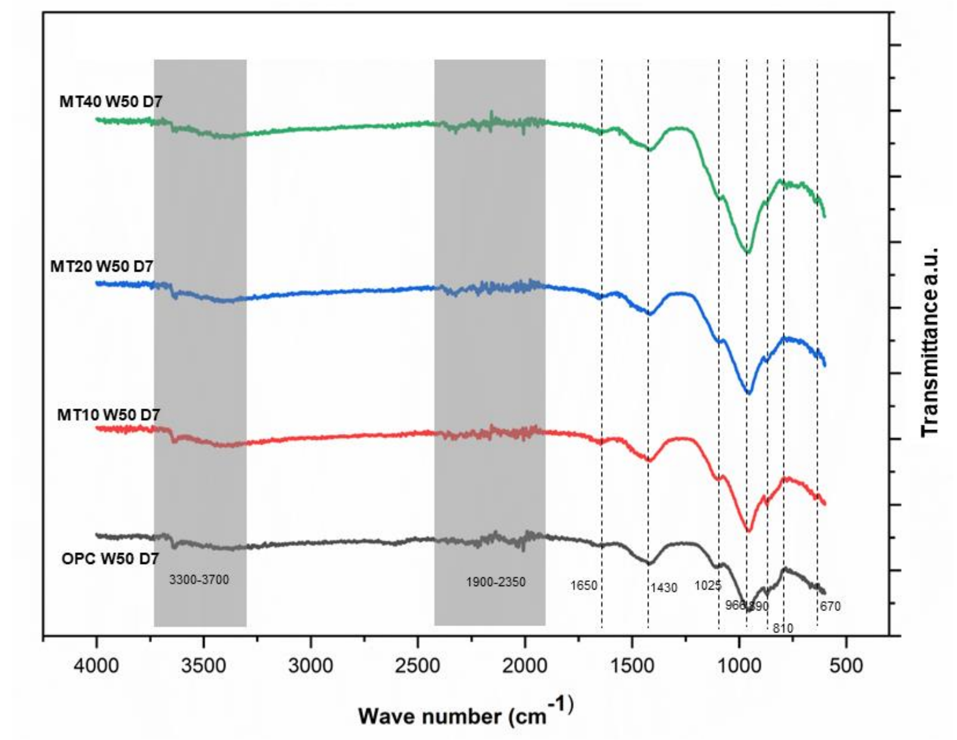
MT40 W50 D7
MT20 W50 D7
MT10 W50 D7
OPC W50 D7
3300-3700
1900-2350
1650
1430
1025
966
890
810
670
4000
3500
3000
2500
2000
1500
1000
500
Wave number (cm^{-1})
Transmittance a.u.

(c)

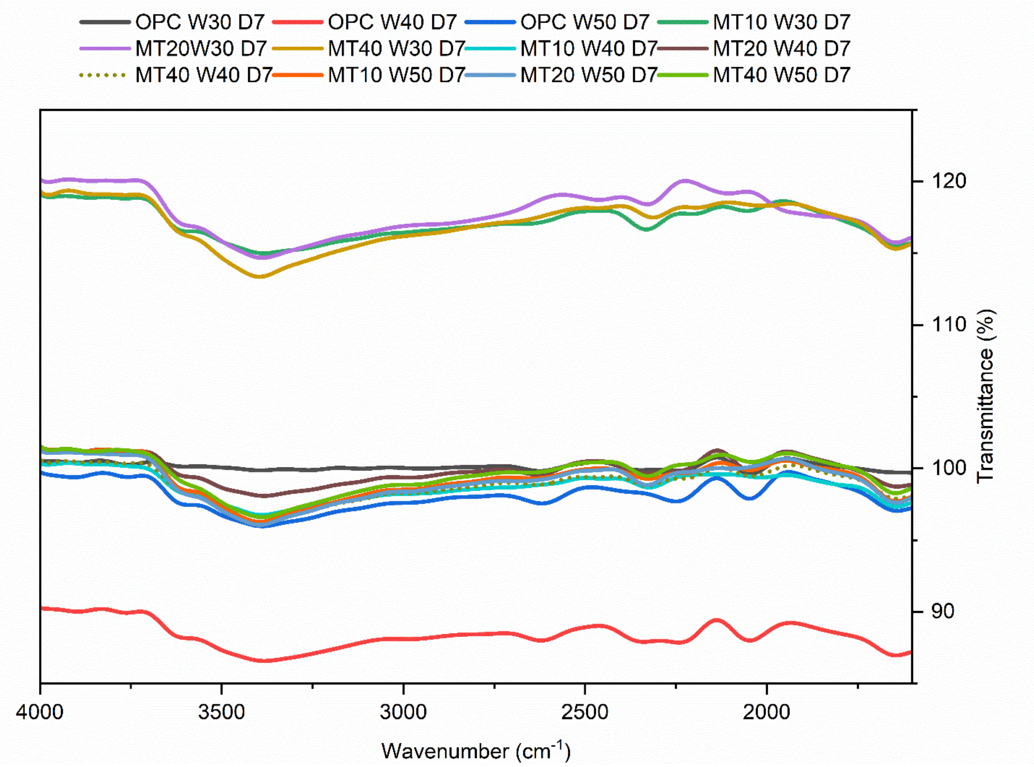

(d)

Fig. 5.23: FTIR spectral patterns of cementitious pastes containing 0%, 10%, 20% and 40% MTCT850 after 7 days of curing. (a) w/c ratio = 0.3, (b) w/c ratio = 0.4, (c) w/c ratio = 0.5, (d) FTIR spectral region corresponding to 1500 cm^{-1} to 4000 cm^{-1}

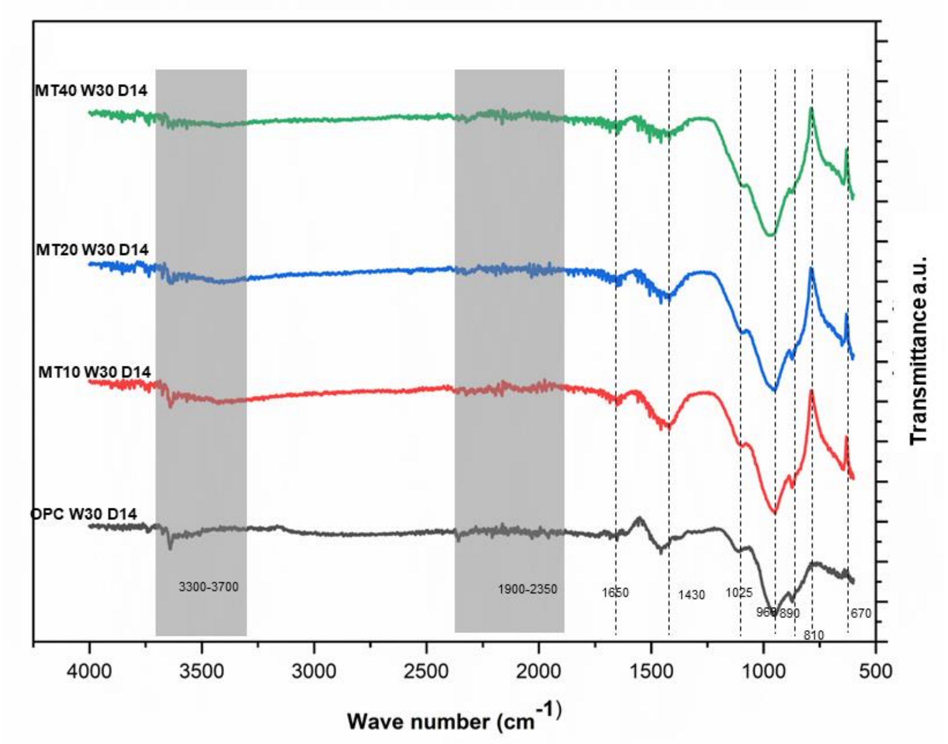

(a)

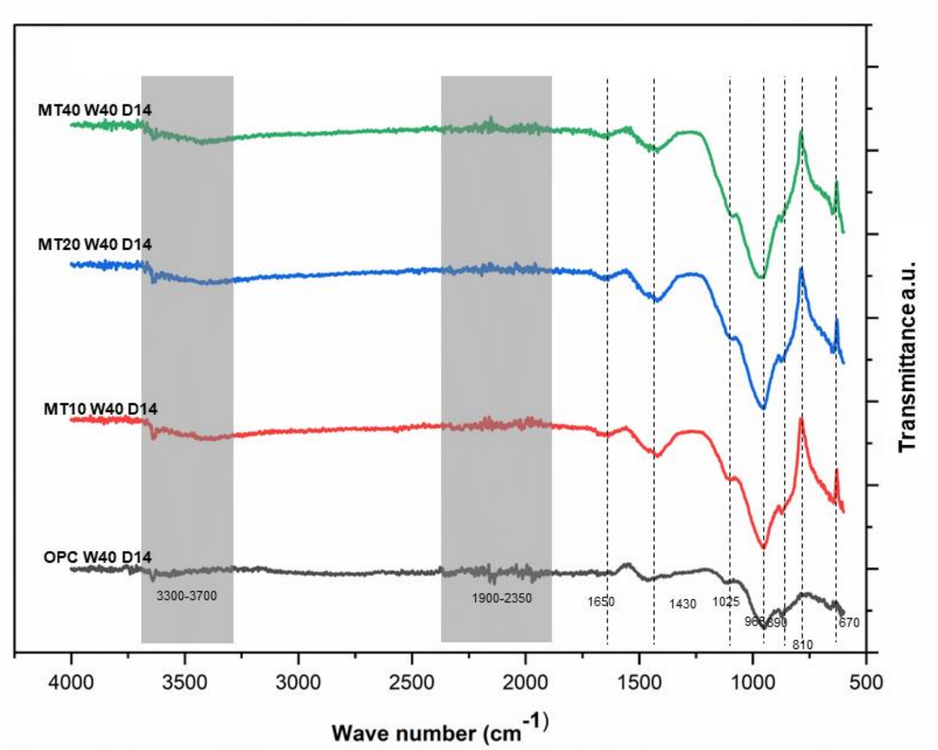

MT40 W40 D14
MT20 W40 D14
MT10 W40 D14
OPC W40 D14
3300-3700
1900-2350
1650
1430
1025
966
890
810
670
4000
3500
3000
2500
2000
1500
1000
500
Wave number (cm^{-1})
Transmittance a.u.

(b)

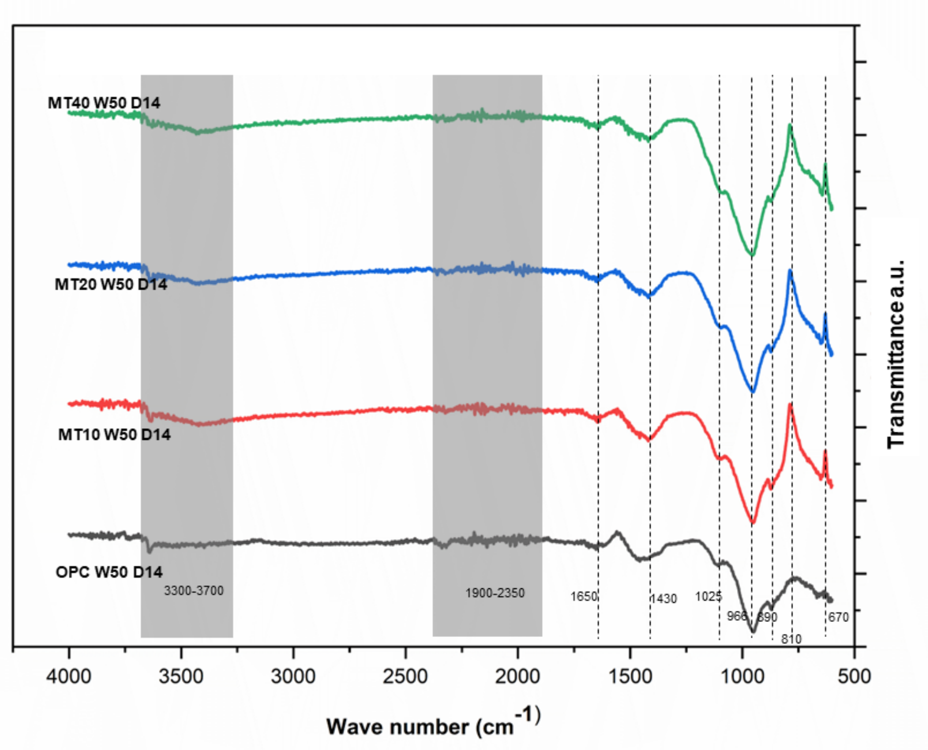

MT40 W50 D14
MT20 W50 D14
MT10 W50 D14
OPC W50 D14
3300-3700
1900-2350
1650
1430
1025
966
890
810
670
4000
3500
3000
2500
2000
1500
1000
500
Wave number (cm^{-1})
Transmittance a.u.

(c)

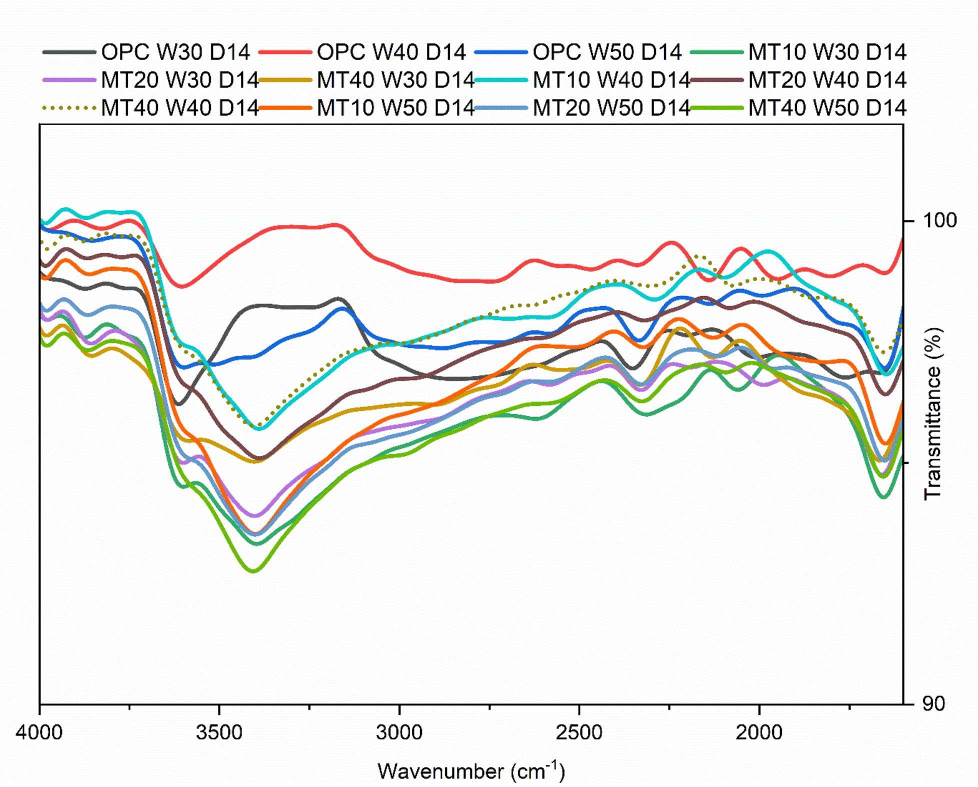

(d)

Fig. 5.24: FTIR spectral patterns of cementitious pastes containing 0%, 10%, 20% and 40% MTCT850 after 14 days of curing. (a) w/c ratio = 0.3, (b) w/c ratio = 0.4, (c) w/c ratio = 0.5, (d) FTIR spectral region corresponding to 1500 cm^{-1} to 4000 cm^{-1}

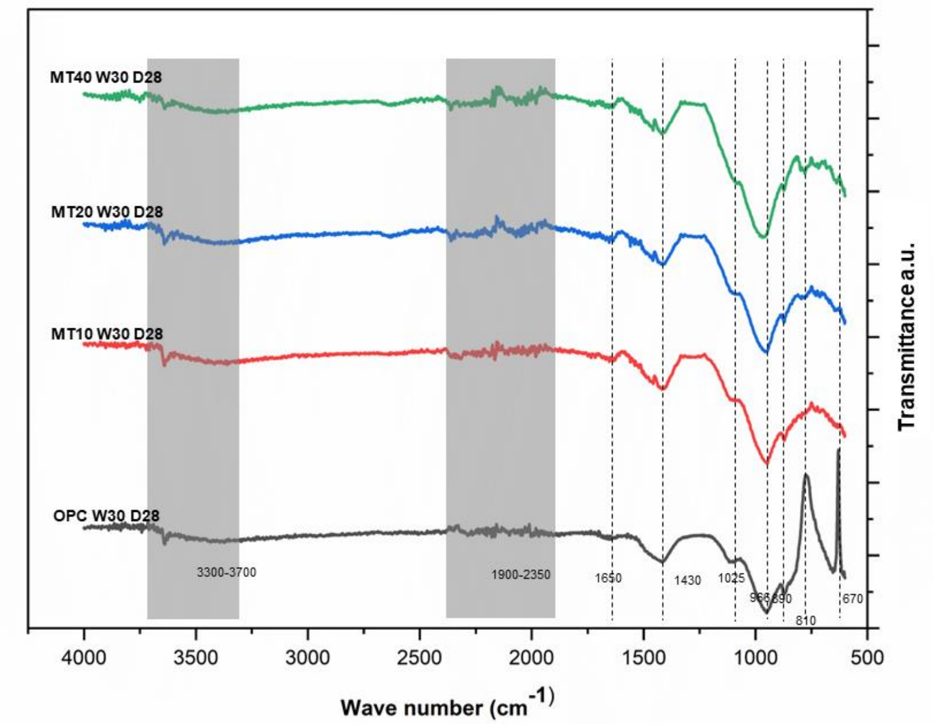

(a)

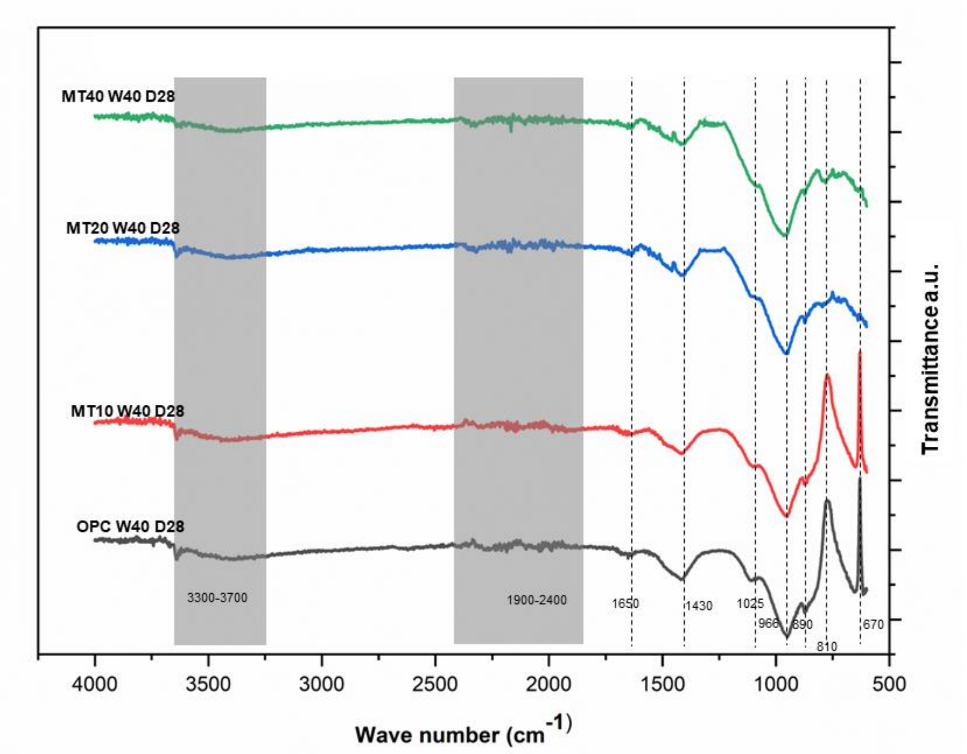
MT40 W40 D28
MT20 W40 D28
MT10 W40 D28
OPC W40 D28
3300-3700
1900-2400
1650
1430
1025
966
890
810
670
Transmittance a.u.
4000
3500
3000
2500
2000
1500
1000
500
Wave number (cm^{-1})

(b)

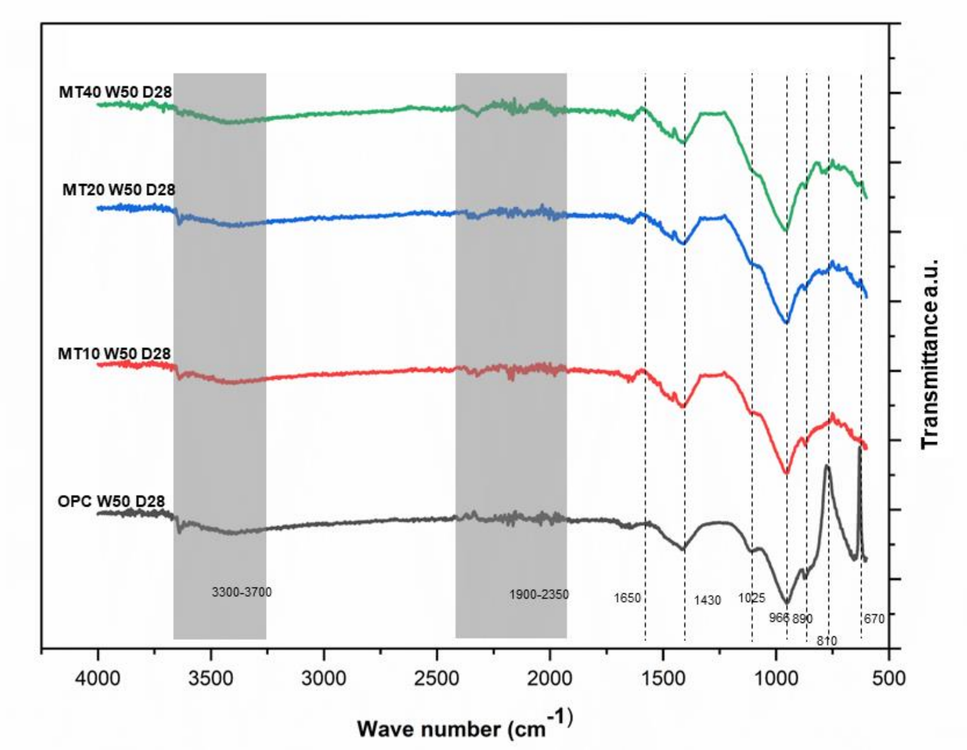
MT40 W50 D28
MT20 W50 D28
MT10 W50 D28
OPC W50 D28
3300-3700
1900-2350
1650
1430
1025
966
890
810
670
Transmittance a.u.
4000
3500
3000
2500
2000
1500
1000
500
Wave number (cm^{-1})

(c)

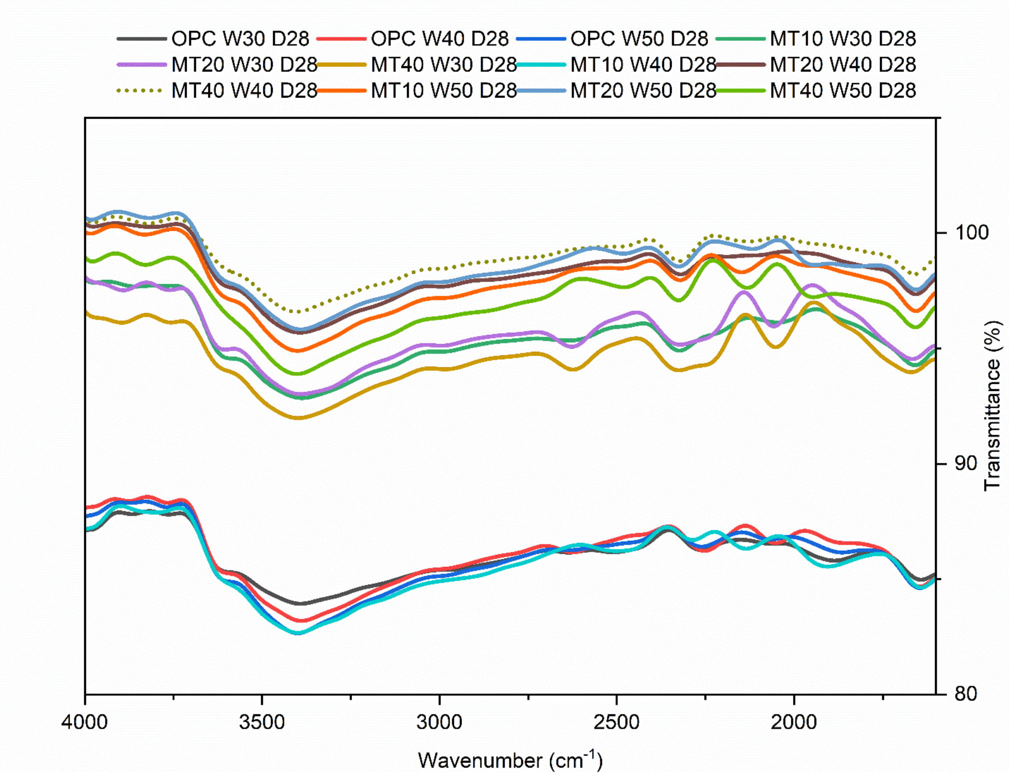

(d)

Fig. 5.25: FTIR spectral patterns of cementitious pastes containing 0%, 10%, 20% and 40% MTCT850 after 28 days of curing. (a) w/c ratio = 0.3, (b) w/c ratio = 0.4, (c) w/c ratio = 0.5, (d) FTIR spectral region corresponding to 1500 cm^{-1} to 4000 cm^{-1}

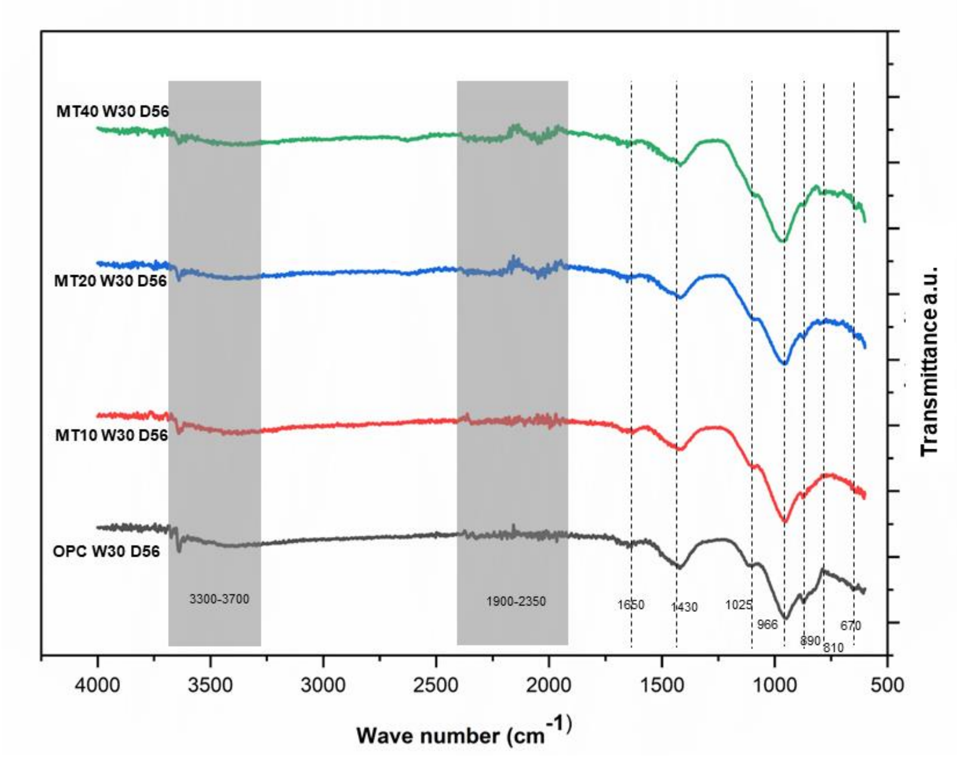

(a)

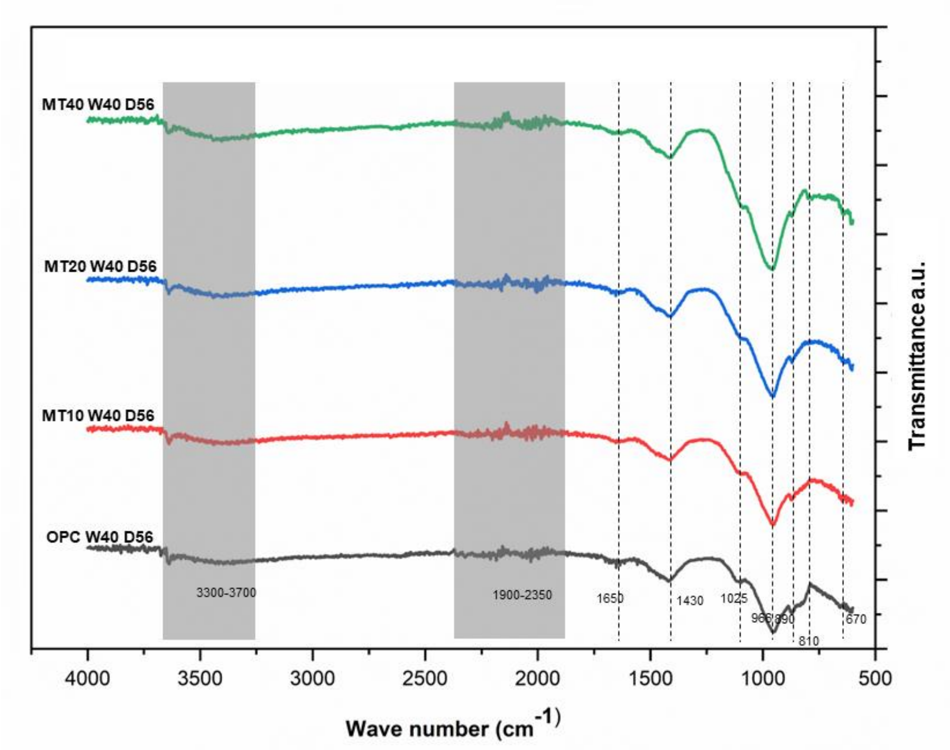
MT40 W40 D56
MT20 W40 D56
MT10 W40 D56
OPC W40 D56
3300-3700
1900-2350
1650
1430
1025
966
890
810
670
Transmittance a.u.
4000
3500
3000
2500
2000
1500
1000
500
Wave number (cm-1)

(b)

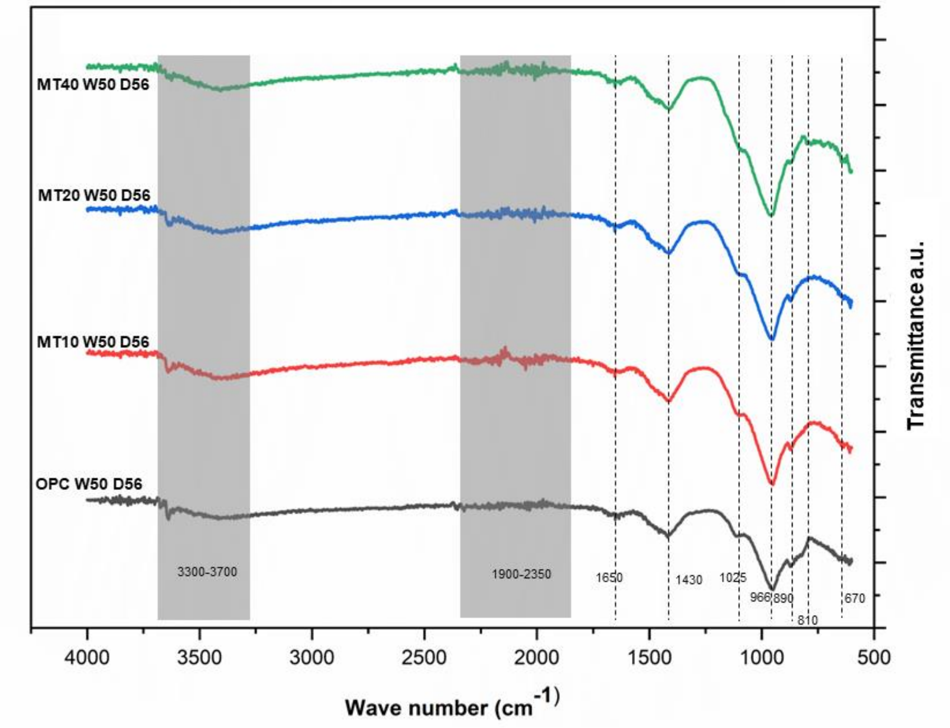
MT40 W50 D56
MT20 W50 D56
MT10 W50 D56
OPC W50 D56
3300-3700
1900-2350
1650
1430
1025
966
890
810
670
Transmittance a.u.
4000
3500
3000
2500
2000
1500
1000
500
Wave number (cm-1)

(c)

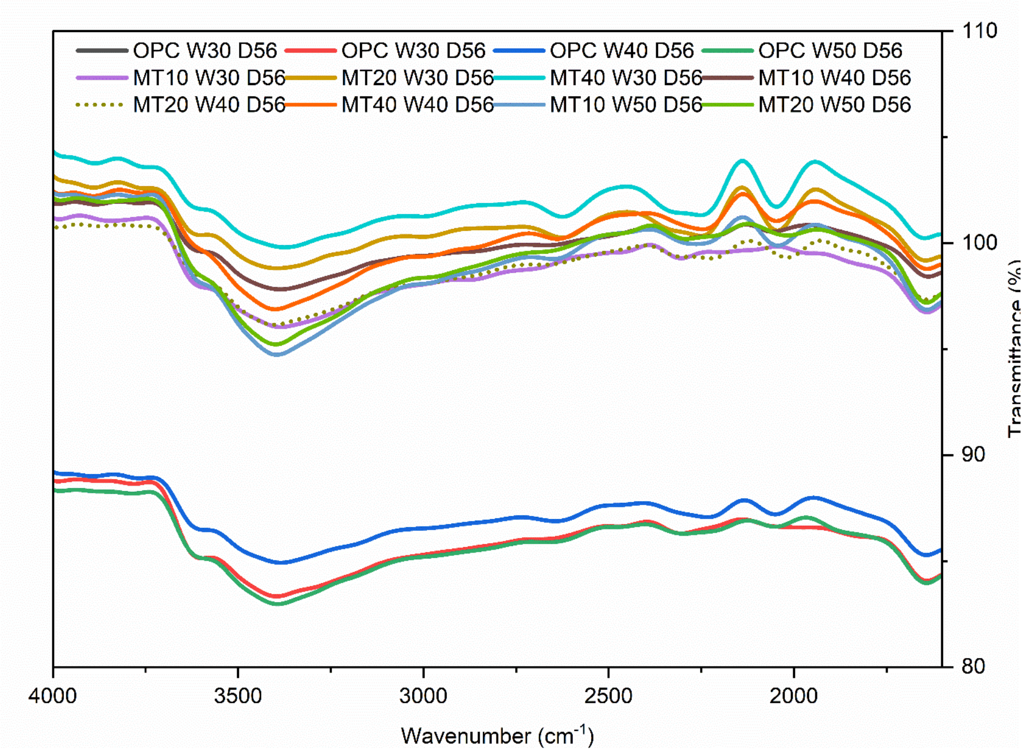

(d)

Fig. 5.26: FTIR spectral patterns of cementitious pastes containing 0%, 10%, 20% and 40% MTCT850 after 56 days of curing. (a) w/c ratio = 0.3, (b) w/c ratio = 0.4, (c) w/c ratio = 0.5, (d) FTIR spectral region corresponding to 1500 cm^{-1} to 4000 cm^{-1}.

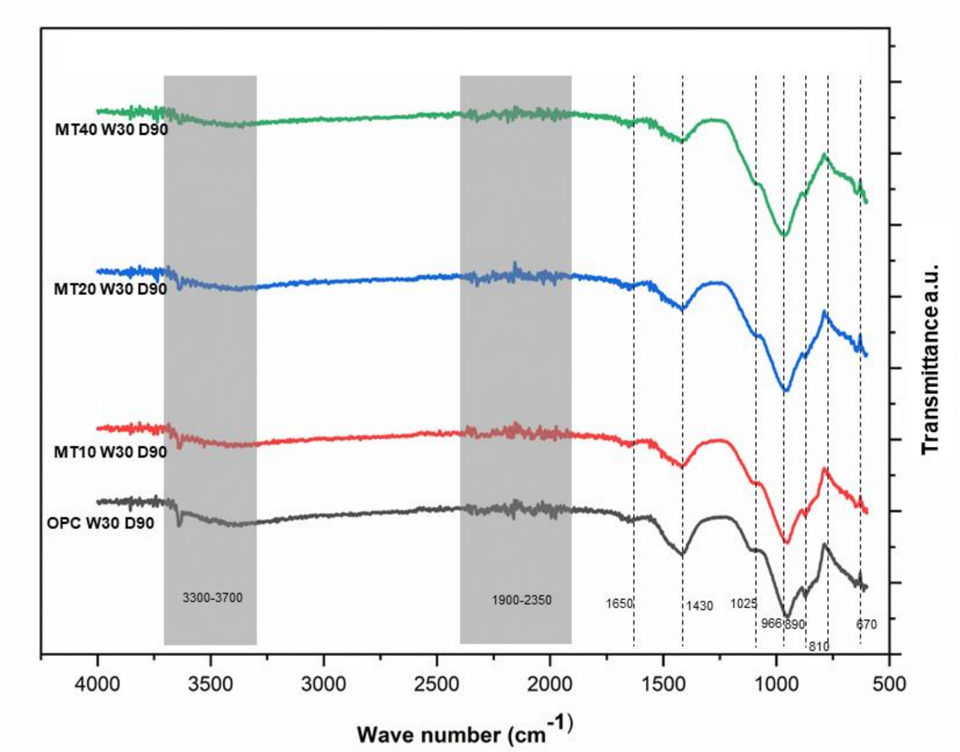

(a)

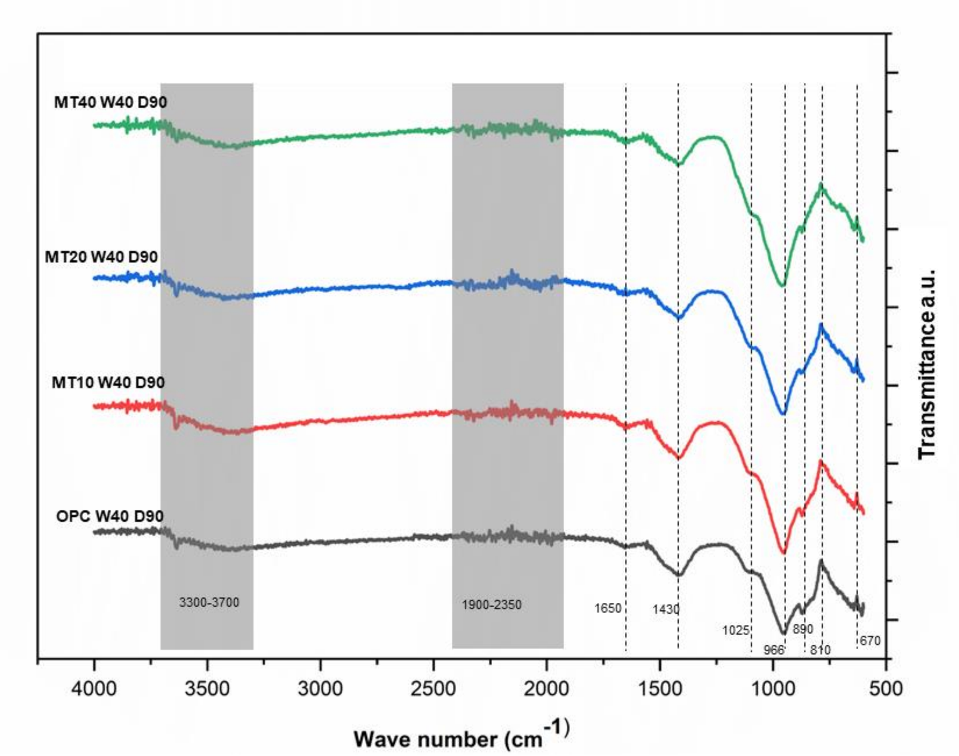
MT40 W40 D90
MT20 W40 D90
MT10 W40 D90
OPC W40 D90
3300-3700
1900-2350
1650
1430
1025
966
890
810
670
4000
3500
3000
2500
2000
1500
1000
500
Wave number (cm^{-1})
Transmittance a.u.

(b)

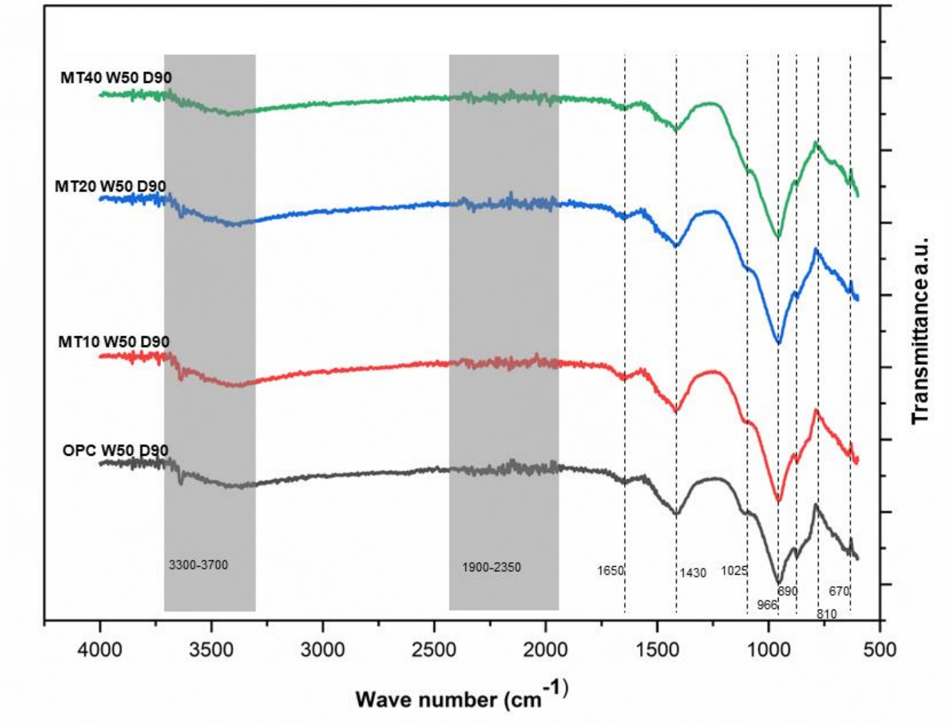
MT40 W50 D90
MT20 W50 D90
MT10 W50 D90
OPC W50 D90
3300-3700
1900-2350
1650
1430
1025
966
890
810
670
4000
3500
3000
2500
2000
1500
1000
500
Wave number (cm^{-1})
Transmittance a.u.

(c)

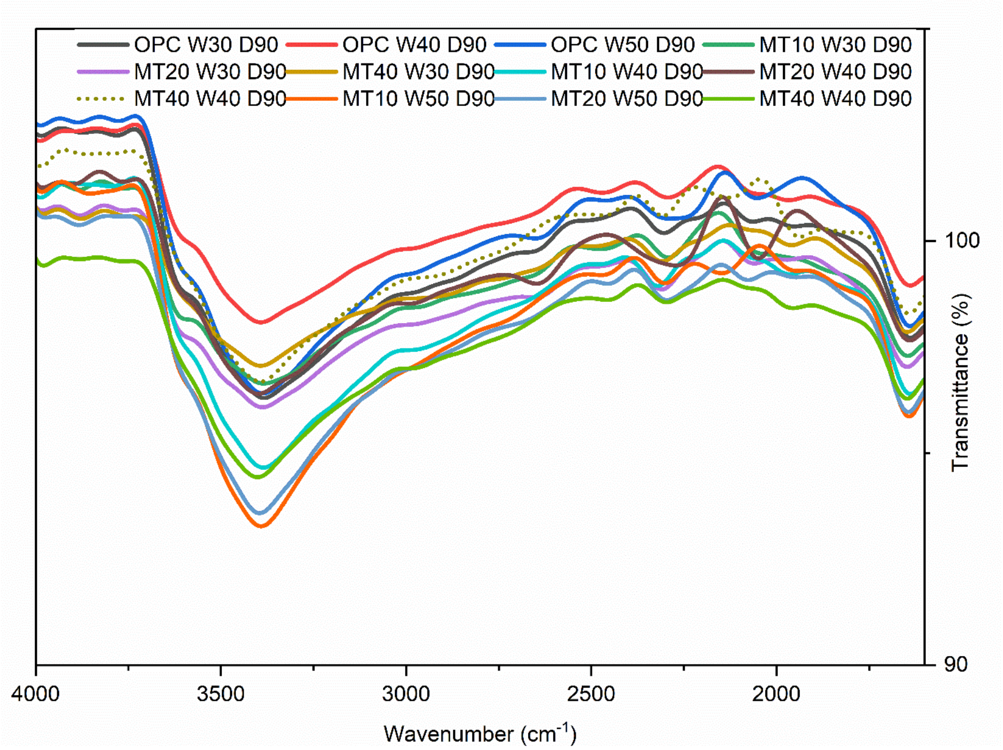

(d)

Fig. 5.27: FTIR spectral patterns of cementitious pastes containing 0%, 10%, 20% and 40% MTCT850 after 90 days of curing. (a) w/c ratio = 0.3, (b) w/c ratio = 0.4, (c) w/c ratio = 0.5, (d) FTIR spectral region corresponding to 1500 cm^{-1} to 4000 cm^{-1}

The spectral patterns of ST and OPC samples at 7 days are given in Fig. 5.28 (a) to (d). In Fig. 5.28 (a) an absorbance peak was observed at 795 cm^{-1} for OPC samples, and the same peak was observed at 788 cm^{-1} for all the ST samples. This region corresponds to Si-O tetrahedral bonds. Based on the XRD observations of the cementitious pastes these correspond to belite and quartz. As the ST samples have both quartz and belite present in them their intensity is higher than that of OPC (which was about 40-50% of ST). The peaks at 861 cm^{-1}, 955 cm^{-1}, and 1105 cm^{-1} are integrated together. In case of ST samples these peaks are found at 874 cm^{-1}, 963 cm^{-1} and 1103 cm^{-1} for all ST10, ST20 and ST40 mixes. The intensity of these peaks for OPC was about 30% the intensity of these peaks for ST. These peaks represent the stretching and bending vibrations of Si-O and Al-O bonds. The formation of hydration products such as C-S-H and ettringite from alite, belite, ferrite and aluminate involve modification in these bonds present in those phases. Also, as indicated by XRD analysis the ST samples have phases such as quartz, feldspar, zeolitic calcium aluminium silicate which also has Si and Al in them. This contributes to higher intensity of these peaks in ST samples. The peaks observed at 810 cm^{-1}, 966 cm^{-1}, and 1025 cm^{-1} for OPC, and the equivalent peaks slightly moved to 874 cm^{-1}, 963 cm^{-1}, and 1103 cm^{-1} for ST mixes, are indicative of the C-S-H bands. These peaks represent the formation of Q^1, Q^2, and, Q^3 andQ^4 species in Si-O bonds. The relatively small displacement of these peaks in ST mixes is related to the changes of silica chains in C-S-H. High silica content in STCT750 causes a decrease in the concentration of Ca2+ ions and results in polymerization of C-S-H chains. In FTIR spectroscopy, the phenomenon is observed as a displacement of the peaks towards a higher wave number. This is caused by a decrease in the presence of Q1 species in the production of calcium-silicate-hydrate (C-S-H) compounds[287].

The S-O peaks corresponding to gypsum and anhydrite [235] at 1175 cm^{-1} , 1156 cm^{-1} , and 1117 cm^{-1} merge with the Si-O peaks and Al-O peaks. The stretching and bending in these bonds extend as a shoulder formation towards the peaks between 1400-1450 cm^{-1} corresponding to the C-O bonds. This shoulder formation is more discernible in case of ST samples due to the presence of anhydrite in STCT750. Based on the findings from XRD these peaks represent the calcium carbonate phases present in OPC samples and the hemi carbonate and calcium carbonate phases present in ST samples. The higher intensity of the peaks in ST confirms the findings from XRD that the hemi carbonate phases are found only in ST samples. The peaks between 1650 cm^{-1} and 1660 cm^{-1} are found only in case of ST samples. This represents the bending and stretching vibrations of water molecules and is generally associated with gypsum and in case of ST mixes it also indicates the water adsorbed in zeolitic C-A-S phases. The band corresponding to wavenumber 1900 – 2350 cm^{-1} represent the presence and bending of O-H bonds The band corresponding to wavenumber 3300-3700 cm^{-1} correspond to O-H stretching vibrations in water molecules and the sharp peak at 3600 cm^{-1} correspond to portlandite and peaks at 3526 cm^{-1} and 3402 cm^{-1} correspond to gypsum. Similar observations were also made in Fig. 5.28 (b) and (c).

The peak spectrum for OPC and ST samples at 14 days are given in Figs. 5.29 (a) through (c). At 14 days the peaks corresponding to S-O bonds at 670 cm^{-1} become more visible. Also, the peaks corresponding to Si-O tetrahedral bonds become more intensified indicating structural changes in phases containing those bonds such as quartz and belite with hydration. This leads to asymmetric bending of the peak at 890 cm^{-1} towards the lower wave number side.

The OPC mixes also exhibit formation of peaks at 1650 cm^{-1} indicates the formation of phases with adsorbed water such as C-S-H. The band corresponding to O-H bonds between 1900 – 2350 cm^{-1} and O-H stretching vibrations in water molecules between 3300-3700 cm^{-1} were also observed.

Figs 5.30, 5.32 and 5.33 show spectrum of the OPC and ST cementitious pastes at 28 days, 56 days, and 90 days. The peaks were observed at the same locations as in case of 7 and 14 days, indicating the presence of same functional groups. However, the shapes and intensity of those peaks keep changing with proportion of ST and OPC representing the changes that happen during hydration.

The changes in the position and morphology of the peaks indicate the shifts in the chemical bonding within the OPC and ST. The X-ray diffraction (XRD) data provides evidence of the consumption of the alite and belite phases throughout the hydration process. Furthermore, it should be emphasised that the microscope (SEM) images provide evidence of the existence of secondary hydration products, including crumpled and flaky C-S-H, as well as a denser matrix. This collective observation indicates the changes in both the chemical composition and morphology of the hydration products that occur during the curing and hydration processes of the samples as time progresses.

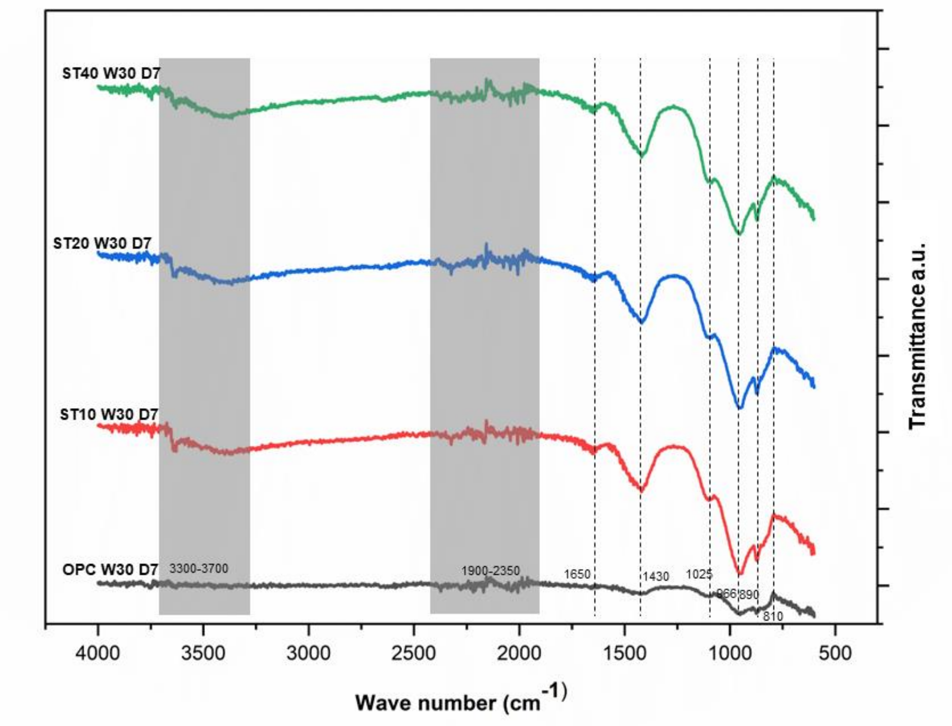
ST40 W30 D7
ST20 W30 D7
ST10 W30 D7
OPC W30 D7
3300-3700
1900-2350
1650
1430
1025
966
890
810
4000
3500
3000
2500
2000
1500
1000
500
Wave number (cm^{-1})
Transmittance a.u.

(a)

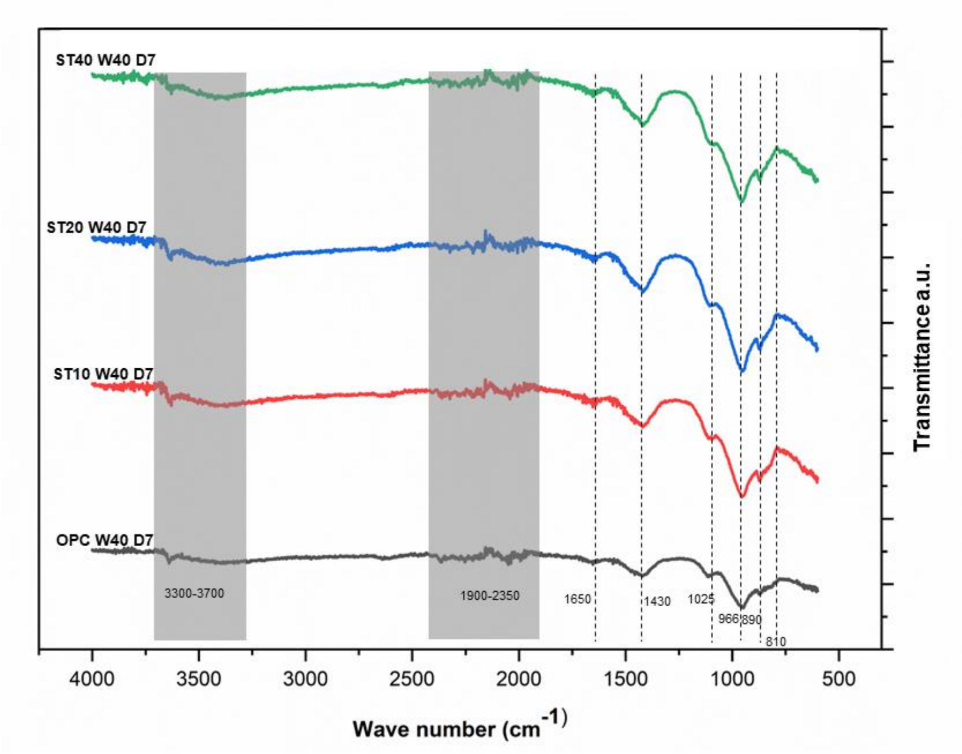
ST40 W40 D7
ST20 W40 D7
ST10 W40 D7
OPC W40 D7
3300-3700
1900-2350
1650
1430
1025
966
890
810
4000
3500
3000
2500
2000
1500
1000
500
Wave number (cm^{-1})
Transmittance a.u.

(b)

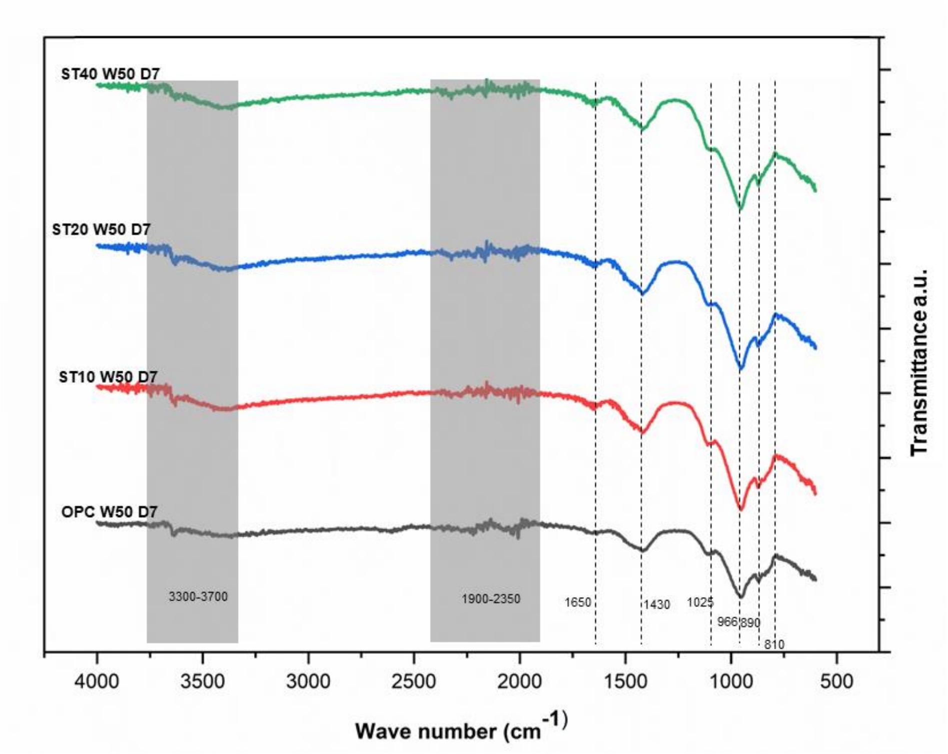

(c)

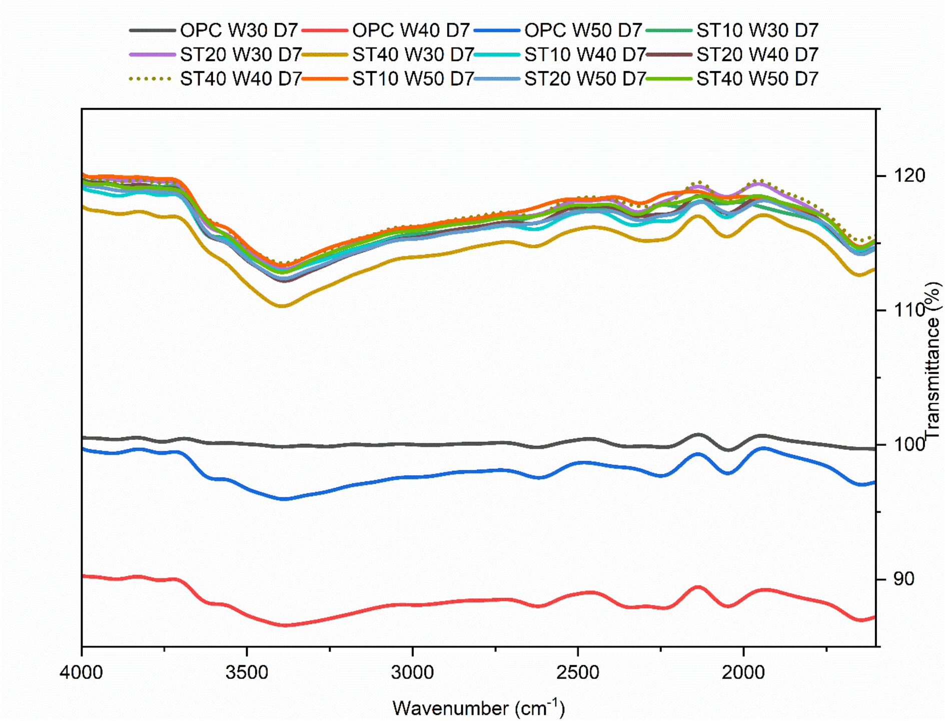

(d)

Fig. 5.28: FTIR spectral patterns of cementitious pastes containing 0%, 10%, 20% and 40% STCT750 after 7 days of curing. (a) w/c ratio = 0.3, (b) w/c ratio = 0.4, (c) w/c ratio = 0.5, (d) FTIR spectral region corresponding to 1500 cm^{-1} to 4000 cm^{-1}.

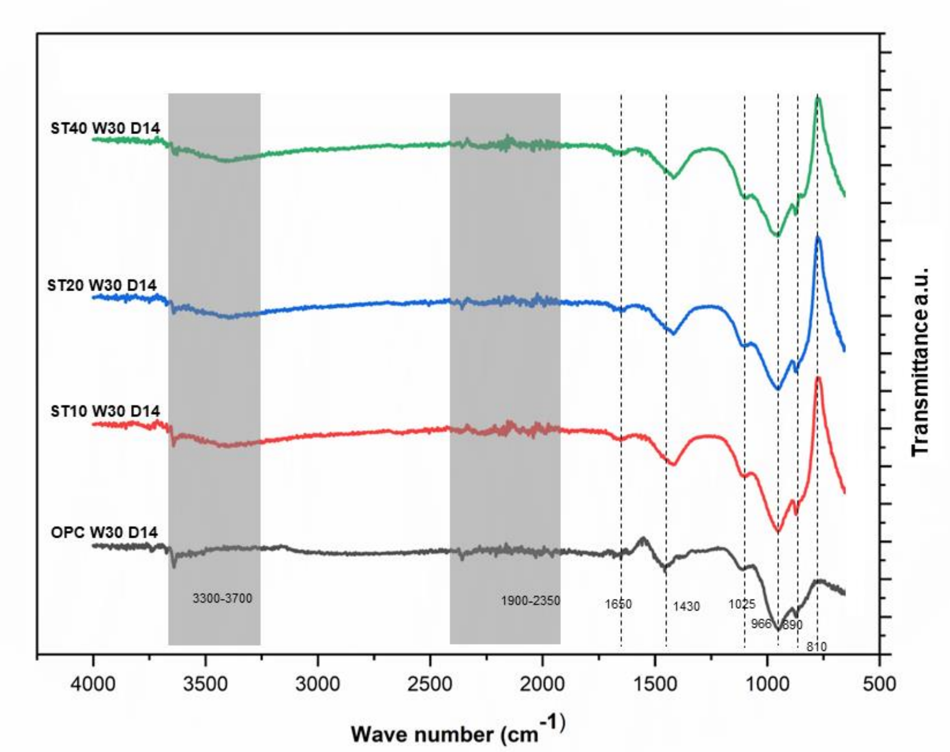
ST40 W30 D14
ST20 W30 D14
ST10 W30 D14
OPC W30 D14
3300-3700
1900-2350
1650
1430
1025
966
890
810
4000
3500
3000
2500
2000
1500
1000
500
Wave number (cm^{-1})
Transmittance a.u.

(a)

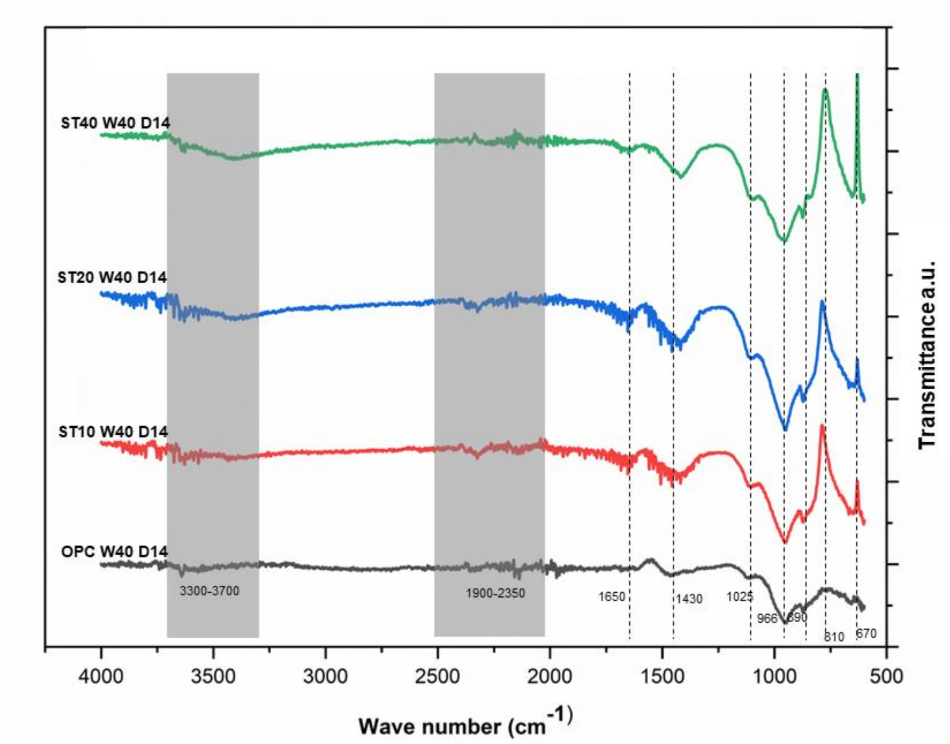
ST40 W40 D14
ST20 W40 D14
ST10 W40 D14
OPC W40 D14
3300-3700
1900-2350
1650
1430
1025
966
890
810
670
4000
3500
3000
2500
2000
1500
1000
500
Wave number (cm^{-1})
Transmittance a.u.

(b)

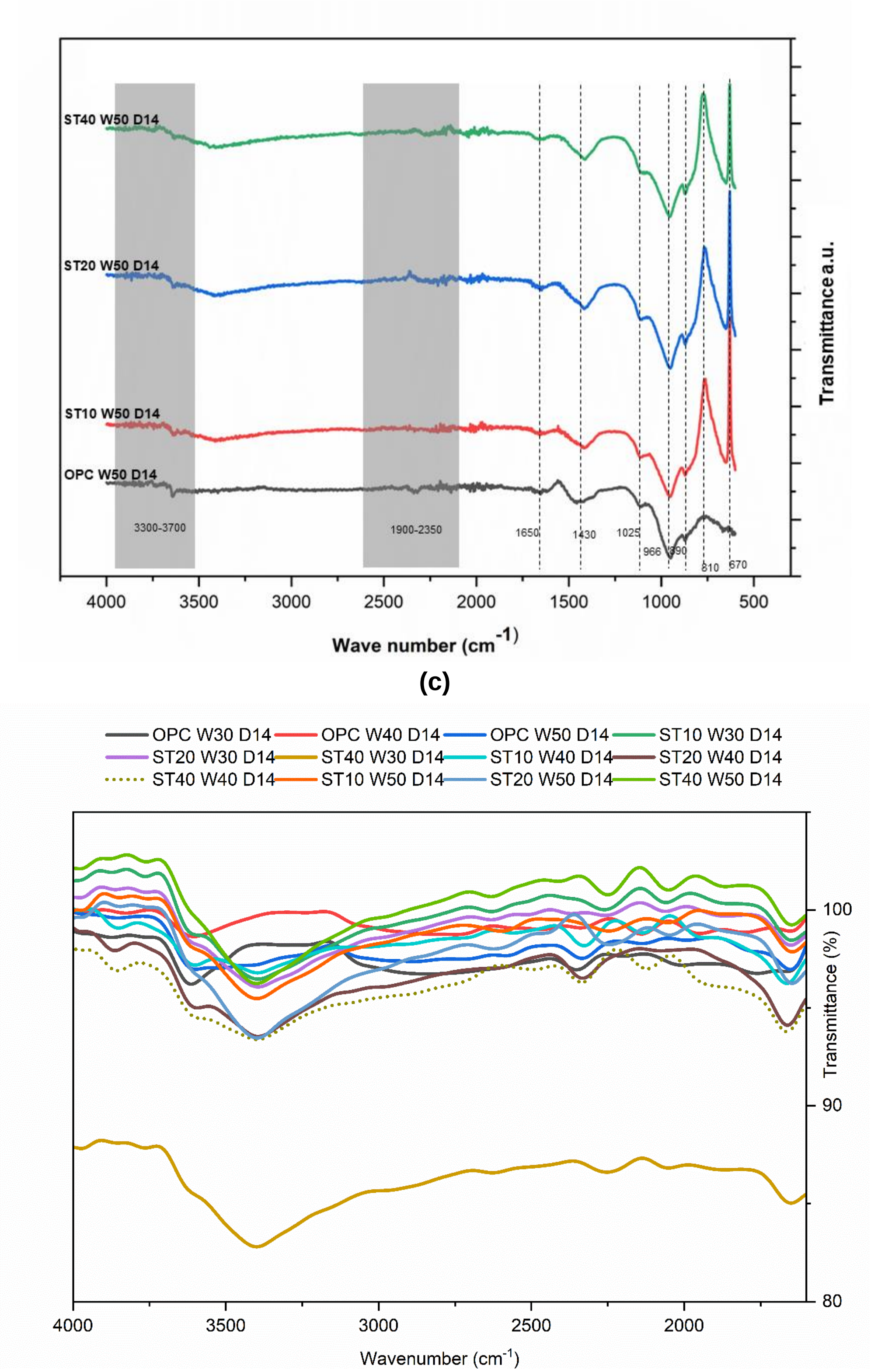

(c)

(d)

Fig. 5.29: FTIR spectral patterns of cementitious pastes containing 0%, 10%, 20% and 40% STCT750 after 14 days of curing. (a) w/c ratio = 0.3, (b) w/c ratio = 0.4, (c) w/c ratio = 0.5, (d) FTIR spectral region corresponding to 1500 cm^{-1} to 4000 cm^{-1}.

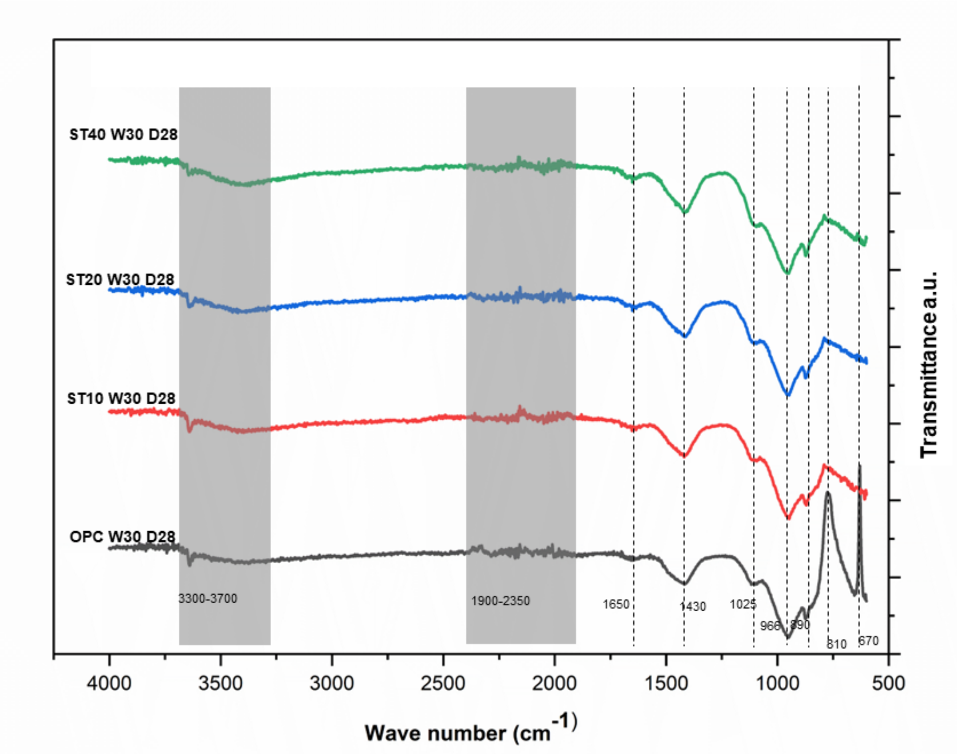
ST40 W30 D28
ST20 W30 D28
ST10 W30 D28
OPC W30 D28
3300-3700
1900-2350
1650
1430
1025
966
890
810
670
4000
3500
3000
2500
2000
1500
1000
500
Wave number (cm^{-1})
Transmittance a.u.

(a)

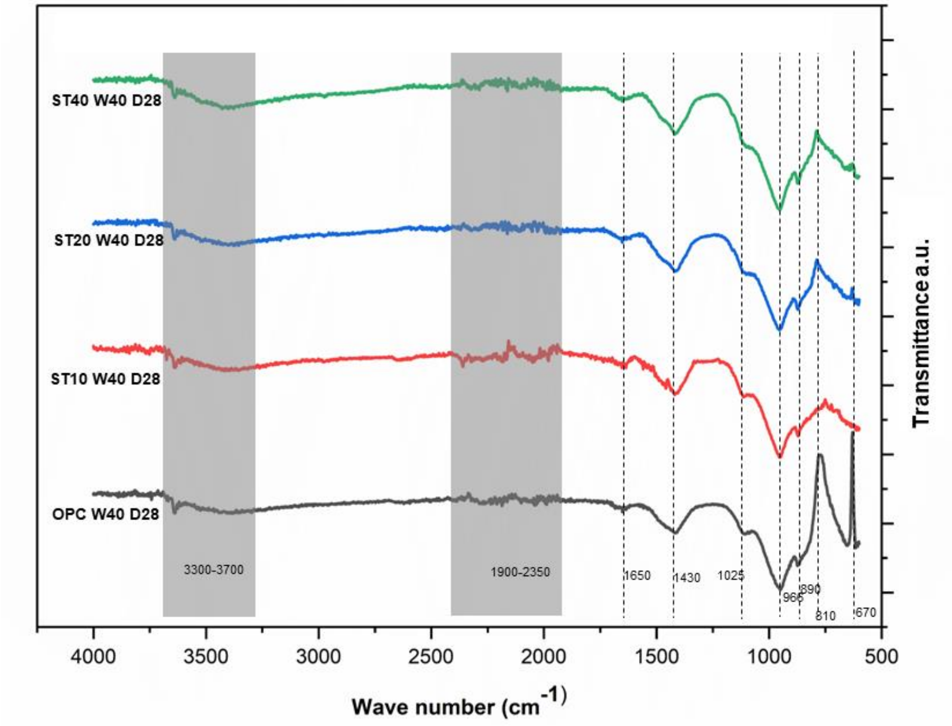
ST40 W40 D28
ST20 W40 D28
ST10 W40 D28
OPC W40 D28
3300-3700
1900-2350
1650
1430
1025
966
890
810
670
4000
3500
3000
2500
2000
1500
1000
500
Wave number (cm^{-1})
Transmittance a.u.

(b)

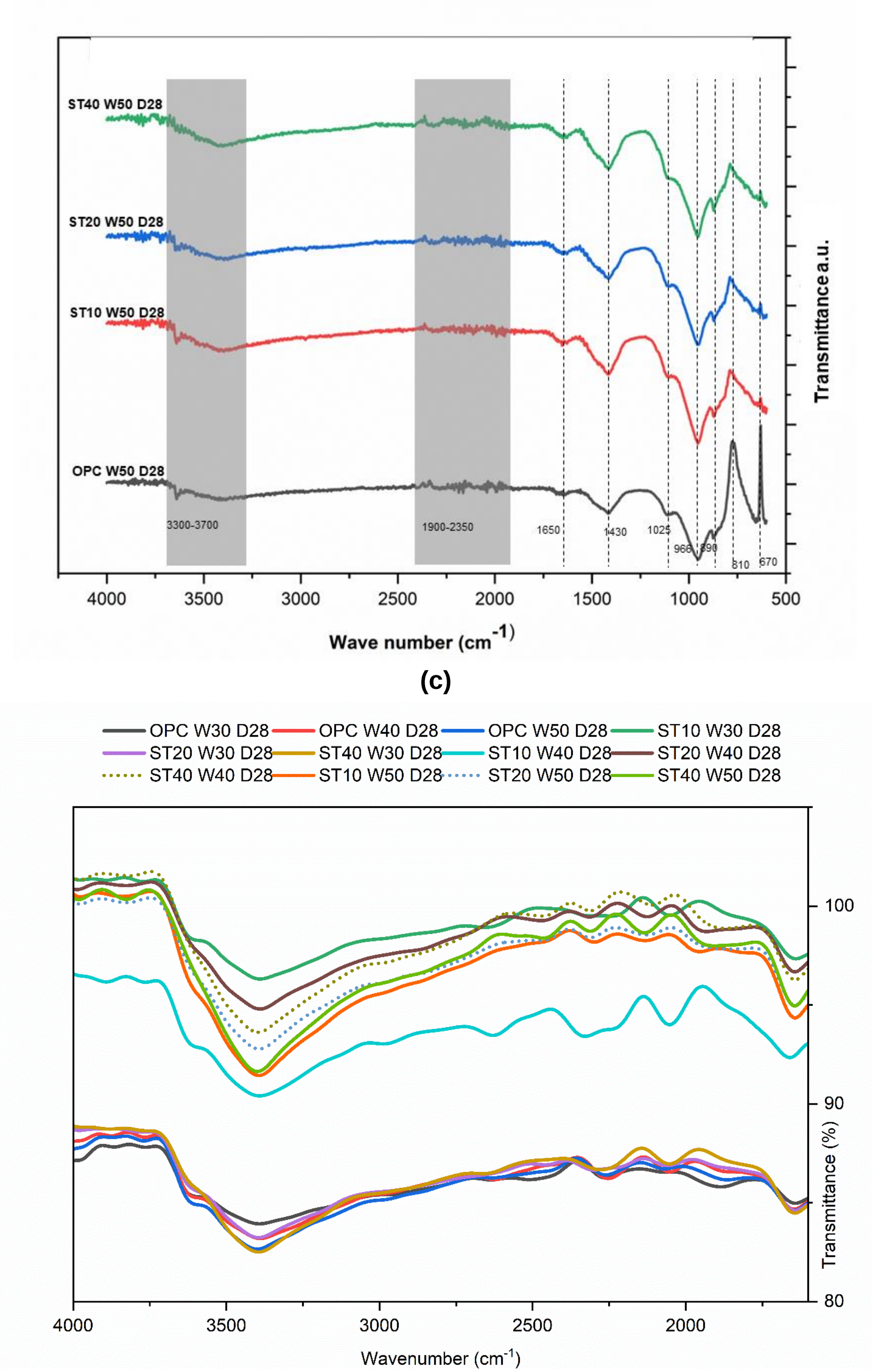

(c)

(d)

Fig. 5.30: FTIR spectral patterns of cementitious pastes containing 0%, 10%, 20% and 40% STCT750 after 28 days of curing. (a) w/c ratio = 0.3, (b) w/c ratio = 0.4, (c) w/c ratio = 0.5, (d) FTIR spectral region corresponding to 1500 cm^{-1} to 4000 cm^{-1}.

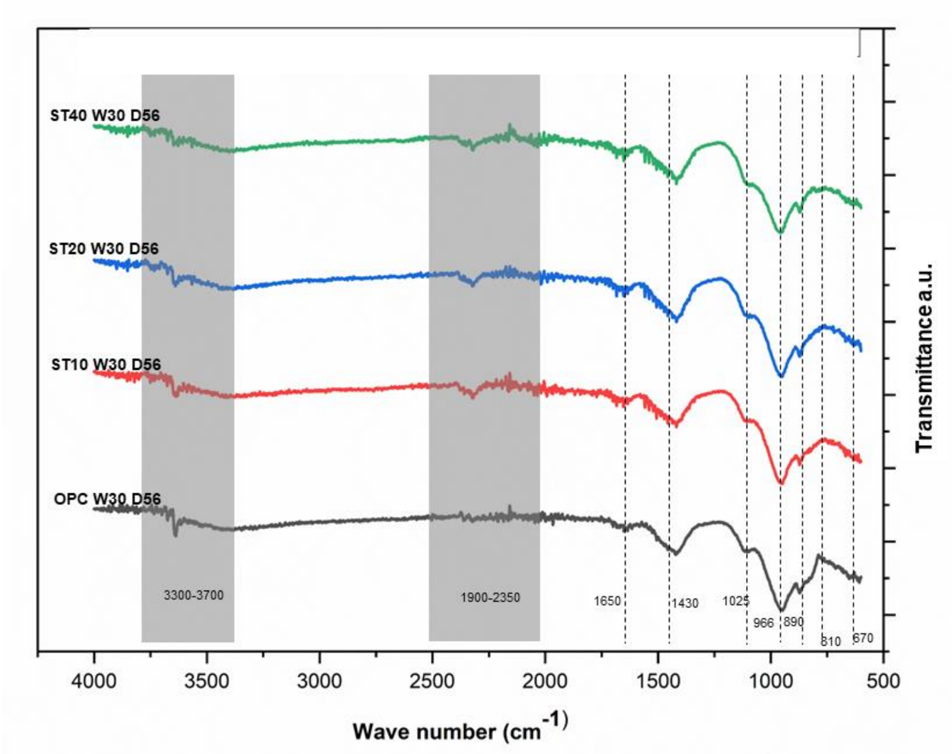
ST40 W30 D56
ST20 W30 D56
ST10 W30 D56
OPC W30 D56
3300-3700
1900-2350
1650
1430
1025
966
890
810
670
4000
3500
3000
2500
2000
1500
1000
500
Wave number (cm^{-1})
Transmittance a.u.

(a)

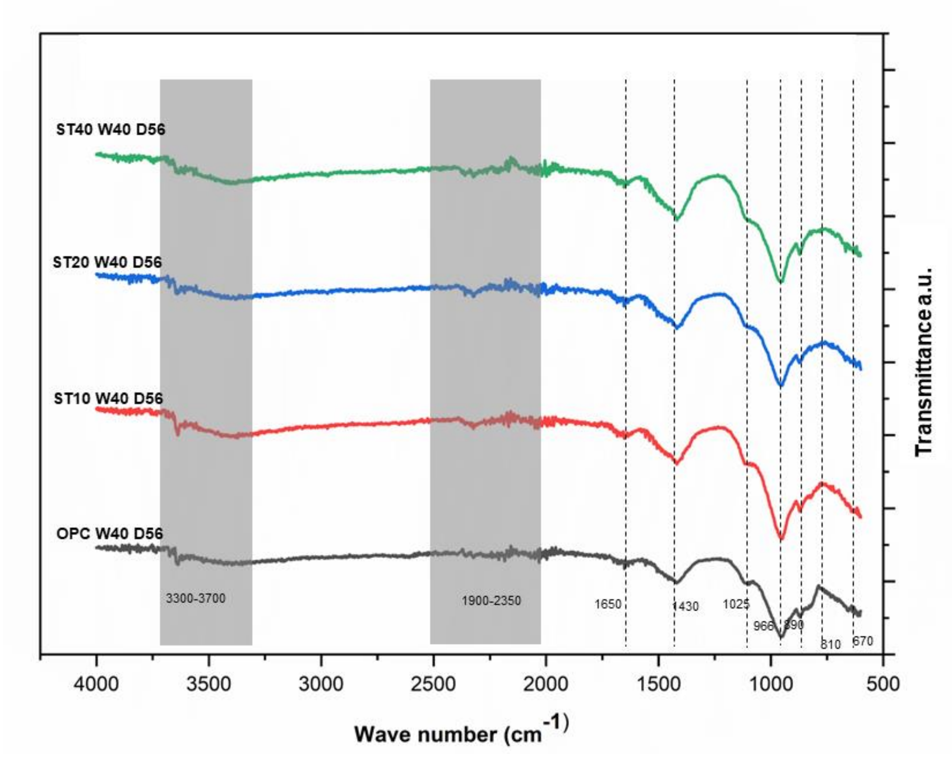
ST40 W40 D56
ST20 W40 D56
ST10 W40 D56
OPC W40 D56
3300-3700
1900-2350
1650
1430
1025
966
890
810
670
4000
3500
3000
2500
2000
1500
1000
500
Wave number (cm^{-1})
Transmittance a.u.

(b)

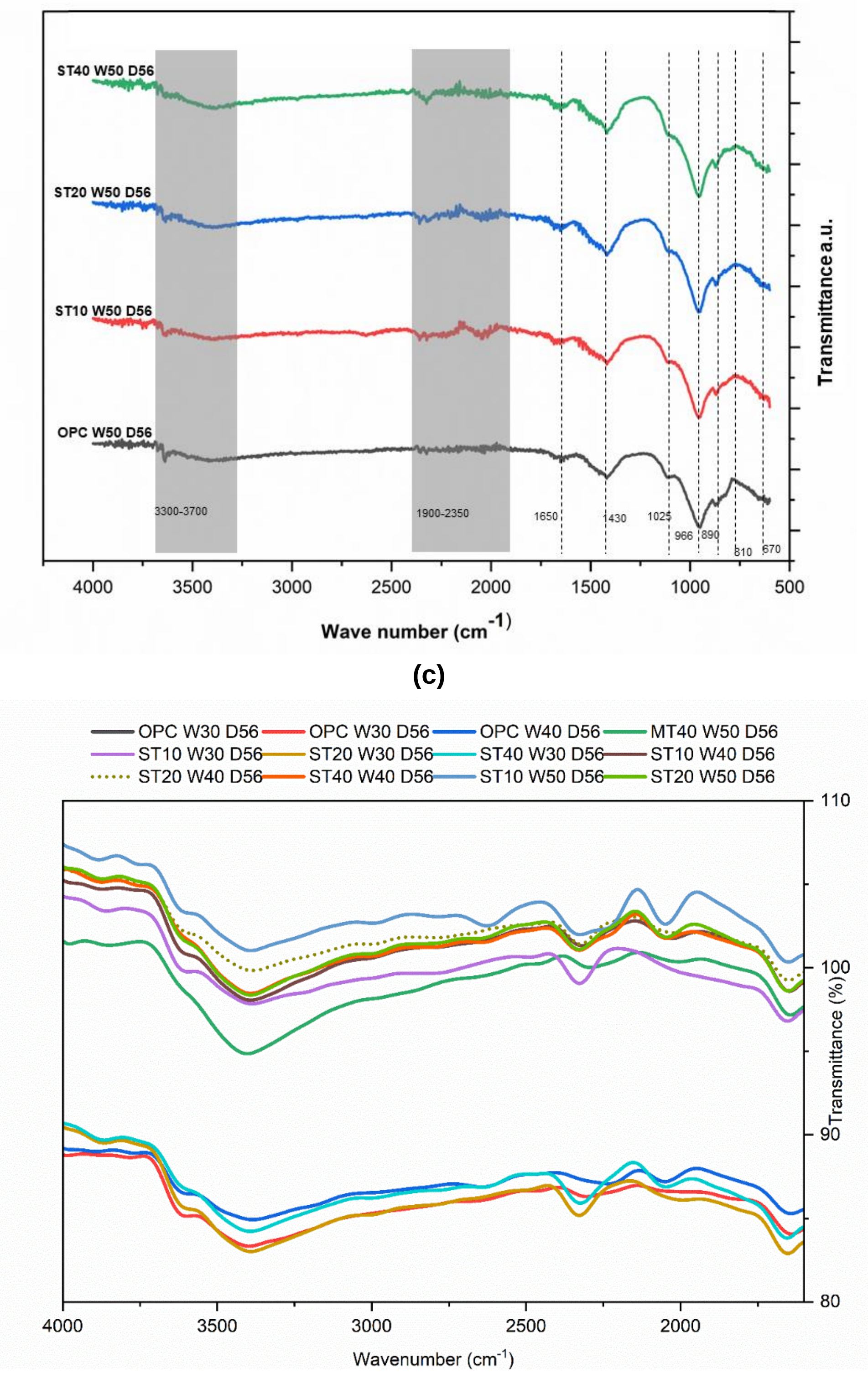

(c)

(d)

Fig. 5.31: FTIR spectral patterns of cementitious pastes containing 0%, 10%, 20% and 40% STCT750 after 56 days of curing. (a) w/c ratio = 0.3, (b) w/c ratio = 0.4, (c) w/c ratio = 0.5, (d) FTIR spectral region corresponding to 1500 cm^{-1} to 4000 cm^{-1}.

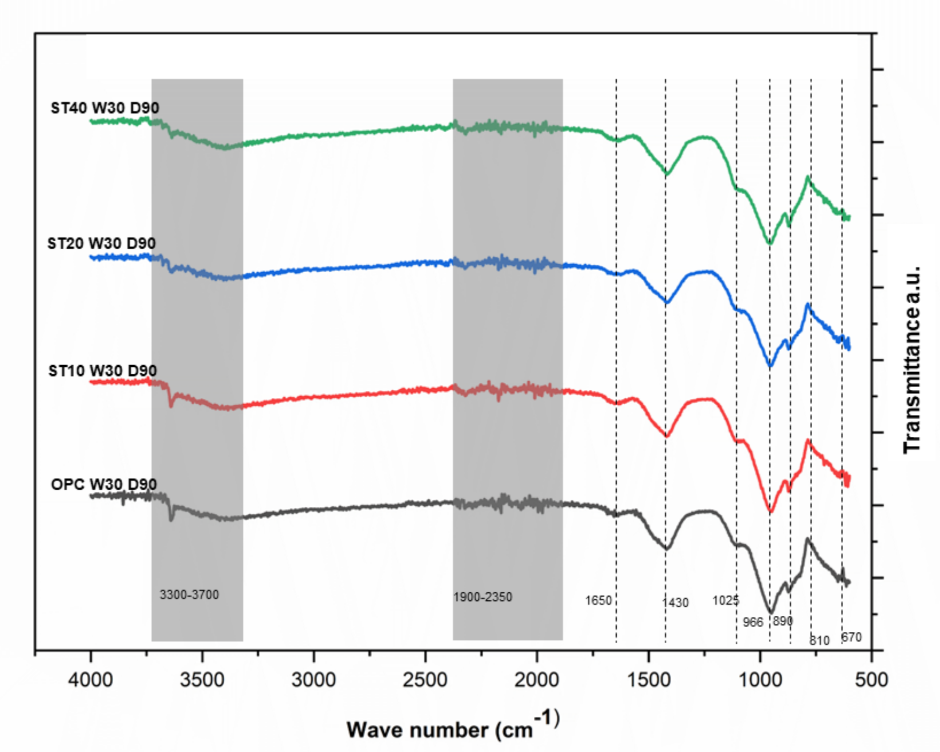
ST40 W30 D90
ST20 W30 D90
ST10 W30 D90
OPC W30 D90
3300-3700
1900-2350
1650
1430
1025
966
890
810
670
4000
3500
3000
2500
2000
1500
1000
500
Wave number (cm^{-1})
Transmittance a.u.

(a)

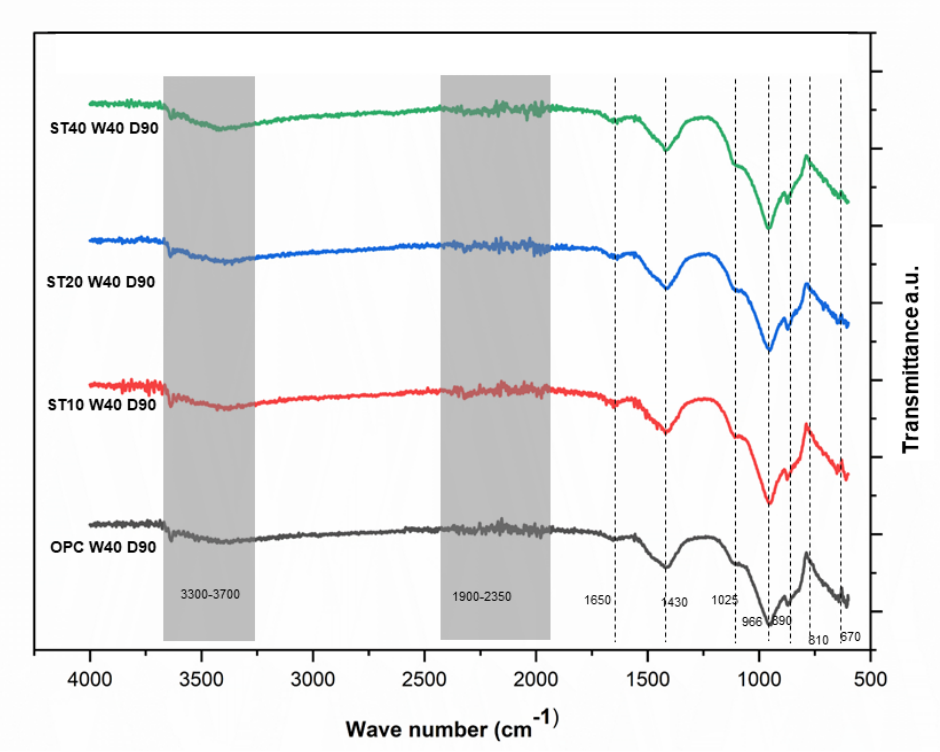
ST40 W40 D90
ST20 W40 D90
ST10 W40 D90
OPC W40 D90
3300-3700
1900-2350
1650
1430
1025
966
890
810
670
4000
3500
3000
2500
2000
1500
1000
500
Wave number (cm^{-1})
Transmittance a.u.

(b)

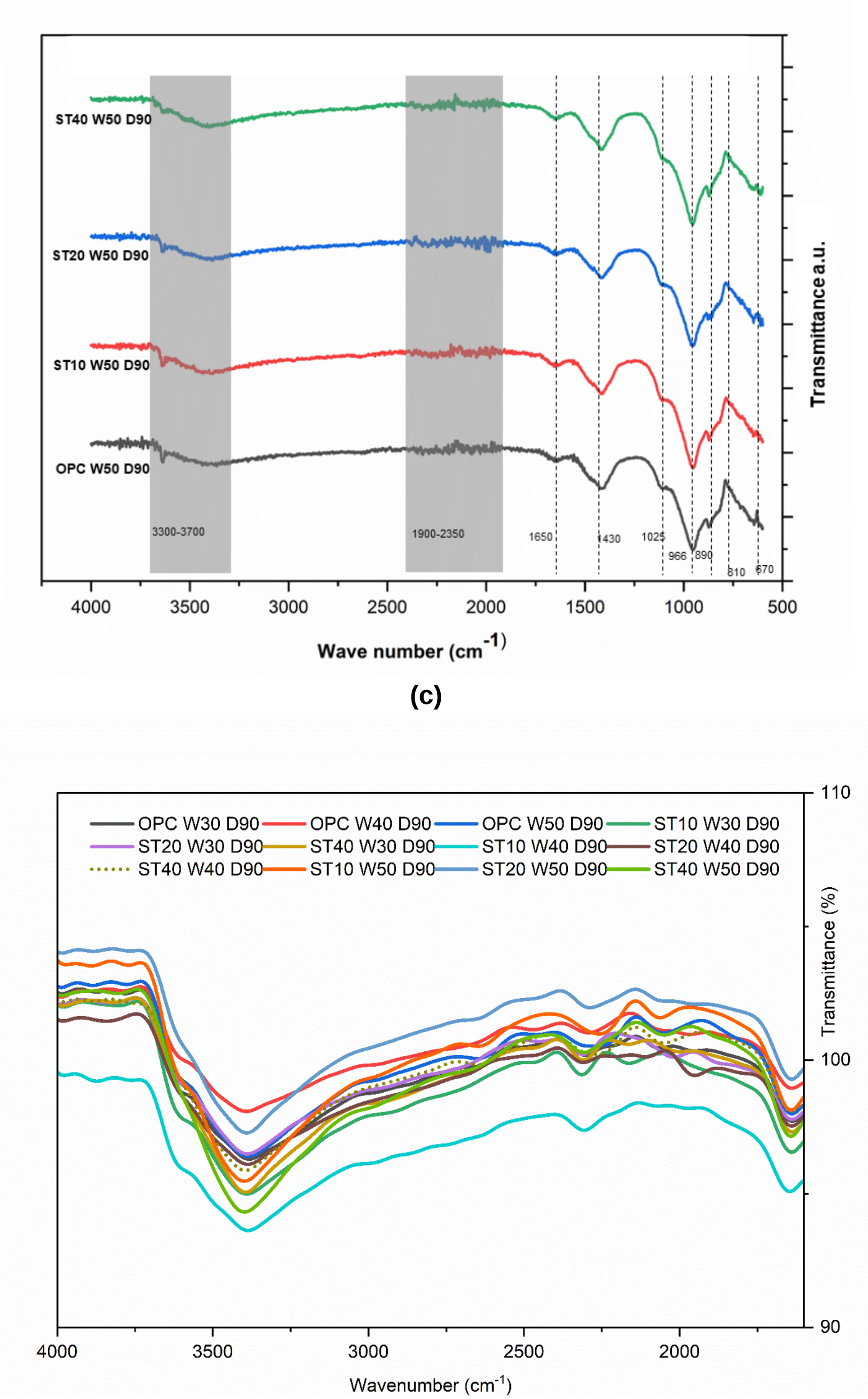

(c)

(d)

Fig. 5.32: FTIR spectral patterns of cementitious pastes containing 0%, 10%, 20% and 40% STCT750 after 90 days of curing. (a) w/c ratio = 0.3, (b) w/c ratio = 0.4, (c) w/c ratio = 0.5, (d) FTIR spectral region corresponding to 1500 cm^{-1} to 4000 cm^{-1}.

5.7 Strength Development and Density

The compressive strength of mortar containing varying percentages (10%, 20%, and 40%) of MTCT850 and STCT750 were compared to the compressive strength of OPC at 7, 14, 28, 56, and 90 days. The results of the same are given in Fig. 5.33

Figure 5.33 shows that the compressive strength of OPC at 7 days was 52.16 MPa and the same for MT mixes was between 36.49 MPa and 48.62 MPa. Similarly at 90 days the compressive strength of OPC was 70.68 MPa and MT mixes was 51.8 MPa and 63.8 MPa. At all ages MT20 mixes performed better than other MT mixes.

ST samples had a strength lower than that of OPC. The compressive strength of ST samples at 7 days ranged between 47.2 MPa to 52.8 MPa. And the same for 90 days ranged between 63 MPa to 69.8 MPa, with ST20 exhibiting highest strength at all ages.

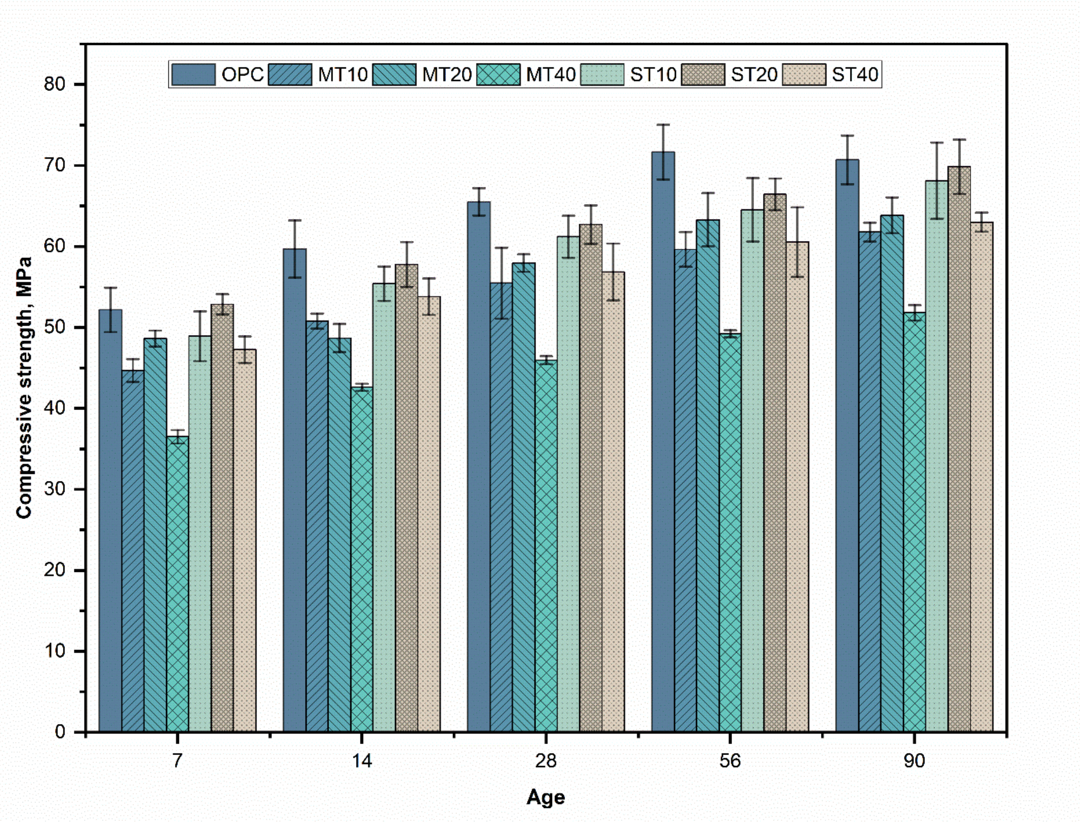

Fig. 5.33: Compressive strength of mortar mixes at the ages 7, 14, 28, 56 and 90 days. with 0%,10%, 20%, and 40% MTCT850 and STCT750.

5.7.1 Strength activity index

Figure 5.34 (a) and (b) illustrate the strength activity index of the MT and ST samples respectively. These values are calculated from the strength values represented in Fig. 5.33 using the Eq. 5.6. Though ASTM C618 [290] recommends a replacement percentage of 20% for strength activity index calculations, the present study reports the results of both 10% and 40% along with 20% for comparison.

$$Strength\ Activity\ Index = \frac{Compressive\ strength\ of\ mortar\ with\ mineral\ waste}{Compressive\ strength\ of\ portland\ cement\ mortar} \quad (5.6)$$

It is evident from Figure 5.34 (a) that the strength activity index of MT20 varied between 82% and 93%, which was higher than that of MT10 (ranging from 83% to 87%) and MT40 (ranging from 69% to 73%). The results indicated that mixes containing 20% MTCT850 exhibited better results compared to other mixes, with a 90-day compressive strength approximately 90% of that observed in OPC mixes. Similarly, Fig. 5.34 (b) illustrates the strength activity index of the ST samples, which varied between 90% and 96% for ST10, 92% and 101% for ST20, and 85% and 91% for ST40. These results indicate that ST20 exhibits the highest compressive strength among the tested mixes, thus making it the optimal mix in terms of strength. However, it is important to note that all the mixes containing 10% and 20% STCT750 exhibited a minimum of 90% of the compressive strength of Ordinary Portland Cement (OPC) at all tested ages.

The strength activity indices observed in the present study are similar to that of calcined kaolinite and bentonite clays which were in range of 67% - 128% (for 20% replacement) [291]. Similar observations were also made with calcined London clay where the strength activity indices were reported to be above 75% whereas granulated blast furnace slag had a strength activity index greater than 100 after 14 days of curing [252].

All of the strength activity indices of the MT and ST mixes, except for MT40, evaluated in the present study were higher than the limit of 75% recommended by the ASTM standard. The strength activity index values of the mixes were consistent with age or varied only within a range of 10%. This indicates that the strength increase of the MT and ST mixes with age were comparable to that of OPC mixtures. This observation is in contrast to other slow reactive supplemental cementitious materials like fly ash in case of which the strength activity index increases with age of hydration.

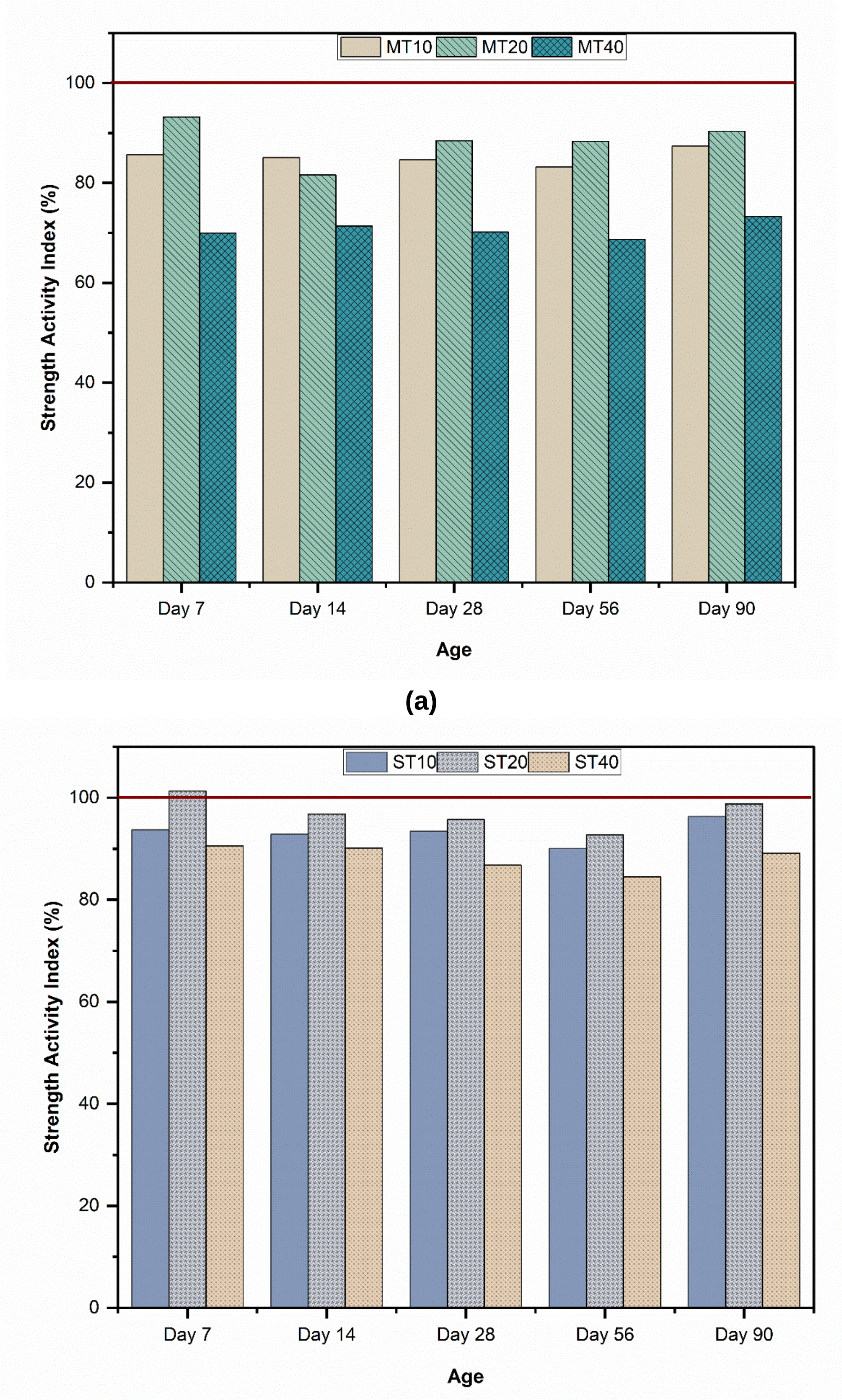

(a)

(b)

Fig. 5.34: Strength activity index of the mixes at 7, 14, 28, 56 and 90 days. (a) with 10%, 20%, and 40% MTCT850 and (b) with 10%, 20%, and 40% STCT750.

5.7.2 Strength development

The strength gain at different ages is represented by the ratio of strength of a mix at any age to the strength of mix at 7 days. The observed strength gain is given in Fig. 5.35. The trend indicates that the compressive strength of the samples increased with age. The compressive strength of OPC exhibited a 14% increase at 14 days, a 25% increase at 28 days, a 37% increase at 56 days, and approximately a 36% increase at 90 days, relative to the strength observed at 7 days. The aforementioned percentages for MT10 were found to be 13%, 24%, 33%, and 38%. Similarly, the percentages for MT20 were determined to be 0%, 19%, 30%, and 31%. Lastly, the percentages for MT40 were observed to be 17%, 26%, 35%, and 42%.

Figure 5.35 shows that in comparison to the 7-day compressive strength value, the compressive strength of ST10 samples exhibited an increase of 13% at 14 days, 25% at 28 days, 32% at 56 days, and 39% at 90 days. These percentages for ST20 were 9%, 18%, 25%, and 32%, while the percentages for ST40 were 13%, 20%, 28%, and 33%.

The data indicates that the strength gain of ordinary Portland cement (OPC) reaches a plateau after 56 days, while the mixes including MTCT850 and STCT750 continue to display a progressive increase in strength gain. The presence of crumpled foil C-S-H observed in the microstructure, in conjunction with these observations, suggests the occurrence of secondary hydration reactions and matrix densification during later stages [274].

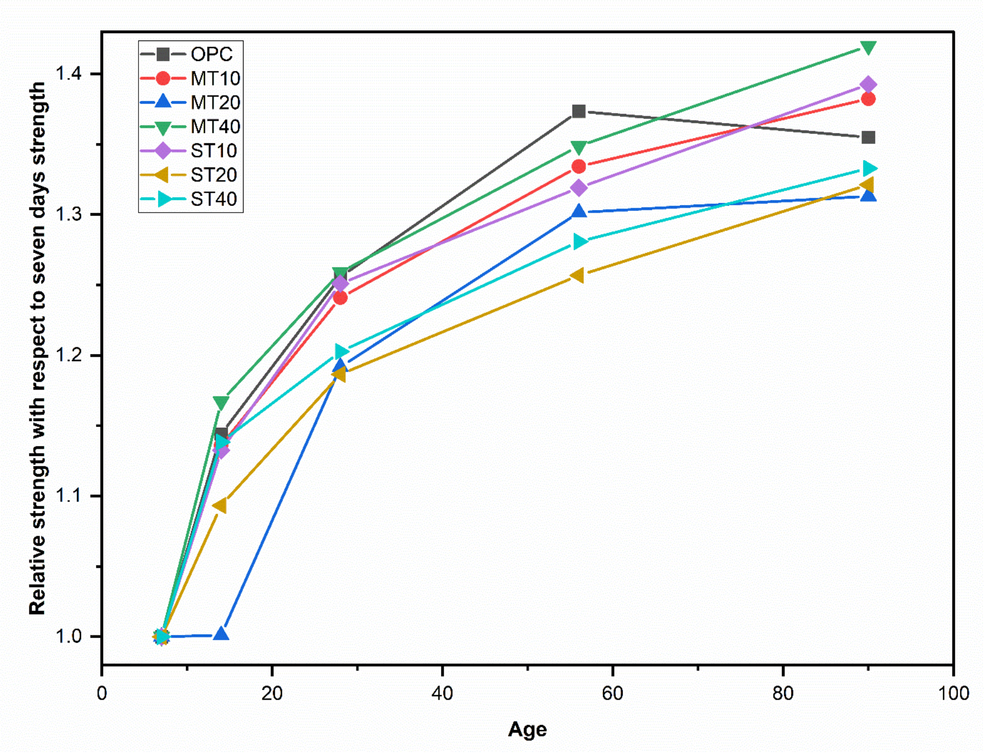

Fig. 5.35: Compressive strength development of mortar mixes with 0%,10%, 20%, and 40% MTCT850 and STCT750 in comparison to 7 days strength.

5.7.3 Density

The saturated surface dry densities of the samples were determined at the age of test, immediately after removal from curing tank. The samples were tested in triplicates and the average test values are reported in Fig. 5.36.

Figure 5.36 (a) illustrates the density range of OPC and MT sample sand indicates no significant variations between the densities of OPC and MT samples. Although the loose particle density of MTCT850 (0.7 g/cc) was lower than that of cement (1.2 g/cc) resulting in higher volume of powder in MT mixes, the observed comparable or higher density can be attributed to the fine particle size of the mine tailings as compared to the sand, resulting in improved packing density of the mortar prepared. The loose particle density is mentioned here as an indicative for the sample specific gravity. It was determined by filling a known volume of container with the sample without compaction. To ensure uniformity the samples were dropped through a funnel and a height of fall of 10 mm was maintained.

Figure 5.36 (b) illustrates the density variations of the ST samples. Similar to MT mixes although the mixes containing STCT750 lower loose particle density (0.72 g/cc) causing higher powder content in ST mixes than the OPC, the comparable or higher density observed can be attributed to the fine particle size of the STCT750, resulting in improved packing density of the mortar.

The findings of the study can be compared with other observations were the strength of the mixes with optimum percentage of replacement were better than the other replacement percentages [77]. This can be attributed to the better packing density, optimum ratio of Si and Ca to facilitate the formation of secondary C-S-H at later ages [191].

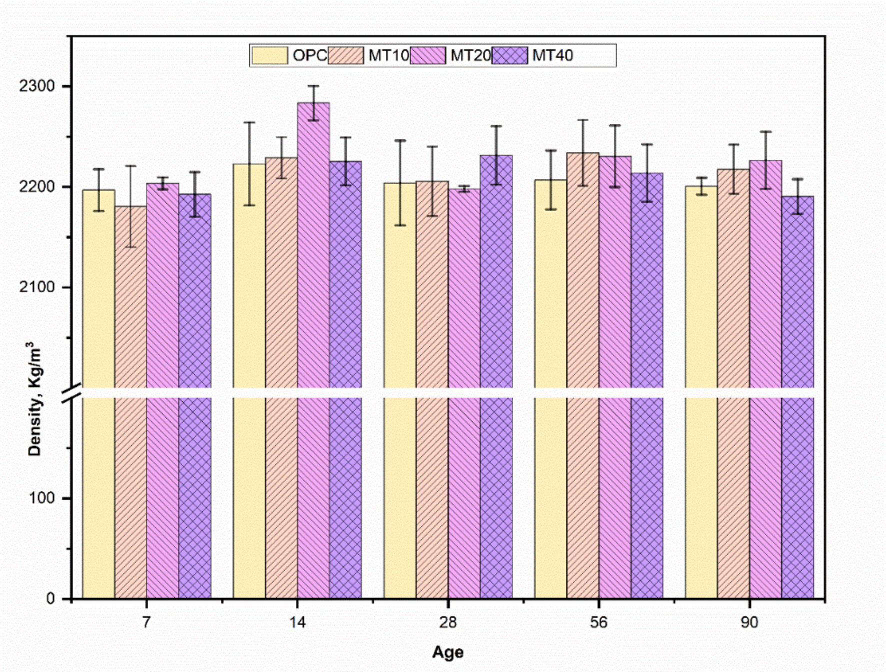

(a)

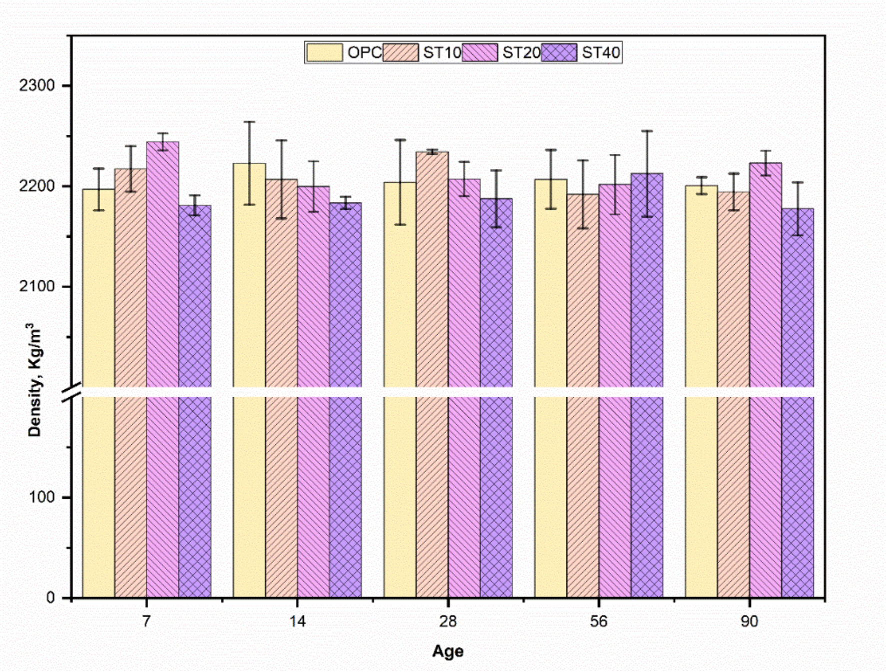

(b)

Fig. 5.36: Density of mortar mixes at the ages 7, 14, 28, 56 and 90 days. (a) with 0%,10%, 20%, and 40% MTCT850 and (b) (a) with 0%,10%, 20%, and 40% STCT750

5.8 Durability

Concrete durability according to American Concrete Institute is defined as, “the ability of concrete to resist weathering action, chemical attack, abrasion, and other conditions of service” [292]. Durability of concrete is dependent on the transport processes of the moisture and other harmful materials and ions inside concrete. In the current study sorptivity and carbonation tests are used as durability indicators.

5.8.1 Sorptivity

Sorptivity test of mortar represents the ability of the mortar to absorb and transmit water through it via capillary suction. It gives an insight into pore structure and connectivity of the pores in the material being tested [244]. Lower value of sorptivity indicates a more compact microstructure with less connectivity of pores.

Figure 5.37 (a) presents the sorptivity coefficient of MT samples in comparison to OPC. The data indicates a noticeable decrease in the sorptivity of the samples as the percentage of MTCT850 increased at the age of 28 days. Specifically, the sorptivity values for MT10, MT20, and MT40 were approximately 95%, 88%, and 86% respectively, in comparison to the sorptivity of OPC samples.

The sorptivity test results for samples of ST and OPC are presented in Figure 5.37 (b). At the 28-day mark, the sorptivity of the ST10 and ST20 samples exhibited a lower value compared to that of the Ordinary Portland Cement (OPC), with reductions of approximately 84% and 82% respectively. Conversely, the sorptivity of the ST40 sample was marginally higher than that of OPC, with a difference of 1.2%.

These observations in OPC, MT and ST can be explained by using the findings reported in past studies. In certain instances, there was an observed correlation between the increase in the percentage of replacement and the increase in water absorption and porosity [68] . However, in other cases, the mixes exhibited improved performance in terms of water absorption when the replacement percentage reached an optimal level [77]. The phenomenon described by Martinez et al. [118] for this behaviour is attributed to the existence of capillary pores and macropores. Despite the overall pore volume, it is observed that capillary pores tend to fill more rapidly, while macropores exhibit a slower filling rate. Hence, the sorptivity of the observed mixes is influenced by the size of capillary pores or macropores, regardless of the total pore volume, when expressed as a function of time.

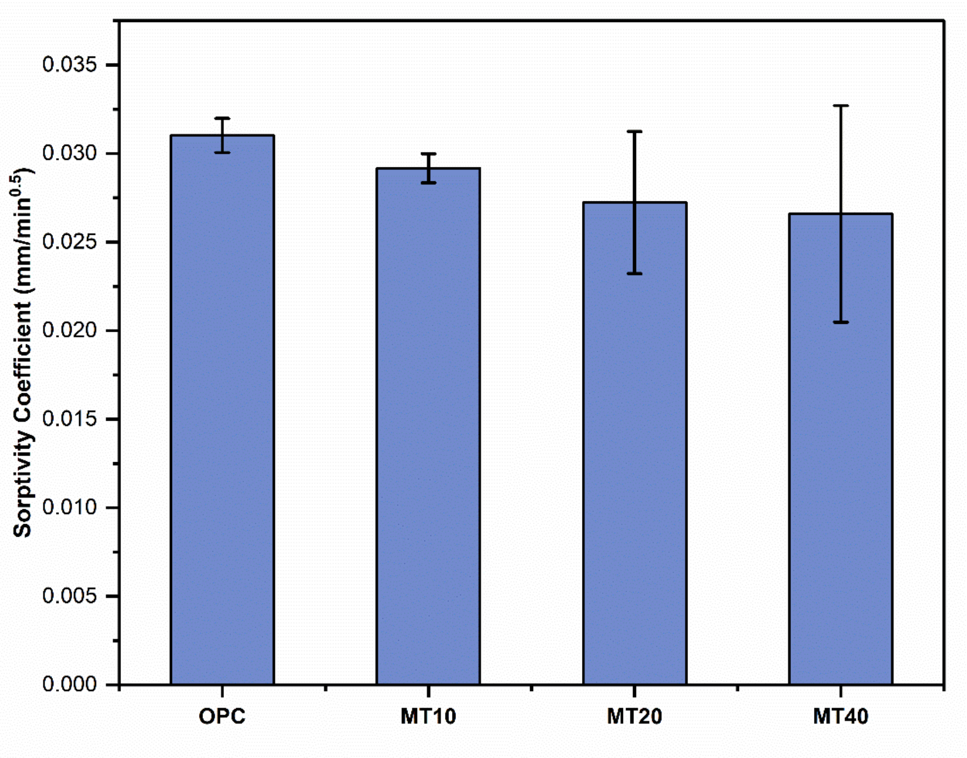

(a)

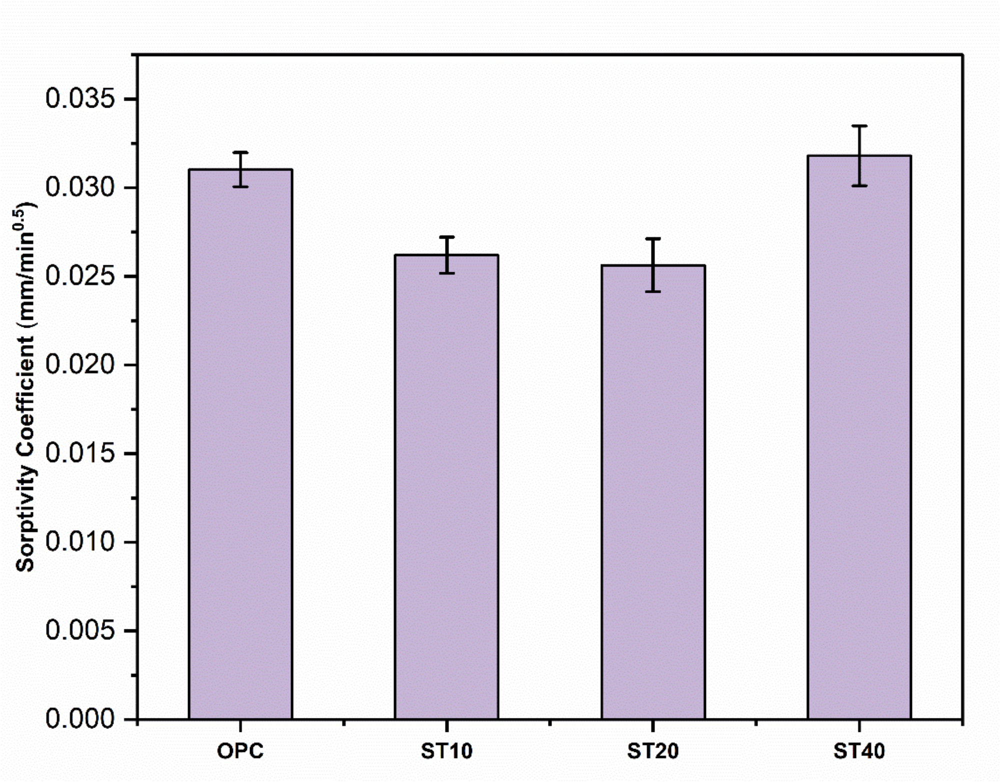

(b)

Fig. 5.37: Sorptivity coefficient of mortar samples at 28 and 56 days (a) with 0%,10%, 20%, and 40% MTCT850 and (b) (a) with 0%,10%, 20%, and 40% STCT750.

5.8.2 Carbonation

The British European standard defines carbonation as the process of reaction of alkaline components (e.g., calcium hydroxide) in the cement paste with atmospheric carbon dioxide resulting in the reduction of pH of the mortar or concrete [243] . The mechanism of carbonation of concrete with SCM is different from the mechanism of carbonation of concrete with OPC [293]. In the present study carbonation of OPC, MT and ST mortar samples were monitored at 7, 28 and 56 days in both normal environment and accelerated carbonation environment using carbonation chamber.

Performing carbonation tests with increase in concentration of CO_2 (accelerated carbonation) is a common practice for performance evaluation. In general, the accelerated carbonation and normal carbonation have a correlation of $R^2 = 0.69$ and 0.15. It depends on various products including the CO_2 concentration and the type of cement [293]. In the present study both the accelerated and natural carbonation depths are compared for a particular duration of exposure to see if the mixes follow a similar trend of carbonation at different concentrations of CO_2.

The carbonation trends in samples containing MTCT850 and OPC are depicted in Figure 5.38 (a), while their respective carbonation coefficients are presented in Figure 5.38 (b). The carbonation coefficient is given by Eq, 5.7 and is usually determined by the slope of the curve plotted between square root of time and depth of carbonation.

$$k = \frac{X_{c(t)}}{\sqrt{t}} \qquad (5.7)$$

where

k - Carbonation coefficient
$X_{c(t)}$ - Depth of carbonation at t
t - Duration of exposure

The data presented in Figure 5.38 (a) indicates that the samples placed in the carbonation chamber displayed a higher depth of carbonation. Following a 7-day exposure period in a carbonation chamber, it was observed that the depth of carbonation remained at 0 mm for all samples, except for the MT40 sample, which exhibited a depth of carbonation measuring 0.19 mm.

After a 28-day period in the carbonation chamber, it was observed that both OPC and MT20 samples exhibited an equal depth of carbonation, measuring 0.27 mm. Furthermore, within the MT mixes, there was a noticeable correlation between the percentage of MTCT850 and the depth of carbonation. Specifically, the depth of carbonation increased from 0.24 mm for MT10 to 1.4 mm for MT40. In the companion chamber, the depth of carbonation was measured to be 0.09 mm for OPC, 0.05 mm for MT40, and 0 mm for both MT10 and MT20.

After a period of 56 days, all samples exhibited indications of carbonation. The depth of carbonation measured was found to be 0.73 mm, 0.60 mm, 0.79 mm, and 2.33 mm for the OPC, MT10, MT20, and MT40 samples, respectively, when subjected to accelerated carbonation. In contrast, the samples placed in the companion chamber displayed carbonation depths of 0.35 mm, 0.17 mm, 0.18 mm, and 0.23 mm, respectively.

The carbonation coefficients depicted in Figure 5.38 (b) also demonstrates this performance. Among the various mixes tested, MT 10 exhibited superior performance compared to the other mixes, while MT 20 demonstrated performance comparable to that of OPC.

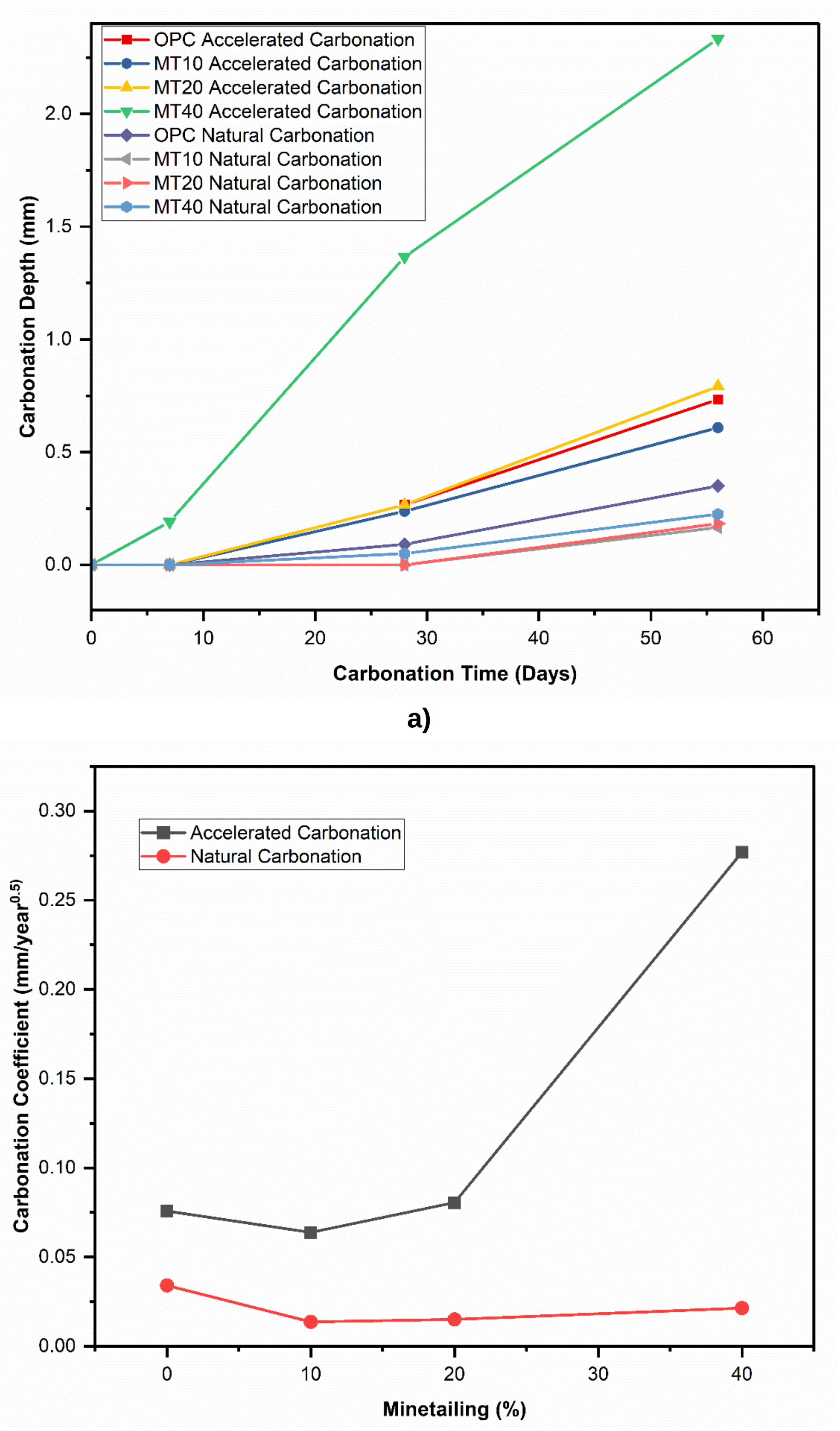

a)

(b)

Fig. 5.38: Carbonation trend observed in samples containing 0%,10%, 20%, and 40% of MTCT850 (a) carbonation depth vs time (b) carbonation coefficient vs % of MTCT850.

Figure 5.39 (a) presents the carbonation trend of samples containing STCT750 and OPC, while Figure 5.39 (b) provides the corresponding carbonation coefficients. The figure illustrates that the depth of carbonation was consistently 0 mm for all samples, with the exception of the ST40 samples in the carbonation chamber. In this case, the depth of carbonation measured 0.19 mm after 7 days.

For samples in the carbonation chamber the depth of carbonation at 28 days was found to be lower (0.1 mm) in samples ST10 and ST20 compared to those of the OPC (0.3 mm). The carbonation depth observed for ST40 was measured to be 0.5 mm. In the case of samples placed in the companion chamber, the OPC samples exhibited a carbonation depth of 0.09 mm, while the ST40 sample displayed a carbonation depth of 0.03 mm. Conversely, the carbonation depths for the ST10 and ST20 samples were measured as 0 mm.

After a period of 56 days, all samples exhibited indications of carbonation. The measured depths of carbonation were found to be 0.73 mm, 0.55 mm, 0.57 mm, and 1.44 mm for the samples composed of ordinary Portland cement (OPC), ST10, ST20, and ST40, respectively, when subjected to accelerated carbonation. In contrast, the depths of carbonation for the samples placed in the companion chamber were measured to be 0.35 mm, 0.08 mm, 0.09 mm, and 0.29 mm, respectively.

This phenomenon is also depicted in the carbonation coefficient as illustrated in Figure 5.39 (b). The performance exhibited by ST10 and ST20 was better than that of OPC.

Similar to the findings of the current study, previous studies have also documented a reduction in carbonation depth at the optimal percentage of mineral waste addition [71] as well as an increase in carbonation with higher levels of mineral waste addition [294] The decrease in carbonation observed at the optimal replacement percentage can be attributed to the densification of the microstructure. However, the introduction of mineral waste and the subsequent formation of secondary C-S-H in concrete leads to the consumption of portlandite, rendering it more prone to carbonation [129] Therefore, the carbonation process is a consequence of factors such as pore structure, transport properties, hydrate phase assemblage, and pore solution chemistry [293]

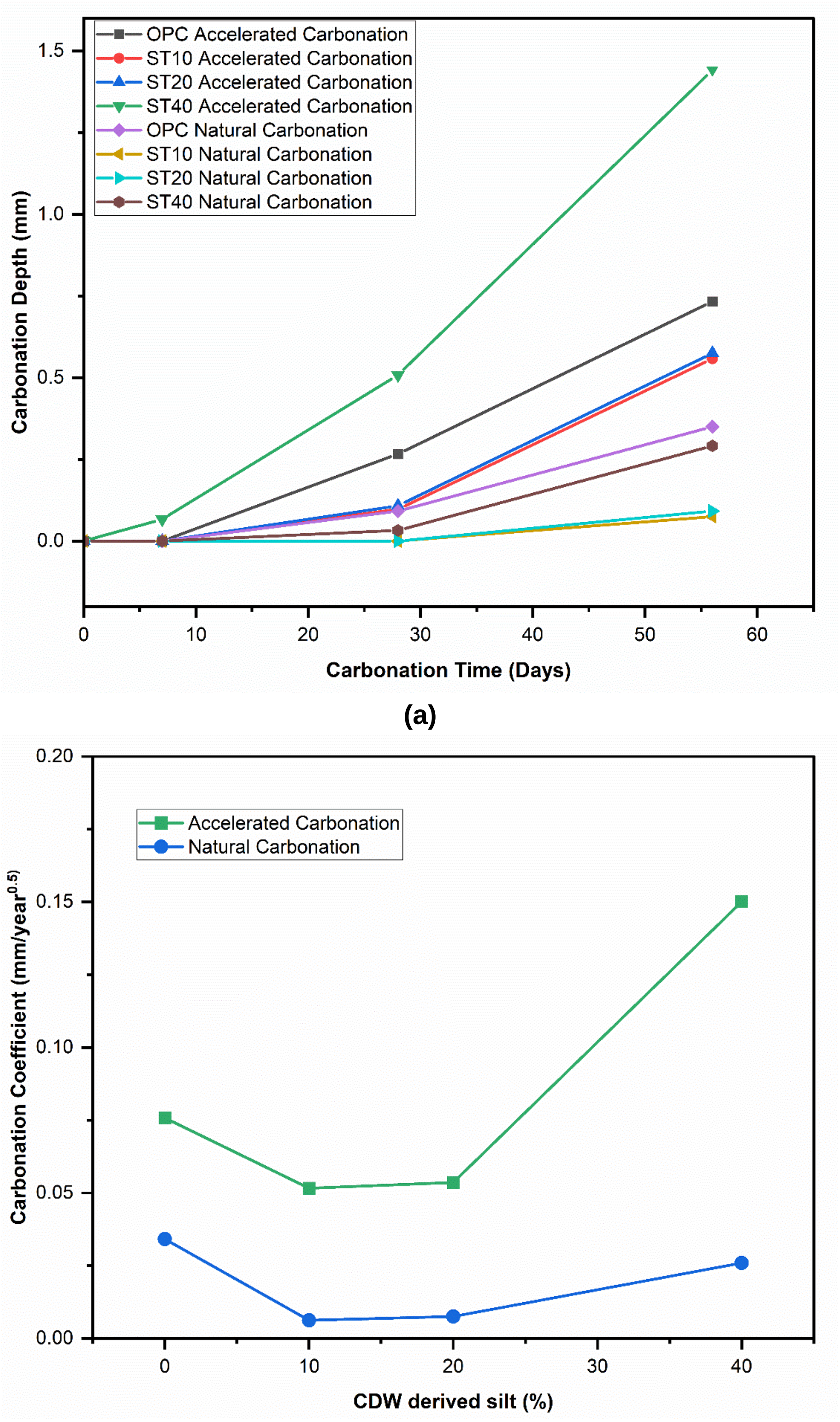

(a)

(b)

Fig. 5.39: Carbonation trend observed in samples containing 0%,10%, 20%, and 40% of STCT750 (a) carbonation depth vs time (b) carbonation coefficient vs % of STCT750.

5.9 Shrinkage and expansion

The drying shrinkage and expansion of the mortar samples with OPC, MTCT850 and STCT750 and w/c ratio 0.4 were monitored and are reported in Figs. 5.40 and 5.41.

The drying shrinkage and expansion of OPC and MT samples monitored for 150 days are reported in Figs. 5.40 (a) and (b). From Fig. 5.40 (a) it can be seen that the drying shrinkage increases with time and the rate of shrinkage is higher in the earlier period up to 7 days and decreases after that. At the end of 3 days the shrinkage values were 0.031%, 0.028%, 0.037% and 0.037% for OPC, MT10, MT20 and MT40 respectively, showing that the mixes with higher powder content, MT20 and MT40 exhibited higher shrinkage. At the end of 7 days the shrinkage of OPC was about 0.065 % and MT10, MT20 and MT40 were 0.054%, 0.064%, and 0.057%. At the end of 150 days, it appeared that the MT40 mixes exhibited least shrinkage strain with 0.105%, followed by MT10 and OPC with 0.120% and 0.125%. The MT20 samples exhibited the highest shrinkage of 0.140%.

The Fig 5.40 (b) showing expansion strain of the samples. There were increase and decrease in strain values with passage of time, however it is to be noted that all of MT samples exhibited strain above zero, indicated there is swelling in sample and hence it can be inferred that there is still demand for water.

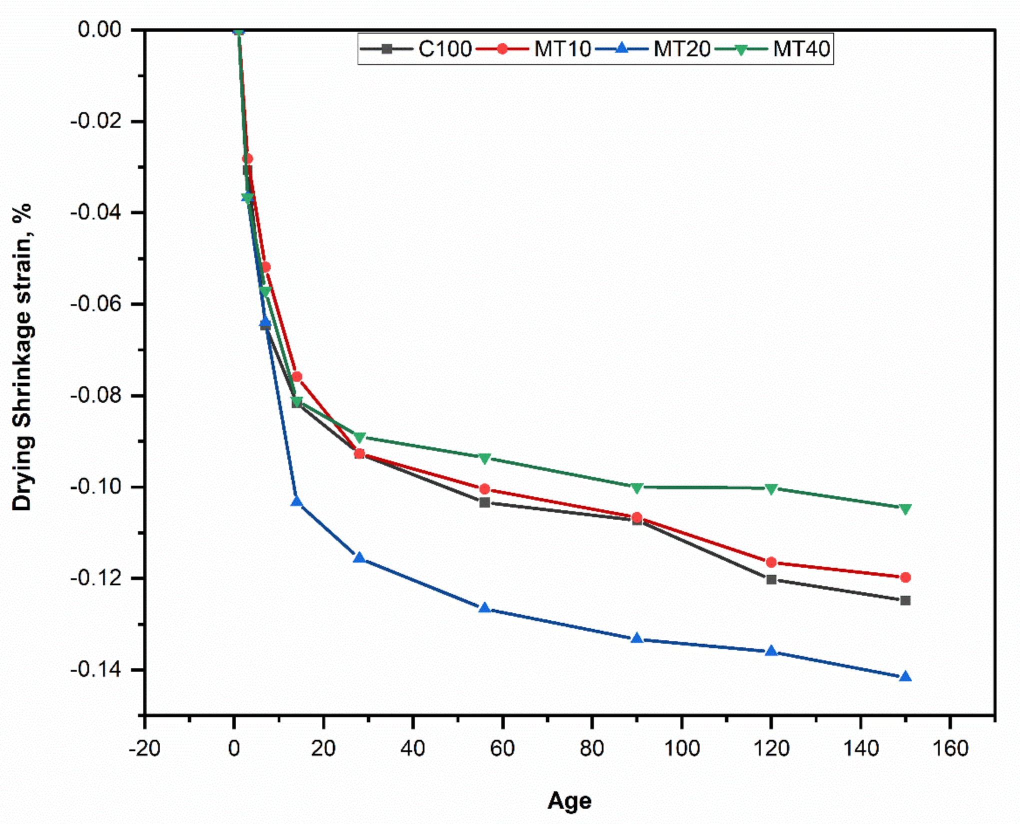

(a)

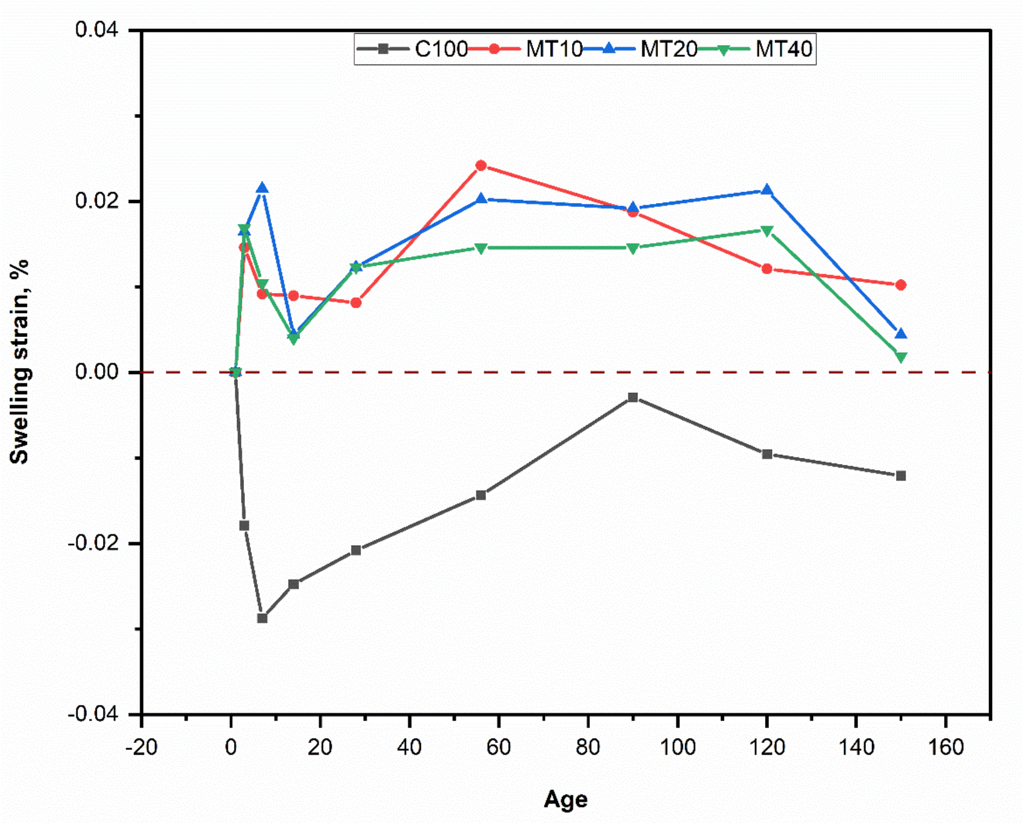

(b)

Fig. 5.40: Shrinkage and expansion observed in samples containing 0%,10%, 20%, and 40% of MTCT850 (a) Shrinkage (b) Expansion.

The drying shrinkage and expansion of OPC and ST samples monitored for 150 days are reported in Figs. 5.41 (a) and (b). As in case of MT samples it can be seen that the drying shrinkage of ST increases with time and the rate of shrinkage decreased after 7 days. At the end of 3 days the shrinkage values were 0.031%, 0.039%, 0.014% and 0.02% for OPC, ST10, ST20 and ST40 respectively, At the end of 7 days the shrinkage of OPC was about 0.065 % and ST10, ST20 and ST40 were 0.066%, 0.066%, and 0.073%. At the end of 150 days, it appeared that the ST40 mixes exhibited least shrinkage strain with 0.129%, following OPC with 0.120% strain. The strain values for ST10 and ST20 were 0.149% and 0.135%. The ST10 samples exhibited the highest shrinkage at the end of 150 days. The Fig 5.41 (b) showing expansion strain of the samples.

There was no particular trend with respect to expansion. There were increase and decrease in strain values with passage of time, however it is to be noted that the order of magnitude of the strain was much less than that of the drying shrinkage and was within the range of -0.04% to 0.02%.

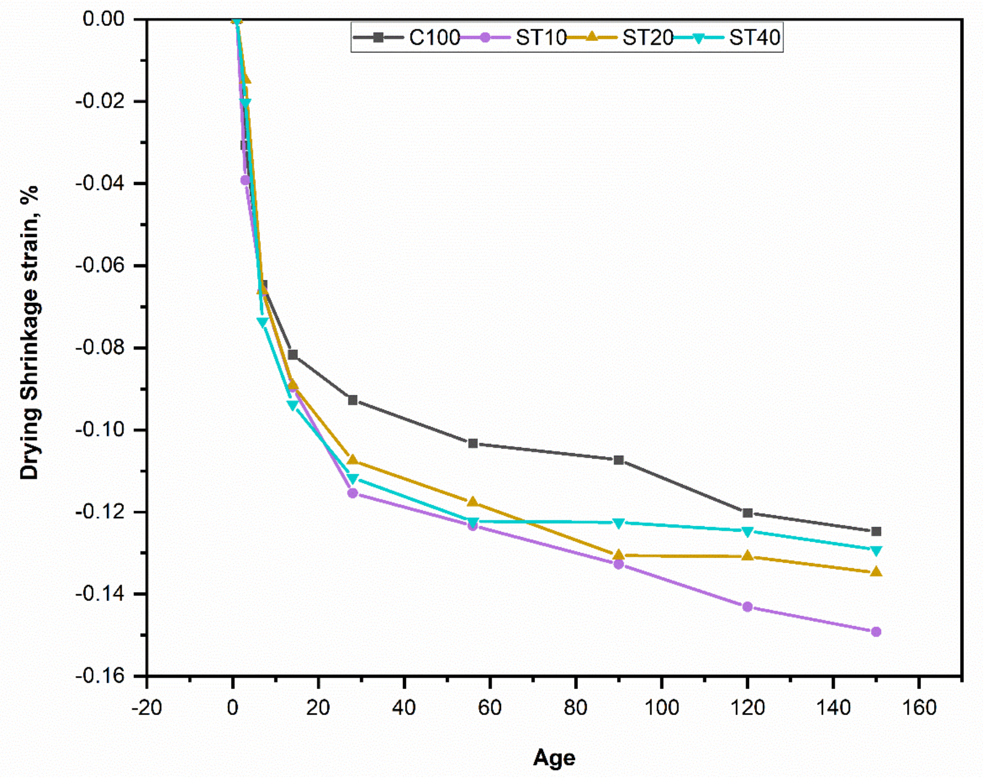

(a)

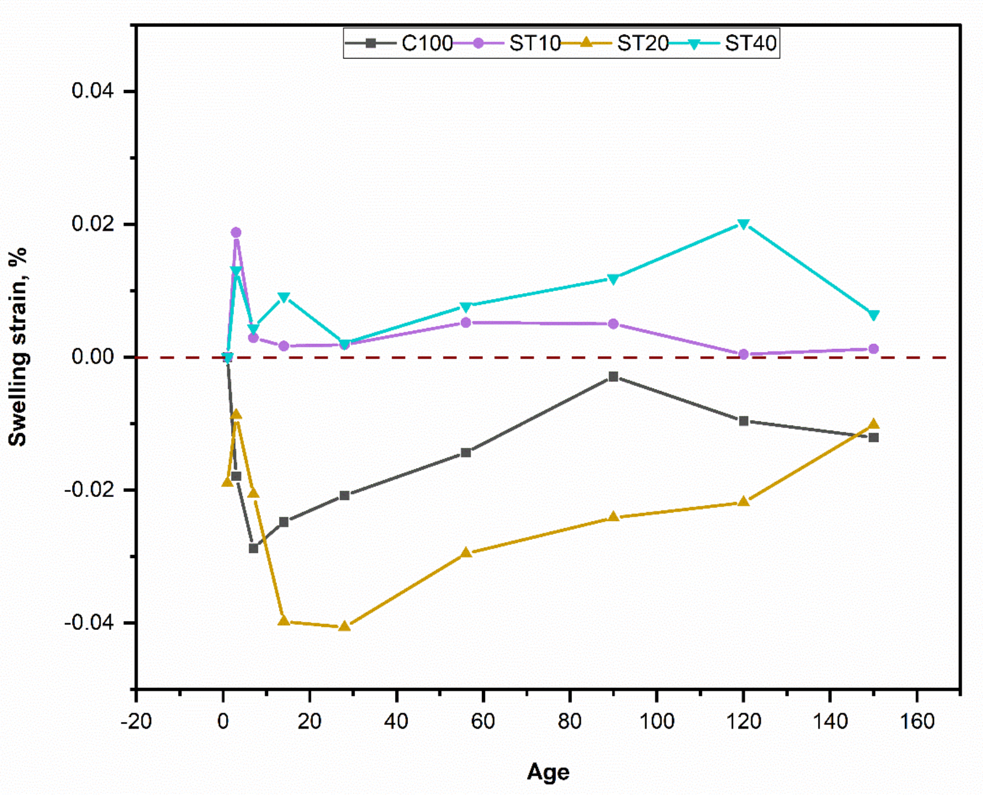

(b)

Fig. 5.41: Shrinkage and expansion observed in samples containing 0%,10%, 20%, and 40% of STCT750 (a) Shrinkage (b) Expansion.

The observed shrinkage strain depicted in Figures 5.40 (a) and (b) is a result of various factors, including pore structure, strain induced by drying shrinkage, and the counteracting effects of the strength developed by the samples and the carbonation products. When considering the MT samples, it was observed that the MT20 mixes demonstrated a notable increase in compressive strength at an early age but exhibited a slower rate of strength gain over a period of 90 days (31% increase from 7 days to 90 days). On the other hand, the MT40 mixes displayed lower early age strength, but demonstrated a higher percentage of strength gain (41% increase from 7 days to 90 days). The observed phenomenon of higher shrinkage in MT40 at early ages and lower shrinkage at later ages can be considered as a potential correlation. Despite the higher powder content, MT40 mixes exhibit higher strength gain and demonstrate better resistance to shrinkage. The performance of MT40 and MT10 was superior to that of OPC.

In contrast, when examining the case of ST mixes, it is observed that the ST10 mixes demonstrated greater strength development within a 90-day period. However, upon considering the sorptivity results, it becomes evident that there is no discernible relationship between the percentage of STCT750 and the pore structure and pore connectivity in the samples. The shrinkage strain observed at 150 days appears to decrease when the percentage of STCT750 increases, likely due to the influence of pore structure, pore network, and water retention capacities of different mixes. Nevertheless, it was observed that all of the ST mixes exhibited higher magnitude of shrinkage when compared to ordinary Portland cement (OPC).

5.10 Conclusions

The performance of the cementitious matrices was assessed across various criteria. Based on the findings from initial setting time tests and isothermal calorimetry for 72 hours, it was observed that the mixes containing MTCT850 and STCT750 exhibited a lower reactivity compared to the OPC mixes. The setting time was observed to increase, while the heat of hydration was found to decrease as the percentage of OPC replacement increased. The heat of hydration of the mixes with MTCT850 and STCT750 were found to be about 66% - 97% of the heat of hydration of OPC mixes across different water to cementitious binder ratios adopted. However, the heat of hydration exhibited by mixes containing 10% and 20% MTCT850 is comparable to or greater than that observed in mixes incorporating silica fume and fly ash. The heat of hydration observed in mixes with 10% STCT750 was found to be greater than that observed in mixes containing silica fume and fly ash. It is to be noted that the heat of hydration was measured only for a period of 72 hours from the time of mixing. Also, the calorimetry studies also indicated the contribution of the added mineral wastes to the heat of hydration by various phenomenon including participation in hydration, creation of additional nucleation sites for hydrate and increase the water to cement ratio due to replacement of cement.

Nonetheless, the examination of mineralogical properties and microstructure of the cementitious pastes over a period of 7 to 90 days at different ages revealed an ongoing process of hydration and enhancement in microstructure as the OPC, MT, and ST mixes aged. The aforementioned studies also demonstrated changes in the chemical, morphological, and physical characteristics of the hydration products that were developed. The XRD analysis of the samples with MTCT850 and STCT750 showed presence of minerals such as biotite, quartz, feldspar, oligoclase from the raw mineral waste. This observation was also confirmed by the SEM images which showed the presence of unhydrated MTCT850 and STCT750 particles in the cement paste samples, especially at early ages of hydration, lower water to cementitious binder ratio and higher percentage replacement of cement by mineral waste. The microstructural analysis also showed the densification of matrix with age and delayed nucleation of CH crystals indicating secondary hydration. The FTIR studies revealed ongoing variations in the chemical makeup and molecular bonding in the hydration products within the identical mix at various ages as well as different mixes.

The strength tests revealed at the end of 90 days the OPC samples had a strength of 70.68 MPa, and the MT mixes exhibited strength in the range of 51.8 MPa and 63.8 MPa, and the same was ST mixes were 63 MPa to 69.8 MPa. Based on the observed strength development, it can be determined that the MT20 and ST20 mixes can be considered the optimum mixes. Interestingly, though the ST mixes exhibited lower heat of hydration than MT mixes in the R3 tests (As discussed in Chapter 4 section 4.8) the ST samples exhibited a strength activity index of 84.5% - 101.3% whereas the MT mixes exhibited a strength activity index of 68.7% 93.2%. This can be attributed to the fact that the STCT750 has higher CaO content as the source STR has about 21% CaO as compared to MTCT850. Based on the high SiO_2 and CaO contents of the STCT750 it can be inferred that the material has a potential to self-react when it comes in contact with water and exhibit latent hydraulic property. The further confirmation of this phenomenon can be performed by determining the bound water content of the R3 samples using thermogravimetry tests and classification of supplementary cementitious material into different categories such as Inert, pozzolanic less reactive, latent hydraulic less reactive, latent hydraulic more reactive and latent hydraulic more reactive. The thermogravimetric study on the paste samples shall also provide more insight with respect to CaO consumption of the samples. The strength activity indices of all the ST and MT mixes, except MT40, were higher than the recommended value of 75% by ASTM C618. The results of the strength activity index, along with the calorimetry data that indicate the heat of hydration contribution from MTCT850 and STCT750. This provides evidence that the mineral wastes utilised in the study are suitable as a supplementary cementitious material (SCM).

The MT20 and ST20 mixes also displayed better performance compared to OPC in terms of carbonation and demonstrated satisfactory performance in terms of sorptivity. In terms of shrinkage, it was observed that the MT40 and ST40 mixes exhibited better resistance to shrinkage compared to the other mixes.

CHAPTER 6
CARBON FOOTPRINT AND ENERGY CONSIDERATIONS

6.1 Introduction

This chapter discusses the environmental benefits of utilizing activated mineral waste, specifically mine tailings and construction and demolition waste (CDW) derived silt, as a cement replacement material. The activation process adopted in this study involves calcination, which helps conversion of some non-reactive phases in these mineral waste to reactive phases This makes the materials more suitable for use as supplementary cementitious materials. The analysis in this chapter estimates the CO_2 emissions, energy consumption associated with the activation of material and compares the same with that of production of OPC. The long-term availability of mineral wastes is also discussed.

6.2 Ordinary Portland Cement

The global cement production was about 4.1 billion tonnes in the year 2022 [2]. This contributes to about 3.7 trillion kg of carbon dioxide emissions at a rate of 866 kg/ t of cement [3], 60-70% of emissions originate from decarbonization of limestone and 20 - 30% from the burning of fuel and operations associated with the cement plant [3] with 30 % and 70% being the most commonly adopted quantities [295]. For the purpose of this study, the CO_2 from decarbonization is assumed to be 70% and from fuel is assumed to be 30%.

The production of cement is an energy intensive process, and the most significant uses of energy are i) fuel required for production of clinker and ii) electricity required to power all drives and operate the plant. The clinkerisation process requires about 3000 - 4000 MJ/t of clinker and the cement plant consumes about 60 – 150 kWh/t [296]. The steps in plant operation include quarrying, processing, and transport, crushing, grinding, homogenization, cement grinding, packing and dispatch [297].

Past studies [12,298] assessed the efficiency of various cement kilns and performed an energy analysis. The findings from the study are reported in Table 6.1. It is to be noted that the study obtained these values with an optimistic kiln efficiency of 61.5% and therefore the values are adjusted to 55% kiln efficiency as this is mostly observed to be in the range of 51 – 57% [12].

Table 6.1: Energy Analysis of a cement kiln for production of cement clinker

Equipment/ Process	**Energy Consumed (MJ/ t)**
Feed	1735.4
Calciner fuel & calciner primary air	809.6
Kiln fuel & Kiln Primary air	755.2
Cooling fans	92.2
Total	**3392.4 MJ/t**

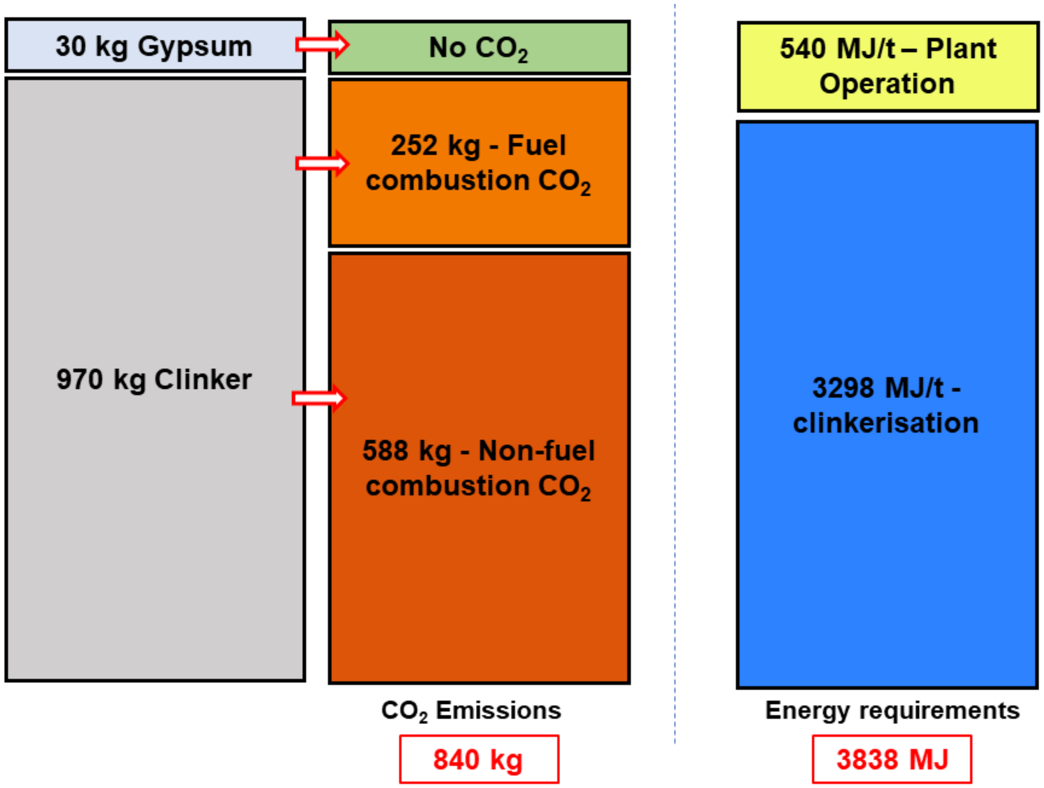

Fig. 6.1: Composition of OPC and the associated CO_2 emissions and energy consumption.

Worldwide efforts are focused on reducing global warming and mitigating greenhouse gas emissions and attempts have been made to reduce the CO_2 emissions from the clinker production by addition of fly ash, silica fume, granulated blast furnace slag and other mineral admixtures into cement as a secondary main constituent.

6.3 Fly ash and Granulated Blast Furnace Slag

The utilization of fly ash and granulated blast furnace slag as substitutes for cement has been extensively investigated [9]. These materials have been employed as replacement for cement in various applications, leading to the consumption of significant quantities of stockpiled fly ash and blast furnace slag in cement production, as well as in mortar and concrete. This has resulted in the recovery and recycling of materials that would otherwise have been dumped in landfill. This approach has also helped in reducing carbon emissions linked to cement manufacturing and enhancing the strength and durability of concrete [14].

Nonetheless, the perpetual availability of these resources is not guaranteed. The gradual transition from non-renewable power sources to renewable power sources will lead to a decrease in the availability of fly ash [14], a byproduct derived from coal-based power generation. This situation could potentially result in a scarcity of fly ash or necessitate the long-distance transportation of fly ash, thereby undermining the efficacy of utilizing fly ash as a means to mitigate carbon emissions.

Likewise, blast furnace slag is a residual material generated during the process of production of iron from Basic Oxygen Furnaces. Most of these furnaces are being converted to electric arc furnaces due to efficiency considerations [14]. Electric arc furnaces do not produce blast furnace slag, leading to a global reduction in the production of granulated blast furnace slag. Predictions expect a consumption of existing stockpiles of fly ash and granulated blast furnace slag by around 2023 and 2025 in the UK leading to a potential shortage and raising the need for these materials to be outsourced from other global sources [14] .

The depletion of current sources may result in a potential scarcity of fly ash and granulated blast furnace slag. Particularly in the present scenario, it is projected that the global urban population will exceed 6680 million by 2050, as compared to the current urban population of 4378 million [6]. This trend has the potential to impart substantial strain on existing infrastructure, thereby necessitating new construction and causing an increased demand for construction materials. Therefore, it is necessary to evaluate the possibility of using locally available industrial by-product or waste material as a cement replacement.

6.4 Mineral Waste

The global efforts under the aegis of climate action [17] and EU's “Clean planet for all” [21], recommends clean energy technologies such as photovoltaic conversion, harvesting wind and thermal energy, storage of these energies, electric mobility, and digital technologies (ICT, robotics, 3D printing). Production of these technological equipment requires very high amounts of critical and non-critical minerals posing an increased demand on mining activities [21].

The UK has the record of extensive mining for critical and non-critical minerals historically. Even currently the UK is a home for many ore forming minerals which are mined for many major commodities such as galena (PbS) for lead (Pb), sphalerite (ZnS) for zinc (Zn), and chalcopyrite (CuFeS2) for copper (Cu). The other major commodities produced in the UK include iron (Fe), tin (Sn), tungsten (W), gold (Au), titanium (Ti), aluminium (Al), manganese (Mn), uranium (U), and chromium (Cr) [299]. Apart from these major commodities, the UK produces about 18 critical raw materials as byproducts of mining operations; these elements include Antimony, Rare earth elements, Niobium, Graphite, Tungsten, Platinum, Magnesium, Silicon, Palladium, Tantalum, Tin, Cobalt, Bismuth, Manganese, Lithium, Titanium, Nickel, and Molybdenum [299]. A similar trend for mining is found globally with China being the dominant supplier of more than 20 critical raw materials and other countries like USA, South Africa and Brazil being the dominant suppliers of specific minerals [300,301].

All of these mining activities are associated with production of mineral wastes, especially mine tailing. The current estimate of stored/ dumped quantity of mine tailing is 217 billion tonnes and the predicted annual growth is 12.3 km^3 [19,20]. This number encompasses the waste from active, inactive, and closed facilities. This shall further increase with the increased mining to meet the production associated with “Clean planet for all”, program. Mineral waste will therefore become a more suitable source to be explored for use in cements.

On the other hand, CDW is the largest waste stream in the EU in terms of mass contributing to 374 million tonnes in the EU, in 2016 [302]. Considering this, the EU developed a waste framework directive which targeted re-use, recycling, and other material recovery of about 70% of the non-hazardous construction and demolition waste [42]. The global market for managing CDW witnessed a growth from $179.51 billion in 2022 to $188.81 billion in 2023 [30]. This suggests that there is an increase in recycling of CDW and a recent report [31] shows that in 2021 of the total 253 Mt of aggregates consumed in the UK, 63 Mt were recycled aggregates. Therefore, the fine fractions generated from CDW recycling is also proportionately increasing, making them good potential candidates for use in cement.

6.5 Energy consumption and Carbon Dioxide Emissions for Processing Mineral Waste

6.5.1 Energy consumption

In this study, a laboratory furnace was utilized to process mineral waste. Consequently, the energy calculation and estimation for large-scale production was conducted directly rather than relying on extrapolation. The calculations are derived from the discussions presented in section 6.2 and employ a methodology akin to that employed in the study referenced [252], considering the specific heat capacity of the material. However, as this approach has its own limitations the accuracy of the approach is also validated by using the same approach to find the specific heat capacity of the standard minerals and comparing the same with their actual specific heat capacity.

“The specific heat capacity of a material describes how much energy is required to change the temperature of 1 unit mass of that material by 1 unit temperature” [303] [23].

As the mineral waste used in the study is a mixture of various minerals the specific heat capacity value is estimated as the sum of specific heat capacity of the constituents of the mineral waste. The use of mineral composition for estimation of specific heat capacity would have been more accurate, however, the mineral waste used int study contain about 40% amorphous phases which are not specifically identified by XRD and also the existing minerals change from one phase to another during the process of activation. Therefore, the oxide composition of the material as obtained from X-ray fluorescence analysis is used for estimation of specific heat capacity.

The specific heat capacities of mineral waste can be estimated by adding the heat capacities of its constituent oxides given in Table 6.2.

Table 6.2: Heat capacities of the oxides present in mineral waste obtained from literature [304,305]

Oxides	Heat Capacity J $K^{-1}mol^{-1}$	Molecular weight	Heat Capacity J $K^{-1}kg^{-1}$
SiO_2	44.42	60.09	739.22
Al_2O_3	79.01	101.96	774.91
Fe_2O_3	104.77	159.69	656.08
Na_2O	68.56	61.98	1106.16

MgO	37.26	40.30	924.57
K_2O	84.53	94.20	897.35
CaO	42.42	56.08	756.42
SO_3	180	80.06	2248.31
TiO_2	55.10	79.90	689.61
BaO	47.06	153.34	306.90
Mn_3O_4	99.04	228.81	432.85
V_2O_5	127.37	181.89	700.26
ZnO	41.07	81.38	504.67
ZrO_2	56.21	123.22	456.18
NiO	44.29	74.71	592.83
P_2O_5	105.86	141.94	745.81

It is important to note that the light elements, ranging from hydrogen (H) to sodium (Na), possess lower energy levels, rendering them insignificant for detection by the X-ray fluorescence analyser's detector. Hence, these oxides (except Na), including the carbon content of the sample, were not quantified by XRF analysis and were omitted from the specific heat capacity calculations. The calculation also does not consider the exothermic or endothermic processes and also ignores the latent heat reactions that occur during the changes in state, for examples in case of oxides such as SO_3 and K_2O. Furthermore, it is assumed for the purpose of this computation that the specific heat capacity values remain constant regardless of changes in temperature.

As these calculations involve a few assumptions to simplify the process it is essential to validate the accuracy of the approach. To validate the accuracy of the results the specific heat capacities of certain known minerals are calculated using this approach and compared with their actual specific heat capacity and reported in Table 6.3. The chemical composition of quartz, aragonite, muscovite, and biotite obtained from literature [306–309] were used for calculations.

$$Specific\ Heat\ capacity\ of\ Quartz$$

$$= \frac{1}{100}[100 \times C_v(SiO_2)]$$

$$= \frac{1}{100} \times [\ 100 \times 739.22]$$

= 739.22 J/ kgK

$$Specific\ Heat\ capacity\ of\ Aragonite$$

$$= \frac{1}{100}[56.03 \times C_v(CaO) + 43.97 \times C_v(SiO_2)$$

$$= \frac{1}{100} \times [\ 56.03 \times 756.42 + \ 43.97 \times 846]$$

= 795.8 J/ kgK

$$Specific\ Heat\ capacity\ of\ Muscovite$$

$$= \frac{1}{100}[44.25 \times C_v(SiO_2) + 34.67 \times C_v(Al_2O_3) + 1.47 \times\ C_v(Fe_2O_3)$$
$$+ 0.54 \times (Na_2O) + 1.07 \times C_v(MgO) + 10.74 \times C_v(K_2O) + 0.23 \times C_v(CaO)$$
$$+ 0.95 \times C_v(H_2O)]$$

$$= \frac{1}{100}[44.25 \times 739.22 + 34.67 \times 774.91 + 1.47 \times 656.08 + 0.54 \times 1106.16$$
$$+ 1.07 \times 924.57 + 10.74 \times 897.35 + 0.23 \times 756.42$$
$$+ 0.95 \times 4182]$$

= 759.12 J/ kgK

$$Specific\ Heat\ capacity\ of\ Biotite$$

$$= \frac{1}{100}[37.93 \times C_v(SiO_2) + 14.09 \times C_v(Al_2O_3) + 7.19 \times\ C_v(Fe_2O_3)$$
$$+ 13.35 \times C_v(FeO)\ + 11.88 \times C_v(MgO) + 9.35 \times C_v(K_2O) + 0.06 \times C_v(F_2O)$$
$$+ 0.11 \times CaO) +\ 0.12 \times (Na_2O) + 3.16 \times C_v(TiO_2)]$$

$$= \frac{1}{100}[37.93 \times 739.22 + 14.09 \times 774.91 + 7.19 \times 1106.1 + 13.35 \times 1039$$
$$+ 11.88 \times 924.57 + 9.35 \times 897.35 + 0.06 \times 315 + 0.11 \times 756.42$$
$$+ 0.12 \times 1106.16 + 3.16 \times 689.61]$$

= 825.69 J/ kgK

Table 6.3: Estimated and actual specific heat capacities of minerals

Compound	**Estimated specific heat capacity (J/ kgK)**	**Actual specific heat capacity (J/ kgK)**	**Variation (%)**
Quartz	739.22	740	0.10
Aragonite	795.8	812.5	2.05
Muscovite	759.12	760	0.12
Biotite	825.69	770	7.23

From Table 6.3 it can be seen that the specific heat capacity of pure minerals estimated by the above methods was an approximation to the actual specific heat capacity of the mineral. The difference between the actual and estimated values ranged from 0.10% to 7.23% for the considered minerals. Though not accurate, in absence of other necessary data this estimation provides an insight into determination of energy required for the calcination of the mineral waste used in this study.

The oxide composition of the MTCT850 discussed in Chapter 4. Section 4.3 is used for the estimation of the specific heat capacity. As the obtained values are in percentages the corresponding values for one kilogram of the material is used in the calculation.

$$
\begin{aligned}
&Specific\ Heat\ capacity\ of\ MTR \\
&= \frac{1}{100}[58.46 \times C_v(SiO_2) + 14.56 \times C_v(Al_2O_3) + 9.72 \times\ C_v(Fe_2O_3) \\
&+ 4.36 \times (Na_2O) + 5.91 \times C_v(MgO) + 2.31 \times C_v(K_2O) + 2.43 \times C_v(CaO) \\
&+ 0.27 \times C_v(SO_3) + 1.08 \times C_v(TiO_2) + 0.43 \times C_v(BaO) + 0.02 \times C_v(Mn_3O_4) \\
&+ 0.05 \times C_v(V_2O_5) + 0.06 \times C_v(ZnO) + 0.03 \times C_v(ZrO_2) + 0.03 \times C_v(NiO) \\
&+ 0.19 \times C_v(P_2O_5)
\end{aligned}
$$

$$
\begin{aligned}
&= \tfrac{1}{100} \times [\ 58.46 \times 739.22 + 14.56 \times 774.91 + 9.72\ \times 656.08 + 4.36 \times 1106.16 + \\
&5.91 \times 924.57 + 2.31 \times 897.35 + 2.43 \times 756.42 + 0.27 \times 2248.31 + 1.08 \times \\
&689.61 + 0.43 \times 306.90 + 0.02 \times 432.85 + 0.05 \times 700.26 + 0.06 \times 504.67 + \\
&0.03 \times 456 + 0.03 \times 592.83 + 0.19 \times 745.81]
\end{aligned}
$$

= 768.04 J/ kgK

The obtained specific heat capacity of the MTR is similar to that of majority of aluminosilicate minerals such as albite 730 J/ kgK, biotite 770 J/ kgK, muscovite 760 J/ kgK, phlogophite 780 J/ kgK, and quartz 740 J/ kgK. [310]

The amount of energy required to raise the temperature of the mineral waste to a required temperature is given in Eq. 6.1[252]:

$$E = m \times c \times \Delta T \quad \text{……………………………….. Eq. (6.1)}$$

where,

E = Energy in kWh
m = mass of material
c = Specific heat capacity in J/kgK
ΔT = Temperature change in ºC

In the case of MTCT850, the temperature of the material has to be increased from room temperature (21ºC) to 850ºC. Therefore, the energy required for calcination of 1 tonne is calculated as below,

E_{MT} = 1000 × 768.04 × (850-21)
= 637 MJ
= 176.9 kWh

Similarly, for STCT750, the specific heat capacity is calculated as below,

$$
\begin{aligned}
&Specific\ Heat\ capacity\ of\ STR \\
&\quad = \frac{1}{100}[56.87 \times C_v(SiO_2) + 10.16 \times C_v(Al_2O_3) + 5.53 \times\ C_v(Fe_2O_3) \\
&\quad + 0.45 \times (Na_2O) + 1.25 \times C_v(MgO) + 1.67 \times (K_2O) + 21 \times C_v(CaO) \\
&\quad + 1.39 \times C_v(SO_3) + 0.71 \times C_v(TiO_2) + 0.48 \times C_v(BaO) + 0.06 \times C_v(Mn_3O_4) \\
&\quad + 0.02 \times C_v(V_2O_5) + 0.02 \times C_v(ZnO) + 0.04 \times C_v(ZrO_2) + 0.02 \times C_v(NiO) \\
&\quad + 0.29 \times C_v(P_2O_5
\end{aligned}
$$

$$
\begin{aligned}
&= \tfrac{1}{100} \times [\ 56.87 \times 739.22 + 10.16 \times 774.91 + 5.53\ \times 656.08 + 0.45 \times 1106.16 + \\
&1.25 \times 924.57 + 1.67 \times 897.35 + 21 \times 756.42 + 1.39 \times 2248.31 + 0.71 \times \\
&689.61 + 0.48 \times 306.90 + 0.06 \times 432.85 + 0.02 \times 700.26 + 0.02 \times 504.67 + \\
&0.04 \times 456 + 0.02 \times 592.83 + 0.29 \times 745.81]
\end{aligned}
$$

= 766.36 J/ kgK

Similar to MTR, STR has a specific heat capacity similar to that of silicate and aluminosilicate minerals.

And using Eq. 6.1, the energy required is determined as follows,

$$
\begin{aligned}
E_{ST} &= 1000 \times 766.36 \times (750\text{-}21) \\
&= 559\ \text{MJ} \\
&= \mathbf{155.28kWh}
\end{aligned}
$$

The energy values given in this section represent the amount of energy necessary for the calcination process of the feed material. In order to determine the total energy needed, taking into account a kiln efficiency of 55% (comparable to the value presented in section 6.2), the energy estimations are provided in Table 6.2. To estimate the fuel requirements for a reduced calcination temperature, the values for calciner fuel and kiln fuel from Table 6.1 are proportionally reduced. The cement calcining temperature has been established to be 1450 ^{o}C. For the MTCT850, a factor of 850/1450 is employed, while for the STCT750, a factor of 750/1450 is utilised. However, the energy demand curve is a complex process including various factors such as type of fuel, moisture content of the feed, chemical composition of the feed, latent heat associated with phase changes and chemical changes of the feed [311,312]. Unfortunately. Detailed data regarding these factors are not available for the materials used in the study and are not included in the scope of the study. As a result, though considering a linear relationship is expected to give a slight overestimation of the energy requirements the same has been employed for the estimation in this study due to the lack of available data.

The data presented in Table 6.4 illustrates that the energy savings achieved in the production of one metric tonne of MTCT850 amount to 38.7%, while for STCT750 the energy savings reach 45.6%. It is to be noted that the processed mineral waste can directly be mixed with cement and does not require milling, unlike clinker. However, due to variation in energy values with the feed material and lack of availability of specific data this savings is not considered as a part of calculations in this study. The study assumes a plant operation energy of 540 MJ/ t for all cementitious binders.

Table 6.4: Energy Analysis of a kiln for production of mineral waste for use in cementitious binders

Equipment/ Process	**Energy Consumed (MJ/ t) MTCT850**	**Energy Consumed (MJ/ t) STCT750**
Feed (Obtained from calculations in section 6.5.1, adjusted to 55% efficiency)	1158	1016
Calciner fuel & calciner primary air	477	429
Kiln fuel & Kiln Primary air	445	400
Cooling fans	-	-
Total	2080	1845

6.5.2 Carbon dioxide emissions

In a comparable manner, when examining carbon dioxide emissions, it is postulated that the amount of CO_2 released during the combustion of fuels for calcination of mineral waste is equivalent to that generated during the clinkerisation process. The values mentioned earlier have been appropriately scaled down to correlate with the corresponding decrease in calcination temperature.

Loss on ignition values correspond to the sum of decomposition of organic matter, hydroxides and decarbonization during heating. However, in this study, with respect to the decarbonization-related CO_2 emissions, it was conservatively assumed that all the loss on ignition values presented in Table 4.1 of Chapter 4 originate from the decarbonization process of the material. Hence, it is assumed that the decarbonization the decarbonization of STCT750 is associated with an 18.43% (of weight of mineral waste) of CO_2 emissions. However, similar approach might not be suitable for MTCT850 as the loss in weight is associated with the direct oxidation of graphite in MTR. The Rietveld analysis of samples revealed that the MTR samples contained about 13% of graphite.

Approximately 14% of the total energy utilised in the production of 1 tonne of clinker is attributed to plant operations, amounting to 540 MJ per tonne [297]. Since it is assumed that the value remains constant for all the blends, it is also assumed that the corresponding percentage of fuel consumption and hence the carbon di oxide emissions remains constant. The remaining 86% of carbon dioxide emissions resulting from fuel combustion can be accounted for the reduction in calcination temperature. The CO_2 emissions associated with gypsum production is considered zero [313]. The tabulated values of CO_2 emissions are presented in Table 6.5.

Table 6.5: CO_2 Emissions for production of OPC and Mineral waste processing

Type	**kg/ t of Clinker**	**kg/ t of MTCT850**	**kg/ t of STCT750**
Fuel combustion CO_2 for plant operation	37	37	37
Fuel combustion CO_2 for Calcination/ clinkerisation	223	131	116
Decarbonisation CO_2	606	477	190
Total	866	645	313

The energy and carbon considerations for the different cementitious binders prepared in the current study are presented in Figure 6.2 (a) to (c) for MT mixes and Figure 6.3 (a) to (c) for ST mixes, as indicated by the aforementioned findings.

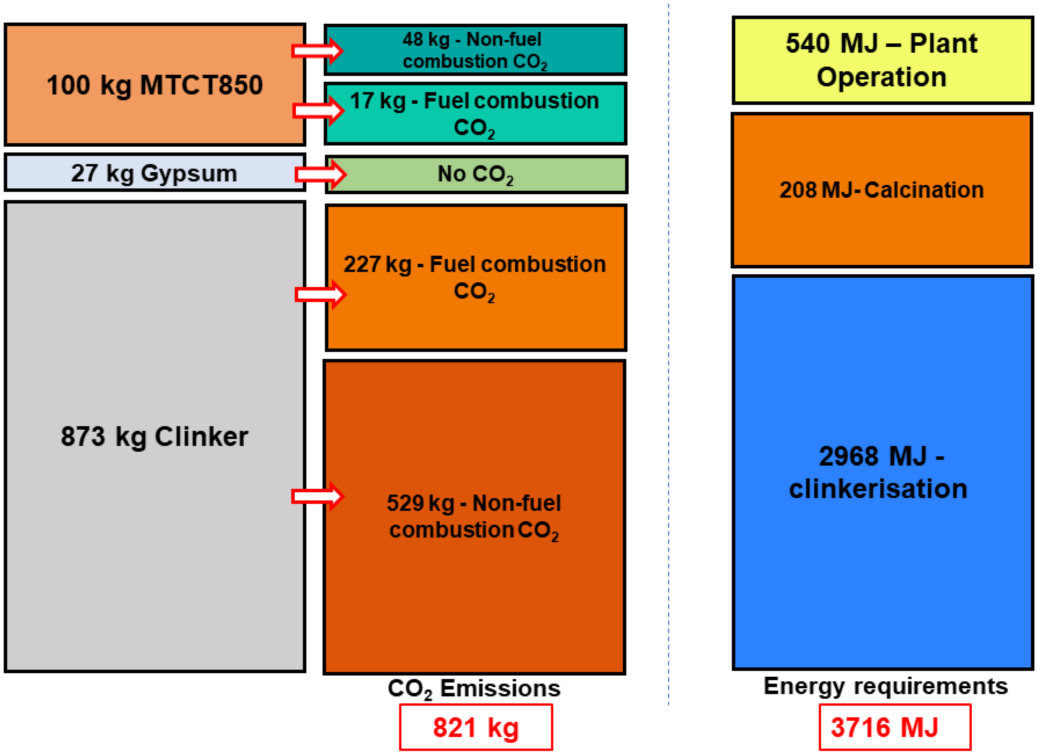

(a)

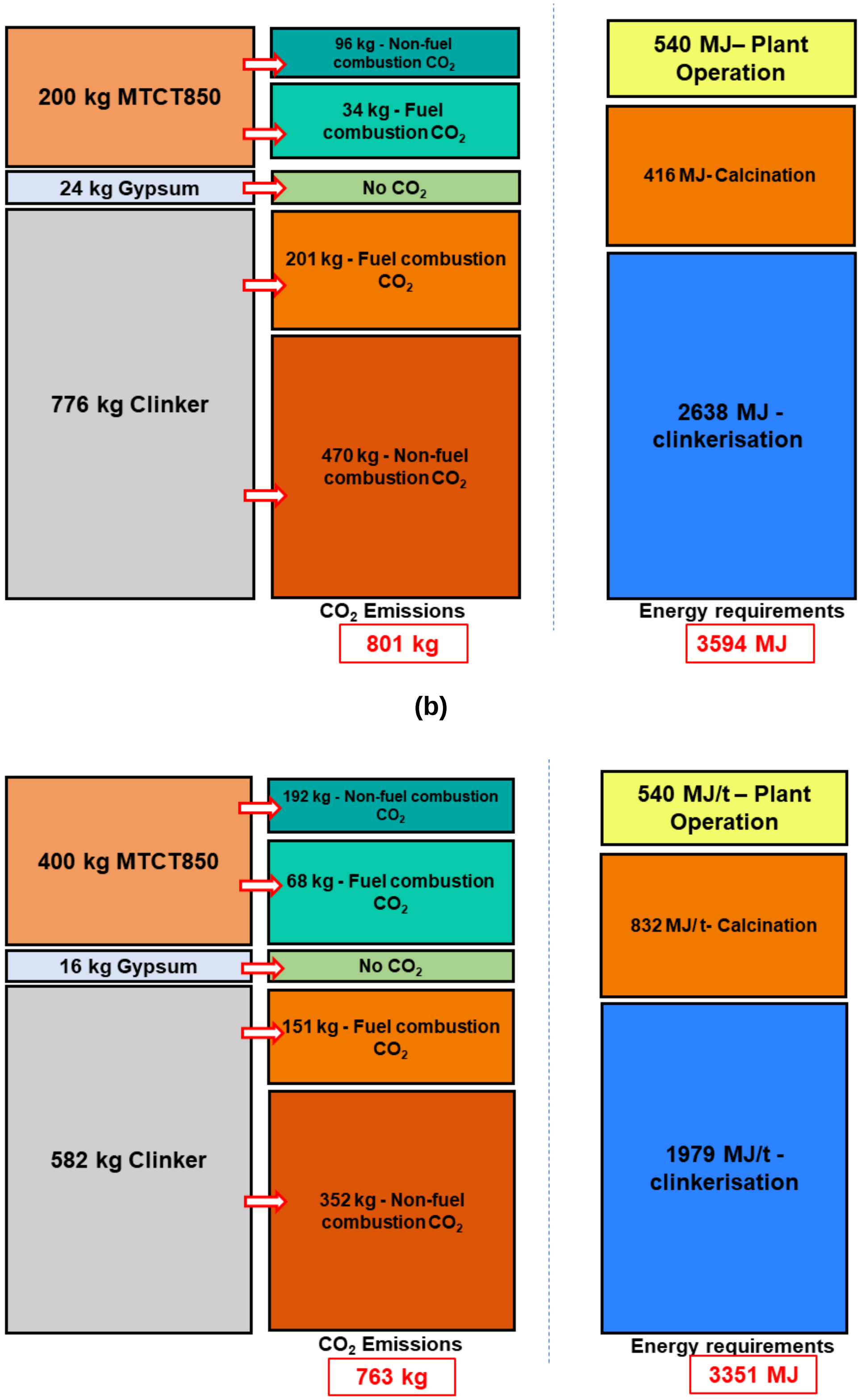

(b)

(c)

Fig. 6.2: Composition of cementitious binder with MTCT850 and the associated CO_2 emissions and energy consumption. (a) 10% cement replacement (b) 20% cement replacement (c) 40% cement replacement.

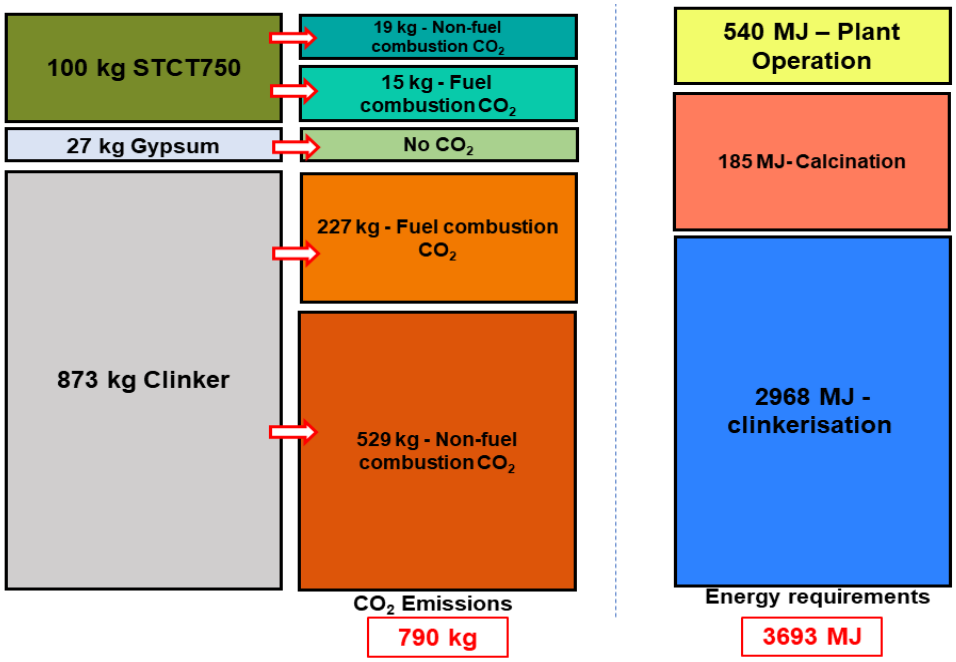
100 kg STCT750
27 kg Gypsum
873 kg Clinker
19 kg - Non-fuel combustion CO_2
15 kg - Fuel combustion CO_2
No CO_2
227 kg - Fuel combustion CO_2
529 kg - Non-fuel combustion CO_2
CO_2 Emissions
790 kg
540 MJ – Plant Operation
185 MJ - Calcination
2968 MJ - clinkerisation
Energy requirements
3693 MJ

(a)

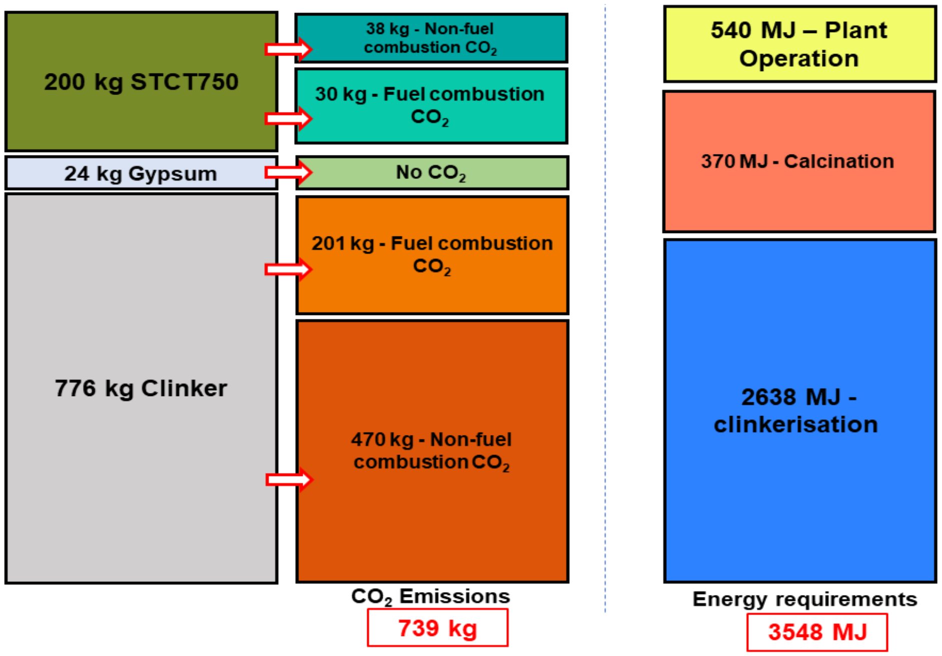
200 kg STCT750
24 kg Gypsum
776 kg Clinker
38 kg - Non-fuel combustion CO_2
30 kg - Fuel combustion CO_2
No CO_2
201 kg - Fuel combustion CO_2
470 kg - Non-fuel combustion CO_2
CO_2 Emissions
739 kg
540 MJ – Plant Operation
370 MJ - Calcination
2638 MJ - clinkerisation
Energy requirements
3548 MJ

(b)

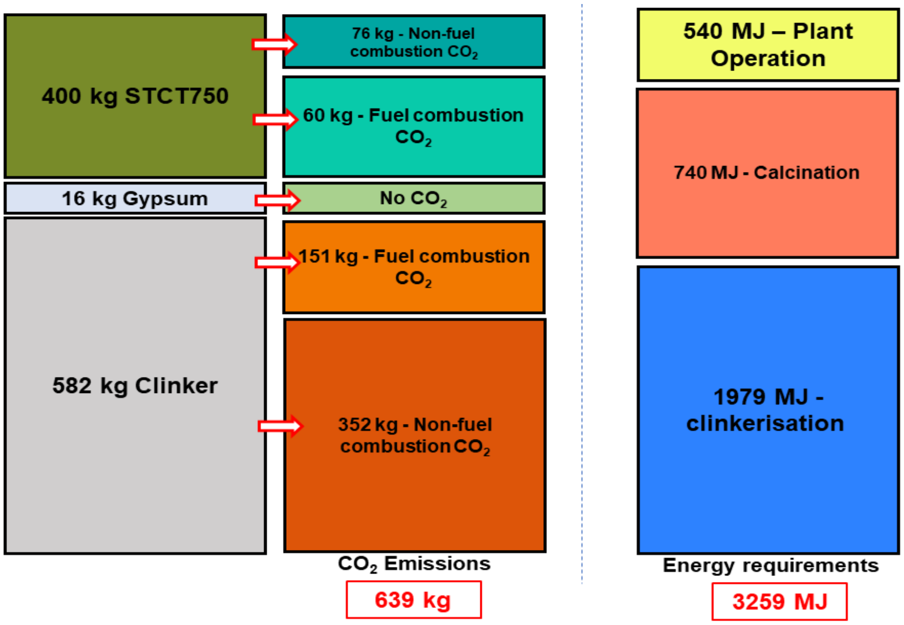

(c)

Fig. 6.3: Composition of cementitious binder with STCT750 and the associated CO_2 emissions and energy consumption. (a) 10% cement replacement (b) 20% cement replacement (c) 40% replacement.

And these finding are summed up in Figure 6.4. from which it is evident that the amounts of carbon dioxide emissions exhibited a reduction of 2.23%, 4.6%, and 9.2% when the replacement of MTCT850 was 10%, 20%, and 40% respectively. Likewise, the energy consumption showed a reduction of 3.2%, 6.5%, and 12.8%. Similarly, for STCT750, the reduction in carbon dioxide emissions were 6%, 12% and 24% for 10%, 20% and 40% replacement and the reduction in energy consumption was 3.8%, 7.6% and 15.2%.

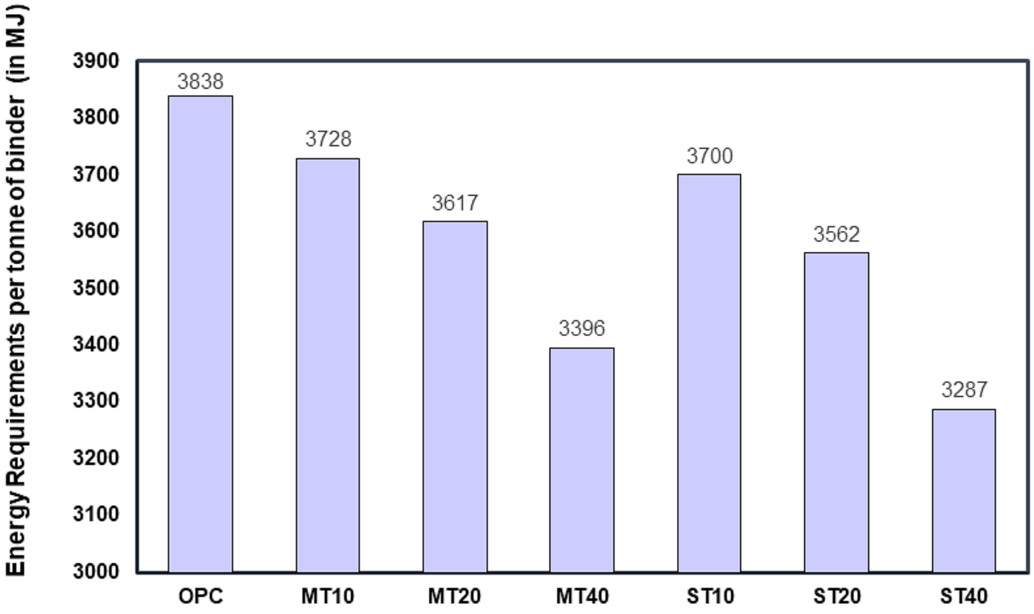

(a)

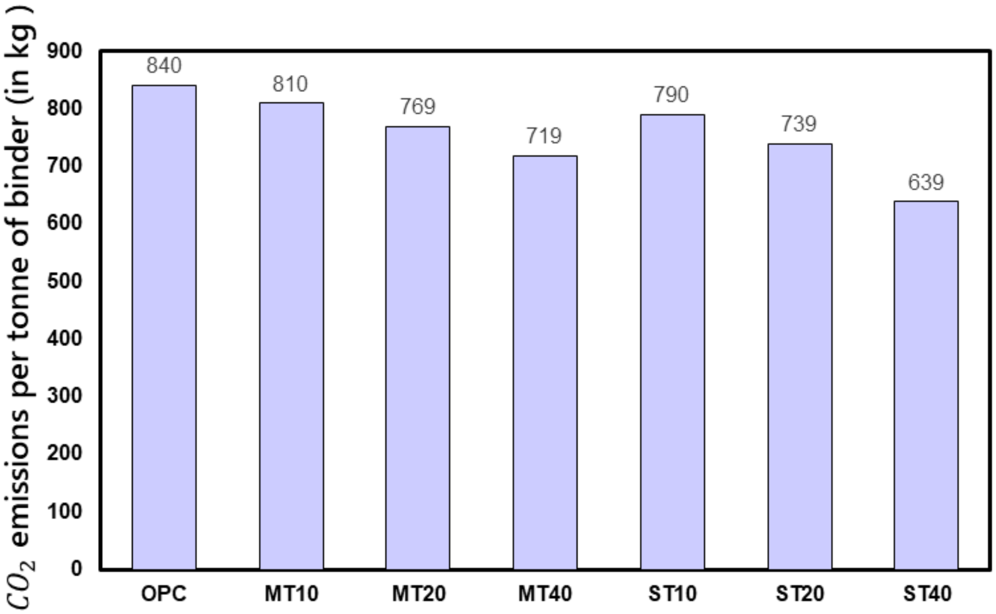

(b)

Fig. 6.4: (a) Energy requirements and (b) CO_2 emissions per tonne of binder with different percentages of mineral waste.

6.6 Conclusions

Growing demand for Ordinary Portland Cement (OPC) and the environmental burden linked to its production, including energy consumption, greenhouse gas emissions, and strain on raw materials, have underscored the urgency to mitigate these impacts. Despite the demonstrated efficacy of materials such as fly ash and granulated blast furnace slag in mitigating the detrimental impacts associated with cement production, it is worth noting that the availability of these resources is progressively diminishing.

In contrast, the endeavours undertaken by diverse governmental organisations as a part of climate action to mitigate emissions are complemented by the net-zero approach, which advocates for waste reduction and reuse. However, it is important to note that the clean energy and zero emissions approach also entails a significant reliance on mineral resources. These processes, in turn, generate additional mineral wastes. Upon examination of mining operations in both the United Kingdom and globally, it becomes evident that they are widely dispersed. The appeal of their utilisation extends beyond the waste-to-wealth perspective, encompassing considerations of their availability as well.

Furthermore, based on the information provided in the chapter, it is evident that the utilisation of these materials results in a reduction of carbon dioxide emissions ranging from 2.2% to 15.2 % when adopting a conservative approach. Additionally, energy consumption is decreased by approximately 3% to 15%, equivalent to a range of 122 to 579 MJ/ tonne of binder.

CHAPTER 7
CONCLUSIONS AND RECOMMENDATIONS

7.1 Executive Summary

Civil infrastructure growth will keep expanding to meet the needs of modern urban societies., for decades to come. The growth in civil infrastructure is closely associated with the use of natural resources for the manufacture of construction. Concrete is the dominant construction material and the key element in most infrastructure assets.

Portland cement used in preparation of concrete is one of the most used and manufactured materials in the planet [1] with about 4.1 billion tonnes being produced annually accounting for ~8% of global anthropogenic CO_2 emissions. The process of cement manufacturing is characterised by a high demand for energy, particularly during the clinkerisation stage, which consumes around 3.5 GJ/ton [46]. Cement production is widely recognised as a significant contributor to carbon emissions.

Despite ongoing efforts to address the growing demands and mitigate the environmental effects of cement production through the utilisation of supplementary cementitious materials, alternative cements [1,4,9], alternative fuels [10–12], and alternative technologies [10,13], this would not be enough to meet more than 10 -15% of the projected demands[8]. The production of well-established supplementary cementitious such as fly ash and granulated blast furnace slag are in decline [14]. The global initiatives on climate action [17] recommend more environment friendly technologies, including shift in steel industry from blast furnace to electric arc furnace. This will result in the production of granulated blast furnace slag will also decrease. Similarly, all the coal fuelled power plants will gradually shift towards a greener fuel making the availability of fly ash scarce Though, it might not be a pivotal shift immediately across the globe, these changes might affect the availability of these materials locally. This makes it vital to explore other sources for use in cementitious binders as an addition or a replacement.

The global initiatives on climate action, as well as the European Union's "Clean planet for all" campaign, also advocate for the adoption of clean energy technologies including photovoltaic conversion, wind and thermal energy harvesting, energy storage, electric mobility, and digital technologies such as robotics, and 3D printing [17,21]. The production of all these items is extremely dependent on minerals necessitating significant quantities of such materials. Such an increase in demand will also pose a need to explore lower quality ores for extraction. The use of low-quality ore also means production of more quantities of waste in the process.

The mining waste arises in a lot of forms including coarse wastes such as stripped soil, weathered rock, and fine-grained wastes such as tailings red mud, coal refuse, wash slime and any other unusable waste left after mineral processing etc [22,23]. These fine wastes are typically of particle size less than 1 mm [22]. Solid form mineral wastes are disposed in landfills. The fine wastes are in general disposed in form of slurry to avoid air pollution due to fine particles during transport and disposal [22]. The slurry is disposed into a cell, confinement, pond, or dam [23], called mine tailing dam. Mineral wastes may be alkaline, contain metals and acidic substances [24]. Thus, making mineral waste management a crucial issue as the physico-chemical characteristics of the wastes have severe impact on the soil and ground water including acid drainage [25]. Besides the physico chemical characteristics of the wastes, the sheer quantity itself poses major environmental issues, especially on occurrence of mine tailing dam failure.

Construction and demolition waste (CDW) is another significant source of waste generation worldwide, accounting for a substantial percentage of the total waste generated in many countries. Considering this EU developed waste framework directive which targeted re-use, recycling, and other material recovery of about 70% of the non-hazardous construction and demolition waste. A recent report [31] shows that in 2021 of the total 253 Mt of aggregates consumed in the UK, 63 Mt were recycled aggregates. Nevertheless, the primary emphasis of these recycling facilities is on the recycling of larger aggregates and certain finer fractions [32,33]. The finer fractions in the size range of silt particles are unused and are disposed of in a landfill. Therefore, there is an increasing proportion of finer fractions generated from CDW recycling contributing to the increasing volumes of waste in landfill.

As the construction sector keeps utilising large volumes of pristine natural, non-renewable, materials for the manufacture of cement and concrete, the Construction and Building materials research under Horizon 2020 program of Europe 2020 strategy promotes materials for energy efficiency including materials with low embodied energy and materials capable of reusing a high waste content [34].

One such waste that can be used in construction is the mineral waste or mining and quarrying wastes. Every year more than 700 million tons of mineral wastes are being disposed in landfills globally [34] and in UK mineral wastes constitute about 35% of the total waste disposed [35]. The mine tailing derived from mining processes and CDW silt derived from CDW recycling processes constitute a significant quantity of the total mineral waste.

Therefore, this study focuses on developing a suitable treatment for mineral waste for its use as a binder precursor. Considering this the primary objective of the current investigation was:

To utilize mineral wastes in the development of alternative cementitious binders which will lead to cement-based systems less dependent on pristine natural resources and with lower embodied energy.

This aim was achieved through the following steps.

- The mineral wastes were characterised and assessed for their suitability to be used in cementitious binder.

- An optimal treatment process was determined to convert non-reactive, crystalline, and inert phases of the mineral waste to amorphous and reactive phases.

- Binders prepared with mineral wastes were evaluated for their performance in cementitious matrices.

The key findings from the above objectives are summarised in the following sections:

7.2 Conclusions

The experimental methodology was designed to meet the objectives also in consideration with the scope and limitations. The research was carried out in three phases. In the initial stage, analyses were performed to characterise the raw mining tailings and CDW derived silt. Different activation methods were employed, taking into consideration the mineralogical characteristics. The research entailed analysis and comparison of the characteristics of untreated mine tailings and treated mine tailings, along with untreated CDW derived silt and treated CDW derived silt. In the second phase of the study, the samples that were activated optimally were chosen. Following this, paste mixes were prepared by replacing 10%, 20%, and 40% of cement with activated mineral waste and with water to binder ratio 0.3, 0.4 and 0.5. The evaluation included an assessment of the microstructure development and mineralogical characteristics of the aforementioned paste mixes. The strength development and durability properties of mortar mixes with various percentages of cement replacement (10%, 20%, and 40%) and a water to binder ratio of 0.4. were evaluated in phase III.

Mineral wastes characterisation

Mineral wastes investigated in this study, namely mine tailings and CDW derived silt exhibited a high silica composition, containing approximately 54-58% SiO_2. It was found that the mine tailings exhibited a comparatively smaller particle size compared to the CDW derived silt, as indicated by their respective D_{90} values of 67 µm and 75 µm. These mineral wastes were a complex mix of various minerals including chlorite, clinochlore, kaolinite, muscovite, phlogopite, biotite, quartz, hornblende, graphite, anhydrite, and plagioclase minerals such as oligoclase, anorthite, and albite for mine tailing, and hematite, k-feldspar, gypsum, orthoclase, ferrosilite, hornblende, feldspar, anhydrite, microcline, albite, illite, quartz, chlorite, muscovite, phlogopite, and calcite for CDW derived silt.

Mineral activation and assessment

The selection of activation methods was determined based on the mineralogical composition of mineral waste. As the initial XRD of mine tailing indicated presence of kaolinite and phlogopite, the calcination temperatures were chosen to be above 650^{o}C. Literature reports that heating above 900 ^{o}C in presence of clay minerals such as kaolinite, illite leads to formation of new crystalline alumino silicate mineral phases such as mullite, which may reduce the reactivity of the activated mineral waste [227,228]. Therefore, calcination temperatures of 650^{o}C, 750^{o}C and 850 ^{o}C were adopted for mine tailing. In the case of CDW derived silt the preliminary analysis indicates presence of calcite whose decomposition temperature is between 700^{o}C and 800 ^{o}C [229]. Calcination temperature of 750^{o}C and 850 ^{o}C were adopted for CDW derived silt.

The initial screening of mine tailing and CDW derived silt with XRD indicated presence of minerals of hardness 2-7 in the Mohs hardness scale. Therefore, milling was conducted using tungsten carbide balls and a tungsten carbide coated container of hardness 9 in the Mohs scale. Milling times of 30 minutes, 60 minutes and 90 minutes were adopted.

The calcination and ball milling regimes adopted for the samples induced alterations in physical structure, mineral phases and morphology. Reduction in particle size was observed in samples following milling. The median particle sizes (D_{50}) of mine tailing were reduced by 37.82%, 46.67% and 55.54% from the initial particle size after 30, 60 and minutes of milling. And the D_{50} values reduced by 52% 66.7% and 72 % after 30 minutes, 60 minutes and 90 minutes of milling. The results obtained from X-ray diffraction and Rietveld analysis revealed the oxidation of graphite and decomposition of clinochlore, and chlorite in mine tailings, as well as the decomposition of calcite and gypsum in CDW derived silt. Alterations in the quantities of all the mineral phases have been observed in both mine tailing and CDW derived silt with all the activation methods adopted. The reactivity assessment of the raw and treated samples was performed by dissolution tests and adapted R3 tests. The dissolution tests indicated the solubility of Al and Si from the mineral waste in an alkaline environment, here 8M NaOH. The adapted R3 tests measured the heat of hydration of the material in tailing within a simulated cementitious matrix. It was found that the mine tailing samples calcined at 850 ^{o}C (MTCT850) and CDW silt samples calcined at 750 ^{o}C (STCT750) exhibited higher heat of hydration compared to other samples. These samples also indicated Si and Al solubility higher than the raw mineral waste. Based on these observations MTCT850 and STCT750 were considered to be the samples subjected to optimum treatment and were used for preparation of cementitious matrices.

The enhanced reactivity of the mineral wastes subjected to this specific temperature was rationalised through the findings from the microstructure study using scanning electron microscopy and transmission electron microscopy. The analysis reveals that the untreated mine tailings and CDW derived silt exhibit a polycrystalline structure with irregular shape. The mineral waste calcined at 650°C showed a more crystalline morphology whereas in samples calcined at a temperature of 750°C and 850°C, the calcined mineral wastes exhibited an increased glassy appearance, accompanied by the presence of sintering and necking indicating the initiation of primary crystallite formation. The glassy appearance indicates the amorphization and defects in the crystal structure of the observed phases. Upon further heating to a higher temperature the mineral waste would have led to formation of newer crystalline phases which might further reduce the reactivity of the sample [259]. Similarly, the microstructure shows that the milling process imparted significant physical changes to the material such as reduced particle size, appearance of flakier particles and cracks in the larger particles. However, as observed from the findings of XRD milling did not have any significant effect on reduction in crystallinity.

Performance of activated minerals in cementitious matrices

The findings from initial setting time tests and isothermal calorimetry for 72 hours, revealed that the mixes containing MTCT850 and STCT750 as a cement replacement exhibited a lower heat of hydration compared to the OPC mixes. The setting time was observed to increase, while the heat of hydration was found to decrease as the percentage of OPC replacement by mineral waste increased. The reason for the time delay can be ascribed to the presence of mineral phases, such as quartz, oligoclase, anorthite, and biotite, which collectively make up approximately 47% of MTCT850 and do not participate readily in hydration reactions. Similarly, in the case of STCT750 the presence of quartz, and orthoclase which are inert and do not participate in cement hydration reactions, while anhydrite turns into gypsum upon reaction with water. The paste mixes with STCT750 suggests the presence of quartz, orthoclase which is inert and does not participate in cement hydration reactions, as well as anhydrite. Anhydrite which is an anhydrous form of calcium sulphate readily transforms to gypsum upon exposure to water. The presence of gypsum actively retards the setting of cement and thus contributes to a delayed initial setting time.

The examination of mineralogical properties and microstructure of the cementitious pastes over a period of 7 to 90 days at different ages revealed an ongoing process of hydration. The XRD analysis showed presence of biotite, quartz, feldspar, oligoclase from the mineral waste. This observation was also confirmed by the SEM images which showed the presence of unhydrated MTCT850 and STCT750 particles in the cement paste samples, especially at early ages of hydration, lower water to cementitious binder ratio and higher percentage replacement of cement by mineral waste. The FTIR studies revealed ongoing variations in the chemical makeup and molecular bonding in the hydration products confirming the densification of matrix and ongoing hydration as observed in the microstructure.

The strength tests revealed at the end of 90 days the OPC samples had a strength of 70.68 MPa, and the MT mixes exhibited strength in the range of 51.8 MPa and 63.8 MPa, and the same was ST mixes were 63 MPa to 69.8 MPa. Based on the observed strength development, it can be determined that the mixes with 20% MTCT850 (MT20) and mixes with 20% STCT750 (ST20) can be considered the optimum mixes.

The MT20 and ST20 mixes also displayed better performance compared to OPC in terms of carbonation and demonstrated satisfactory performance in terms of sorptivity.

The utilisation of mineral wastes results in a reduction of carbon dioxide emissions ranging from 6% to 27% and energy consumption is decreased by approximately 3% to 15%, equivalent to a range of 122 to 579 MJ/ tonne of binder depending on the percentage of replacement.

The aforementioned tests produced findings that both collectively and individually suggest that the treatment processes employed, (i.e.) calcination and ball milling, has resulted in effective alterations to the particle size, morphology, and mineralogy of the material. This demonstrates that the strategy for selection of treatment process for the material based on its mineralogical composition has proven to be successful. The mine tailing and CDW derived silt, when subjected to suitable treatment, demonstrated promise as a viable component in high-strength cement, with replacement levels of up to 20 percent. Though the initial hydration reactions and early age strength of the mixes indicated a slower reactivity of the mineral wastes, the microstructure and later age strength development indicate continuous hydration of the mineral waste. This strength gain trend is similar to that of a slow reactive pozzolan such as fly ash. In later ages of hydration and strength development (90 days), the specimens exhibited a strength of 50 MPa or above even at a replacement level of 40%.

In conclusion, the extensive testing and analysis of cement mixes containing MTCT850 and STCT750 as mineral waste replacements for OPC have yielded valuable insights. While these mixes initially exhibited delayed setting times and reduced heat of hydration due to the presence of inert mineral phases, further investigations over a 90-day period revealed ongoing hydration processes. The MT20 and ST20 mixes, with a 20% replacement level, have been identified as the optimum mixes in terms of strength, carbonation resistance, and sorptivity, demonstrating their potential as eco-friendly and high-strength cementitious materials. The key findings of the study can be summed up as represented in Fig. 7.1 which shows that thought there is a reduction in strength of 11% for MT20 and 4% for ST20 mixes at 28 days, the other performances make these binders a sustainable alternative for high strength cementitious materials.

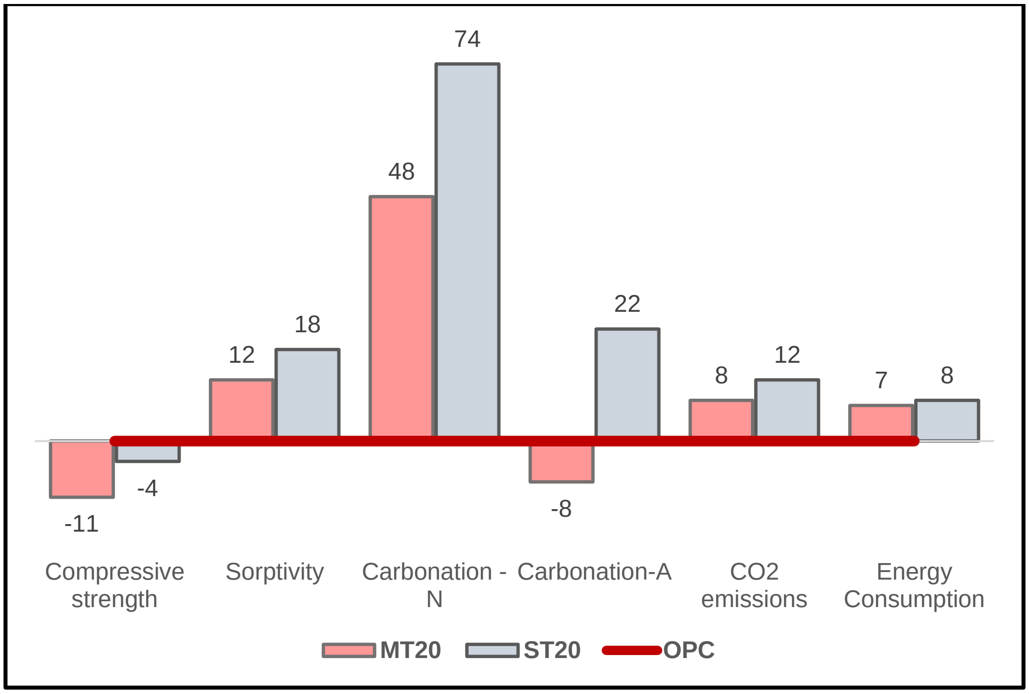

Fig. 7.1: Performance of MT20 and ST 20 mixes.

Furthermore, the utilisation of mineral waste in the production of cement not only leads to significant reductions in carbon dioxide emissions and energy usage, but also serves as a suitable way for upcycling the mineral waste which would otherwise be disposed of in landfills. This study underscores the viability of incorporating mineral waste as a sustainable and high-performance component in modern cement formulations, with even higher replacement levels showing promise in the long term.

7.3 Limitations and Future Directions

This section not only outlines the scope and achievements of our research but also lays out the short comings of the present study and a roadmap for potential avenues of exploration in future studies, which promise to bring forth a more comprehensive comprehension of this intriguing material and its practical implications.

The current investigation encompassed the characterization of mineral waste by examining its microstructure, mineralogy, and chemical composition. Although the investigation initially included the examination of the material's thermal behaviour by thermogravimetric analysis, this aspect of the study was unfortunately not executed due to equipment-related issues which unfortunately impeded the completion of some planned experiments or tests. Despite these constraints, the data and results obtained from other tests within the confines of this study still provide valuable insights and contribute to the overall understanding of the subject matter. However, the future studies with thermogravimetric analysis shall provide better insights into the changes that occurred during the calcination process and portlandite consumption in cement pastes at different ages of hydration.

The present study employed thermal activation by calcination at 650^{o}C, 750^{o}C and 850^{o}C, and mechano-chemical activation by ball milling for 30 minutes, 60 minutes and 90 minutes. These activation methods were selected based on the mineralogical composition and previous research findings. This study did not investigate the effects of higher temperatures of calcination or longer durations of milling. The potential for investigating higher calcination temperatures can be explored based on the results obtained from thermogravimetric analysis. Furthermore, within the realm of mechano-chemical activation, one can investigate the effects of extended milling durations, varying ball to powder ratios, and variable ball sizes.

The potential for investigating the combined utilisation of activation methods is worth considering. This may involve the employing calcination and milling techniques together, or alternatively, the calcination process might be conducted in the presence of an alkali substance. Another possibility is to activate the material through alkali treatment subsequent to ball milling or calcination.

The evaluation of reactivity of the activated material was carried out using adapted R3 tests at 60 ^{o}C and dissolution in 8 M NaOH for 6 hours. These tests can be performed in different temperatures or with different concentration of NaOH and different duration of dissolution. This shall provide a comprehensive idea about the reactivity of the material at different experimental conditions.

The duration of heat of hydration investigations can be extended in order to correlate with the compressive strength of the samples.

The sorptivity studies shall be performed at different ages to infer the pore structure development and the effect of carbonation on the sample shall be determined by SEM and XRD examination of the carbonated samples. Despite these unavoidable limitations, the data and results acquired from the various assessments conducted within the confines of this study have yielded valuable insights, enriching our collective understanding of the mineral waste used. The findings of the studies presented alongside the limitations provide directions for future work before the practical application of the material in field.

The present study utilised a laboratory furnace and a laboratory ball mill for the purpose of material activation. However, in the context of large-scale field applications, it is crucial to acknowledge that the activation process can require the utilisation of different technologies or equipment that operate based on similar principles. This underscores the significance of gaining a comprehensive understanding of the material and the transformations that occur during activation, as this knowledge is pivotal for the effective upcycling of the material in a large-scale context.

In addition, it is imperative to investigate the variations in mineral wastes originating from similar and different processes, sources, and locations. This necessitates the classification of these materials into distinct categories and the formulation of a framework that aids in the selection of the appropriate treatment process based on this classification. Furthermore, it is imperative to formulate a comprehensive approach for the pre-processing and separation of heavy metals, if present, while also considering the environmental implications linked to their incorporation in cementitious binders. Such a holistic approach is vital for achieving sustainable and environmentally responsible practices in the management and repurposing of these materials.

Future study in this topic should encompass not only the technical dimensions of mineral waste utilisation but also acknowledge and address the existing constraints and problems that impede the widespread implementation and large-scale valorisation. Key points to emphasize include the urgent need for a more profound understanding of these materials, the development of appropriate legislation and standards, and addressing environmental concerns related to heavy metal content. Furthermore, collaborative efforts among researchers, industry stakeholders, and regulatory bodies are essential to propel this emerging field forward and establish sustainable practices for mineral waste management and repurposing. This is a nascent area with significant potential, but it requires comprehensive multidisciplinary efforts to overcome existing hurdles and unlock its full benefits for a greener future.

REFERENCES

[1] F.Birol., Technology Roadmap: Low-Carbon Transition in the Cement Industry, International Energy Agency, (2018) 66.

[2] The European Cement Association, Cembureau Activity report 2022, (2022).

[3] F. Winnefeld, A. Leemann, A. German, B. Lothenbach, CO_2 storage in cement and concrete by mineral carbonation, Curr Opin Green Sustain Chem 38 (2022) 100672. https://doi.org/10.1016/j.cogsc.2022.100672.

[4] I.H. Shah, S.A. Miller, D. Jiang, R.J. Myers, Cement substitution with secondary materials can reduce annual global CO_2 emissions by up to 1.3 gigatons, Nat Commun 13 (2022) 1–11. https://doi.org/10.1038/s41467-022-33289-7.

[5] United Nations Department of Economic and Social Affairs Population Division, World Population Prospects 2022: Summary of Results, UN DESA/PO, 2022. www.un.org/development/ desa/pd/.

[6] United Nations Human Settlements Programme (UN-Habitat), Envisaging the Future of Cities, 2022.

[7] THE 17 GOALS | Sustainable Development, (n.d.). https://sdgs.un.org/goals (accessed August 21, 2023).

[8] G. Habert, S.A. Miller, V.M. John, J.L. Provis, A. Favier, A. Horvath, K.L. Scrivener, Environmental impacts and decarbonization strategies in the cement and concrete industries, Nat Rev Earth Environ 1 (2020) 559–573. https://doi.org/10.1038/s43017-020-0093-3.

[9] F.M. Lea, C.H. Desch, Lea's Chemistry of Cement and Concrete, Elsevier, 2019. https://doi.org/10.1016/C2013-0-19325-7.

[10] X. Xu, B. Huang, L. Liu, Z. Cao, X. Gao, R. Mao, L. Duan, Y. Chen, Y. Wang, G. Liu, Modernizing cement manufacturing in China leads to substantial environmental gains, Commun Earth Environ 3 (2022) 1–9. https://doi.org/10.1038/s43247-022-00579-3.

[11] V. Kosajan, Z. Wen, F. Fei, C.D. Dinga, Z. Wang, P. Liu, Comprehensive assessment of cement kiln co-processing under MSW sustainable management requirements, Resour Conserv Recycl 174 (2021) 105816. https://doi.org/10.1016/j.resconrec.2021.105816.

[12] A. Atmaca, R. Yumrutaş, Analysis of the parameters affecting energy consumption of a rotary kiln in cement industry, Appl Therm Eng 66 (2014) 435–444. https://doi.org/10.1016/j.applthermaleng.2014.02.038.

[13] A. Cantini, L. Leoni, F. De Carlo, M. Salvio, C. Martini, F. Martini, Technological energy efficiency improvements in cement industries, Sustainability (Switzerland) 13 (2021). https://doi.org/10.3390/su13073810.

[14] S. Alberici, J. de Beer, I. van der Hoorn, M. Staats, Fly ash and blast furnace slag for cement manufacturing, Department for Business Energy and Industrial Strategy UK 35 (2017) 35. https://assets.publishing.service.gov.uk/government/uploads/system/uploads/attachment_data/file/660888/fly-ash-blast-furnace-slag-cement-manufacturing.pdf.

[15] Steel industry makes 'pivotal' shift towards lower-carbon production - Carbon Brief, (n.d.). https://www.carbonbrief.org/steel-industry-makes-pivotal-shift-towards-lower-carbon-production/ (accessed August 22, 2023).

[16] V. Logar, I. Škrjanc, The Influence of Electric-Arc-Furnace Input Feeds on its Electrical Energy Consumption, Journal of Sustainable Metallurgy 7 (2021) 1013–1026. https://doi.org/10.1007/S40831-021-00390-Y.

[17] Introduction to Climate Action | UNFCCC, (n.d.). https://unfccc.int/climate-action/introduction-climate-action (accessed August 16, 2023).

[18] D.J. Harrison, A.J. Bloodworth, J. Eyre, M. Macfarlane, C.J. Mitchell, P. Scott, E.J. Steadman, Utilisation of mineral waste: case studies, Economic Minerals and Geochemical Baseline Programme Commissioned Reserach Report CR/02/227N (2002) 92pp.

[19] Visualizing the size of mine tailings - MINING.COM, (n.d.). https://www.mining.com/web/visualizing-the-size-of-mine-tailings/ (accessed August 14, 2023).

[20] UN, Global Industry Standard on Tailings Management, (2020).

[21] S. Bobba, S. Carrara, J. Huisman, F. Mathieux, C. Pavel, Critical Raw Materials for Strategic Technologies and Sectors in the EU - a Foresight Study, 2020. https://doi.org/10.2873/58081.

[22] G. Blight, Mine Waste: A Brief Overview of Origins, Quantities, and Methods of Storage, Waste (2011) 77–88. https://doi.org/10.1016/B978-0-12-381475-3.10005-1.

[23] J.S. Adiansyah, M. Rosano, S. Vink, G. Keir, A framework for a sustainable approach to mine tailings management: Disposal strategies, J Clean Prod 108 (2015) 1050–1062. https://doi.org/10.1016/j.jclepro.2015.07.139.

[24] A. Saedi, A. Jamshidi-Zanjani, A.K. Darban, A review on different methods of activating tailings to improve their cementitious property as cemented paste and reusability, J Environ Manage 270 (2020) 110881. https://doi.org/10.1016/j.jenvman.2020.110881.

[25] D. Kossoff, W.E. Dubbin, M. Alfredsson, S.J. Edwards, M.G. Macklin, K.A. Hudson-Edwards, Mine tailings dams: Characteristics, failure, environmental impacts, and remediation, Applied Geochemistry 51 (2014) 229–245. https://doi.org/10.1016/j.apgeochem.2014.09.010.

[26] B. Bussière, Colloquium 2004: Hydrogeotechnical properties of hard rock tailings from metal mines and emerging geoenvironmental disposal approaches, Canadian Geotechnical Journal 44 (2007) 1019–1052. https://doi.org/10.1139/T07-040.

[27] J.S. Adiansyah, N. Haque, M. Rosano, W. Biswas, Application of a life cycle assessment to compare environmental performance in coal mine tailings management, J Environ Manage 199 (2017) 181–191. https://doi.org/10.1016/j.jenvman.2017.05.050.

[28] Construction and demolition waste, (n.d.). https://environment.ec.europa.eu/topics/waste-and-recycling/construction-and-demolition-waste_en (accessed April 2, 2023).

[29] Construction and demolition sites - Do you know what's in your waste? - Creating a better place, (n.d.). https://environmentagency.blog.gov.uk/2021/03/28/construction-and-demolition-sites-do-you-know-whats-in-your-waste/ (accessed August 6, 2023).

[30] Construction And Demolition Waste Management Global Market Report 2023, (n.d.). https://www.researchandmarkets.com/reports/5766698/construction-demolition-waste-management-global (accessed August 14, 2023).

[31] MPA, Mineral Products Today, Mineral Products Association (n.d.).

[32] L. Qiao, Y. Tang, Y. Li, M. Liu, X. Yuan, Q. Wang, Q. Ma, Life cycle assessment of three typical recycled products from construction and demolition waste, J Clean Prod 376 (2022) 134139. https://doi.org/10.1016/j.jclepro.2022.134139.

[33] M. Behera, S.K. Bhattacharyya, A.K. Minocha, R. Deoliya, S. Maiti, Recycled aggregate from C&D waste & its use in concrete - A breakthrough towards sustainability in construction sector: A review, Constr Build Mater 68 (2014) 501–516. https://doi.org/10.1016/j.conbuildmat.2014.07.003.

[34] F. Pacheco-Torgal, Eco-efficient construction and building materials research under the EU Framework Programme Horizon 2020, Constr Build Mater 51 (2014) 151–162. https://doi.org/10.1016/j.conbuildmat.2013.10.058.

[35] C. Mitchell, Mineral waste in the UK, (n.d.).

[36] A.M.T. Simonsen, S. Solismaa, H.K. Hansen, P.E. Jensen, Evaluation of mine tailings' potential as supplementary cementitious materials based on chemical, mineralogical and physical characteristics, Waste Management 102 (2020) 710–721. https://doi.org/10.1016/j.wasman.2019.11.037.

[37] N. Sedira, J. Castro-Gomes, G. Kastiukas, X. Zhou, A. Vargas, A review on mineral waste for chemical-activated binders: Mineralogical and chemical characteristics, Mining Science 24 (2017) 29–58. https://doi.org/10.5277/msc172402.

[38] P. Kinnunen, A. Ismailov, S. Solismaa, H. Sreenivasan, M.L. Räisänen, E. Levänen, M. Illikainen, Recycling mine tailings in chemically bonded ceramics – A review, J Clean Prod 174 (2018) 634–649. https://doi.org/10.1016/j.jclepro.2017.10.280.

[39] X. Liu, N. Zhang, Utilization of red mud in cement production: A review, Waste Management and Research 29 (2011) 1053–1063. https://doi.org/10.1177/0734242X11407653.

[40] R. Argane, M. Benzaazoua, R. Hakkou, A. Bouamrane, A comparative study on the practical use of low sulfide base-metal tailings as aggregates for rendering and masonry mortars, J Clean Prod 112 (2016) 914–925. https://doi.org/10.1016/j.jclepro.2015.06.004.

[41] A. Saedi, A. Jamshidi-Zanjani, A.K. Darban, A review on different methods of activating tailings to improve their cementitious property as cemented paste and reusability, J Environ Manage 270 (2020) 110881. https://doi.org/10.1016/j.jenvman.2020.110881.

[42] Waste Framework Directive, (n.d.). https://environment.ec.europa.eu/topics/waste-and-recycling/waste-framework-directive_en (accessed August 14, 2023).

[43] OECD, Global Material Resources Outlook to 2060, OECD Publishing, Paris, 2019. https://doi.org/https://doi.org/10.1787/9789264307452-en.

[44] A. Torres, J. Brandt, K. Lear, J. Liu, A looming tragedy of the sand commons, Science 357 (2017) 970–971. https://doi.org/10.1126/science.aao0503.

[45] S.-E. Ouldboukhitine, R. Belarbi, I. Jaffal, A. Trabelsi, Assessment of green roof thermal behavior: A coupled heat and mass transfer model, Build Environ 46 (2011) 2624–2631. https://doi.org/10.1016/j.buildenv.2011.06.021.

[46] Cement - IEA, (n.d.). https://www.iea.org/energy-system/industry/cement (accessed August 4, 2023).

[47] J. Lehne, F. Preston, Chatham House Report: Making Concrete Change - Innovation in Low-carbon Cement and Concrete, 2018.

[48] International Energy Agency, Technology Roadmap - Low carbon Transisition in the Cement Industry Foldout, 2018. https://doi.org/10.1007/springerreference_7300.

[49] EU Commission, The European Green Deal, European Commission 53 (2019) 24.

[50] K.L. Scrivener, V.M. John, E.M. Gartner, Eco-efficient cements: Potential economically viable solutions for a low-CO_2 cement-based materials industry, Cem Concr Res 114 (2018) 2–26. https://doi.org/10.1016/j.cemconres.2018.03.015.

[51] W. Shanks, C.F. Dunant, M.P. Drewniok, R.C. Lupton, A. Serrenho, J.M. Allwood, How much cement can we do without? Lessons from cement material flows in the UK, Resour Conserv Recycl 141 (2019) 441–454. https://doi.org/10.1016/j.resconrec.2018.11.002.

[52] M.C.G. Juenger, R. Snellings, S.A. Bernal, Supplementary cementitious materials: New sources, characterization, and performance insights, Cem Concr Res 122 (2019) 257–273. https://doi.org/10.1016/j.cemconres.2019.05.008.

[53] C. Reichl, M. Schatz, World Mining Data 2021, Vienna, 2021.

[54] Home | United Nations Development Programme, (n.d.). https://www.undp.org/ (accessed August 6, 2023).

[55] Responsible Mining Foundation, Responsible Mining Index Methodology 2020, (2020) 138.

[56] J.R. Owen, D. Kemp, Lèbre, K. Svobodova, G. Pérez Murillo, Catastrophic tailings dam failures and disaster risk disclosure, International Journal of Disaster Risk Reduction 42 (2020). https://doi.org/10.1016/j.ijdrr.2019.101361.

[57] B. Oberle, S. Bringezu, S. Hatfield-dodds, S. Hellweg, H. Schandl, J. Clement, C. Authors, L. Cabernard, N. Che, D. Chen, H. Droz-georget, P. Ekins, M. Fischer-kowalski, M. Flörke, S. Frank, A. Froemelt, A. Geschke, M. Haupt, P. Havlik, R. Hüfner, M. Lenzen, M. Lieber, B. Liu, Y. Lu, S. Lutter, J. Mehr, A. Miatto, D. Newth, C. Oberschelp, S. Pfister, E. Piccoli, R. Schaldach, J. Schüngel, T. Sonderegger, A. Sudheshwar, E. Van Der Voet, C. Walker, J. West, Z. Wang, B. Zhu, Global Resources Outlook 2019: Natural resources for the future we want, United Nations Environment Programme, 2019.

[58] R. Argane, M. El Adnani, M. Benzaazoua, H. Bouzahzah, A. Khalil, R. Hakkou, Y. Taha, Geochemical behavior and environmental risks related to the use of abandoned base-metal tailings as construction material in the upper-Moulouya district, Morocco, Environmental Science and Pollution Research 23 (2016) 598–611. https://doi.org/10.1007/s11356-015-5292-y.

[59] M.A. Longhi, E.D. Rodríguez, S.A. Bernal, J.L. Provis, A.P. Kirchheim, Valorisation of a kaolin mining waste for the production of geopolymers, J Clean Prod 115 (2016) 265–272. https://doi.org/10.1016/j.jclepro.2015.12.011.

[60] Y.W. Choi, Y.J. Kim, O. Choi, K.M. Lee, M. Lachemi, Utilization of tailings from tungsten mine waste as a substitution material for cement, Constr Build Mater 23 (2009) 2481–2486. https://doi.org/10.1016/j.conbuildmat.2009.02.006.

[61] I. Vangelatos, G.N. Angelopoulos, D. Boufounos, Utilization of ferroalumina as raw material in the production of Ordinary Portland Cement, J Hazard Mater 168 (2009) 473–478. https://doi.org/10.1016/j.jhazmat.2009.02.049.

[62] C. Ince, S. Derogar, K. Gurkaya, R.J. Ball, Properties, durability and cost efficiency of cement and hydrated lime mortars reusing copper mine tailings of Lefke-Xeros in Cyprus, Constr Build Mater 268 (2021) 121070. https://doi.org/10.1016/j.conbuildmat.2020.121070.

[63] A.P. Vilela, T.M.C. Eugênio, F.F. de Oliveira, J.F. Mendes, A.G.C. Ribeiro, L.E.V. de S. Brandão Vaz, R.F. Mendes, Technological properties of soil-cement bricks produced with iron ore mining waste, Constr Build Mater 262 (2020) 120883. https://doi.org/10.1016/j.conbuildmat.2020.120883.

[64] B. Wang, L. Yan, Q. Fu, B. Kasal, A Comprehensive Review on Recycled Aggregate and Recycled Aggregate Concrete, Resour Conserv Recycl 171 (2021) 105565. https://doi.org/10.1016/j.resconrec.2021.105565.

[65] G. Bai, C. Zhu, C. Liu, B. Liu, An evaluation of the recycled aggregate characteristics and the recycled aggregate concrete mechanical properties, Constr Build Mater 240 (2020) 117978. https://doi.org/10.1016/j.conbuildmat.2019.117978.

[66] M. Surya, V.V.L.K. Rao, P. Lakshmy, Mechanical, durability, and time-dependent properties of recycled aggregate concrete with fly ash, ACI Mater J 112 (2015) 653–661. https://doi.org/10.14359/51687853.

[67] L. Yu, Z. Zhang, X. Huang, B. Jiao, D. Li, Enhancement experiment on cementitious activity of copper-mine tailings in a geopolymer system, Fibers 5 (2017) 1–15. https://doi.org/10.3390/fib5040047.

[68] O. Onuaguluchi, Ö. Eren, Recycling of copper tailings as an additive in cement mortars, Constr Build Mater 37 (2012) 723–727. https://doi.org/10.1016/j.conbuildmat.2012.08.009.

[69] F. Pacheco-Torgal, J. Castro-Gomes, S. Jalali, Tungsten mine waste geopolymeric binder: Preliminary hydration products investigations, Constr Build Mater 23 (2009) 200–209. https://doi.org/10.1016/j.conbuildmat.2008.01.003.

[70] N. Cristelo, J. Coelho, M. Oliveira, N.C. Consoli, Á. Palomo, A. Fernández-Jiménez, Recycling and application of mine tailings in alkali-activated cements and mortars-strength development and environmental assessment, Applied Sciences (Switzerland) 10 (2020). https://doi.org/10.3390/app10062084.

[71] C. Ince, Reusing gold-mine tailings in cement mortars: Mechanical properties and socio-economic developments for the Lefke-Xeros area of Cyprus, J Clean Prod 238 (2019) 117871. https://doi.org/10.1016/j.jclepro.2019.117871.

[72] P. Savva, M.F. Petrou, Highly absorptive normal weight aggregates for internal curing of concrete, Constr Build Mater 179 (2018) 80–88. https://doi.org/10.1016/j.conbuildmat.2018.05.205.

[73] P. Savva, D. Nicolaides, M.F. Petrou, Internal curing for mitigating high temperature concreting effects, Constr Build Mater 179 (2018) 598–604. https://doi.org/10.1016/j.conbuildmat.2018.04.032.

[74] M. Alazhari, T. Sharma, A. Heath, R. Cooper, K. Paine, Application of expanded perlite encapsulated bacteria and growth media for self-healing concrete, Constr Build Mater 160 (2018) 610–619. https://doi.org/10.1016/j.conbuildmat.2017.11.086.

[75] R. Alghamri, A. Kanellopoulos, C. Litina, Preparation and polymeric encapsulation of powder mineral pellets for self-healing cement based materials, Constr Build Mater 186 (2018) 247–262. https://doi.org/10.1016/j.conbuildmat.2018.07.128.

[76] Y.W. Choi, Y.J. Kim, O. Choi, K.M. Lee, M. Lachemi, Utilization of tailings from tungsten mine waste as a substitution material for cement, Constr Build Mater 23 (2009) 2481–2486. https://doi.org/10.1016/j.conbuildmat.2009.02.006.

[77] J. Esmaeili, H. Aslani, Use of copper mine tailing in concrete: strength characteristics and durability performance, J Mater Cycles Waste Manag 21 (2019) 729–741. https://doi.org/10.1007/s10163-019-00831-7.

[78] Z.R. Wang, B. Li, H.B. Liu, Y.X. Zhang, X. Qin, Degradation characteristics of graphite tailings cement mortar subjected to freeze-thaw cycles, Constr Build Mater 234 (2020) 117422. https://doi.org/10.1016/j.conbuildmat.2019.117422.

[79] A.M.T. Simonsen, S. Solismaa, H.K. Hansen, P.E. Jensen, Evaluation of mine tailings' potential as supplementary cementitious materials based on chemical, mineralogical and physical characteristics, Waste Management 102 (2020) 710–721. https://doi.org/10.1016/j.wasman.2019.11.037.

[80] R. Lupo, M. Tyrer, C.R. Cheeseman, S. Donatello, Manufactured aggregate from waste materials, Sustainable Construction Materials and Technologies - International Conference on Sustainable Construction Materials and Technologies (2007) 763–767. https://doi.org/10.13140/2.1.1612.6722.

[81] J. Kiventerä, P. Perumal, J. Yliniemi, M. Illikainen, Mine tailings as a raw material in alkali activation: A review, International Journal of Minerals, Metallurgy and Materials 27 (2020) 1009–1020. https://doi.org/10.1007/s12613-020-2129-6.

[82] R. Argane, M. El Adnani, M. Benzaazoua, H. Bouzahzah, A. Khalil, R. Hakkou, Y. Taha, Geochemical behavior and environmental risks related to the use of abandoned base-metal tailings as construction material in the upper-Moulouya district, Morocco, Environmental Science and Pollution Research 23 (2016) 598–611. https://doi.org/10.1007/s11356-015-5292-y.

[83] Sid 5, New technologies to allow beneficial reuse of silt from construction and demolition waste recycling washing plant, Research Project Report (WR0204 (WRT 236)) Submitted to Defra, Science Directorate 5 (2009) 1–25.

[84] R. Argane, M. Benzaazoua, A. Bouamrane, R. Hakkou, Cement hydration and durability of low sulfide tailings-based renders: A case study in Moroccan constructions, Miner Eng 76 (2015) 97–108. https://doi.org/10.1016/j.mineng.2014.10.022.

[85] H. Liu, K. Liu, Z. Lan, D. Zhang, Mechanical and Electrical Characteristics of Graphite Tailing Concrete, Advances in Materials Science and Engineering 2018 (2018). https://doi.org/10.1155/2018/9297628.

[86] G. Yao, Q. Liu, J. Wang, P. Wu, X. Lyu, Effect of mechanical grinding on pozzolanic activity and hydration properties of siliceous gold ore tailings, J Clean Prod 217 (2019) 12–21. https://doi.org/10.1016/j.jclepro.2019.01.175.

[87] K. Peng, H. Yang, J. Ouyang, Tungsten tailing powders activated for use as cementitious material, Powder Technol 286 (2015) 678–683. https://doi.org/10.1016/j.powtec.2015.09.012.

[88] C. Ince, Reusing gold-mine tailings in cement mortars: Mechanical properties and socio-economic developments for the Lefke-Xeros area of Cyprus, J Clean Prod 238 (2019) 117871. https://doi.org/10.1016/j.jclepro.2019.117871.

[89] C. Lampris, R. Lupo, C.R. Cheeseman, Geopolymerisation of silt generated from construction and demolition waste washing plants, Waste Management 29 (2009) 368–373. https://doi.org/10.1016/j.wasman.2008.04.007.

[90] C. Shi, P. V. Krivenko, D. Roy, Alkali-Activated Cements and Concretes, CRC Press 03 (2003).

[91] M. Kovac, A. Sicakova, M. Spak, Testing the Supplementary Cementitious Material Based on GGBFS and Zeolite for Prediction of the Activity Index, (2018) 1287. https://doi.org/10.3390/proceedings2201287.

[92] A. Sicakova, M. Kovac, Technological characterisation of selected mineral additives, IOP Conference Series: Materials Science and Engineering, Construmet (2018) 1–6. https://doi.org/10.1088/1757-899X/385/1/012048.

[93] P. Kinnunen, A. Ismailov, S. Solismaa, H. Sreenivasan, M.L. Räisänen, E. Levänen, M. Illikainen, Recycling mine tailings in chemically bonded ceramics – A review, J Clean Prod 174 (2018) 634–649. https://doi.org/10.1016/j.jclepro.2017.10.280.

[94] J. Ye, W. Zhang, D. Shi, Properties of an aged geopolymer synthesized from calcined ore-dressing tailing of bauxite and slag, Cem Concr Res 100 (2017) 23–31. https://doi.org/10.1016/j.cemconres.2017.05.017.

[95] S. Aydln, C.Ç. Klzlltepe, Valorization of Boron Mine Tailings in Alkali-Activated Mortars, Journal of Materials in Civil Engineering 31 (2019) 1–12. https://doi.org/10.1061/(ASCE)MT.1943-5533.0002871.

[96] M. Frías, M.I. Sanchez De Rojas, R. García, A. Juan Valdés, C. Medina, Effect of activated coal mining wastes on the properties of blended cement, Cem Concr Compos 34 (2012) 678–683. https://doi.org/10.1016/j.cemconcomp.2012.02.006.

[97] J. Zheng, Y. Zhu, Z. Zhao, Utilization of limestone powder and water-reducing admixture in cemented paste backfill of coarse copper mine tailings, Constr Build Mater 124 (2016) 31–36. https://doi.org/10.1016/j.conbuildmat.2016.07.055.

[98] Y. Chen, Y. Zhang, T. Chen, Y. Zhao, S. Bao, Preparation of eco-friendly construction bricks from hematite tailings, Constr Build Mater 25 (2011) 2107–2111. https://doi.org/10.1016/j.conbuildmat.2010.11.025.

[99] M.A. Longhi, E.D. Rodríguez, S.A. Bernal, J.L. Provis, A.P. Kirchheim, Valorisation of a kaolin mining waste for the production of geopolymers, J Clean Prod 115 (2016) 265–272. https://doi.org/10.1016/j.jclepro.2015.12.011.

[100] H. Liu, K. Liu, Z. Lan, D. Zhang, Mechanical and Electrical Characteristics of Graphite Tailing Concrete, Advances in Materials Science and Engineering 2018 (2018). https://doi.org/10.1155/2018/9297628.

[101] S. Moukannaa, M. Loutou, M. Benzaazoua, L. Vitola, J. Alami, R. Hakkou, Recycling of phosphate mine tailings for the production of geopolymers, J Clean Prod 185 (2018) 891–903. https://doi.org/10.1016/j.jclepro.2018.03.094.

[102] S. Pyo, M. Tafesse, B.J. Kim, H.K. Kim, Effects of quartz-based mine tailings on characteristics and leaching behavior of ultra-high performance concrete, Constr Build Mater 166 (2018) 110–117. https://doi.org/10.1016/j.conbuildmat.2018.01.087.

[103] K. Peng, H. Yang, J. Ouyang, Tungsten tailing powders activated for use as cementitious material, Powder Technol 286 (2015) 678–683. https://doi.org/10.1016/j.powtec.2015.09.012.

[104] B. Wei, Y. Zhang, S. Bao, Preparation of geopolymers from vanadium tailings by mechanical activation, Constr Build Mater 145 (2017) 236–242. https://doi.org/10.1016/j.conbuildmat.2017.03.234.

[105] Q. Wan, F. Rao, S. Song, R. Morales-Estrella, X. Xie, X. Tong, Chemical forms of lead immobilization in alkali-activated binders based on mine tailings, Cem Concr Compos 92 (2018) 198–204. https://doi.org/10.1016/j.cemconcomp.2018.06.011.

[106] H. Paiva, J. Yliniemi, M. Illikainen, F. Rocha, V.M. Ferreira, Mine tailings geopolymers as awaste management solution for a more sustainable habitat, Sustainability (Switzerland) 11 (2019). https://doi.org/10.3390/su11040995.

[107] S. Aydln, C.Ç. Klzlltepe, Valorization of Boron Mine Tailings in Alkali-Activated Mortars, Journal of Materials in Civil Engineering 31 (2019) 1–12. https://doi.org/10.1061/(ASCE)MT.1943-5533.0002871.

[108] S. Ahmari, L. Zhang, Utilization of cement kiln dust (CKD) to enhance mine tailings-based geopolymer bricks, Constr Build Mater 40 (2013) 1002–1011. https://doi.org/10.1016/j.conbuildmat.2012.11.069.

[109] S. Moukannaa, A. Nazari, A. Bagheri, M. Loutou, J.G. Sanjayan, R. Hakkou, Alkaline fused phosphate mine tailings for geopolymer mortar synthesis: Thermal stability, mechanical and microstructural properties, J Non Cryst Solids 511 (2019) 76–85. https://doi.org/10.1016/j.jnoncrysol.2018.12.031.

[110] Y. Chen, Y. Zhang, T. Chen, T. Liu, J. Huang, Preparation and characterization of red porcelain tiles with hematite tailings, Constr Build Mater 38 (2013) 1083–1088. https://doi.org/10.1016/j.conbuildmat.2012.06.056.

[111] S. Wang, Preparation of foam concrete from graphite tailing, Adv Mat Res 356–360 (2012) 1994–1997. https://doi.org/10.4028/www.scientific.net/AMR.356-360.1994.

[112] M. Benzaazoua, H. Bouzahzah, Y. Taha, L. Kormos, D. Kabombo, F. Lessard, B. Bussière, I. Demers, M. Kongolo, Integrated environmental management of

pyrrhotite tailings at Raglan Mine: Part 1 challenges of desulphurization process and reactivity prediction, J Clean Prod 162 (2017) 86–95. https://doi.org/10.1016/j.jclepro.2017.05.161.

[113] G. Zhang, Y. Yan, Z. Hu, B. Xiao, Investigation on preparation of pyrite tailings-based mineral admixture with photocatalytic activity, Constr Build Mater 138 (2017) 26–34. https://doi.org/10.1016/j.conbuildmat.2017.01.134.

[114] H. Xu, J.S.J. Van Deventer, The geopolymerisation of alumino-silicate minerals, Int J Miner Process 59 (2000) 247–266. https://doi.org/10.1016/S0301-7516(99)00074-5.

[115] H. Xu, J.S.J. Van Deventer, Factors affecting the geopolymerization of alkali-feldspars, Minerals and Metallurgical Processing 19 (2002) 209–214. https://doi.org/10.1007/bf03403271.

[116] K. Zheng, J. Zhou, M. Gbozee, Influences of phosphate tailings on hydration and properties of Portland cement, Constr Build Mater 98 (2015) 593–601. https://doi.org/10.1016/j.conbuildmat.2015.08.115.

[117] R. Hakkou, M. Benzaazoua, B. Bussière, Valorization of Phosphate Waste Rocks and Sludge from the Moroccan Phosphate Mines: Challenges and Perspectives, Procedia Eng 138 (2016) 110–118. https://doi.org/10.1016/j.proeng.2016.02.068.

[118] L. Caneda-Martínez, C. Medina, M.I. Sánchez de Rojas, M. Frías, Water transport in binary eco-cements containing coal mining waste, Cem Concr Compos 104 (2019) 103373. https://doi.org/10.1016/j.cemconcomp.2019.103373.

[119] L. Caneda-Martínez, M. Frías, C. Medina, M.I.S. de Rojas, N. Rebolledo, J. Sánchez, Evaluation of chloride transport in blended cement mortars containing coal mining waste, Constr Build Mater 190 (2018) 200–210. https://doi.org/10.1016/j.conbuildmat.2018.09.158.

[120] S. Ahmari, L. Zhang, Production of eco-friendly bricks from copper mine tailings through geopolymerization, Constr Build Mater 29 (2012) 323–331. https://doi.org/10.1016/j.conbuildmat.2011.10.048.

[121] I. Sheikhhosseini, M. Mohsen, V. Toufigh, Improvement of poorly graded sandy soil by using copper mine tailing dam sediments-based geopolymer and silica fume, Constr Build Mater 281 (2021) 122591. https://doi.org/10.1016/j.conbuildmat.2021.122591.

[122] I. Silva, J.P. Castro-Gomes, A. Albuquerque, Effect of immersion in water partially alkali-activated materials obtained of tungsten mine waste mud, Constr Build Mater 35 (2012) 117–124. https://doi.org/10.1016/j.conbuildmat.2012.02.069.

[123] X. Jiao, Y. Zhang, T. Chen, Thermal stability of a silica-rich vanadium tailing based geopolymer, Constr Build Mater 38 (2013) 43–47. https://doi.org/10.1016/j.conbuildmat.2012.06.076.

[124] F. Lessard, B. Bussière, J. Côté, M. Benzaazoua, V. Boulanger-Martel, L. Marcoux, Integrated environmental management of pyrrhotite tailings at Raglan Mine: Part 2 desulphurized tailings as cover material, J Clean Prod 186 (2018) 883–893. https://doi.org/10.1016/j.jclepro.2018.03.132.

[125] Z. Wei, J. Zhao, W. Wang, Y. Yang, S. Zhuang, Utilizing gold mine tailings to produce sintered bricks, Constr Build Mater 282 (2021) 122655. https://doi.org/10.1016/j.conbuildmat.2021.122655.

[126] N. Zhang, A. Hedayat, H.G. Bolaños Sosa, J.J. González Cárdenas, G.E. Salas Álvarez, V.B. Ascuña Rivera, Damage evaluation and deformation behavior of mine tailing-based Geopolymer under uniaxial cyclic compression, Ceram Int 47 (2021) 10773–10785. https://doi.org/10.1016/j.ceramint.2020.12.194.

[127] B. Koohestani, P. Mokhtari, E. Yilmaz, F. Mahdipour, A.K. Darban, Geopolymerization mechanism of binder-free mine tailings by sodium silicate, Constr Build Mater 268 (2021) 121217. https://doi.org/10.1016/j.conbuildmat.2020.121217.

[128] C. Goulart Bezerra, C.A. Abelha Rocha, I.S. de Siqueira, R.D. Toledo Filho, Feasibility of iron-rich ore tailing as supplementary cementitious material in cement pastes, Constr Build Mater 303 (2021) 124496. https://doi.org/10.1016/j.conbuildmat.2021.124496.

[129] Y. Cheng, F. Huang, S. Qi, W. Li, R. Liu, G. Li, Durability of concrete incorporated with siliceous iron tailings, Constr Build Mater 242 (2020) 118147. https://doi.org/10.1016/j.conbuildmat.2020.118147.

[130] H. Xu, J.S.J. Van Deventer, Effect of source materials on geopolymerization, Ind Eng Chem Res 42 (2003) 1698–1706. https://doi.org/10.1021/ie0206958.

[131] J. Li, M. Hitch, Mechanical activation of magnesium silicates for mineral carbonation , a review, Miner Eng 128 (2018) 69–83. https://doi.org/10.1016/j.mineng.2018.08.034.

[132] I. Tole, K. Habermehl-Cwirzen, A. Cwirzen, Mechanochemical activation of natural clay minerals: an alternative to produce sustainable cementitious binders – review, Mineral Petrol 113 (2019). https://doi.org/10.1007/s00710-019-00666-y.

[133] P. Baláž, M. Achimovicová, M. Baláž, P. Billik, C.Z. Zara, J.M. Criado, F. Delogu, E. Dutková, E. Gaffet, F.J. Gotor, R. Kumar, I. Mitov, T. Rojac, M. Senna, A. Streletskii, W.C. Krystyna, Hallmarks of mechanochemistry: From nanoparticles to technology, Chem Soc Rev 42 (2013) 7571–7637. https://doi.org/10.1039/c3cs35468g.

[134] F. Pacheco-Torgal, J.A. Labrincha, C. Leonelli, A. Palomo, P. Chindaprasirt, Handbook of Alkali-Activated Cements, Mortars and Concretes, 2014. https://doi.org/10.1016/C2013-0-16511-7.

[135] B. Wei, Y. Zhang, S. Bao, Preparation of geopolymers from vanadium tailings by mechanical activation, Constr Build Mater 145 (2017) 236–242. https://doi.org/10.1016/j.conbuildmat.2017.03.234.

[136] G. Yao, Q. Liu, J. Wang, P. Wu, X. Lyu, Effect of mechanical grinding on pozzolanic activity and hydration properties of siliceous gold ore tailings, J Clean Prod 217 (2019) 12–21. https://doi.org/10.1016/j.jclepro.2019.01.175.

[137] I. Tole, K. Habermehl-Cwirzen, A. Cwirzen, Mechanochemical activation of natural clay minerals: an alternative to produce sustainable cementitious binders – review, Mineral Petrol 113 (2019). https://doi.org/10.1007/s00710-019-00666-y.

[138] J. Li, M. Hitch, Mechanical activation of magnesium silicates for mineral carbonation , a review, Miner Eng 128 (2018) 69–83. https://doi.org/10.1016/j.mineng.2018.08.034.

[139] J.M. Franco de Carvalho, K. Defáveri, J.C. Mendes, W. Schmidt, H.C. Kühne, R.A.F. Peixoto, Influence of particle size-designed recycled mineral admixtures on the properties of cement-based composites, Constr Build Mater 272 (2021). https://doi.org/10.1016/j.conbuildmat.2020.121640.

[140] G. Yao, Q. Wang, Z. Wang, J. Wang, X. Lyu, Activation of hydration properties of iron ore tailings and their application as supplementary cementitious materials in cement, Powder Technol 360 (2020) 863–871. https://doi.org/10.1016/j.powtec.2019.11.002.

[141] M. Zbik, R.S.C. Smart, Influence of dry grinding on talc and kaolinite morphology: Inhibition of nano-bubble formation and improved dispersion, Miner Eng 18 (2005) 969–976. https://doi.org/10.1016/j.mineng.2005.01.005.

[142] H. Niu, P. Kinnunen, H. Sreenivasan, E. Adesanya, M. Illikainen, Structural collapse in phlogopite mica-rich mine tailings induced by mechanochemical treatment and implications to alkali activation potential, Miner Eng 151 (2020) 106331. https://doi.org/10.1016/j.mineng.2020.106331.

[143] G. Yao, Z. Wang, J. Yao, X. Cong, C. Anning, X. Lyu, Pozzolanic activity and hydration properties of feldspar after mechanical activation, Powder Technol 383 (2021) 167–174. https://doi.org/10.1016/j.powtec.2021.01.042.

[144] L. Yu, Z. Zhang, X. Huang, B. Jiao, D. Li, Enhancement experiment on cementitious activity of copper-mine tailings in a geopolymer system, Fibers 5 (2017) 1–15. https://doi.org/10.3390/fib5040047.

[145] Y. Cheng, F. Huang, W. Li, R. Liu, G. Li, J. Wei, Test research on the effects of mechanochemically activated iron tailings on the compressive strength of concrete, Constr Build Mater 118 (2016) 164–170. https://doi.org/10.1016/j.conbuildmat.2016.05.020.

[146] P. Perumal, H. Niu, J. Kiventerä, P. Kinnunen, M. Illikainen, Upcycling of mechanically treated silicate mine tailings as alkali activated binders, Miner Eng 158 (2020) 106587. https://doi.org/10.1016/j.mineng.2020.106587.

[147] R. Menezes, F. Farias, M.F. Oliveira, L.N.L. Santana, G.A. Neves, H.L. Lira, H.C. Ferreira, Kaolin processing waste applied in the manufacturing of ceramic tiles and

mullite bodies, Waste Management and Research 27 (2009) 78–86. https://doi.org/10.1177/0734242X07085338.

[148] F. Vargas, M. Lopez, Development of a new supplementary cementitious material from the activation of copper tailings: Mechanical performance and analysis of factors, J Clean Prod 182 (2018) 427–436. https://doi.org/10.1016/j.jclepro.2018.01.223.

[149] R. Fernandez, F. Martirena, K.L. Scrivener, The origin of the pozzolanic activity of calcined clay minerals: A comparison between kaolinite, illite and montmorillonite, Cem Concr Res 41 (2011) 113–122. https://doi.org/10.1016/j.cemconres.2010.09.013.

[150] D. Feng, J.L. Provis, J.S.J. Van Deventer, Thermal activation of albite for the synthesis of one-part mix geopolymers, Journal of the American Ceramic Society 95 (2012) 565–572. https://doi.org/10.1111/j.1551-2916.2011.04925.x.

[151] N. Sedira, J. Castro-Gomes, Study of an alkali-activated binder based on tungsten mining mud and brick powder waste, MATEC Web of Conferences 163 (2018) 1–8. https://doi.org/10.1051/matecconf/201816306002.

[152] J. Kiventerä, J. Yliniemi, L. Golek, J. Deja, V. Ferreira, M. Illikainen, Utilization of sulphidic mine tailings in alkali-activated materials, MATEC Web of Conferences 274 (2019) 01001. https://doi.org/10.1051/matecconf/201927401001.

[153] A. Mette, T. Simonsen, S. Solismaa, H.K. Hansen, P.E. Jensen, Evaluation of mine tailings ’ potential as supplementary cementitious materials based on chemical , mineralogical and physical characteristics, Waste Management 102 (2020) 710–721. https://doi.org/10.1016/j.wasman.2019.11.037.

[154] C. Yang, C. Cui, J. Qin, X. Cui, Characteristics of the fired bricks with low-silicon iron tailings, Constr Build Mater 70 (2014) 36–42. https://doi.org/10.1016/j.conbuildmat.2014.07.075.

[155] N. Sedira, J. Castro-Gomes, M. Magrinho, Red clay brick and tungsten mining waste-based alkali-activated binder: Microstructural and mechanical properties, Constr Build Mater 190 (2018) 1034–1048. https://doi.org/10.1016/j.conbuildmat.2018.09.153.

[156] W. Liu, T. Wu, Z. Li, X. Hao, A. Lu, Preparation and characterization of ceramic substrate from tungsten mine tailings, Constr Build Mater 77 (2015) 139–144. https://doi.org/10.1016/j.conbuildmat.2014.12.094.

[157] G. Young, M. Yang, Preparation and characterization of Portland cement clinker from iron ore tailings, Constr Build Mater 197 (2019) 152–156. https://doi.org/10.1016/j.conbuildmat.2018.11.236.

[158] A. Buchwald, M. Hohmann, K. Posern, E. Brendler, The suitability of thermally activated illite/smectite clay as raw material for geopolymer binders, Appl Clay Sci 46 (2009) 300–304. https://doi.org/10.1016/j.clay.2009.08.026.

[159] H. He, Q. Yue, Y. Qi, B. Gao, Y. Zhao, H. Yu, J. Li, Q. Li, Y. Wang, The effect of incorporation of red mud on the properties of clay ceramic bodies, Appl Clay Sci 70 (2012) 67–73. https://doi.org/10.1016/j.clay.2012.09.022.

[160] T.P. Chang, J.Y. Shih, K.M. Yang, T.C. Hsiao, Material properties of portland cement paste with nano-montmorillonite, J Mater Sci 42 (2007) 7478–7487. https://doi.org/10.1007/s10853-006-1462-0.

[161] F. Pacheco-Torgal, S. Jalali, Influence of sodium carbonate addition on the thermal reactivity of tungsten mine waste mud based binders, Constr Build Mater 24 (2010) 56–60. https://doi.org/10.1016/j.conbuildmat.2009.08.018.

[162] F. Pacheco-Torgal, S. Jalali, Influence of sodium carbonate addition on the thermal reactivity of tungsten mine waste mud based binders, Constr Build Mater 24 (2010) 56–60. https://doi.org/10.1016/j.conbuildmat.2009.08.018.

[163] C.R. Kaze, G.L. Lecomte-Nana, E. Kamseu, P.S. Camacho, A.S. Yorkshire, J.L. Provis, M. Duttine, A. Wattiaux, U.C. Melo, Mechanical and physical properties of inorganic polymer cement made of iron-rich laterite and lateritic clay: A comparative study, Cem Concr Res 140 (2021). https://doi.org/10.1016/j.cemconres.2020.106320.

[164] A. Hajimohammadi, J.S.J. van Deventer, Dissolution behaviour of source materials for synthesis of geopolymer binders: A kinetic approach, Int J Miner Process 153 (2016) 80–86. https://doi.org/10.1016/j.minpro.2016.05.014.

[165] R. Obenaus-Emler, M. Falah, M. Illikainen, Assessment of mine tailings as precursors for alkali-activated materials for on-site applications, Constr Build Mater 246 (2020) 118470. https://doi.org/https://doi.org/10.1016/j.conbuildmat.2020.118470.

[166] H. Xu, J.S.J. Van Deventer, Geopolymerisation of multiple minerals, Miner Eng 15 (2002) 1131–1139. https://doi.org/10.1016/S0892-6875(02)00255-8.

[167] F. Pacheco-Torgal, J.P. Castro-Gomes, S. Jalali, Investigations on mix design of tungsten mine waste geopolymeric binder, Constr Build Mater 22 (2008) 1939–1949. https://doi.org/10.1016/j.conbuildmat.2007.07.015.

[168] P. Duxson, J.L. Provis, G.C. Lukey, S.W. Mallicoat, W.M. Kriven, J.S.J. Van Deventer, Understanding the relationship between geopolymer composition, microstructure and mechanical properties, Colloids Surf A Physicochem Eng Asp 269 (2005) 47–58. https://doi.org/10.1016/j.colsurfa.2005.06.060.

[169] Y.M. Liew, H. Kamarudin, A.M. Mustafa Al Bakri, M. Bnhussain, M. Luqman, I. Khairul Nizar, C.M. Ruzaidi, C.Y. Heah, Optimization of solids-to-liquid and alkali activator ratios of calcined kaolin geopolymeric powder, Constr Build Mater 37 (2012) 440–451. https://doi.org/10.1016/j.conbuildmat.2012.07.075.

[170] H. Xu, J.S.J. Van Deventer, Factors affecting the geopolymerization of alkali-feldspars, Minerals and Metallurgical Processing 19 (2002) 209–214. https://doi.org/10.1007/bf03403271.

[171] A. Fernandes, M. Magrinho, J. Castro-Gomes, Leaching of alkali-activated tungsten mining waste materials by electrical conductivity and DRX, MATEC Web of Conferences 274 (2019) 02002. https://doi.org/10.1051/matecconf/201927402002.

[172] J. Kiventerä, I. Lancellotti, M. Catauro, F.D. Poggetto, C. Leonelli, M. Illikainen, Alkali activation as new option for gold mine tailings inertization, J Clean Prod 187 (2018) 76–84. https://doi.org/10.1016/j.jclepro.2018.03.182.

[173] H. Paiva, J. Yliniemi, M. Illikainen, F. Rocha, V.M. Ferreira, Mine tailings geopolymers as awaste management solution for a more sustainable habitat, Sustainability (Switzerland) 11 (2019). https://doi.org/10.3390/su11040995.

[174] S. Moukannaa, M. Loutou, M. Benzaazoua, L. Vitola, J. Alami, R. Hakkou, Recycling of phosphate mine tailings for the production of geopolymers, J Clean Prod 185 (2018) 891–903. https://doi.org/10.1016/j.jclepro.2018.03.094.

[175] J. Kiventerä, I. Lancellotti, M. Catauro, F.D. Poggetto, C. Leonelli, M. Illikainen, Alkali activation as new option for gold mine tailings inertization, J Clean Prod 187 (2018) 76–84. https://doi.org/10.1016/j.jclepro.2018.03.182.

[176] H. Xu, J.S.J. Van Deventer, Effect of source materials on geopolymerization, Ind Eng Chem Res 42 (2003) 1698–1706. https://doi.org/10.1021/ie0206958.

[177] B. Koohestani, P. Mokhtari, E. Yilmaz, F. Mahdipour, A.K. Darban, Geopolymerization mechanism of binder-free mine tailings by sodium silicate, Constr Build Mater 268 (2021) 121217. https://doi.org/10.1016/j.conbuildmat.2020.121217.

[178] J. Kiventerä, P. Perumal, J. Yliniemi, M. Illikainen, Mine tailings as a raw material in alkali activation: A review, International Journal of Minerals, Metallurgy and Materials 27 (2020) 1009–1020. https://doi.org/10.1007/s12613-020-2129-6.

[179] A. Peys, A.P. Douvalis, V. Hallet, H. Rahier, B. Blanpain, Y. Pontikes, Inorganic Polymers From CaO-FeOx-SiO2 Slag: The Start of Oxidation of Fe and the Formation of a Mixed Valence Binder, Front Mater 6 (2019) 1–10. https://doi.org/10.3389/fmats.2019.00212.

[180] R. Obenaus-Emler, M. Falah, M. Illikainen, Assessment of mine tailings as precursors for alkali-activated materials for on-site applications, Constr Build Mater 246 (2020) 118470. https://doi.org/10.1016/j.conbuildmat.2020.118470.

[181] S.A. Bernal, E.D. Rodríguez, A.P. Kirchheim, J.L. Provis, Management and valorisation of wastes through use in producing alkali-activated cement materials, Journal of Chemical Technology and Biotechnology 91 (2016) 2365–2388. https://doi.org/10.1002/jctb.4927.

[182] N. Sedira, J. Castro-Gomes, M. Magrinho, Red clay brick and tungsten mining waste-based alkali-activated binder: Microstructural and mechanical properties, Constr Build Mater 190 (2018) 1034–1048. https://doi.org/10.1016/j.conbuildmat.2018.09.153.

[183] N. Sedira, J. Castro-Gomes, Effect of activators on hybrid alkaline binder based on tungsten mining waste and ground granulated blast furnace slag, Constr Build Mater 232 (2020) 117176. https://doi.org/10.1016/j.conbuildmat.2019.117176.

[184] P.H.R. Borges, F.C.R. Ramos, T.R. Caetano, T.H. Panzerra, H. Santos, Reuse of iron ore tailings in the production of geopolymer mortars, Revista Escola de Minas 72 (2019) 581–587. https://doi.org/10.1590/0370-44672017720169.

[185] K. doCarmoeSilvaDefáveri, L. dosSantos, R.A.F. Peixoto, G.J. Brigolini, J. FrancodeCarvalho, K. do Carmo e Silva Defáveri, L.F. dos Santos, J.M. Franco de Carvalho, R.A.F. Peixoto, G.J. Brigolini, Iron ore tailing-based geopolymer containing glass wool residue: A study of mechanical and microstructural properties, Constr Build Mater 220 (2019) 375–385. https://doi.org/10.1016/j.conbuildmat.2019.05.181.

[186] N. Sedira, J. Castro-Gomes, Effect of activators on hybrid alkaline binder based on tungsten mining waste and ground granulated blast furnace slag, Constr Build Mater 232 (2020) 117176. https://doi.org/10.1016/j.conbuildmat.2019.117176.

[187] A. Wang, H. Liu, X. Hao, Y. Wang, X. Liu, Z. Li, Geopolymer synthesis using garnet tailings from molybdenum mines, Minerals 9 (2019). https://doi.org/10.3390/min9010048.

[188] J. Zheng, Y. Zhu, Z. Zhao, Utilization of limestone powder and water-reducing admixture in cemented paste backfill of coarse copper mine tailings, Constr Build Mater 124 (2016) 31–36. https://doi.org/10.1016/j.conbuildmat.2016.07.055.

[189] C.R. Wu, Z.Q. Hong, Y.H. Yin, S.C. Kou, Mechanical activated waste magnetite tailing as pozzolanic material substitute for cement in the preparation of cement products, Constr Build Mater 252 (2020) 119129. https://doi.org/10.1016/j.conbuildmat.2020.119129.

[190] L. Caneda-Martínez, C. Medina, M.I. Sánchez de Rojas, M. Frías, Water transport in binary eco-cements containing coal mining waste, Cem Concr Compos 104 (2019) 103373. https://doi.org/10.1016/j.cemconcomp.2019.103373.

[191] S. Liu, L. Wang, Q. Li, J. Song, Hydration properties of Portland cement-copper tailing powder composite binder, Constr Build Mater 251 (2020) 118882. https://doi.org/10.1016/j.conbuildmat.2020.118882.

[192] F. Rao, Q. Liu, Geopolymerization and its potential application in mine tailings consolidation: A review, Mineral Processing and Extractive Metallurgy Review 36 (2015) 399–409. https://doi.org/10.1080/08827508.2015.1055625.

[193] J. Kiventerä, L. Golek, J. Yliniemi, V. Ferreira, J. Deja, M. Illikainen, Utilization of sulphidic tailings from gold mine as a raw material in geopolymerization, Int J Miner Process 149 (2016) 104–110. https://doi.org/10.1016/j.minpro.2016.02.012.

[194] P. Perumal, K. Piekkari, H. Sreenivasan, P. Kinnunen, M. Illikainen, One-part geopolymers from mining residues – Effect of thermal treatment on three different tailings, Miner Eng 144 (2019) 106026. https://doi.org/10.1016/j.mineng.2019.106026.

[195] C. Ince, S. Derogar, K. Gurkaya, R.J. Ball, Properties, durability and cost efficiency of cement and hydrated lime mortars reusing copper mine tailings of Lefke-Xeros in Cyprus, Constr Build Mater 268 (2021) 121070. https://doi.org/10.1016/j.conbuildmat.2020.121070.

[196] B. Malagón, G. Fernández, J.M. De Luis, R. Rodríguez, Feasibility study on the utilization of coal mining waste for Portland clinker production, Environmental Science and Pollution Research 27 (2020) 21–32. https://doi.org/10.1007/s11356-019-05150-w.

[197] K. Zheng, J. Zhou, M. Gbozee, Influences of phosphate tailings on hydration and properties of Portland cement, Constr Build Mater 98 (2015) 593–601. https://doi.org/10.1016/j.conbuildmat.2015.08.115.

[198] C.R. Wu, Z.Q. Hong, Y.H. Yin, S.C. Kou, Mechanical activated waste magnetite tailing as pozzolanic material substitute for cement in the preparation of cement products, Constr Build Mater 252 (2020) 119129. https://doi.org/10.1016/j.conbuildmat.2020.119129.

[199] S. Liu, L. Wang, Q. Li, J. Song, Hydration properties of Portland cement-copper tailing powder composite binder, Constr Build Mater 251 (2020) 118882. https://doi.org/10.1016/j.conbuildmat.2020.118882.

[200] S. Siddique, J.G. Jang, Assessment of molybdenum mine tailings as filler in cement mortar, Journal of Building Engineering 31 (2020) 101322. https://doi.org/10.1016/j.jobe.2020.101322.

[201] I. Vegas, M. Cano, I. Arribas, M. Frías, O. Rodríguez, Physical-mechanical behavior of binary cements blended with thermally activated coal mining waste, Constr Build Mater 99 (2015) 169–174. https://doi.org/10.1016/j.conbuildmat.2015.07.189.

[202] B. Malagón, G. Fernández, J.M. De Luis, R. Rodríguez, Feasibility study on the utilization of coal mining waste for Portland clinker production, Environmental Science and Pollution Research 27 (2020) 21–32. https://doi.org/10.1007/s11356-019-05150-w.

[203] X. Jiao, Y. Zhang, T. Chen, S. Bao, T. Liu, J. Huang, Geopolymerisation of a silica-rich tailing, Miner Eng 24 (2011) 1710–1712. https://doi.org/10.1016/j.mineng.2011.09.008.

[204] F. Pacheco-Torgal, J.P. Castro-Gomes, S. Jalali, Investigations on mix design of tungsten mine waste geopolymeric binder, Constr Build Mater 22 (2008) 1939–1949. https://doi.org/10.1016/j.conbuildmat.2007.07.015.

[205] D. Feng, J.L. Provis, J.S.J. Van Deventer, Thermal activation of albite for the synthesis of one-part mix geopolymers, Journal of the American Ceramic Society 95 (2012) 565–572. https://doi.org/10.1111/j.1551-2916.2011.04925.x.

[206] F. Rao, Q. Liu, Geopolymerization and its potential application in mine tailings consolidation: A review, Mineral Processing and Extractive Metallurgy Review 36 (2015) 399–409. https://doi.org/10.1080/08827508.2015.1055625.

[207] X. Jiao, Y. Zhang, T. Chen, S. Bao, T. Liu, J. Huang, Geopolymerisation of a silica-rich tailing, Miner Eng 24 (2011) 1710–1712. https://doi.org/10.1016/j.mineng.2011.09.008.

[208] R.A.M. Figueiredo, P.R.G. Brandão, M. Soutsos, A.B. Henriques, A. Fourie, D.B. Mazzinghy, Producing sodium silicate powder from iron ore tailings for use as an activator in one-part geopolymer binders, Mater Lett 288 (2021) 129333. https://doi.org/10.1016/j.matlet.2021.129333.

[209] L. Caneda-Martínez, M. Frías, C. Medina, M.I.S. de Rojas, N. Rebolledo, J. Sánchez, Evaluation of chloride transport in blended cement mortars containing coal mining waste, Constr Build Mater 190 (2018) 200–210. https://doi.org/10.1016/j.conbuildmat.2018.09.158.

[210] J. Esmaeili, H. Aslani, Use of copper mine tailing in concrete: strength characteristics and durability performance, J Mater Cycles Waste Manag 21 (2019) 729–741. https://doi.org/10.1007/s10163-019-00831-7.

[211] F. Vargas, M. Lopez, Development of a new supplementary cementitious material from the activation of copper tailings: Mechanical performance and analysis of factors, J Clean Prod 182 (2018) 427–436. https://doi.org/10.1016/j.jclepro.2018.01.223.

[212] X. Liu, N. Zhang, H. Sun, J. Zhang, L. Li, Structural investigation relating to the cementitious activity of bauxite residue - Red mud, Cem Concr Res 41 (2011) 847–853. https://doi.org/10.1016/j.cemconres.2011.04.004.

[213] S. Jian, W. Gao, Y. Lv, H. Tan, X. Li, B. Li, W. Huang, Potential utilization of copper tailings in the preparation of low heat cement clinker, Constr Build Mater 252 (2020) 119130. https://doi.org/10.1016/j.conbuildmat.2020.119130.

[214] S. Siddique, J.G. Jang, Assessment of molybdenum mine tailings as filler in cement mortar, Journal of Building Engineering 31 (2020) 101322. https://doi.org/10.1016/j.jobe.2020.101322.

[215] S. Ahmari, L. Zhang, Durability and leaching behavior of mine tailings-based geopolymer bricks, Constr Build Mater 44 (2013) 743–750. https://doi.org/10.1016/j.conbuildmat.2013.03.075.

[216] M. Falah, K. Ohenoja, R. Obenaus-Emler, P. Kinnunen, M. Illikainen, Improvement of mechanical strength of alkali-activated materials using micro low-alumina mine tailings, Constr Build Mater 248 (2020) 118659. https://doi.org/10.1016/j.conbuildmat.2020.118659.

[217] Z.R. Wang, B. Li, H.B. Liu, Y.X. Zhang, X. Qin, Degradation characteristics of graphite tailings cement mortar subjected to freeze-thaw cycles, Constr Build Mater 234 (2020) 117422. https://doi.org/10.1016/j.conbuildmat.2019.117422.

[218] L. Caneda-Martínez, J. Sánchez, C. Medina, M. Isabel Sánchez de Rojas, J. Torres, M. Frías, Reuse of coal mining waste to lengthen the service life of cementitious matrices, Cem Concr Compos 99 (2019) 72–79. https://doi.org/10.1016/j.cemconcomp.2019.03.007.

[219] EPA Guidelines, TOXICITY CHARACTERISTIC LEACHING PROCEDURE, Method 1311, 148 (n.d.) 148–162.

[220] EUROPEAN COMMISSION, Commission notice on technical guidance on the classification of waste, Official Journal of the European Union C 124 (2018) 134.

[221] J.P. Castro-Gomes, A.P. Silva, R.P. Cano, J. Durán Suarez, A. Albuquerque, Potential for reuse of tungsten mining waste-rock in technical-artistic value added products, J Clean Prod 25 (2012) 34–41. https://doi.org/10.1016/j.jclepro.2011.11.064.

[222] M. Gou, L. Zhou, N.W.Y. Then, Utilization of tailings in cement and concrete: A review, Science and Engineering of Composite Materials 26 (2019) 449–464. https://doi.org/10.1515/secm-2019-0029.

[223] J. Nouairi, W. Hajjaji, C.S. Costa, L. Senff, C. Patinha, E. Ferreira da Silva, J.A. Labrincha, F. Rocha, M. Medhioub, Study of Zn-Pb ore tailings and their potential in cement technology, Journal of African Earth Sciences 139 (2018) 165–172. https://doi.org/10.1016/j.jafrearsci.2017.11.004.

[224] Near-zero-waste recycling of low-grade sulphidic mining waste for critical-metal, mineral and construction raw-material production in a circular economy, (n.d.). https://h2020-nemo.eu/ (accessed September 15, 2021).

[225] T.E. of Encyclopaedia. Britannica, Munsell colour system, Encyclopedia Britannica (2018).

[226] S. Maruthupandian, A. Chaliasou, A. Kanellopoulos, Recycling mine tailings as precursors for cementitious binders – Methods, challenges and future outlook, Constr Build Mater 312 (2021) 125333. https://doi.org/10.1016/j.conbuildmat.2021.125333.

[227] P. Perumal, K. Piekkari, H. Sreenivasan, P. Kinnunen, M. Illikainen, One-part geopolymers from mining residues – Effect of thermal treatment on three different tailings, Miner Eng 144 (2019) 106026. https://doi.org/10.1016/j.mineng.2019.106026.

[228] S. Hollanders, Mineralogical study of the pozzolanic properties of calcined clays, (2017) 236. https://limo.libis.be/primo-explore/fulldisplay?docid=LIRIAS1727587&context=L&vid=Lirias&search_scope=Lirias&tab=default_tab&lang=en_US&fromSitemap=1.

[229] K.S.P. Karunadasa, C.H. Manoratne, H.M.T.G.A. Pitawala, R.M.G. Rajapakse, Thermal decomposition of calcium carbonate (calcite polymorph) as examined by in-situ high-temperature X-ray powder diffraction, Journal of Physics and Chemistry of Solids 134 (2019) 21–28. https://doi.org/10.1016/J.JPCS.2019.05.023.

[230] The Mohs Hardness Scale And Chart For Select Gems, (n.d.). https://www.gemsociety.org/article/select-gems-ordered-mohs-hardness/ (accessed September 4, 2023).

[231] H. Shin, S. Lee, H. Suk Jung, J.B. Kim, Effect of ball size and powder loading on the milling efficiency of a laboratory-scale wet ball mill, Ceram Int 39 (2013) 8963–8968. https://doi.org/10.1016/j.ceramint.2013.04.093.

[232] K. Scrivener, R. Snellings, B. Lothenbach, A Practical Guide to Microstructural Analysis of Cementitious Materials, 1st ed., CRC Press, Taylor and Francis Group, 2016.

[233] T. Degen, M. Sadki, E. Bron, U. König, G. Nénert;, The HighScore suite, (2014) S13–S18.

[234] T.S. Qureshi, the Role of Expansive Minerals in the Autogenous and Autonomic Self-Healing of Cement Based Materials, PhD Thesis, University of Cambridge (2016).

[235] N. V. Chukanov, Infrared spectra of mineral species: Extended library, 2014. http://link.springer.com/10.1007/978-94-007-7128-4.

[236] A. Hajimohammadi, J.L. Provis, J.S.J. Van Deventer, The effect of silica availability on the mechanism of geopolymerisation, Cem Concr Res 41 (2011) 210–216. https://doi.org/10.1016/j.cemconres.2011.02.001.

[237] S. Ramanathan, REACTIVITY OF SUPPLEMENTARY CEMENTITIOUS MATERIALS IN MODEL SYSTEMS AND CEMENTITIOUS PASTES, PhD Thesis Submitted to University of Miami (2021) 249.

[238] F. Avet, R. Snellings, A. Alujas, M. Ben, K. Scrivener, Cement and Concrete Research Development of a new rapid , relevant and reliable (R 3) test method to evaluate the pozzolanic reactivity of calcined kaolinitic clays, Cem Concr Res 85 (2016) 1–11. https://doi.org/10.1016/j.cemconres.2016.02.015.

[239] F. Avet, R. Snellings, A. Alujas Diaz, M. Ben Haha, K. Scrivener, Development of a new rapid, relevant and reliable (R3) test method to evaluate the pozzolanic reactivity of calcined kaolinitic clays, Cem Concr Res 85 (2016) 1–11. https://doi.org/10.1016/j.cemconres.2016.02.015.

[240] A. C1897-20, Standard Test Methods for Measuring the Reactivity of Supplementary Cementitious Materials by Isothermal Calorimetry and Bound Water, ASTM International, West Conshohocken, PA 04 (2020) 1–5. https://doi.org/10.1520/C1897-20.2.

[241] BS EN 196-3:2016, Methods of testing cement Determination of setting times and soundness, BS EN Standards (2016) 1–18.

[242] BS EN 12617-4:2002, Products and systems for the protection and repair of concrete structures. Test methods Determination of shrinkage and expansion, BS EN Standards (2002) 1–18.

[243] BS EN 13295:2004, Products and systems for the protection and repair of concrete structures.Test methods. Determination of resistance to carbonation, BS EN Standards (2004).

[244] Surface tests to determine transport properties of concrete – II: analytical models to calculate permeability, Transport Properties of Concrete (2021) 41–58. https://doi.org/10.1016/B978-0-12-820249-4.00004-3.

[245] A. Kanellopoulos, P. Giannaros, A. Al-Tabbaa, The effect of varying volume fraction of microcapsules on fresh, mechanical and self-healing properties of mortars, Constr Build Mater 122 (2016) 577–593. https://doi.org/10.1016/j.conbuildmat.2016.06.119.

[246] H. Liu, K. Liu, Z. Lan, D. Zhang, Mechanical and Electrical Characteristics of Graphite Tailing Concrete, Advances in Materials Science and Engineering 2018 (2018). https://doi.org/10.1155/2018/9297628.

[247] Y. Peng, Y. Liu, B. Zhan, G. Xu, Preparation of autoclaved aerated concrete by using graphite tailings as an alternative silica source, Constr Build Mater 267 (2021) 121792. https://doi.org/10.1016/j.conbuildmat.2020.121792.

[248] F.C. Chang, M.Y. Lee, S.L. Lo, J.D. Lin, Artificial aggregate made from waste stone sludge and waste silt, J Environ Manage 91 (2010) 2289–2294. https://doi.org/10.1016/j.jenvman.2010.06.011.

[249] M.A. Glinicki, K. Gibas, Influence of high-calcium fly ash on the chloride ion penetration into concrete, Non-Traditional Cement and Concrete IV (2011) 420–428.

[250] K. Gibas, M. Glinicki, G. Nowowiejski, Evaluation of impermeability of concrete containing calcareous fly ash in respect to environmental media, Roads and Bridges - Drogi i Mosty 12 (2013) 159–171. https://doi.org/10.7409/rabdim.013.012.

[251] P.T. Durdziński, Hydration of multi-component cements containing clinker, slag, type-V fly ash and limestone, 6834 (2016) 1–225.

[252] D. Zhou, Developing Supplementary Cementitious Materials From Waste London Clay, Imperial College London (2016) 236. https://spiral.imperial.ac.uk/handle/10044/1/44528.

[253] K. Komnitsas, D. Zaharaki, Geopolymerisation: A review and prospects for the minerals industry, Miner Eng 20 (2007) 1261–1277. https://doi.org/10.1016/j.mineng.2007.07.011.

[254] I.O. Faniyi, O. Fasakin, B. Olofinjana, A.S. Adekunle, T. V. Oluwasusi, M.A. Eleruja, E.O.B. Ajayi, The comparative analyses of reduced graphene oxide (RGO) prepared via green, mild and chemical approaches, SN Appl Sci 1 (2019) 1–7. https://doi.org/10.1007/s42452-019-1188-7.

[255] R. Ellerbrock, M. Stein, J. Schaller, Comparing amorphous silica, short-range-ordered silicates and silicic acid species by FTIR, Sci Rep 12 (2022). https://doi.org/10.1038/s41598-022-15882-4.

[256] M. Illikainen, P. Perumal, J. Kiventer, Influence of alkali source on properties of alkali activated silicate tailings, 271 (2021). https://doi.org/10.1016/j.matchemphys.2021.124932.

[257] Gypsum – Database of ATR-FT-IR spectra of various materials, (n.d.). https://spectra.chem.ut.ee/paint/fillers/gypsum/ (accessed April 18, 2024).

[258] X. Ren, L. Zhang, D. Ramey, B. Waterman, S. Ormsby, Utilization of aluminum sludge (AS) to enhance mine tailings-based geopolymer, J Mater Sci 50 (2015) 1370–1381. https://doi.org/10.1007/s10853-014-8697-y.

[259] S. Luo, M. Liu, L. Yang, J. Chang, W. Yang, X. Yan, H. Yu, Y. Shen, Utilization of waste from alumina industry to produce sustainable cement-based materials, Constr Build Mater 229 (2019) 116795. https://doi.org/10.1016/j.conbuildmat.2019.116795.

[260] M.M.H. Al Omari, I.S. Rashid, N.A. Qinna, A.M. Jaber, A.A. Badwan, Calcium Carbonate, 2016. https://doi.org/10.1016/bs.podrm.2015.11.003.

[261] Ö. Bozkaya, H. Yalçın, M.C. Göncüoğlu, Diagenetic and very low-grade metamorphic characteristics of the Paleozoic series of the Istanbul Terrane (NW Turkey), Swiss J Geosci 105 (2012) 183–201. https://doi.org/10.1007/s00015-012-0108-2.

[262] R. Zhao, Z.C. Tian, Z. Zhao, Effect of calcination temperature on rare earth tailing catalysts for catalytic methane combustion, Green Processing and Synthesis 9 (2020) 734–743. https://doi.org/10.1515/gps-2020-0053.

[263] K. Berent, S. Komarek, R. Lach, W. Pyda, The Effect of Calcination Temperature on the Structure and Performance of Nanocrystalline Mayenite Powders, (2019).

[264] S. Ramanathan, L.R. Pestana, P. Suraneni, Reaction kinetics of supplementary cementitious materials in reactivity tests, Cement 8 (2022) 100022. https://doi.org/10.1016/j.cement.2022.100022.

[265] P.P. Sivakumar, S. Matthys, N. De Belie, E. Gruyaert, Reactivity assessment of modified ferro silicate slag by R3 method, Applied Sciences (Switzerland) 11 (2021) 1–14. https://doi.org/10.3390/app11010366.

[266] P. Suraneni, J. Weiss, Examining the pozzolanicity of supplementary cementitious materials using isothermal calorimetry and thermogravimetric analysis, Cem Concr Compos 83 (2017) 273–278. https://doi.org/10.1016/j.cemconcomp.2017.07.009.

[267] M. Frías, O. Rodriguez, R. Vigil De La Villa, R. García, S. Martínez-Ramiréz, L.J. Fernández-Carrasco, I. Vegas, The Influence of Activated Coal Mining Wastes on the Mineralogy of Blended Cement Pastes, Journal of the American Ceramic Society 99 (2016) 300–307. https://doi.org/10.1111/jace.13840.

[268] L. Luo, Y. Zhang, S. Bao, T. Chen, Utilization of Iron Ore Tailings as Raw Material for Portland Cement Clinker Production, Advances in Materials Science and Engineering 2016 (2016). https://doi.org/10.1155/2016/1596047.

[269] L.N. Warr, IMA–CNMNC approved mineral symbols, Mineral Mag 85 (2021) 291–320. https://doi.org/10.1180/mgm.2021.43.

[270] M. Zajac, A. Rossberg, G. Le Saout, B. Lothenbach, Influence of limestone and anhydrite on the hydration of Portland cements, Cem Concr Compos 46 (2014) 99–108. https://doi.org/10.1016/j.cemconcomp.2013.11.007.

[271] S. Mabroum, A. Aboulayt, Y. Taha, M. Benzaazoua, N. Semlal, R. Hakkou, Elaboration of geopolymers based on clays by-products from phosphate mines for construction applications, J Clean Prod 261 (2020) 121317. https://doi.org/10.1016/j.jclepro.2020.121317.

[272] R. Snellings, A. Salze, K.L. Scrivener, Use of X-ray diffraction to quantify amorphous supplementary cementitious materials in anhydrous and hydrated blended cements, Cem Concr Res 64 (2014) 89–98. https://doi.org/10.1016/j.cemconres.2014.06.011.

[273] J.M. Soler, Thermodynamic Description of the Solubility of C-S-H Gels in Hydrated Portland Cement, (2007) 33.

[274] Z. Zhang, G.W. Scherer, A. Bauer, Morphology of cementitious material during early hydration, Cem Concr Res 107 (2018) 85–100. https://doi.org/10.1016/j.cemconres.2018.02.004.

[275] F. Basquiroto de Souza, E. Shamsaei, K. Sagoe-Crentsil, W. Duan, Proposed mechanism for the enhanced microstructure of graphene oxide–Portland cement composites, Journal of Building Engineering 54 (2022) 104604. https://doi.org/10.1016/j.jobe.2022.104604.

[276] M.G. Margalha, A.S. Silva, M. do Rosário Veiga, J. de Brito, R.J. Ball, G.C. Allen, Microstructural Changes of Lime Putty during Aging, Journal of Materials in Civil Engineering 25 (2013) 1524–1532. https://doi.org/10.1061/(asce)mt.1943-5533.0000687.

[277] H. Choi, H. Choi, M. Inoue, R. Sengoku, Control of the polymorphism of calcium carbonate produced by self-healing in the cracked part of cementitious materials, Applied Sciences (Switzerland) 7 (2017) 1–16. https://doi.org/10.3390/app7060546.

[278] Q. Hu, J. Zhang, H. Teng, U. Becker, Growth process and crystallographic properties of ammonia-induced vaterite, American Mineralogist 97 (2012) 1437–1445. https://doi.org/10.2138/am.2012.3983.

[279] S. Kadir, A.P. Önen-Hall, S.N. Aydin, C. Yakicier, N. Akarsu, M. Tuncer, Environmental effect and genetic influence: A regional cancer predisposition survey in the Zonguldak region of Northwest Turkey, Environmental Geology 54 (2008) 391–409. https://doi.org/10.1007/s00254-007-0826-3.

[280] Y.H. Wu, R. Huang, C.J. Tsai, W.T. Lin, Recycling of sustainable co-firing fly ashes as an alkali activator for GGBS in blended cements, Materials 8 (2015) 784–798. https://doi.org/10.3390/ma8020784.

[281] Hudson Institute of Mineralogy, Biotite, (n.d.).

[282] M. Gomes-Pimentel, M. Rubens Cardoso da Silva, D. de Cássia S. Viveiros, M.S. Picanço, Manganese mining waste as a novel supplementary material in Portland cement, Mater Lett 309 (2022) 131459. https://doi.org/10.1016/j.matlet.2021.131459.

[283] J.F. Muñoz, E. Li, R. Liu, J. Youtcheff, Effect of the SI to AL Ratio of Amorphous Nanoaluminosilicates on the Hydration Reaction of Portland Cement, Journal of Materials in Civil Engineering 30 (2018) 1–12. https://doi.org/10.1061/(asce)mt.1943-5533.0002332.

[284] Y.C. Li, X.B. Min, Y. Ke, L.Y. Chai, M.Q. Shi, C.J. Tang, Q.W. Wang, Y.J. Liang, J. Lei, D.G. Liu, Utilization of red mud and Pb/Zn smelter waste for the synthesis of a red mud-based cementitious material, J Hazard Mater 344 (2018) 343–349. https://doi.org/10.1016/j.jhazmat.2017.10.046.

[285] M. Khachani, A. El Hamidi, M. Halim, S. Arsalane, Non-isothermal kinetic and thermodynamic studies of the dehydroxylation process of synthetic calcium hydroxide Ca (OH) 2, (2014).

[286] M. Maier, N. Beuntner, K.C. Thienel, Mineralogical characterization and reactivity test of common clays suitable as supplementary cementitious material, Appl Clay Sci 202 (2021) 105990. https://doi.org/10.1016/j.clay.2021.105990.

[287] R. Zarzuela, M. Luna, L.M. Carrascosa, M.P. Yeste, I. Garcia-Lodeiro, M.T. Blanco-Varela, M.A. Cauqui, J.M. Rodríguez-Izquierdo, M.J. Mosquera, Producing C-S-H gel by reaction between silica oligomers and portlandite: A promising approach to repair cementitious materials, Cem Concr Res 130 (2020). https://doi.org/10.1016/j.cemconres.2020.106008.

[288] M. Horgnies, J.J. Chen, C. Bouillon, Overview about the use of fourier transform infrared spectroscopy to study cementitious materials, in: WIT Transactions on Engineering Sciences, WITPress, 2013: pp. 251–262. https://doi.org/10.2495/MC130221.

[289] M. Frías, R.V. De La Villa, M.S. De Rojas, C. Medina, A. Juan Valdés, Scientific aspects of kaolinite based coal mining wastes in pozzolan/ Ca(OH) 2 system, Journal of the American Ceramic Society 95 (2012) 386–391. https://doi.org/10.1111/j.1551-2916.2011.04985.x.

[290] P. Suraneni, L. Burris, C.R. Shearer, R.D. Hooton, ASTM C618 Fly Ash Specification: Comparison with Other Specifications, Shortcomings, and Solutions., ACI Mater J 118 (2021) 157–168. https://doi.org/10.14359/51725994.

[291] A. Tironi, M.A. Trezza, A.N. Scian, E.F. Irassar, Assessment of pozzolanic activity of different calcined clays, Cem Concr Compos 37 (2013) 319–327. https://doi.org/10.1016/j.cemconcomp.2013.01.002.

[292] M. Al-Jabari, Introduction to concrete chemistry, Integral Waterproofing of Concrete Structures: Advanced Protection Technologies of Concrete by Pore Blocking and Lining (2022) 1–36. https://doi.org/10.1016/B978-0-12-824354-1.00001-5.

[293] S. von Greve-Dierfeld, B. Lothenbach, A. Vollpracht, B. Wu, B. Huet, C. Andrade, C. Medina, C. Thiel, E. Gruyaert, H. Vanoutrive, I.F. Saéz del Bosque, I. Ignjatovic, J. Elsen, J.L. Provis, K. Scrivener, K.C. Thienel, K. Sideris, M. Zajac, N. Alderete, Ö. Cizer, P. Van den Heede, R.D. Hooton, S. Kamali-Bernard, S.A. Bernal, Z. Zhao, Z. Shi, N. De Belie, Understanding the carbonation of concrete with supplementary cementitious materials: a critical review by RILEM TC 281-CCC, 2020. https://doi.org/10.1617/s11527-020-01558-w.

[294] Y. Cheng, F. Huang, S. Qi, W. Li, R. Liu, G. Li, Durability of concrete incorporated with siliceous iron tailings, Constr Build Mater 242 (2020) 118147. https://doi.org/10.1016/j.conbuildmat.2020.118147.

[295] A.S. Basavaraj, R. Gettu, Life Cycle Assessment As a Tool in Sustainability Assessment of Concrete Systems: Why and How?, Indian Concrete Journal 96 (2022) 8–27.

[296] WBCSD, Getting the Numbers Right: Cement Industry Energy and CO_2 Performance, World Business Council for Sustainable Development (2011) 42. http://www.wbcsdcement.org/pdf/CSI GNR Report final_updated Nov11_LR.pdf.

[297] N. Sahoo, A. Kumar, Samsher, Review on energy conservation and emission reduction approaches for cement industry, Environ Dev 44 (2022) 100767. https://doi.org/10.1016/j.envdev.2022.100767.

[298] A.I. Okoji, A.N. Anozie, J.A. Omoleye, A.E. Taiwo, F.N. Osuolale, Energetic assessment of a precalcining rotary kiln in a cement plant using process simulator and neural networks, Alexandria Engineering Journal 61 (2022) 5097–5109. https://doi.org/10.1016/j.aej.2021.10.010.

[299] E. Deady, K.M. Goodenough, D. Currie, A. Lacinska, H. Grant, M. Patton, M. Cooper, P. Josso, R.A. Shaw, P. Everett, T. Bide, The National Grid and other Ordnance

Survey data Potential for Critical Raw Material Prospectivity in the UK, (2023). www.bgs.ac.uk.

[300] European Commission, Communication from the Commission: On the Review of the List of Critical Raw Materials for the EU and the Implementation of the Raw Materials Initiative, European Commission: Brussels, Belgium (2014) COM no. 297.

[301] Critical raw materials, (n.d.). https://single-market-economy.ec.europa.eu/sectors/raw-materials/areas-specific-interest/critical-raw-materials_en (accessed August 14, 2023).

[302] European Environment Agency., Construction and demolition waste : challenges and opportunities in a circular economy., (n.d.).

[303] M. Awais, A.A. Bhuiyan, S. Salehin, M.M. Ehsan, B. Khan, M.H. Rahman, Synthesis, heat transport mechanisms and thermophysical properties of nanofluids: A critical overview, International Journal of Thermofluids 10 (2021). https://doi.org/10.1016/j.ijft.2021.100086.

[304] Specific Heat for all the elements in the Periodic Table, (n.d.). https://periodictable.com/Properties/A/SpecificHeat.an.html (accessed August 16, 2023).

[305] J. Leitner, P. Chuchvalec, D. Sedmidubský, A. Strejc, P. Abrman, Estimation of heat capacities of solid mixed oxides, Thermochim Acta 395 (2002) 27–46. https://doi.org/10.1016/S0040-6031(02)00177-6.

[306] U. Riaz Muhammad Nawaz Shareef, I. Bibi, N. Khan Niazi, G. Murtaza, Potassium Release Kinetics from Dioctahedral and Trioctahedral Minerals under Alkaline Conditions, 2018. https://www.researchgate.net/publication/324484905.

[307] Aragonite Mineral Data, Mineralogy Database (n.d.). https://webmineral.com/data/Aragonite.shtml (accessed April 9, 2024).

[308] Biotite mineral data, Mineralogy Database (n.d.). https://webmineral.com/data/Biotite.shtml (accessed April 9, 2024).

[309] Mineralogical Society of America, American Mineralogist International Journal of Earth and Planetary Materials Research, (n.d.). http://www.minsocam.org/ammin/AM24/AM24_255. (accessed April 9, 2024).

[310] D.W. Waples, J.S. Waples, A review and evaluation of specific heat capacities of rocks, minerals, and subsurface fluids. Part 2: Fluids and porous rocks, Natural Resources Research 13 (2004) 123–130. https://doi.org/10.1023/B:NARR.0000032648.15016.49.

[311] O. Justus, V.I. Ugonabo, Optimization of Heat Consumption in a Rotary Cement Kiln, 2019. www.rsisinternational.org.

[312] D. Gauthier, European Cement Research Academy Chairman of the advisory board: Evaluation of the energy performance of cement kilns in the context of co-processing

Evaluation of the energy performance of cement kilns in the context of co-processing, n.d. www.ecra-online.org.

[313] M. Sharma, S. Bishnoi, F. Martirena, K. Scrivener, Limestone calcined clay cement and concrete: A state-of-the-art review, Cem Concr Res 149 (2021) 106564. https://doi.org/10.1016/j.cemconres.2021.106564.

[314] Perumal, Illikainen, Alkali Activation of Silicate Mine-Tailings: Response to Different Activator Sources, Proc West Mark Ed Assoc Conf 34 (2019) 10. https://doi.org/10.3390/proceedings2019034010.

[315] T. Luukkonen, Z. Abdollahnejad, J. Yliniemi, P. Kinnunen, M. Illikainen, One-part alkali-activated materials: A review, Cem Concr Res 103 (2018) 21–34. https://doi.org/10.1016/j.cemconres.2017.10.001.

[316] X.Y. Huang, W. Ni, W.H. Cui, Z.J. Wang, L.P. Zhu, Preparation of autoclaved aerated concrete using copper tailings and blast furnace slag, Constr Build Mater 27 (2012) 1–5. https://doi.org/10.1016/j.conbuildmat.2011.08.034.

[317] G. Zhang, Y. Yan, Z. Hu, B. Xiao, Investigation on preparation of pyrite tailings-based mineral admixture with photocatalytic activity, Constr Build Mater 138 (2017) 26–34. https://doi.org/10.1016/j.conbuildmat.2017.01.134.

[318] C. Li, Q. Wen, M. Hong, Z. Liang, Z. Zhuang, Y. Yu, Heavy metals leaching in bricks made from lead and zinc mine tailings with varied chemical components, Constr Build Mater 134 (2017) 443–451. https://doi.org/10.1016/j.conbuildmat.2016.12.076.

[319] H. Xu, J.S.J. Van Deventer, The geopolymerisation of alumino-silicate minerals, Int J Miner Process 59 (2000) 247–266. https://doi.org/10.1016/S0301-7516(99)00074-5.

[320] S. Moukannaa, A. Nazari, A. Bagheri, M. Loutou, J.G. Sanjayan, R. Hakkou, Alkaline fused phosphate mine tailings for geopolymer mortar synthesis: Thermal stability, mechanical and microstructural properties, J Non Cryst Solids 511 (2019) 76–85. https://doi.org/10.1016/j.jnoncrysol.2018.12.031.

[321] C. Yang, C. Cui, J. Qin, X. Cui, Characteristics of the fired bricks with low-silicon iron tailings, Constr Build Mater 70 (2014) 36–42. https://doi.org/10.1016/j.conbuildmat.2014.07.075.

[322] T. Luukkonen, Z. Abdollahnejad, J. Yliniemi, P. Kinnunen, M. Illikainen, One-part alkali-activated materials: A review, Cem Concr Res 103 (2018) 21–34. https://doi.org/10.1016/j.cemconres.2017.10.001.

[323] G. Yao, Z. Wang, J. Yao, X. Cong, C. Anning, X. Lyu, Pozzolanic activity and hydration properties of feldspar after mechanical activation, Powder Technol 383 (2021) 167–174. https://doi.org/10.1016/j.powtec.2021.01.042.

[324] P. Krivenko, O. Kovalchuk, A. Pasko, T. Croymans, M. Hult, G. Lutter, N. Vandevenne, S. Schreurs, W. Schroeyers, Development of alkali activated cements

and concrete mixture design with high volumes of red mud, Constr Build Mater 151 (2017) 819–826. https://doi.org/10.1016/j.conbuildmat.2017.06.031.

[325] R. Fernandez, F. Martirena, K.L. Scrivener, The origin of the pozzolanic activity of calcined clay minerals: A comparison between kaolinite, illite and montmorillonite, Cem Concr Res 41 (2011) 113–122. https://doi.org/10.1016/j.cemconres.2010.09.013.

[326] A. McIntosh, S.E.M. Lawther, J. Kwasny, M.N. Soutsos, D. Cleland, S. Nanukuttan, Selection and characterisation of geological materials for use as geopolymer precursors, Advances in Applied Ceramics 114 (2015) 378–385. https://doi.org/10.1179/1743676115Y.0000000055.

[327] K. Komnitsas, D. Zaharaki, Geopolymerisation: A review and prospects for the minerals industry, Miner Eng 20 (2007) 1261–1277. https://doi.org/10.1016/j.mineng.2007.07.011.

[328] Y. Chen, Y. Zhang, T. Chen, T. Liu, J. Huang, Preparation and characterization of red porcelain tiles with hematite tailings, Constr Build Mater 38 (2013) 1083–1088. https://doi.org/10.1016/j.conbuildmat.2012.06.056.

[329] H. Lindgreen, M. Geiker, H. Krøyer, N. Springer, J. Skibsted, Microstructure engineering of Portland cement pastes and mortars through addition of ultrafine layer silicates, Cem Concr Compos 30 (2008) 686–699. https://doi.org/10.1016/j.cemconcomp.2008.05.003.

[330] S.H. Hartikainen, H. Helinä Hartikainen, Phosphorus retention by phlogopite-rich mine tailings, Applied Geochemistry 23 (2008) 2716–2723. https://doi.org/10.1016/j.apgeochem.2008.06.004.

[331] H. Sreenivasan, P. Kinnunen, E.P. Heikkinen, M. Illikainen, Thermally treated phlogopite as magnesium-rich precursor for alkali activation purpose, Miner Eng 113 (2017) 47–54. https://doi.org/10.1016/j.mineng.2017.08.003.

[332] M.G. Sephton, J.A. Webb, S. McKnight, Applications of Portland cement blended with fly ash and acid mine drainage treatment sludge to control acid mine drainage generation from waste rocks, Applied Geochemistry 103 (2019) 1–14. https://doi.org/10.1016/j.apgeochem.2019.02.005.

[333] A. Hajimohammadi, J.S.J. van Deventer, Dissolution behaviour of source materials for synthesis of geopolymer binders: A kinetic approach, Int J Miner Process 153 (2016) 80–86. https://doi.org/10.1016/j.minpro.2016.05.014.

APPENDIX A1

Table A.1: Reactivity and activation of minerals present in mineral waste

Mineral/ Mineral group reported	Reactivity/ Property in raw form	Activation possibility	Literature
Albite	A crystalline alumina silicate mineral with formula $NaAlSi_3O_8$. Slow reactive and stable up to 1000 ^oC under normal conditions	Albite was completely amorphized when calcined at 1000 ^oC or 1150°C in presence of 50% NaOH or Na_2CO_3 respectively. Albite was observed to be stable at temperatures below 1000°C	[205,314]
Amphibole	Inosilicate minerals of double chain SiO_4 tetrahedra with a better dissolubility as compared to Quartz	The amphibole phases decreased significantly when mixed with blast furnace slag, cement clinker and finely ground to a powder and mixed with warm water and cured at a temperature of 48±1 ^oC. Also, shall be used as a precursor for geopolymer.	[93,315,316]
Anatase	Anatase is a mineral form of TiO_2 and is crystalline. Anatase is less stable as compared to Rutile.	TiO_2 shall be immobilised in presence of phyllosilicates such as kaolinites. Admixtures prepared with anatase, alkali and phyllosilicates by calcination at 800 ^oC were found to improve compressive strength.by about 37%	[317]
Ankerite	Ankerite is $Ca(Fe, Mg, Mn)(CO_3)_2$, and has properties similar to dolomite	Being a carbonate mineral ankerite is prone to decomposition at a temperature range of 650 ^oC to 850 ^oC	[40]
Anorthite	Anorthite ($(Ca,Na)(Si,Al)_4O_8$) is a member of plagioclase feldspar member series	Quartz, calcite, and chlorite decompose to form anorthite at a firing temperature of about 1100 ^oC and contribute to the strength bricks and	[76,154,170,318]

		ceramics. However, Anorthite partially melts to liquid phase at 1200 °C. In presence of NaOH/ KOH dissolution of Si and Al in Anorthite happens to form reactive components	
Apatite	Apatite is a group of phosphate mineral including hydroxyapatite ($Ca_5(PO_4)_3(OH)$), fluorapatite ($Ca_5(PO_4)_3F_2$) and chlorapatite ($Ca_5(PO_4)_3Cl_2$)	Apatite indicated no/ lesser solubility in presence of alkali. However, shall be used in heavy metal encapsulation in ceramics. In a basic environment at a temperature of about 550 °C the phosphates from apatite and Al react leading to decrease in apatite peaks.	[93,197]
Arsenopyrite	Arsenopyrite (FeAsS) is a hard Iron Arsenic Sulphide crystal. þ	When arsenopyrite was heated to 550 °C using microwaves Pyrite was formed. Arsenopyrite reacts with alkali and leaches As.	[102,193]
Augite	Augite is a chain silicate mineral with a stoichiometric formula $(Ca, Mg, Fe)_2(Si, Al)_2O_6$	Augite reacted when mixed with blast furnace slag, cement clinker and finely ground to a powder and mixed with warm water and cured at a temperature of 48±1 °C.	[316,319]
Barite	Barite is a Barium sulphate mineral of formula $BaSO_4$	When used in mortar without treatment remained unaltered even till 180 days	[84]
Biotite	Biotite is a phyllosilicate mineral within the mica group of formula $K(Mg,Fe)_3AlSi_3O_{10}(F,OH)_2$ for the ith member	Biotite underwent partial decomposition in presence of sodium silicate	[320]
Caldecahydrite	$CaAl_2O_4$ $10H_2O$	It can be used in combination with other silicate minerals or other source of silica shall be considered for the use in binders	[173]

Calcite	Calcite is calcium carbonate mineral of formula $CaCO_3$	The decomposition occurs completely at about 800 °C under calcination and at about 550 °C under alkali fusion.	[267,320]
Chlorite	Chlorite is a group of phyllosilicate minerals and shall contribute to pozzolanic properties in raw form	Reactivity shall be improved by calcination	[79]
Clinochlore	Clinochlore is a member of chlorite group of minerals with the formula $(Mg,Fe)_6(Si,Al)_4O_{10}(OH)_8$	Structural decomposition of Clinochlore occurs at about 505 °C of calcination.	[155,321]
Colemanite	Colemanite is a borate mineral of formula $Ca_2B_6O_{11}.5H_2O$	Colemanite decomposed forming CaO upon calcination up to 600 °C	[95]
Corundum	Corundum is an Al_2O_3 mineral phase with better stability and crystallinity	Corundum disappeared on sintering above 1100 °C indicating decomposition and fusing to form other minerals depending on the elements present in the matrix	[156]
Diaspore	Diaspore is an aluminium hydroxide mineral AlO(OH)	Diaspore turns to Corundum when calcined at a temperature of 800 °C for 1 h The specific temperature of decomposition was at 510 °C – 540 °C.	[94]. [61]
Diopside	Diopside is a pyroxene mineral of formula, $CaMgSi_2O_6$	Alkaline roasting of diopside in presence of NaOH at 450 °C led to its decomposition.	[123]
Dolomite	Dolomite has a general formula of $MgCO_3{\cdot}CaCO_3$.	Can play a role as an activator of pozzolans and shall also be used as a replacement of limestone. The peaks of dolomite, decreased significantly when mixed with blast furnace slag, cement clinker, and finely ground to a powder and mixed with warm water and cured at a temperature of 48±1 C.	[79,316,320]

		The decomposition of dolomite by dehydration and decarbonation processes complete at 850 °C of calcination.	
Feldspar	Feldspars are group of silicate minerals with calcium, aluminium, and potassium in it.	Completely dissolves in presence of a 10 M NaOH and shall be used as a precursor for alkali activated materials. Also decomposes while clinkering at a temperature of 1450 ^{o}C Grinding up to 200 minutes increased the pozzolanic activity index of feldspar from 61% to 84%.	[157,322,323]
Fluorite	Fluorite or fluorspar is a calcium fluorite mineral CaF_2	When used in mortar without treatment remained unaltered even till 180 days	[84]
Garnet	Garnet is a group of aluminium silicate minerals. It has high hardness, structural and chemical stability, and low cementitious property. It is also reported to have solidified chromium in it. It	Garnet minerals exhibited low dissolution in presence of alkali such as KOH and NaOH. However, garnet exhibited excellent geopolymerisation in presence of 20% metakaolin and 30% sodium silicate	[103,187,319]
Gypsum	Calcium sulphate mineral reacts with water and leads to expansion., $CaSO_4$. $2H_2O$	Percentage shall be limited to 3.5 – 4% in the cement. Gypsum also reacts with alkalis and participates in geopolymerisation	[79,193]
Hematite	Hematite is an Iron mineral of formula Fe_2O_3 and is abundant on the earth's crust.	Hematite in an alkaline medium produced by sodium metasilicate and in presence of other minerals reacted to form kinoferrosilite. Hematite also exhibited a thermal stability up to a temperature of 950 ^{o}C.	[158,159,324]

		At temperatures greater than 1000 ^{o}C Hematite decomposed to produce magnetite and oxygen.	
Hydroboracite	Hydroboracite is a hydrated borate mineral of formula, $CaMg(B_3O_4((OH)_3)_2.3(H_2O)$	Hydroboracite decomposed at 600 ^{o}C of calcination	[95]
Illite	Illite is a type of phyllosilicate clay mineral	At 10% of NaOH, Illite was dissolved at a temperature of 550 °C and Na-rich sodium aluminium silicate was formed. The dehydroxylation of illite generally occurs between 600 °C and 800 °C but the presence of alkali elements enhances the release of H_2O by hydrolysis and then the completion of the dehydroxylation process, however this hydroxylation has smaller effect on crystallinity.	[320,325]
Kaolinite	$Al_2Si_2O_5(OH)_4$ or kaolinite is an alumina silicate crystalline mineral with Si/Al ratio equal to one. It in natural form shall act as an inert filler for supply of Al^{3+} ions	Turns to amorphous metakaolinite phases on calcination 750°C. This is one of the most important minerals used in geopolymerisation, A study considered geopolymerisation of sixteen different minerals mixed with kaolin. All sixteen mixes indicated higher strength in case of kaolinite addition, due to increased dissolution of alumina in the matrix. However, kaolinite on calcination at 950°C recrystallizes and reduces the reactivity	[227,253,319,326]
Magnetite	Magnetite is an iron mineral with chemical formula, Fe_3O_4	Magnetite exhibited lesser dissolution and reactivity in presence of alkali and phases were	[327]

		unaltered even after 28 days.	
Mica	Mica is a group of phyllosilicate mineral.	It shall contribute to pozzolanic properties. The behaviour shall be improved by calcination till dehydroxylation	[79]
Montmorillonite	A soft phyllosilicate clay mineral system. On contact with water montmorillonite can swell many times its original volume	600-800 ^{o}C of calcination exhibited decrease in surface area and increased consumption of $Ca(OH)_2$. However calcined montmorillonite does not have much influence on the microstructure. However, montmorillonite on grinding to a nano size becomes amorphous and improves microstructure and reduces permeability of concrete	[160,325]
Mullite	Mullite is an alumina silicate mineral of formula $Al_6Si_2O_{13}$	Mullite when formed in bricks and ceramics as a product of firing up to 1200 ^{o}C contributed to mechanical properties. However, in raw materials Mullite phases were found to be inert in presence of alkali.	[70,328]
Muscovite	Phyllosilicate mineral of aluminium and potassium of formula $KAl_3SiO_{10}(OH)_2$	80 minutes of grinding reduces the crystallinity of muscovite by 37%. However, muscovite is identified to be mostly inert in case of alkali activation	[70,136]
Orthoclase	Orthoclase is a Feldspar mineral with formula $KAlSi_3O_8$	Orthoclase is capable of dissolution in alkali environment and hence geopolymerisation	[170]
Palygorskite	Magnesium aluminium phyllosilicate clay mineral with water absorption capacity about 300% or more	Addition to cement leads to formation of interconnected fine pores.	[329]

Pentlandite	Pentlandite is a sulphide mineral of formula $(Fe,Ni)_9S_8$	Pentlandite on oxidation leads to acid mine drainage	[25]
Phlogopite	Phlogopite is an end member of the biotite series of mica group $(KMg_3AlSi_3O_{10}(OH)_2$	The peaks phlogopite, decreased significantly when mixed with blast furnace slag, cement clinker and finely ground to a powder and mixed with warm water and cured at a temperature of 48±1ºC. Melting, quenching and grinding of phlogopite improved alkali activity by 40%. Calcination of phlogopite up to 1200°C improved the reactivity and at 1600°C was completely amorphous.	[93,316,330,331]
Pyrite	Iron sulphide mineral (FeS_2) in presence of water and oxidation leads to acid mine drainage	On hydration in presence of OPC pyrites produce ettringite and in presence of alkalis pyrites undergo alkali oxidation	[84,193]
Pyrrhotite	Iron sulphide mineral of formula $Fe_{1-x}S$,	Leads to acid mine drainage on oxidation and is more reactive than pyrite	[193,332]
Quartz	Inert silicate mineral, SiO_2	Mine tailings with high amount of quartz has been used as aggregates	[178]
Rutile	TiO_2. More inert compared to anatase. Contributes to photocatalytic effect		[317]
Sanidine	K- Feldspar $K(AlSi_3O_8)$	Sanidine acted as a source of AL in alkali environment, however complete dissolution did not take place.	[108,120]
Siderite	Crystalline Iron carbonate mineral	Transformed to magnetite on calcination	[165,221]
Smithsonite	$ZnCO_3$	Calcination leads to decarboxylation	[58]
Talc	Talc is a phyllosilicate mineral	Milling more than 30 minutes led to reaggregation of particles.	[333]